

42413691

MONASH UNIVERSITY
THESIS ACCEPTED IN SATISFACTION OF THE
REQUIREMENTS FOR THE DEGREE OF
DOCTOR OF PHILOSOPHY

ON..... 21 September 2004.....

.....

Sec. Research Graduate School Committee

Under the Copyright Act 1968, this thesis must be used only under the normal conditions of scholarly fair dealing for the purposes of research, criticism or review. In particular no results or conclusions should be extracted from it, nor should it be copied or closely paraphrased in whole or in part without the written consent of the author. Proper written acknowledgement should be made for any assistance obtained from this thesis.

**A THEORETICAL AND
EXPERIMENTAL STUDY OF A RAPID
PRESSURE SWING ADSORPTION
SYSTEM FOR AIR SEPARATION**

Richard Shannon Todd

Bachelor of Engineering (Chemical) (Honours), Monash University

**A thesis submitted in partial fulfillment of the requirements for the degree of
Doctor of Philosophy**



**Department of Chemical Engineering
Monash University**

October 2003

TABLE OF CONTENTS

Declaration vii

Acknowledgements ix

Abstract..... xi

Nomenclature..... xiii

List of Tables..... xix

List of Figures..... xxi

List of Publications..... xxvii

Chapter 1: Introduction..... 1

 1.1 Qualitative Discussion on Rapid Pressure Swing Adsorption 1

 1.1.1 Rapid Swing versus Rapid Cycle PSA 2

 1.1.2 Why RPSA over Conventional PSA? 5

 1.1.3 RPSA Process Application - Oxygen Enrichment from Air..... 6

 1.2 A Discussion on the Fundamental Transport Mechanisms 9

 1.2.1 Transport at the Interpellet Level..... 9

 1.2.2 Transport between the Interpellet and Intrapellet Regions 14

 1.2.3 Transport at the Intrapellet Level..... 14

 1.3 Temperature Transients - Is Non-Isothermal Behaviour Important? 16

 1.4 Why is such a Detailed Analysis of an RPSA Cycle Important? 17

 1.5 Objectives of this Study 18

Chapter 2: Mass Transfer at the Intrapellet Level 21

 2.1 Previous Studies on Intrapellet Mass Transfer and Adsorption 22

 2.1.1 Fick plus Equimolar Counterdiffusion Mass Transfer Model 22

 2.1.2 Maxwell-Stefan Mass Transfer Model 25

 2.2 Conservation and Flux Equations for the Pellet Model 27

 2.2.1 Isobaric Diffusion Transport Mechanism 30

| | |
|--|----|
| 2.2.2 Viscous Flow Transport Mechanism..... | 33 |
| 2.2.3 Surface Diffusion Transport Mechanism..... | 34 |
| 2.2.4 Limiting Forms of the Flux Equations..... | 35 |
| 2.2.5 Numerical Solution of the Discretised Pellet Model..... | 39 |
| 2.3 LDF Approximation to the Conservation Equations..... | 39 |
| 2.3.1 Isothermal LDFP and LDFS Models..... | 40 |
| 2.3.2 Non-Isothermal LDFP Model..... | 42 |
| 2.4 An Overview of the Mass Transfer Models Investigated..... | 43 |
| 2.5 Validation of SimPell using a Known Analytical Solution..... | 44 |
| 2.6 Cyclic Boundary Conditions: Isothermal Behaviour..... | 47 |
| 2.6.1 Square-Wave Boundary Conditions..... | 50 |
| 2.6.2 RPSA Boundary Conditions..... | 55 |
| 2.7 Cyclic Boundary Conditions: Non-Isothermal Behaviour..... | 60 |
| 2.7.1 Square-Wave Boundary Conditions..... | 61 |
| 2.7.2 RPSA Boundary Conditions..... | 63 |
| 2.8 Concluding Remarks..... | 66 |
| Chapter 3: Combined Intra-Interpellet Model for an Adsorption Process..... | 69 |
| 3.1 Previous Models for RPSA Process Simulation..... | 70 |
| 3.1.1 Instantaneous Local Equilibrium (ILE) Model..... | 70 |
| 3.1.2 Linear Driving Force (LDF) Mass Transfer Model..... | 71 |
| 3.1.3 Coupling the Intra- and Interpellet Equations..... | 72 |
| 3.1.4 Acceleration Techniques for Cyclic Adsorption Simulation..... | 73 |
| 3.2 Overview of the Adsorption Process Simulator..... | 76 |
| 3.2.1 The Impact of Numerical Dispersion on Adsorption Simulation..... | 77 |
| 3.2.2 Non-Isothermal Conservation Equations with the DPM..... | 78 |
| 3.2.3 Non-Isothermal Conservation Equations with the LDFP Model..... | 80 |
| 3.2.4 Conservation of Momentum at the Interpellet Level..... | 81 |
| 3.2.5 Conservation of Energy for the Column Wall..... | 82 |
| 3.2.6 Void Volume and Product Tank Models..... | 82 |
| 3.2.7 Numerical Solution of the Governing Conservation Equations..... | 84 |
| 3.3 Novel CPU Optimisation Techniques Introduced into NDGNAS..... | 87 |
| 3.3.1 Mass-transfer Model Switch (MMS)..... | 87 |
| 3.3.2 Use of an Improved ODE Integrator - BzzOde..... | 89 |
| 3.4 CPU Comparisons using Analytical Test Cases..... | 91 |
| 3.4.1 Three Component Similarity Solution..... | 92 |
| 3.4.2 Rosen Solution..... | 95 |

| | |
|---|-----|
| 3.5 CPU Improvements with the MMS and BzzOde for an RPSA Cycle..... | 97 |
| 3.5.1 Isothermal Simulation - RPSA Cases 1, 2 and 3..... | 99 |
| 3.5.2 Non-Isothermal Simulation - RPSA Cases 4, 5 and 6..... | 103 |
| 3.6 Concluding Remarks..... | 106 |
| 3.6.1 Note Regarding Incompatibility of BzzOde on Unix Workstation..... | 107 |
| Chapter 4: Experimental Determination of the Intrapellet Transport Coefficients..... | 109 |
| 4.1 Sorbent of Experimental Interest: Zeochem LiLSX..... | 109 |
| 4.1.1 Equilibrium Isotherm for Zeochem LiLSX..... | 110 |
| 4.1.2 Physical Properties for Zeochem LiLSX..... | 112 |
| 4.2 Previous Studies on Transport through a Porous Medium..... | 115 |
| 4.2.1 Non-Adsorbing Methods Proposed in the Literature..... | 115 |
| 4.2.2 Methods that Include Adsorption and Diffusion..... | 118 |
| 4.2.3 Mathematical Description of the Transport Coefficient..... | 128 |
| 4.2.4 Motivation Behind Methods used to Find VF+DGM Coefficients..... | 131 |
| 4.3 Knudsen Diffusion and Viscous Flow Transport Coefficients..... | 132 |
| 4.3.1 Modelling Required to Estimate Transport Coefficients..... | 132 |
| 4.3.2 Experimental Mass-transfer Unit (EMU)..... | 135 |
| 4.3.3 Calibrating Numerical Flow and Heat Transfer Coefficients..... | 137 |
| 4.3.4 Temperature Profiles in the Sample Volume..... | 145 |
| 4.3.5 Comparing EMU and NDGNAS Results to Find C_K and C_V | 151 |
| 4.3.6 Impact of Non-Isothermal Behaviour with Sorbent Pellets..... | 157 |
| 4.4 Molecular Diffusion Transport Coefficient..... | 164 |
| 4.4.1 Model Options Activated within NDGNAS to Ascertain C_m | 164 |
| 4.4.2 LUB Apparatus for Binary Chromatographic Experiments..... | 166 |
| 4.4.3 Fitting C_m to Breakthrough Run 3..... | 173 |
| 4.4.4 Sensitivity Analysis of Breakthrough Run 3..... | 180 |
| 4.4.5 LUB and NDGNAS Results from Remaining Breakthrough Runs..... | 183 |
| 4.4.6 Verifying Intrapellet Mass Transfer as the Limiting Resistance..... | 187 |
| 4.5 Concluding Remarks..... | 189 |
| Chapter 5: Experimental Determination of the Interpellet Coefficients for Pressure Drop..... | 191 |
| Part I. Momentum Equation under Non-Adsorbing Conditions..... | 192 |
| 5.1 Derivation of the Steady State and Full Momentum Balance..... | 194 |
| 5.1.1 Solution of the Equations for a Single Component System..... | 196 |
| 5.2 Steady State Pressure Drop Coefficients κ_{viscous} and κ_{kinetic} | 198 |
| 5.2.1 Using the LUB Apparatus for Steady State Experiments..... | 198 |

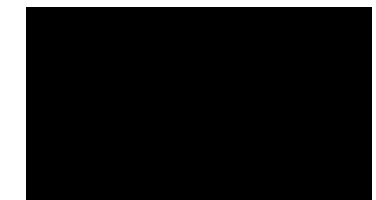
| | |
|--|-----|
| 5.2.2 Experimental Estimates of κ_{viscous} and κ_{kinetic} for Zeochem LiLSX..... | 198 |
| 5.3 Pressure Drop During Co-Current Depressurisation..... | 199 |
| 5.3.1 Using the LUB Apparatus for Depressurisation Experiments..... | 200 |
| 5.3.2 Comparison of Experimental and Numerical Pressure Profiles | 202 |
| 5.3.3 Validating the Isothermal Assumption | 206 |
| Part II. Momentum Equation for an Adsorbing Bed of Porous Pellets | 209 |
| 5.4 Previous Studies that Consider Pressure Drop and Adsorption..... | 209 |
| 5.4.1 Adsorption Models that Incorporate Darcy's Law | 209 |
| 5.4.2 Adsorption Models that Incorporate the Ergun Equation..... | 210 |
| 5.5 Pressure Drop During Co-Current Depressurisation..... | 213 |
| 5.6 Pressure Drop During Breakthrough Runs | 218 |
| 5.6.1 The Issue of Temperature Measurement in the LUB Apparatus | 220 |
| 5.7 Concluding Remarks..... | 223 |
| Chapter 6: Comparing Mathematical Predictions Against Pilot Plant Data..... | 225 |
| 6.1 Previous Studies that have Investigated RPSA | 225 |
| 6.2 Description of the RPSA Pilot Plant | 232 |
| 6.2.1 One-Bed as Opposed to Two-Bed Operation | 232 |
| 6.2.2 Solenoid and Modulating Valves..... | 232 |
| 6.2.3 Adsorption Column Design..... | 233 |
| 6.2.4 In-Line Process Equipment to Measure Operating Conditions | 234 |
| 6.2.5 PLC Control and Remote Data Acquisition | 236 |
| 6.3 One-Bed, Four Step Cycle of Experimental Interest..... | 236 |
| 6.3.1 Target Values for End of Step Pressures and Product Purity | 238 |
| 6.3.2 Cycle Times Investigated | 240 |
| 6.3.3 Defining Parameters of Experimental Interest..... | 241 |
| 6.4 Simulating the RPSA Pilot Plant with NDGNAS..... | 242 |
| 6.4.1 Experimentally Fitting Product Tank Response | 243 |
| 6.4.2 Defining CSS from Experimental and Numerical Data..... | 244 |
| 6.4.3 An Appropriate Level of Axial and Radial Discretisation?..... | 246 |
| 6.4.4 Implementing Numerical Control Loops..... | 248 |
| 6.5 Introducing the Simplified RPSA Analysis | 249 |
| 6.6 Results - RPSA Pilot Plant versus NDGNAS Data | 251 |
| 6.6.1 Experimental Results Obtained from a Repeat of RPSA Run 2..... | 261 |
| 6.6.2 Maintaining CSS at the Shortest Cycle Time - RPSA Run 18..... | 262 |
| 6.7 Discussion - Mathematical Predictions versus Experimental Data..... | 264 |
| 6.7.1 Quantifying Mismatch between Simulated and Experimental Results..... | 264 |

| | |
|---|-----|
| 6.7.2 Comparing Overall Process Performance at CSS..... | 267 |
| 6.7.3 Comparing Pressure Profiles at CSS | 281 |
| 6.7.4 Comparing Temperature Profiles at CSS..... | 285 |
| 6.7.5 Adiabatic versus Non-Isothermal Assumption | 292 |
| 6.7.6 Comparing Temperature Profiles from Teague & Edgar (1999)..... | 294 |
| 6.8 Concluding Remarks..... | 296 |
| 6.8.1 Effective Diffusion Coefficients from the RPSA Pilot Plant..... | 298 |
| Chapter 7: Conclusions, Recommendations and Future Work..... | 299 |
| 7.1 Conclusions..... | 299 |
| 7.2 Recommendations and Future Work..... | 301 |
| Appendix A: Derivation of SimPell | 303 |
| A.1 Differential Form of the Conservation Equations | 303 |
| A.1.1 Isothermal Conditions..... | 303 |
| A.1.2 Non-Isothermal Conditions..... | 304 |
| A.2 Numerical Solution of the Discretised Pellet Model..... | 306 |
| A.2.1 Isothermal Conditions..... | 308 |
| A.2.2 Non-Isothermal Conditions..... | 308 |
| A.2.3 Finding Intrapellet Molar Flux at each Finite Volume Boundary..... | 309 |
| A.3 Derivation of the Linear Driving Force Model | 311 |
| A.3.1 Isothermal Conditions..... | 311 |
| A.3.2 Non-Isothermal Conditions..... | 313 |
| A.4 Definition of Cyclic Steady State Applied within SimPell | 314 |
| Appendix B: Derivation of NDGNAS..... | 317 |
| B.1 Isothermal Conditions | 318 |
| B.1.1 Conservation Equation with the DPM | 318 |
| B.1.2 Conservation Equation with the LDFP Model..... | 318 |
| B.2 Non-Isothermal Conditions | 319 |
| B.2.1 Intra- and Interpellet Temperatures Differ: $T_B \neq T_P$ | 319 |
| B.2.2 Intra- and Interpellet Temperatures are Equivalent: $T_B = T_P = T$ | 320 |
| B.3 Numerical Solution of the Conservation Equations | 321 |
| B.3.1 Isothermal Conditions | 323 |
| B.3.2 Non-Isothermal Conditions and $T_B \neq T_P$ | 323 |
| B.3.3 Non-Isothermal Conditions and $T_B = T_P = T$ | 324 |

| | |
|--|-----|
| B.3.4 Additional Model Options Established within NDGNAS | 326 |
| B.4 Definition of Cyclic Steady State Applied within NDGNAS | 326 |
| Appendix C: Simplified RPSA Analysis..... | 329 |
| C.1 Mass Balance Over One Cycle..... | 329 |
| C.2 Introducing Non-Isothermal Behaviour - Simple Energy Balance | 333 |
| C.2.1 Proposed Solution Strategy..... | 335 |
| Appendix D: Details on Each Experimental Apparatus | 337 |
| D.1 Experimental Mass-transfer Unit (EMU)..... | 337 |
| D.2 Length of Unused Bed (LUB) Apparatus | 340 |
| D.3 RPSA Pilot Plant..... | 344 |
| List of References..... | 351 |

DECLARATION

This thesis contains no material that has been accepted for the award of any other degree or diploma in any university or other institution. To the best knowledge of the author, this thesis contains no material previously published or written by another person except where due reference is made in the text.



Richard S. Todd

Department of Chemical Engineering

Monash University

October 2003

ACKNOWLEDGEMENTS

There are a number of people I would like to acknowledge for their contributions over the course of my Ph.D. candidature. Technical staff within the Department of Chemical Engineering at Monash University provided valuable assistance with the experimental and computational aspects of this project: John Barnard, Paul Beardsley, Ross Ellingham, Peter Froud, Gamini Ganegoda, Ron Graham and Roy Harrip. Many thanks also go to the administrative staff of the Chemical Engineering Department at Monash University: Yvonne Arnold, Chris Goodwin, Stelios Konstantinidis, Judy Lawlor and Irene Murray. The efforts of Ralph Day and Bill Sinclair (IWI Cryoquip) with the design and construction of the RPSA pilot plant is greatly appreciated.

The contribution of Dr. Guido Buzzi Ferraris and Dr. Davide Manca (Polytechnic of Milan, Italy) with BzzOde and the associated discussion is very much appreciated, as well as Dr. John Andrews (Department of Chemical Engineering, Monash University) in relation to the multicomponent similarity solution. Thanks also go to my fellow colleagues Dr. Chris Beh, Dr. Jianming He, Graeme Short and Dr. Simon Wilson for their insightful discussions regarding adsorption and the like. I would especially like to thank my supervisor Dr. Paul Webley for providing the knowledge, expertise and inspiration required to complete this project and to our industrial sponsor, Air Products and Chemicals Inc., for providing financial support with the construction of all three experimental units: the EMU, LUB apparatus and RPSA pilot plant.

Finally, a very special thank you goes to my family and friends: Richard, Pauline, Robert, James, Timothy & Christian Todd and Cathy Reynolds for their support, and to all the progressive/death metal bands out there whose music inspired me through countless hours of writing, programming and data analysis.

ABSTRACT

The separation of a multicomponent gas stream using the phenomenon of adsorption provides an efficient unit operation for the chemical and allied industries. In recent years the development of novel sorbent materials and process cycles has led to more economical systems. One particular cycle that is of academic and industrial interest is Rapid Pressure Swing Adsorption (RPSA). A survey of the journal and patent literature reveals oxygen enrichment from air is the primary application for RPSA and hence forms the process of experimental and theoretical interest throughout this dissertation. It is commonly assumed that macropore diffusion control limits intrapellet mass transfer with the air-zeolite system for oxygen enrichment and this has been imposed on all single pellet and full bed simulations. While an RPSA cycle can improve oxygen productivity in relation to a traditional PSA cycle, the mechanisms that dictate heat and mass transport are complicated making mathematical modelling difficult. To accurately assess process performance at the RPSA limit requires a detailed mathematical and/or experimental program to be devised. As experimental studies are costly and time consuming, significant advantages can be gained from the development and verification of a detailed mathematical model that is applicable at the RPSA limit. It is the intention of this study to investigate various aspects of process modelling at the RPSA limit and to quantify physical parameters that define this model.

Throughout the adsorption literature the Linear Driving Force (LDF) model has been commonly used to describe intrapellet mass transfer at the RPSA limit while the isothermal assumption varies from study to study. Single pellet studies indicate the LDF model underestimates working capacity over a sorbent pellet by as much as 50% when compared to the Viscous Flow plus Dusty Gas Model (VF+DGM) approach at dimensionless times $\theta_i (= D_i^e t / R_p^2)$ below the commonly imposed RPSA limit of 0.1. Relative errors between the various mechanisms of intrapellet mass transfer imposed on a single sorbent pellet were also found to be independent of the isothermal versus non-isothermal assumption.

Combining a Discretised Pellet Model (DPM) using the VF+DGM intrapellet flux equation into a full process simulator for an adsorption cycle imposes significant computational overheads when non-isothermal behavior arises. For this reason two CPU optimisation schemes have been investigated to reduce the burden of simulating an RPSA cycle to CSS. The first technique exploits computational improvements when handling Newton matrix factorisation through a refinement of the Jacobian matrix algorithm of the ODE integrator BzzOde [Buzzi Ferraris & Manca (1998)].

while the second technique uses a Mass-transfer Model Switch (MMS) that extrapolates CSS profiles from the LDF model to initial conditions for the computationally intensive DPM. Both techniques reduced the CPU time required to achieve CSS without altering CSS results in their absence.

Having developed a full process simulator for an adsorption cycle that uses a VF+DGM approach to intrapellet mass transfer, called NDGNAS, the characterisation of certain transport parameters are required. The most important of these include intrapellet transport coefficients of the VF+DGM and the viscous-kinetic constants of the steady state momentum equation (i.e. Ergun equation). A volumetric device that performs single component uptake experiments using nitrogen allowed the Knudsen diffusion coefficient to be obtained, while determination of the viscous flow transport coefficient was not satisfactorily resolved with the volumetric device. Binary component breakthrough experiments performed on a chromatographic device allowed the molecular diffusion transport coefficient to be found. These transport coefficients were in good agreement with existing literature estimates. Dynamic experiments performed on the chromatographic apparatus revealed the Ergun equation accurately reproduces pressure profiles obtained from the full momentum balance under inert conditions using experimentally calibrated viscous and kinetic constants. The Ergun equation also reproduced pressure profiles well under adsorbing conditions using the same viscous and kinetic constants obtained from steady state experiments.

With NDGNAS fully calibrated, separation performance was compared using RPSA pilot plant data. While the DPM and LDF model both match performance well at the long cycle time, the LDF model significantly underestimated separation performance at the shortest cycle time in comparison to the DPM. Although mismatch between experimental and numerical values could be attributed to errors in regressed equilibrium isotherm parameters using Ideal Adsorbed Solution Theory (IAST), the DPM did successfully reproduce RPSA pilot plant trends across the entire PSA-RPSA operating regime that the LDF model did not. In addition to the VF+DGM intrapellet flux equation, non-isothermal behaviour was also found to be a critical component of RPSA process operation. Severe temperature gradients as a function of axial position were predicted and experimentally observed at the shortest cycle time investigated.

NOMENCLATURE

| | |
|-----------------|--|
| A | Cross sectional area (m^2) |
| a_i | The i -th coefficient of an n -th order polynomial (<i>various units</i>) |
| B | Permeability coefficient of the intrapellet pore network (m^2) |
| Bi | Biot number (-) |
| b | Pre-exponential term within the isotherm equation ($bar.a^{-1}$) |
| C | Transport coefficient related to the intrapellet pore structure (-) |
| c | Heat capacity at constant pressure per unit gmole ($J gmole^{-1} K^{-1}$) |
| \hat{c} | Heat capacity at constant pressure per unit kg of sorbent ($J kg^{-1} K^{-1}$) |
| D | Diffusion coefficient ($m^2 s^{-1}$) |
| d | Diameter (m) |
| E | Working capacity error used in chapter 2 (%) |
| E | CSS error tolerance parameter (<i>various units</i>) |
| Fo | Fourier number (-) |
| G | Gibbs free energy per unit gmole ($J gmole^{-1}$) |
| H | Enthalpy per unit gmole ($J gmole^{-1}$) |
| \hat{H} | Enthalpy per unit kg of sorbent ($J kg^{-1}$) |
| H | Henry's law gradient of linear equilibrium isotherm ($gmole kg^{-1} bar.a^{-1}$) |
| h | Heat transfer coefficient ($W m^{-2} K^{-1}$) |
| J_0 | Zeroth order Bessel function of the first kind (-) |
| J_1 | First order Bessel function of the first kind (-) |
| $K_{laminar}$ | K factor for laminar flow in a pipe (m) |
| $K_{turbulent}$ | K factor for turbulent flow in a pipe ($kg^{1/2} s^{-1} bar.a^{-1/2} m^{1/2}$) |
| K_{valve} | Flow coefficient of the compressible valve equation (-) |
| k | Mass transfer coefficient (s^{-1}) |
| k_0 | Knudsen diffusion transport coefficient of Abassi <i>et. al.</i> (1983) (m) |
| L | Length (m) |
| L_i | The i -th term of an N_L -th order Lagrange interpolating polynomial (-) |
| M | Molecular weight ($g gmole^{-1}$) |
| Ma | Mach number (-) |
| m | Mass of sorbent (kg) |
| m | Affinity parameter within the equilibrium isotherm equation ($gmole kg^{-1}$) |
| N | Intrapellet molar flux per unit area ($gmole m^{-2} s^{-1}$) |

| | |
|----------------|--|
| N | Total mole flow used in simplified RPSA analysis (gmole cycle ⁻¹) |
| N_c | Number of components present within system (-) |
| N_{css} | Number of cycles required to achieve cyclic steady state (-) |
| N_{eq} | Number of equations passed to ODE integrator (-) |
| N_L | Order of Lagrange interpolating polynomial (-) |
| N_r | Number of radial control volumes within pellet (-) |
| N_z | Number of axial control volumes within bed (-) |
| Nu | Nusselt number (-) |
| n | Moles adsorbed per kilogram of sorbent (gmole kg ⁻¹) |
| P_{ax} | Probability factor for axial dispersion in Eq. (4.32) (-) |
| Pe_B | Peclet number at the bed or interpellet level (-) |
| Pe_P | Peclet number at the pellet level (-) |
| p | Pressure (bar.a) |
| Q | Activation energy within the equilibrium isotherm equation (J gmole ⁻¹) |
| q | Heat of adsorption (J gmole ⁻¹) |
| R | Radius (m) |
| R | Universal gas constant (8.314×10^{-5} bar.a m ³ gmole ⁻¹ K ⁻¹) |
| Re | Reynolds number based on internal pipe diameter (-) |
| Re_P | Reynolds number based on pellet diameter, pellet Reynolds number (-) |
| \mathfrak{R} | Ratio operator between old and new PSA process (-) |
| r | Intrapellet radial coordinate for spherical geometry (m) |
| r | Interpellet radial coordinate for cylindrical geometry (m) |
| S | Entropy per unit gmole (J gmole ⁻¹) |
| SG | Specific gravity (-) |
| Sc | Schmidt number (-) |
| T | Temperature (K) |
| t | Time (s) |
| U | Internal energy per unit gmole (J gmole ⁻¹) |
| \hat{U} | Internal energy per unit kg of sorbent (J kg ⁻¹) |
| V | Volume (m ³) |
| v | Velocity, interstitial gas velocity in bed, superficial gas velocity in pipe (m s ⁻¹) |
| X | Solution vector obtained from ODE integrator (<i>various units</i>) |
| X | Fraction of feed gas lost in purge out stream from simplified RPSA analysis (-) |
| $Y_{compress}$ | Compressibility factor (-) |
| y | Mole fraction in gas phase, mole fraction of oxygen in simplified RPSA analysis (-) |
| z | Interpellet axial coordinate for cylindrical geometry (m) |

Greek Letters

| | |
|----------------------------|--|
| $\alpha_1, \alpha_2 \dots$ | Upper limit of a summation loop, used when defining a GSSE (-) |
| α_m | Positive roots of $\alpha_m J_1(\alpha_m R) - (h_{b,w}/\lambda_g^B) \alpha_m J_0(\alpha_m R) = 0$ (m ⁻¹) |
| α_n | Positive roots of $\alpha_n \tan(\alpha_n L) - (h_{b,w}/\lambda_g^B) = 0$ (m ⁻¹) |
| γ | Ratio of heat capacities = $c_g / (c_g - R)$ for an ideal gas (-) |
| δ | Intrapellet pore diameter (m) |
| Γ | Thermodynamic correction factor (-) |
| ϵ | Void volume ((m ³ void) (m ³ total) ⁻¹) |
| ϵ_{tol} | Vector of tolerances that define CSS (<i>various units</i>) |
| Ξ | Surface chemical potential per unit gmole of adsorbed species (J gmole ⁻¹) |
| $\hat{\Xi}$ | Surface chemical potential per unit kg of sorbent (J kg ⁻¹) |
| ξ | Equilibrium isotherm and surface potential derivatives of Eq. (A.14) (J kg ⁻¹ K ⁻¹) |
| ρ | Density in terms of gmole (gmole m ⁻³) |
| $\hat{\rho}$ | Density in terms of kg (kg m ⁻³) |
| σ | Lennard-Jones collision diameter (Angstrom) |
| η | Pellet effectiveness factor in simplified RPSA analysis (-) |
| θ | Dimensionless time = $D^* t / R_p^2$ (-) |
| ϑ | Fraction of occupied adsorption sites (-) |
| κ | Numerical constant of the steady state pressure drop equation (-) |
| λ | Thermal conductivity (W m ⁻¹ K ⁻¹) |
| μ | Gas phase viscosity (Pascal s) |
| τ | Intrapellet tortuosity factor ((m actual length) (m shortest length) ⁻¹) |
| \bar{x} | Similarity variable = $\bar{z}/\bar{t}^{1/2}$ (-) |
| Ω | Numerical constant of the LDF model (-) |
| $\Omega_{ij}^{(1,1)*}$ | Dimensionless transport collision integral (-) |
| ∇ | Operator that defines a difference between two finite volume boundary values |

Subscripts/Superscripts

| | |
|--------------|--|
| A | Parameter related to ambient conditions |
| a | Parameter related to adsorbed phase |
| ax | Parameter related to axial dispersion |
| ads | Parameter related to the adsorption step of a two step cycle |
| B | Parameter related to the interpellet (bed void) region of sorbent bed |
| BD | Blowdown stream related to the simplified RPSA cycle |
| bed | Parameter related to total packed section of a sorbent bed |
| bottom | Parameter related to the lower void volume below sorbent bed |
| col | Parameter related to the outside dimension of the adsorption column |
| cycle | Parameter related to one full cycle of a PSA process |
| D | Parameter related to the diffusive component of intrapellet flux |
| down | Parameter related to a downstream quantity |
| e | Effective coefficient |
| energy | Parameter related to the accumulation of energy over cycle when determining CSS |
| eq | Parameter at equilibrium conditions |
| eqv | Equivalent spherical diameter for a distribution of pellet sizes |
| FD | Feed stream related to the simplified RPSA cycle |
| g | Parameter related to gas phase |
| grad | Parameter related to the gradient of energy accumulation when determining CSS |
| heat | Parameter related to dimensionless analysis involving heat transfer correlations |
| i, j, k, n | Counter variables for loops in N_c , N_r and/or N_z . |
| K | Parameter related to the mechanism of Knudsen diffusion |
| kinetic | Parameter related to the kinetic term in the steady state pressure drop equation |
| m | Parameter related to the mechanism of molecular diffusion |
| m, n, p, q | Counter variables in loops not related to N_c , N_r or N_z |
| mass | Parameter related to dimensionless analysis involving mass transfer correlations |
| max | Related to the maximum value of that parameter |
| mole | Parameter related to the accumulation of mass over cycle when determining CSS |
| min | Related to the minimum value of that parameter |
| P | Parameter related to the intrapellet region inside a sorbent pellet |
| PD | Product stream related to the simplified RPSA cycle |
| PG in | Purge in stream related to the simplified RPSA cycle |
| PG out | Purge out stream related to the simplified RPSA cycle |
| ref | Reference quantity |
| rms | Parameter related to the root mean square error of X when determining CSS |

| | |
|---------|--|
| S | Parameter related to the surface (micropore) diffusion component of intrapellet flux |
| s | Parameter related to the skeletal material of a pellet |
| sat | Parameter related to adsorption at saturation conditions |
| T | Parameter related to the total or combined regions of the system |
| tank | Parameter related to the product tank |
| therm | Parameter related to thermal diffusivity |
| top | Parameter related to the upper void volume above sorbent bed |
| up | Parameter related to an upstream quantity |
| v | Parameter related to the viscous flow component of intrapellet flux |
| viscous | Parameter related to the viscous term in the steady state pressure drop equation |
| - | Dimensionless quantity |
| ~ | Volume averaged quantity |

Abbreviations

| | |
|----------|--|
| ADSIM | ADsorption SIMulator (commercial software package from AspenTech (1997)) |
| APCI | Air Products and Chemicals Inc. |
| ASAP2010 | Accelerated Surface Area and Porosimetry unit, model 2010 |
| BC | Boundary Condition |
| BzzOde | ODE solver developed by Dr. G. Buzzi Ferraris and Dr. D. Manca |
| CSS | Cyclic Steady State |
| DFT | Density Functional Theory |
| DGM | Dusty Gas Model |
| DP | Differential Pressure |
| DPM | Discretised Pellet Model |
| DTM | Dry Test Meter for measuring accumulated gas flow |
| EMU | Experimental Mass-transfer Unit |
| FFL | Fick's First Law of diffusion |
| GLDF | Glueckauf Linear Driving Force |
| GSSE | Global Sum Squared Error |
| IAST | Ideal Adsorbed Solution Theory |
| IC | Initial Condition |
| ILE | Instantaneous Local Equilibrium |
| IUPAC | International Union of Pure and Applied Chemistry |
| J | Jacobian (matrix) |
| LDF | Linear Driving Force |
| LDFP | Partial pressure form of the LDF model |

| | |
|--------|--|
| LDFS | Surface diffusion form of the LDF model |
| LSODE | Livermore Solver for Ordinary Differential Equations |
| LSX | Low Silica-to-alumina ratio X-type zeolite |
| MMS | Mass-transfer Model Switch |
| MINSA | Monash Integrated Numerical Simulator for Adsorption (software developed at Monash University by Dr. J. He and Dr. P. A. Webley) |
| MTZ | Mass Transfer Zone |
| MV | Modulating Valve |
| N | Newton (matrix) |
| NDGNAS | N-component Dusty Gas model for Numerical Adsorption Simulation (software developed as part of this Ph.D. project) |
| ODE | Ordinary Differential Equation |
| PDE | Partial Differential Equation |
| PLC | Programmable Logic Controller |
| PSA | Pressure Swing Adsorption |
| QUICK | Quadratic Upstream Interpolation using Convective Kinematics |
| RPSA | Rapid Pressure Swing Adsorption |
| SCADA | Supervisory Control And Data Acquisition |
| SimPel | Simulation of Pellet model (software developed as part of this Ph.D. project) |
| SIMPAC | SIMulator for Packed bed Adsorption Cycles (proprietary software of APCI) |
| SMART | Sharp and Monotonic Algorithm for Realistic Transport by convection |
| SV | Solenoid (on-off) Valve |
| VF+DGM | Viscous Flow plus Dusty Gas Model |
| VODE | Variable coefficient Ordinary Differential Equation solver |
| WC | Working Capacity |
| WS | Working Selectivity |

LIST OF TABLES

| | | |
|-------------|---|----------|
| Table 1.1: | Brief overview of RPSA patents obtained from the US database. | 6 |
| Table 2.1: | Isotherm and sorbent parameters applied to all simulations in §2.6 and 2.7. | 49 |
| Table 2.2: | CSS tolerance parameters applied to all simulations in §2.6 and §2.7. | 49 |
| Table 3.1: | ODE integrator results from similarity solution of Andrews & Scott (2000). | 93 |
| Table 3.2: | ODE integrator results from the Rosen solution. | 95 |
| Table 3.3: | Magnitude of the tolerances applied to each CSS parameter used by NDGNAS when simulating the four-step, one-bed RPSA cycle of Fig. 3.6. | 98 |
| Table 3.4: | Integrator performance statistics for isothermal RPSA case 1 through 3. | 100 |
| Table 3.5: | CSS performance results for isothermal RPSA case 1 through 3. | 100 |
| Table 3.6: | Integrator performance statistics for non-isothermal RPSA case 4 through 6. | 104 |
| Table 3.7: | CSS performance results for non-isothermal RPSA case 4 through 6. | 104 |
| Table 4.1: | Dual-site Langmuir equilibrium isotherm parameters for Zeochem LiLSX. | 111 |
| Table 4.2: | Distribution of pellet diameters obtained with Zeochem LiLSX. | 112 |
| Table 4.3: | Physical properties obtained experimentally for Zeochem LiLSX. | 113 |
| Table 4.4: | Summary of experimental operating conditions for all blank and dust EMU runs. | 140 |
| Table 4.5: | Fitted NDGNAS flow coefficients for three different boundary conditions along with the product tank-to-wall heat transfer coefficient using blank and dust results. | 141 |
| Table 4.6: | Summary of experimental operating conditions across all EMU pellet runs. | 151 |
| Table 4.7: | Dependence on the level of radial discretisation within the pellet to the optimised transport coefficients obtained across all EMU pellet runs. | 154 |
| Table 4.8: | Physical properties of the adsorption column applied within NDGNAS. | 169 |
| Table 4.9: | Summary of experimental conditions investigated across each breakthrough run. | 170 |
| Table 4.10: | Dependence on level of radial discretisation within pellet to the optimised molecular transport coefficient obtained from breakthrough run 3. | 174 |
| Table 4.11: | Tabular summary of LUB versus NDGNAS data from each breakthrough run obtained with $N_r = 5$ and $C_m = 0.166$ | 183 |

| | | |
|-------------|---|----------|
| Table 5.1: | Initial conditions obtained experimentally from the LUB apparatus for both depressurisation runs performed with 99.996 mol%He. | 202 |
| Table 5.2: | Initial conditions obtained experimentally from the LUB apparatus for both depressurisation runs performed with an adsorbing gas. | 213 |
| Table 6.1: | Published studies that have investigated RPSA process performance. | 226 |
| Table 6.2: | Parameters that were controlled around the RPSA pilot plant. | 238 |
| Table 6.3: | Individual step and cycle times considered on the RPSA pilot plant. | 240 |
| Table 6.4: | A summary of experimental parameters that characterise the RPSA pilot plant. | 243 |
| Table 6.5: | Magnitude of the tolerances applied to each CSS parameter used by NDGNAS when simulating RPSA pilot plant data. | 245 |
| Table 6.6: | Tabular summary of experimentally obtained step times, product purity and end of step pressures that identify the operating conditions for each RPSA run. | 251 |
| Table 6.7: | Comparing experimental and numerical parameters of interest as outlined in §6.3.3. | 254 |
| Table 6.8: | Experimental results obtained from RPSA runs 2 (repeat) and 2. | 261 |
| Table 6.9: | NDGNAS predictions at CSS for RPSA run 7 and RPSA run 9 under various assumptions for intrapellet mass transfer and interpellet pressure drop. | 273 |
| Table 6.10: | Numerical performance results obtained from RPSA runs 2 and 8 under non-isothermal and adiabatic conditions with the LDFP model activated on NDGNAS. | 293 |
| Table 6.11: | Effective diffusion coefficients for nitrogen and oxygen in Zeochem LiLSX over a range of operating conditions experimentally investigated. | 298 |
| Table A.1: | Parameters that define CSS within SimPell. | 314 |
| Table B.1: | Parameters that define CSS within NDGNAS. | 327 |
| Table C.1: | Experimental and numerical values of fraction of feed lost as purge out, X . | 330 |
| Table D.1: | Equipment specifications on the EMU. | 337 |
| Table D.2: | Equipment specifications on the LUB apparatus. | 340 |
| Table D.3: | Equipment specifications on the RPSA pilot plant. | 344 |

LIST OF FIGURES

| | | |
|--------------|--|----------|
| Figure 1.1: | Schematic arrangement of a three-step rapid swing PSA cycle. | 3 |
| Figure 1.2: | Pictorial representation of the various mechanisms that dictate mass transfer within a packed bed of sorbent pellets. | 11 |
| Figure 2.1: | Pictorial representation using an electrical analog for combined intrapellet diffusive and viscous fluxes, developed from Mason & Evans (1969). | 29 |
| Figure 2.2: | Effective diffusivity as a function of pressure and pore diameter. | 36 |
| Figure 2.3: | Plot of Ω_i versus θ_i for both the Nakao & Suzuki (1983) and Alpay & Scott (1992) LDFS models. | 41 |
| Figure 2.4: | Flowchart indicating the relationship and assumptions between various models for intrapellet mass transfer investigated in this dissertation. | 44 |
| Figure 2.5: | Dimensionless adsorbed phase loading for nitrogen from start up to CSS with the VF+DGM using $\bar{t}_{ads} = 0.11$ and $\bar{t}_{ads} = 0.0087$. | 46 |
| Figure 2.6: | Dimensionless nitrogen partial pressure profiles at CSS for $N_r = 5$ and $N_r = 30$ with the VF+DGM using $\bar{t}_{ads} = 0.11$ and $\bar{t}_{ads} = 0.0087$. | 46 |
| Figure 2.7: | WC error with isothermal square-wave BC and $N_r = 30$ for nitrogen and oxygen. | 51 |
| Figure 2.8: | Dimensionless adsorbed phase loading for oxygen within a macroporous pellet. | 52 |
| Figure 2.9: | Difference in the WC between $N_r = 5$ and $N_r = 30$ with isothermal square-wave BC for nitrogen and oxygen. | 54 |
| Figure 2.10: | Partial pressure boundary conditions obtained from MINSA for a two-step RPSA cycle. | 56 |
| Figure 2.11: | WC error with isothermal RPSA BC and $N_r = 30$ for nitrogen at $z = 0.23$ m and $z = 0.97$ m. | 57 |
| Figure 2.12: | WC error with isothermal RPSA BC and $N_r = 30$ for oxygen at $z = 0.23$ m and $z = 0.97$ m. | 57 |
| Figure 2.13: | Volume-averaged adsorbed phase loading profiles for nitrogen at CSS. | 58 |
| Figure 2.14: | Difference in the WC between $N_r = 5$ and $N_r = 30$ with isothermal RPSA BC for nitrogen at $z = 0.23$ m and $z = 0.97$ m. | 59 |
| Figure 2.15: | Difference in the WC between $N_r = 5$ and $N_r = 30$ with isothermal RPSA BC for oxygen at $z = 0.23$ m and $z = 0.97$ m. | 59 |

| | |
|--|----------|
| Figure 2.16: WC error with non-isothermal square-wave BC and $N_r = 30$ for nitrogen and oxygen. | 61 |
| Figure 2.17: Plot of maximum minus minimum temperature across the pellet at CSS with square-wave BC and $N_r = 30$. | 63 |
| Figure 2.18: WC error with non-isothermal RPSA BC and $N_r = 30$ for nitrogen and oxygen. | 64 |
| Figure 2.19: Plot of maximum minus minimum temperature across the pellet at CSS with RPSA BC and $N_r = 30$. | 65 |
| Figure 3.1: Schematic diagram of the numerical discretisation scheme for the adsorption column showing void volumes and source/sink tanks. | 86 |
| Figure 3.2: Experimental temperature profiles obtained for a 12 s RPSA cycle producing 76 mol%O ₂ over a 3.00:1.01 bar.a pressure window. | 87 |
| Figure 3.3: Flowchart outlining implementation of the Mass-transfer Model Switch. | 89 |
| Figure 3.4: Output profiles from the similarity solution of Andrews & Scott (2000). | 93 |
| Figure 3.5: Output profiles from the Rosen solution. | 96 |
| Figure 3.6: Four-step one-bed RPSA cycle. | 97 |
| Figure 3.7: End of step composition profiles at CSS from the DPM and LDFP model with $N_z = 20$ for RPSA case 2. | 101 |
| Figure 3.8: Pressure profiles at CSS from the DPM and LDFP model with $N_z = 20$ for RPSA case 2 showing end of step profiles and history data obtained at $z = 0$ and $z = L_{bed}$. | 102 |
| Figure 3.9: End of step temperature profiles at CSS from the DPM and LDFP model with $N_z = 20$ for RPSA case 5. | 105 |
| Figure 3.10: End of step temperature profiles at CSS with and without the MMS for RPSA case 5. | 105 |
| Figure 4.1: Equilibrium isotherm for pure component nitrogen and oxygen obtained at three different temperatures using the equilibrium measuring device, along with the corresponding analytical fit using regressed dual-site Langmuir isotherm parameters. | 111 |
| Figure 4.2: Representative sample of Zeochem LiLSX sorbent pellets. | 112 |
| Figure 4.3: Intrapellet pore size distribution obtained from nitrogen adsorption (DFT) and mercury intrusion porosimetry (Hg intrusion) for Zeochem LiLSX. | 114 |
| Figure 4.4: Basic mode of operation for a steady state Wicke-Kallenbach cell. | 115 |

| | |
|--|----------|
| Figure 4.5: Basic schematic arrangement of one EMU run from start, $t = 0$, to end, $t \gg 0.1$. | 136 |
| Figure 4.6: Experimental versus numerical pressure response for blank and dust runs 1 through 6. | 142 |
| Figure 4.7: Comparative plot of the Crane Co. (1976) compressibility criterion and Re at small values of time obtained from NDGNAS for each regime of flow with blank run 3 and dust run 3. | 144 |
| Figure 4.8: A schematic arrangement drawing of the EMU sample volume showing the experimental location of the thermocouple tip and vessel dimensions. | 146 |
| Figure 4.9: Experimental versus numerical profiles obtained from blank runs 7 and 8 using regime iii. | 148 |
| Figure 4.10: GSSE of Eq. (4.15) versus the two independent fitting parameters C_K and C_v obtained from the initial parameter search using $N_r = 30$. | 153 |
| Figure 4.11: NDGNAS and EMU pressure profiles obtained for each dust and pellet run using $N_r = 30$. | 155 |
| Figure 4.12: First order sensitivity coefficients of p^{blank} obtained from NDGNAS as a function of the Knudsen and viscous flow transport coefficients and the pellet-to-bed heat transfer coefficient for various dust and pellet runs. | 159 |
| Figure 4.13: EMU and NDGNAS temperature profiles, presented over two different times scales, obtained in the sample volume for each dust and pellet run with the ice water bath. | 163 |
| Figure 4.14: Schematic diagram outlining the procedure initiated for one breakthrough experiment performed on the LUB apparatus. | 167 |
| Figure 4.15: GSSE of Eq. (4.25) as a function of the one independent fitting parameter C_m for breakthrough run 3 using NDGNAS with $N_r = 3$ and the rigorous wall model activated. | 174 |
| Figure 4.16: NDGNAS breakthrough curves obtained from the rigorous wall model and adiabatic simulations of breakthrough run 3 in comparison to LUB data. | 178 |
| Figure 4.17: NDGNAS temperature profiles obtained from the rigorous wall model and adiabatic simulations of breakthrough run 3 in comparison to experimental temperature profiles. | 179 |
| Figure 4.18: First order sensitivity coefficients of y_i^B as a function of C_K , C_v and C_m obtained from breakthrough run 3 using NDGNAS. | 181 |
| Figure 4.19: Comparison of LUB and NDGNAS breakthrough curves obtained with the rigorous wall model activated for NDGNAS. | 184 |

| | |
|--|----------|
| Figure 4.20: A comparison of LUB and NDGNAS temperature profiles obtained with the rigorous wall model activated. | 186 |
| Figure 4.21: Peclet mass transfer number at the bed scale and Biot mass transfer number obtained from NDGNAS data for each gas mixture at $z = 1.55$ m, the location of the oxygen analyser, for breakthrough runs 1, 3 and 6. | 188 |
| Figure 5.1: Friction factor f versus modified pellet Reynolds number $Re_p / (1 - \epsilon_B)$ for Zeochem LiLSX. | 199 |
| Figure 5.2: Schematic diagram outlining the procedure initiated for one co-current depressurisation experiment on the LUB apparatus. | 200 |
| Figure 5.3: Experimental and numerical pressure profiles obtained from depress run 1 using the approximate model. Relative error in pressure obtained from depress run 1. | 204 |
| Figure 5.4: Experimental and numerical pressure profiles obtained from depress run 2 using the approximate model. Relative error in pressure obtained from depress run 2. | 205 |
| Figure 5.5: Experimental temperature profiles obtained from depress run 2. | 206 |
| Figure 5.6: Experimental and numerical pressure profiles obtained from depress run 3. | 214 |
| Figure 5.7: Experimental and numerical temperature profiles obtained from depress run 3. | 215 |
| Figure 5.8: Experimental and numerical pressure profiles obtained from depress run 4. | 216 |
| Figure 5.9: Experimental and numerical temperature profiles obtained from depress run 4. | 217 |
| Figure 5.10: Experimental and numerical pressure drop and temperature profiles from breakthrough run 1 using gas mixture A. | 219 |
| Figure 5.11: Experimental and numerical pressure drop and temperature profiles from breakthrough run 3 with gas mixture B. | 219 |
| Figure 5.12: Experimental and numerical pressure drop and temperature profiles from breakthrough run 6 with gas mixture C. | 220 |
| Figure 6.1: One-bed, four-step cycle initiated on the RPSA pilot plant. | 237 |
| Figure 6.2: Experimental temperature and product purity that track changes in ambient temperature once a steady CSS condition has been achieved. | 246 |
| Figure 6.3: Experimental temperature and product purity at CSS from RPSA run 18 over a twelve hour period. | 262 |
| Figure 6.4: Experimental pressure profiles obtained at CSS from RPSA run 18. | 263 |

| | |
|--|----------|
| Figure 6.5: True binary versus IAST fitted adiabatic working selectivity of APCI LiLSX and APCI Class 2 MCI. | 266 |
| Figure 6.6: Comparing process performance results between RPSA pilot plant data, NDGNAS and simplified RPSA analysis over a 4.00:1.20 pressure window at a target purity of 90 mol%O ₂ for specific productivity and recovery. | 270 |
| Figure 6.7: Comparing process performance results between RPSA pilot plant data, NDGNAS and simplified RPSA analysis over a 4.00:1.20 pressure window at a target purity of 80 mol%O ₂ for specific productivity and recovery. | 271 |
| Figure 6.8: Composition profiles obtained from RPSA run 7 using six different modelling options within NDGNAS at the end of step 1, 2, 3 and 4. | 274 |
| Figure 6.9: Composition profiles obtained from RPSA run 9 using six different modelling options within NDGNAS at the end of step 1, 2, 3 and 4. | 275 |
| Figure 6.10: Magnitude of pressure gradient across sorbent bed obtained experimentally and numerically under various modelling options for RPSA runs 7 and 9. | 277 |
| Figure 6.11: Comparing process performance results between RPSA pilot plant data, NDGNAS and simplified RPSA analysis over a 5.00:1.20 pressure window at a target purity of 90 mol%O ₂ for specific productivity and recovery. | 278 |
| Figure 6.12: Comparing process performance results between RPSA pilot plant data, NDGNAS and simplified RPSA analysis over a 5.00:1.20 pressure window at a target purity of 80 mol%O ₂ for specific productivity and recovery. | 279 |
| Figure 6.13: Comparing experimental versus simulated pressure profiles with time at CSS over a 4.00:1.20 bar.a pressure window using both intrapellet mass transfer models of NDGNAS. | 282 |
| Figure 6.14: Comparing experimental versus simulated pressure profiles with time at CSS over a 5.00:1.20 bar.a pressure window using both intrapellet mass transfer models of NDGNAS. | 283 |
| Figure 6.15: Comparing experimental versus simulated temperature profiles with time at CSS over a 4.00:1.20 bar.a pressure window using both intrapellet mass transfer models of NDGNAS. | 286 |
| Figure 6.16: Comparing experimental versus simulated temperature profiles with time at CSS over a 5.00:1.20 bar.a pressure window using both intrapellet mass transfer models of NDGNAS. | 287 |
| Figure 6.17: NDGNAS end of step composition profiles for nitrogen obtained with the DPM and LDFP model from RPSA run 2 and RPSA run 9. | 289 |

| | |
|--|----------|
| Figure 6.18: Comparing experimental versus simulated end of step temperature profiles at CSS with a 4.00:1.20 bar.a pressure window using both intrapellet mass transfer models of NDGNAS. | 290 |
| Figure 6.19: Comparing experimental versus simulated end of step temperature profiles at CSS with a 5.00:1.20 bar.a pressure window using both intrapellet mass transfer models of NDGNAS. | 291 |
| Figure 6.20: Comparing adiabatic versus non-isothermal temperature profiles obtained with the LDFP model activated in NDGNAS from RPSA runs 2 and 8. | 294 |
| Figure 6.21: Comparing experimental versus numerical temperature profiles obtained by Teague & Edgar (1999) against those obtained in this dissertation. | 295 |
| Figure A.1: Cutaway diagram of a spherical sorbent pellet showing the arrangement of control volumes. | 307 |
| Figure B.1: Diagram of a single control volume within the sorbent bed detailing the mechanisms that dictate heat and mass transfer. | 321 |
| Figure C.1: System boundary and streams of interest for the simplified RPSA analysis. | 329 |
| Figure C.2: Qualitative representation of temperature profiles assumed to arise at the end of the feed and blowdown steps. | 333 |
| Figure C.3: Flowchart outlining calculation procedure for the simplified RPSA analysis. | 335 |
| Figure D.1: Detailed piping and instrumentation diagram of the EMU. | 338 |
| Figure D.2: Various photos of the EMU. | 339 |
| Figure D.3: Detailed arrangement drawing of the LUB adsorption column. | 341 |
| Figure D.4: Detailed piping and instrumentation diagram of LUB apparatus. | 342 |
| Figure D.5: Various photos of the LUB apparatus. | 343 |
| Figure D.6: Detailed arrangement drawing of the RPSA pilot plant adsorption column. | 345 |
| Figure D.7: Detailed piping and instrumentation diagram of the RPSA pilot plant. | 346 |
| Figure D.8: Various photos of the RPSA pilot plant and adsorption column. | 347 |
| Figure D.9: Detailed arrangement drawing of the top flange and bottom flange. | 348 |
| Figure D.10: Photos of the RPSA pilot plant valve manifolds and column internals. | 349 |

LIST OF PUBLICATIONS

Webley P. A., Beh C., He J., Wilson S. & Todd R. S. (2000) Numerical Simulation and Experimental Validation of Multiple-Layer, Non-Isothermal, Bulk Gas Pressure Swing Adsorption, 658 – 662, *Proc. 2nd. Pacific Basin Conf. Adsorption Science and Technology*, Brisbane, Queensland, Australia, 14-18 May

Todd R. S., Beh C. C. K., Wilson S. J. & Webley P. A. (2001) Simplified Modelling of Pressure Driven Flow in Pressure Swing Adsorption Processes, 5 – 8, *Proc. Monash Graduate Fluids Conference*, Melbourne, Victoria, Australia, 5 July

Todd R. S. & Webley P. A. (2001) Low Purity Oxygen Production by Rapid Pressure Swing Adsorption, *Proc. 6th. World Congress Chemical Engineering*, Melbourne, Victoria, Australia, 23-27 September

Wilson S. J., Todd R. S. & Webley P. A. (2001) Damping Thermal Swings in Oxygen Vacuum Swing Adsorption (VSA), *Proc. 6th. World Congress Chemical Engineering*, Melbourne, Victoria, Australia, 23-27 September

Beh C. C. K., Todd R. S. & Webley P. A. (2001) Capturing Mass Transfer Effects using Neural Network Models. Case Study - Breakthrough Fronts for N₂/O₂ Separation, *Proc. 6th. World Congress Chemical Engineering*, Melbourne, Victoria, Australia, 23-27 September

Wilson S. J., Beh C. C. K., Webley P. A. & Todd R. S. (2001) The Effects of a Readily Adsorbed Trace Component (Water) in a Bulk Separation PSA Process: The Case of Oxygen VSA, *Ind. Eng. Chem. Res.*, **40**, 2702 – 2713

Todd R. S., He J., Webley P. A., Beh C., Wilson S. & Lloyd M. A. (2001) Fast Finite-Volume Method for PSA/VSA Cycle Simulation - Experimental Validation, *Ind. Eng. Chem. Res.*, **40**, 3217 – 3224

Todd R. S. & Webley P. A. (2002) Limitations of the LDF/Equimolar Counterdiffusion Assumption for Mass Transport within Porous Adsorbent Pellets, *Chem. Eng. Sci.*, **57**, 4227 – 4242

Todd R. S. & Webley P.A. (2002) Experimental and Numerical Investigation of the Ergun Equation for Pressure Drop with Adsorption, *AIChE Annual Meeting*, Indianapolis, Indiana, USA, 3-8 November

Todd R. S. & Webley P.A. (2002) Limitations of the LDF and Equimolar Counterdiffusion Assumption for an Adsorbent Pellet under Non-Isothermal Conditions, *AIChE Annual Meeting*, Indianapolis, Indiana, USA, 3-8 November

Webley P. A., Todd R. S., Elkhishin E. & Yee B. (2002) Linear Driving Force Rate Constants for Adsorbent Mixtures, *AIChE Annual Meeting*, Indianapolis, Indiana, USA, 3-8 November

Todd R. S., Buzzi Ferraris G., Manca D. & Webley P. A. (2003) Improved ODE Integrator and Mass Transfer Approach for Simulating a Cyclic Adsorption Process, *Comput. & Chem. Eng.*, **27**, 883 – 899

Webley P.A. & Todd R. S. (2003) Kinetics of Mixed Adsorbent Systems in Gas-Solid Adsorption, *Adsorption Science & Technology*, **21**, 9 – 34

Todd R. S., Webley P. A., Whitley R. D., Chiang R. L. & LaBuda M. J. (2003) Knudsen Diffusion and Viscous Flow Dusty-Gas Coefficients for Pelletised Zeolites from Kinetic Uptake Experiments, *8th. International Conference on Fundamentals of Adsorption (FOA8)*, Sedona, Arizona, USA, 22-28 May 2004

Todd R. S., Webley P. A., Whitley R. D., Chiang R. L. & LaBuda M. J. (2004) Dusty Gas Coefficients for a Pelletised Zeolite Under Macropore Diffusion Control. Part 1: Knudsen Diffusion and Viscous Flow Coefficients, *Currently under review*

Todd R. S. & Webley P. A. (2004) Dusty Gas Coefficients for a Pelletised Zeolite Under Macropore Diffusion Control. Part 2: Molecular Diffusion Coefficient, *Currently under review*

Todd R. S. & Webley P. A. (2004) Pressure Drop in a Packed Bed Under Non-Adsorbing and Adsorbing Conditions, *Currently under review*

Todd R. S. & Webley P. A. (2004) Comparing LDF and DGM Predictions Against Pilot Plant Data for Air Separation Under RPSA Conditions, *Currently under review*

CHAPTER 1

INTRODUCTION

Adsorption describes the interaction and subsequent retention of a fluid molecule (sorbate) onto the atoms that make up the surface of a solid (sorbent) material. When a multicomponent gas or liquid stream is exposed to a suitably tailored sorbent, particular components will be selectively adsorbed to leave behind a depleted fluid mixture that can be recovered as an enriched product stream. Thus, adsorption provides a simple and cost effective means of separating bulk and trace component mixtures within the chemical industry. Commercial adsorption processes typically operate in a scheduled batch-like manner, removing the more-strongly adsorbed component(s) on a designated “feed plus make product” step and then regenerating the sorbent via desorption and purge on subsequent process steps. Multiple sorbent beds and/or buffer tanks are often used to provide a continuous supply of product gas to the downstream consumer. Different methods of sorbent regeneration and cycle configurations will not be the subject of this dissertation and the texts of Ruthven (1984a), Suzuki (1990), Ruthven *et. al.* (1994), Tien (1994), Yang (1997) and Thomas & Crittenden (1998) provide an excellent background to adsorption and adsorption separation processes. Only one particular process, gas-phase Pressure Swing Adsorption (PSA)[†] will be considered in this dissertation. By virtue of its name, PSA involves the adsorption and subsequent desorption of the more-strongly adsorbed component(s) by changing the absolute pressure of the bulk gas phase.

1.1 Qualitative Discussion on Rapid Pressure Swing Adsorption

The last twenty years has seen rapid growth in the development of PSA, particularly in relation to three key process applications: air dehumidification, hydrogen enrichment and air separation [Cassidy & Holmes (1984), Suzuki (1988), LeVan (1998), Ruthven (2000), Sircar (2001, 2002)]. A large number of these developments relate to improved sorbent materials and arrangement (i.e. monolithic structures) that are more efficient at removing certain components from the fluid stream, thereby improving adsorption-desorption capacity per unit mass of sorbent. This is an active area of research for the major gas companies with Air Products and Chemicals Inc. [Golden *et. al.* (2003)], the BOC group [Lu *et. al.* (2003)] and PraxAir [Ackley *et. al.* (2003)] all awarded

[†] The term PSA is used within this dissertation to denote a pressure swing cycle that involves adsorption at super-atmospheric pressure and desorption at atmospheric pressure.

patents related to this field in the first half of 2003 alone. Other developments have focused on new process and cycle configurations. One particular process development that is of current research and commercial interest is Rapid Pressure Swing Adsorption (RPSA). Although RPSA is classified as a distinct adsorption separation process, the actual boundary between a PSA and RPSA cycle is not quite so well defined.

Industrial literature (i.e. patents) indirectly define RPSA as any PSA process with a total cycle time below approximately thirty seconds. This definition provides a rule of thumb below which constraints such as valve dynamics, pellet attrition, mass transfer, bed pressure drop and fluidisation become an integral part of system design. The *academic literature* provides an alternative definition based on a dimensionless rather than absolute time argument. Dimensionless time $\theta (=D^2 t/R_p^2)$ commonly substitutes absolute time within the governing pellet conservation equations when they are recast into dimensionless form. Accordingly, as θ falls below a critical value, taken to be 0.1, the solution of these conservation equations using a simplified mathematical approach often fails. This is closely related to the internal mechanisms that dictate mass transfer within the sorbent pellet and as such places no constraints on equipment design or operation.

Although both definitions can sometimes contradict each other (i.e. certain combinations of small pellets and short cycles can give absolute times less than thirty seconds while dimensionless time is greater than 0.1), they do indicate mass transfer and pressure drop play a central role in the design and operation of any RPSA process.

1.1.1 Rapid Swing versus Rapid Cycle PSA

A review of the published literature reveals two distinct fields of "RPSA" have emerged. The first process configuration can be classified rapid swing PSA while the second can be classified rapid cycle PSA. The main difference between these two configurations resides in the scheduling of individual process steps and the form of the axial pressure profile that arises through the bed.

The basic rapid swing PSA cycle involves the pressurisation of a single sorbent bed with feed gas while product is simultaneously withdrawn from the other end, followed by counter-current depressurisation. In some cases an intermediate co-current depressurisation step is used between feed and counter-current depressurisation to increase product recovery. The typical arrangement of a rapid swing PSA cycle is shown in Fig. 1.1 along with some characteristic pressure profiles that arise over each step. In some cases the axial pressure gradient is steep enough such that product

gas can be continuously withdrawn during counter-current depressurisation [Turnock & Kadlec (1971)].

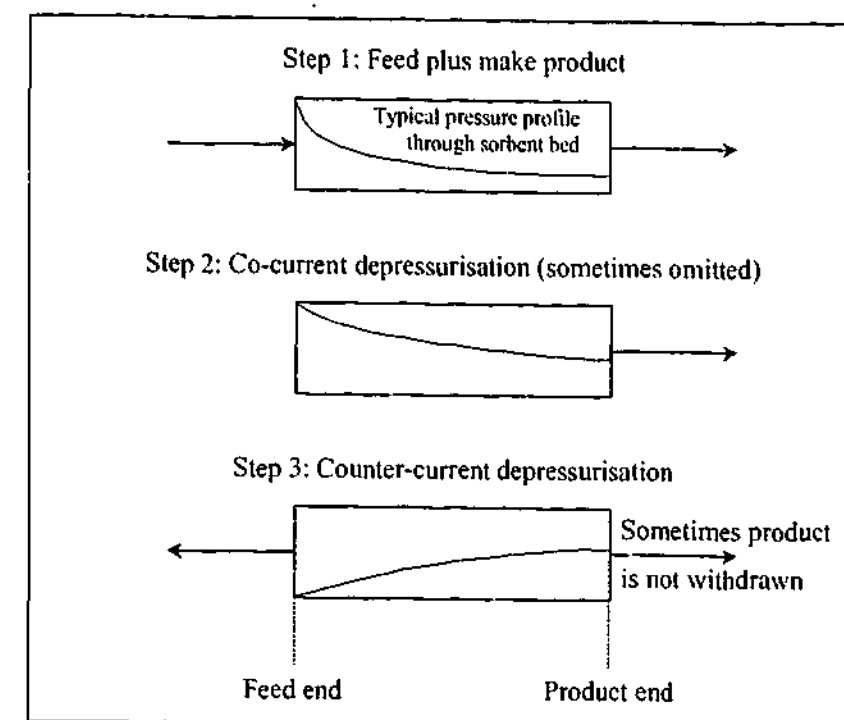


Figure 1.1: Schematic arrangement of a three-step rapid swing PSA cycle. Note that co-current depressurisation (step 2) is sometimes referred to as feed delay. The general shape of the axial pressure profile during each step is also depicted through the sorbent bed.

Eliminating the need for multiple sorbent beds makes rapid swing PSA inherently cheaper and simpler than an equivalent PSA process due to a reduction in the number of valves, vessels, ancillary process equipment and most importantly, sorbent material. This makes rapid swing PSA a suitable candidate for academic research with Turnock & Kadlec (1971), Kowler & Kadlec (1972), Jones & Keller (1981), Pritchard & Simpson (1986), Jianyu & Zhenhua (1990), Hart & Thomas (1991), Alpay *et al.* (1993, 1994), Chou & Wu (1994), Chou & Kuang (1996), Murray (1996), Suzuki *et al.* (1996, 1997), Zhu (1996), Horváth & Suzuki (1998), Zhang *et al.* (1998), Choong (2000) and Arvind *et al.* (2002) all having considered this particular configuration.

With pressure swinging rapidly over a cycle, the time scale for mass transfer within a single sorbent pellet is now comparable to the duration of each process operating step. To minimise this resistance to mass transfer the size of individual sorbent pellets needs to be reduced. A survey of the aforementioned studies reveals pellet size is generally less than 1.0×10^{-3} m, which in turn gives rise to the large axial pressure gradient. This axial pressure gradient means a relatively small region of the bed located near the feed entrance is swinging between high and low pressure: the upper portion of the bed essentially remains at one relatively uniform pressure with respect to the lower half of the bed.

The region between high and low pressure ultimately defines the working capacity for nitrogen adsorption and desorption over a cycle and hence the amount of separation that can occur. With a reduced portion of the bed swinging between high and low pressure the amount of gas that can be separated per unit mass of sorbent is reduced. A reduced working capacity limits the recovery of product gas with respect to an equivalent cycle where the entire bed is swinging between high and low pressure. Low recovery also means a large portion of the mechanical work imparted upon the feed stream is discharged through the exhaust line during counter-current depressurisation. Hence energy costs (based on volume of product gas obtained per unit volume of feed gas required) and oxygen recovery are two primary reasons why large-scale rapid swing PSA is not commercially practiced.

Rapid swing PSA operates over a completely different cycle arrangement with respect to a traditional PSA cycle. On the other hand, rapid cycle PSA can be thought of as a traditional PSA cycle that has been reduced in time to the point where the academic and/or industrial definition of "rapid PSA" is now relevant. All the essential elements of the conventional cycle remain except here the time scale for mass transfer within a single sorbent pellet is now comparable to the duration of each process operating step. Although axial pressure gradients may be important, their severity is not as pronounced as for the rapid swing process. The ultimate limit in separation performance is therefore attributed to mechanisms that limit heat and/or mass transfer within the sorbent bed. Although academic studies related to rapid cycle PSA are not as common as their rapid swing counterparts, the pursuit of rapid cycle PSA is the common goal of industry when a review of the patent literature is made (see Table 1.1).

The distinction between rapid swing and rapid cycle PSA will not be made through this dissertation so the term "RPSA" will in general refer to both process configurations. Although attention is focused on rapid cycle PSA, the models and experimental units presented in this dissertation are also applicable to rapid swing PSA. Rapid cycle as opposed to rapid swing PSA is considered in this dissertation for two reasons:

- i. Rapid swing PSA has been extensively studied for oxygen enrichment and it is not the intension of the author to repeat this body of work. The same cannot be said for rapid cycle PSA, however, providing one key area of adsorption research that has received little attention.
- ii. Recent trends from industry is to push PSA into the rapid cycle regime rather than adopt rapid swing PSA, so the findings of this study have a direct bearing on current research efforts that are of relevance to the industrial sector.

1.1.2 Why RPSA over Conventional PSA?

Rota & Wankat (1990) presented a set of scaling rules based on the dimensionless form of the governing conservation equations that demonstrate the potential improvements offered with shorter cycle times. Using a complete set of design results from an existing installation or simulation, a ratio operator $\mathfrak{R}(\psi)$ was introduced that equates these "old" conditions to a "new" process where ψ represents any dependent or independent parameter.

$$\mathfrak{R}(\psi) = \frac{\psi_{\text{new plant}}}{\psi_{\text{old plant}}} \quad (1.1)$$

With an equivalent product purity and recovery between the old and new configuration, $\mathfrak{R}(\text{purity}) = \mathfrak{R}(\text{recovery}) = 1$, the following scaling rules were obtained.

$$\mathfrak{R}(\text{productivity}) = \mathfrak{R}(\text{cycle time})^{-1} \quad (1.2)$$

$$\mathfrak{R}(\text{bed length}) = \mathfrak{R}(\text{cycle time}) \quad (1.3)$$

$$\mathfrak{R}(\text{bed diameter}) = \mathfrak{R}(\text{molar feed rate per unit time})^{0.5} \quad (1.4)$$

$$\mathfrak{R}(\text{pellet diameter}) = \mathfrak{R}(\text{cycle time})^{0.5} \quad (1.5)$$

These particular scaling rules relate to a non-isothermal process that exhibits internal mass transfer limitations at the pellet level. Equation (1.2) demonstrates sorbent productivity increases as cycle time decreases, giving rise to smaller inventories of sorbent per unit volume of product gas that provides one key driver for the miniaturisation principle of RPSA. Equations (1.3) through (1.5) indicate shorter cycle times also lead to shorter, wider beds packed with smaller diameter pellets.

In theory, an infinitely short cycle time requires an infinitely small volume of sorbent to achieve a particular separation according to Eq. (1.2). So what in practice limits the attainment of such an operating condition if physical equipment dimensions and actuation times, at least hypothetically, were not a constraint? Equations (1.2) through (1.5) imply the solution of the governing conservation equations between the long and short cycle time configurations both possess identical profiles in dimensionless units and the same mechanisms dictate heat and mass transfer throughout the adsorption column. The assumptions underlying these mechanisms break down at the RPSA limit and consequently the validity of such a model is restricted. The question now becomes "with

the validity of a simplified mathematical model failing at this RPSA limit, what improvements can be made from a modelling perspective to drive future research towards improved RPSA technology?"

Before digressing into a qualitative discussion of the various mechanisms that need to be considered, a background to the industrial relevance of RPSA will be introduced first.

1.1.3 RPSA Process Application - Oxygen Enrichment from Air

While PSA and Vacuum Swing Adsorption (VSA)[†] [Kumar (1996)] have proven themselves to be viable separation technologies, RPSA has only found limited process applications with the most prominent being medical-grade oxygen generation. Currently this market is experiencing double-digit growth rates, offering a lucrative business portfolio in the coming years for several gas supply companies [APCI (2001)]. The impact of RPSA on medical-grade oxygen generation is further revealed through a literature search within the US patent database [<http://www.uspto.gov>] for process applications directly related to RPSA (Table 1.1).

Table 1.1: Brief overview of RPSA patents obtained from the US database [<http://www.uspto.gov>].

| Inventor(s) | Cycle Description | Process Application | Incremental Improvement |
|----------------------|--|--|---|
| Eriksson (1979) | 1-bed, 2-step cycle invoked by a piston moving back and forth below the bed at a frequency of 0.1 to 10 RPM, total cycle time ranging from 600 to 6 s. | Oxygen enrichment from air feed stream. | Limitations of valve wear with existing PSA units overcome by using a moving piston below the bed to invoke pressurisation and depressurisation. Although no reference to RPSA made, operating frequency of 10 RPM is within the RPSA regime. |
| Earls & Long (1980) | 2 or 3-bed process operated over 4 or 6-step cycle of total duration 18 s or less. Pressurisation performed via backflow of product gas and/or inflow of feed gas. | Oxygen enrichment from air for medical applications. | Provide a lightweight and compact unit with improved recovery, start-up time and productivity by employing shorter cycle times in comparison to conventional PSA. |
| Jones et. al. (1980) | Single bed, 2 or 3-step RPSA process operated under various cycle times, all of which are less than 30 s. | O ₂ enrichment from air for medical applications: H ₂ enrichment from CH ₄ , CO, CO ₂ ; and N ₂ enrichment from N ₂ -C ₂ H ₄ and H ₂ from H ₂ -C ₂ H ₄ . | RPSA unit with increased recovery and productivity (in relation to work of Turnock & Kadlec (1971) and Kowler & Kadlec (1972)) by having feed plus feed delay step times less than half the counter-current depressurisation step time. |

[†] The term VSA is used within this dissertation to denote a pressure swing cycle that involves adsorption at pressures slightly above atmospheric and desorption at sub-atmospheric pressure.

Table 1.1 continued

| Inventor(s) | Cycle Description | Process Application | Incremental Improvement |
|---------------------------|---|---|--|
| Keller & Kuo (1982) | Single bed, 2-step cycle invoked by pistons moving back and forth above/below the bed at a frequency of 45-50 RPM (total cycles times around 1.2-1.3 s). | Proposed for a multitude of applications, while O ₂ /N ₂ enrichment from air the only process investigated experimentally. | Reduced operating costs and improved productivity afforded with pistons used to invoke pressure changes and hence flow through the bed. Ratio of bottom-to-top piston stroke length and phase lag needs to be optimised for a particular separation. |
| Dangieri & Cassidy (1983) | RPSA process using between 2 and 10-beds operated over 3 or 4-step cycle of total duration 20 s or less. | O ₂ enrichment from air for portable oxygen generators and military aircraft breathing systems. | Increased feed pressure and temporary stop on feed flow before passage to next bed improves productivity without affecting purity or process size. |
| Miller & Theis (1989) | 2-bed, 2-step cycle operated over a bed of carbon molecular sieve with a total cycle time in the range of 3 to 9 s. | Oxygen enrichment to high purity (99.6 mol%) for portable oxygen generators and military aircraft breathing systems. | The disclosed cycle does not require purge flow during bed regeneration to achieve high purity, thereby minimising the consumption of feed gas for efficient operation. |
| Wells (1991) | 1-bed, 2-step cycle operated over a pressure window of 0.1 bar or less with a frequency of around 50 to 200 cycles per second, termed acoustic pressure swing gas separation. | No system explicitly cited, but oxygen enrichment from air for medical purposes mentioned in patents related to the prior art. | Provide a PSA system that substantially reduces energy consumption with a lower pressure ratio operated at high frequencies. Pressure variations induced by a thermally driven gas resonance device. |
| Sircar (1991) | 2 (or more) bed, 2-step (equal time) RPSA cycle called split bed RPSA as flow restriction present between beds to allow for purge. Total cycles times in the range 6 to 60 s. | Potential applications include N ₂ and O ₂ enrichment from air, air dehumidification and H ₂ enrichment from CO-CO ₂ -CH ₄ -N ₂ -H ₂ feedstocks. | Continuous processing of feed and removal of product gas allowed. Provides efficient use of sorbent capacity while reducing sorbent inventory and ancillary equipment size. |
| Hirooka et. al. (1992) | 2-bed RPSA process operated over a 6-step (26 to 76 s duration), 8-step (32 to 92 s duration) or 10-step (34 to 102 s duration) cycle. Each takes advantage of continuous use of vacuum pump. | Oxygen enrichment from air feed steam. | Exploits high production rate of fast cycles, high recovery of multi-bed system and optimum power consumption of vacuum pump as pump is always on-line to the bed throughout the cycle. |

Table 1.1 continued

| Inventor(s) | Cycle Description | Process Application | Incremental Improvement |
|--------------------------|---|---|--|
| Kulish & Swank (1998) | 6-bed, 6-step cycle with "piping network" between beds and associated inlet/outlet lines machined into a plate that rotates above the stationary sorbent beds. Total cycle time of approximately 12 s. | Oxygen enrichment from air for use as a portable medical oxygen generator (preferred embodiment). | Provides an oxygen concentrator that is quiet, utilises less energy, and is more efficient, lightweight and compact than previous disclosures. <i>Note: This patent was reissued in May 2000 (US Patent 6,068,680) by the same authors.</i> |
| Keefer & McLean (2000) | 2, 3 or 6 sorbent laminate sheets (\equiv beds) are rotated between claw pumps to invoke a VSA cycle. Frequency of 100 to 300 cycles per minute quoted. | O ₂ enrichment from air and H ₂ purification (particularly aimed at advanced energy generation systems such as fuel cells). | This patent claims radical miniaturisation of vacuum PSA systems will result. Very high efficiencies using much more compact equipment claimed in this disclosure. |
| Maheshwary et al. (2001) | 2-bed, 5-step cycle operated over a PSA pressure window with total cycle time between 5 and 60 s, or a VSA window with total cycle time between 5 and 120 s. | Oxygen enrichment from air feed steam. | The disclosed process maximises air blower and vacuum pump "on-line" time to sorbent bed to achieve higher productivity and lower power consumption in relation to existing process arrangements. |
| Keefer & McLean (2003) | 3-bed cycle operated over a range of process steps to invoke a PSA or VSA cycle. Each bed equivalent to the laminate sheets disclosed by Keefer & McLean (2000). Steps invoked by rotating beds between feed pump and exhaust line. | Oxygen enrichment from air feed steam for medical applications. | Rotating sorbent sheets between feed and vacuum pump allows high frequency operation that provides high energy efficiency and compact machinery with low capital cost. |
| Ackley & Zhong (2003) | 2-bed, 6-step cycle with total cycle time below 10 s (preferred embodiment). Sorbent with high intrinsic mass transfer rate disclosed by Ackley et al. (2003) the basis for process improvement. | Oxygen enrichment from air for use as a portable medical oxygen generator. | The use of sorbent with high intrinsic diffusivities allows fast cycles to be performed that significantly reduces the size, weight and power consumption of this unit in comparison to other medical oxygen generators. |

Mature oxygen enrichment technologies associated with traditional PSA and VSA processes have found numerous applications within the chemical industry. Some of these include on-site delivery of oxygen to provide an enriched combustion oxidant for waste incineration, steel production and nonferrous metal recovery; biological processes for the treatment of wastewater and bioremediation of contaminated soil; and delignification processes to reduce chlorine consumption in the pulp and paper industry [Shelley (1991), Michael (1997)]. More recently the use of low purity oxygen, around 28-50 mol%O₂, rather than air was found to improve efficiency with

minimal capital outlay and process downtime for three applications; acrylonitrile manufacture, aluminium smelting and sulphur recovery [Parkinson et al. (1999)]. Significant growth in the consumption of low purity oxygen was also predicted in the coming years as environmental and economical constraints tighten. Although RPSA is not yet considered economically viable for these process applications, future developments, particularly in relation to enhanced sorbent materials disclosed recently in patent form, does not preclude RPSA from breaking down some of these boundaries traditionally held by PSA and VSA. For this reason, oxygen enrichment from air using molecular sieve zeolites will form the system of experimental and theoretical analysis throughout this dissertation.

1.2 A Discussion on the Fundamental Transport Mechanisms

As described in §1.1, a major driver towards the development of future adsorption processes lies in the development of improved sorbent materials. However, these improved materials with better adsorption-desorption capacity must ultimately find their way into a real process for commercial applications that should operate within the RPSA regime to maximise product output per unit mass of sorbent. The issue now becomes "how should this material be loaded into a commercial process; should it be in pellet form and if so, what is the optimum diameter to balance pressure drop and mass transfer; or should it be in a structured form (such as a monolith) to minimise pressure drop, but what impact does this have on mass transfer?" From here, material development largely becomes proprietary with accumulated knowledge the standard from which a final product is made. To propose a mathematical model that quantifies some of these possibilities around the RPSA limit would prove a valuable tool to the design engineer.

This requires a fundamental understanding of the mechanisms that dictate heat and mass transfer within a gas phase adsorption process. A collection of these important mechanisms can be grouped across two distinct regions of the sorbent bed. The first relates to the bed void or *interpellet* region associated with empty void space between individual sorbent pellets: while the second relates to the gas, solid and adsorbed phases located inside each sorbent pellet, commonly termed the *intrapellet* region.

1.2.1 Transport at the Interpellet Level

As the pressure cycles above and/or below a packed bed, gas motion correspondingly changes so that bulk movement is directed towards the region of lowest absolute pressure. In addition to these external forcing boundary conditions, pressure gradients can form within the bed as a result of flow resistance exerted by individual sorbent pellets on the moving gas stream via drag forces. At

low flow rates where the pellet Reynolds number Re_p is of order 1 this flow resistance is proportional to the first power of interstitial velocity v_B and inversely proportional to the square of the equivalent spherical pellet diameter $d_{p,eqv}$ in analogy with the Hagen-Poiseuille relationship for laminar flow [McCabe *et. al.* (1993, p 153)].

$$-\frac{\partial p^B}{\partial z} \propto \frac{v_B}{d_{p,eqv}^2} \text{ for } Re_p < 5 \quad (1.6)$$

As Re_p increases the tortuous flow path around an individual sorbent pellet now gives rise to local losses associated with the contraction and subsequent expansion of the gas phase. These local losses that arise under laminar conditions result in a flow transition that several researchers incorrectly assign as the onset of turbulence [Niven (2002)]. At the fully-turbulent limit an analogy similar to that for turbulent flow in a pipe gives rise to the following relationship for v_B and $d_{p,eqv}$ in relation to flow resistance [McCabe *et. al.* (1993, pp 153-154)].

$$-\frac{\partial p^B}{\partial z} \propto \frac{v_B^2}{d_{p,eqv}} \text{ for } Re_p > 1000 \quad (1.7)$$

At the intermediate Re_p regime a linear combination of the viscous and kinetic energy loss terms has been proposed [Ergun & Orning (1949)]. Using Eqs. (1.6) and (1.7) smaller pellet diameters and higher feed flow rates give rise to larger interpellet pressure drops, hence the need for shorter, wider adsorption columns to partially offset this limitation. The use of structured packings with adsorbing material coated on the surface is one method that has been recently proposed to minimise interpellet pressure drop. Although early data indicates structured sorbents can improve separation performance in relation to pelletised sorbents for some processes [Jaffe & Contescu (2002a), Jaffe *et. al.* (2002b)], this dissertation will not consider the use or modelling of structured sorbents. Instead, attention will be focused towards the use of sorbent materials in spherical pelletised form.

For a packed bed of sorbent material the non-linear relationship between velocity, pressure drop, bed length and pellet size does not provide a simple criterion to ascertain the overall impact of flow resistance under RPSA conditions. For this reason experimental data needs to be obtained under non-adsorbing conditions to independently characterise pressure drop. In conjunction with a mathematical description of pressure driven flow through a packed bed, the impact of pressure drop at the interpellet level can be quantified. This provides one particular research topic addressed within this dissertation.

While interpellet pressure drop is an important mechanism to consider under RPSA conditions, shorter, wider columns with smaller sorbent pellets give rise to other phenomena that can influence the transport of gas from one axial position to another.

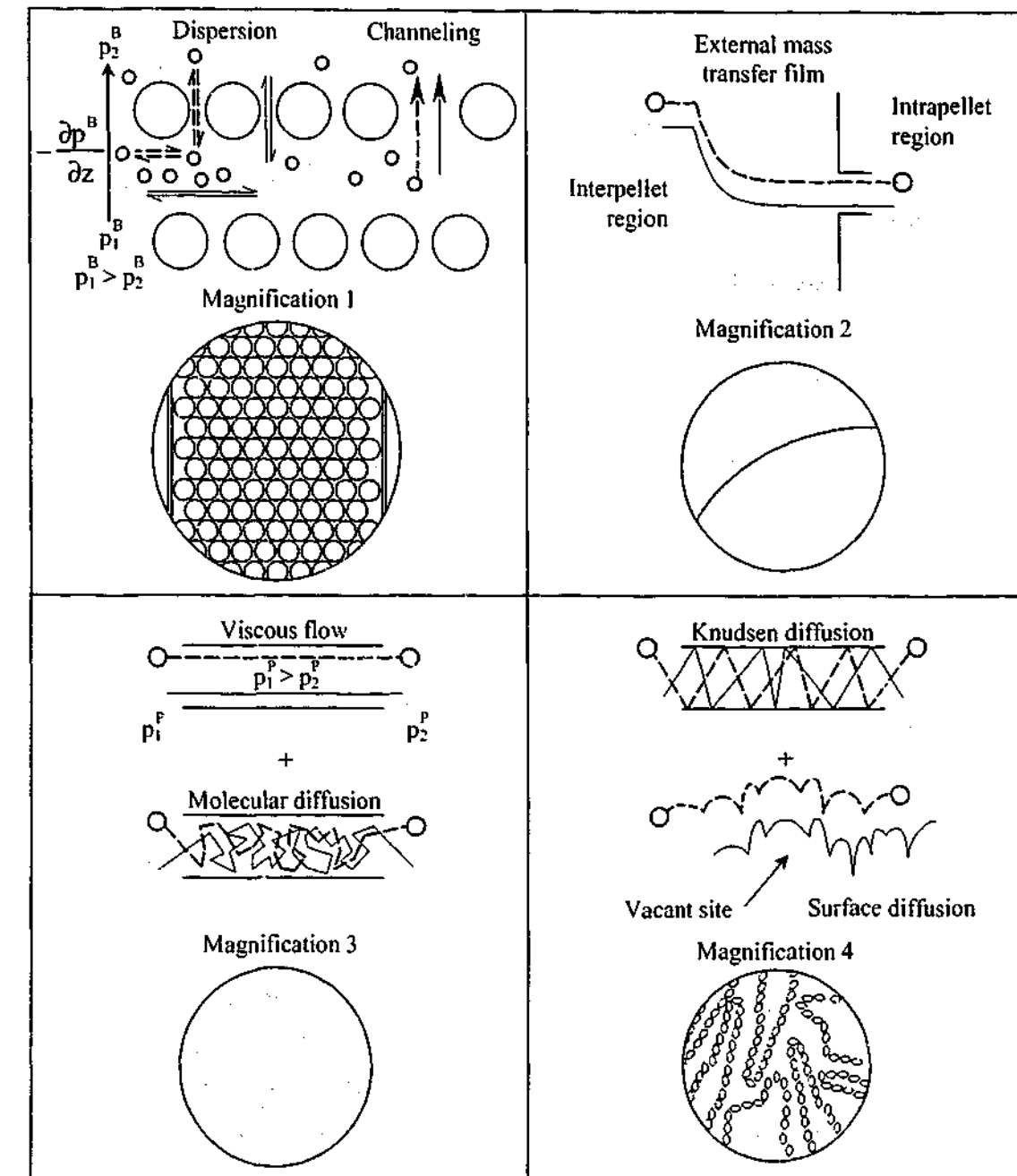


Figure 1.2: Pictorial representation of the various mechanisms that dictate mass transfer within a packed bed of sorbent pellets. Developed from Tien (1994, p 72) and Krishna & Wesselingh (1997).

Diffusion of interpellet gas in addition to the splitting and recombining of flow around sorbent pellets will contribute towards dispersion while channeling can occur when non-uniformities exist in the packing arrangement of sorbent material. Magnification 1 of Fig. 1.2 provides a simplified pictorial analogy of these mechanisms.

Axial Dispersion

The presence of spatial composition gradients will result in dispersion of the gas phase [Choong *et al.* (1998)]. While radial dispersion is often desirable given it minimises concentration profiles formed at regions perpendicular to gas flow, dispersion in the axial direction is undesirable as it can cause premature breakthrough of the strongly-adsorbed component(s) through the upper layers of the bed [Tien (1994, p 72)]. The impact of axial dispersion can be assessed through the magnitude of the dimensionless Peclet mass transfer number at the bed or interpellet scale, $Pe_{B,mass}$ [Liao & Shiau (2000)].

$$Pe_{B,mass} = \frac{v_B L_{bed}}{D_{ax}^e} \quad (1.8)$$

D_{ax}^e represents the effective axial dispersion coefficient, usually calculated from a correlation of the Peclet mass transfer number at the pellet scale, $Pe_{p,mass} (= v_B d_{p,eqv} / D_{ax}^e)$. Correlations for $Pe_{p,mass}$ often involve two additive components, one attributed to turbulent mixing and the other to molecular diffusion. Although D_{ax}^e has been well characterised for non-porous materials [Langer *et al.* (1978)], these same authors suggest independent analysis is required for each specific system when the packing material is porous and catalytic reaction/adsorption occurs. Gunn (1987) addressed this issue and proposed a general correlation for D_{ax}^e that matches experimental data well for both porous and non-porous packing materials of spherical and cylindrical geometry. Complicated equations for materials that are well-packed or not well-packed were presented, with an additional parameter appearing in the not well-packed correlation to describe the dimensionless variance of the radial velocity profile. Assuming a bed of sorbent material is well-packed, typical estimates on the effective axial dispersion coefficient obtained from the correlation of Gunn (1987) for spherical geometry gives D_{ax}^e around $10^{-3} \text{ m}^2 \text{ s}^{-1}$ for operating conditions experimentally encountered throughout this dissertation.

Liao & Shiau (2000) solved the isothermal, axially dispersed plug flow model using the separation of variables technique for linear equilibrium isotherms to assess the impact of axial dispersion within an adsorption system. For values of $Pe_{B,mass}$ greater than 80 the impact of axial dispersion on column profiles was negligible. At the opposite limit where $Pe_{B,mass}$ is less than approximately 10 column profiles were largely influenced by axial dispersion. At intermediate values between these two limits axial dispersion partially contributed to the transport of gas through the interpellet region. The commercial simulation package ADSIM assigns similar values, 100 and 30

respectively, for these two limits [Asp & Tech (1997)]. From these limiting conditions and Eq. (1.8) the product $v_B L_{bed}$ needs to be approximately $0.1 \text{ m}^2 \text{ s}^{-1}$ or higher to neglect axial dispersion. Experimental data presented in this dissertation was performed in a regime where this constraint was satisfied.

Langer *et al.* (1978) indicate a further complication arises for pellets with a diameter below $3.0 \times 10^{-3} \text{ m}$. At these smaller diameters pellets tend to cluster and create small dead zones to interpellet gas flow, effectively increasing axial dispersion that may increase the limiting value of $v_B L_{bed}$ required to maintain the plug flow assumption. Although this particular constraint is difficult to quantify, it is assumed that values of $v_B L_{bed}$ experimentally achieved throughout this dissertation are high enough to neglect axial dispersion of the interpellet gas phase. There is the potential, however, to introduce artificial axial dispersion within a plug flow model via numerical discretisation schemes. This issue will be discussed separately in chapters 3 and 4.

Flow Channeling

Flow channeling is associated with the uneven distribution of pellets and is often difficult to quantify given the random orientation of the sorbent once packed. Flow channelling also becomes a dominant mechanism at low column-to-pellet diameter ratios as the high porosity region located between the pellet layer adjoining the column wall significantly increases velocity in comparison to central regions several pellet diameters away from the wall.

Varying limits on this column-to-pellet diameter ratio have been proposed, ranging from 10 [Gunn (1987)] to 20 [LeVan & Vermeulen (1984)] to 30 for Newtonian and 50 for non-Newtonian fluids [Cohen & Metzner (1981)]. Experimental and numerical data obtained by Vortmeyer & Michael (1985) and Mohamadinejad *et al.* (2000) have found porosity fluctuations at the wall still influence bed profiles with a column-to-pellet diameter ratio of 21 and 15 respectively. Tobis & Vortmeyer (1988) found the experimental data of LeVan & Vermeulen (1984) was also influenced by porosity effects at the wall for a column-to-pellet diameter ratio greater than 100.

From this rather preliminary survey it would appear that column-to-pellet diameter ratios no smaller than 30 should be experimentally maintained, although Tobis & Vortmeyer (1988) suggest otherwise. For the purpose of process modelling, however, it is assumed that a column-to-pellet diameter ratio greater than or equal to 30 is adequate to neglect channeling and allow gas flow to be uniformly distributed over each axial cross-section of the bed [Mohamadinejad *et al.* (2000)]. In this dissertation, experimental values of column-to-pellet diameter ratio are approximately 30:1 in the Length of Unused Bed (LUB) apparatus and 92:1 in the RPSA pilot plant.

1.2.2 Transport between the Interpellet and Intrapellet Regions

As gas composition changes within the interpellet region a concentration gradient forms between the interpellet and intrapellet regions. This driving force causes gas to migrate across the external mass transfer film present at the surface of the pellet and enter/leave the intrapellet pore volume (magnification 2 of Fig. 1.2). The external mass transfer film can be considered a function of the hydrodynamic flow conditions, Re_p , and ratio of the viscous-to-diffusional resistance, Sc , within the interpellet region [Choong & Scott (1998)]. The impact of this external film resistance can be characterised through the dimensionless Biot mass transfer number, Bi_{mass} , which compares the magnitude of the external film coefficient $k_{p,B}$ in relation to the mechanisms of intrapellet mass transfer, defined through an effective intrapellet diffusion coefficient D_i^e .

$$Bi_{mass} = \frac{k_{p,B} R_p}{D_i^e} \quad (1.9)$$

One correlation for Bi_{mass} in terms of Re_p and Sc is given by the following [Yang (1997, p 123)].

$$Bi_{mass} = \frac{0.179}{\epsilon_B} \frac{D_{m,i}}{D_i^e} Re_p^{0.641} Sc^{1/3} \quad (1.10)$$

$D_{m,i}/D_i^e$ is typically of order 10 while $Re_p^{0.641} Sc^{1/3}$ is also of order 10 or higher, implying Bi_{mass} is greater than 1 [Ruthven (1984a, p 217), Yang (1997, p 124)]. This result indicates the transport of gas via intrapellet mass transfer limits the uptake rate of material from the interpellet phase. On this basis external film mass transfer resistance can be neglected across a large range of RPSA operating conditions, leaving intrapellet mass transfer as the limiting mechanism.

1.2.3 Transport at the Intrapellet Level

Commercial sorbent pellets typically used within oxygen RPSA processes are an amalgam of synthetically manufactured aluminosilicate zeolite crystals formed into pellets though the addition of a suitable clay-binding agent. The resulting intrapellet pore space exhibits a bimodal distribution between individual crystals on the micropore scale ($\delta < 2.0 \times 10^{-9}$ m) and interconnecting pore channels between crystals on the macropore scale ($\delta > 5.0 \times 10^{-8}$ m). Intermediate pores between these two limits encompass the mesoporous region (2.0×10^{-9} m $< \delta < 5.0 \times 10^{-8}$ m) in accordance with the IUPAC classification. The clay-binding agent, which often constitutes 10 to 20% of the

total pellet mass, is added to improve crush strength and abrasion resistance of individual zeolite crystals when operated over a PSA cycle [Ruthven (1984a, pp 19-23)]

Macropore Diffusion

From the pellet surface, gas can be assumed to enter macropore channels where molecule-molecule collisions dominate over molecule-wall collisions. Under these conditions molecular diffusion and viscous flow are the dominant modes of gas transport through the pellet (magnification 3 of Fig. 1.2). These channels primarily act as "superhighways" for the transport of gas to the pore opening of an individual zeolite crystal or micropore where the active surface area for adsorption is located.

Micropore Diffusion

Once a micropore is entered gas can then interact with and migrate between active cationic sites located within the three-dimensional cage structure of an individual zeolite crystal, represented by hexagons in magnification 4 of Fig. 1.2. Gas molecules can also migrate within the adsorbed phase to an unoccupied adsorption site by a series of activated jumps that represents surface or micropore diffusion. In this region Knudsen diffusion can also be important if a gas molecule is not readily adsorbed at the cationic surface.

At the intermediate or mesopore level between magnifications 3 and 4 of Fig. 1.2, all four mechanisms may contribute to the total molar flux. In reality, however, the internal structure of a single sorbent pellet is a heterogeneous distribution of pore sizes randomly positioned throughout the pellet. This often reduces a quantitative description of intrapellet mass transfer to an idealised model that separately accounts for at most two distinct pore sizes, one for the macropore and another for the micropore domain that incorporates the above mentioned transport mechanisms at each limit. Even at this rather simplified level a great deal of variation exists in the type of mass transfer model one can use. This requires experimental uptake rate data for the adsorption of gas onto the zeolite to be obtained and then deconvoluted using an appropriate mathematical model incorporating the aforementioned gas transport mechanisms. The form of these models and appropriate experimental techniques will occupy a second research topic of this dissertation.

1.3 Temperature Transients - Is Non-Isothermal Behaviour Important?

When a sorbate molecule is adsorbed from the surrounding gas phase it loses one degree of freedom as it is now constrained on a "two-dimensional surface". Hence the entropy of the molecule decreases when it undergoes adsorption ($\Delta S < 0$, i.e. has gone from a state of disorder to order). Adsorption is a spontaneous process so the Gibbs free energy of the sorbate molecule decreases ($\Delta G < 0$). If we assume the sorbate molecule experiences no temperature change before and after adsorption occurs, the thermodynamic relationship $G = H - T S$ [Çengel & Boles (1994, p 635)] becomes $\Delta G = \Delta H - T \Delta S$ and heat must be liberated by a sorbate molecule during adsorption, $\Delta H < 0$ [Thomas & Crittenden (1998, p 32)]. In reality, however, the sorbate molecule along with the surrounding sorbent and gas phase take up this heat and, according to the first law of thermodynamics, system temperature increases.

If the local temperature of the system is continuously changing the magnitude of intra- and interpellet transport coefficients, which are in general a function of temperature, will also change. A further complicating factor in these situations is the presence of a radial temperature profile that have been:

- i. experimentally observed in columns that do not behave adiabatically [Pentchev *et al.* (2002)] and,
- ii. theoretically predicted in columns where the temperature wave due to the heat of adsorption travels faster than the mass transfer zone [Farooq & Ruthven (1990a)].

Given intra- and interpellet transport processes are coupled in a non-linear manner the overall impact of these temperature transients on system performance is difficult to characterise at this preliminary stage. However, one example of an adsorption separation process that is strongly influenced by temperature transients is oxygen enrichment from air [Wilson (2001), Wilson *et al.* (2001), Wilson & Webley (2002)], the particular PSA process that is of theoretical and experimental interest in this dissertation. From the accumulated knowledge and literature on oxygen PSA/VSA obtained within the adsorption research group at Monash University, non-isothermal behaviour is an important aspect of process operation to consider. This also occupies another field of research that will be considered within this dissertation.

1.4 Why is such a Detailed Analysis of an RPSA Cycle Important?

The architecture of a mathematical model that incorporates the full complexities of the aforementioned physical mechanisms poses a significant challenge computationally, with many variables changing rapidly in time across several domains. In addition, non-isothermal effects associated with a bulk gas separation further complicates the analysis, ultimately leading to a coupled set of non-linear Partial Differential Equations (PDEs).

So why does a model of this complexity warrant investigation over a more traditional and somewhat simplified approach? The physics that describe an adsorption process are coupled in a complex and non-linear manner, limiting the ability to separate one mechanism from the other experimentally. The only realistic way to investigate the importance of each mechanism is through mathematical modelling that allows one to manipulate the magnitude of various parameters in a systematic way around their design values, akin to sensitivity analysis [Leis & Kramer (1988)]. This statement, however, implies the proposed mathematical model adequately captures all of the important phenomena described in §1.2 and §1.3.

Any mathematical model used in this manner should provide an independent method of quantifying each transport coefficient that does not require additional fitting against experimental RPSA data. While methods for establishing some parameters such as pressure drop coefficients within the steady state Ergun equation are well established [Ergun (1952)], methods to independently determine transport coefficients for the "most appropriate" intrapellet mass transfer model are subjective at best. The importance of mass transfer parameters on a rigorous PSA simulator SIMPAC [Kumar *et al.* (1994)] highlighted the fact that small changes made around design input values can affect predicted separation [Hartzog & Sircar (1995)]. For an RPSA process where intrapellet mass transfer is important [Serbezov & Sotirchos (1999)], the selection of an appropriate mass transfer model along with experimental characterisation of these parameters has a large bearing on the predictive ability of the mathematical model.

From this point of view a more fundamental approach is required when the intrusion of intrapellet mass transfer, interpellet pressure drop and temperature transients cannot be neglected. This in turn requires a transparent method of determining physical parameters of the sorbent that can be used as a set of general transport coefficients over a range of experimental conditions independent of the PSA/RPSA operating limit.

1.5 Objectives of this Study

The previous discussion has highlighted several mechanisms that dictate process operation when cycle time approaches the RPSA limit. The ability to predict performance over a range of operating conditions using a model that incorporates these mechanisms is the central theme underlying this dissertation. Therefore, the overall objectives can be summarised as follows:

- i. Develop and validate a detailed adsorption process model that includes a rigorous treatment of mass transfer at the intra- and interpellet level. This also requires efficient numerical techniques to be introduced for the solution of a coupled set of non-linear, first order Ordinary Differential Equations (ODEs).
- ii. Identify the mechanisms that contribute to the transport of gas at the pellet level under macropore diffusion control. Identify the limiting assumptions imposed on existing mass transfer models, such as the Linear Driving Force (LDF) model when simulating adsorption-desorption phenomena within an individual sorbent pellet at the RPSA limit.
- iii. Develop and conduct an independent set of experiments to calibrate the coefficients that describe intra- and interpellet mass transfer within a PSA system for the detailed process model.
- iv. Construct and operate a pilot scale RPSA facility to determine the effect of cycle time reduction on PSA performance and use both the detailed process model and a simplified mechanistic model to explain observed trends in terms of interpellet pressure drop, non-isothermal behaviour and intrapellet mass transfer.

Although theoretical arguments and mathematical models developed throughout this dissertation are general to any PSA cycle, the *enrichment of oxygen from a binary air feed mixture will be the only system considered*. This dissertation is presented over five analysis chapters. The progression of each chapter follows a deliberate methodology that starts at the intrapellet level for an assumed macroporous sorbent pellet (chapter 2) and then progresses to a full process simulator that incorporates the intra- and interpellet conservation equations together in their complete form (chapter 3). Chapter 3 also presents novel CPU optimisation techniques and additional modelling options required to simulate a true RPSA process.

From here, chapter 4 experimentally quantifies transport coefficients at the intrapellet level using the process model as a tool to deconvolute experimental data. In addition to mass transfer parameters, chapter 4 also presents equilibrium isotherm and density/voidage parameters for one particular LiLSX sorbent material that will feature prominently in the experimental analysis. The first part of chapter 5 investigates pressure driven flow through a packed bed of sorbent material under non-adsorbing conditions using both the steady state and full momentum balance. The

second part of this same chapter validates the steady state momentum balance, the Ergun equation, for numerical simulation with experimental data obtained under adsorbing conditions. The final analysis chapter, chapter 6, incorporates all the elements of the first five chapters to compare experimental data obtained from a pilot scale RPSA facility. The detailed process model is used in this chapter to examine the impact of different intrapellet mass transfer models on predicted separation performance. Chapter 6 also compares experimental and numerical results with a simplified predictive model that allows certain qualitative trends in process performance to be understood.

Based on this summary, standard thesis formatting that presents an independent chapter for a literature review has not been adopted and instead a review of the relevant literature at the beginning of each chapter has been made. It is the opinion of the author that a chapter-by-chapter review of the existing literature provides a more relevant and in-depth assessment that ultimately serves as an introduction to the analysis of that particular chapter.

CHAPTER 2

MASS TRANSFER AT THE INTRAPELLET LEVEL

The first analysis chapter of this dissertation examines various assumptions on the transport of gas within a porous sorbent pellet under macropore diffusion control through the development of a rigorous mathematical model. The individual objectives for this chapter are as follows:

- i. Introduce the accumulated literature on mass transfer modelling at the intrapellet level and discuss the need for a detailed mathematical model under RPSA conditions.
 - ii. Validate the numerical implementation of this mathematical model using a known analytical solution.
 - iii. Discuss limitations of the conventional Linear Driving Force (LDF) and equimolar counterdiffusion assumptions in relation to Maxwell-Stefan theory for a two-step adsorption-desorption cycle over a single sorbent pellet under isothermal and non-isothermal conditions.
-

Early models developed for PSA and RPSA cycles alike assumed local equilibrium between the interpellet gas and intrapellet adsorbed phase [Turnock & Kadlec (1971), Shendalam & Mitchell (1972)]. While local equilibrium is a suitable assumption for long cycles that operate over many minutes, typical oxygen PSA and RPSA cycles operate in a regime where intrapellet mass transfer cannot be neglected. Doong & Yang (1986) suggest a model that assumes local equilibrium will begin to deviate from a model that incorporates mass transfer when the dimensionless time parameter θ falls below 43. This situation is most pronounced at the RPSA limit where θ can fall below 1.

Before digressing into a review of the published literature, it is important to quantify this dimensionless time parameter $\theta (= D^e t / R_p^2)$ given it is extensively used to characterise mass transfer at the intrapellet level. When the effective diffusion coefficient is assumed constant, θ usually substitutes dimensional time when the intrapellet conservation equations are recast into dimensionless form. Although time will not explicitly reduce to this form when a Maxwell-Stefan approach to intrapellet mass transfer is adopted, the use of the θ parameter is maintained throughout this dissertation as a guide to the PSA/RPSA limit previously defined by other researchers.

The magnitude of θ is usually in reference to the "adsorption" step(s) of a general PSA cycle given mass transfer has a strong influence on the shape of the breakthrough front and purity of the eluting product gas. Time is usually taken as the difference between start and end absolute time of these step(s). The diffusion coefficient is evaluated at the pressure, temperature and composition experienced over the relevant process step(s), which can be assumed constant or determined through an appropriate averaging technique. In addition, the diffusion coefficient is evaluated in micropore (or surface) diffusion form as often a linear equilibrium isotherm is imposed on the governing conservation equation. This requires the gas phase effective diffusion coefficient D^e to be divided by $[\epsilon_p + \hat{\rho}_p RT_p (\partial n_{i,eq}^p / \partial p_i^p)]$ to maintain θ on an equivalent basis with that considered previously. This means N_c unique values for θ arise, denoted θ_i for $i = 1 \dots N_c$, given each component in general has a different equilibrium isotherm gradient for $\partial n_{i,eq}^p / \partial p_i^p$.

2.1 Previous Studies on Intrapellet Mass Transfer and Adsorption

To quantify the uptake rate of an adsorbing component from the bulk gas phase a large number of models have been proposed [Do (1998)]. These can be broken down into two distinct categories that are delineated through the constitutive flux model.

2.1.1 Fick plus Equimolar Counterdiffusion Mass Transfer Model

The Fick plus equimolar counterdiffusion model, also referred to as Fick's second law of diffusion, has formed the governing flux equation for a large majority of mass transfer models proposed in the literature. Within this subset, the lumped-parameter LDF model has proven the most popular. Glueckauf & Coates (1947) originally derived the LDF model by assuming the rate of diffusion into the pellets, which they referred to as grains, is proportional to the amount still required to produce equilibrium. This is expressed in the following form where $n_{i,eq}^B$ denotes the adsorbed phase concentration in equilibrium with the bulk phase and \tilde{n}_i^p the volume-averaged adsorbed phase concentration over the pellet.

$$\frac{\partial \tilde{n}_i^p}{\partial t} = k_i (n_{i,eq}^B - \tilde{n}_i^p) \text{ for } i = 1 \dots N_c \quad (2.1)$$

k_i was described as a diffusion factor denoting the time in which a sorbent pellet reaches 1/e of its equilibrium capacity. The expression $k_i = D_i^e / (2\psi R_p)^2$ was proposed where ψ depends on the geometry of the pellets ($\psi < 1/2$). Glueckauf (1955) independently derived the LDF model of Eq.

(2.1) starting from Fick's second law of diffusion, providing an analytical expression for the LDF coefficient k_i using successive integration by parts for a continuously varying change in concentration at the pellet surface.

$$k_i = \frac{\Omega_i D_i^e}{R_p^2} \text{ where } \Omega_i = 15 \text{ for } i = 1 \dots N_c \quad (2.2)$$

The Glueckauf & Coates (1947) and Glueckauf (1955) LDF (GLDF) models were best suited to an equilibrium isotherm that exhibits a linear or slightly favourable gradient where the operating conditions were assumed to be relatively close to equilibrium. Alternative functional relationships on $d\tilde{n}_i^p/dt$ have been proposed using different isotherm shapes, one example being the quadratic driving force model of Vermeulen (1953) for irreversible adsorption. However, common equilibrium isotherm gradients observed with nitrogen and oxygen on molecular sieve zeolite exhibits a moderately favourable (i.e. reversible) shape implying the GLDF form is the most appropriate.

One argument central to the GLDF model is the assumption the time rate of change of concentration at the pellet surface can be approximated by the time rate of change of the volume-averaged pellet concentration, $(dn_i/dt)_{R_p} \approx d\tilde{n}_i^p/dt$. When θ_i falls below a critical value this assumption breaks down and the pellet no longer operates at conditions close to equilibrium. Glueckauf (1955), Jury (1967) and Nakao & Suzuki (1983) indicate the critical θ value is 0.10 while Do & Rice (1986) suggest this same limit to be 0.05. To overcome this constraint with the GLDF model under RPSA conditions, several modifications to the governing form of the linearised rate equation have been proposed. These can be conveniently classified into two categories. The first considers alternative functional relationships on the intrapellet concentration profile while the second investigates time dependence on the GLDF constant Ω_i .

Higher Order Intrapellet Concentration Profiles

Liaw *et al.* (1979) demonstrated the GLDF approximation, Eqs. (2.1) and (2.2), is equivalent to the intrapellet concentration profile being parabolic in form under a linear equilibrium isotherm using Fick's second law of diffusion. From this argument extensions to higher order concentration profiles have been investigated. Sircar & Hufton (2000) demonstrate any functional relationship of the form $a_0(t) + a_n(t) F(r)$ can be used in conjunction with Fick's second law of diffusion to model the intrapellet concentration profile provided $F(r)$ is a continuous function in r over $0 \leq r \leq R_p$ that satisfies $dF(r)/dr = 0$ at $r = 0$.

Do & Rice (1986) and Lai & Tan (1991) imposed a quartic intrapellet concentration profile of the form $a_0 + a_2 r^2 + a_4 r^4$ while Do & Mayfield (1987), Bhaskar & Do (1989), Li & Yang (1999) and Basagaoglu *et al.* (2000) considered an n -th order intrapellet profile of the form $a_0 + a_n r^n$. Buzanowski & Yang (1989, 1991a) proposed an extended LDF model using a cubic intrapellet concentration profile of the form $a_0 + a_2 r^2 + a_3 r^3$ to obtain an empirical correction parameter that is added to the standard GLDF model of Eq. (2.1). Do & Rice (1995) considered two different intrapellet approximations, both second order, for the estimation of initial and long time scale pellet uptake profiles for batch adsorption experiments. Tomida & McCoy (1987) transform a general n -th order intrapellet polynomial profile, $\sum_{m=0}^{n/2} a_{2m} r^{2m}$ into the Laplace domain demonstrating this form better approximates the exact analytical solution as more terms are progressively retained within the summation.

Time Corrections on the LDF Coefficient Ω_i

The second modelling alternative at the RPSA limit considers the GLDF constant Ω_i to be a function of cycle time. Nakao & Suzuki (1983) devised a numerical procedure that forces the LDF model to match the working capacity of the analytical solution at Cyclic Steady State (CSS) by adjusting Ω_i for square-wave changes in boundary conditions under equal step times. Alpay & Scott (1992) applied penetration theory for short contact times and obtained an analytical result to the numerical procedure of Nakao & Suzuki (1983) for spherical pellet geometry under equal step times. Scott (1994) extended this to include slab and cylindrical geometries. Carta (1993) transposed the analytical solution of the diffusion equation, along with the LDF model, into the Laplace domain in order to match the working capacities. The resulting infinite series contains the coefficient Ω_i that must be found numerically for a particular value of θ_i . Buzanowski & Yang (1991b) proposed $d\tilde{n}_i^p/dt = n_{i,eq}^b D_i^c [(2.4/\sqrt{\pi\theta_i}) - 2.4]/R_p^2$, a non-driving force approximation that was obtained from a short-time approximation of the analytical solution for $\theta_i \leq 0.1$. Hsuen (2000) proposed an n -th order approximation for Ω_i of the form $a_0 + a_n \theta^n$ during the adsorption step, using the two coefficients a_0 and a_n as fitting parameters to minimise the error between the approximate and exact solutions.

Each of these studies can be thought of as manipulating the original GLDF formulation to match adsorption-desorption response (i.e. working capacity) under short contact times for a sorbent pellet. Harriott (1993) indicates conventional rate laws such as the LDF model fail at short contact times because the concentration history at the pellet surface is not accounted for through the assumption $(dn_i/dt)_{R_p} \approx d\tilde{n}_i^p/dt$. Harriott (1993) then proposed a memory integral method based

on convolution of the unit step response that considers the pellet surface only for dynamic simulation, reducing the solution procedure by eliminating the pellet conservation equations. Through suitable approximations to the kernel of the memory integral the LDF model is recovered.

An additional level of complexity using Ficks' second law of diffusion can be imposed by numerically solving the discretised set of conservation equations over the pellet. Do (1990) used a perturbation method to reduce the complexity of an isothermal pellet model that incorporates all three transport mechanisms (external film, macropore and micropore diffusion) to six degenerate models that considers at most two of these transport mechanisms under various limiting conditions. Brunovská *et al.* (1978) investigated the response of a sorbent pellet under non-isothermal conditions, concluding a process with steep isotherms and high heat of adsorption such as adsorption on zeolites will generate significant temperature deviations that invalidates the isothermal assumption.

2.1.2 Maxwell-Stefan Mass Transfer Model

All of the models considered thus far have incorporated the Fick formulation with equimolar counterdiffusion to describe intrapellet mass transfer. Krishna (1993a) highlighted several flaws inherent with this constitutive model for mass transfer and cites Maxwell-Stefan theory as the only quantitatively correct formulation for multicomponent diffusion.

Within the literature the terms "Maxwell-Stefan" and "Dusty Gas Model (DGM)" are sometimes used interchangeably to describe diffusion through a porous medium, which is not correct. The DGM is only one particular solution to the general Maxwell-Stefan equations for the diffusion of an N_c component gas mixture through an " $N_c + 1$ "th pseudo-species, the so-called dust medium. These dust molecules are fixed in space such that $N_{N_c+1} = 0$ and so provide frictional resistance to the movement of unconstrained gas molecules around them. This frictional resistance between gas-dust molecules manifests as Knudsen diffusion within the DGM and gas-gas interactions as molecular diffusion when formal kinetic theory arguments are applied [Evans *et al.* (1961)]. Hence the DGM refers to one limiting form of the Maxwell-Stefan equations for multicomponent diffusion through a porous medium whereas Maxwell-Stefan theory provides the mechanics through which multicomponent diffusion is quantified. Additional flux contributions from surface diffusion and viscous flow are linearly added to the molecular-Knudsen diffusion terms of the DGM to yield the total intrapellet flux for component i .

The DGM has followed a complex path of rediscoveries and reformulations since its development in the 1860's by James Clerk Maxwell and later in the 1870's by Josef Stefan. This rather lengthy

discussion is reviewed in detail through the monographs of Cunningham & Williams (1980, chapter 6) and Mason & Malinauskas (1983, chapter 1) and so is not repeated here. Only recently, however, has the DGM been considered in unifying the mechanisms of mass transfer typically encountered over a PSA cycle [Krishna (1993b)].

O'Shea & Liapis (1990) provide one of the earliest studies to adopt the DGM under adsorption conditions, investigating the propane-butane-activated carbon system with a process time scale of hours. Simulation results suggest the deviations between a simple and complex pellet model for this system only manifest in situations where steep concentration or temperature gradients form within the pellet. Scholl & Mersmann (1991a, 1991b) developed a non-isothermal, non-isobaric pellet model for single component uptake curves from an inert carrier stream and concluded the formation of intrapellet pressure gradients and hence viscous flow was negligible with most trace component PSA systems. Simulation of a system that has the bulk component adsorbing, however, was not performed.

Given the complexities that exist in solving the full set of intrapellet transport equations for most practical PSA systems, Mendes *et al.* (1994, 1995, 1996) proposed an approximation based on the LDF assumption. The so-called Linear Driving Force approximation to the Dusty Gas (LDF-DG) model was derived by curve-fitting four parameters for each component to the overall diffusion mechanism predicted using a full DGM-viscous flow-surface diffusion pellet model. Each of these parameters is then used to determine an appropriate k_i value in Eq. (2.1). The first parameter is evaluated at CSS using square wave perturbations over a two step cycle to equate the total cumulative flux at the pellet surface, while the second parameter, a "phase lag" parameter, is used to modify the LDF response when smoother boundary conditions are imposed. Two additional parameters were then introduced to quantify intrapellet viscous flow and surface diffusion. These LDF-DG model approximations were derived under isothermal conditions for a binary system using linear and Langmuir isotherms. A complicated empirical equation for each parameter was obtained.

Serbezov & Sotirchos (1997a) examined the DGM and Fick formulations with and without viscous flow in conjunction with the LDF model for binary and quaternary gas mixtures under PSA conditions. They concluded the Fick plus equimolar counterdiffusion and LDF models do not even qualitatively predict dynamic pellet response in relation to the DGM with viscous flow under RPSA conditions. Serbezov & Sotirchos (1998) extended this analysis to the air-5A system under non-isothermal conditions and concluded intrapellet temperature gradients and inter-intrapellet temperature differences are negligible.

Do & Do (1998a) developed an isothermal model for transient uptake from the bulk phase using the DGM coupled with viscous flow and surface diffusion for a single capillary and an activated carbon pellet. Comparisons between numerical and experimental data for the nitrogen-ethane-propane system over activated carbon show good quantitative agreement. Do & Do (1998b) extended this analysis to consider non-isothermal behaviour. Mugge *et al.* (2000, 2001) examined uptake curves on activated carbon extrudates using the non-isothermal, non-isobaric DGM with viscous flow and surface diffusion. They found all intrapellet transport mechanisms contributed to the total molar flux, where the surface diffusion coefficient was used as the single fitting parameter to experimental data.

An analogy with the Maxwell-Stefan model for molecular-Knudsen diffusion (DGM) has also been developed for surface diffusion, where the " $N_c + 1$ "th component now becomes the vacant adsorption sites and the remaining N_c terms the adsorbed phase molecules for each component. Krishna (1990), Krishna (1995), Krishna & van den Broeke (1995), Do & Do (1998b) and Krishna *et al.* (1999) have adopted this Maxwell-Stefan approach to surface diffusion for various zeolite and activated carbon systems.

Although by no means exhaustive, this introductory discussion has outlined a variety of analytical and numerical techniques previously used to quantify mass transfer at the pellet level under PSA conditions. The rest of this chapter will focus on the development and implementation of various models that describe mass transfer at the intrapellet level, particularly around the RPSA limit^{††}.

2.2 Conservation and Flux Equations for the Pellet Model

Only a select number of the governing conservation equations will be presented in this discussion and appendix A should be referenced for a complete derivation. The form of the conservation of mass and energy for an isotropic sorbent pellet of spherical geometry can be written as follows.

$$\left(\frac{\epsilon_p}{RT_p} + \hat{\rho}_p \frac{\partial n_{i,eq}^p}{\partial p_i^p} \right) \frac{\partial p_i^p}{\partial t} + \sum_{j=1, j \neq i}^{N_c} \left(\hat{\rho}_p \frac{\partial n_{i,eq}^p}{\partial p_j^p} \right) \frac{\partial p_j^p}{\partial t} + \left(\hat{\rho}_p \frac{\partial n_{i,eq}^p}{\partial T_p} - \frac{\epsilon_p p_i^p}{RT_p^2} \right) \frac{\partial T_p}{\partial t} = - \frac{1}{r^2} \frac{\partial}{\partial r} (r^2 N_i) \quad \text{for } i = 1 \dots N_c \quad (2.3)$$

^{††} Please note the isothermal analysis of this chapter has been recently published in Chemical Engineering Science [Todd & Webley (2002a)] while the non-isothermal analysis was presented at the 2002 AIChE annual meeting in Indianapolis [Todd & Webley (2002b)]

$$\left\{ \hat{\rho}_p \hat{c}_s + \sum_{i=1}^{N_c} \left[\frac{\epsilon_p \rho_i^p}{RT_p} \left(c_{g,i}^p - \frac{H_{g,i}^p}{T_p} \right) + \hat{\rho}_p n_{i,eq}^p c_{g,i}^p + \hat{\rho}_p (H_{g,i}^p - q_i^p) \frac{\partial n_{i,eq}^p}{\partial T_p} \right] \right\} \frac{\partial T_p}{\partial t} + \left[\sum_{i=1}^{N_c} \frac{\partial p_i^p}{\partial t} \left(\frac{\epsilon_p H_{g,i}^p}{RT_p} - \epsilon_p 10^5 + \sum_{j=1}^{N_c} \hat{\rho}_p (H_{g,j}^p - q_j^p) \frac{\partial n_{j,eq}^p}{\partial p_i^p} \right) \right] = -\frac{1}{r^2} \frac{\partial}{\partial r} \left(r^2 \sum_{i=1}^{N_c} N_i H_{g,i}^p \right) - \frac{1}{r^2} \frac{\partial}{\partial r} \left(r^2 \lambda_p^e \frac{\partial T_p}{\partial r} \right) \quad (2.4)$$

To simulate an isothermal process the temporal derivative on temperature contained in Eq. (2.3) is set to zero and the conservation of energy, Eq. (2.4), becomes redundant. For this reason the equivalent isothermal pellet model is not shown here but can be found in §A.1 of appendix A. In its current form the conservation of energy allows finite temperature gradients to form within the pellet. However the final working version of the pellet model assumes a uniform radial temperature profile exists. To assess the validity of this assumption it is common to ascertain the magnitude of the dimensionless Biot and Fourier heat transfer numbers, Bi_{heat} and Fo_{heat} respectively, for a sorbent pellet.

The dimensionless Biot heat transfer number defines the ratio of the external-to-internal heat transfer rates ($Bi_{heat} = h_{p,b} R_p / 3\lambda_p^e$), which for most practical adsorption processes is less than one [Ruthven (1984a, p 217), Yang (1997, p 124)]. This indicates the resistance to heat transfer lies within the external film, a result confirmed by experimental data obtained for a single zeolite [Ilavský *et al.* (1980)] and catalyst pellet [Kehoe & Butt (1972), Carberry (1975)]. The dimensionless Fourier heat transfer number provides a dimensionless estimate of the time required to dissipate a temperature gradient between $r = 0$ and $r = R_p$. Fo_{heat} is of the form $t_{heat} D_{therm}^e / R_p^2$ [Incropera & DeWitt (1990, p 238)], where t_{heat} is a characteristic time for intrapellet heat transfer and D_{therm}^e represents thermal diffusivity, given by $\lambda_p^e / \hat{\rho}_p \hat{c}_s$. Typical values of thermal diffusivity for a sorbent pellet range between 10^{-6} and $10^{-7} \text{ m}^2 \text{ s}^{-1}$ [Murray (1996)], while R_p is of order 10^{-3} m . When $Bi_{heat} < 1$, $Fo_{heat} = 1$ indicates the pellet is less than 10% away from thermal equilibrium [Incropera & DeWitt (1990, p 250)], giving rise to a heat transfer time t_{heat} of approximately 1 s. This dimensionless analysis, however, neglects internal generation of heat that occurs during gas adsorption and the effective R_p value to use in Fo_{heat} could be at least one order of magnitude smaller.

Estimates of internal heat transfer rates using Fo_{heat} and intra- to interpellet heat transfer resistance through Bi_{heat} indicate the uniform temperature assumption for a sorbent pellet is well justified,

allowing the conservation of energy to be integrated over the entire pellet domain to develop one unique equation for $\partial T_p / \partial t$. The conservation equations, Eqs. (2.3) and (2.4) require a constitutive relationship for the molar flux N_i within the pellet. As shown previously, Fig. 1.2, there are four intrapellet mass transfer mechanisms that limit instantaneous uptake of gas from the interpellet region. Further to this each mechanism occurs to varying extents within two distinct regions of the pellet: macropores, where viscous flow and molecular diffusion is dominant and micropores, where surface and Knudsen diffusion is dominant. The total intrapellet molar flux for component i can be thought of as the summation of three individual transport mechanisms, where Knudsen and molecular diffusion are coupled.

$$N_i = N_i^D (\text{molecular + Knudsen diffusion}) + N_i^V (\text{viscous flow}) + N_i^S (\text{surface diffusion}) \quad \text{for } i = 1 \dots N_c \quad (2.5)$$

The assumption of a uniform intrapellet temperature profile eliminates thermal diffusion and transpiration becoming additional diffusive mechanisms within N_i^D . An analogy with circuit theory is shown in Fig. 2.1 that pictorially describes the interaction between each of the four transport mechanisms on the overall molar flux for component i . According to Fig. 2.1 molecular and Knudsen diffusion add like resistors in series (through the concentration gradient or driving force $\partial p_i^p / \partial r$, equivalent to voltage) and surface diffusion, viscous flow and molecular-Knudsen diffusion add like resistors in parallel (equivalent to current). This mnemonic explanation has been used several times when deriving the intrapellet molar flux through alternative theoretical arguments [Mason & Evans (1969), Jackson (1977), Mason & Malinauskas (1983), Serbezov & Sotirchos (1997a)].

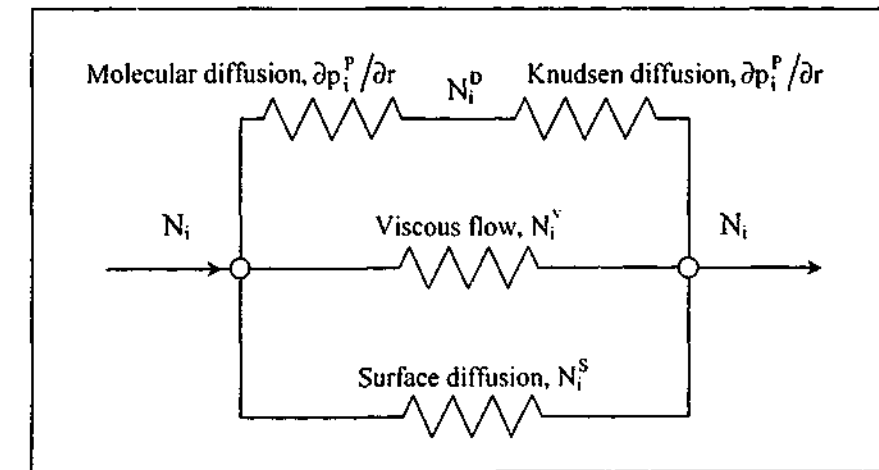


Figure 2.1: Pictorial representation using an electrical analog for combined intrapellet diffusive and viscous fluxes, developed from Mason & Evans (1969).

Coupling Knudsen and molecular transport into the one diffusive mechanism, N_i^D , is a direct result of unifying arguments from the DGM for gas transport across the macropore-mesopore-micropore size range. It will be shown later the mechanism that gives rise to Knudsen diffusion is still retained at the macropore limit. Hence Knudsen diffusion is not exclusively restricted to the micropore domain when considered through Maxwell-Stefan theory.

2.2.1 Isobaric Diffusion Transport Mechanism

A rigorous kinetic theory model of the isobaric diffusion mechanism, derived from momentum transfer arguments, is given by the following [Jackson (1977, p 23)].

Dusty Gas Model (DGM) constitutive equation

$$\frac{N_i^D}{D_{K,i}^e} + \sum_{j=1, j \neq i}^{N_c} \left(\frac{y_j^p N_i^D - y_i^p N_j^D}{D_{m,ij}^e} \right) = -\frac{1}{RT_p} \frac{\partial p_i^p}{\partial r} \quad \text{for } i = 1 \dots N_c \quad (2.6)$$

When Eq. (2.6) is coupled with the intrapellet conservation equations the resulting pellet model is abbreviated the DGM. Effective diffusion coefficients (or inverse drag coefficients as described by some researchers) arise from the extended diffusion path an N_c component gas mixture must traverse when moving around stationary dust molecules. For this dissertation it is assumed the functionality of these variables can be represented in the following manner.

$$D_{m,ij}^e = C_m D_{m,ij} \quad \text{and} \quad D_{K,i}^e = C_K D_{K,i} \quad \text{for } i, j = 1 \dots N_c \text{ and } i \neq j \quad (2.7)$$

The transport coefficients C_m and C_K are commonly defined in the literature as (ϵ_p/τ_m) and (ϵ_p/τ_K) respectively. The voidage correction factor ϵ_p indicates the volume available for diffusion is only a small fraction of the total intrapellet volume. The tortuosity correction factor τ , usually greater than 1, reduces the magnitude of the true or "unhindered" diffusion coefficient by an amount that represents the interconnectedness of randomly oriented pore channels surrounding the structural matrix for each transport mechanism. The molecular diffusion coefficient $D_{m,ij}$ is often correlated from kinetic theory using the first approximation to the Chapman-Enskog procedure at low gas densities [Hirschfelder *et al.* (1954, p 539)].

$$D_{m,ij} = 1.8829 \times 10^{-7} \frac{\sqrt{T_p^3 (M_i + M_j) / M_i M_j}}{p^p \sigma_{ij}^2 \Omega_{ij}^{(1,1)*}} \quad \text{for } i, j = 1 \dots N_c \text{ and } i \neq j \quad (2.8)$$

The Knudsen coefficient $D_{K,i}$ can be evaluated using Eq. (2.8) for the interaction between a gas and dust molecule within the pseudo " $N_c + 1$ " component mixture [Evans *et al.* (1961)]. Alternatively, the Knudsen coefficient can be found from the mean speed of gas molecules at low pressure using Maxwell's distribution function [Present (1958, p 60)]. These two formulations are equivalent and the final result can be represented in the following manner.

$$D_{K,i} = \frac{2}{3} \left(\frac{8 \cdot 10^5 RT_p}{\pi M_i / 10^3} \right)^{1/2} \frac{\delta}{2} \approx 48.5 \left(\frac{T_p}{M_i} \right)^{1/2} \delta \quad \text{for } i = 1 \dots N_c \quad (2.9)$$

Although the DGM is derived from rigorous kinetic theory arguments proposed by Maxwell and Stefan [Taylor & Krishna (1993, pp 14-17)], Mason & Evans (1969) demonstrated a simpler approach can be used that involves the diffusion of a gas mixture at the two limits of intrapellet pore size under isobaric conditions. In the molecular diffusion regime where the dimension of the pore is assumed larger than the mean free path between molecule collisions, the binary version of the Fick model including bulk gas flow can be written in the following form.

$$\frac{y_j^p N_i^D - y_i^p N_j^D}{D_{m,ij}} = -\frac{1}{RT_p} \frac{\partial p_i^p}{\partial r} \quad \text{for } i = 1, 2 \text{ and } i \neq j \quad (2.10)$$

The term on the left-hand side of Eq. (2.10) represents the momentum transferred from species i to species j and $\partial p_i^p / \partial r$ represents the rate of change of momentum for species i per unit volume. Extending this argument to N_c components simply adds additional momentum transfer terms between each combination for species i and j ($j \neq i$) to the left-hand side of Eq. (2.10).

$$\sum_{j=1, j \neq i}^{N_c} \left(\frac{y_j^p N_i^D - y_i^p N_j^D}{D_{m,ij}} \right) = -\frac{1}{RT_p} \frac{\partial p_i^p}{\partial r} \quad \text{for } i = 1 \dots N_c \quad (2.11)$$

At the opposite limit where the mean free path length of an individual molecule is larger than the intrapellet pore dimension such that molecule-wall collisions dominate, the mechanism of Knudsen diffusion prevails [Present (1958, pp 55-60)].

$$N_i^D = -\frac{D_{K,i}}{RT} \frac{\partial p_i^p}{\partial r} \quad \text{for } i = 1 \dots N_c \quad (2.12)$$

Using the argument that momentum transfer terms are linearly additive through the partial pressure derivative (Fig. 2.1) couples Eqs. (2.11) and (2.12) through the intermediate regime between molecular and Knudsen flow. To do this requires some information regarding the pathway for gas transport and so the diffusion coefficients are scaled by the equivalent transport coefficients defined in Eq. (2.7).

$$\frac{N_i^D}{D_{k,i}^c} + \sum_{j=1, j \neq i}^{N_c} \left(\frac{y_j^p N_j^D - y_i^p N_i^D}{D_{m,ij}^c} \right) = -\frac{1}{RT_p} \frac{\partial p_i^p}{\partial r} \quad \text{for } i = 1 \dots N_c \quad (2.13)$$

Equation (2.13) is fully consistent with the DGM of Eq. (2.6) and so provides an additional method of obtaining the flux equations using a Fick formulation. It should be noted that this derivation is built upon weak physical arguments borrowed from the final form of the kinetic theory result. It does, however, provide a conceptual picture for combined Knudsen and molecular transport for the case where intrapellet pore diameter δ is comparable to the mean free path length between gas molecule collisions.

If the assumption of equimolar counterdiffusion is now imposed within the pellet such that bulk gas motion is zero, a simplified diffusion equation results. At the limit of molecular diffusion for a binary system flowing under isobaric conditions the molar flux reduces to Fick's first law of diffusion.

$$N_i^D \equiv -\frac{D_{m,ij}}{RT} \frac{\partial p_i^p}{\partial r} \quad \text{for } i = 1, 2 \text{ and } i \neq j \quad (2.14)$$

Applying the momentum transfer argument of Fig. 2.1 to combine Eq. (2.14) with the Knudsen result, Eq. (2.12), gives the following where the diffusion coefficients are scaled by the equivalent transport coefficients of Eq. (2.7) for a porous medium.

$$N_i^D = -\frac{\left(\frac{1}{D_{k,i}^c} + \frac{1}{D_{m,ij}^c} \right)^{-1}}{RT_p} \frac{\partial p_i^p}{\partial r} \quad \text{for } i = 1, 2 \text{ and } i \neq j \quad (2.15)$$

To extend this concept to an N_c component system is not obvious and a modified molecular diffusion coefficient is used [Serbezov & Sotirchos (1997a)].

Fick's First Law (FFL) constitutive equation

$$N_i^D = -\frac{\left(\frac{1}{D_{k,i}^c} + \frac{1}{D_{m,i}^c} \right)^{-1}}{RT_p} \frac{\partial p_i^p}{\partial r} \quad \text{for } i = 1 \dots N_c \quad (2.16)$$

Equation (2.16) is equivalent to Fick's first law of diffusion [Crank (1975, p 2)]. When this is coupled with the intrapellet conservation equations the resulting pellet model is abbreviated FFL. The modified molecular diffusion coefficient $D_{m,i}^c$ is often correlated using the Wilke approximation [Wilke (1950a)].

$$D_{m,i}^c = \frac{1 - y_i^p}{\left(\sum_{j=1, j \neq i}^{N_c} y_j^p / D_{m,ij}^c \right)} \quad \text{for } N_c \geq 2 \quad (2.17)$$

For a binary system, Eq. (2.17) reduces to $D_{m,ij}^c$. The diffusion coefficient defined within the FFL is equivalent to the Bosanquet formulation for diffusion within a porous medium [Pollard & Present (1948)], providing some insight into the applicability of the Bosanquet assumption.

2.2.2 Viscous Flow Transport Mechanism

The previous section presented equations for the diffusive component of the intrapellet molar flux. Coupled with this transport mechanism is viscous flow that arises when finite pressure gradients form across the pellet. This mechanism is obtained by considering pressure driven flow within a single capillary, Poiseuille flow, and extrapolating the result to a porous medium through the introduction of an effective transport coefficient.

$$N_i^V = -\frac{y_i^p}{RT_p} \left(\frac{B^c p^p}{10^{-5} \mu_p} \right) \frac{\partial p^p}{\partial r} \quad \text{for } i = 1 \dots N_c \quad (2.18)$$

The factor 10^{-5} converts viscosity from units of Pa s to bar.s. Mixture viscosity at low gas density, μ_p , is found using the Wilke approximation [Wilke (1950b)] from the correlation of Stiel & Thodos (1961) for pure component viscosity. The effective pellet permeability coefficient B^c applies a transport coefficient C_v , similar to that for $D_{m,ij}^c$ and $D_{k,i}^c$ of Eq. (2.7), to the analytical value of B^c obtained for a single tube of circular cross section [Jackson (1977, pp 14-15)].

$$B^c = C_v \frac{\delta^2}{32} \text{ where } C_v = \epsilon_p / \tau_v \quad (2.19)$$

Combining the result of Eq. (2.6) with Eq. (2.18) through Eq. (2.5) with $N_i^S = 0$ provides one single transport equation for the combined mechanisms of viscous flow and diffusion.

Viscous Flow plus Dusty Gas Model (VF+DGM) constitutive equation

$$\frac{N_i}{D_{k,i}^c} + \sum_{j=1, j \neq i}^{N_c} \left(\frac{y_j^p N_i - y_i^p N_j}{D_{m,ij}^c} \right) = -\frac{1}{RT_p} \frac{\partial p_i^p}{\partial r} - \frac{p_i^p}{RT_p} \left(\frac{B^c}{10^{-5} \mu_p D_{k,i}^c} \right) \frac{\partial p^p}{\partial r} \text{ for } i = 1 \dots N_c \quad (2.20)$$

Equation (2.20) is termed the viscous flow plus dusty gas model and when coupled with the intrapellet conservation equations is abbreviated the VF+DGM.

2.2.3 Surface Diffusion Transport Mechanism

The mechanism of surface diffusion (also called solid, configurational, intra-crystalline or micropore diffusion) is important for strongly adsorbed species or highly microporous materials such as activated carbon [Krishna & Wesselingh (1997)]. Under these conditions it is assumed that adsorbed molecules never escape the force field of the surrounding pore walls, even at the center of the pore. Diffusion occurs through an activated process where adsorbed molecules migrate between regions of low potential energy or vacant sites. Krishna (1990, 1993b) and Krishna & Wesselingh (1997) examined surface diffusion using similar arguments to those proposed through the DGM for gas phase diffusion, where now the vacant sites are considered to be the " N_c+1 "th pseudo-species of the N_c component system. As with the DGM, these vacant sites are assumed stationary such that $N_{N_c+1}^S = 0$.

$$\frac{1}{\hat{p}_p \epsilon_p n_{eq,sat}^p} \left[\frac{N_i^S}{D_{s,i}} + \sum_{j=1, j \neq i}^{N_c} \left(\frac{\vartheta_j N_i^S - \vartheta_i N_j^S}{D_{s,ij}} \right) \right] = -\frac{\vartheta_i}{RT_p} \frac{\partial \Xi_i}{\partial r} \text{ for } i = 1 \dots N_c \quad (2.21)$$

The first term in the [] bracket on the left hand side of Eq. (2.21) accounts for the frictional resistance exerted on species i by vacant sites and the second term in the [] bracket to the friction exerted by adsorbed species j on the surface transport of component i . The surface diffusion flux N_i^S for component i in Eq. (2.21) is defined as $\hat{p}_p \epsilon_p n_{eq,sat}^p \vartheta_i v_i^S$, where $n_{eq,sat}^p$ represents the total saturation concentration of adsorbed species, ϑ_i the fraction of adsorbed sites occupied by species

i and v_i^S a surface velocity for component i . $\partial \Xi_i / \partial r$ is the surface chemical potential gradient that tends to move species i along the surface, which can be expressed in terms of the gradient in surface occupancy through the introduction of a thermodynamic correction factor Γ_{ij} .

$$\frac{\vartheta_i}{RT_p} \frac{\partial \Xi_i}{\partial r} = \sum_{j=1}^{N_c} \left(\Gamma_{ij} \frac{\partial \vartheta_j}{\partial r} \right) \text{ where } \Gamma_{ij} = \vartheta_i \frac{\partial \ln p_i^p}{\partial \vartheta_j} \text{ for } i = 1 \dots N_c \quad (2.22)$$

The thermodynamic correction factor Γ_{ij} is related to the equilibrium isotherm and hence is particular to each type of isotherm equation. The binary surface diffusion coefficient $D_{s,ij}$ represents the exchange of species j with species i at an adsorption site. The diffusivity coefficient $D_{s,i}$ between adsorbed species i and vacant sites is analogous to Knudsen diffusivity within the DGM and can be related to surface coverage and atomic jump frequency [Riekert (1971), Reed & Ehrlich (1981), Zhadanov (1988)].

2.2.4 Limiting forms of the Flux Equations

Combining the foregoing analysis for each mechanism through Eq. (2.5) allows a unified picture of transport within a porous sorbent pellet to be constructed. However the implicit nature of each transport mechanism in relation to the corresponding driving force often means a simple analytical form to the complete transport equation is not readily available. A comparison of the relative magnitude of each transport coefficient, represented here as effective diffusivities, can be seen at various limits of pressure and intrapellet pore diameter in Fig. 2.2. From this, two limiting forms of the transport equations can be derived for two extremes of intrapellet pore dimension and/or pressure.

Micropore/Low Pressure Limit

At the limit of small pore size and/or pressure the mean free path length is comparable to the intrapellet pore dimension. Equation (2.8) indicates $D_{m,ij}^c$ is proportional to $1/p^p$ and Eq. (2.9) shows $D_{k,i}^c$ is proportional to δ . From this $1/D_{m,ij}^c \ll 1/D_{k,i}^c$ and the DGM reduces to Knudsen diffusion [Hite & Jackson (1977)]. The permeability coefficient B^c of Eq. (2.19) is proportional to the square of δ , allowing viscous flow in Eq. (2.5) to be neglected. Assuming the contribution to transport via surface diffusion is negligible, the following transport equation is derived.

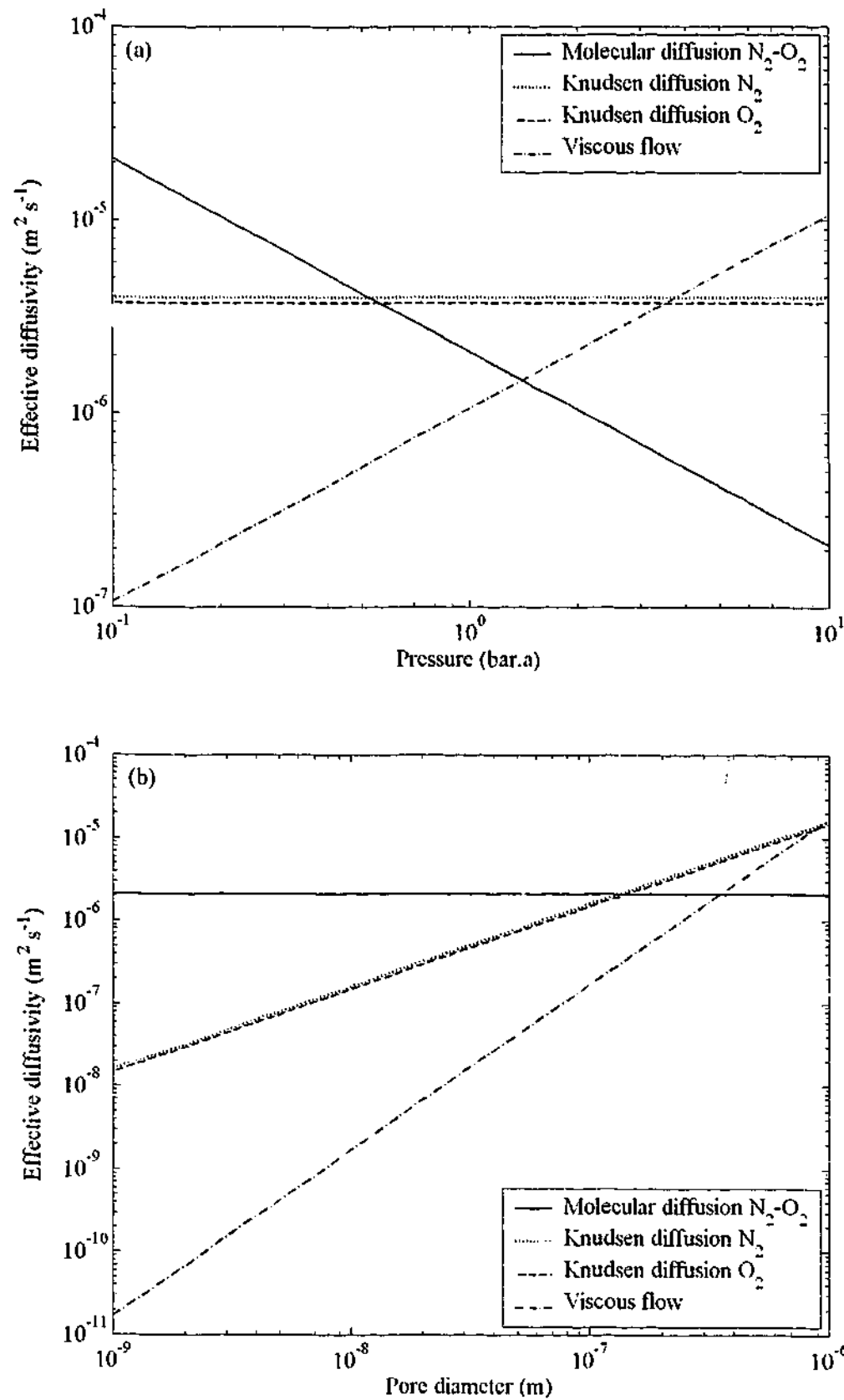


Figure 2.2: (a) Effective diffusivity as a function of pressure at $T_p = 300$ K, $\delta = 2.5 \times 10^{-7}$ m and $C_k = C_m = C_s = 0.1$. (b) Effective diffusivity as a function of pore diameter at $T_p = 300$ K, $p^p = 1$ bar.a and C_k, C_m and $C_s = 0.1$

$$N_i = -\frac{D_{k,i}^c}{RT_p} \frac{\partial p_i^p}{\partial r} \quad \text{for } i = 1 \dots N_c \quad (2.23)$$

Although surface diffusion cannot be neglected in most practical situations at the micropore limit, the result of Eq. (2.23) is used within this dissertation solely for analytical verification of various numerical models and to investigate the impact of equimolar counterdiffusion at the macro-mesopore limit. Outside of these two cases discussed in this chapter and §3.4.2, no reference to micropore diffusion control will be made.

Macropore/High Pressure Limit

Although it may seem customary under these conditions to ignore Knudsen diffusion from the DGM, doing so will lead to an inconsistent set of diffusion equations. Dropping the term $N_i^p/D_{k,i}^c$ out of Eq. (2.6) and summing for all i results in the left hand side j -summation vanishing where as in general, the right hand side does not [Jackson (1977, p 37)]. To overcome this inconsistency the DGM is combined with the viscous flux of Eq. (2.18) and rearranged using Eq. (2.5) with $N_i^s = 0$ to yield the following [Jackson (1977, pp 34-36)].

$$\sum_{i=1}^{N_c} \left(\frac{N_i}{D_{k,i}^c} \right) = -\frac{1}{RT_p} \left[1 + \left(\frac{B^c p^p}{\mu_p} \right) \sum_{j=1}^{N_c} \left(\frac{y_j^p}{D_{k,j}^c} \right) \right] \frac{\partial p^p}{\partial r} \quad (2.24)$$

$$\sum_{j=1, j \neq i}^{N_c} \left\{ (y_j^p N_i - y_i^p N_j) \left[\frac{1}{D_{m,ij}^c} + \frac{1}{D_{k,i}^c D_{k,j}^c \sum_{k=1}^{N_c} (y_k^p / D_{k,k}^c)} \right] \right\} = -\frac{p^p}{RT_p} \frac{\partial y_i^p}{\partial r} - \frac{y_i^p}{RT_p} \left[1 - \frac{1}{D_{k,i}^c} \sum_{j=1}^{N_c} \left(\frac{y_j^p}{D_{k,j}^c} \right)^{-1} \right] \frac{\partial p^p}{\partial r} \quad \text{for } i = 1 \dots N_c \quad (2.25)$$

At the limit of large pore size and/or pressure the term $(B^c p^p / \mu_p) \sum_{i=1}^{N_c} (y_i^p / D_{k,i}^c)$, which is proportional to p^p and δ , is assumed to be much greater than 1. Exploiting the dependence of $D_{m,ij}^c$ and $D_{k,i}^c$ on p^p and δ already mentioned shows that for the macropore limit, Eqs. (2.24) and (2.25) reduce to the following [Jackson (1977, p 40)].

$$\sum_{i=1}^{N_c} \left(\frac{N_i}{D_{k,i}^c} \right) = - \frac{B^c p^p}{\mu_p RT_p} \left(\sum_{i=1}^{N_c} \frac{y_i^p}{D_{k,i}^c} \right) \frac{\partial p^p}{\partial r} \quad \text{for } i = 1 \dots N_c \quad (2.26)$$

$$\sum_{j=1, j \neq i}^{N_c} \left(\frac{y_j^p N_i - y_i^p N_j}{D_{m,ij}^c} \right) = - \frac{p^p}{RT_p} \frac{\partial y_i^p}{\partial r} - \frac{y_i^p}{RT_p} \left[1 - \frac{1}{D_{k,i}^c} \sum_{j=1}^{N_c} \left(\frac{y_j^p}{D_{k,j}^c} \right)^{-1} \right] \frac{\partial p^p}{\partial r} \quad \text{for } i = 1 \dots N_c \quad (2.27)$$

Equations (2.26) and (2.27) suggest Knudsen diffusion also controls mass transfer at the macropore limit. Closer inspection reveals the ratio of these coefficients is present. Using Eq. (2.9), a ratio of the Knudsen coefficients reduces to the ratio of the square root of molecular weight so Eqs. (2.26) and (2.27) depend on the magnitude of the molecular diffusion and permeability coefficients only as expected.

It is useful, however, to note the mechanism that gives rise to Knudsen diffusion within the DGM does not disappear, suggesting the interaction between a gas and dust molecule even at the macropore limit is still an essential aspect of the model to maintain. In reality the limit of a completely macroporous sorbent pellet is rarely encountered so the individual mechanisms of molecular-Knudsen diffusion are maintained within the pellet model for all cases considered in this dissertation.

For zeolite sorbents commonly used with the enrichment of oxygen from air, macropore diffusion control is attributed as the limiting mechanism for intrapellet mass transfer [Ruthven (1984a, pp 154-155), Ruthven & Xu (1993), Aipay *et al.* (1994), Murray (1996), Suzuki *et al.* (1996), Arvind *et al.* (2002), Rittig *et al.* (2002, 2003), Valyon *et al.* (2003)]. The mechanisms of molecular diffusion and viscous flow are commonly associated with macropore diffusion control while Knudsen diffusion is present because of the coupled nature of diffusion described using Maxwell-Stefan theory (i.e. Eqs. (2.26) and (2.27)). Therefore, macropore diffusion control neglects any contribution from surface diffusion to the overall transport of gas through a sorbent pellet. To investigate this assumption further, consider the time scale for surface diffusion within a single zeolite crystal (i.e. micropore channel) within a sorbent pellet. Ruthven & Xu (1993) found the half time for surface diffusion of oxygen and nitrogen within 5A crystals was approximately 3×10^{-4} s at ambient conditions. They also point out that "diffusion in 5A is substantially slower than in 13X reflecting the smaller pore size of 5A". From this one can assume the resistance to surface diffusion in X-type zeolites is many orders of magnitude smaller than mechanisms associated with macropore diffusion control.

2.2.5 Numerical Solution of the Discretised Pellet Model

The conservation equations imposed on the VF+DGM, DGM and FFL are each a function of the N_c partial pressure and temperature derivatives. Also the multipliers on each of the derivative terms are in themselves functions of the dependent variables. This often precludes an analytical solution from being found in all but the simplest of cases, requiring a numerical approach to solve the conservation equations in their most general form. The finite volume method[†] [Botte *et al.* (2000)] is used exclusively throughout this dissertation to ensure a mass balance performed over the discretised region closes to integrator tolerance, irrespective of the spatial resolution. The pellet domain is divided into N_r spherical regions of equal volume [Sun & LeVan (1995)] and the conservation of mass, Eq. (2.3) integrated over each spherical control volume. The conservation of energy neglects radial temperature gradients so the finite volume in this case is the entire pellet, providing one ODE for temperature. In the interest of space the discretised form of the conservation equations are not presented here but rather can be found in §A.2 of appendix A.

The resulting set of $N_r N_c$ partial pressure ODEs for each intrapellet flux equation along with the corresponding temperature ODE is integrated in the time domain using VODE [Brown *et al.* (1989)]. A custom written Fortran90 program was developed to interface directly with VODE and provide the necessary subroutines to invoke any user-defined cycle on the pellet. The final working version of this program is called SimPell (short for Simulation of Pellet model) which essentially solves a Discretised Pellet Model (DPM) for each of the three previously highlighted intrapellet flux models using the same set of boundary conditions.

2.3 LDF Approximation to the Conservation Equations

In addition to three DPMs, SimPell also contains two LDF approximations to the governing conservation equations. These LDF approximations eliminate the need to discretise the radial domain by volume-averaging the conservation of mass over the entire pellet. This reduces the intrapellet PDE for component i to a single ODE that only requires the molar flux entering and leaving the pellet at $r = R_p$ to elucidate dynamic response (see §A.3 of appendix A for a more detailed discussion).

[†] The finite volume method can be defined as a discretisation scheme that starts by integrating the differential equations over a set of predefined control volumes [Morton (1996, p 215)].

2.3.1 Isothermal LDFP and LDFS Models

Integrating the conservation of mass, Eq. (2.3), over the entire pellet domain gives the following.

$$\left(\frac{\varepsilon_p}{RT_p} + \hat{\rho}_p \frac{\partial \tilde{n}_{i,eq}^p}{\partial p_i^p} \right) \frac{d\tilde{p}_i^p}{dt} + \sum_{j=1, j \neq i}^{N_c} \left(\hat{\rho}_p \frac{\partial \tilde{n}_{i,eq}^p}{\partial p_j^p} \right) \frac{d\tilde{p}_j^p}{dt} = -\frac{3}{R_p} N_{i,R_p} \quad \text{for } i = 1 \dots N_c \quad (2.28)$$

The surface molar flux term N_{i,R_p} can be found by equating the n -th order analysis of Do & Mayfield (1987) with the cycle time corrected Ω_i analysis of Nakao & Suzuki (1983). The resulting conservation equation is termed the partial pressure form of the linear driving force (LDFP) model and is written as follows.

Intrapellet conservation of mass using the isothermal LDFP model

$$\left(\varepsilon_p + \hat{\rho}_p RT_p \frac{\partial \tilde{n}_{i,eq}^p}{\partial p_i^p} \right) \frac{d\tilde{p}_i^p}{dt} + \sum_{j=1, j \neq i}^{N_c} \left(\hat{\rho}_p RT_p \frac{\partial \tilde{n}_{i,eq}^p}{\partial p_j^p} \right) \frac{d\tilde{p}_j^p}{dt} = \frac{\Omega_i D_i^c}{R_p^2} (p_i^B - \tilde{p}_i^p) \quad \text{for } i = 1 \dots N_c \quad (2.29)$$

Although Eq. (2.29) is not in the LDF form of Eq. (2.1), it is general in the functional equilibrium isotherm adopted for the adsorbed phase and correctly accounts for the intrapellet gas void that some LDF models incorrectly omit [Chahbani & Tondeur (1998, 2000)]. The difference between the interpellet and volume-averaged intrapellet partial pressure on the right hand side of Eq. (2.29) is linear and for this reason is defined as a *linear* approximation to the driving force for mass transfer into a sorbent pellet with an RPSA corrected numerical constant Ω_i . This and subsequent LDF models used in this dissertation are hence relevant across the PSA and RPSA cycle regime, at least to the approximations discussed in §A.3 of appendix A. If linear, uncoupled equilibrium isotherms for $n_{i,eq}^p$ is imposed on Eq. (2.29) and both sides of the equation are multiplied by the linear equilibrium isotherm gradient H_i , the surface diffusion form of the linear driving force (LDFS) model is obtained.

Intrapellet conservation of mass with the isothermal LDFS model

$$\frac{d\tilde{n}_i^p}{dt} = \left(\frac{D_i^c}{\varepsilon_p + \hat{\rho}_p RT_p H_i} \right) \frac{\Omega_i}{R_p^2} (n_{i,eq}^B - \tilde{n}_i^p) \quad \text{for } i = 1 \dots N_c \quad (2.30)$$

Equation (2.30) is the most common form of the LDF model in use and is equivalent to the LDF model of Eq. (2.1). The term $[D_i^c / (\varepsilon_p + \hat{\rho}_p RT_p H_i)]$ can be thought of as a surface diffusion

coefficient and is equivalent to the LDFQ model of Suzuki (1990, p 161) where Suzuki uses a Q to denote the adsorbed phase. This also highlights why $[\varepsilon_p + \hat{\rho}_p RT_p (\partial n_{i,eq}^p / \partial p_i^p)]$ is introduced into the definition of θ mentioned at the beginning of this chapter. Equation (2.30) is strictly applicable to a linear, uncoupled equilibrium isotherm operated under isothermal conditions and for this reason will only be used in cases where these assumptions hold.

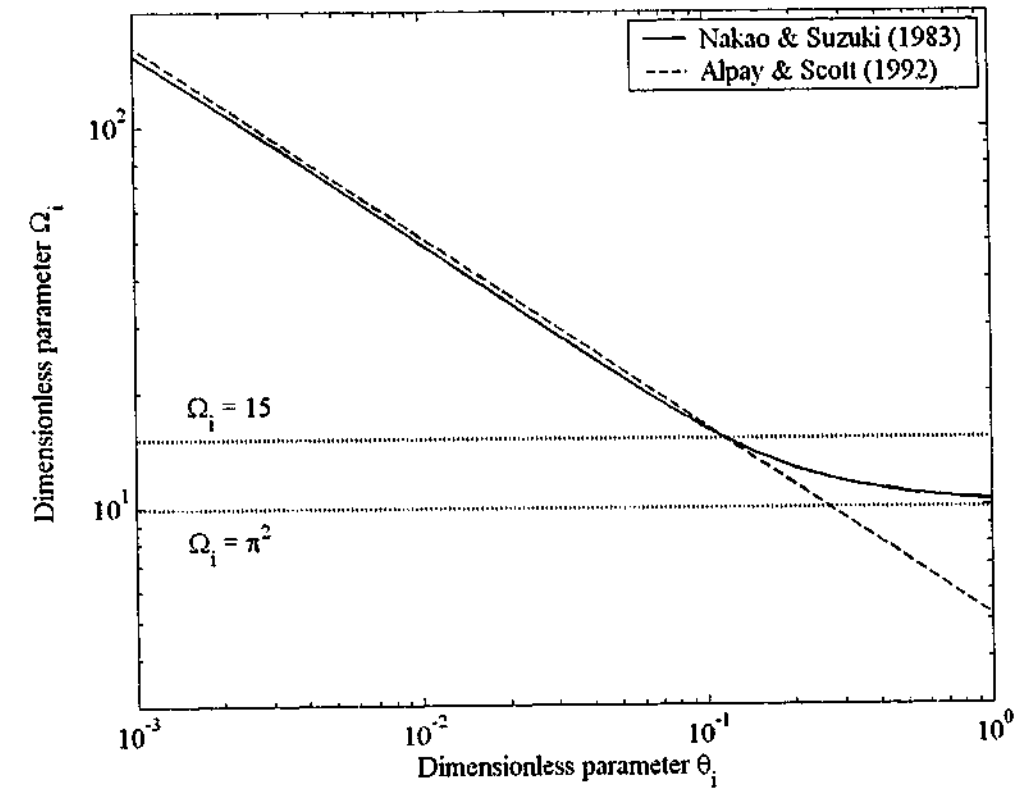


Figure 2.3: Plot of Ω_i versus θ_i for both the Nakao & Suzuki (1983) and Alpay & Scott (1992) LDFS models. The asymptotes $\Omega_i = \pi^2$ and $\Omega_i = 15$ are also shown.

As mentioned earlier, the time corrected value for Ω_i is found using the correlation of Nakao & Suzuki (1983). This is adopted for several reasons.

- i. The Nakao & Suzuki (1983) correlation circumvents limitations on the GLDF assumption when θ_i falls below the critical value.
- ii. The Ω_i correlation of Nakao & Suzuki (1983) is equivalent to the Ω_i correlations developed by Buzanowski & Yang (1989), Alpay & Scott (1992) and Carta (1993). Theoretical arguments underpinning the Nakao & Suzuki (1983) correlation have been well defined in these subsequent studies.

A plot of Ω_i versus θ_i for the Nakao & Suzuki (1983) and Alpay & Scott (1992) correlations are shown in Fig. 2.3. The correlation of Buzanowski & Yang (1989) and Carta (1993) are not shown, but are equivalent to the Nakao & Suzuki (1983) and Alpay & Scott (1992) lines of Fig. 2.3

respectively. Also shown on Fig. 2.3 are the lines $\Omega_i = \pi^2$, which is the asymptote for Ω_i as $\theta_i \rightarrow \infty$ from the Nakao & Suzuki (1983) analysis and $\Omega_i = 15$, the numerical value obtained by Glueckauf (1955). The Alpay & Scott (1992) penetration theory result approaches zero continuously as $\theta_i \rightarrow \infty$. Penetration theory assumes the pellet is infinitely deep such that adsorbed phase concentration at the center is unaffected by surface changes. For $\theta_i > 0.1$ the entire pellet volume begins to follow the dynamic response of the surface (i.e. GLDF assumption) so the asymptote $\Omega_i = \pi^2$ is applied from this point.

The LDF-DG model approximation of Mendes *et al.* (1994, 1995, 1996) is not used here given their coefficient Ω_i is purely empirical in nature and curve-fitted to the DPM through a trial-and-error approach. Any results that suggest the LDF-DG model approximation does not match the DPM only manifest through estimation of their four fitting parameters, providing no insight into the governing flux model imposed. Mendes *et al.* (1996) state the difference between the LDF-DG model approximation versus the DPM approach is approximately 10% over a range of boundary conditions, already providing an estimate of the errors expected with this approach.

2.3.2 Non-Isothermal LDFP Model

The method of integrating both conservation equations across the radial domain ($0 \leq r \leq R_p$) also carries over here. However the LDFS model is no longer considered and the LDFP is exclusively used to maintain consistent treatments between the intrapellet gas, adsorbed and solid phases in relation to the DPMs. For a linear, uncoupled equilibrium isotherm operated under non-isothermal conditions both the LDFS and LDFP provide equivalent results given the LDFS is essentially a simplification of the LDFP model. However, the conservation of energy and mass are now coupled such that the LDFS model cannot be represented in a form consistent with that given by Eq. (2.1) (i.e. the LDFS model now contains the temperature derivative $d\tilde{T}_p/dt$ in addition to the loading derivative $d\tilde{n}_i^p/dt$, eliminating the simplistic nature of the LDFS approach).

For this reason the LDFS model is applied only for the isothermal pellet simulations of this chapter where linear equilibrium isotherms are imposed. Non-isothermal simulations presented later in this chapter and all isothermal/non-isothermal pellet-bed model simulations of chapters 3 onward apply the LDFP model. The resulting form of the conservation of mass and energy respectively with the LDFP model is given by the following.

Intrapellet conservation of mass with the non-isothermal LDFP model

$$\left(\varepsilon_p + \hat{\rho}_p R \tilde{T}_p \frac{\partial \tilde{n}_{i,eq}^p}{\partial \tilde{p}_i^p} \right) \frac{d\tilde{p}_i^p}{dt} + \sum_{j=1, j \neq i}^{N_c} \left(\hat{\rho}_p R \tilde{T}_p \frac{\partial \tilde{n}_{j,eq}^p}{\partial \tilde{p}_j^p} \right) \frac{d\tilde{p}_j^p}{dt} + \left(\hat{\rho}_p R \tilde{T}_p \frac{\partial \tilde{n}_{i,eq}^p}{\partial \tilde{T}_p} - \frac{\varepsilon_p \tilde{p}_i^p}{\tilde{T}_p} \right) \frac{d\tilde{T}_p}{dt} = \frac{\Omega_i D_i^c}{R_p^2} (\tilde{p}_i^b - \tilde{p}_i^p) \text{ for } i = 1 \dots N_c \quad (2.31)$$

Intrapellet conservation of energy with the LDFP model

$$\left\{ \hat{\rho}_p \tilde{c}_s + \sum_{i=1}^{N_c} \left[\frac{\varepsilon_p \tilde{p}_i^p}{R \tilde{T}_p} \left(\tilde{c}_{g,i}^p - \frac{\tilde{H}_{g,i}^p}{\tilde{T}_p} \right) + \hat{\rho}_p \tilde{n}_{i,eq}^p \tilde{c}_{g,i}^p + \hat{\rho}_p (\tilde{H}_{g,i}^p - \tilde{q}_i^p) \frac{\partial \tilde{n}_{i,eq}^p}{\partial \tilde{T}_p} \right] \right\} \frac{d\tilde{T}_p}{dt} + \left\{ \sum_{i=1}^{N_c} \left[\frac{\varepsilon_p \tilde{H}_{g,i}^p}{R \tilde{T}_p} - \varepsilon_p 10^5 + \sum_{j=1}^{N_c} \hat{\rho}_p (\tilde{H}_{g,j}^p - \tilde{q}_j^p) \frac{\partial \tilde{n}_{j,eq}^p}{\partial \tilde{p}_j^p} \right] \frac{d\tilde{p}_j^p}{dt} \right\} = \sum_{i=1}^{N_c} \left[\frac{\Omega_i D_i^c}{R \tilde{T}_p R_p^2} (\tilde{p}_i^b - \tilde{p}_i^p) \left(H_{g,i} |_{R_p} \right) \right] - \frac{3h_{p,B}}{R_p} (\tilde{T}_p - T_B) \quad (2.32)$$

2.4 An Overview of the Mass Transfer Models Investigated

The preceding discussion highlighted several mass transfer models that can be used to simulate intrapellet mass transfer. This represents only a small sample of all possible models that could be invoked. A convenient map that shows the relationship between each of the mass transfer models developed in this dissertation is shown in Fig. 2.4. This highlights the individual assumptions on each constitutive flux equation and how these flux equations relate to the conservation of mass and energy over the pellet. Broken lines that couple a particular constitutive flux equation to the corresponding conservation equation has been highlighted already in the preceding discussion, along with their abbreviated names.

Three of these models radially discretise the pellet domain using the finite volume technique, indicated on Fig. 2.4 by a broken arrow crossing the grey shaded region. The other two models provide analytical solutions through relevant assumptions imposed on the governing conservation and constitutive equation and hence do not require radial discretisation. These models do not cross the grey shaded region of Fig. 2.4 and are denoted by LDF in their name to indicate a modified form of the linear driving force assumption has been imposed.

Some of these mass transfer models will be considered in isolated studies of this chapter to elucidate the impact of various assumptions on gas transport, such as the DGM, FFL and LDFS,

while others will be considered at length throughout this dissertation including the VF+DGM and LDFP.

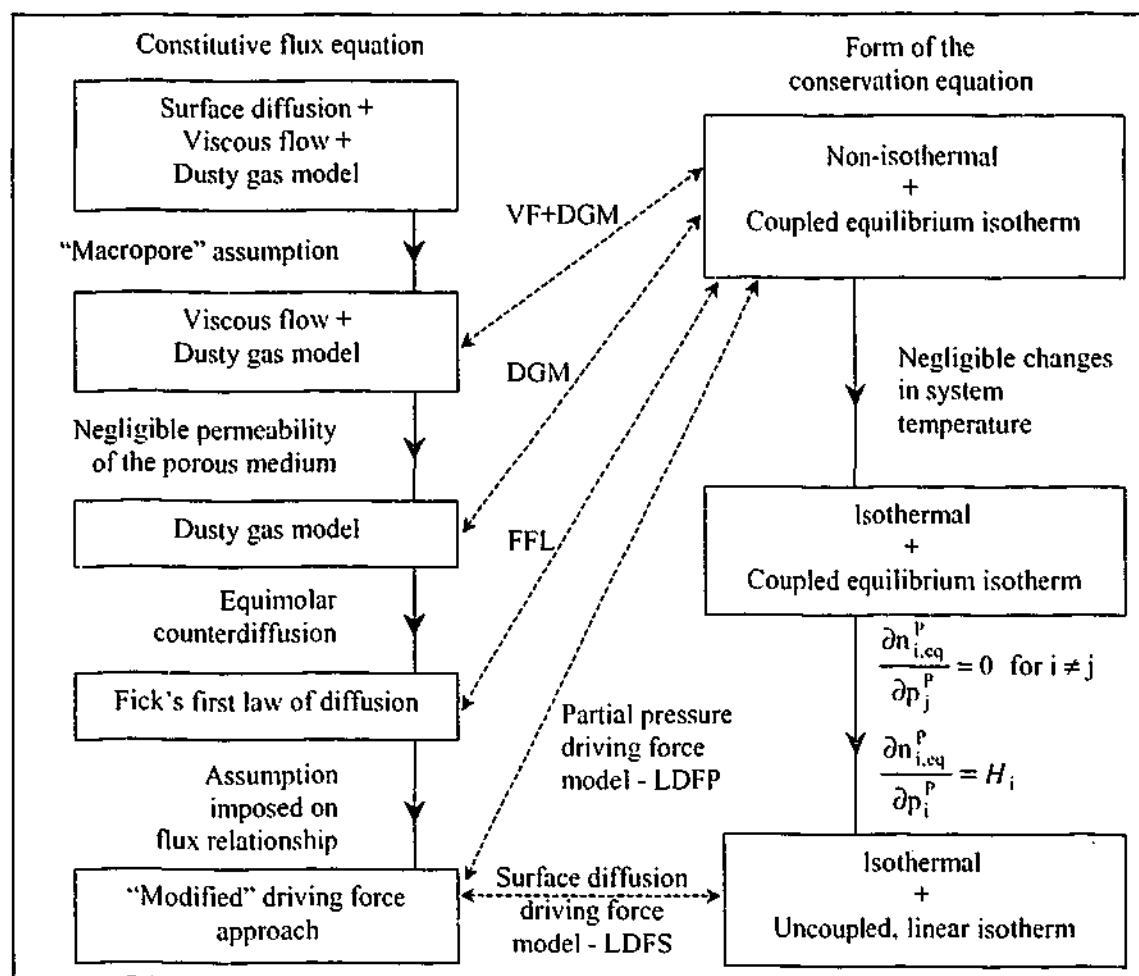


Figure 2.4: Flowchart indicating the relationship and assumptions between various models for intrapellet mass transfer investigated in this dissertation. Any broken arrow that crosses the grey shaded area requires radial discretisation of the conservation equation.

2.5 Validation of SimPell using a Known Analytical Solution

Given the complex, non-linear form of the PDEs relating to the DPM an analytical test is not readily available in their complete form. Under the assumption of isothermal behaviour, small pore diameter and linear uncoupled equilibrium isotherms a convenient simplification to the conservation of mass lends itself to a tractable analytical solution. For very small pore diameters within the micropore range Knudsen diffusion dominates, Eq. (2.23), and the conservation equation using the VF+DGM, DGM and FFL all reduce to the following.

$$(\epsilon_p + \hat{\rho}_p RT_p H_i) \frac{\partial p_i^p}{\partial t} = \frac{D_{K,i}^c}{r^2} \frac{\partial}{\partial r} \left(r^2 \frac{\partial p_i^p}{\partial r} \right) \text{ for } i = 1 \dots N_c \quad (2.33)$$

The analytical solution to Eq. (2.33) is derived by introducing the dimensionless variables $\bar{p}_i^p = p_i^p / p_{ref}$, $\bar{r} = r / R_p$, $\bar{t} = t D_{K,i}^c / R_p^2 (\epsilon_p + \hat{\rho}_p RT_p H_i)^{-1}$ and $\bar{\zeta}_i = \bar{p}_i^p \bar{r}$ [Carslaw & Jaeger (1993, p 94)]. A bar (–) above a variable denotes that quantity is in dimensionless form except $\bar{\zeta}_i$, which is a new dimensionless variable. The analytical solution for an instantaneous increase in partial pressure at $r = R_p$ to p_{ref} for a set period of time, denoted \bar{t}_{ads} , is given by the following. The Boundary and Initial Conditions (BC and IC respectively) are provided for completeness.

$$\text{BC 1: } \bar{\zeta}_i = 1 \text{ at } \bar{r} = 1 \text{ for } 0 < \bar{t} \leq \bar{t}_{ads}$$

$$\text{BC 2: } \bar{\zeta}_i = 0 \text{ at } \bar{r} = 0 \text{ for } 0 < \bar{t} \leq \bar{t}_{ads}$$

$$\text{IC 1: } \bar{\zeta}_i = \psi(\bar{r}) \text{ for } \bar{t} = 0 \text{ over } 0 \leq \bar{r} \leq 1$$

$$\bar{\zeta}_i(\bar{r}, 0 < \bar{t} \leq \bar{t}_{ads}) = \bar{r} + 2 \sum_{m=1}^{\infty} \left\{ \sin(m\pi\bar{r}) \exp(-m^2\pi^2\bar{t}) \int_0^{\bar{r}} [\psi(\bar{r}') - \bar{r}'] \sin(m\pi\bar{r}') d\bar{r}' \right\} \quad (2.34)$$

For an instantaneous decrease in \bar{p}_i^p to zero at the pellet surface for the same duration of time, the BCs, IC and analytical solution are as follows.

$$\text{BC 1: } \bar{\zeta}_i = 0 \text{ at } \bar{r} = 1 \text{ for } \bar{t}_{ads} < \bar{t} \leq 2\bar{t}_{ads}$$

$$\text{BC 2: } \bar{\zeta}_i = 0 \text{ at } \bar{r} = 0 \text{ for } \bar{t}_{ads} < \bar{t} \leq 2\bar{t}_{ads}$$

$$\text{IC 1: } \bar{\zeta}_i = \psi'(\bar{r}) \text{ at } \bar{t} = \bar{t}_{ads} \text{ over } 0 \leq \bar{r} \leq 1$$

$$\bar{\zeta}_i(\bar{r}, \bar{t}_{ads} < \bar{t} \leq 2\bar{t}_{ads}) = 2 \sum_{m=1}^{\infty} \left[\sin(m\pi\bar{r}) \exp(-m^2\pi^2\bar{t}) \int_0^{\bar{r}} \psi'(\bar{r}') \sin(m\pi\bar{r}') d\bar{r}' \right] \quad (2.35)$$

Two comparisons using different values for the dimensionless adsorption half time \bar{t}_{ads} are considered. To attain CSS Eqs. (2.34) and (2.35) are solved using a successive substitution approach until the total difference in dimensionless loading between the start and end of the cycle is less than a pre-defined tolerance (1.0×10^{-6}). Both cases consider a two-component mixture of nitrogen and oxygen. The assumption imposed on the current analysis is that the Knudsen coefficient is many orders of magnitude larger than the molecular diffusion and viscous flow coefficients. Hence the VF+DGM, DGM and FFL results are all equivalent to within tolerances applied on the ODE integrator ($RelTol = AbsTol = 10^{-7}$). For this reason *the VF+DGM results only are graphed with identical results obtained for the DGM and FFL*. Intrapellet pore size is very small ($\delta = 1.0 \times 10^{-11}$ m) and total pressure relatively low (1.0 bar.a) to maintain Knudsen diffusion as the limiting diffusion mechanism.

The first analytical test case for SimPell considered the nitrogen mole fraction cycling between an upper value of 0.78 and a lower value of 0.0 (balance oxygen) for a dimensionless adsorption half time of $\bar{t}_{ads} = 0.11$ based on nitrogen. The second dimensionless adsorption half time is $\bar{t}_{ads} = 0.0087$, also based on nitrogen, operated over the same boundary conditions. Given nitrogen is the gas species under consideration the initial conditions are a pre-saturated pellet of pure oxygen at 1.0 bar.a. Two different levels of pellet discretisation are considered that will be used in subsequent RPSA simulations of this chapter. The first applied $N_r = 5$ while the second set of simulations ran with $N_r = 30$. Figures 2.5a and 2.5b show the evolution from start up to CSS for the integrated loading over the pellet with time for both \bar{t}_{ads} values. Figures 2.6a and 2.6b present four pellet profiles at CSS with the DGM for the two values of \bar{t}_{ads} .

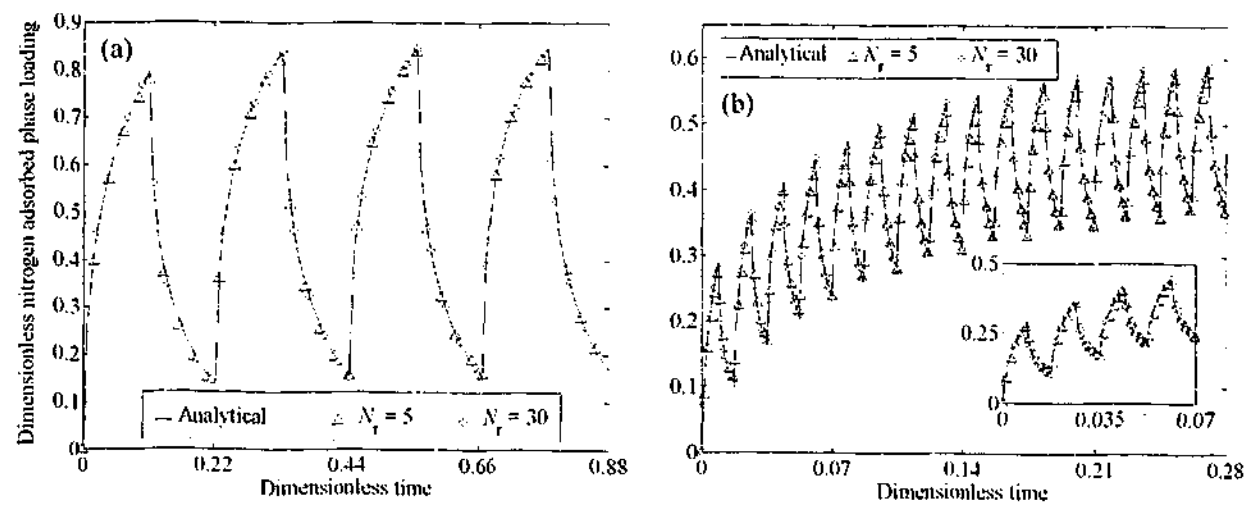


Figure 2.5: Dimensionless adsorbed phase loading for nitrogen from start up to CSS with the VF+DGM using (a) $\bar{t}_{ads} = 0.11$ and (b) $\bar{t}_{ads} = 0.0087$.

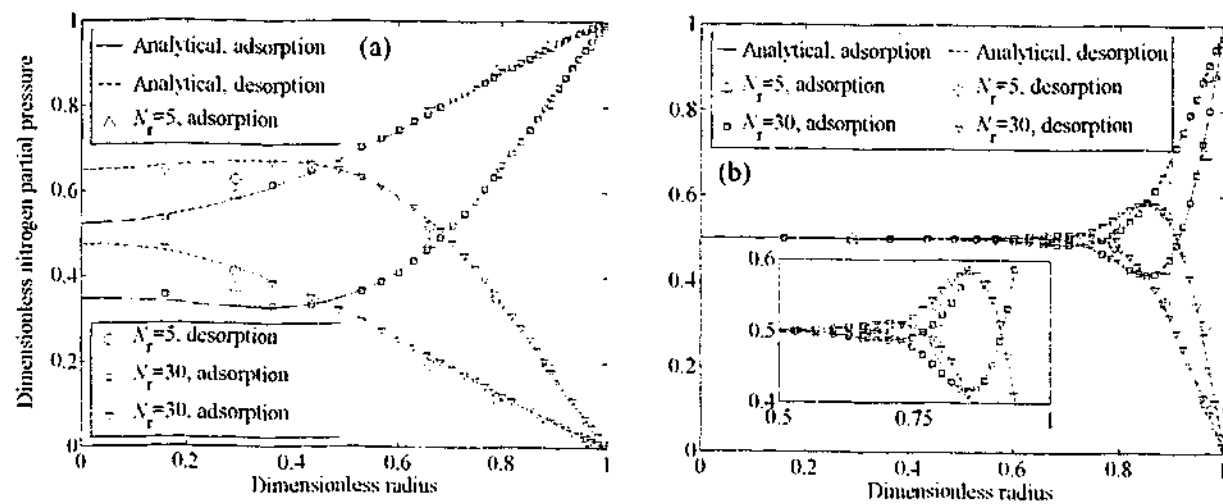


Figure 2.6: Dimensionless nitrogen partial pressure profiles at CSS for $N_r = 5$ and $N_r = 30$ with the VF+DGM using (a) $\bar{t}_{ads} = 0.11$ and (b) $\bar{t}_{ads} = 0.0087$.

Figures 2.5 and 2.6 show both levels of radial discretisation capture analytical profiles well, even when a minimal number of radial nodes are used through the pellet ($N_r = 5$). From these graphs, iso-volumetric discretisation coupled with the finite volume method provides an efficient and accurate numerical scheme for solving the pellet model. This result becomes important for cyclic simulation where a minimal number of radial nodes within the pellet are desired to reduce computational overheads without compromising model accuracy.

2.6 Cyclic Boundary Conditions: Isothermal Behaviour

The fundamental driving force behind an adsorption based separation is predicated on the ability to load one or several components from the feed stream over the adsorption step and subsequently remove it on the desorption step. From this the parameter that best defines process performance when evaluating deviations between a VF+DGM, DGM, FFL, LDFP and LDFS approach is the Working Capacity (WC). WC defines the difference in the amount of material adsorbed and desorbed across each step of the cycle and can be calculated as follows.

$$WC_i = \bar{n}_{i, \text{start step}}^p - \bar{n}_{i, \text{end step}}^p \quad \text{for } i = 1 \dots N_c \quad (2.36)$$

For the VF+DGM, DGM and FFL \bar{n}_i^p is equal to the summation of $\bar{n}_{i, \text{eq}, k}^p (\nabla_k^3 r / R_p^3)$ over each control volume. For a two-step cycle, the simplest RPSA cycle one can consider, WC for each step also defines WC for the cycle given the difference in volume-averaged adsorbed phase loading at the beginning and end of the adsorption step is the negative of the corresponding WC for the desorption step at CSS. Given four different mass transfer models are considered, any difference in the working capacity between one model to the next provides an indication of the error imposed by that relevant assumption, as indicated in Fig. 2.4.

Errors between the LDFS or LDFP versus FFL only manifest in the form of the boundary conditions imposed on the pellet when the method of Nakao & Suzuki (1983) is used with a linear isotherm. Differences that arise between the FFL versus DGM only manifest through the assumption of equimolar counterdiffusion within the pellet. Finally, differences that arise between the VF+DGM versus DGM can only manifest in the assumption of negligible intrapellet permeability. Each of these errors can be characterised using the relative WC difference between the first and second listed model. This gives rise to three relative errors denoted $E_{i,m}$ that apply to both isothermal and non-isothermal simulations performed in this chapter. Each of these relative errors is a function of just one particular assumption on the intrapellet flux equation.

$$E_{i,(\text{LDFS or LDFP}) \text{ vs FFL}} = \left(\frac{WC_{i,(\text{LDFS or LDFP})} - WC_{i,\text{FFL}}}{WC_{i,\text{FFL}}} \right) \times 100 \text{ for } i = 1 \dots N_c \quad (2.37)$$

$$E_{i,\text{FFL vs DGM}} = \left(\frac{WC_{i,\text{FFL}} - WC_{i,\text{DGM}}}{WC_{i,\text{DGM}}} \right) \times 100 \text{ for } i = 1 \dots N_c \quad (2.38)$$

$$E_{i,\text{DGM vs VF+DGM}} = \left(\frac{WC_{i,\text{DGM}} - WC_{i,\text{VF+DGM}}}{WC_{i,\text{VF+DGM}}} \right) \times 100 \text{ for } i = 1 \dots N_c \quad (2.39)$$

Equations (2.37) through (2.39) indicate that if $E_{i,m}$ is positive, the first listed mass transfer model over-predicts adsorbed phase loading relative to the second listed model and if negative, under-predicts the second listed model. To ensure a valid comparison is made between all mass transfer models a linear equilibrium isotherm extrapolated from the results of Miller (1987) for 13X molecular sieve zeolite is used.

$$n_{i,\text{eq}}^p = H_i p_i^p \text{ where } H_i = H_{i,0} \exp\left(\frac{Q_i}{RT_p}\right) \text{ for } i = 1 \dots N_c \quad (2.40)$$

Although Miller (1987) considered a non-linear functional form on the equilibrium isotherm equation, the linear curve fitted equation used here agrees with the data to a very good approximation. Isotherm and sorbent parameters used for each simulation of this chapter are provided in Table 2.1.

A successive substitution approach to CSS is adopted within SimPell. To determine when CSS is achieved, a procedure very similar to that outlined by Todd *et al.* (2001) is adopted at the pellet scale. Refer to §A.4 of appendix A for a description of the CSS check implemented within SimPell. The magnitude assigned to each CSS tolerance parameter can be found in Table 2.2. These were selected on the basis that further tightening simply increased the number of cycles to simulate for a negligible change in the pellet profiles with respect to ODE tolerances. The ODE tolerances RelTol and AbsTol of VODE were both set to 10^{-7} in all simulations. A two-step RPSA cycle of high pressure adsorption followed by low pressure desorption will be exclusively used in this discussion, to maintain the validity of theoretical arguments considered with the LDFS/LDFP correlation for Ω_i .

Table 2.1: Isotherm and sorbent parameters applied to all simulations in §2.6 and §2.7.

| Parameter | Magnitude | Units |
|-------------------------|-----------------------|--|
| $H_{\text{nitrogen},0}$ | 2.47×10^{-4} | gmole kg ⁻¹ bar.a ⁻¹ |
| Q_{nitrogen} | 17,350 | J gmole ⁻¹ |
| $H_{\text{oxygen},0}$ | 9.78×10^{-4} | gmole kg ⁻¹ bar.a ⁻¹ |
| Q_{oxygen} | 11,180 | J gmole ⁻¹ |
| R_p | 0.75×10^{-3} | m |
| δ (macroporous) | 1.0×10^{-7} | m |
| δ (mesoporous) | 1.0×10^{-8} | m |
| δ (microporous) | 1.0×10^{-9} | m |
| $\hat{\rho}_p$ | 1,270 | kg m ⁻³ |
| \hat{c}_s | 1,000 | J kg ⁻¹ |
| ϵ_p | 0.60 | (m ³ void) (m ³ total) ⁻¹ |
| C_K, C_m and C_v | 0.20 | - |

Table 2.2: CSS tolerance parameters applied to all simulations in §2.6 and §2.7. A complete definition of these parameters can be found in Table A.1 of appendix A.

| Parameter | Magnitude | Units |
|---|----------------------|---|
| $E_{j,\text{max}}^p$ for p_i^p | 5.0×10^{-6} | bar.a for $i = 1 \dots N_c$ ($j = 1 \dots N_c$) |
| $E_{j,\text{max}}^p$ for T_p | 3.0×10^{-3} | K ($j = N_c + 1$) |
| $E_{j,\text{rms}}^p$ for p_i^p | 5.0×10^{-6} | bar.a for $i = 1 \dots N_c$ ($j = 1 \dots N_c$) |
| $E_{j,\text{rms}}^p$ for T_p | 3.0×10^{-3} | K ($j = N_c + 1$) |
| $E_{i,\text{mole}}^p$ | 5.0×10^{-4} | % for $i = 1 \dots N_c$ |
| E_{energy}^p and E_{grad}^p | 3.0×10^{-2} | % |

For each simulation, three different pore sizes within the pellet are used to replicate different regimes for the limiting mechanism of mass transfer when adopting the IUPAC classification. The first pore size lies within the macropore range where the molecular/viscous flow mechanisms dominate over the Knudsen mechanism. The third pore size lies within the micropore range where Knudsen diffusion dominates over molecular diffusion and viscous flow. The second pore size lies at the mesopore or intermediate level where all three mechanisms are comparable in magnitude.

2.6.1 Square-Wave Boundary Conditions

The first set of boundary conditions impose a square-wave change in composition and pressure at the pellet surface under isothermal conditions, reminiscent of the conditions that typically arise over a PSA cycle. Under these conditions the LDFS model is used for comparison to FFL.

$$\text{BC during step 1: } \left. \begin{array}{l} p^p = 3.21 \text{ bar.a} \\ y_{\text{nitrogen}}^p = 0.762 \\ T_p = 297.2 \text{ K} \end{array} \right\} \text{ at } r = R_p \text{ for } 0 < t \leq \frac{1}{2} t_{\text{cycle}} \quad (2.41)$$

$$\text{BC during step 2: } \left. \begin{array}{l} p^p = 1.20 \text{ bar.a} \\ y_{\text{nitrogen}}^p = 0.831 \\ T_p = 297.2 \text{ K} \end{array} \right\} \text{ at } r = R_p \text{ for } \frac{1}{2} t_{\text{cycle}} < t \leq t_{\text{cycle}} \quad (2.42)$$

To maintain consistency between the molecular and Knudsen diffusion coefficients, the average pressure and composition from the instantaneous change in boundary conditions over the cycle are used. This also applies to the permeability coefficient of the VF+DGM. This reduces each diffusion and permeability coefficient to a constant. For each pore size ten simulations at varying θ_i were considered. As the magnitude of θ_i decreased from values around 1.0 to that approaching 0.001, the corresponding number of cycles required for the pellet to reach CSS increased. Approximately 2 to 3 cycles were required on average to reach CSS from the initial conditions when θ_i is close to 1.0, whereas 300 to 500 were required as θ_i approached 0.001. Within SimPell the FFL is taken as the standard by which CSS is determined (i.e. once FFL has reached CSS the simulation is terminated). The FFL is selected due to the fact that this flux model has the smallest magnitude for transport into/out of the pellet and hence will take the longest to wash out arbitrary initial conditions. The DGM and VF+DGM contain additional transport mechanisms that increase the quantity of gas passing into/out of the pellet, moving these to CSS more rapidly.

Approximately two to four minutes of simulation time was required for each run on a 650 MHz Compaq XP1000 Dec-Alpha workstation. The resulting WC error plots using Eqs. (2.37) through (2.39) for nitrogen and oxygen respectively are shown in Figs. 2.7a and 2.7b. WC error for the LDFS versus FFL model is essentially zero as expected from the cycle time corrected correlation of Nakao & Suzuki (1983). The error between the FFL versus DGM on the same two plots is quite substantial, exceeding -30% in the macroporous case as θ_i approaches 0.1. Below $\theta_i = 0.1$, $E_{\text{LDFS vs DGM}}$ begins to asymptote towards a relatively steady error well in excess of that expected from a diffusion model that incorporates equimolar counterdiffusion.

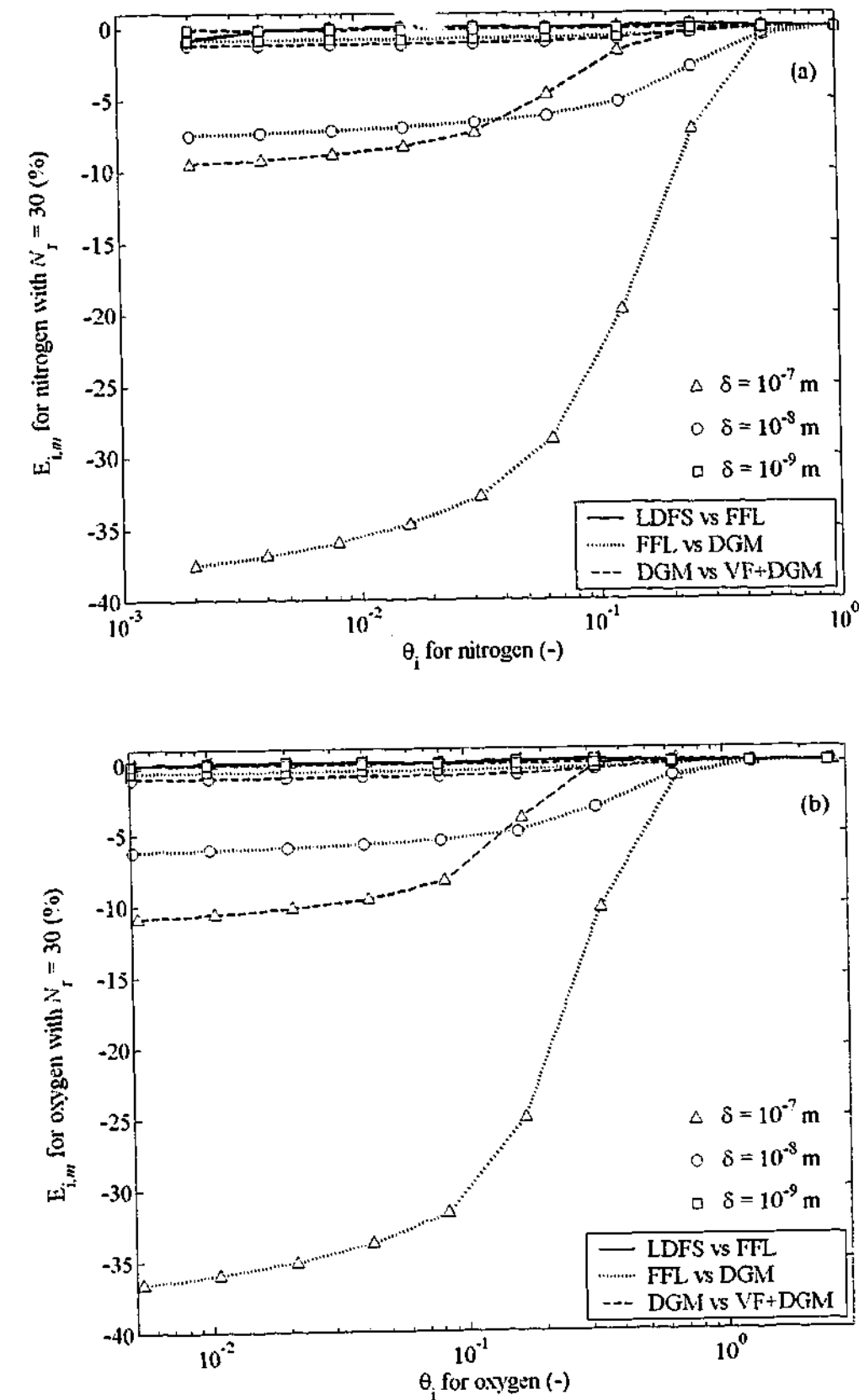


Figure 2.7: WC error with isothermal square-wave BC and $N_r = 30$ for (a) nitrogen and (b) oxygen.

Asymptotic behaviour in WC error is observed as $\theta_i \rightarrow 0$ due to the effective working region for adsorption and desorption being progressively reduced to a relatively thin layer near the pellet surface. This indicates nitrogen and oxygen do not penetrate much further into the pellet once θ_i

drops below 0.1 due to additional contributions from bulk motion and viscous flow in relation to the LDF and FFL assumption. At the mesoporous level the FFL versus DGM error is approximately -8%, approaching zero as the micropore limit is approached. At the micropore limit the Knudsen mechanism dominates over molecular diffusion and viscous flow such that mass transfer is now dominated by the individual species composition gradient. Hence the magnitude of the flux coupling terms associated with bulk gas motion at the micropore level is negligible.

Errors from the FFL versus DGM for each run was negative, indicating the contribution from bulk gas motion assists separative performance by sweeping gas into the pellet more rapidly than composition gradients alone contribute. WC errors between the DGM versus VF+DGM are relatively small across all pore sizes, not exceeding -10%, implying viscous flow under these conditions contributes marginally to gas transport when compared to the mechanism of bulk gas motion (DGM).

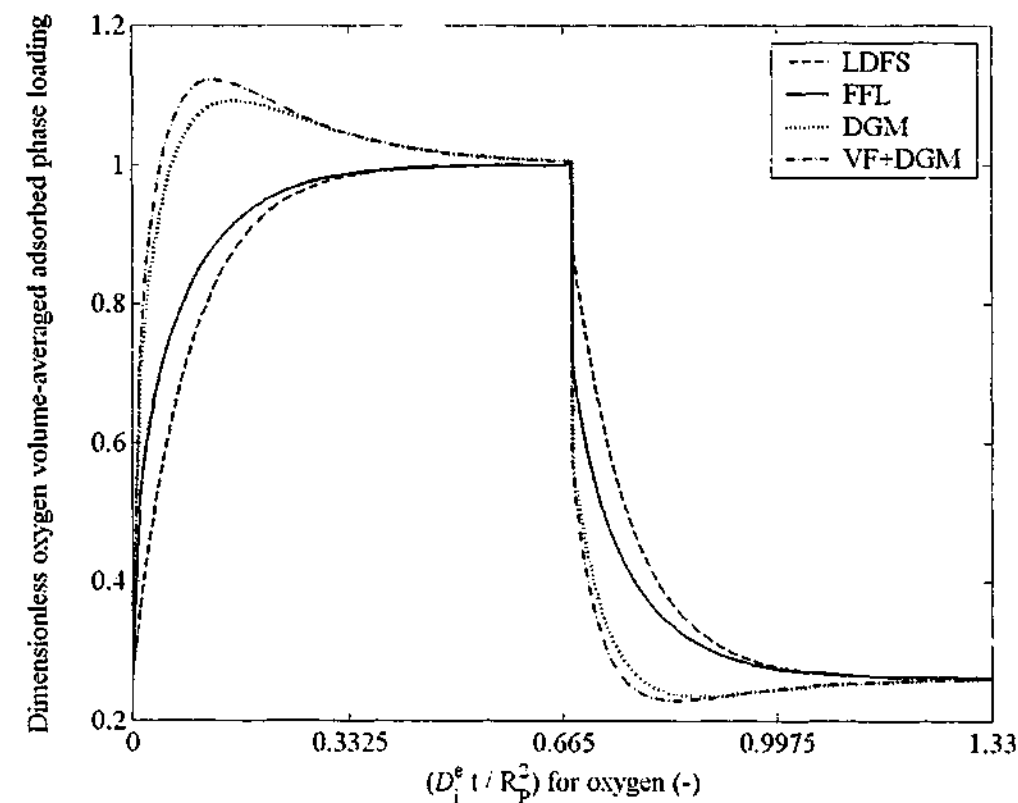


Figure 2.8: Dimensionless adsorbed phase loading for oxygen within a macroporous pellet. $\theta_{\text{oxygen}} = 0.665$ and $N_r = 30$ using isothermal square-wave BC.

To demonstrate the importance of bulk gas motion and viscous flow at the macropore limit, Fig. 2.8 presents the dimensionless adsorbed phase loading versus dimensionless time for oxygen obtained with $\theta_{\text{oxygen}} = 0.665$. The adsorbed phase loading has been non-dimensionalised by dividing the volume-averaged loading over the pellet with the equilibrium loading from external gas phase conditions at high pressure. At the onset of a pressure increase the oxygen adsorbed

phase loading rapidly overshoots equilibrium conditions using the VF+DGM and DGM. Oxygen and nitrogen have similar magnitudes for their transport coefficients and both diffuse at similar rates within the macropore channels. However, nitrogen is selectively adsorbed over oxygen by approximately 3:1 and initially nitrogen adsorbs across the surface layers of the pellet. Due to the rapid transport and subsequent uptake of nitrogen in the pellet, bulk gas motion and viscous flow also sweep oxygen into the pellet. This rapidly convected oxygen is allowed to equilibrate at a pressure close to external gas conditions in the absence of nitrogen across a majority of the pellet. As nitrogen begins to penetrate further into the pellet, oxygen is selectively desorbed and flows out of the pellet causing a decrease in oxygen loading towards the equilibrium value.

With a reduction in pressure the pellet initially desorbs oxygen/nitrogen and almost instantaneously sweeps this gas out of the pellet. Once the pellet has rapidly equilibrated to external gas pressure the intrapellet composition is now enriched with nitrogen, causing the pellet to undershoot oxygen adsorbed phase loading. The external gas phase composition is not all that dissimilar to the composition at the end of step 1 and from here nitrogen diffuses out of the pellet and oxygen in. As diffusion occurs and the composition gradient equilibrates, oxygen adsorbed phase loading increases. These overshoot/undershoot profiles are common when a lesser-adsorbed component is present in a system where bulk gas motion and viscous flow rapidly convects gas faster than diffusion alone, such as hydrogen purification [Serbezov & Sotirchos (1997a)]. These transients occur in the opposite direction of the predicted FFL and LDFS response.

The time scale for bulk gas motion and viscous flow within the pellet at the limit of a long step ($\theta_i > 1$) is only a small fraction of the total step time, allowing the pellet to equilibrate towards bulk gas conditions before commencement of the next step. This means the FFL and LDFS predict WC well as the equilibrium adsorbed phase composition between the start and end of the step ultimately dictates WC once overshoot/undershoot no longer occurs [Lu *et al.* (1992)]. As step time decreases, bulk gas motion, viscous flow and the overall step time are comparable in magnitude. Transport into and out of the pellet is now dominated by bulk gas motion (DGM) and viscous flow (VF+DGM) rather than composition gradients (FFL and LDFS) indicating equimolar counterdiffusion is now neglecting the dominant modes of gas transport.

Figures 2.7a and 2.7b relate to simulation data with $N_r = 30$. Each simulation performed with $N_r = 30$ was repeated using $N_r = 5$. Results between these two levels of discretisation were compared to assess the impact of node resolution on the reproducibility of WC for the pellet. A comparative plot of these discretisation levels, shown as a relative error in the WC for each intrapellet flux model for each pore size is shown in Figs. 2.9a and 2.9b.

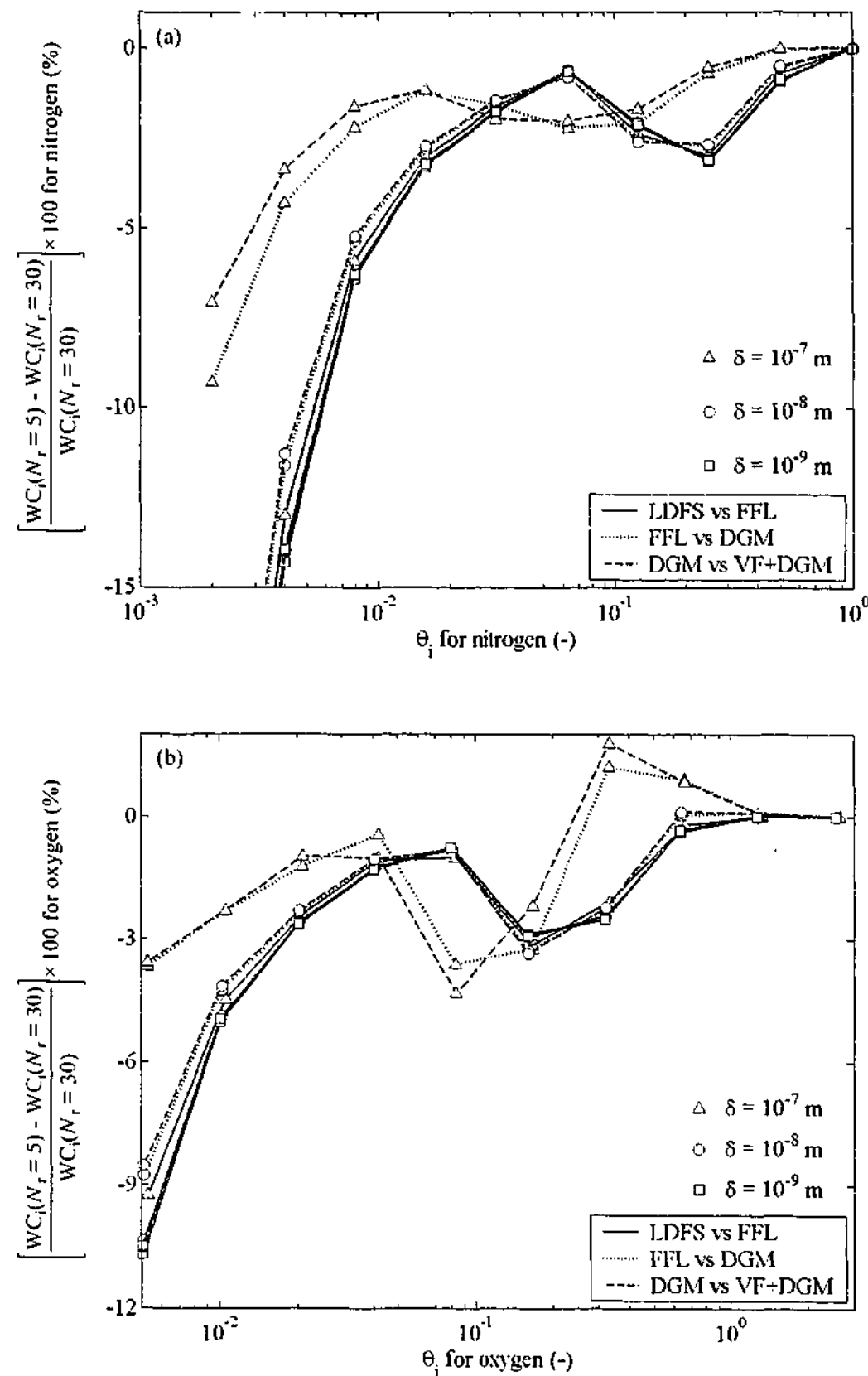


Figure 2.9: Difference in the WC between $N_r = 5$ and $N_r = 30$ with isothermal square-wave BC for (a) nitrogen and (b) oxygen.

Figure 2.9 shows both levels of discretisation follow each other well for $\theta_i > 0.01$. Below this limit WC for the two levels of discretisation diverge. For relatively large values of θ_i the effective

utilisation of the pellet for adsorption/desorption capacity is large with the entire domain effectively swinging between conditions imposed at the pellet surface. As θ_i decreases below 0.1 the adsorption/desorption zone progressively moves towards the outer layers of the pellet, leaving the inner regions relatively unaffected by external surface changes. Fewer nodes are now being used in the pellet to estimate the intrapellet concentration profile that ultimately dictates transport across the pellet surface. In the extreme case as few as one or two nodes (when $N_r = 5$) are being used to estimate $\partial p_i^p / \partial r$ at $r = R_p$. For conditions where θ_i could be expected to approach these lower limits the level of radial discretisation becomes critical in assessing the validity of a DPM approach.

2.6.2 RPSA Boundary Conditions

Over a PSA cycle both composition and total pressure fluctuate periodically with time to varying extents throughout the adsorption bed. Near the entrance nitrogen mole fraction varies from air composition (78 mol% N_2) to near unity at the end of the counter-current desorption step while the top of the bed (product end) may be substantially pure oxygen varying only in total pressure. Near the mass transfer zone compositions vary rapidly with oxygen leaving and nitrogen entering the pellet as the mass transfer zone traverses the bed. Together with rapid pressure changes this could lead to some unusual non-Fick fluxes in the pellet.

To capture these boundary conditions the adsorption simulator MINSA [Todd *et al.* (2001)] was used to simulate the two-step RPSA cycle described previously to CSS utilizing the LDFS model. MINSA discretises the bed into N_z axial nodes, $N_z = 30$ in this case, and solves for gas composition, pressure, temperature and loading at each node. The gas composition and pressure at each axial node was recorded as a function of time over a cycle at CSS and subsequently used as the boundary condition for the VF+DGM, DGM, FFL and LDFS models of SimPell.

Partial pressure profiles obtained from MINSA at axial positions 0.23 m and 0.97 m for $\delta = 1.0 \times 10^{-7}$ m are shown in Fig. 2.10, where both positions will be used as separate boundary conditions on SimPell. Different locations in the bed give qualitatively similar trends for a two-step cycle, with the absolute values changing to reflect the gradual increase in oxygen concentration along the axial domain of the bed. The remaining boundary conditions for the other two pore sizes are qualitatively similar to those shown in Fig. 2.10 and so are not presented for brevity. As was the case for square-wave boundary conditions of §2.6.1, the LDFS model is compared with the FFL. Hence any deviations that arise between the LDFS versus FFL

formulation will be a direct result of the square-wave assumption on boundary conditions at the pellet surface.

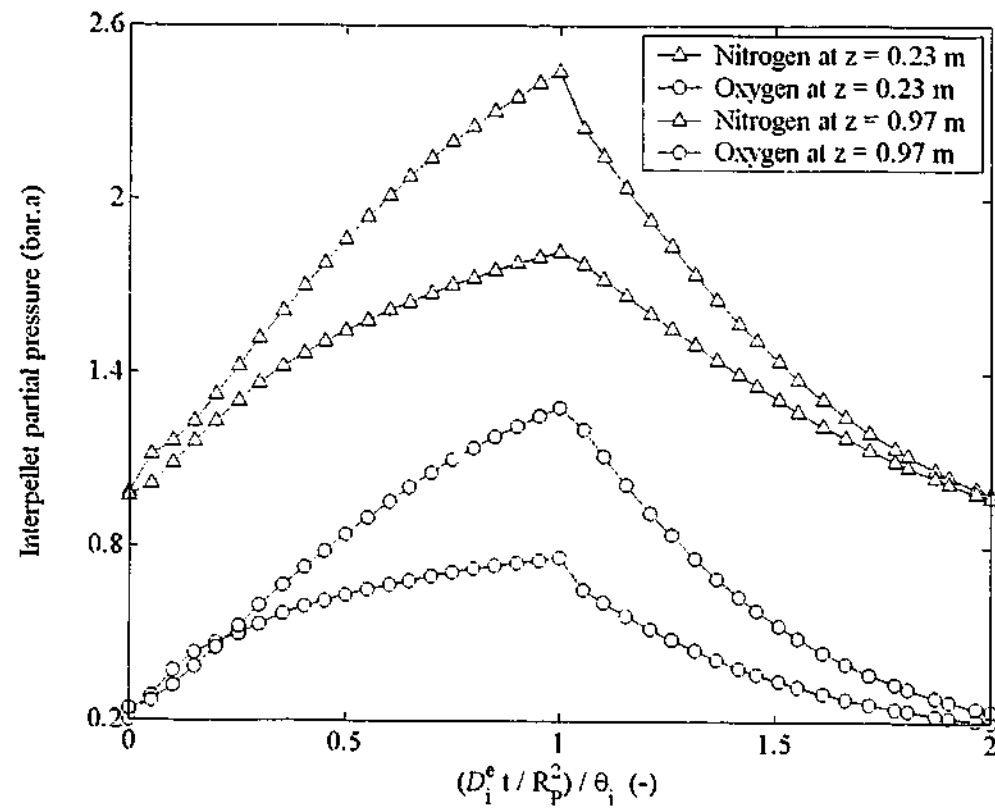


Figure 2.10: Partial pressure boundary conditions obtained from MINSA for a two-step RPSA cycle.

Figure 2.11 shows the error plots for nitrogen at two different axial positions in the bed using RPSA boundary conditions while Figure 2.12 shows the same results for oxygen. A difference of approximately 3 to 10% is observed between the LDFS versus FFL error and FFL versus DGM at both axial locations, whereas the difference between the DGM versus VF+DGM at both locations is much smaller, around 1 to 2%. As was the case for square-wave boundary conditions, the error between the FFL versus DGM approach is large, exceeding -30% for the macroporous case as θ_1 approaches 0.1. This error progressively decreases in magnitude as the microporous limit is reached. What has dramatically changed between the square-wave and RPSA boundary conditions, however, is the magnitude of the error between the LDFS versus FFL approach. No longer does this error assume the value zero but steadily decreases below zero as θ_1 decreases, showing a more pronounced error than the assumption of equimolar counterdiffusion over the cycle. This indicates the time corrected Ω_1 value underestimates WC in comparison to the FFL approach.

For square-wave perturbations the initial step change causes gas to rapidly diffuse into the pellet, gradually tailing off as equilibrium is approached. The corresponding cycle corrected Ω_1 value of Nakao & Suzuki (1983) accounts for this step change and forces the LDFS model to fit the FFL WC result at the endpoints of each step. Although the transient uptake periods during each step do

not necessarily match, at the end of each step they do in order to predict WC for the pellet. This time corrected Ω_1 value multiplied by the driving force for a varying boundary condition no longer tracks WC predicted from the FFL model.

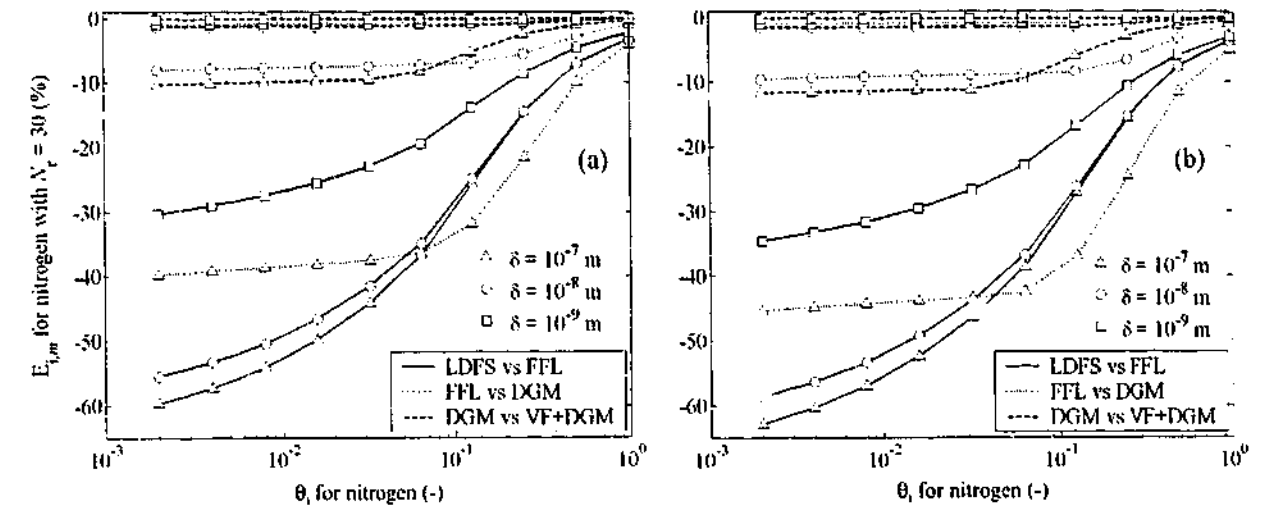


Figure 2.11: WC error with isothermal RPSA BC and $N_r = 30$ for nitrogen at (a) $z = 0.23$ m and (b) $z = 0.97$ m.

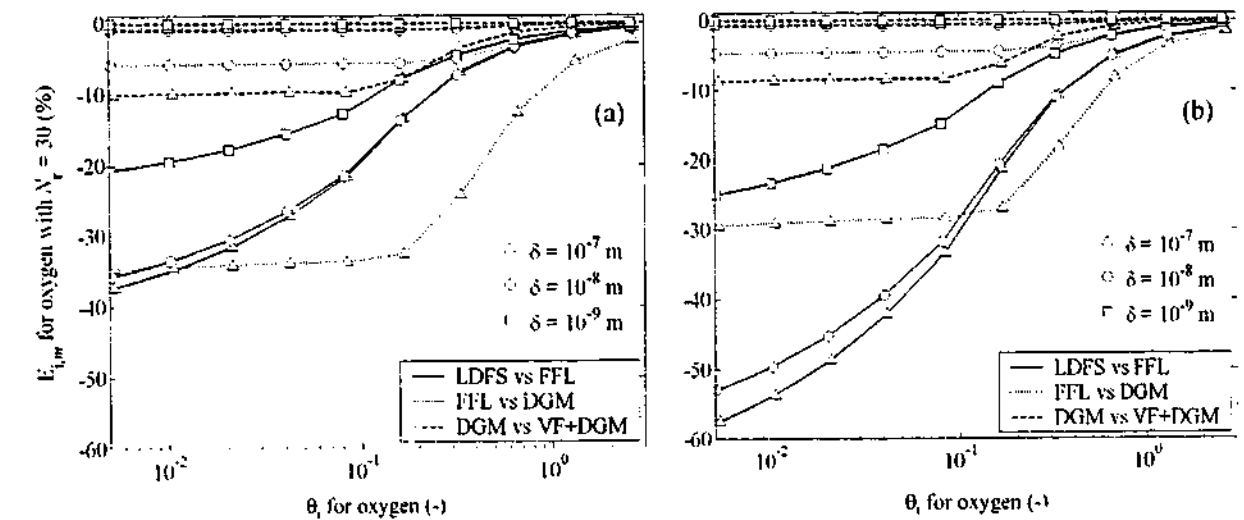


Figure 2.12: WC error with isothermal RPSA BC and $N_r = 30$ for oxygen at (a) $z = 0.23$ m and (b) $z = 0.97$ m.

One particular loading profile with time is shown in Fig. 2.13 to discuss this result. Quantitatively similar trends for nitrogen and oxygen are observed with each pellet simulation performed under RPSA conditions. The LDFS model has effectively introduced a phase lag into the loading profile that increases in magnitude as θ_1 decreases, which requires a small portion of θ_1 for each step to overcome. At the onset of adsorption for example, the bulk gas phase composition slowly increases as air begins to flow around the pellet. However, the average pellet phase loading from the LDFS model estimates the pellet is at a composition still higher than the bulk gas resulting in mass transfer from the pellet to the bulk gas. At this point all three pellet models begin to adsorb

nitrogen in the outer layers of the pellet, showing a gradual increase in nitrogen loading as this penetration distance increases while the LDFS is still desorbing nitrogen. A qualitatively similar argument over the early stages of the desorption step follows from here as well.

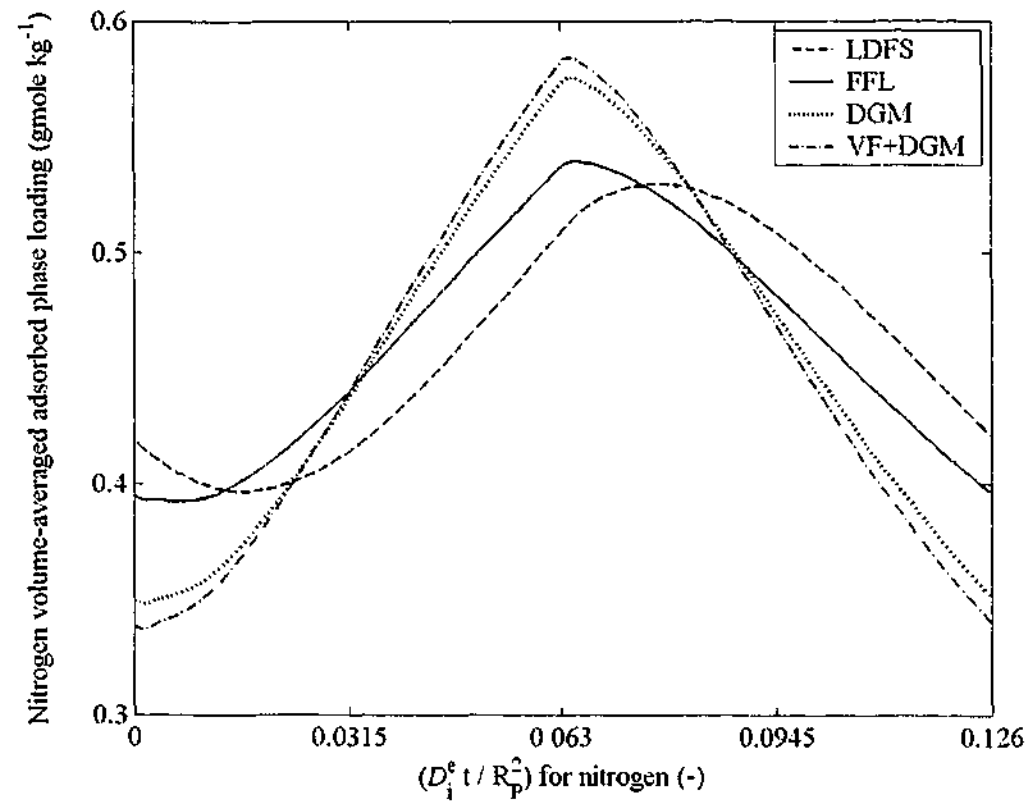


Figure 2.13: Volume-averaged adsorbed phase loading profiles for nitrogen at CSS ($z = 0.23$ m, $\theta_{\text{nitrogen}} = 0.063$ and $\delta = 1.0 \times 10^{-7}$ m).

A similar result was observed for the LDF-DG model approximation of Mendes *et al.* (2001a). This indicates the time corrected Ω_i value is incorrectly assigned where now the LDFS model needs to be multiplied by a constant larger than the Nakao & Suzuki (1983) value in order to close the cycle in terms of WC. If one were to alter the cycle and consider a new process where the form of the boundary conditions differed from those above, a different Ω_i value again would be required to correctly predict WC. Hence an infinite number of possible Ω_i values arise once different cycle and process regimes are investigated and the generality of an adsorption process simulator for design and optimisation is lost in the complexities of these corrected mass transfer coefficients. This is one argument against the application and extension of the LDF-DG model of Mendes *et al.* (1994, 1995, 1996) to include additional process effects such as non-isothermal behaviour.

Alternative forms of the LDFS model that employ variations on the intrapellet concentration profile when starting with the FFL model will suffer the same fate as these time corrected Ω_i values simply due to the unpredictable nature of the boundary conditions experienced at any one point in the bed. Model mismatch associated with cyclically varying boundary conditions will have

a greater impact than any inaccuracies associated with the form of the concentration profile adopted.

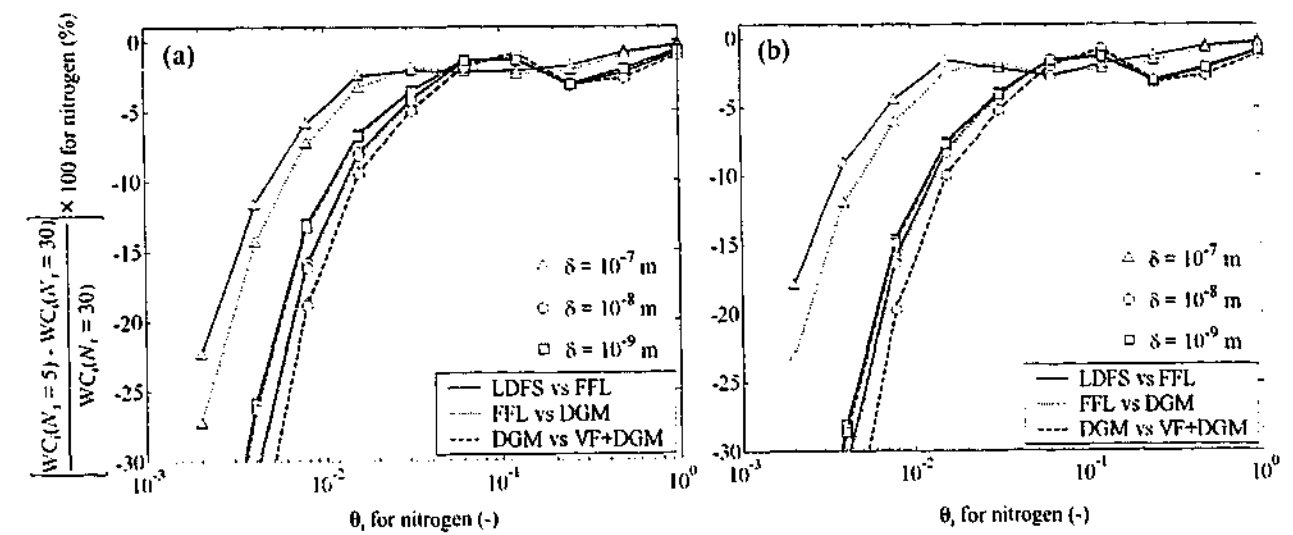


Figure 2.14: Difference in WC between $N_r = 5$ and $N_r = 30$ with isothermal RPSA BC for nitrogen at (a) $z = 0.23$ m and (b) $z = 0.97$ m.

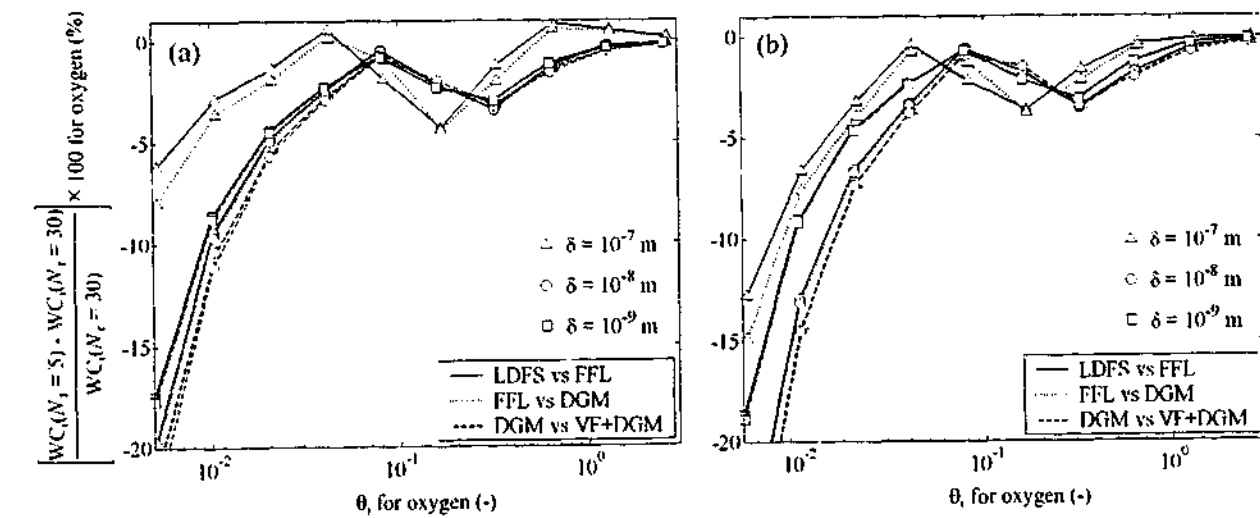


Figure 2.15: Difference in WC between $N_r = 5$ and $N_r = 30$ with isothermal RPSA BC for oxygen at (a) $z = 0.23$ m and (b) $z = 0.97$ m.

As was the case with square-wave boundary conditions the difference in predicted errors for the two levels of discretisation show similar trends (Figs. 2.14 and 2.15). The magnitude of the error for nitrogen is somewhat larger here than it was before but again show the discretised pellet model approach diverges rather rapidly for $\theta_i < 0.01$.

2.7 Cyclic Boundary Conditions: Non-Isothermal Behaviour

The discussion thus far has concentrated on the response of the pellet using various mass transfer models under isothermal conditions. A reduction in the internal degrees of freedom a gas molecule experiences when adsorbed onto the active cationic molecule within a single zeolite crystal results in the liberation of heat, causing the pellet to change temperature (§1.3). These temperature deviations require the conservation of energy to be coupled with the conservation of mass to accurately represent the operating behaviour expected within a real system. For this reason the analysis of §2.6 now incorporates the conservation of energy over the pellet domain.

To maintain an equivalent set of boundary conditions from the isothermal counterparts of §2.6.1 and §2.6.2 energy exchange via film heat transfer or Newton's law of cooling [Bird *et al.* (1960, p 267)] to and from the pellet surface is neglected. This forces the intra- to interpellet heat transfer coefficient $h_{p,B}$ to zero with convection becoming the only mechanism through which energy enters and leaves the pellet. Neglecting external film heat transfer isolates the major contribution of energy transferred between these two regions to maintain all dynamic changes within the intrapellet region only. Hence the bulk gas phase surrounding the pellet assumes one uniform temperature, 297.15 K, as imposed on each isothermal simulation. Although energy exchange via convection is only a small fraction of the energy transferred by external film heat transfer it is essential to maintain convection for closure of the energy balance both over an individual cycle and at CSS given the enthalpy term $H_{g,i}|_{R_p}$ contains the reference temperature T_{ref} .

In addition to setting $h_{p,B} = 0$, temperature dependence on the molecular and Knudsen diffusion coefficients is also neglected and one temperature, that of the bulk gas at 297.15 K, is used for these terms. Given the pressure and gas composition dependence on the diffusion and viscous flow coefficients are also taken as constant at the average conditions over the cycle the molecular-Knudsen-viscous flow coefficients take on the same constant values imposed under isothermal conditions.

Unlike the equivalent set of isothermal simulations that implicitly assume closure in the accumulation of energy at cycle 1, here the CSS check for closure in the accumulation of energy is performed cycle-by-cycle. This significantly increases the number of cycles required to reach CSS. CSS was attained in approximately 500-600 cycles with θ_i around 1.0, while several thousand were required as θ_i approached 0.001. Slow convergence to CSS with decreasing θ_i is attributed to the small accumulation of energy within the pellet over a cycle given enthalpy entering and leaving at $r = R_p$ is several orders of magnitude smaller than energy released/absorbed at the

zeolite surface when external film heat transfer is neglected. Each simulation in this section required around one to three days of CPU time on average using the same Dec-Alpha workstation quoted in §2.6.1 with VODE ($RelTol = AbsTol = 10^{-7}$). Linear equilibrium isotherms are used throughout this chapter so the values for $Q_{nitrogen}$ and Q_{oxygen} assigned in Table 2.1 also represent the isosteric heat of adsorption for nitrogen and oxygen, $q_{nitrogen}^p$ and q_{oxygen}^p , respectively.

2.7.1 Square-Wave Boundary Conditions

WC errors, Eqs. (2.37) through (2.39), are also used to quantify deviations observed between each mass transfer model under non-isothermal conditions, shown in Figs. 2.16a and 2.16b. These results show WC error under non-isothermal conditions follow the equivalent trend from the isothermal run. The one exception now is the non-zero deviation observed between the LDFP versus FFL model. The only mechanism that gives rise to a non-zero error between these two models is non-isothermal behaviour, introducing an additional operating parameter that can alter Ω_i .

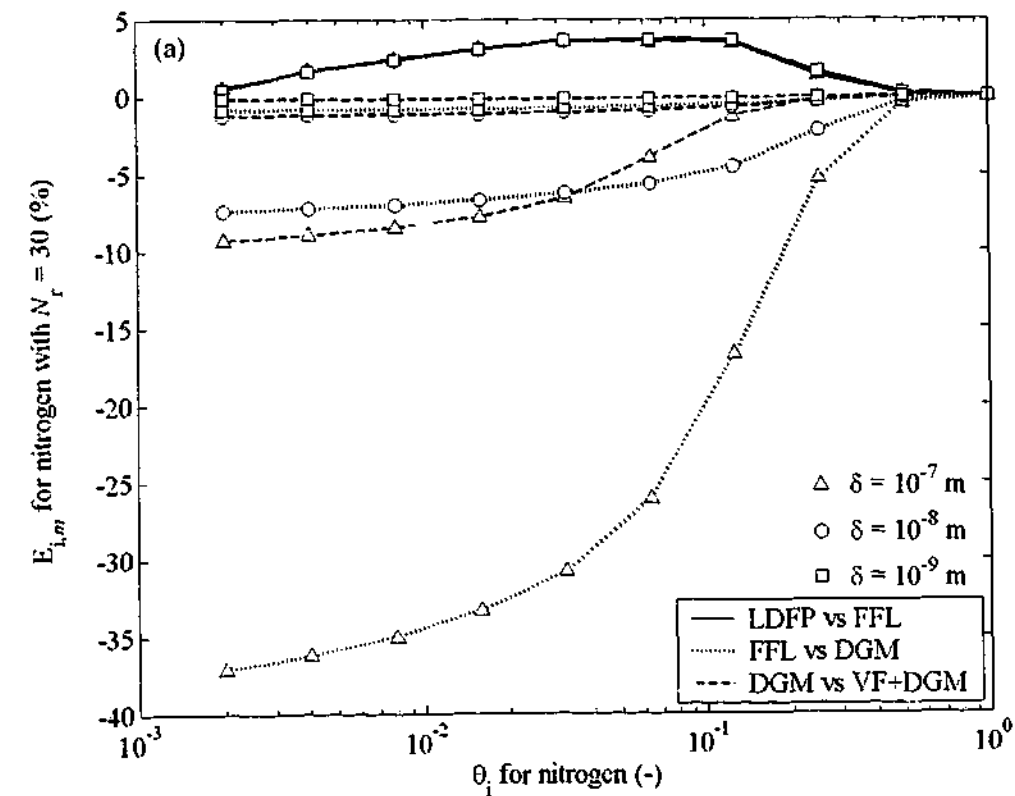


Figure 2.16: WC error with non-isothermal square-wave BC and $N_r = 30$ for (a) nitrogen and (b) oxygen.

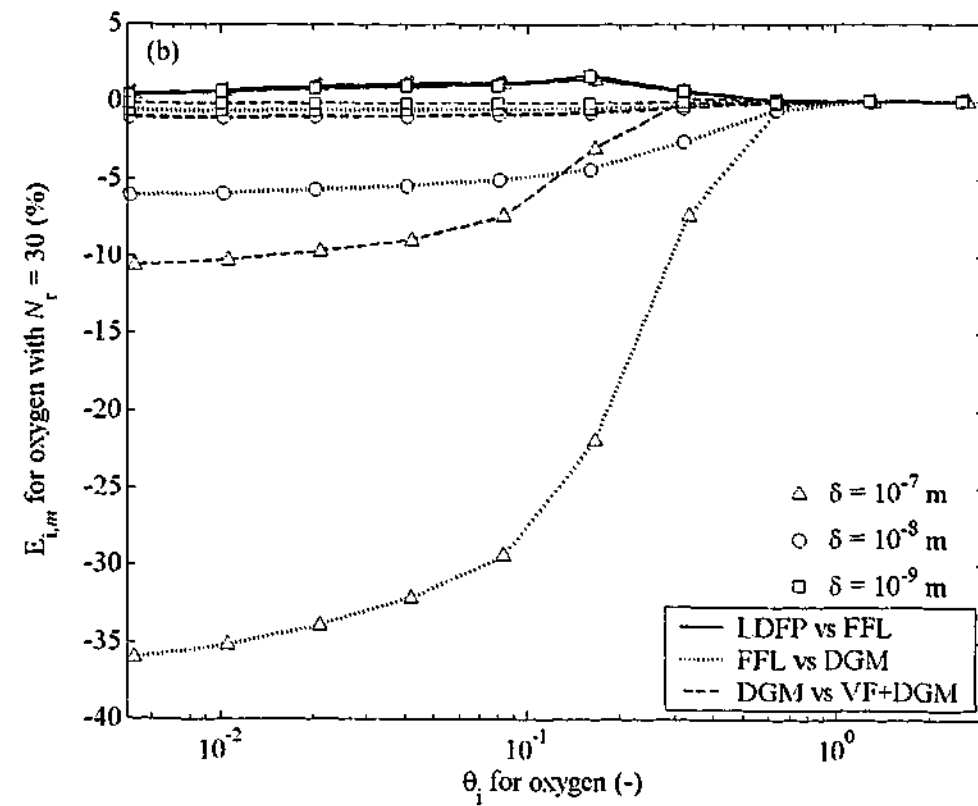
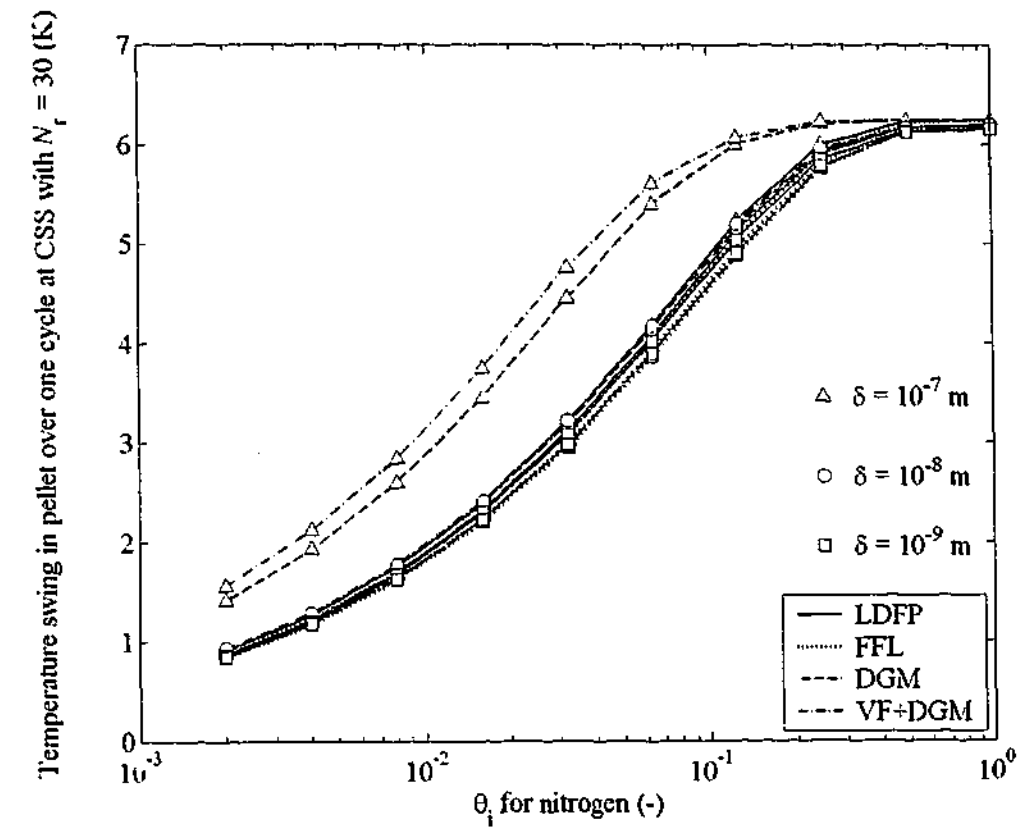


Figure 2.16 continued

The LDFP model overestimates WC given the driving force for pellet uptake has been slightly reduced from the inverse temperature dependence on H_i within the isotherm equation in relation to the isothermal case. Although there is an observed difference it is relatively small, $E_{i,LDFP \text{ vs FFL}} < 5\%$, and was found to be independent of pore size suggesting the Nakao & Suzuki (1983) method is relatively well justified when the equivalent non-isothermal case is considered. The assumption of equimolar counterdiffusion again gives rise to the largest errors observed between each of the mass transfer models and as before is most pronounced at the macropore limit.

One explanation for the relatively close agreement between the isothermal and equivalent non-isothermal WC error can be seen through a plot of the maximum temperature swing calculated for the pellet over the cycle (Fig. 2.17). With the exception of the VF+DGM and DGM, each predicted temperature swing is in close agreement. Figure 2.17 indicates an error of approximately 10% or less in predicted WC will give rise to a temperature swing that generally agrees to within a degree. This indicates non-isothermal behaviour does not significantly alter the relative importance of equimolar counterdiffusion for a macro- mesoporous pellet.

Figure 2.17: Plot of maximum minus minimum temperature across the pellet at CSS with square-wave BC and $N_r = 30$.

2.7.2 RPSA Boundary Conditions

Within a real PSA process the boundary conditions experienced at the surface of a pellet at any point in the bed are generally not square-wave in form. Hence boundary conditions obtained from MINSA under isothermal conditions are now considered here as boundary conditions to SimPell. Again external film heat transfer is neglected to maintain all dynamics solely at the intrapellet level.

Although two different axial positions within the bed were considered in §2.6.2, this analysis focuses only on the lower point in the bed, $z = 0.23$ m. Results observed at the lower axial coordinate show similar trends to other regions for this particular two-step cycle. The resulting error plots for nitrogen and oxygen at $z = 0.23$ m is shown in Figs. 2.18a and 2.18b respectively. WC errors between each mass transfer model demonstrate the assumption of equimolar counterdiffusion introduces a similar deviation to that found when isothermal conditions were imposed. This error (FFL versus DGM) reduces in magnitude as pore size decreases, a direct result of the lessening impact bulk gas motion and viscous flow has on intrapellet mass transfer at the micropore limit. The error between the LDFP versus FFL is well in excess of -30% when the RPSA limit is exceeded, a result that was also observed for the equivalent isothermal runs. The

time corrected Ω_i parameter is again lower than that required to close the cycle in terms of WC and the introduction of non-isothermal behaviour further complicates the procedure invoked to find Ω_i .

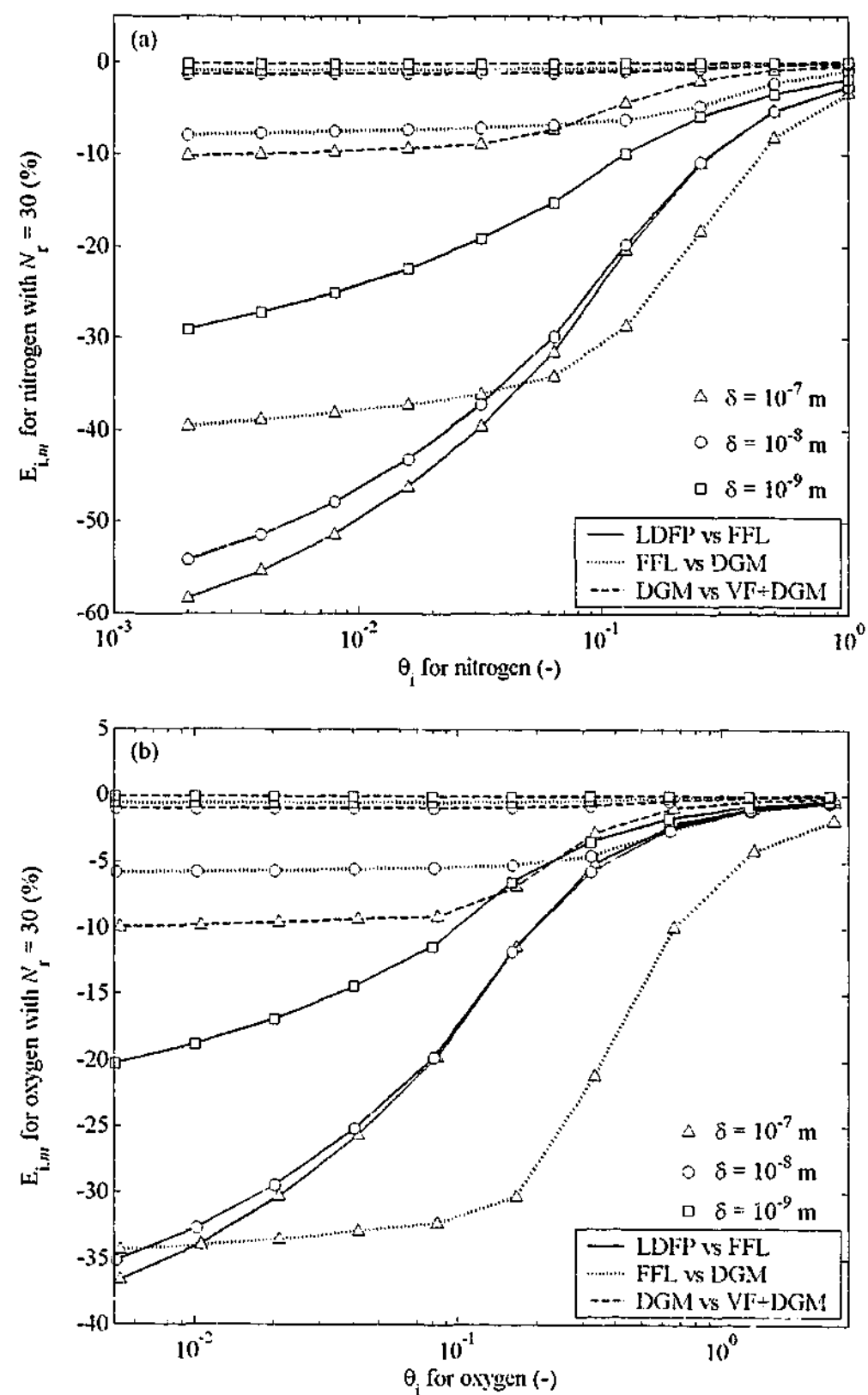


Figure 2.18: WC error with non-isothermal RPSA BC and $N_r = 30$ for (a) nitrogen and (b) oxygen.

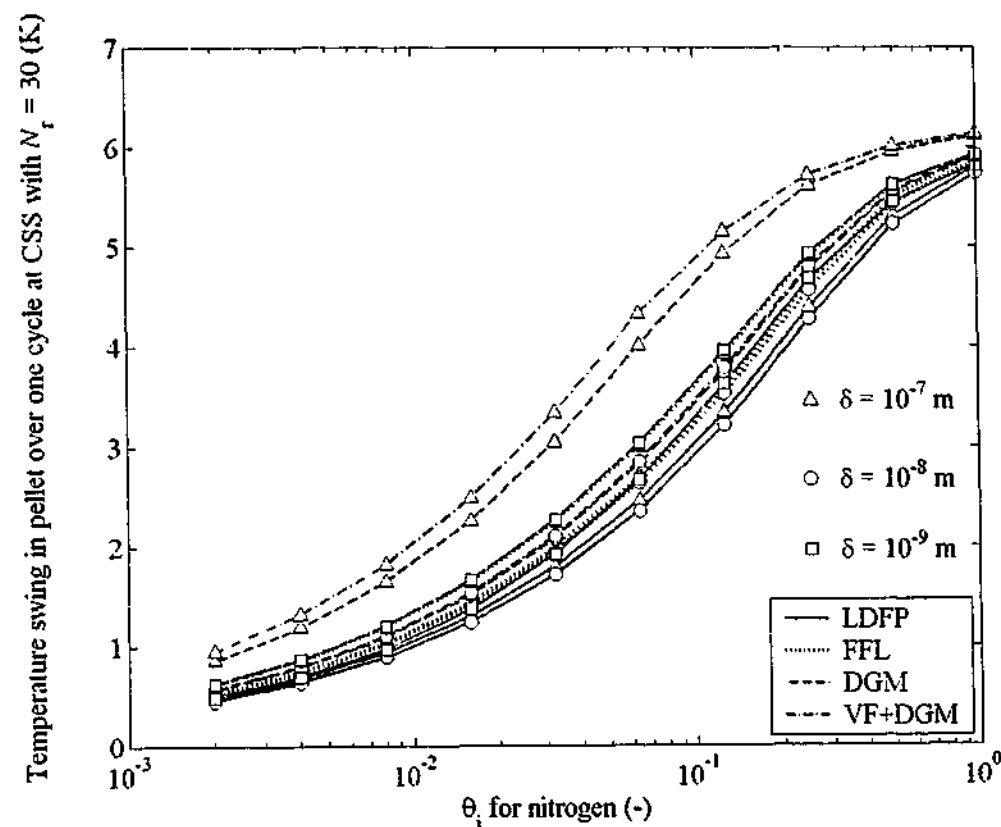


Figure 2.19: Plot of maximum minus minimum temperature across the pellet at CSS with RPSA BC and $N_r = 30$.

With the time corrected Ω_i parameter now underestimating WC in relation to FFL, slightly larger deviations are observed for the maximum versus minimum temperature swing across the pellet (Fig. 2.19). This deviation, however, is still within one degree of the total predicted swing in temperature across the pellet observed for square-wave BC. Predicted temperature swing across the pellet is in very good agreement between the two discretisation schemes, $N_r = 5$ versus $N_r = 30$, using both square-wave and RPSA boundary conditions. In addition, sensitivity on WC from both discretisation schemes is almost identical to the isothermal results of Fig. 2.9 for square-wave BC and Figs. 2.14 and 2.15 for RPSA BC. For brevity it is deemed unnecessary to present these additional graphs in this discussion.

Figures 2.17 and 2.19 both indicate temperature swing across the pellet decreases in magnitude as $\theta_i \rightarrow 0$. At the limit of a long cycle, $\theta_i \rightarrow \infty$, the entire pellet will reach equilibrium with the surrounding gas phase and liberate heat across the entire radial domain. Heat liberated at the crystal surface is transferred across all intrapellet phases (i.e. thermal equilibrium assumed) increasing the internal energy that correspondingly increases the pellet temperature. As cycle time progressively decreases the effective working region for adsorption and desorption moves towards the outer layers of the pellet. Despite a reduced intrapellet volume providing the effective working capacity, the region available for energy accumulation still spans $0 \leq r \leq R_p$ under thermal

equilibrium and hence the gas, solid and adsorbed phases still accumulate energy to the same extent as for an infinitely long cycle time. A smaller amount of heat being liberated over an approximately constant thermal mass means the temperature will increase by a smaller amount. At the extreme limit of RPSA, near-isothermal behaviour would be attained given the small amount of heat liberated across a differential layer of the pellet at $r = R_p$ in relation to thermal capacitance.

At some point, however, the assumption of thermal equilibrium within the pellet will break down and the ability to accumulate energy across the entire pellet domain will be limited by the rate at which heat can be conducted through the pellet. This comes back to the Fourier heat transfer analysis performed at the start of §2.2, which revealed $\partial T_p/\partial r$ can be assumed to equal zero for contact times greater than 0.1 s for a sorbent pellet where internal heat generation is present. These contact times relate to a dimensionless time θ_i of approximately 0.01, 0.004 and 0.001 when $\delta = 1.0 \times 10^{-7}$ m, 1.0×10^{-8} m and 1.0×10^{-9} m respectively for nitrogen and oxygen in X-type zeolite pellets. This suggests a second RPSA regime will arise for θ_i less than 0.01 that is limited by heat conduction within the pellet. However, for most systems of industrial relevance this is not a practical operating regime and the pursuit of SimPell with a radially varying temperature profile is not considered at this point.

2.8 Concluding Remarks

A detailed model has been introduced to quantify the dynamic response of a sorbent pellet that is subjected to a range of pressure swing conditions. For the particular case of oxygen enrichment from air macropore diffusion control was imposed such that viscous flow, molecular and Knudsen diffusion become the dominant modes of intrapellet mass transfer.

A two-step cycle with square-wave and RPSA boundary conditions indicate equimolar counterdiffusion is one assumption that gives rise to large deviations in the predicted working capacity for a sorbent pellet when approaching and exceeding the RPSA limit with a macroporous pellet. At the micropore limit bulk gas motion and viscous flow comprise a small percentage of the total intrapellet molar flux and equimolar counterdiffusion is relatively well justified. However, most sorbents commonly used for the enrichment of oxygen from air operate in the macropore diffusion control regime for mass transfer. This invalidates the basic assumption that underlies the FFL and LDFS/LDFP models. In addition the use of time corrected Ω_i parameters, such as the method of Nakao & Suzuki (1983), further limits the use of linear driving force approximations in situations where boundary conditions other than square-wave in form persist. Errors introduced

with a time corrected Ω_i parameter and equimolar counterdiffusion were most pronounced at the short time limit, $\theta_i < 1.0$.

Deviations between the LDFS/LDFP, FFL, DGM and VF+DGM intrapellet flux models were similar in magnitude in the presence or absence of temperature variations. This implies equimolar counterdiffusion and time corrected Ω_i parameters are limiting assumptions on the transport of oxygen and nitrogen within a sorbent pellet under RPSA conditions irrespective of the isothermal or non-isothermal assumption. This observation implies $\partial T_p/\partial r = 0$, which is valid for the nitrogen-oxygen-zeolite system when $\theta_i > \approx 0.01$.

CHAPTER 3

COMBINED INTRA-INTERPELLET MODEL FOR AN ADSORPTION PROCESS

Chapter 3 expands the single pellet simulator of chapter 2, SimPel, into a full numerical simulator for a general PSA process, called NDGNAS. To minimise computational time associated with the successive substitution approach to CSS, two novel CPU optimisation techniques are introduced into NDGNAS. The individual objectives for this chapter are as follows:

- i. Assess current process models described in the literature to justify the development of a detailed numerical simulator for a general PSA process.
 - ii. Investigate both CPU optimisation techniques using two analytical solutions and several RPSA test cases to assess their merits.
-

Over the course of a true PSA/RPSA cycle the operating conditions that exist at each position within the sorbent bed at any point in time is a complex function of the boundary conditions and physical processes occurring simultaneously within the bed. Convective gas motion between each pellet, diffusive and viscous flow through randomly oriented pore channels of the sorbent and non-isothermal effects associated with the adsorption of a quantity of gas onto the zeolite crystal are just a small collection of the important physical processes to be considered. Given some of these transport mechanisms occur over different time scales, one cycle will not mirror the response of the previous cycle(s) until a steady periodic or CSS condition is achieved. CSS for an adsorption process implies that each transport mechanism no longer introduces any transients outside of those resulting from external forcing boundary conditions. Under non-isothermal conditions several thousand cycles may be required to attain CSS [Wilson *et. al.* (2002)].

For this reason mathematical models of varying complexity have been developed to understand and quantify results obtained from a pilot and/or industrial scale adsorption process. The advantage of developing a mathematical model lies in the ability to obtain real process operating data without recourse to a lengthy or expensive experimental program.

3.1 Previous Models for RPSA Process Simulation

Adsorption models begin with the conservation of mass, energy and momentum for an adsorbing bed of porous sorbent pellets under pressure swing conditions. Assumptions imposed upon the model from this stage of development will define the level of sophistication achieved through process simulation. Low-level models provide a ball park estimate that may be useful when assessing general trends in process performance for a particular separation. High-level models, on the other hand, can be applied to more detailed analyses that include the design of a new installation tailored for a particular separation or to optimise an existing process [Hartzog & Sircar (1995)].

Broadly speaking, these hierarchies of adsorption process models can be grouped into three categories that are delineated by the particular form of the mass transfer model invoked [Serbezov & Sotirchos (1999)].

- i. The first and simplest of these is based on the Instantaneous Local Equilibrium (ILE) assumption, where interpellet gas and intrapellet adsorbed phase concentrations are assumed to be in equilibrium at each axial coordinate within the bed.
- ii. The second and most common assumes a lumped-parameter mass transfer model (i.e. LDF) approximates intrapellet mass transfer resistance, where the pellet conservation equations are volume-averaged over the entire pellet domain.
- iii. The third and most fundamental couples the intra- and interpellet conservation equations together in their most complete form.

3.1.1 Instantaneous Local Equilibrium (ILE) Model

The assumption of ILE often provides an analytical solution for a cyclic adsorption process through the method of characteristics given the hyperbolic nature of the governing PDEs. PSA process models incorporating the ILE assumption have been developed with varying levels of process sophistication. The early PSA models of Shendalam & Mitchell (1972) and Chan *et al.* (1981) considered ILE for trace separations where the assumption of isothermal, isobaric behaviour matches process conditions reasonably well. Later, Knaebel & Hill (1985) extended this analysis to consider isothermal, bulk component separations while Matz & Knaebel (1988) introduced incomplete purge. Further studies by Chiang (1996) and Park *et al.* (1999) have extended the analysis of Matz & Knaebel (1988) to introduce additional process steps.

The ILE assumption was also used in the earliest study of an RPSA cycle to predict the enrichment of nitrogen from a nitrogen-methane feed mixture [Turnock & Kadlec (1971)]. A finite difference

approximation to the conservation of mass coupled with the method of characteristics was applied. Kowler & Kadlec (1972) performed an optimisation study of the aforementioned RPSA process using an equilibrium model coupled with a well-mixed cells-in-series method to solve the resulting set of PDEs. Hart & Thomas (1991) considered an equilibrium model for the separation of methane from methane-carbon dioxide mixtures using a two-step RPSA cycle. Subsequent studies by Lee & Kadlec (1988), Vaporicyan & Kadlec (1987, 1989) and Zhang & Cheng (2000) have extended the ILE model to include a simultaneous reaction within a catalytic-sorbent bed termed Rapid Pressure Swing Reaction.

3.1.2 Linear Driving Force (LDF) Mass Transfer Model

In reality, however, most practical PSA and RPSA cycles do not operate under ILE given the finite resistance to mass transfer present at the intrapellet level. This leads into the second class of mathematical models that now endeavour to describe process operation at a more fundamental level by incorporating the mechanisms of intrapellet mass transfer through an appropriate lumped parameter model. Under these conditions an analytical solution to the governing conservation equation generally apply to an isothermal, isobaric feed step that initially contains uniform bed profiles [Cen & Yang (1986)]. The work of Hirose & Minoda (1986) provides one of the few analytical solutions obtained for a cyclic RPSA process that adopts an LDF model. Their solution was derived by truncating a power series expansion of dimensionless composition at the second term under the assumption of short cycle times for a two-step RPSA cycle to evaluate product gas composition. The assumption of a single adsorbable component fed in trace quantities under isothermal, isobaric, plug flow conditions with a linear isotherm was imposed.

In general, however, a large majority of cyclic adsorption models are not amenable to an analytical solution and recourse to a numerical procedure is required. Common numerical methods that have been used to solve the resulting set of PDEs with the LDF model over an RPSA cycle include a finite difference technique [Doong & Yang (1988)], spline interpolation coupled with a collocation scheme [Baron (1993), Serbezov & Sotirchos (1997b)], a well mixed cells-in-series model [Singh & Jones (1997)], orthogonal collocation [Murray (1996), Oh & Pantelidies (1996), Zhu *et al.* (1996), Betlem *et al.* (1998), Farooq *et al.* (1998), Choong (2000), Sheikh *et al.* (2001)], a Galerkin finite element technique [Teague & Edgar (1999)] and the method of lines [Foeth *et al.* (1995), Ko & Moon (2000), Huang & Chou (2003)]. An alternative model formulation involving an electrical analogue simulation of an RPSA process using the lumped-parameter LDF mass transfer model was developed by Guan & Ye (1990), which was applied in the studies of Guan & Ye (1993), Crittenden *et al.* (1994) and Crittenden *et al.* (1995).

Although the LDF model provides a simplified approximation to the intrapellet conservation equation, problems can arise with this formulation under RPSA conditions. Various alternatives to the GLDF model described in chapter 2 have been incorporated into full process simulators. The time dependent Ω_i parameter developed by Nakao & Suzuki (1983) was applied in the ultra rapid PSA process of Suzuki *et al.* (1996). The penetration theory result of Alpay & Scott (1992) for Ω_i was applied in the studies of Alpay *et al.* (1993, 1994), Murray (1996), Choong (2000) and Cheng *et al.* (1998). Two alternative formulations on Ω_i for a four-step PSA cycle were developed by Raghavan *et al.* (1986) using numerical analysis and Kapoor & Yang (1989) using experimental data. Both of these studies altered Ω_i at short cycle times to better match process performance obtained from simulated and experimental data respectively. However Raghavan *et al.* (1986) extrapolated an asymptotic value of 40 for Ω_i as the cycle time approaches zero whereas Kapoor & Yang (1989) extrapolated this same value to be 110. From a survey of the RPSA literature no cyclic adsorption simulation using an intrapellet concentration profile higher than second order could be found. A great deal of these higher order intrapellet concentration profiles result in a modified form of the LDF mass transfer coefficient k_i that, ultimately, are not all that dissimilar to a formulation where k_i is modified using a time dependent Ω_i parameter. For this reason the pursuit of higher order intrapellet concentration profiles using the LDF model from this preliminary discussion and chapter 2 appears futile.

3.1.3 Coupling the Intra- and Interpellet Equations

The LDF model and its numerous variants have been well documented in the literature when simulating intrapellet mass transfer resistance for an RPSA cycle. The foregoing discussion also highlights the fact that sometimes these models provide a contradicting set of mass transfer parameters to use for a particular cycle regime that, unfortunately, are not applicable to different cycle/process regimes. For this reason selection of an appropriate mass transfer model for an RPSA cycle is often subject to a large set of often limiting constraints. To overcome this requires a more fundamental approach to intrapellet mass transfer that couples the intra- and interpellet conservation equations directly without the use of a lumped parameter approach. However, this analysis significantly complicates the solution procedure. To provide an analytical solution for the bed profiles that couples the intra- and interpellet conservation equations has only been considered using FFL under the isothermal, isobaric, trace adsorbing component assumption for the feed plus make product step when started from uniform initial conditions [Rosen (1952), Kawazoe & Takeuchi (1974), Rasmuson & Neretnieks (1980), Rasmuson (1981), Rasmuson (1982), Carta (1988)]. To the best knowledge of the author an analytical solution to these coupled conservation equations using any intrapellet flux model has yet to be developed for a cyclic PSA/RPSA process.

Further complicating this analysis is the assumption of equimolar counterdiffusion, which neglects the dominant mode of gas transport when applied to the separation of a gas mixture where the macropore dimension contains the limiting regime for mass transfer. The most rigorous set of constitutive equations developed to date exploits the momentum transfer arguments of Maxwell and Stefan for an N_c component gas mixture diffusing through a porous medium (chapter 2). Despite the DGM being reintroduced to the academic community over 40 years ago [Evans *et al.* (1961)] only a handful of dissertations [Mendes (1993), Serbezov (1997)] and articles published recently can be found on the simulation of a PSA/RPSA cycle incorporating Maxwell-Stefan theory with a DPM.

Serbezov & Sotirchos (1999) considered an isothermal and non-isothermal four-step Skarstrom cycle of 88-120 s for the enrichment of oxygen from air. By varying R_p they were able to simulate a process that exhibited severe intrapellet mass transfer limitations ($\theta_i \approx 0.08$) and found the LDF model and DPM with $N_2 = 1$ deviated significantly in predicted oxygen product purity to a DPM with $N_2 = 4$ by almost 10 mol%O₂. Mendes (2001b) compared simulation results to experimental data for the enrichment of oxygen from air over a Skarstrom cycle and Skarstrom cycle with co-current pressure equalisation using the LDF-DG model approximation. With total cycle times in the range 60-240 s reasonable agreement between simulated and experimental results were found. However, results obtained through a DPM were not compared. Mendes *et al.* (2001a) consider an isothermal binary component VF+DGM formulation in conjunction with various LDF-DG model approximations using a four-step PSA cycle. Under short cycle times the inclusion of a curve-fitted phase lag parameter in addition to the diffusion and viscous transport parameters of the LDF-DG model approximation were required to achieve a similar product gas composition to that of the VF+DGM with a DPM.

3.1.4 Acceleration Techniques for Cyclic Adsorption Simulation

Process models described thus far invoke a successive substitution solution strategy. Successive substitution uses the state vector X of bed operating parameters obtained at the end of cycle i , $X_i(t=t_{\text{cycle}})$, as initial conditions for the next simulated cycle, $X_{i+1}(t=0)$. This procedure continues indefinitely until the difference in X at the end of each step j between two concurrent cycles i and $i - 1$ is smaller than a predefined tolerance.

$$\text{abs}[X_{i,j}(t=t_j) - X_{i-1,j}(t=t_j)] < \epsilon_{\text{tol}} \text{ for } j = 1 \text{ to number of steps in cycle} \quad (3.1)$$

This procedure, however, is at best linear in convergence to CSS [Smith & Westerberg (1992)]. Given these slow convergence rates observed with traditional adsorption process simulators, several acceleration methods have been proposed.

Complete Discretisation

By virtue of its name, complete discretisation reduces the temporal and spatial domain of an adsorption model to a grid of space-time coordinates over which the governing PDEs are discretised. Both finite element [Harriott (1996)] and finite difference [Nilchan & Pantelides (1998), Ko & Moon (2000, 2002) and Ko *et al.* (2002, 2003)] schemes have been applied. A very large set of non-linear algebraic equations result, with each equation defining one particular operating parameter such as p_i^B , p_i^P and T_B at one particular spatial coordinate within the bed for just one increment in time over the cycle. An additional constraint is the periodicity condition that states all parameters evaluated at the start of the cycle match the corresponding parameters at the end of the cycle to within ϵ_{tol} . In theory only one inversion of the algebraic equation set is required to ascertain CSS. However the number of algebraic equations that need to be inverted presents an enormous computational workload and often convergence is not guaranteed across several or even one inversion of the equation set [Harriott (1996), Ko *et al.* (2003)].

Although CPU comparisons demonstrate complete discretisation is superior to successive substitution for the simulation of an isothermal RPSA cycle using the LDF model for oxygen enrichment [Nilchan & Pantelides (1998), Ko & Moon (2000, 2002), Ko *et al.* (2003)], the extension to a non-isothermal cycle using the DPM is still untested. Further to this, Nilchan & Pantelides (1998) and Ko *et al.* (2003) found poor agreement between complete discretisation and successive substitution results at CSS under RPSA conditions.

Shooting Methods

Direct determination via a shooting method integrates the spatially discretised ODEs as per successive substitution except here, X_i is now manipulated through the periodicity condition of Eq. (3.1). This manipulation provides a new state vector X that is closer to CSS than simply setting $X_i(t=t_{cycle}) = X_{i+1}(t=0)$ and performing traditional successive substitution. The periodicity condition is introduced through a generic function f , given by $X_{i+1} - X_i$, where X_{i+1} is found by setting $f=0$ [Smith & Westerberg (1992)]. The evaluation of f is performed using Newton's method, which requires a numerically intensive Jacobian matrix (**J**-matrix) to be found. Several algorithms have been investigated to handle the calculation of the **J**-matrix.

Smith & Westerberg (1992) employ the quasi-Newton method of Broyden, Croft & LeVan (1994) applied Newton's method while Kvamsdal & Hertzberg (1995) investigated a range of methods including the quasi-Newton Broyden method, Aitken (quadratic interpolation method), Muller (secant method) and a damped Newton-based method (within the Broyden scheme). Each of the aforementioned studies investigated an isothermal, trace component separation with mass transfer described by the LDF model. More recently Ding & LeVan (2001) developed a hybrid Newton-Broyden method that was used in conjunction with an iterative-secant algorithm for an isothermal, trace component PSA and temperature swing adsorption cycle.

An alternative algorithm based on the Newton-Picard method of Lust *et al.* (1998) for cyclically operated reactors and separators has been recently developed [van Noorden *et al.* (2002)]. An improved estimate of the CSS solution vector is obtained from $X_{i+1} = X_i + \Delta X_i$ by breaking down ΔX_i into two separate subspaces based on a user defined eigenvalue from the **J**-matrix. Although successive substitution had to simulate more cycles to achieve CSS, the Broyden method required less cycles given the Newton-Picard method performs additional calculations that determine stability of the computed CSS condition [van Noorden *et al.* (2002)]. van Noorden *et al.* (2003) combined a first order gradient method with the Newton-Picard method to optimise an isothermal RPSA cycle for oxygen enrichment using the LDF model with cycle time, feed pressure and step time duration as the manipulated variables.

Accelerated Successive Substitution

Accelerated successive substitution can be classified as a technique that is incorporated into an existing simulator that exploits a certain level of "process intuition" to manipulate the solution vector X in a systematic fashion while successive substitution is underway.

ADSIM invokes cycle jumping at a pre-determined point during the simulation from user-defined information that extrapolates bed profiles over a set number of cycles along a particular trajectory [AspenTech (1997)]. Todd *et al.* (2001) developed a node refinement scheme that progressively increases spatial node resolution (N_z systematically increases), with the results at CSS obtained from a low-level node resolution becoming the new extrapolated initial conditions for a refined spatial node resolution. Wilson & Webley (2002) provide an accelerated method of determining CSS temperature profiles by decomposing the energy balance using a short- and long-time scale temperature approximation $T = T_{short} + T_{long}$. Choong *et al.* (2002) (first disclosed in Choong (2000)) proposed an extrapolator technique based on the quasi-linear convergence of product purity to CSS for an isothermal RPSA cycle using the LDF model. Development of the quasi-

linear region for product purity required approximately one-quarter of N_{css} so a four-fold decrease in simulation time was achieved.

While the preceding discussion is not a complete treatise, it does highlight the current status of RPSA process modelling and solution strategies currently proposed in the literature. Although rigorous models for the intrapellet conservation equation have been proposed, their application to a true RPSA cycle is still relatively obscure. Even more elusive is an appropriate acceleration technique for a non-isothermal RPSA cycle that uses a DPM. The remainder of this chapter will focus on the development of a bed model for cyclic PSA/RPSA simulation that incorporates a DPM along with two novel methods of optimising CPU time not yet reported for a cyclic non-isothermal RPSA process[†].

3.2 Overview of the Adsorption Process Simulator

The following discussion presents the final form of each conservation equation only, with a complete derivation for both isothermal and non-isothermal conditions provided in §B.1 and §B.2 of appendix B respectively. In addition, non-isothermal conservation equations only are presented here given the isothermal form can be easily deduced by eliminating $\partial T/\partial t$ from the conservation of mass and neglecting the conservation of energy. Three variations on the conservation of energy have been developed within the final working version of the adsorption simulator.

- i. The process is isothermal and no temperature gradients arise within the bed.
- ii. Intrapellet temperature T_p is identical to the interpellet temperature T_b , which assumes the pellet-to-bed heat transfer coefficient is infinite ($h_{p,b} \rightarrow \infty$).
- iii. Intrapellet temperature is different to interpellet temperature and energy exchange between these two regions is governed by enthalpy passing into/out of the pellets in conjunction with external film heat transfer resistance.

Isothermal conditions will not be used in conjunction with experimental data for the obvious reason that significant temperature excursions are observed. Therefore option i. above is only considered in this chapter for the comparison of two CPU optimisation techniques that have been developed. A large majority of numerical analyses performed within the remaining chapters of this dissertation use option ii., the most common assumption that has been shown to adequately represent pellet scale dynamics over a range of operating conditions [Serbezov & Sotirchos (1998)]. However, one isolated analysis in §4.3.6 will also compare simulation data using option

[†] Please note, however, that CPU optimisation techniques and the related discussion of this chapter have been recently published in *Computers and Chemical Engineering* [Todd *et al.* (2003)].

iii. above. For this reason the following discussion presents the governing conservation equations for both options ii. and iii. It is acknowledged, however, that experimental difficulties inherent with the measurement of T_p and T_b simultaneously over the course of any experiment limits the general use of this modelling option outside of numerical comparisons in §4.3.6. When describing the governing set of conservation equations for option ii. above no distinction will be made between the intrapellet temperature T_p and interpellet temperature T_b , so a generic temperature T will be used for these combined regions.

No radial profiles in composition, pressure or temperature are assumed across the constant cross sectional area of the sorbent bed. This assumes gas is flowing axially through a cylindrical column where no channeling occurs (§1.2.1). Given most PSA/RPSA processes operate at conditions well removed from the critical point of each component, ideal gas behaviour is assumed.

3.2.1 The Impact of Numerical Dispersion on Adsorption Simulation

Second order dispersion terms associated with the interpellet phase are neglected in accordance with the discussion of §1.2.1. However, axial dispersion can be artificially introduced through a numerical discretisation procedure when the conservation equations cannot be solved analytically.

Webley & He (2000) quantified the impact of numerical dispersion for a trace separation with linear equilibrium isotherms over a single breakthrough step using a finite volume discretisation method. They found 10 to 15 nodes were required within the MTZ to minimise numerical dispersion. For a cyclic process where initial bed profiles are smeared as a result of the preceding counter-current depressurisation and purge steps, Webley & He (2000) indicate the number of nodes can be greatly reduced in order to match experimental results and simulation data without the intrusion of numerical dispersion. Provided the discretisation scheme maintains approximately 10 nodes within the MTZ for the breakthrough experiments of chapters 4 and 5 and the node resolution has little impact on predicted RPSA performance, numerical dispersion is relatively small and can be assumed to offset any error introduced by neglecting axial dispersion in the real system.

3.2.2 Non-Isothermal Conservation Equations with the DPM

Intra- and Interpellet Temperatures Differ: $T_B \neq T_P$

The differential form of the conservation of mass and energy respectively at the intrapellet level is given by the following two equations.

$$\left(\frac{\epsilon_P}{RT_P} + \hat{\rho}_P \frac{\partial n_{i,eq}^P}{\partial p_i^P} \right) \frac{\partial p_i^P}{\partial t} + \sum_{j=1, j \neq i}^{N_c} \left(\hat{\rho}_P \frac{\partial n_{i,eq}^P}{\partial p_j^P} \right) \frac{\partial p_j^P}{\partial t} + \left(\hat{\rho}_P \frac{\partial n_{i,eq}^P}{\partial T_P} - \frac{\epsilon_P p_i^P}{RT_P^2} \right) \frac{\partial T_P}{\partial t} = -\frac{1}{r^2} \frac{\partial}{\partial r} (r^2 N_i)$$

for $i = 1 \dots N_c$ (3.2)

$$\int_0^{R_P} \left[\epsilon_P \frac{\partial \left(\sum_{i=1}^{N_c} \rho_{g,i}^P U_{g,i}^P \right)}{\partial t} + \hat{\rho}_P \frac{\partial \left(\sum_{i=1}^{N_c} \hat{U}_{a,i}^P \right)}{\partial t} + \hat{\rho}_P \frac{\partial \hat{U}_s^P}{\partial t} \right] r^2 dr = -R_P^2 \left[\sum_{i=1}^{N_c} (N_{i,R_P} H_{g,i}^P) + h_{P,B} (T_P - T_B) \right]$$

(3.3)

Any arbitrary flux relationship described in chapter 2 can be used within Eqs. (3.2) and (3.3). In the programs current form a user-defined flag selects this constitutive model. An analytical form to the integrated derivatives for each of the internal energy terms is not possible so Eq. (3.3) represents the most general form of the intrapellet conservation of energy under non-isothermal conditions when T_P is not a function of r . The discretisation scheme applied within the pellet allows Eq. (3.3) to be simplified to a form suitable for numerical implementation. The conservation of mass and energy at the interpellet level are written as follows.

$$\frac{1}{RT_B} \frac{\partial p_i^B}{\partial t} - \frac{p_i^B}{RT_B^2} \frac{\partial T}{\partial t} = -\frac{\partial}{\partial z} \left(\frac{p_i^B v_B}{RT_B} \right) + \left(\frac{1 - \epsilon_B}{\epsilon_B} \right) \frac{3}{R_P} N_{i,R_P} \text{ for } i = 1 \dots N_c \quad (3.4)$$

$$\frac{\partial \left(\sum_{i=1}^{N_c} \rho_{g,i}^B U_{g,i}^B \right)}{\partial t} = -\frac{\partial}{\partial z} \left[\sum_{i=1}^{N_c} \left(\frac{p_i^B v_B}{RT_B} H_{g,i}^B \right) \right] - \frac{4h_{B,W}}{d_{bed} \epsilon_B} (T_B - T_W)$$

$$+ \frac{(1 - \epsilon_B)}{\epsilon_B} \frac{3}{R_P} \left[\sum_{i=1}^{N_c} (N_{i,R_P} H_{g,i}^P) + h_{P,B} (T_P - T_B) \right] \quad (3.5)$$

Intra- and Interpellet Temperatures are Equivalent: $T_B = T_P = T$

The conservation of mass at the intra- and interpellet level is identical to Eqs. (3.2) and (3.4) except here one generic temperature, T , is used.

$$\left(\frac{\epsilon_P}{RT} + \hat{\rho}_P \frac{\partial n_{i,eq}^P}{\partial p_i^P} \right) \frac{\partial p_i^P}{\partial t} + \sum_{j=1, j \neq i}^{N_c} \left(\hat{\rho}_P \frac{\partial n_{i,eq}^P}{\partial p_j^P} \right) \frac{\partial p_j^P}{\partial t} + \left(\hat{\rho}_P \frac{\partial n_{i,eq}^P}{\partial T} - \frac{\epsilon_P p_i^P}{RT^2} \right) \frac{\partial T}{\partial t} = -\frac{1}{r^2} \frac{\partial}{\partial r} (r^2 N_i)$$

for $i = 1 \dots N_c$ (3.6)

$$\frac{1}{RT} \frac{\partial p_i^B}{\partial t} - \frac{p_i^B}{RT^2} \frac{\partial T}{\partial t} = -\frac{\partial}{\partial z} \left(\frac{p_i^B v_B}{RT} \right) + \left(\frac{1 - \epsilon_B}{\epsilon_B} \right) \frac{3}{R_P} N_{i,R_P} \text{ for } i = 1 \dots N_c \quad (3.7)$$

In order to combine the conservation of energy across the intra- and interpellet regions, Eq. (3.3) needs to be multiplied through by $-3(1 - \epsilon_B)/\epsilon_B R_P^2$. This allows the left hand side of Eq. (3.3) to replace $3(1 - \epsilon_B) \left[\sum_{i=1}^{N_c} (N_{i,R_P} H_{g,i}^P) + h_{P,B} (T_P - T_B) \right] / \epsilon_B R_P$ on the right hand side of Eq. (3.5).

$$\frac{\partial \left(\sum_{i=1}^{N_c} \rho_{g,i}^B U_{g,i}^B \right)}{\partial t} + \frac{3(1 - \epsilon_B)}{\epsilon_B} R_P \int_0^{R_P} \left[\epsilon_P \frac{\partial \left(\sum_{i=1}^{N_c} \rho_{g,i}^P U_{g,i}^P \right)}{\partial t} + \hat{\rho}_P \frac{\partial \left(\sum_{i=1}^{N_c} \hat{U}_{a,i}^P \right)}{\partial t} + \hat{\rho}_P \frac{\partial \hat{U}_s^P}{\partial t} \right] \frac{r^2 dr}{R_P^3}$$

$$= -\frac{\partial}{\partial z} \left[\sum_{i=1}^{N_c} \left(\frac{p_i^B v_B}{RT} H_{g,i}^B \right) \right] - \frac{4h_{B,W}}{d_{bed} \epsilon_B} (T - T_W) \quad (3.8)$$

Negligible Transport of Energy by Axial Conduction

Both forms of the conservation of energy at the interpellet level, Eqs. (3.5) and (3.8), neglect energy transport by axial conduction. To further investigate this assumption consider a simplified version of the conservation of energy that includes axial conduction with no heat generation or dissipation for the transient flow of gas through an inert bed of sorbent material where no composition gradients form [Bird *et al.* (1960, p 322)].

$$\left[\left(\frac{1 - \epsilon_B}{\epsilon_B} \right) \hat{\rho}_P \hat{c}_s + \rho_g^B \sum_{i=1}^{N_c} y_i^B (c_{g,i}^B - 10^5 R) \right] \frac{\partial T}{\partial t} = -\frac{\lambda_{ax}^c}{\epsilon_B} \frac{\partial^2 T}{\partial z^2} - \rho_g^B \left(\sum_{i=1}^{N_c} y_i^B c_{g,i}^B \right) v_B \frac{\partial T}{\partial z} \quad (3.9)$$

Recasting Eq. (3.9) in dimensionless form gives rise to one governing dimensionless group, the bed scale Peclet heat transfer number $Pe_{B,heat}$, that compares the coefficients of energy transport by convection and conduction [Incropera & DeWitt (1990, p 353)].

$$Pe_{B,heat} = \left[\rho_g^B \left(\sum_{i=1}^{N_c} y_i^B c_{g,i}^B \right) / \lambda_{ax}^c \right] \epsilon_B v_B L_{bed} \quad (3.10)$$

When $Pe_{B,heat} \gg 1$ the mechanism of convection dominates the transport of energy through the bed while conduction dominates transport at the opposite limit, $Pe_{B,heat} \ll 1$. At intermediate values of $Pe_{B,heat}$ both convection and conduction contribute to the transport of energy. Values of $Pe_{B,heat}$ that characterise oxygen RPSA are typically 200 or greater, implying the transport of energy by conduction is small in relation to the transport of energy by convection. This conclusion also holds true when compared to the analogous discussion for the bed scale Peclet mass transfer number (§1.2.1). While the foregoing analysis is based on a simplified version of the conservation of energy, it does directly compare the essential components of interpellet energy transport common with any detailed adsorption-inclusive model. The addition of heat generation, dissipation and accumulation terms will not dramatically alter the relative importance of energy transport by convection or conduction ascertained from this simple analysis.

3.2.3 Non-Isothermal Conservation Equations with the LDFP Model

No LDFP model simulation performed in this dissertation invokes the non-isothermal option of letting intrapellet temperature T_p differ from interpellet temperature T_B . This effectively leaves the DPM as the only mass transfer model considered throughout this dissertation that activates option iii. for $T_p \neq T_B$ described at the start of §3.2. The non-isothermal LDFP model is therefore presented for the case where $T_p = T_B$ only and no reference is made for the case where $T_p \neq T_B$. This statement allows the intra- and interpellet temperatures to be written in terms of one generic temperature, T . Although the form of the LDFP model does not represent the more common LDFS form typically used in the literature, it does correctly account for the intrapellet gas phase [Chabanhi & Tondeur (1998, 2000)] while incorporating the analytical form required on the equilibrium isotherm derivatives when non-linear isotherm equations are present. The corresponding form of the interpellet conservation equation is as follows.

$$\frac{1}{RT} \frac{\partial p_i^B}{\partial t} - \frac{p_i^B}{RT^2} \frac{\partial T}{\partial t} = - \frac{\partial}{\partial z} \left(\frac{p_i^B v_B}{RT} \right) - \left(\frac{1 - \epsilon_B}{\epsilon_B} \right) \frac{\Omega_i D_i^c}{RTR_p^2} (p_i^B - \tilde{p}_i^p) \quad \text{for } i = 1 \dots N_c \quad (3.11)$$

The conservation of mass at the interpellet level is solved in conjunction with the volume-averaged conservation of mass for the intrapellet region, Eq. (2.31).

$$\begin{aligned} \left(\epsilon_p + \hat{\rho}_p RT \frac{\partial \tilde{n}_{i,eq}^p}{\partial p_i^p} \right) \frac{d\tilde{p}_i^p}{dt} + \sum_{j=1, j \neq i}^{N_c} \left(\hat{\rho}_p RT \frac{\partial \tilde{n}_{i,eq}^p}{\partial p_j^p} \right) \frac{d\tilde{p}_j^p}{dt} + \left(\hat{\rho}_p RT \frac{\partial \tilde{n}_{i,eq}^p}{\partial T} - \frac{\epsilon_p \tilde{p}_i^p}{T} \right) \frac{\partial T}{\partial t} \\ = \frac{\Omega_i D_i^c}{R_p^2} (p_i^B - \tilde{p}_i^p) \quad \text{for } i = 1 \dots N_c \end{aligned} \quad (3.12)$$

The corresponding conservation of energy in its most fundamental form for the combined regions is equivalent to the DPM conservation of energy. Axial conduction is neglected based on the magnitude of $Pe_{B,heat}$ discussed in §3.2.2.

$$\begin{aligned} \frac{\partial \left(\sum_{i=1}^{N_c} \rho_{g,i}^B U_{g,i}^B \right)}{\partial t} + \frac{3(1 - \epsilon_B) R_p}{\epsilon_B} \left[\epsilon_p \frac{\partial \left(\sum_{i=1}^{N_c} \rho_{g,i}^p U_{g,i}^p \right)}{\partial t} + \hat{\rho}_p \frac{\partial \left(\sum_{i=1}^{N_c} \hat{U}_{a,i} \right)}{\partial t} + \hat{\rho}_p \frac{\partial \hat{U}_s^p}{\partial t} \right] \frac{r^2 dr}{R_p^3} \\ = - \frac{\partial}{\partial z} \left[\sum_{i=1}^{N_c} \left(\frac{p_i^B v_B}{RT} H_{g,i}^B \right) \right] - \frac{4h_{B,w}}{d_{bed} \epsilon_B} (T - T_w) \end{aligned} \quad (3.13)$$

The analytical form of the integrated radial derivatives using the LDFP model is not presented here for brevity but can be found in §B.3 of appendix B.

3.2.4 Conservation of Momentum at the Interpellet Level

In addition to the conservation of mass and energy for the intra- and interpellet regions, an additional relationship for the conservation of momentum at the interpellet level is required. This equation relates the change in bed velocity to the axial pressure gradient that arises from frictional losses associated with gas flow through a packed bed. This particular aspect of the model will be discussed at length in chapter 5 in relation to both the steady state and full momentum balance. Conclusions from chapter 5 indicate the steady state form of the momentum balance, the Ergun equation, adequately describes interpellet pressure profiles within a sorbent bed under adsorbing and non-adsorbing conditions, providing the momentum balance that is to be used within the adsorption simulator.

$$10^5 \frac{\partial p^B}{\partial z} = - \left[\frac{\kappa_{viscous} \mu_B}{d_{p,eqv}^2} \left(\frac{1 - \epsilon_B}{\epsilon_B} \right)^2 \right] v_B - \left[\frac{\kappa_{kinetic} \hat{\rho}_g^B}{d_{p,eqv}} \left(\frac{1 - \epsilon_B}{\epsilon_B} \right) \right] v_B |v_B| \quad (3.14)$$

3.2.5 Conservation of Energy for the Column Wall

Most industrial installations operate at conditions close to adiabatic given their large internal diameter [Farooq & Ruthven (1990a)]. Most laboratory systems rarely achieve adiabatic behaviour due to limitations on the physical size of process equipment. Small diameter metal walled columns can provide a significant energy source/sink that forces the process to operate somewhere between isothermal and adiabatic [Pentchev *et al.* (2002)]. From this, two methods are available to ensure physical mechanisms predicted within a laboratory sized installation can be scaled to the appropriate industrial capacity.

The first method uses an adsorption column that achieves near adiabatic behaviour when operated over a PSA cycle. Wilson (2001) provides one method that attains near-adiabatic behaviour on a laboratory scale VSA process. A column of internal diameter 0.010 m, lined with a 0.125×10^{-3} m mylar film encased within a polyurethane-insulated wall of outside diameter 0.300 m was reported. The physical strength of this design, however, limits the pressure window to mild VSA conditions and is not recommended for process operating conditions typical of an RPSA cycle.

To maintain physical integrity thick walled metal columns are required. Hence a rigorous wall energy balance is required to describe the exchange of energy between the sorbent bed, column walls and the surrounding environment. The conservation of energy for the wall includes film heat transfer from the sorbent bed to the wall, accumulation and axial conduction of energy along the wall and film heat transfer from the external face of the wall to the environment. Combining these mechanisms gives rise to the following conservation equation.

$$\hat{\rho}_w \hat{c}_w \frac{\partial T_w}{\partial t} = \lambda_w \frac{\partial^2 T_w}{\partial z^2} + \frac{4d_{bed} h_{B,W}}{(d_{col}^2 - d_{bed}^2)} (T_B - T_w) - \frac{4d_{col} h_{W,A}}{(d_{col}^2 - d_{bed}^2)} (T_w - T_A) \quad (3.15)$$

Within Eq. (3.15) $d_{col} = d_{bed} + 2 \Delta z_w$. The term $(d_{col}^2 - d_{bed}^2)$ arises due to annular geometry of the differential element considered along the column wall.

3.2.6 Void Volume and Product Tank Models

To complement the previously defined set of conservation equations, void volumes located above and below the sorbent bed interface are included to represent empty space that dampens the response of a pressure and/or composition change between the seat of the solenoid valve and packed bed interface. A non-isothermal CSTR model that is uniform throughout in pressure is used. To identify the upper and lower regions, the lower void (before $z = 0$) is denoted "bottom"

and upper void (beyond $z = L_B$) denoted "top". This terminology makes experimental versus numerical comparisons of chapter 6 very easy to distinguish. Each equation is written for gas flowing in the positive z direction (i.e. from $z = 0$ to $z = L_{bed}$), so when gas flow is reversed the velocities change sign. The conservation of mass within the bottom and top void volumes respectively are as follows.

$$\frac{V_{bottom}}{RT_{bottom}} \frac{dp_i^{bottom}}{dt} - \frac{V_{bottom} p_i^{bottom}}{RT_{bottom}^2} \frac{dT_{bottom}}{dt} = \left(\frac{p_i v_A}{RT} \right)_{in \text{ at bottom}} - \left(\frac{p_i^B v_B \epsilon_B A_{bed}}{RT_B} \right)_{z=0} \quad \text{for } i = 1 \dots N_c \quad (3.16)$$

$$\frac{V_{top}}{RT_{top}} \frac{dp_i^{top}}{dt} - \frac{V_{top} p_i^{top}}{RT_{top}^2} \frac{dT_{top}}{dt} = \left(\frac{p_i^B v_B \epsilon_B A_{bed}}{RT_B} \right)_{z=L_{bed}} - \left(\frac{p_i v_A}{RT} \right)_{out \text{ at top}} \quad \text{for } i = 1 \dots N_c \quad (3.17)$$

The conservation of energy for the bottom and top void volumes respectively are as follows.

$$\left[\sum_{i=1}^{N_c} \left(\frac{V p_i}{RT} \right)_{bottom} \left(c_{g,i} - \frac{H_{g,i}}{T} \right)_{bottom} \right] \frac{dT_{bottom}}{dt} + \sum_{i=1}^{N_c} \left[V_{bottom} \frac{dp_i^{bottom}}{dt} \left(\frac{H_{g,i}}{RT} - 10^5 \right)_{bottom} \right] \\ = \left(\sum_{i=1}^{N_c} \frac{p_i v_A}{RT} H_{g,i} \right)_{in \text{ at bottom}} - \left(\sum_{i=1}^{N_c} \frac{p_i^B v_B \epsilon_B A_{bed}}{RT_B} H_{g,i}^B \right)_{z=0} \\ - \pi d_{bed} L_{bottom} h_{bottom,W} (T_{bottom} - T_w) \quad (3.18)$$

$$\left[\sum_{i=1}^{N_c} \left(\frac{V p_i}{RT} \right)_{top} \left(c_{g,i} - \frac{H_{g,i}}{T} \right)_{top} \right] \frac{dT_{top}}{dt} + \sum_{i=1}^{N_c} \left[V_{top} \frac{dp_i^{top}}{dt} \left(\frac{H_{g,i}}{RT} - 10^5 \right)_{top} \right] \\ = \left(\sum_{i=1}^{N_c} \frac{p_i^B v_B \epsilon_B A_{bed}}{RT_B} H_{g,i}^B \right)_{z=L_{bed}} - \left(\sum_{i=1}^{N_c} \frac{p_i v_A}{RT} H_{g,i} \right)_{out \text{ at top}} \\ - \pi d_{bed} L_{top} h_{top,W} (T_{top} - T_w) \quad (3.19)$$

Product gas is obtained from a PSA cycle during a select number of process steps. For this reason most PSA systems locate a buffer tank after the adsorption column(s) to provide a constant supply of product gas to the downstream consumer. An analogous CSTR model to the bottom and top void volumes is also applied to the product tank. To maintain gas compression terms an independent conservation of energy is written for the product tank. For ease of simulation it is assumed that gas leaving the adsorption column also enters the product tank with the same enthalpy. This implies the rate of heat transfer from the pipe to environment is relatively slow in comparison to the time scale for movement of gas between the column and product tank. Although

perfect mixing may not be representative of true hydrodynamics within the product tank, for the sake of process simulation this is assumed to be a relatively close approximation.

$$\frac{V_{\text{tank}}}{RT_{\text{tank}}} \frac{dp_i^{\text{tank}}}{dt} - \frac{V_{\text{tank}} p_i^{\text{tank}}}{RT_{\text{tank}}^2} \frac{dT_{\text{tank}}}{dt} = \left(\frac{p_i v A}{RT} \right)_{\text{out of column}} - \left(\frac{p_i v A}{RT} \right)_{\text{out of tank}} \quad \text{for } i = 1 \dots N_c \quad (3.20)$$

$$\begin{aligned} & \left[\sum_{i=1}^{N_c} \frac{V_{\text{tank}} p_i^{\text{tank}}}{RT_{\text{tank}}} \left(c_{g,i}^{\text{tank}} - \frac{H_{g,i}^{\text{tank}}}{T_{\text{tank}}} \right) \right] \frac{dT_{\text{tank}}}{dt} + \sum_{i=1}^{N_c} \left[V_{\text{tank}} \frac{dp_i^{\text{tank}}}{dt} \left(\frac{H_{g,i}^{\text{tank}}}{RT_{\text{tank}}} - 10^5 \right) \right] \\ & = \left(\sum_{i=1}^{N_c} \frac{p_i v A}{RT} H_{g,i} \right)_{\text{out of column}} - \left(\sum_{i=1}^{N_c} \frac{p_i v A}{RT} H_{g,i} \right)_{\text{out of tank}} \\ & - \left(\pi d_{\text{tank}} L_{\text{tank}} + 2 \frac{\pi d_{\text{tank}}^2}{4} \right) h_{\text{tank,W}} (T_{\text{tank}} - T_W) \end{aligned} \quad (3.21)$$

When the top void volume is active during a simulation, the terms $(p_i v A / RT)_{\text{out of column}}$ and $\left(\sum_{i=1}^{N_c} p_i v A H_{g,i} / RT \right)_{\text{out of column}}$ in Eqs. (3.20) and (3.21) represent the mole and enthalpy flow of gas leaving this void respectively. When the top void volume is not active, these same two terms represent the mole and enthalpy flow of gas leaving the sorbent bed interface at $z = L_{\text{bed}}$.

3.2.7 Numerical Solution of the Governing Conservation Equations

The governing set of interpellet conservation equations has simply added an extra level of model complexity to the non-linear set of intrapellet conservation equations discussed in chapter 2. This excludes analytical techniques being used so an appropriate numerical strategy is required. To ensure the governing set of equations remain in conservative form such that mass and energy entering and leaving the simulation balances the amount accumulated to within ODE integrator tolerances, the axial domain of the sorbent bed and radial domain of the pellet (if required) is discretised using the finite volume method introduced in §2.2.5. This reduces temporal and spatially dependent PDEs to a relatively large number of temporal ODEs. A detailed discussion on the discretised form of the interpellet conservation equations will not be presented here for brevity, but can be found in §B.3 of appendix B for both the DPM and LDFP model in isothermal and non-isothermal form.

When the DPM is activated, the finite volume method transforms the set of $(N_c + 1)$ non-isothermal bed void PDEs into a set of $N_z (N_c + 1)$ ODEs over the axial domain of the bed. In addition to the discretised bed void ODEs an additional set of $N_c N_r$ ODEs for the intrapellet model

at each axial volume within the bed is required. Hence a total of $N_z [(1 + N_r) N_c + 1]$ ODEs are to be solved across the intra-interpellet domain using the DPM.

Similarly, the finite volume method transforms the set of $(N_c + 1)$ non-isothermal bed void PDEs for the LDFP model into a set of $N_z (N_c + 1)$ ODEs over the axial domain of the bed. The LDFP model also requires an additional $N_c N_z$ ODEs according to Eq. (3.12) to be included into the set of $N_z (N_c + 1)$ conservation equations. Hence a total of $N_z (2 N_c + 1)$ ODEs are to be solved using the LDFP formulation across the intra-interpellet domain. From this it is readily seen the LDFP formulation is equivalent to the single radial node case of the DPM ($N_r = 1$).

Along with these $N_z [(1 + N_r) N_c + 1]$ ODEs for the DPM and $N_z (2 N_c + 1)$ ODEs for the LDFP model a further $2 (N_c + 1)$ ODEs are established to accumulate mass and enthalpy entering and leaving the adsorption column, which can be physically interpreted as “numerical” mass and enthalpy flow meters. These extra ODEs allow independent mass and energy balance closure checks to be performed. Further to this, an additional group of ODEs can be established through appropriate settings on user-defined input flags. These ODEs are designated “optional” as they are not always activated on every run discussed in this dissertation.

- i. When implementing $T_p \neq T_b$ for the DPM, an extra N_z ODEs are required.
- ii. For the rigorous wall model, an extra N_z ODEs are required.
- iii. When bottom and top void volumes are included, an extra $2 (N_c + 1)$ ODEs are required. Also, an extra 2 ODEs are required for the wall when option ii. above is activated.
- iv. For the rigorous product tank model, an extra $N_c + 1$ ODEs are required.

The total number of ODEs passed to the ODE integrator, N_{eq} , with all simulation options “active” are set out by the following.

$$N_{\text{eq}} (\text{DPM}) = N_c [5 + (1 + N_r) N_z] + 3 N_z + 7 \quad (3.22)$$

$$N_{\text{eq}} (\text{LDFP}) = N_c (5 + 2 N_z) + 2 N_z + 7 \quad (3.23)$$

The complete set of discretised ODEs have been incorporated into a custom written Fortran90 program that is essentially an addendum to SimPell. The final working version of this program is called NDGNAS (acronym for N-component Dusty Gas model for Numerical Adsorption Simulation, pronounced indigenous). NDGNAS is a new and independent adsorption simulator in relation to MINSA [Webley *et al.* (2000), Webley & He (2000), Todd *et al.* (2001)]. Extensive testing of NDGNAS against MINSA revealed identical predictions across a range of model options common to both simulators. Comparative plots of NDGNAS and MINSA profiles, however, are

deemed unnecessary for presentation in this dissertation. Within NDGNAS, both ends of the adsorption column are connected to source and/or sink tanks that communicate gas into or out of the simulation. Any number of tanks can be assigned, with the user specifying the relevant tank connected to the top and bottom of the column. These additional tanks can be set using a rigorous model identical in form to the "CSTR product tank" or designated "infinite" to provide a fixed composition, temperature and pressure (i.e. atmospheric conditions).

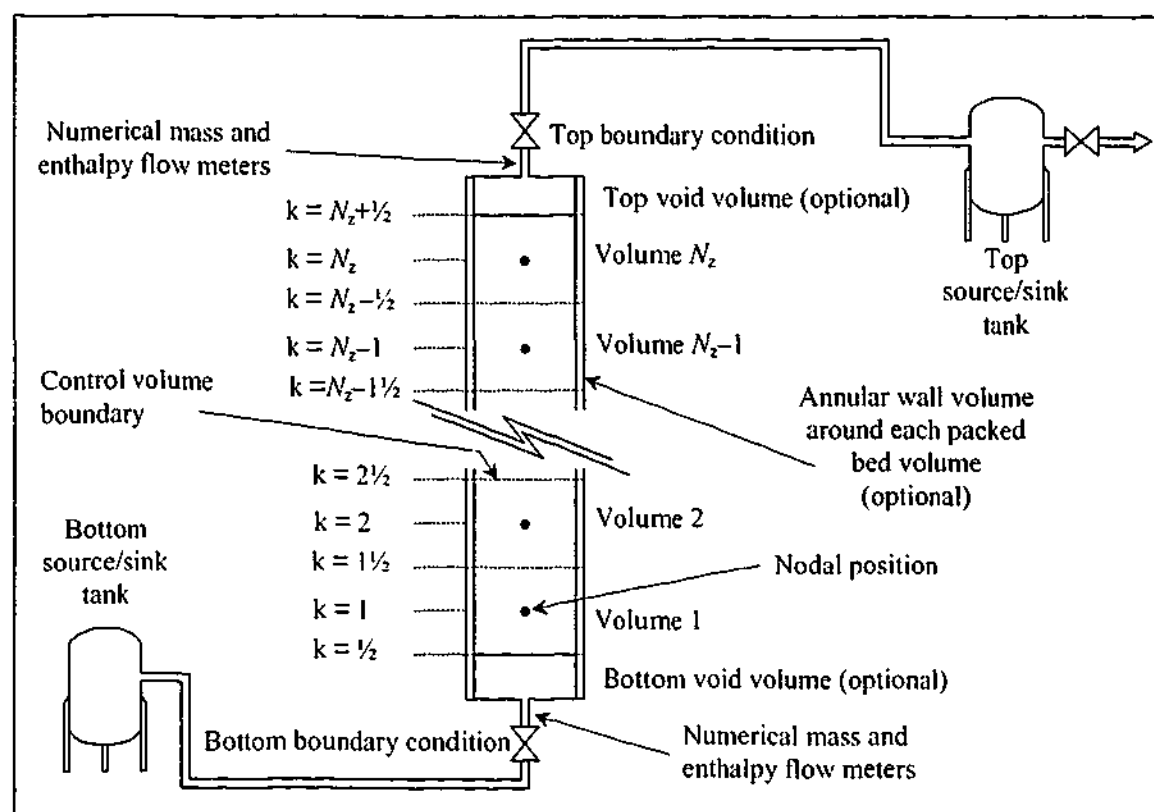


Figure 3.1: Schematic diagram of the numerical discretisation scheme for the adsorption column showing void volumes and source/sink tanks. The parameter k in this diagram represents a control volume counter that starts numbering from node 1 at the bottom of the bed. For convenience, control volume boundaries are denoted "half-a- k " above or below node position " k ".

Outside of the rigorous product tank model, however, this dissertation will use "infinite" volume tanks for source/sink gas being passed to or from the adsorption column except chapter 6. In chapter 6, a new option was included that allows experimental product tank profiles to be used for reasons that will become clear through chapter 4. A diagram that helps to explain the numerical arrangement of the adsorption process is shown schematically in Fig. 3.1.

3.3 Novel CPU Optimisation Techniques Introduced into NDGNAS

The foregoing discussion has presented a complex set of coupled, non-linear PDEs and subsequently, an even larger set of discretised ODEs that describe the operation of a generic PSA cycle.

3.3.1 Mass-transfer Model Switch (MMS)

Solution of these discretised ODEs presents a challenge computationally given the slow convergence rate to CSS mentioned in §3.1.4. As an example, temperature profiles obtained from our RPSA pilot plant producing 76 mol%O₂ over a 3.00:1.01 bar.a pressure window indicates a minimum of 2500 cycles from start-up are required to approach CSS (Fig. 3.2). The total cycle time is 12 s and a four-step, one-bed cycle similar to that presented in §3.5 is used. While experimental data is not the subject of this chapter, these profiles are presented merely to demonstrate the difficulties that arise with the simulation of such a process and why the conservation of energy is an important factor in PSA modelling for bulk gas separation.

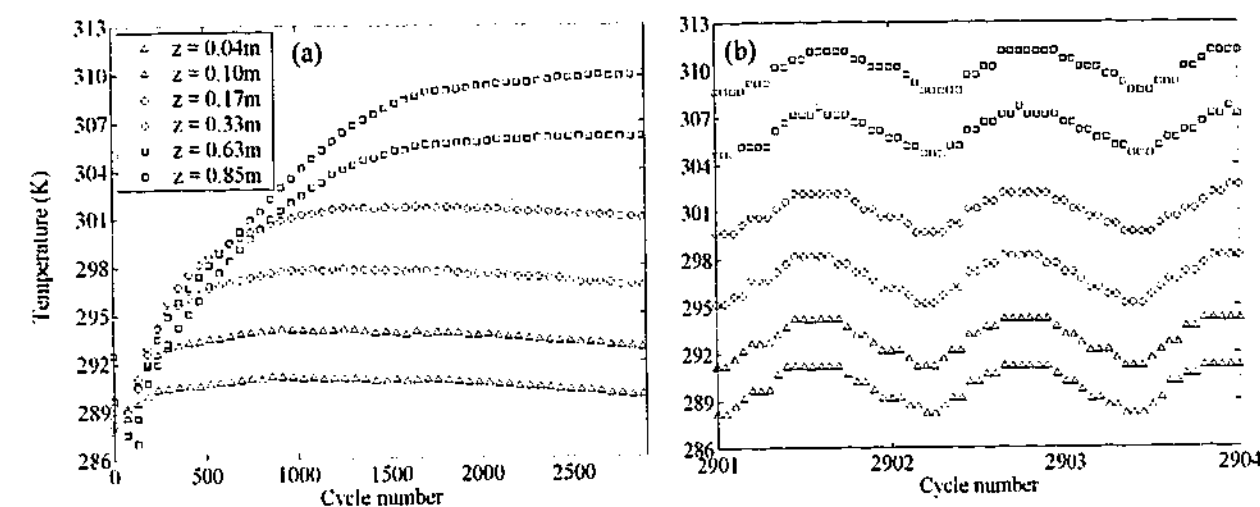


Figure 3.2: Experimental temperature profiles obtained for a 12 s RPSA cycle producing 76 mol%O₂ over a 3.00:1.01 bar.a pressure window. (a) Long time scale temperature profiles showing the evolution of temperature from start-up to the onset of CSS. (b) Short time scale temperature profiles at the onset of CSS.

An examination of the energy source-sink terms within this process show two distinct time scales exist for the generation and dissipation of energy within the bed [Wilson & Webley (2002)]. Temperature swing associated with adsorption-desorption phenomena is attributed to changing pressure, which occurs on the time scale of seconds. This is represented by wave-like temperature fluctuations in Fig. 3.2b. Over the time scale of hours, however, is the movement of this energy via gas convection through the bed resulting from the ratio $\rho_g^B c_g^B / \hat{\rho}_{bed} \hat{c}_s \ll 1$. This is demonstrated

by slowly converging temperature profiles, cycle-by-cycle, in Fig. 3.2a. The final form of the axial temperature profile results from closure of the energy generated and consumed via reversible adsorption to the energy convected into and out of the bed over a cycle.

Starting from arbitrary initial conditions, which is generally the case when the final form of the temperature profile is not known, often requires many thousands of cycles to be simulated. Tracking the evolution of this temperature profile from cycle 1 to N_{CSS} using the computationally expensive DPM is prohibitive. An efficient and robust method needs to be developed that minimises the duration of time a DPM is activated while maintaining strict closure in the accumulation of energy to pre-determined tolerances. Unlike other numerical models considered for an RPSA system, NDGNAS is developed with both the LDFP model and DPM activated at some point during the simulation. This has the added advantage of executing the program just once to obtain CSS results from both the DPM and LDFP model.

When NDGNAS begins and bed profiles are far removed from CSS, the computationally simpler LDFP model is activated. Although the LDFP model does show inadequacies in predicting mass transfer dynamics when compared to the DPM, this is of secondary importance to the evolution of the temperature profile. Capturing adsorption-desorption phenomena with an LDFP model provides a first estimate of the temperature swing expected over a cycle that ultimately gives rise to the CSS temperature profile. Once the LDFP model has reached CSS these bed profiles are then extrapolated to the DPM and the simulator restarts with a better estimate of CSS profiles than if started from cycle 1 with the DPM, hence the name Mass-transfer Model Switch (MMS). A flowchart outlining the implementation of the MMS within NDGNAS is shown in Fig. 3.3.

For the MMS to prove successful a consistent definition of CSS is required that is independent of spatial discretisation and mass transfer model. The definition of CSS introduced by Todd *et al.* (2001) satisfies this criterion provided a conservative discretisation scheme is adopted, which checks for closure in mass and energy accumulation over a cycle as well as closure in bed profiles at the start and end of each step between two concurrent cycles. The equation set considered here, however, does not check for closure of the intrapellet partial pressure profile between two concurrent cycles when the DPM is active. NDGNAS assumes volume averaged adsorbed phase loading can be used to ascertain closure at the pellet scale. A combination of the finite volume method and CSS check of Todd *et al.* (2001) will be demonstrated later in this chapter to reproduce CSS that is relatively insensitive to the level of spatial discretisation. Please refer to §B.4 of appendix B for a detailed description of the CSS check adopted within NDGNAS. The underlying concept behind this development is to provide CSS results entirely consistent with a

kinetic theory (VF+DGM) approach to mass transfer without the burden of simulating the DPM from cycle 1 to N_{CSS} .

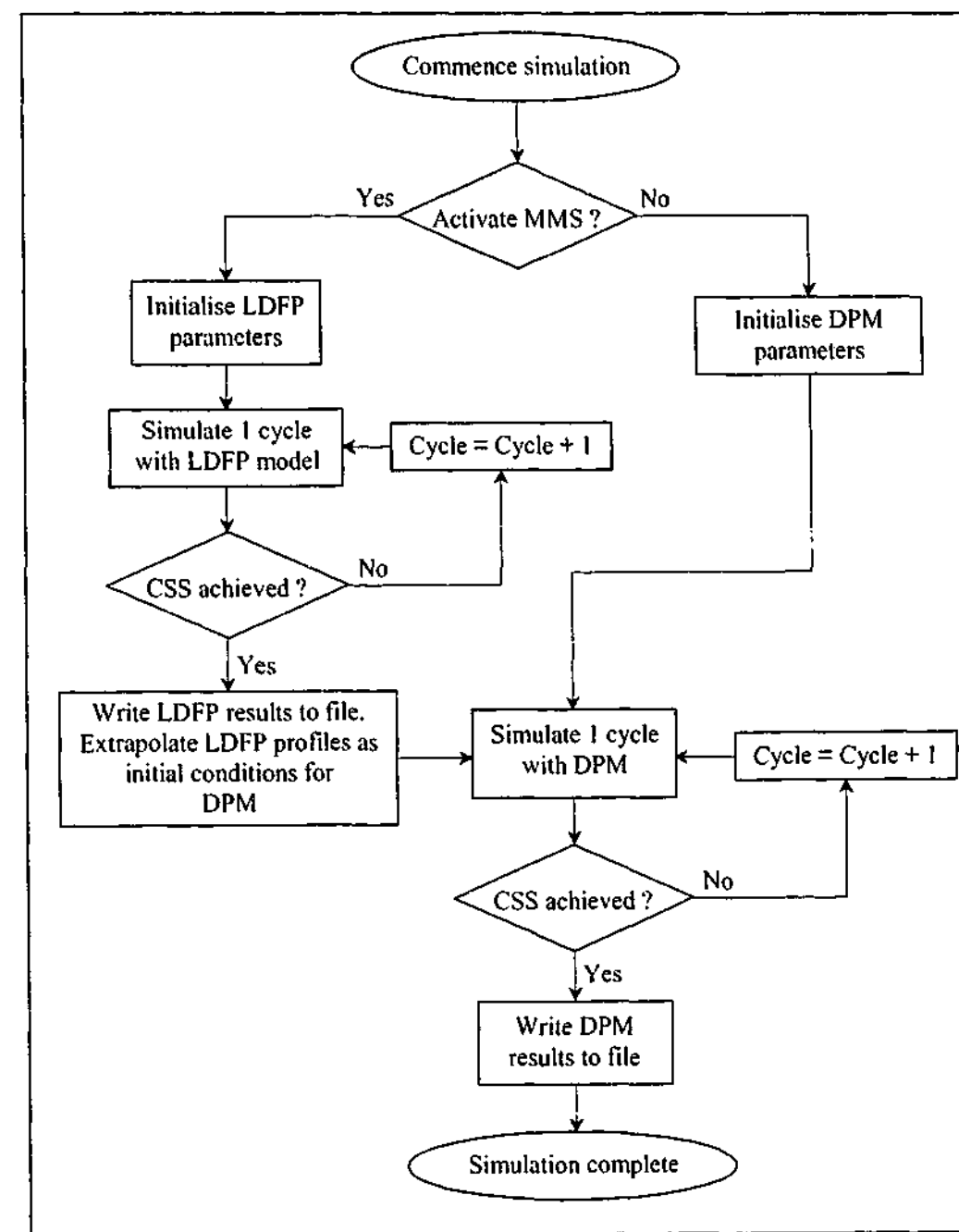


Figure 3.3: Flowchart outlining the implementation of the Mass-transfer Model Switch (MMS).

3.3.2 Use of an Improved ODE Integrator - BzzOde

The MMS provides one method to optimise the CPU time required in simulating an RPSA process to CSS. This method faithfully reproduces the actual performance of a real process via successive substitution, checking for CSS at the end of each cycle. This method is expensive computationally and often requires a large number of cycles to reach CSS under non-isothermal conditions. The speed at which CSS is achieved, however, ultimately depends on the ability of the ODE integrator

to numerically solve the resulting set of N_{eq} ODEs for the system in their discretised form. A further complication is that often the operating conditions expected over a typical cycle will change for different case studies and the ability to provide an analytical **J**-matrix for the system is often impractical. This also limits the practicality of various ODE integrators that invoke an iterative Krylov linear solver based on a preconditioning matrix as the sparsity of the system may not be known *a priori* when general cycle/boundary condition options and user input flags to a PSA simulator are established. Hence the preconditioned Krylov option of VODE and the sparse matrix factorization of BzzOde will not be considered in the following discussion.

For process models that involve a medium-to-large number of ODEs, the **J**-matrix calculation using finite difference quotients and subsequent Newton matrix (**P**-matrix) factorisation becomes the limiting step towards optimising CPU performance [Buzzi Ferraris & Manca (1998)]. One of the early integrators developed for the numerical solution of stiff systems of ODEs was LSODE, based on algorithmic and interface improvements to the Gear package of Hindmarsh [Petzold (1983)]. LSODE calculates a full numerical **J**-matrix through an extra set of N_{eq} calls to the time derivative subroutine, attempting to keep the **P**-matrix constant for a limited number of steps and re-evaluating the **J**-matrix each time the **P**-matrix requires re-factoring. This integrator becomes CPU intensive, however, when a medium-to-large number of ODEs are to be solved. To overcome some of these issues with the **J**-matrix evaluations of LSODE, VODE was developed. VODE provides algorithmic improvements by storing and reusing the **J**-matrix when the **P**-matrix requires re-factoring, continuing in this manner until pre-defined criteria are met and the **J**-matrix requires re-evaluation [Brown *et al.* (1989)]. This technique reduces the additional number of time derivative subroutine calls required to update the **J**-matrix and hence optimises CPU time in relation to LSODE. More recently a new class of ODE solver developed in C++ for the solution of stiff and non-stiff ODEs, BzzOde, has shown efficiency and robustness characteristics further advanced on VODE. In addition to capitalising on the object oriented programming construct of the C++ environment, a new consistency check on the validity of the current **J**-matrix was devised. This allows BzzOde to update the **J**-matrix only when strictly necessary and not every 20 steps as VODE enforces.

Due to the fact that the number of calls to the ODE system for updating the **J**-matrix is proportional to the number of variables, BzzOde chooses to update more frequently the **J**-matrix when the dimension of the problem, N_{eq} , is small. On the other hand, BzzOde reduces at the maximum extent the update of the **J**-matrix when a large number of equations are involved. This choice usually reduces the total number of time derivative subroutine calls but increases the number of time increments taken and especially the number of factorizations of the **P**-matrix. The increased number of time increments is quite irrelevant whilst the factorization of a large matrix is

time consuming when the **J**-matrix is considered as a dense matrix. Generally speaking, when chemical engineering problems are involved, CPU time savings due to the reduction of calls to the time derivative subroutine are more relevant than the increase of **P**-matrix factorizations [Buzzi Ferraris & Manca (1998)]. With this, BzzOde was shown to reduce CPU time when solving medium and large sets of stiff ODEs in comparison to VODE and other Fortran based ODE integrators.

Given the solution of a typical PSA process often involves at least a medium number of stiff ODEs, N_{eq} generally greater than 50, alternative ODE integrators outside of VODE and BzzOde will not be considered in this study. These two integrators are specifically targeted for the optimal solution of medium-to-large ODE systems that other integrators rarely achieve in terms of CPU performance. Absolute CPU times reported in this chapter are well outside those required for program initialisation and termination procedures performed within the Windows98 operating system. Hence a direct comparison between absolute CPU time from each ODE integrator can be made. When a select number of cases from §3.5 of this chapter were repeated absolute CPU time was comparable to that reported in Tables 3.4 and 3.6 to within 10-25 s. Integrator performance and CSS parameters obtained from these comparative runs also match very well.

3.4 CPU Comparisons using Analytical Test Cases

Before a true RPSA cycle is considered with respect to each ODE integrator, test cases using known analytical solutions under limiting model assumptions will be performed. This provides a first case comparison of simulation results obtained with each ODE integrator and an independent assessment of CPU improvements afforded with the introduction of BzzOde. Given these comparisons are derived for a single step only and do not involve a cyclic adsorption process the MMS is not considered at this point and only the DPM is used. This is equivalent to deactivating the MMS, simulating just 1 step of 1 cycle and deactivating the CSS criterion of Fig. 3.3. In the programs current format a user-defined flag allocates the simulation as being isothermal or non-isothermal. This flag effectively partitions the subroutine containing time derivatives into two sections where non-isothermal cases are considered separately from isothermal cases, eliminating the redundant energy equations from N_{eq} . In addition, the rigorous wall and product tank models as well as the bottom and top void volume options are deactivated.

3.4.1 Three Component Similarity Solution

To reduce the non-isothermal conservation equations to the equivalent form considered by Andrews & Scott (2000) the following assumptions are imposed.

- ILE is achieved at each axial position within the sorbent bed.
- The combined intra- and interpellet regions behave isothermally.
- The equilibrium isotherm is linear and uncoupled and of the form $n_{i,eq}^p = H_i p_i^B$, where H_i is constant under isothermal conditions. This allows the conservation of mass for the interpellet region to be re-written in the following form.

$$\frac{\partial p_i^B}{\partial t} \left[1 + \left(\frac{1 - \epsilon_B}{\epsilon_B} \right) \beta_p H_i RT \right] = - \frac{\partial}{\partial z} (p_i^B v_B) \quad (3.24)$$

- The Ergun equation reduces to the laminar form commonly referred to as the Blake-Kozeny equation.

$$10^5 \frac{\partial p^B}{\partial z} = - \left[\frac{\kappa_{viscous} \mu_B}{d_{p,eqv}^2} \left(\frac{1 - \epsilon_B}{\epsilon_B} \right)^2 \right] v_B \quad \text{with } \kappa_{viscous} = 150 \quad (3.25)$$

Combining Eqs. (3.24) and (3.25) and introducing the dimensionless variables $\bar{z} = z/L_{bed}$,

$$K_i = \left[1 + \left(\frac{1 - \epsilon_B}{\epsilon_B} \right) \beta_p R T H_i \right]^{-1}, \quad \bar{t} = \frac{p_{ref} t}{L_{bed}^2} \left[\frac{10^{-5} \kappa_{viscous} \mu_B}{d_{p,eqv}^2} \left(\frac{1 - \epsilon_B}{\epsilon_B} \right)^2 \right]^{-1} \quad \text{and } \bar{p}_i^B = p_i^B / p_{ref} \quad \text{gives}$$

the following.

$$\frac{\partial \bar{p}_i^B}{\partial \bar{t}} = K_i \frac{\partial}{\partial \bar{z}} \left(\bar{p}_i^B \frac{\partial \bar{p}_i^B}{\partial \bar{z}} \right) \quad (3.26)$$

The analytical solution of Eq. (3.26) using the similarity variable $\bar{\chi} = \bar{z}/\sqrt{\bar{t}}$ subject to an instantaneous change in pressure at the inlet to the bed for N_c components is given by Andrews & Scott (2000). A particular case study presented bed profiles for the pressurisation of a column of 5A zeolite with $\bar{p}^B = 2.00$ at $\bar{\chi} = 0$, initially containing oxygen, nitrogen and argon with dimensionless partial pressures of 0.21, 0.70 and 0.09 respectively. To simulate this numerically ninety axial nodes ($N_z = 90$) through the bed and five radial nodes ($N_r = 5$) within the pellet was adopted. To simulate equilibrium conditions using a DPM, the transport coefficients for each of the three transport mechanisms of the VF+DGM were set to very large values of the order 10^3 . This forces the effective diffusion coefficients of the diffusive and viscous transport mechanisms to assume a value many orders of magnitude larger than expected under normal operating

conditions, eliminating intrapellet mass transfer as the limiting transport mechanism. For this reason $N_r = 5$ provides sufficient resolution of radial profiles required under equilibrium conditions. This axial-radial node distribution gives $N_{eq} = 1626$ with the energy balance options deactivated.

Table 3.1: ODE integrator results from the similarity solution of Andrews & Scott (2000).

| Integrator | N_{eq} | # Incs | # FC | # JE | # LU | CPU time (s) |
|------------|----------|--------|--------|------|------|--------------|
| BzzOde | 1,626 | 2,186 | 4,581 | 1 | 60 | 942 |
| VODE | 1,626 | 350 | 11,877 | 7 | 55 | 855 |

Incs = Total number of time increments taken.
 # FC = Total number of calls made to the time derivative subroutine.
 # JE = Total number of J-matrix evaluations.
 # LU = Total number of linear system P-matrix factorisations.

The formulation of Andrews & Scott (2000) shows " $N_c - 1$ " shockwaves form within the bed resulting in a stiff set of ODEs. This test case also provides a good example for the inherent stability introduced by the QUICK scheme with SMART smoothing to minimise unwanted oscillations that can form around these shock fronts, shown in Fig. 3.4. For each ODE integrator the location of both shockwaves is well captured, along with the asymptotic form of dimensionless partial and total pressure for $\bar{\chi} \rightarrow \infty$. Each of the two integrators also presented no stability problems in solving for bed profiles, presented here at $t = 20$ s.

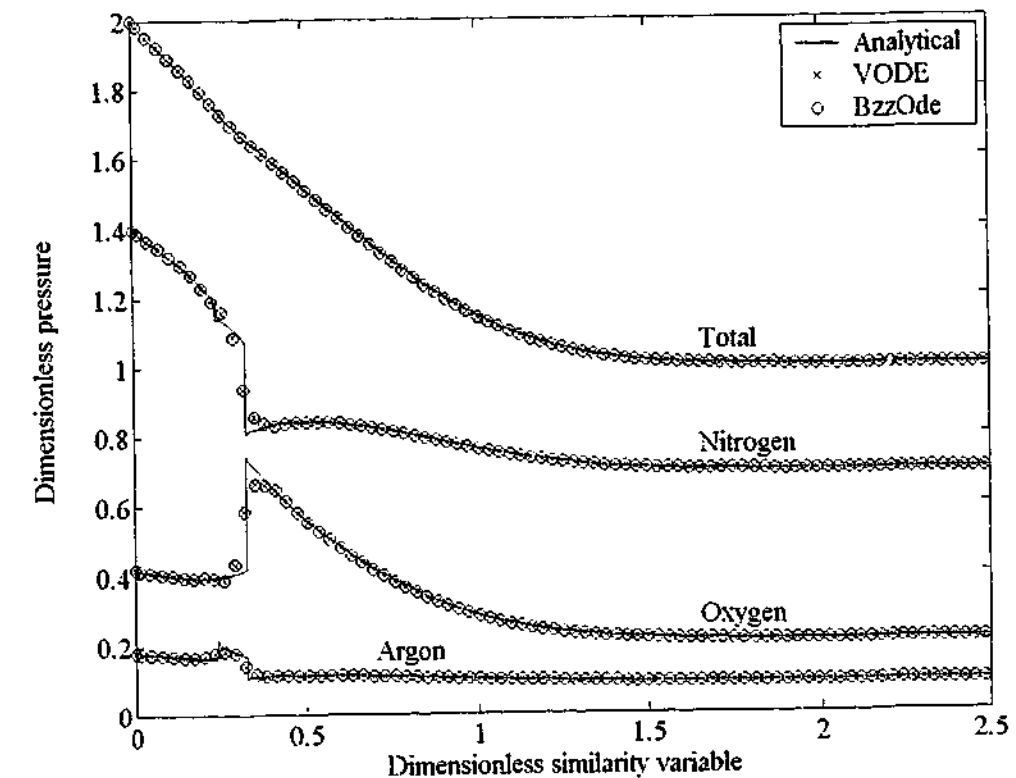


Figure 3.4: Output profiles from the similarity solution of Andrews & Scott (2000).

Overall simulation results are provided in Table 3.1. Although BzzOde required less numerical **J**-matrix evaluations and ensuing time derivative subroutine calls (just the 1 **J**-matrix calculation was performed), the overall simulation time was approximately 10% longer than that of VODE (requiring 7 **J**-matrix calculations). As mentioned previously, this can be attributed to an increased number of **P**-matrix factorizations rather than the increased number of time increments taken. BzzOde performed 60 factorizations to complete the integration whilst VODE performed 55. At the same time, for this problem the number of differential equations is high and consequently the **P**-matrix factorization is quite exacting since the **J**-matrix is considered a dense matrix. As reported in Table 3.1, the number of function calls performed by BzzOde is about 2.6 times less than that of VODE. Due to the significant simplifications of such a problem, evaluation of the ODE system is quite inexpensive when compared to **P**-matrix factorization.

In this problem, the **J**-matrix is structured and quite sparse. Consequently the linear system solution should account for both structure and sparsity of such a matrix. If that feature were implemented a significant reduction in CPU time for the linear system solution could be achieved whilst the total number of time derivative subroutine evaluations would remain constant. Nonetheless, as mentioned earlier, it was decided not to consider structure and sparsity issues due to an imbalance in the comparison between VODE and BzzOde given both routines take advantage of this information differently. This is one aspect of adsorption simulation that could be investigated further for CPU improvements.

For this problem the advantage of having a reduced number of **J**-matrix evaluations and consequently, a reduced number of time derivative subroutine calls is not significant when compared to increased **P**-matrix factorizations. This indicates BzzOde is not universally faster than existing state of the art ODE integrators in every case, but does provide performance results of a similar magnitude. Total mole balance error upon exiting each ODE integrator at $t = 20$ s was 1.4×10^{-11} gmols (BzzOde) and -8.5×10^{-13} gmols (VODE).

3.4.2 Rosen Solution

The original formulation of Rosen (1952) considered the uptake of a single adsorbable component fed in trace quantities from an inert carrier under isothermal and isobaric conditions. The solid diffusion form of Fick's first law was applied within the pellets, so a direct comparison of this with the VF+DGM can only be made under the small pore assumption within the micropore range [Hite & Jackson (1977)]. The limiting form of the intrapellet molar flux under these conditions has been discussed previously in §2.2.4.

For the present case, voids within the pellet are assumed negligible so the intrapellet molar flux effectively represents surface diffusion under the linear, uncoupled isotherm assumption applied in §3.4.1. An analytical solution to the governing intra- and interpellet conservation equations under these assumptions subject to an instantaneous change in feed concentration for an initially clean bed is in the form of an infinite integral with two governing parameters for the case where no external film mass transfer is present [Rosen (1952)].

$$\frac{\rho_g^b}{\rho_{g,feed}} = \frac{1}{2} + \frac{2}{\pi} \int_0^{\infty} \exp(-\omega_1 H_{D1}) \sin(\omega_2 \psi^2 - \omega_1 H_{D2}) \frac{d\psi}{\psi} \quad (3.27)$$

$$\text{where } H_{D1} = \frac{\psi[\sinh(2\psi) + \sin(2\psi)]}{[\cosh(2\psi) - \cos(2\psi)]} - 1, \quad H_{D2} = \frac{x[\sinh(2\psi) - \sin(2\psi)]}{[\cosh(2\psi) - \cos(2\psi)]}$$

$$\omega_1 = \frac{3D_{K,i}^c z}{R_p^2 \epsilon_B v_B} \quad \text{and} \quad \omega_2 = \frac{2D_{K,i}^c}{\hat{\rho}_p R T H_i R_p^2} \left(t - \frac{z}{v_B} \right)$$

Sixty axial nodes ($N_z = 60$) through the bed and eight radial nodes ($N_r = 8$) within the pellet were adopted for a binary component system ($N_c = 2$). This results in a total of 1086 simultaneous ODEs ($N_{eq} = 1086$) that need to be solved over the bed at any one point in time. Again, the energy balance options were deactivated. For this case a distinct difference now arises between the performance of VODE and BzzOde (Table 3.2).

Table 3.2: ODE integrator results from the Rosen solution.

| Integrator | N_{eq} | # Incs | # FC | # JE | # LU | CPU time (s) |
|------------|----------|--------|---------|------|------|--------------|
| BzzOde | 1,086 | 3,109 | 21,907 | 16 | 1176 | 1611 |
| VODE | 1,086 | 2,502 | 301,628 | 274 | 579 | 8271 |

Incs = Total number of time increments taken.

FC = Total number of calls made to the time derivative subroutine.

JE = Total number of **J**-matrix evaluations.

LU = Total number of linear system **P**-matrix factorisations.

Here, the expense of additional time steps and \mathbf{P} -matrix factorizations taken for a reduced number of \mathbf{J} -matrix evaluations and ensuing time derivative subroutine calls far exceeds the performance of VODE, where additional \mathbf{J} -matrix evaluations and time derivative subroutine calls are made for a reduced number of time increments. This difference, which for the previous case resulted in VODE outperforming BzzOde by approximately 10% here results in BzzOde outperforming VODE by over 500%. Further to this slight numerical wiggle is observed around the plateau regions behind and in front of the breakthrough curve from the output results of VODE (Fig. 3.5).

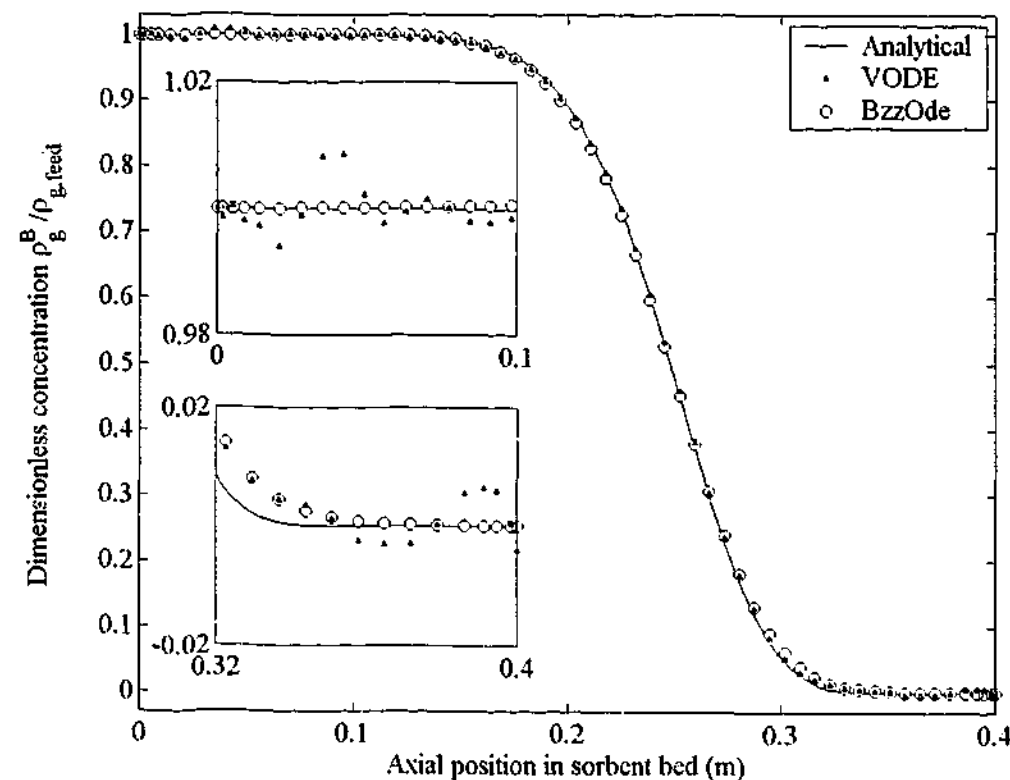


Figure 3.5: Output profiles from the Rosen solution.

Despite VODE accurately capturing the shape of the breakthrough curve along the length of the mass transfer zone, these numerical wiggles suggest some minor instability around the plateau regions may result in cases where very high purity is considered. Interestingly, these numerical wiggles were not observed with BzzOde, nor with any of the profiles obtained from the similarity solution of Andrews & Scott (2000). Mole balance error upon exiting the ODE integrators at $t = 300$ s were 3.0×10^{-10} gmoles (BzzOde) and -1.3×10^{-7} gmoles (VODE).

3.5 CPU Improvements with the MMS and BzzOde for an RPSA Cycle

To explore the ability of each ODE integrator to solve a true RPSA process using the MMS, a one-bed, four-step RPSA cycle that includes a purge step from a well-mixed product tank is considered (Fig. 3.6). One of the reasons for adopting an RPSA cycle of this form is that to date, no modified LDFP correlation readily exists. On this basis the selection of an appropriate LDFP Ω , coefficient appears rather arbitrary.

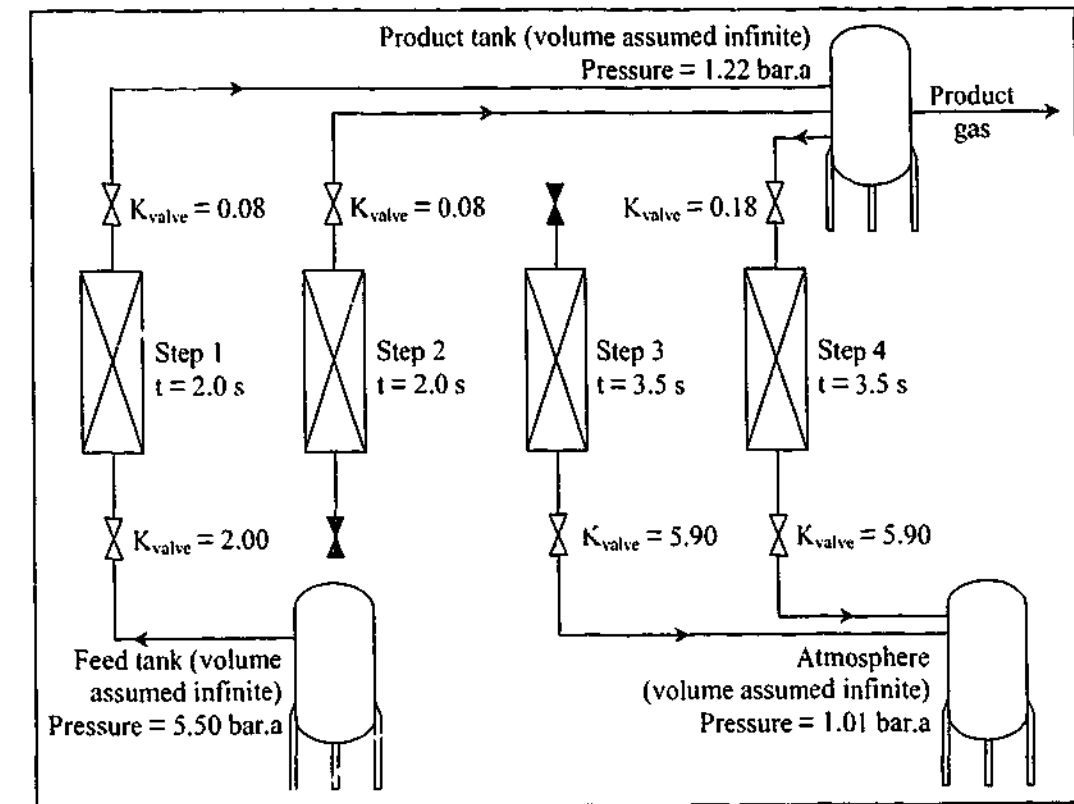


Figure 3.6: Four-step one-bed RPSA cycle.

The process under investigation here is the enrichment of oxygen from a binary air feed stream (78 mol% N_2 and 22 mol% $O_2 + Ar$). The sorbent packed into the bed ($L_{bed} = 1.60$ m, $d_{bed} = 0.12$ m) is spherical pellets of 16 mesh ($d_{p,eq} = 1.15 \times 10^{-3}$ m) 13X molecular sieve zeolite ($\epsilon_B = 0.37$, $\epsilon_p = 0.50$, $\rho_p = 1520$ kg m^{-3}), with the binary component isotherm adopted from the ternary component, single site Langmuir-Sips data of Miller (1987). Inspection of the data from Miller (1987) indicates argon adsorbs with an isotherm gradient very similar to that for oxygen, allowing argon and oxygen to be grouped as the one component. Given the temperature range under consideration here is approximately 297 to 315 K (when a non-isothermal simulation is performed) the Langmuir-Sips exponent for nitrogen of 0.94-0.95 presented by Miller (1987) was set arbitrarily to 1.0 with minimal deviation observed in isotherm loading from his original data. Hence a single site Langmuir isotherm for each component is adopted with all RPSA simulations. Also the dimensionless time parameter θ , is in excess of 0.1 for each component and each step of

the cycle under consideration, suggesting on the surface the LDFP assumption is relatively well justified for the current analysis. This also provides reasonable justification for use of five internal node points ($N_r = 5$) within the pellet for all DPM simulations (chapter 2). For the present set of simulations the rigorous conservation of energy across the column wall and bottom/top void volumes were deactivated as these were deemed unnecessary within the present discussion.

Given the sorbent pellet is a combination of zeolite crystal mixed with a suitable binding agent macropore diffusion resistance associated with the binder phase is often attributed as the limiting mechanism for mass transfer. For this reason an average intrapellet pore diameter δ of 9.0×10^{-8} m, just above the IUPAC classification for the macropore-mesopore boundary of 5.0×10^{-8} m, is adopted. The LDF correlation of Nakao & Suzuki (1983) is used to evaluate the cycle time dependent parameter Ω , for all RPSA simulations which, given θ was greater than 0.1 for all cases, is approximately equal to π^2 .

For each simulation performed in this chapter the CSS check described in §B.4 of appendix B was activated. The magnitude of each CSS tolerance parameter invoked on isothermal and non-isothermal simulations is provided in Table 3.3. For all cases where isothermal behaviour is assumed CSS parameters related to $E_{j,energy}^B$, $E_{j,grad}^B$ and $E_{j,max}^B$ and $E_{j,rms}^B$ for temperature are not required and hence are automatically assumed to be within tolerance when the simulation commences.

Table 3.3: Magnitude of the tolerances applied to each CSS parameter used by NDGNAS when simulating the four-step, one-bed RPSA cycle of Fig. 3.6. A complete definition of these parameters can be found in Table B.1 of appendix B.

| Parameter | Magnitude | Units |
|---------------------------------|----------------------|---|
| $E_{j,max}^B$ for p_i^B | 1.0×10^{-4} | bar.a for $i = 1 \dots N_c$ ($j = 1 \dots N_c$) |
| $E_{j,max}^B$ for n_i^P | 1.0×10^{-4} | gmole kg^{-1} for $i = 1 \dots N_c$ ($j = N_c + 1 \dots 2 N_c$) |
| $E_{j,max}^B$ for T | 8.0×10^{-4} | K ($j = 2 N_c + 1$) |
| $E_{j,rms}^B$ for p_i^B | 1.0×10^{-4} | bar.a for $i = 1 \dots N_c$ ($j = 1 \dots N_c$) |
| $E_{j,rms}^B$ for n_i^P | 1.0×10^{-4} | gmole kg^{-1} for $i = 1 \dots N_c$ ($j = N_c + 1 \dots 2 N_c$) |
| $E_{j,rms}^B$ for T | 2.5×10^{-3} | K ($j = 2 N_c + 1$) |
| $E_{i,mole}^B$ | 5.0×10^{-3} | % for $i = 1 \dots N_c$ |
| E_{energy}^B and E_{grad}^B | 1.0×10^{-1} | % |

3.5.1 Isothermal Simulation - RPSA Cases 1, 2 and 3

The first set of RPSA cycles will investigate the performance of each ODE integrator and the MMS under isothermal conditions (297.15 K). The initial conditions for the bed are $y_{N_2}^B = y_{N_2}^P = 0.20$ (balance oxygen), $p^B = p^P = 1.23$ bar.a and $T = 297.15$ K (RPSA cases 1 and 2), and $y_{N_2}^B = y_{N_2}^P = 0.78$ (balance oxygen) with p^B , p^P and T the same (RPSA case 3). To justify use of the finite volume scheme as a method for reproducing CSS conditions that is relatively insensitive to the level of axial discretisation, two different values for N_z were used. The first applies an axial node resolution of 14 (RPSA case 1) and the second uses an axial node resolution of 20 (RPSA case 2). The third configuration (RPSA case 3) considers a different initial condition with $N_z = 20$. CSS results from BzzOde and VODE for these particular cases are summarised in Tables 3.4 and 3.5.

Initially, BzzOde outperforms VODE by approximately 50% in terms of total CPU time for each RPSA case, attributed to a reduced number of J-matrix calculations in favour of an increase in the number of time steps. Secondly performance results between each ODE integrator match very well. Table 3.5 shows high enrichment of the light component (oxygen) is achieved from the DPM under RPSA conditions (98.8 mol% oxygen + argon) at the expense of product recovery, which is less than 2%. The relative cycle number where the MMS occurred (213-214 with $N_z = 14$ versus 232-234 with $N_z = 20$) also agree suggesting the definition of CSS and cycle number to activate the DPM is well captured along with the final number of cycles required for the DPM.

Although BzzOde outperforms VODE for these cyclic simulations, implementation of the MMS is seen to increase CPU time with the initial conditions selected for RPSA cases 1 and 2. This can be attributed to the rather misleading composition gradient predicted from the LDFP model when initialising the DPM, highlighted in the large discrepancy, almost 10 mol% O_2 , between the CSS product gas purity from the two mass transfer models. Figure 3.7 displays the end of step nitrogen mole fraction profiles at CSS between the LDFP versus DPM runs for RPSA case 2 with $N_z = 20$ (equivalent trends are observed for RPSA cases 1 and 3). The mass transfer zone starts approximately half way into the bed and terminates within the vicinity of the bed outlet. The DPM predicts the axial mole fraction profile steadily decreases towards product gas composition, whereas the LDFP model shows a qualitatively different trend with composition passing through a semi-plateau region before dropping rather rapidly to product gas purity at the outlet of the bed.

Table 3.4: Integrator performance statistics for isothermal RPSA case 1 through 3. The definition for each sub-heading after N_{eq} is identical to those found at the bottom of Table 3.1.

| RPSA case [†] | Integrator | N_{eq} | # Incs | # FC | # JE | # LU | CPU time (s) |
|------------------------|------------|----------|---------|-----------|--------|---------|--------------|
| 1 | BzzOde | 172 | 134,238 | 527,214 | 1,934 | 28,800 | 2,901 |
| | VODE | 172 | 124,185 | 970,593 | 4,511 | 22,652 | 4,751 |
| 1a | BzzOde | 60 | 123,025 | 362,854 | 3,434 | 31,850 | 341 |
| | VODE | 60 | 148,378 | 569,503 | 5,661 | 31,073 | 490 |
| 1b | BzzOde | 172 | 321,249 | 1,125,326 | 6,168 | 73,204 | 4,783 |
| | VODE | 172 | 330,398 | 1,997,799 | 12,307 | 64,808 | 7,504 |
| 2 | BzzOde | 244 | 162,139 | 760,945 | 2,106 | 42,795 | 6,624 |
| | VODE | 244 | 139,223 | 1,540,819 | 5,401 | 25,206 | 10,911 |
| 2a | BzzOde | 84 | 240,771 | 604,452 | 2,847 | 44,136 | 838 |
| | VODE | 84 | 186,287 | 874,950 | 6,907 | 37,248 | 1,051 |
| 2b | BzzOde | 244 | 519,122 | 1,794,042 | 5,995 | 124,482 | 12,127 |
| | VODE | 244 | 407,284 | 3,289,937 | 15,354 | 77,568 | 18,145 |
| 3 | BzzOde | 244 | 320,642 | 1,474,391 | 4,015 | 81,159 | 12,905 |
| | VODE | 244 | 275,468 | 3,009,915 | 10,528 | 50,346 | 21,305 |
| ? | BzzOde | 84 | 235,052 | 598,408 | 2,855 | 46,672 | 827 |
| | VODE | 84 | 181,068 | 861,418 | 6,826 | 36,523 | 1,031 |
| 3b | BzzOde | 244 | 472,547 | 1,778,037 | 6,061 | 111,761 | 11,654 |
| | VODE | 244 | 404,545 | 3,309,157 | 15,392 | 77,253 | 18,397 |

[†] RPSA cases denoted by an "a" show results at the onset of a MMS, where the LDFP model has just finished and the DPM is being initialised. RPSA cases denoted by a "b" show results at the completion of a simulation using the MMS, where the DPM has finished. RPSA cases that do not have an "a" or "b" following the number represent a simulation where the MMS was not activated.

Table 3.5: CSS performance results for isothermal RPSA case 1 through 3.

| RPSA case | Integrator | N_{css} | Purity | Recovery | Output | MB |
|-----------|------------|-----------|--------|----------|--------|------------------------|
| 1 | BzzOde | 167 | 97.73 | 1.258 | 70.66 | 2.8×10^{-6} |
| | VODE | 164 | 97.72 | 1.257 | 70.66 | 8.8×10^{-6} |
| 1a | BzzOde | 214 | 86.79 | 1.803 | 66.93 | 2.5×10^{-13} |
| | VODE | 213 | 86.80 | 1.802 | 66.94 | -3.1×10^{-14} |
| 1b | BzzOde | 456 | 97.53 | 1.256 | 70.52 | 2.7×10^{-6} |
| | VODE | 456 | 97.52 | 1.256 | 70.52 | -1.1×10^{-6} |
| 2 | BzzOde | 173 | 98.93 | 1.257 | 71.45 | -1.2×10^{-6} |
| | VODE | 170 | 98.93 | 1.256 | 71.45 | -3.6×10^{-7} |
| 2a | BzzOde | 232 | 88.47 | 1.826 | 68.10 | 2.0×10^{-14} |
| | VODE | 234 | 88.47 | 1.826 | 68.10 | 1.1×10^{-13} |
| 2b | BzzOde | 504 | 98.79 | 1.257 | 71.35 | -2.9×10^{-6} |
| | VODE | 502 | 98.78 | 1.257 | 71.35 | -1.2×10^{-6} |
| 3 | BzzOde | 331 | 98.82 | 1.251 | 71.34 | 7.1×10^{-7} |
| | VODE | 327 | 98.82 | 1.251 | 71.34 | -3.9×10^{-6} |
| 3a | BzzOde | 219 | 88.25 | 1.817 | 67.91 | -7.9×10^{-13} |
| | VODE | 224 | 88.26 | 1.817 | 67.92 | 6.6×10^{-14} |
| 3b | BzzOde | 493 | 98.82 | 1.251 | 71.34 | -7.3×10^{-7} |
| | VODE | 496 | 98.82 | 1.250 | 71.34 | -8.8×10^{-7} |

The definition for "RPSA case" is identical to that found at the bottom of Table 3.4.

Purity = Average purity of product gas from bed over cycle (mol%O₂).

Recovery = $100 \times \text{gmol O}_2 \text{ obtained as product} / \text{gmol O}_2 \text{ in feed gas} (\%)$.

Output = Product throughput measured in contained kg of oxygen per day ((kg O₂) day⁻¹).

MB = Total mole balance error over cycle (gmol).

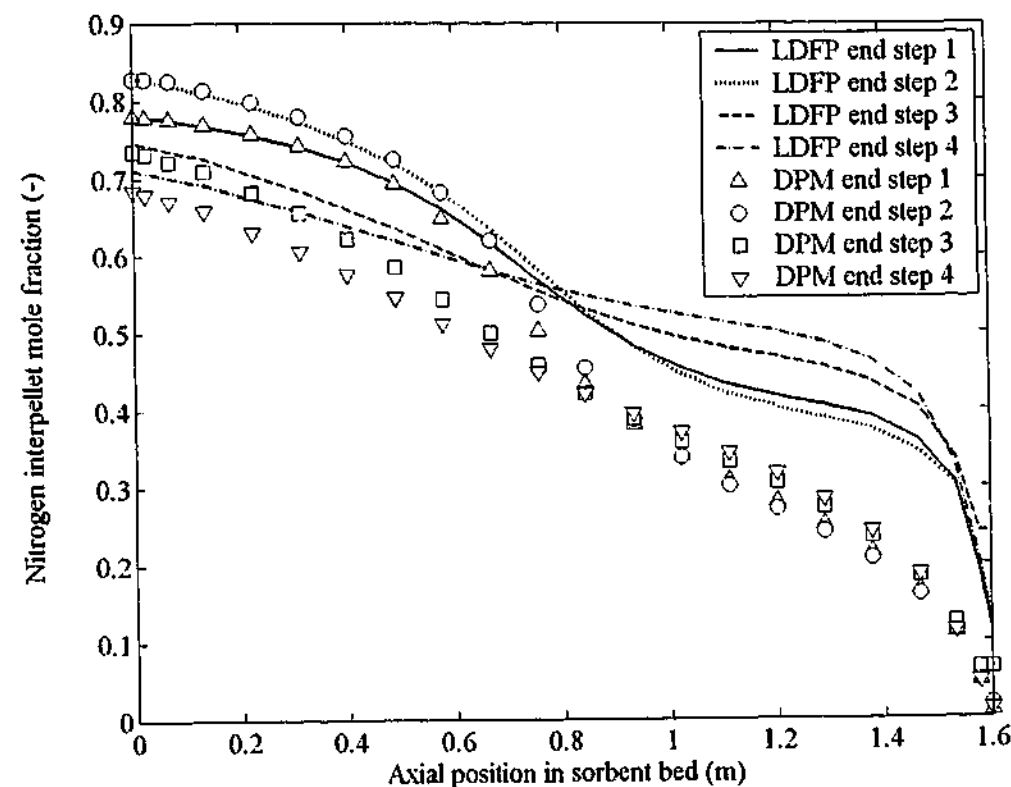


Figure 3.7: End of step composition profiles at CSS from the DPM and LDFP model with $N_2 = 20$ for RPSA case 2.

Comparing CSS pressure profiles for RPSA case 2 at the end of each step, Fig. 3.8a, and for each time increment at the inlet and outlet to the bed, Fig. 3.8b, show only slight differences during feed plus make product (step 1) and from here μ ree very well. This suggests the velocity profile and hence moles passed into/out of the bed are similar and the major differences can be solely attributed to purity discrepancies associated with the uptake rate predicted from the two mass transfer models. This composition profile discrepancy requires an additional 270 cycles of simulation with the DPM to wash out once the LDFP model has reached CSS. In comparison, the DPM started from cycle 1 required less than 180 cycles to reach CSS.

If one started the bed initially with air ($y_{N_2}^B = y_{N_2}^F = 0.78$) rather than 20 mol%N₂ at the same pressure and temperature, a favorable result using the MMS is observed. Here, CSS is achieved after approximately 330 cycles without the MMS activated. When the same input deck was run using the MMS almost identical simulation results to that of RPSA case 2 were observed, where an additional 270 cycles are required to converge to CSS using initial conditions extrapolated from the LDFP model. This result suggests the MMS is relatively insensitive to the initial conditions given the LDFP component of the simulation is only a small fraction of the total CPU time.

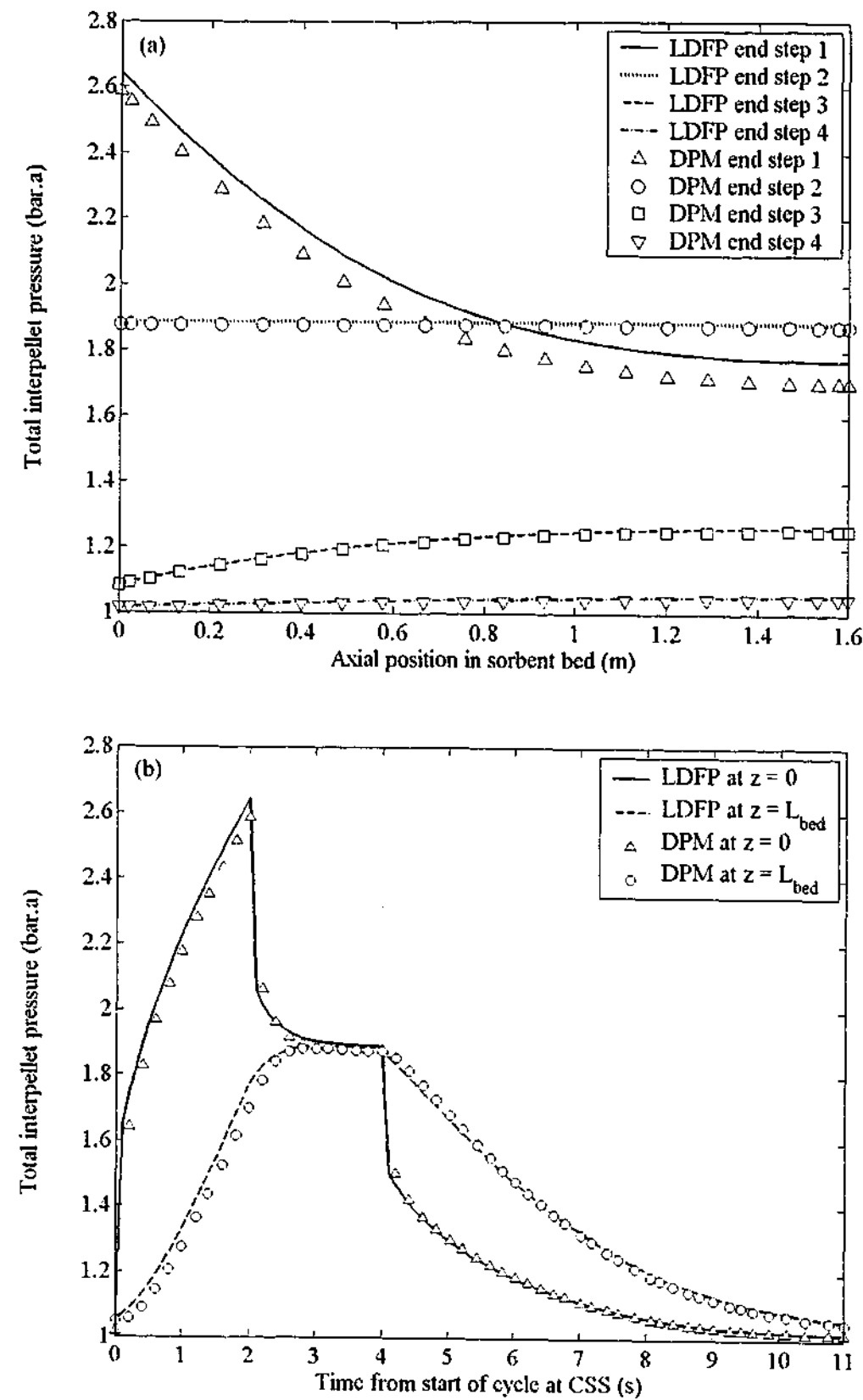


Figure 3.8: Pressure profiles at CSS from the DPM and LDFP model with $N_z = 20$ for RPSA case 2 showing (a) end of step profiles and (b) history data obtained at $z = 0$ and $z = L_{bed}$.

3.5.2 Non-Isothermal Simulation - RPSA Cases 4, 5 and 6

The assumption of isothermal behaviour reduces the number of ODE equations by $N_z + 2$ and also simplifies the definition of CSS given temperature profile and energy accumulation closure is implicitly assumed at cycle one. However, to know *a priori* the final form of the axial temperature profile under non-isothermal conditions is very difficult without experimental data. Given most real PSA processes experience finite temperature deviations over a cycle this complicating physical mechanism often cannot be ignored. The RPSA cycle discussed in Section §3.5.1 is now considered to operate non-isothermally, with the initial conditions imposed here identical to those adopted for the three equivalent isothermal RPSA cases. The first two compare different axial node resolution on the determination of CSS (RPSA case 4 and 5), while the third investigates the impact of a different initial condition on the determination of CSS (RPSA case 6). CSS results from BzzOde and VODE are summarised in Tables 3.6 and 3.7.

Along with computational improvements provided by BzzOde the MMS now provides favorable simulation results in all runs. The relative cycle number where the MMS occurred, along with N_{css} required for the DPM agree well. The impact of non-isothermal behavior in this situation causes feed gas to penetrate further into the bed (reduced adsorption capacity with increasing temperature), dropping the product gas purity to approximately 94 mol%O₂+Ar (Table 3.7). Now that less gas is adsorbed within the bed, the recovery of oxygen plus argon increases slightly from the isothermal runs.

Simulation time with BzzOde and the MMS here is approximately one and a half days (both RPSA cases 5 and 6), as compared to two and a half days and beyond for all other combinations. This result can be attributed to the similar end of step temperature profile predicted by the DPM and LDFP model, shown in Fig. 3.9 for RPSA case 5. Hence the LDFP model has been used to track the slow movement of energy convected through the bed, requiring approximately five hours of simulation time to achieve this task.

From here, thirty hours were required to simulate the DPM to CSS with LDFP model profiles extrapolated as initial conditions. Starting the DPM at cycle 1 required almost sixty hours to reach CSS with BzzOde. Figure 3.10 compares two CSS temperature profiles obtained with and without the MMS. Although RPSA case 5 required approximately half the simulation time the overall temperature profile and operating results are very similar. Unlike the isothermal runs where simulation time with the MMS was sensitive to the initial conditions, non-isothermal runs here

show no preference to the initial conditions whether started from $y_{N_2}^b = y_{N_2}^p = 0.20$ (RPSA cases 4 and 5) or $y_{N_2}^b = y_{N_2}^p = 0.78$ (RPSA case 6).

Table 3.6: Integrator performance statistics of non-isothermal RPSA case 4 through 6. The definition for each sub-heading is identical to that found at the bottom of Tables 3.1 and 3.4.

| RPSA case | Integrator | N_{eq} | # Incs | # FC | # JE | # LU | CPU time (s) |
|-----------|------------|----------|-----------|------------|--------|---------|--------------|
| 4 | BzzOde | 188 | 2,071,039 | 7,013,580 | 20,891 | 617,932 | 95,907 |
| | VODE | 188 | 1,362,324 | 11,747,865 | 50,321 | 483,091 | 148,736 |
| 4a | BzzOde | 76 | 1,212,662 | 3,277,677 | 19,285 | 300,700 | 7,461 |
| | VODE | 76 | 1,218,574 | 5,574,678 | 46,448 | 253,695 | 11,078 |
| 4b | BzzOde | 188 | 2,371,375 | 7,195,176 | 30,852 | 636,199 | 64,581 |
| | VODE | 188 | 1,964,861 | 12,007,244 | 73,993 | 386,908 | 101,777 |
| 5 | BzzOde | 266 | 2,170,947 | 10,212,638 | 25,553 | 525,135 | 213,609 |
| | VODE | 266 | 1,717,306 | 20,044,718 | 64,262 | 310,078 | 351,707 |
| 5a | BzzOde | 106 | 1,836,066 | 5,351,539 | 23,643 | 394,137 | 17,666 |
| | VODE | 106 | 1,525,371 | 8,743,944 | 57,775 | 303,028 | 24,560 |
| 5b | BzzOde | 266 | 3,017,897 | 10,837,395 | 37,269 | 679,880 | 125,983 |
| | VODE | 266 | 2,440,927 | 19,374,965 | 91,831 | 468,859 | 211,407 |
| 6 | BzzOde | 266 | 2,528,903 | 11,326,721 | 27,613 | 588,682 | 239,710 |
| | VODE | 266 | 1,826,863 | 21,782,253 | 70,034 | 323,756 | 376,683 |
| 6a | BzzOde | 106 | 2,130,322 | 6,072,535 | 26,152 | 425,417 | 19,895 |
| | VODE | 106 | 1,698,865 | 9,725,535 | 64,152 | 339,515 | 27,347 |
| 6b | BzzOde | 266 | 3,312,892 | 11,494,488 | 39,539 | 713,386 | 127,333 |
| | VODE | 266 | 2,603,977 | 20,216,364 | 97,755 | 503,074 | 211,555 |

Table 3.7: CSS performance results of non-isothermal RPSA case 4 through 6. The definition for each sub-heading is identical to that found at the bottom of Table 3.5.

| RPSA case | Integrator | N_{css} | Purity | Recovery | Output | MB | EB |
|-----------|------------|-----------|--------|----------|--------|-----------------------|------------------------|
| 4 | BzzOde | 1,794 | 93.23 | 2.011 | 77.08 | -2.0×10^{-5} | -4.9×10^{-12} |
| | VODE | 1,791 | 93.22 | 2.011 | 77.09 | -4.6×10^{-7} | 9.0×10^{-12} |
| 4a | BzzOde | 1,722 | 81.88 | 2.293 | 71.03 | -8.4×10^{-8} | 1.7×10^{-12} |
| | VODE | 1,712 | 81.88 | 2.293 | 71.03 | 1.4×10^{-7} | -5.6×10^{-12} |
| 4b | BzzOde | 2,695 | 93.18 | 2.011 | 76.99 | -1.9×10^{-5} | -1.4×10^{-11} |
| | VODE | 2,690 | 93.18 | 2.012 | 76.99 | -2.6×10^{-6} | -4.6×10^{-13} |
| 5 | BzzOde | 2,019 | 94.07 | 2.105 | 78.17 | 2.8×10^{-6} | -6.0×10^{-12} |
| | VODE | 2,008 | 94.08 | 2.104 | 78.17 | 3.6×10^{-7} | 3.0×10^{-12} |
| 5a | BzzOde | 1,947 | 82.07 | 2.356 | 71.50 | -2.5×10^{-8} | 1.0×10^{-11} |
| | VODE | 1,940 | 82.07 | 2.355 | 71.51 | 2.6×10^{-7} | 1.0×10^{-11} |
| 5b | BzzOde | 3,009 | 94.04 | 2.104 | 78.07 | 2.2×10^{-6} | 6.5×10^{-12} |
| | VODE | 3,003 | 94.04 | 2.104 | 78.07 | -2.4×10^{-6} | -1.6×10^{-11} |
| 6 | BzzOde | 2,192 | 94.08 | 2.100 | 78.09 | 3.9×10^{-6} | 1.0×10^{-12} |
| | VODE | 2,190 | 94.05 | 2.098 | 78.06 | -3.3×10^{-6} | 3.6×10^{-11} |
| 6a | BzzOde | 2,146 | 82.00 | 2.356 | 71.41 | -4.4×10^{-8} | 1.4×10^{-11} |
| | VODE | 2,142 | 82.08 | 2.353 | 71.44 | -1.9×10^{-8} | -5.1×10^{-12} |
| 6b | BzzOde | 3,190 | 94.03 | 2.104 | 78.05 | -2.1×10^{-6} | 3.2×10^{-12} |
| | VODE | 3,191 | 94.07 | 2.099 | 78.05 | -5.1×10^{-6} | 5.6×10^{-13} |

EB = Total energy balance error over cycle (kJ)

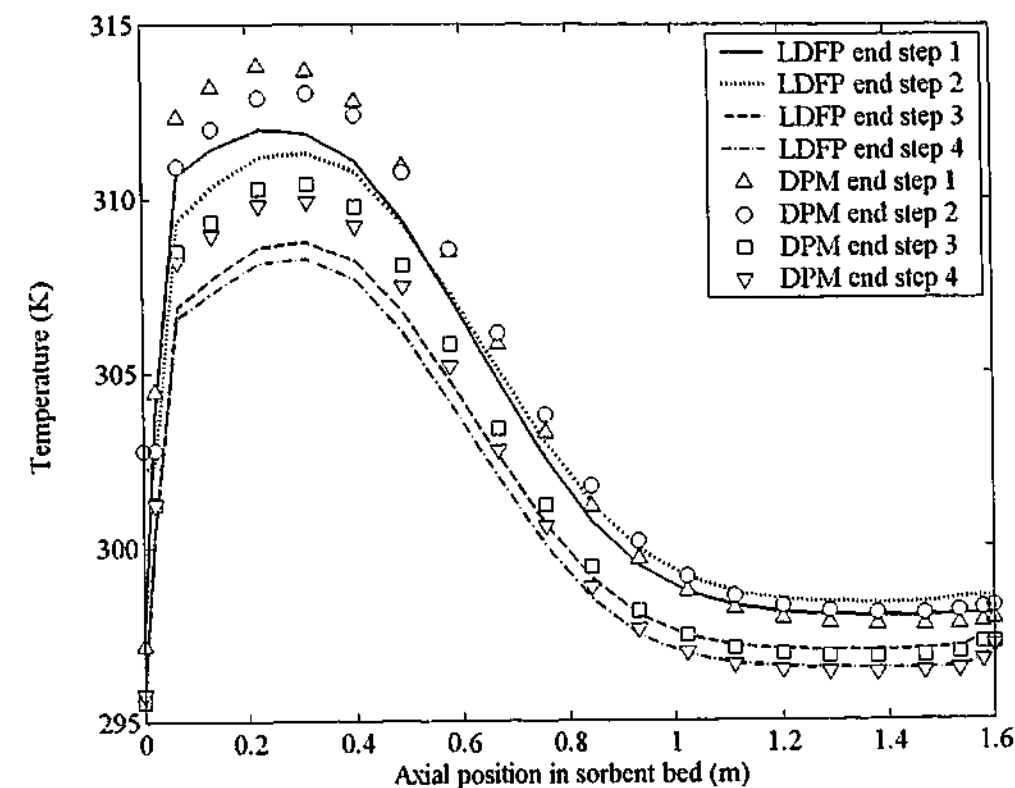


Figure 3.9: End of step temperature profiles at CSS from the DPM and LDFP model with $N_2 = 20$ for RPSA case 5.

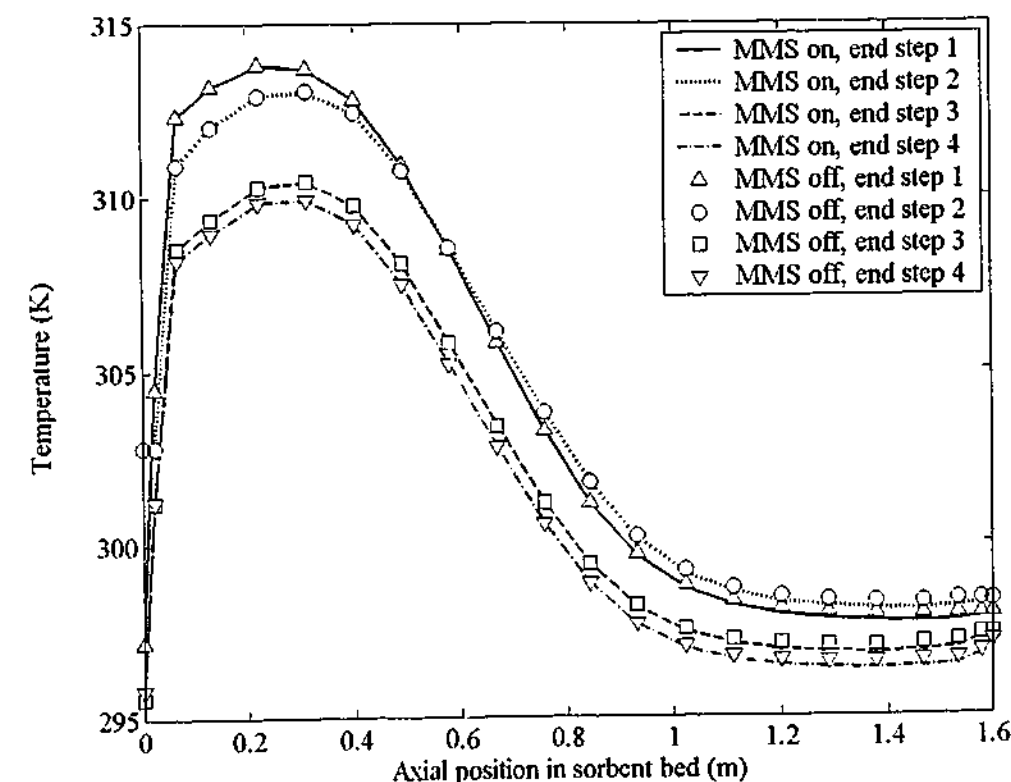


Figure 3.10: End of step temperature profiles at CSS with and without the MMS for RPSA case 5.

3.6 Concluding Remarks

The governing set of conservation equations and ancillary model options that underlie a general PSA cycle have been introduced. A numerical solution to these coupled, nonlinear ODEs is a time consuming exercise when non-isothermal conditions arise and a DPM approach is used for intrapellet mass transfer. Consequently, two methods have been explored that can potentially reduce CPU time required to simulate a PSA process to CSS with a DPM approach to intrapellet mass transfer using successive substitution.

- i. The first exploits computational improvements when handling the P-matrix factorisation using a refinement of the J-matrix update algorithm of BzzOde [Buzzi Ferraris & Manca (1998)].
- ii. The second introduces a MMS, which runs from cycle 1 to N_{css} with the LDFP model then switches automatically to the DPM approach with the initial conditions extrapolated from CSS profiles of the LDFP model.

Initial test cases considered the performance of BzzOde against VODE, a state-of-the art Fortran ODE integrator. CPU comparisons with the similarity solution of Andrews & Scott (2000) show BzzOde performs slightly worse than VODE by 10% but outperforms VODE by over 500% when using the Rosen solution [Rosen (1952)]. These results highlight BzzOde is not universally faster than existing Fortran90 integrators in all cases but at minimum provides comparable simulation performance.

When methods i. and ii. above were considered over a four-step one-bed RPSA process operating under isothermal conditions, CPU improvements with the MMS were found to depend on the initial conditions allocated for the bed. Selecting an initial composition close to that of product gas allowed the DPM alone to reach CSS faster than the MMS. This can be attributed to the rather misleading composition profile predicted at CSS when initiated for the DPM. Under non-isothermal conditions the combination of methods i. and ii. above reduced simulation time by at least 60% in relation to one or both of them being deactivated. This arose from the reduced number of cycles that need to be simulated using a DPM approach. The LDFP model successfully tracked the slow forming temperature profile to CSS providing the DPM with a good estimate of the CSS temperature profile. Methods i. and ii. described previously provide a unique method of determining reproducible CSS results for a non-isothermal RPSA process that is fully consistent with a kinetic theory approach to intrapellet mass transfer.

3.6.1 Note Regarding Incompatibility of BzzOde on Unix Workstation

Conclusions from this chapter highlight the benefits an improved ODE integrator such as BzzOde can provide in relation to existing state of the art ODE integrators for the simulation of an adsorption process. However, generating an executable program that incorporates BzzOde into NDGNAS requires a mixed-language Fortran90/C++ compiler that unfortunately was not available on the Dec-Alpha workstations within the Chemical Engineering department at Monash University.

All runs presented in this chapter were produced from an executable file that ran in Windows98 as kindly generated by Dr. G. Buzzi Ferraris and Dr. D. Manca from the Polytechnic of Milan in Italy. They used the mixed language compiling capabilities of Visual Fortran 6.0 and Visual C++ 6.0 to generate the executable file once provided with the source code for NDGNAS. Given I did not have access to such a compiler on the Unix platform, all subsequent simulations performed beyond chapter 3 with NDGNAS had to use VODE as the ODE integrator. While this does not in any way detract from simulations that are to follow given both integrators provide identical results to within ODE integrator tolerances, CPU improvements offered through BzzOde are not considered from this point onwards. However, running NDGNAS with VODE from the Unix environment on a Dec-Alpha workstation was found to be comparable in terms of CPU time to running NDGNAS with BzzOde from the Windows98 platform for several identical test runs. This means no significant difference in the computational effort of chapters 4 through 6 would be expected in relation to chapter 3.

CHAPTER 4

EXPERIMENTAL DETERMINATION OF THE INTRAPELLET TRANSPORT COEFFICIENTS

NDGNAS contains several transport parameters that need to be experimentally calibrated. This chapter performs a series of experiments using one particular sorbent material of industrial relevance to ascertain intrapellet transport coefficients. The individual objectives for this chapter are as follows:

- i. Provide an overview of the methods currently used to determine intrapellet transport coefficients from various experimental and mathematical techniques.
 - ii. Introduce one particular experimental method that allows the Knudsen diffusion and viscous flow transport coefficients of the VF+DGM, C_K and C_v , respectively, to be found.
 - iii. Introduce a second experimental method that allows the molecular diffusion transport coefficient of the VF+DGM, C_m , to be found.
-

To compare NDGNAS with experimental data obtained from an RPSA pilot plant, several physical properties of the sorbent need to be characterised first. The most important of these include the equilibrium isotherm for $n_{i,eq}^P$, density/void terms of the sorbent material, transport coefficients for each mechanism of intrapellet mass transfer and transport coefficients of the steady state momentum equation. Experimental methods developed in this and subsequent chapters describe intrapellet mass transfer in the presence of adsorption, so equilibrium isotherm and physical pellet properties will be introduced first.

4.1 Sorbent of Experimental Interest: Zeochem LiLSX

One particular sorbent material will form the basis for all experimental analyses within this dissertation. The crystal itself is a Low Silica-to-alumina ratio NaX (LSX) zeolite that has been exchanged with approximately 85% lithium to form LiLSX. For this material the silica-to-alumina ratio is approximately 1. Individual LiLSX crystals have been pelletised through the addition of a clay binding agent to form a spherical pellet of relatively high crush and abrasion resistance, the binder itself constitutes approximately 20% of the pellets final mass. This sorbent is a proprietary material purchased from Zeochem through Air Products and Chemicals Inc. and goes under the

trade name Z10-05-03. This material will be referred to as Zeochem LiLSX for the remainder of this dissertation.

4.1.1 Equilibrium Isotherm for Zeochem LiLSX

Knowledge of the equilibrium isotherm is imperative to quantify performance from any process that involves adsorption. The equilibrium isotherm for nitrogen-oxygen-Zeochem LiLSX was experimentally determined using a volumetric device that was constructed and calibrated in-house at Monash University. Three MKS Baratron pressure transducers are housed on this unit to cover a wide range of pressures. The volume containing sorbent is submerged within a water bath to control temperature to a tolerance of 0.1 K. This device, however, only provides pure component equilibrium data and extrapolation to multicomponent data was performed using Ideal Adsorbed Solution Theory (IAST) [Myers & Prausnitz (1965)].

Before the sorbent was used within any experimental unit, regeneration was performed. A regeneration procedure has been developed in-house that consistently reproduces an equilibrium isotherm that exhibits maximum nitrogen adsorption capacity or acceptable level of pre-adsorbed water per unit mass of sorbent.

- i. To remove water from pores that has undergone capillary condensation, the sorbent is initially heated for twelve hours at 373 K within a furnace under a dry air purge flow at a dew point of -60°C . A common rule of thumb for sorbent regeneration requires this dry air flow rate be three times the packed bed volume per minute.
- ii. Immediately following the twelve hour pre-heat, the sorbent is then subjected to 733 K for eight hours using the same dry air purge flow rate to remove chemisorbed water.

The furnace constructed in-house holds up to 40 kg in one batch, making it possible to regenerate enough sorbent to fill all experimental units. When transferring sorbent into the columns of the RPSA pilot plant and LUB apparatus, exposure to air for only a couple of seconds occurred. Given the quantity of sieve transferred (approximately 11 kg in the RPSA pilot plant and 3 kg in the LUB apparatus), water contamination after regeneration was minimal. Samples used in the equilibrium measuring device and Experimental Mass-transfer Unit (EMU) were transferred and screened within a glove box maintained at a steady -60°C dew point. In all cases water contamination after regeneration was assumed negligible. A dual-site Langmuir isotherm was used to correlate binary component adsorbed phase loadings for oxygen and nitrogen.

$$n_{i,\text{eq}}^p = \frac{m_{i,\text{site } 1} b_{i,\text{site } 1} \exp(Q_{i,\text{site } 1} / 10^5 RT_P) p_i^p}{1 + \sum_{j=1}^{N_c} [b_{j,\text{site } 1} \exp(Q_{j,\text{site } 1} / 10^5 RT_P) p_j^p]} + \frac{m_{i,\text{site } 2} b_{i,\text{site } 2} \exp(Q_{i,\text{site } 2} / 10^5 RT_P) p_i^p}{1 + \sum_{j=1}^{N_c} [b_{j,\text{site } 2} \exp(Q_{j,\text{site } 2} / 10^5 RT_P) p_j^p]} \quad \text{for } i = 1 \dots N_c \quad (4.1)$$

In order for Eq. (4.1) to be thermodynamically consistent $m_{i,\text{site } 1} = m_{i,\text{site } 2}$ [Myers (1983)]. The regressed parameters obtained for Zeochem LiLSX are displayed in Table 4.1 while a comparison of the experimental and fitted pure component equilibrium isotherms for nitrogen and oxygen at three different temperatures; 272.7, 297.5 and 321.9 K is shown in Fig. 4.1.

Table 4.1: Dual-site Langmuir equilibrium isotherm parameters for Zeochem LiLSX.

| Component | $m_{\text{site } 1}$ | $b_{\text{site } 1}$ | $Q_{\text{site } 1}$ |
|-----------|---------------------------|---|--------------------------|
| | (gmole kg ⁻¹) | (bar.a ⁻¹) | (J gmole ⁻¹) |
| Nitrogen | 1.316 ± 0.020 | $1.601 \times 10^{-4} \pm 0.015 \times 10^{-4}$ | $21,540 \pm 50$ |
| Oxygen | 1.625 ± 0.020 | $2.727 \times 10^{-4} \pm 0.015 \times 10^{-4}$ | $13,550 \pm 50$ |
| | $m_{\text{site } 2}$ | $b_{\text{site } 2}$ | $Q_{\text{site } 2}$ |
| | (gmole kg ⁻¹) | (bar.a ⁻¹) | (J gmole ⁻¹) |
| Nitrogen | 1.316 ± 0.020 | $4.379 \times 10^{-6} \pm 0.015 \times 10^{-6}$ | $26,410 \pm 50$ |
| Oxygen | 1.625 ± 0.020 | $1.882 \times 10^{-4} \pm 0.015 \times 10^{-4}$ | $13,610 \pm 50$ |

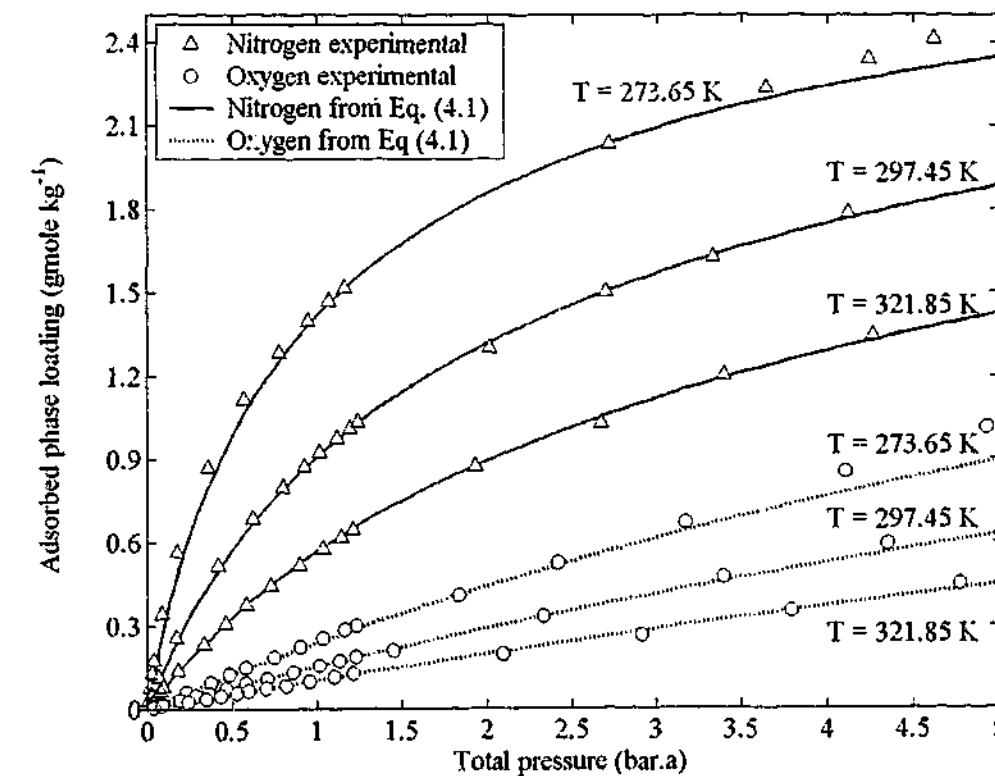


Figure 4.1: Equilibrium isotherm for pure component nitrogen and oxygen obtained at three different temperatures using the equilibrium measuring device, along with the corresponding analytical fit using regressed dual-site Langmuir isotherm parameters.

4.1.2 Physical Properties for Zeochem LiLSX

Pelletised Zeochem LiLSX was not of a uniform diameter so an equivalent diameter $d_{p,eqv}$ was determined. The method used to find $d_{p,eqv}$ involved the screening of approximately 9.5 kg of this material into various size grades.

Table 4.2: Distribution of pellet diameters obtained with Zeochem LiLSX.

| Mass of sorbent weighed before screening commenced = 9473.7 grams | | |
|---|-----------------------|----------------------------|
| Screen size (m) | Mass obtained (grams) | % of total (original) mass |
| 2.0×10^{-3} and greater | 50.4 | 0.53 |
| 1.4×10^{-3} through 2.0×10^{-3} | 7583.7 | 80.05 |
| 1.0×10^{-3} through 1.4×10^{-3} | 1754.4 | 18.51 |
| 0.5×10^{-3} through 1.0×10^{-3} | 28.0 | 0.29 |
| 0.5×10^{-3} and lower | 0.7 | ≈ 0.00 |
| Total | 9417.2 | 99.39 |

Loss of sorbent during screening ≈ 56 grams

Results from the screening process, Table 4.2, indicates a majority of this sorbent, approximately 80%, has a diameter between 1.4×10^{-3} and 2.0×10^{-3} m. Assuming this size range is normally distributed, an equivalent pellet size of 1.7×10^{-3} m is obtained. Although this represents a rather crude way of obtaining an estimate on $d_{p,eqv}$, it was the only practical method readily available. One encouraging result in favour of this value, however, are the experimental estimates obtained for the two steady state pressure drop coefficients $K_{viscous}$ and $K_{kinetic}$ (see §5.2.2). These values lie relatively close to established literature values [Ergun (1952), Macdonald *et al.* (1979)] providing some justification that $d_{p,eqv}$ is close to 1.7×10^{-3} m for assumed spherical geometry.

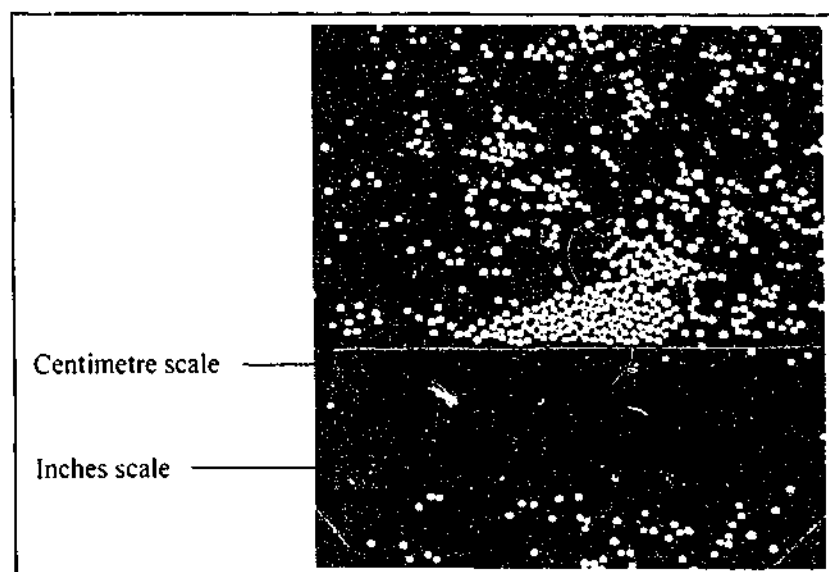


Figure 4.2: Representative sample of Zeochem LiLSX sorbent pellets.

A visual guide to the size distribution of this commercially manufactured material is provided in Fig. 4.2. In order to find interpellet voidage ϵ_B , other physical properties of the sorbent need to be independently calculated first. These include packed bed density $\hat{\rho}_{bed}$, sorbent skeletal density $\hat{\rho}_s$, and intrapellet voidage ϵ_p . Packed bed density was found by dividing the mass of sorbent packed into the LUB and RPSA adsorption columns with the volume occupied. A relatively consistent value was obtained for this parameter with several packings of both apparatuses. The experimental value and associated error can be found in Table 4.3. Skeletal density was obtained using a Micromeritics AccuPyc 1330 helium pycnometer [Webb & Orr (1997, pp 195-199)] for different random samples of Zeochem LiLSX. A relatively consistent estimate was obtained, presented in Table 4.3 with the associated deviation.

Table 4.3: Physical properties obtained experimentally for Zeochem LiLSX.

| Parameter | Magnitude | Units |
|----------------------|-------------------------|--|
| $d_{p,eqv}$ | 1.7 ± 0.2 | $m \times 10^3$ |
| $\hat{\rho}_{bed}$ | 602 ± 11 | $kg m^{-3}$ |
| $\hat{\rho}_s$ | 2416 ± 10 | $kg m^{-3}$ |
| ϵ_p | 0.62 ± 0.04 | $(m^3 \text{ intrapellet gas void}) (m^3 \text{ pellet})^{-1}$ |
| $\epsilon_{p,macro}$ | $0.34 \pm 0.04^\dagger$ | $(m^3 \text{ macropore void}) (m^3 \text{ pellet})^{-1}$ |
| ϵ_B | 0.35 ± 0.06 | $(m^3 \text{ interpellet gas void}) (m^3 \text{ total})^{-1}$ |
| $\hat{\rho}_p$ | 926 ± 77 | $kg m^{-3}$ |
| δ | 2.5 ± 0.4 | $m \times 10^7$ |
| \hat{c}_s | 960^\ddagger | $J kg^{-1} K^{-1}$ |

[†] Discussed at the end of §4.2.3

[‡] Assumed equivalent to fire clay, burnt [Incropera & DeWitt (1990, p A13)]

Intrapellet voidage ϵ_p was found using the equation $[1 - (\text{skeletal volume packed in helium pycnometer}) / (\text{average volume of one sorbent pellet multiplied by the number of pellets in pycnometer sample})]$. From various samples run on the Micromeritics AccuPyc 1330 helium pycnometer (and many mind numbing hours of counting pellets), an experimental estimate of 0.62 ± 0.04 was obtained. With these three parameters characterised, interpellet voidage ϵ_B was then found via a simple equation that relates the respective volume of each region to these parameters, namely $1 - [\hat{\rho}_{bed} / \hat{\rho}_s (1 - \epsilon_p)]$ (Table 4.3). A derived quantity obtained from these parameters is pellet density $\hat{\rho}_p$, which is a measure of the mass of sorbent per unit volume of pellet that includes skeletal material and intrapellet void space. This parameter is given by $\hat{\rho}_s (1 - \epsilon_p)$ and is reported in Table 4.3 along with associated experimental bounds. The final physical property to be quantified is the intrapellet pore diameter δ for the macropore domain. This parameter is required to evaluate the magnitude of the Knudsen diffusion and viscous flow transport coefficients D_K^*

and B^s respectively. Although micropore diffusion is not considered, it is useful at this point to discuss the bidisperse nature of LiLSX pellets. To quantify the micropore dimension, an equilibrium isotherm for nitrogen on Zeochem LiLSX at liquid nitrogen temperatures (77 K) was performed using the Micromeritics ASAP2010 unit. The resulting equilibrium isotherm was then deconvoluted using Density Functional Theory (DFT) [Webb & Orr (1998, pp 81-89)] for slit pore geometry to derive a plot of incremental surface area versus pore size. As nitrogen undergoes negligible adsorption on the clay binder phase that constitutes macropore channels, mercury intrusion (Hg intrusion) porosimetry was employed to quantify the macropore dimension. The Micromeritics AutoPore III unit was used for this purpose [Webb & Orr (1998, p 155)].

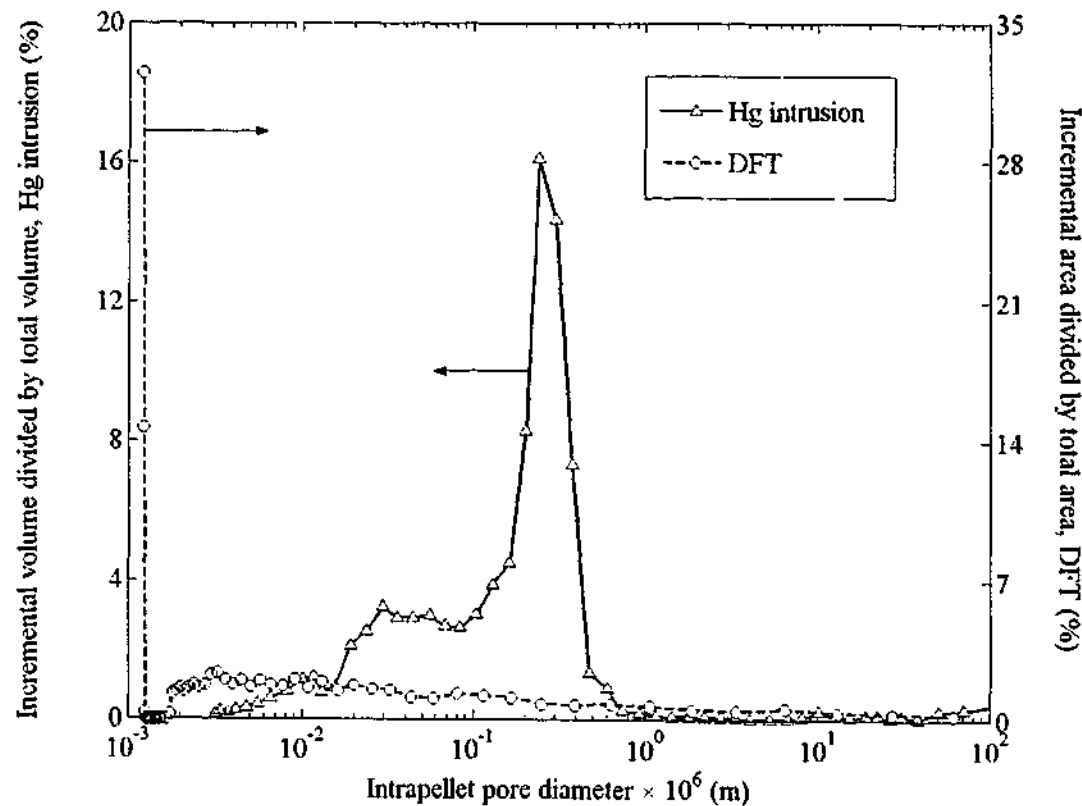


Figure 4.3: Intrapellet pore size distribution obtained from nitrogen adsorption (DFT) and mercury intrusion porosimetry (Hg intrusion) for Zeochem LiLSX.

While surface area is a useful measure of the pore size distribution for nitrogen adsorption, volume is the best descriptor for pore size distribution using Hg intrusion porosimetry. The corresponding results from DFT and Hg intrusion for Zeochem LiLSX are presented in Fig. 4.3, which gives rise to a micropore dimension of approximately 12×10^{-10} m (12 Angstroms) and macropore dimension of approximately $2.5 \pm 0.4 \times 10^{-7}$ m. Although a sharp peak is observed for the macropore dimension at $2.5 \pm 0.4 \times 10^{-7}$ m, there is a relatively long tail in the pore size distribution observed below this value from Hg intrusion porosimetry. This indicates the macropore domain is not truly monodisperse but rather a range of pore sizes exist across this region. Hence the mode of the macropore domain is used.

4.2 Previous Studies on Transport through a Porous Medium

Many experimental and theoretical methods have been investigated to quantify diffusion through porous materials. Some of the earliest methods were developed to measure diffusion under inert conditions while, more recently, methods have been developed to combine the phenomena of adsorption and/or desorption with diffusion. In addition to these and other experimental techniques, purely mathematical descriptions have been formulated to model the diffusion path of a gas molecule within a hypothetical porous medium.

4.2.1 Non-Adsorbing Methods Proposed in the Literature

The understanding of gas transport through porous media was pioneered by the work of Thomas Graham between the 1830s and 1840s [Mason & Evans (1969)]. Although a mathematical treatment of gas transport and the diffusion coefficient was not formulated until 1855 by Fick [Crank (1975, p 2)] the work of Graham laid the foundations by which diffusion coefficients under non-adsorbing conditions are experimentally determined. A common apparatus used to measure diffusion coefficients, which is a variant on Graham's original apparatus is the steady state Wicke-Kallenbach cell, first proposed by Wicke & Kallenbach (1941) to determine the overall diffusion coefficient of carbon dioxide into a nitrogen stream through a porous sample of activated carbon. A diagram of the Wicke-Kallenbach cell is shown in Fig. 4.4.

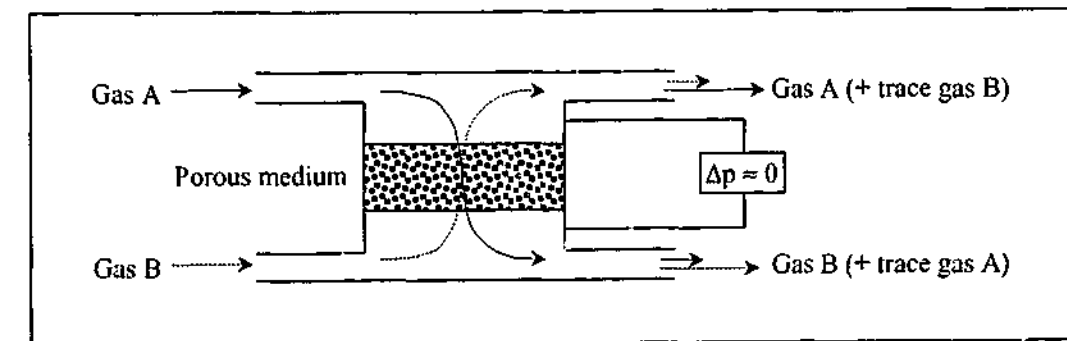


Figure 4.4: Basic mode of operation for a steady state Wicke-Kallenbach cell.

The steady state Wicke-Kallenbach cell requires absolute pressure on both sides of the porous medium to be the same, eliminating any contribution from viscous flow [Mason & Kronstadt (1967)]. This reduces $\partial p^p / \partial r$ in Eq. (2.20) to zero, where r now represents a coordinate system relative to the diffusion path from one side of the porous medium to the other. Therefore, Eq. (2.20) correctly reduces to Graham's law of effusion at the micropore/low pressure limit and Graham's law of diffusion at the macropore/high pressure limit [Mason & Kronstadt (1967)]. For a binary system this can be written as $N_1 \sqrt{M_1} + N_2 \sqrt{M_2} = 0$ or $N_1 / N_2 = -\sqrt{M_2 / M_1}$. The

negative sign is sometimes left out as this simply indicates the two molar fluxes are in opposite directions. Hoogschagen (1953, 1955), Henry *et al.* (1961), Scott & Dullien (1962), Wakao & Smith (1962), Johnson & Stewart (1965), Henry *et al.* (1967), Feng *et al.* (1974), Kaptijn *et al.* (1995), Guo *et al.* (1998) and Haugaard & Livbjerg (1998) have all used the steady state Wicke-Kallenbach cell for a wide range of porous materials to determine an effective diffusion or similarly related transport coefficient.

Although heat transfer limitations are effectively eliminated under steady state conditions using a Wicke-Kallenbach cell [Ruthven (1984b)], this apparatus does contain two inherent limitations:

- i. For systems where adsorption or heterogeneous reaction occurs, the presence of dead end pores may still contribute to the molar flux given these can terminate at an active adsorption or reaction site. Under steady state, non-adsorbing conditions a dead end pore will offer no contribution to the molar flux and hence steady state methods underestimate the effective diffusion or intrapellet transport coefficient [Hopfinger & Altman (1969), Cunningham & Williams (1980, p 225)].
- ii. The steady state Wicke-Kallenbach cell must ensure bypass does not occur around the mounted porous sample otherwise the predicted intrapellet molar flux will be erroneously large. For the sorbent investigated in this dissertation avoiding gas bypass around individually mounted pellets in a Wicke-Kallenbach type apparatus would be difficult to achieve, bringing into doubt experimental results for intrapellet molar flux.

Although confidence in parameters obtained using a steady state Wicke-Kallenbach cell are subjective, Hartmann & Mersmann (1994) found good agreement between simulated and experimental uptake profiles for carbon dioxide on 5A molecular sieve using VF+DGM transport coefficients obtained from a steady state Wicke-Kallenbach cell. Their porous medium constituted nineteen Grace GmbH 5A molecular sieve pellets that were glued into a sample ring using epoxy resin. This "porous" sample ring was then mounted into a steady state Wicke-Kallenbach cell to determine the molecular and Knudsen transport coefficients. An alternative set of experiments applied a pressure gradient across the same porous sample to determine the permeability or viscous flow transport coefficient. Despite favourable results obtained by Hartmann & Mersmann (1994), the steady state Wicke-Kallenbach cell is generally accepted across the published literature as an inadequate method for materials that potentially contain dead end pores.

This has prompted the development of dynamic methods to estimate the effective diffusion or transport coefficient from experimental data. The present discussion is still limited to non-adsorbing conditions and dynamic methods that include adsorption are deferred to §4.2.2.

Dynamic variants on the Wicke-Kallenbach method

Doğu & Smith (1975, 1976) injected a non-adsorbing tracer gas, helium, into an inert carrier stream, nitrogen, within a Wicke-Kallenbach cell arrangement to observe the dynamic change in outlet concentration across a diffusion length on the order of one pellet, in this case a single alumina pellet. As with the steady state Wicke-Kallenbach cell the requirement of equal absolute pressures on both sides of the porous medium is required. Wang & Smith (1983) and Doğu *et al.* (1987) have used this same device for the determination of macro- and micropore diffusion coefficients in a range mono- and bidisperse porous materials. One limitation with this dynamic Wicke-Kallenbach apparatus, however, is the physical dimension of the pellet must be large to obtain a measurable response from the tracer gas injection [Burghardt & Smith (1979)]. Further to this, Burghardt & Smith (1979) note the physical characteristics of this enlarged pellet may not necessarily represent the properties of a commercial pellet formed from the same raw components.

Using a similar device, Burghardt *et al.* (1988) show how a model that imposes a monodisperse structure will underestimate the diffusion coefficient for bidisperse materials given dead end pores are not accounted for. Arnošt & Schneider (1995) also used such a device on four different α -alumina catalyst pellets to evaluate transport coefficients of the DGM and mean transport pore model [Schneider (1978)], both of which are based on Maxwell-Stefan theory.

Valuš & Schneider (1981) devised a unit called "Graham's cell" that is similar to the Wicke-Kallenbach arrangement in Fig. 4.4. In this device, however, gas flows are terminated once steady state is achieved and flow from one side of the porous sample to atmosphere is measured through a calibrated soap bubble flow meter, providing a measure of the intrapellet molar flux. Isobaric conditions are maintained across the porous sample for the entire experiment and several different gas pairs are used on either side of the porous sample. Graham's cell has since been used by Valuš & Schneider (1985a) and Šolcová *et al.* (2001) for the determination of transport parameters related to the mean transport pore model for various porous catalyst pellets.

Novák *et al.* (1988) introduced a dynamic Wicke-Kallenbach cell that operates with one side of the apparatus depicted in Fig. 4.4 closed to flow. At time zero feed gas supplied to the open side of the porous system is changed to a different gas, with pressure on the closed side going through a maximum or minimum before reaching a new steady state. When a light gas (low molecular weight) replaces a heavy gas (high molecular weight) the light gas rapidly diffuses across the porous medium while heavy gas diffuses out slowly, causing pressure in the closed compartment to increase. The converse argument holds when a heavy gas replaces a light gas at time zero. A range of non-adsorbing gas pairs are used to independently fit transport coefficients of the porous

material. This device has since been used by Čapek *et al.* (1997), Hejtmánek *et al.* (1998), Čapek & Seidel-Morgenstern (2001) and Čapek *et al.* (2001) to obtain transport coefficients of the DGM and mean transport pore model for a range of mono- and bidisperse catalyst pellets.

Baiker *et al.* (1982) used a range of commercially available bidisperse catalyst pellets to examine the predictive ability of three different measuring techniques for the estimation of intrapellet diffusion coefficients. Good agreement was found between the steady state and dynamic Wicke-Kallenbach methods, while a non-adsorbing single pellet string column (chromatographic technique) provided similar values but was more sensitive to experimental error.

4.2.2 Methods that Include Adsorption and Diffusion

Exposing a porous material to dynamic changes in composition under non-adsorbing conditions can provide useful information on the mechanism(s) of intrapellet mass transfer. It has also been found that steady state and dynamic methods predict similar transport coefficient(s), provided some account of the pore network is made [Baiker *et al.* (1982), Burghardt *et al.* (1988)]. To complement these techniques, several alternatives have been developed that measure intrapellet mass transfer in the presence of adsorption/desorption. Incorporating adsorption/desorption into the analysis provides the distinct advantage of measuring diffusion rates within a regime that is approaching actual operating conditions expected within the real process.

Dynamic Wicke-Kallenbach Cell under Adsorbing Conditions

The first system discussed in this section can be viewed as an extension of the dynamic Wicke-Kallenbach method from §4.2.1 with the tracer gas introduced at $t = 0$ now being adsorbed onto the porous sample. In this case the observed outlet response is a function of both the adsorption capacity of the porous sample as well as intrapellet mass transfer. Frost (1981) found macropore and micropore diffusion controlled the transport of carbon dioxide through 0.0033 m extrudates of 5A zeolite. Doğu and Ercan (1983) obtained macropore and micropore diffusion coefficients of ethylene in bidisperse α -alumina pellets with helium used as the carrier gas. Hejtmánek *et al.* (1999) extended the experimental study of Hejtmánek *et al.* (1998) to consider the introduction of an adsorbing gas into their dynamic Wicke-Kallenbach device.

Rutherford & Do (1999) introduced a permeation cell that is similar in principle to the dynamic Wicke-Kallenbach cell except here no flow is passed over each face of the porous medium depicted in Fig. 4.4. Instead, two large volumes separate the porous medium. One was filled to a moderately high initial pressure with either helium, nitrogen, argon or oxygen and the other

evacuated to a pressure close to 1.0×10^{-9} bar.a. When the porous medium, in this case activated carbon, was exposed at time zero to these volumes a relatively constant molar flow arose such that intrapellet molar flux at conditions close to steady state could be determined from transient pressure profiles. Rutherford & Do (2000) and Rutherford & Coons (2002) have used this same device to investigate the mechanisms of intrapellet micropore diffusion of various gas species in carbon molecular sieve.

Uptake Experiments - Principle Mode of Operation

An uptake experiment follows the transient response that occurs when an initially evacuated sample of adsorbing material is exposed at time zero to a step change in bulk phase concentration [Ruthven (1984b)]. Within a volumetric device the experimentally measured response is usually pressure. Accurately knowing the volume of each compartment and dynamic pressure response provides a measure of the rate of uptake from the interpellet fluid phase. Gravimetric methods, on the other hand, physically measure the weight change of the sorbent with time as adsorption occurs. Hence the rate of change of sorbent mass with time provides an experimental measure of the uptake rate to the intrapellet adsorbed phase.

A small sample of sorbent, in the order of milligrams to grams, is used within such a device to minimise interpellet pressure drop and axial dispersion. The experimentally measured process response can then be used to adjust a mathematical representation of the system to elucidate intrapellet diffusion or transport coefficient(s). One critical aspect of data interpretation from an uptake device, however, lies in the assumptions imposed on the mathematical model that will be used to deconvolute the experimental transient. In some cases, operating conditions present during the physical experiment fall outside the mathematical models range of validity, leading to erroneous conclusions regarding the magnitude of the resulting coefficient(s) [Ruthven (1984b)]. Sircar (1994) points out the isothermal versus non-isothermal assumption is one very important aspect of any uptake experiment, which he referred to as a differential adsorption test, that should not be neglected. For this reason, data obtained from any uptake device should be scrutinized over a range of operating conditions.

Ruthven (1984b) indicates uptake experiments should be performed over a range of differential sorbate step sizes. Often, mathematical models used to quantify an uptake experiment assume isothermal behaviour with a linear equilibrium isotherm. This allows a tractable analytical solution of the diffusion equation to be derived. Should the differential sorbate step size be too large such that system non-linearities and temperature transients become important, the model will subsequently breakdown. On the other hand if the model does not impose these limiting

assumptions, generally leading to a numerical solution, this test can then be performed over a larger sorbate step size to fully explore the validity of the model. In addition pellet size should also be varied, whether individual zeolite crystals under micropore diffusion control or pelletised zeolite samples under macropore diffusion control are used, to ensure the correct trend in process response with diffusion path length is observed. One such check is R_p^2 dependence on uptake rate under macropore diffusion control for spherical geometry.

Uptake Experiments - Volumetric Method

Riekert (1971) investigated micropore diffusion of various hydrocarbon sorbates through synthetic zeolite crystals of the mordenite, T- and Y-type. Experimental data revealed Fick's second law of diffusion could not adequately resolve the observed trends and two alternative rate models were investigated that represent the migration of adsorbed molecules into or out of a zeolite crystal. Schalles & Danner (1988) presented oxygen and nitrogen uptake profiles on carbon molecular sieve type 3A pellets using a volumetric device that contained a recirculation pump to ensure the gas phase was well mixed. This allowed single and multicomponent uptake profiles to be obtained. Srinivasan *et al.* (1995) investigated uptake profiles of oxygen and nitrogen on carbon molecular sieve using a surface barrier model for micropore diffusion. Czepirski & Laciak (2000) used Fick's second law of diffusion to deconvolute the uptake rate of various pure component gas samples (carbon dioxide, however, was the only data set presented) on activated carbon. Similar studies by Nguyen & Do (2000), Bülow (2002) and Qinglin *et al.* (2003) have also investigated micropore diffusion control of various gas samples in adsorbing materials using a volumetric device.

Do (1995) introduced a new way of performing a volumetric experiment for a pure component adsorbing gas whereby the pressure increase in the sample volume is now performed very slowly using a mass flow controller (experimentally achieved by a vacuum leak valve) such that a constant molar flow enters the sample volume. Using very low pressures and performing the experiment very slowly ensures the linear Henry's law regime is achieved under isothermal conditions. Prasetyo & Do (1998) used this device to measure micropore diffusion coefficients of methane and carbon dioxide in activated carbon pellets while Do *et al.* (2000) introduced non-isothermal behaviour into the analysis to obtain micropore diffusion coefficients of methane, ethane, propane and *n*-butane in activated carbon pellets.

Uptake Experiments - Gravimetric Method

In addition to the aforementioned studies using volumetric techniques, uptake experiments have been performed using the gravimetric method. As was the case with the volumetric device, these experiments have primarily focused on micropore diffusion control. Ruckenstein *et al.* (1971) used a gravimetric technique to measure the weight change of various samples of ion exchange resin exposed to water vapour, sulphur dioxide, carbon dioxide and ammonia. Experimental data was compared to a bidisperse uptake model for a spherical sorbent pellet composed of an internal assemblage of uniformly distributed spherical micro pellets (i.e. zeolite crystals) using Fick's second law of diffusion under isothermal conditions with a linear equilibrium isotherm. Dominguez *et al.* (1988) compared the LDF and Langmuir kinetic models for oxygen and nitrogen uptake on carbon molecular sieve where non-Fick behaviour was observed using a gravimetric device.

Gravimetric techniques have also been widely used in the study of micropore diffusion of hydrocarbon molecules in various zeolite crystals using Fick's second law of diffusion [Ruthven & Loughlin (1971, 1972), Ruthven & Doetsch (1976), Gelbin & Fiedler (1980), Zhu *et al.* (2001), Wloch (2003)]. Ruthven *et al.* (1980) extended the isothermal Fick diffusion model for micropore diffusion to include temperature variations for a linear equilibrium isotherm. Experimental and analytical comparisons of carbon dioxide and *n*-pentane on 4A and 5A molecular sieve crystals allowed the mechanisms of micropore diffusion and heat transfer control to be delineated. Sircar (1983) and Sircar & Kumar (1984) investigated the presence of a surface barrier resistance to heat and mass transfer for the uptake of various hydrocarbons in A- and X-type zeolite crystals and carbon dioxide on 4A. Mugge *et al.* (2000, 2001) developed a non-isothermal Maxwell-Stefan model to describe gravimetric uptake profiles of carbon dioxide, methane and ethane on activated carbon under both macropore and micropore diffusion control.

The results from a volumetric experiment are only limited by the accuracy and response time of the pressure transducer, along with the estimates of volume for the dosing and sample regions. With the correct pressure transducer, uptake rates in the order of a second can be obtained making volumetric experiments a suitable candidate for the study of macropore diffusion control in zeolite pellets. While gravimetric techniques are useful for slowly diffusing molecules, this method is unsuitable for rapid uptake associated with macropore diffusion control in X-type zeolites. This can be attributed to "pan wobble", which occurs when gas suddenly fills the void space at time zero and "flutters" the microbalance, generally lasting anywhere from thirty [Ruckenstein *et al.* (1971)] to fifty seconds [Dominguez *et al.* (1988)] before decaying.

Frequency Response Methods

Frequency response techniques measure the CSS variation in pressure and, in some cases, temperature within an enclosed vessel that contains adsorbing material by virtue of a device that can cyclically modulate the volume such as a piston or agitated bellows section. As the modulating device increases in frequency, the time scale for intrapellet diffusion and heat transfer becomes comparable to the external forcing device and a lag in response arises. Expressions related to the variation in pressure and temperature are complex in form which, when transposed into the real domain, give rise to an in-phase and out-of-phase term. Resistance to heat and mass transfer within a sorbent pellet, in general, occur at slightly different time scales so different mechanisms will dominate at different frequencies. Matching experimental versus numerical in-phase and out-of-phase pressure/temperature profiles allows one to extract parameters related to heat and mass transfer.

Naphtali & Polinski (1963) provide the first reported use of the frequency response method to characterise the dynamics of hydrogen adsorption on a nickel catalyst using the Langmuir rate equation. Yasuda (1982) extended this technique to examine micropore diffusion control of krypton in sodium mordenite pellets. Similar studies by Yasuda *et al.* (1991), Sward & Levan (1999) and Valyon *et al.* (2000) have investigated micropore diffusion control via frequency response techniques using various gas species in adsorbing materials. Onyestyák *et al.* (2000) found macropore diffusion controlled the uptake of ammonia in various A-, X- and Y-type zeolite pellets. Each study mentioned thus far in relation to the frequency response method has assumed isothermal behaviour across all operating conditions. The importance of non-isothermal behaviour within a frequency response device has been highlighted by Sun *et al.* (1994), Jordi & Do (1994) and Song & Rees (1996). Sun *et al.* (1994) found the intrusion of heat effects into the isothermal analysis of Yasuda *et al.* (1991) was incorrectly attributed to the mobility of two different adsorbed species.

Significant improvements in frequency response data acquisition has been recently reported using a non-invasive infrared temperature measuring device with a response time close to 0.001 s and temperature resolution down to 0.002 K [Bourdin *et al.* (1996)]. This has been used by Bourdin *et al.* (1996) to characterise micropore, macropore and external film heat transfer resistance of water in NaX and propane on 5A pellets; and Grenier *et al.* (1999) for micropore diffusion and external film heat transfer resistance of propane in silicalite-1 and carbon dioxide in NaX crystals.

Frequency response is a very powerful technique for measuring a range of intrapellet heat and mass transfer mechanisms within pelletised sorbent materials and individual zeolite crystals. The

distinct advantage frequency response provides over other experimental techniques is the fact that a "zero datum for time" is removed from the analysis given CSS data as a function of frequency only is required. The one disadvantage, however, arises when a solution to the system can only be found numerically. Each data point may require several thousand cycles to achieve CSS via successive substitution under non-isothermal conditions. Hence the task of optimising transport coefficients across a large range of individual "CSS data points" imposes enormous computational overheads when the DPM with a VF+DGM constitutive equation is used.

The Pulsed Field Gradient Nuclear Magnetic Resonance Technique

Nuclear Magnetic Resonance (NMR) has found numerous applications in the study of diffusion, structural imaging and the chemical and physical description of atomic and molecular species [Gladden (1994, 2003)]. One particular NMR technique that has found widespread use in the study of self-diffusion coefficients within a confined system is Pulsed Field Gradient NMR (PFG NMR), which was first applied to liquid systems [Stejskal & Tanner (1965), Boss *et al.* (1967), Tanner & Stejskal (1968)].

PFG NMR introduces radio frequency pulses that are opposite in direction around a magnetic field that is pulsed with a frequency Δt . The initial radio frequency pulse is introduced for a sufficient period and intensity to excite the nuclear spins of sorbate molecules that have a relatively high concentration of unpaired nuclear spins. Once the radio frequency pulse has terminated, the magnetic field pulse is activated to "phase encode" these nuclear spins so that their position at this point in time, $t_{\text{mag field}}$, is known. Between $t_{\text{mag field}}$ and $t_{\text{mag field}} + \Delta t$, the reversed radio frequency pulse is introduced. If the phase encoded nuclei have not moved, the magnetic field pulse that occurs $t_{\text{mag field}} + \Delta t$ later will cancel the first. Due to molecular migration, however, the phase encoded nuclei have moved and cancellation of the second magnetic field pulse is incomplete, giving rise to spin-echo attenuation. Spin-echo attenuation provides a direct measure of the mean square displacement of phase encoded nuclei between the two magnetic field pulses [Ruthven (1984b), Gladden (1994), Stallmach & Kärger (1999)].

PFG NMR has found numerous applications in the study of micropore diffusion control in various sorbent materials using ^1H [Vasenkov *et al.* (2001), Jobic *et al.* (2003), Pel *et al.* (2003)], ^{13}C [Kärger *et al.* (1993), Stallmach *et al.* (1993)], ^{19}F [Snurr & Kärger (1997)] and ^{129}Xe [Kärger *et al.* (1990), Labouriau *et al.* (1999)] as the probe nucleus. ^{129}Xe PFG NMR has also been used to study interpellet flow around individual pellets of 13X zeolite pellets of diameter 2.0×10^{-3} m [Kaiser *et al.* (2000)]. Recently, researchers at Air Products and Chemicals Inc. have investigated the use of PFG NMR using ^{15}N -labelled N_2 in various A- and X-type zeolite crystals and pellets

[McDaniel *et al.* (1996), Bär *et al.* (1997), Rittig *et al.* (2002, 2003)]. At low temperatures between 135 and 190 K, strong dependence on micropore diffusion for nitrogen in A- and X-type zeolite crystals was observed. At higher temperatures micropore diffusion control diminished as diffusion between zeolite crystals became significant [Bär *et al.* (1997)]. Rittig *et al.* (2002, 2003) applied the long range diffusion model of Kärger *et al.* (1981) to investigate diffusion on a scale that is longer than individual zeolite crystals but smaller than the dimension of the pellet. This provided macropore tortuosity coefficients of 2.8 and 2.0 for two different 5A pellets and 1.5 for 13X pellets using ^{13}C -labelled CO and CH_4 , ^1H -labelled CH_4 and ^{15}N -labelled N_2 . A recent review by Kärger *et al.* (2003) has further highlighted the potential of PFG NMR for the characterization of macropore diffusion using multicomponent gas mixtures.

Chromatographic Methods

The chromatographic method examines the output response of a packed bed of pellets that is subjected to a pulse or step change in feed composition from the inlet end at time zero. The broadening of the response peak from its initial injection is therefore related to the mechanisms of mass transfer resistance at the intra- and interpellet level [Ruthven (1984b)]. This response, however, makes data interpretation difficult given all resistances to mass transfer within a packed bed described in §1.2 are now locked up in one measured process output response. Care must be exercised with chromatographic results to ensure that:

- i. all extraneous mechanisms of mass transfer not desired in the output response, such as axial dispersion, are suitably minimised or
- ii. a separate set of experiments are performed to quantify the impact of each mechanism on the output response by changing parameters such as feed composition or pellet size.

Despite these limitations, the chromatographic technique has appeared numerous times across the published literature for the determination of macro- and micropore diffusion control under adsorbing conditions.

Cui *et al.* (1990) compare the tortuosity coefficient predicted from the chromatographic and Wicke-Kallenbach methods for microporous alumina to highlight the inconsistent tortuosity coefficient predicted from a Wicke-Kallenbach cell when processes other than diffusion such as adsorption or chemical reaction occur within the pellet. Hashimoto & Smith (1974) elucidated macro- and micropore diffusion coefficients from chromatographic experiments using moments analysis for the adsorption of 0.5 mol% *n*-butane from a helium carrier stream over bidisperse alumina pellets. Ruthven *et al.* (1975) assumed isobaric, non-isothermal, plug flow operating conditions using the LDF model to describe micropore diffusion control of propylene, 1-butene and *cis*-2-butene flowing in an inert carrier stream over 5A zeolite pellets. Experimentally fitted

mass transfer coefficients revealed parameters obtained under the isothermal assumption, when used for a non-isothermal system, will delay the point of breakthrough. Andrieu & Smith (1980) investigated micropore diffusion control of carbon dioxide in a packed bed of activated carbon. Matching experimental data using the moments method revealed macropore diffusion control was also a significant mechanism that limited the uptake rate of carbon dioxide. Boniface & Ruthven (1985), Kim (1990), Farooq (1995), Nijhuis *et al.* (1997) and Chun & Lee (2000) have also used the chromatographic method to determine intrapellet diffusion coefficients over a range of sorbent materials.

Anderson *et al.* (1998) developed a positron emission profiling technique to measure composition profiles in packed beds of various acid exchanged sodium based zeolite pellets. This device measures gamma photons that are emitted when a fast positron particle (that is released from the radioactive decay of a neutron deficient nucleus, ^{11}C in this case) annihilates with its antimatter equivalent, the electron. This technique provides spatial resolution down to 0.003 m and temporal resolution down to 0.5 s, providing the distinct advantage of measuring interpellet profiles throughout the chromatographic experiment. Noordhoek *et al.* (1998) used results from positron emission profiling to propose new micropore diffusion coefficients for various acid exchanged zeolites using ^{11}C -labelled *n*-hexane. Provided the response time of process measuring instruments is sufficiently rapid and the mathematical model correctly accounts for mass transfer across the intra- and interpellet levels, the chromatographic technique can provide quantitative information on macropore diffusion control in pelletised X-type zeolites.

Single Pellet String Column - A Chromatographic Technique

One variant on the chromatographic method that was proposed to overcome interpellet axial dispersion is a single pellet string column. This particular device arranges individual pellets one after the other as per a chromatographic column except here the confining walls are just wide enough to allow a single pellet to occupy the cross sectional area. Relatively large void regions are present around each pellet, allowing high velocities to be maintained that minimises broadening of the pulse injection peak from interpellet pressure drop and axial dispersion. To minimise fluid bypassing along the wall, the ratio of column-to-pellet diameter needs to be in the range 1.1-1.4 [Scott *et al.* (1974)].

Valuš & Schneider (1985b) used a slightly modified arrangement by physically stacking cylindrical pellets of α -alumina on top of each other, which meant that no adjustable parameters were required from separate experiments. Six tracer-carrier gas pairs were used over ten different samples of bidisperse α -alumina pellets to elucidate transport parameters. Schneider & Gelbin

(1985) used this data, in conjunction with other data sets on diffusion in porous media to show that intrapellet transport parameters cannot be adequately determined from data obtained using mercury porosimetry alone. Sharma *et al.* (1991) used a single pellet string column with 13 different commercial catalyst pellets to estimate the effective tortuosity coefficient of the intrapellet pore network using various literature correlations. They found tortuosity varied strongly with internal porosity ϵ_p and macropore diffusion was an important component of the total molar flux for bidisperse materials. Delmas & Ruthven (1995) used a device that contained 100×10^{-6} m crystals of NaX zeolite packed within a 150×10^{-6} m capillary column for the determination of micropore diffusion coefficients of *n*-butane, *n*-hexane, cyclohexane, *n*-octane, benzene and decalin. The mechanism of axial dispersion in a single pellet string column has been quantified by Hsiang & Haynes (1977) for spherical pellets and Šolcová & Schneider (1994) for cylindrical pellets.

Differential Adsorption Bed - Another Chromatographic Technique

Another variant on the chromatographic technique for adsorption studies is the differential adsorption bed, first used by Carlson & Dranoff (1985) to characterise micropore diffusion of ethane in 4A zeolite crystals. This apparatus uses a very short length of sorbent with very high gas flow rates to rapidly dissipate heat generated within the sorbent and minimise interpellet dispersion. Once flow through the differential adsorption bed has terminated, it is heated and desorbed gas collected in a separate volume and analysed off-line to determine bed content up to the point where feed flow was terminated. By terminating feed flow at different points in time, a complete picture of the uptake rate with time can be obtained. This method has the advantage of allowing multi-component gas mixtures to be analysed.

Mayfield & Do (1991) investigated macro- and micropore diffusion of ethane, *n*-butane and *n*-pentane through activated carbon that exhibits a bimodal pore distribution using the Fick diffusion equation. Do & Do (1998a) adopted a Maxwell-Stefan approach to multicomponent transport of nitrogen-ethane-propane gas mixtures in activated carbon pellets of slab and cylindrical geometry. Do & Wang (1998) used the differential adsorption bed technique to examine single component uptake curves of ethane, propane, *n*-butane, benzene, toluene, carbon dioxide and sulphur dioxide on activated carbon using a micropore model that assumes the sorbent pellet has a size distribution of slit-shaped channels. Do & Do (2001) found good agreement of rate parameters obtained from differential adsorption bed experiments for micropore diffusion of methane, ethane, *n*-butane, *n*-hexane, benzene and ethanol on activated carbon with other adsorption/diffusion measuring devices. Wang *et al.* (2001) compared five different mass transfer models for single and multicomponent uptake rates of ethane and propane on activated carbon using the differential

adsorption bed technique. While the differential adsorption bed is a powerful technique for gas-zeolite systems where pellet saturation occurs over the timescale of minutes to hours, this has yet to be applied to a system where pellet saturation occurs within a fraction of a second, such as oxygen and nitrogen uptake in macropore diffusion controlled X-type zeolite pellets.

Zero Length Column - Another form of Chromatography

The zero length column is similar in spirit to a differential adsorption bed experiment except here the desorption response of a pre-saturated sample is continually measured from $t = 0$ without terminating feed gas flow. Again, the adsorption bed is very short such that interpellet dispersion is negligible, hence the name "zero length" column. Also, carrier gas flow rate is high to minimise external film heat and mass transfer resistance [Eiç & Ruthven (1988)].

MacDougall *et al.* (1999) obtained micropore diffusion coefficients and equilibrium parameters for sulfur hexafluoride in silicalite zeolite crystals between 303 and 434 K. A similar study by Cavalcante *et al.* (2000) for micropore diffusion of ortho- and para-xylene in aluminophosphate molecular sieve samples was performed at temperatures between 423 and 453 K. Eiç *et al.* (2002) investigated micropore diffusion and immobilization mechanisms of toluene in silicalite-1 zeolite crystals between 348 and 451 K. Brandani *et al.* (2000a) compared the analytical approximation of Brandani (1998) for para-xylene on silicalite zeolite crystals of diameter 50×10^{-10} m that exhibits a non-linear isotherm. Similar studies by Brandani *et al.* (1995a, 1995b, 1996, 1997, 2000b), Cavalcante *et al.* (1997), Loos *et al.* (2000) and Duncan & Möller (2002) have all investigated micropore diffusion control in zeolite crystals under the isothermal assumption using a zero length column. The mathematical model for a zero length column experiment has also been extended to account for non-isothermal behaviour [Brandani *et al.* (1998), Brandani (2002)].

While micropore diffusion is the most common mechanism that has been investigated in the published literature using zero length column techniques, this device has also been used to investigate macropore diffusion control inside pelletised samples of 5A beads for the transport of oxygen and nitrogen at ambient conditions [Ruthven & Xu (1993)]. These results indicate macropore diffusion is the dominant mechanism of intrapellet mass transfer within a pelletised zeolite pellet at ambient conditions.

The Spinning Basket - A Hybrid Uptake/Chromatographic Method

The spinning basket can be classified as a hybrid between an uptake and chromatographic method. This apparatus essentially measures the change in outlet concentration from a pulse or step change in feed concentration that is introduced into the vessel at time zero, this aspect of the experiment being similar in spirit to a chromatographic method. The internal arrangement of the vessel, however, is similar to that of an uptake device where a small sample of porous material, in the order of milligrams to grams, is housed. The only difference here is the porous sample is rapidly rotated inside a cage structure that is mounted on a stirrer. The advantage in rapidly spinning the porous material, as opposed to using a stationary batch, lies in the ability to experimentally verify the point where interpellet mechanisms such as axial dispersion and external film heat and mass transfer resistance become insignificant. By increasing stirrer speed the outlet response with time will eventually asymptote to a reading that does not change with stirrer speed. This condition experimentally verifies interpellet mechanisms have been suitably reduced to an insignificant level [Kolaczowski & Ullah (1989)].

Such a device has been successfully applied to determine intrapellet diffusion coefficients for adsorbing [Ma & Lee (1976)] and reacting [Kolaczowski & Ullah (1989)] systems. Provided the outlet device measuring composition change is suitably rapid, this technique also appears suitable to measure rapid diffusion dynamics for macropore limited X-type pellets.

4.2.3 Mathematical Description of the Transport Coefficient

In addition to the aforementioned experimental techniques, various researchers have adopted a purely mathematical description of transport in porous media. A similar analogy carries over from methods described in §4.2.1 and §4.2.2 in the fact that transport has been considered under conditions where the porous medium is either inert or active to adsorption.

Mathematical Treatment under Non-Adsorbing Conditions

Early models of transport in porous materials, typically a catalyst pellet, were based on simplified models that were developed to characterise transport under non-adsorbing conditions. Wakao & Smith (1962) developed an analytical expression based on three mechanisms of intrapellet mass transfer: macropore, micropore and macro-micropore series diffusion that predicts a tortuosity coefficient $\tau = 1/\epsilon$. Weisz & Schwartz (1962) predicted $\tau = \sqrt{3}/\epsilon$ using an array of cells that are visualized as cubes or spheres that have a fraction, ϵ , of their surface open to the neighbouring cell, where the open surface is randomly oriented in space. Weissberg (1963) obtained the formula $\tau =$

$1 - \frac{1}{2} \ln \epsilon$ in a porous medium that constitutes randomly packed spheres of either uniform or non-uniform size that do not overlap. Neale & Nader (1973) developed a model for impermeable spherical particles that have an arbitrary size distribution to obtain the result $\tau = (3 - \epsilon)/2$. Beeckment & Froment (1982) found $\tau = 4$ based on a simplified model of reaction and diffusion in a porous catalyst that consists of cylindrical pores with no dead ends.

With the advent of modern computers, the mathematical treatment of transport under non-adsorbing conditions has been extended to the investigation of a tagged gas molecule being introduced into a hypothetical porous medium. It is generally assumed in this instance that the porous medium will scatter gas molecules in a random direction when they collide with the pore wall. Equations that describe transport at different levels of pore opening, from the Knudsen to molecular level are then used to simulate the motion of individual gas molecules.

Evans *et al.* (1980) and Nakano & Evans (1983) consider the pore walls to be made up of an assemblage of spheres that were regularly and randomly arranged. A tagged gas molecule was introduced at one face of the porous medium and the fraction of molecules that reach a distance L before leaving the porous structure was recorded using a Monte Carlo simulation technique. This procedure was repeated several thousand times to obtain an explicit expression for the effective Knudsen transport mechanism that does not require any tortuosity coefficient. Similarly, Burganos (1998) developed an expression for the Knudsen mechanism using a binary or pixelated method that blanks out sections of a three dimensional grid to represent the structure obtained from microscopic imaging techniques. Reyes & Jensen (1985) applied a Bethe lattice network approximation of the porous material to investigate effective transport coefficients at the pore level using the VF+DGM.

Abassi *et al.* (1983) extended the analysis of Evans *et al.* (1980) and Nakano & Evans (1983) to consider diffusion at the macropore level while Reyes & Iglesia (1991) used a similar approach with spheres of varying size to define transport at the Knudsen, transition and molecular regime. Burganos & Sotirchos (1987, 1988, 1989), Sotirchos & Burganos (1988), Sotirchos (1989, 1992), and Tomadakis & Sotirchos (1993) have also simulated transport at the Knudsen, transition and molecular regimes using the DGM and VF+DGM for capillary structures with various cross-linking configurations. Bhatia (1985, 1986) developed a random walk theory for transport in random pore networks to demonstrate short-range memory effects of diffusion in the pore structure can influence predicted tortuosities, which was extended to cubic networks by Deepak & Bhatia (1994).

Mathematical Treatment under Adsorbing Conditions

Within this subsection, two methods have evolved for the simulation of transport in a porous medium in the presence of a sink term for adsorption. The first can be regarded as an extension of the "tagged gas molecule in a hypothetical porous medium" technique developed for non-adsorbing media. Common examples include the sorption and surface diffusion of a binary component system in a cylindrical, nonintersecting channel [Paleker & Rajadhyaksha (1985)], an extension of the random-walk theory of Bhatia (1985, 1986) to micropore diffusion [Bhatia (1988)] and the simulation of mass transfer in a pellet of interconnecting capillaries using the DGM in conjunction with micropore diffusion [Gladden (1991)].

The second technique involves a molecular dynamics approach to the transport of gas within a porous medium that is limited by micropore diffusion of adsorbing molecules within the crystal structure of individual zeolite crystals. This has been used to describe the transport of hydrocarbon molecules in silicalite [Demontis *et al.* (1990), June *et al.* (1990, 1992), Nowak *et al.* (1991), Maginn *et al.* (1996), Runnebaum & Maginn (1997)] and ZSM-5 [Smit & den Ouden (1988)] zeolite crystals. Experimental data obtained from Jobic (2000) using quasi-elastic neutron scattering agreed well with molecular dynamic simulations for short *n*-alkanes in ZSM-5, but significant deviations were observed for long chain *n*-alkanes. Jobic (2000) indicates further improvements in model representations of sorbate-sorbent systems will reduce these discrepancies between experimental and theoretical results under micropore diffusion control.

While methods described under non-adsorbing conditions have some analogy with the transport of oxygen and nitrogen in macropore channels of X-type zeolite pellets, the use of molecular modelling techniques common to the study of micropore diffusion is not practical at the macropore level. Studies that consider transport under non-adsorbing conditions, however, assume porosity used in the calculation of effective diffusion or transport coefficients, ϵ , relates to the region where transport is occurring, which will be referred to here as $\epsilon_{p,macro}$. From the IZA database for zeolite structures [Baerlocher *et al.* (2001), Robinson & Lillerud (2001)] it is possible to obtain a crystal density for low silica Faujasite type zeolites of approximately 1410 kg m^{-3} . Neglecting the difference between binder and crystals and using pellet density from Table 4.3 it is possible to estimate a macropore void fraction $\epsilon_{p,macro}$ of 0.34. A quick check on this number can be made by estimating the total porosity from data that indicates X type zeolites have a porosity of 51% [Szostak (1992)]. Assuming 20% binder, the total porosity obtained is 0.61, which agrees very well with the experimental result of 0.62 from Table 4.3.

4.2.4 Motivation Behind Methods Used to Find VF+DGM Coefficients

A large variety of methods have been proposed in the literature to quantify the transport of gas through an adsorbing zeolite crystal/pellet, which is still an active area of research today [Kärger (2003)]. Although by no means complete, the previous discussion does indicate a large majority of these studies investigate micropore diffusion control within zeolite crystals with much less emphasis placed on macropore diffusion control in pelletised materials. There is an even smaller body of work that has experimentally investigated the VF+DGM flux model for a sorbent pellet that exhibits macropore diffusion control, with use of the DGM mainly concentrated in the mathematical description of transport in porous materials discussed in §4.2.3. From this perspective the most appropriate technique to use on such a system appears rather arbitrary and will ultimately be dictated by the response time of equipment used on the experimental apparatus as opposed to any swaying arguments from the literature.

Chapter 2 highlighted the importance of the VF+DGM formulation in situations where the macropore domain contains the limiting intrapellet transport mechanism. Although marginal differences were observed between the DGM and VF+DGM constitutive models from chapter 2, viscous flow is maintained within this analysis as an additional contribution to the transport of gas at the macropore limit. The inclusion of viscous flow does not complicate the solution strategy in any significant way over the DGM approach as simply one extra term arises within the overall flux equation at each control volume boundary within the DPM (i.e. compare Eqs. (2.6) and (2.20)).

The ability to estimate all three structural parameters of the VF+DGM intrapellet flux model from one experiment is very difficult given the measured process response, usually one parameter such as composition or pressure, will invariably contain all three transport mechanisms. The degrees of freedom available to manipulate each coefficient limits the amount of information contained within one particular experiment. For this reason each structural parameter is obtained from an experiment that isolates each particular transport mechanism. The first set of experiments isolates Knudsen diffusion and viscous flow using a volumetric uptake device. The second unit performs chromatographic experiments to elucidate the structural parameter related to molecular diffusion. A large number of experiments over and above those required to calibrate each transport parameter was obtained to verify system response using the numerical adsorption simulator NDGNAS. These two techniques were arbitrarily selected for experimental analysis based simply on the availability and response time of equipment items.

4.3 Knudsen Diffusion and Viscous Flow Transport Coefficients

The first set of experiments isolate the mechanisms of Knudsen diffusion and viscous flow using a volumetric device. The N_c component summation for molecular diffusion within the VF+DGM of Eq. (2.20) is effectively eliminated by using a pure component gas, in this case nitrogen. A pure component gas also eliminates the presence of external film mass transfer resistance at the surface of the pellet.

4.3.1 Modelling Required to Estimate Transport Coefficients

The mathematical analysis of chapter 2 described intrapellet mass transfer in terms of a transport coefficient C that alters the magnitude of the "unhindered" diffusion/flow coefficient to account for the tortuous network of a porous medium. The remaining discussion of this subsection outlines a particular set of modelling conditions that allows C_k and C_v to be manipulated with respect to experimental data.

The first requirement from NDGNAS is to remove any dependence on mass transfer at the interpellet level. Although axial dispersion and external film mass transfer resistance do not arise for a pure component system, dependence on the steady state pressure drop coefficients κ_{viscous} and κ_{kinetic} needs to be reduced. A volumetric device houses a small mass of sorbent within a sample volume that can be assumed uniform throughout in pressure and temperature. This allows the entire sorbent bed and associated void volumes to be treated as one single control volume, i.e. the sorbent pellets and associated void regions are contained within a CSTR. The sorbent pellets exchange mass directly with the entire void space and this void space communicates directly with a separate volume that passes gas into and/or out of the single control volume. The separate volume that communicates with the single control volume sorbent bed is modelled using the rigorous product tank model, which also behaves like a CSTR.

The second requirement is that flow between the single control volume sorbent bed and product tank be calibrated against data obtained from an independent set of experiments. Fitting coefficients that characterise flow between these two regions should be consistent over the full range of temperatures and pressures investigated. These same parameters should also reproduce pressure profiles during a volumetric experiment that is independent of the material contained within the single control volume sorbent bed.

The form of the conservation of energy adopted within this dissertation contains gas compression terms that can produce significant temperature variations at the onset of a rapid pressure change. In

addition to fitting flow parameters between the two volumes using the above listed experiments, heat transfer coefficients between the single node control volume/product tank and surrounding environment also need to be established. To facilitate this procedure an analytical solution for two-dimensional non-steady conduction within the sample volume will be used in conjunction with NDGNAS results to assess the importance of heat transfer coefficients and their relative magnitude.

These combined assumptions reduce the interpellet conservation of mass and energy respectively to the following form. Note that:

- i. A single component is being used so all i summations from 1 to N_c are unnecessary.
- ii. The volume occupied by the pellets is subtracted from the combined empty sample volume V_B , with m_p representing the mass of sorbent pellets and $\hat{\rho}_p$ the density of the pellets that includes intrapellet pore space and skeletal material.
- iii. Although numerical discretisation of the interpellet region is not required, these variables will still be denoted with a tilde (\sim) to draw attention to the fact a "single control volume" CSTR model is being used.

$$\frac{[V_{\text{bed}} - (m_p/\hat{\rho}_p)]}{R\tilde{T}_B} \left(\frac{d\tilde{p}^B}{dt} - \frac{\tilde{p}^B}{\tilde{T}_B} \frac{d\tilde{T}_B}{dt} \right) = (\rho_g A v)_{\text{tank,bed}} + \left(\frac{m_p/\hat{\rho}_p}{4\pi R_p^3/3} \right) 4\pi R_p^2 N_{R_p} \quad (4.2)$$

$$\left(V_{\text{bed}} - \frac{m_p}{\hat{\rho}_p} \right) \left[\frac{\tilde{p}^B}{R\tilde{T}_B} \left(\tilde{c}_s^B - \frac{\tilde{H}_g^B}{\tilde{T}_B} \right) \frac{d\tilde{T}_B}{dt} + \left(\frac{\tilde{H}_g^B}{R\tilde{T}_B} - 10^5 \right) \frac{d\tilde{p}^B}{dt} \right] = (\rho_g A v H_g)_{\text{tank,bed}} + \left(\frac{m_p}{\hat{\rho}_p} \frac{3}{4\pi R_p^3} \right) 4\pi R_p^2 \left[(H_g N)_{R_p} + h_{p,B} (\tilde{T}_p - \tilde{T}_B) \right] - [h_{B,W} A_{B,W} (\tilde{T}_B - T_W)] \quad (4.3)$$

As gas is flowing from the dosing to sample volume, $(\rho_g A v)_{\text{tank,bed}}$ is positive when entering the sample volume and negative when leaving the dosing volume. Equations (4.2) and (4.3) require a certain number of physical parameters to be quantified. These include the size of the empty sample volume V_{bed} , the surface area of the vessel $A_{B,W}$, the coefficients that define flow between the two CSTRs, the mass of sorbent added to the sample volume m_p , the pellet-to-bed heat transfer coefficient $h_{p,B}$ and the bed-to-wall heat transfer coefficient $h_{B,W}$. V_{bed} is measured by difference when introducing helium into the empty sample volume and again with a known volume of non-porous displacement material [Webb & Orr (1995, pp 95-98)], while m_p is measured directly using scales accurate to 0.01×10^{-3} kg. $h_{p,B}$ is not readily determined from experimental data and this parameter will be discussed separately when examining the impact of $T_B = T_p$ versus $T_B \neq T_p$.

suffice to say this parameter has little impact on simulation results. This leaves $(\rho_g A v)_{\text{tank,bed}}$ and $h_{\text{B,W}}$ to be found using appropriate experimental runs. $A_{\text{B,W}}$ is calculated using an approximate estimate of the surface dimensions of the sample volume, which is $3.4 \times 10^{-3} \text{ m}^2$.

The equivalent ODEs for the intrapellet region is presented in finite volume form to allow analytical expressions for energy accumulation in the solid, adsorbed and gas phases to be defined.

$$\left(\frac{\varepsilon_p}{R\tilde{T}_p} + \hat{\rho}_p \frac{\partial \tilde{n}_{\text{eq}}^p}{\partial \tilde{p}^p} \right) \frac{d\tilde{p}_k^p}{dt} + \left(\hat{\rho}_p \frac{\partial \tilde{n}_{\text{eq}}^p}{\partial \tilde{T}_p} \right) \frac{d\tilde{T}_p}{dt} = -\frac{3}{\nabla_k r^3} \nabla_k (r^2 N) \text{ for } k = 1 \dots N_r \quad (4.4)$$

$$\begin{aligned} & \left[\hat{\rho}_p c_s + \sum_{k=1}^{N_r} \frac{\nabla_k r^3}{R_p^3} \left[\frac{\varepsilon_p \tilde{p}_k^p}{R\tilde{T}_p} \left(\tilde{c}_g^p - \frac{\tilde{H}_g^p}{\tilde{T}_p} \right) + \hat{\rho}_p \tilde{n}_{\text{eq},k}^p \tilde{c}_g^p + \hat{\rho}_p (\tilde{H}_g^p - \tilde{q}_{k,p}^p) \frac{\partial \tilde{n}_{\text{eq}}^p}{\partial \tilde{T}_p} \right] \right] \frac{d\tilde{T}_p}{dt} \\ & + \sum_{k=1}^{N_r} \frac{\nabla_k r^3}{R_p^3} \left[\frac{\varepsilon_p \tilde{H}_g^p}{R\tilde{T}_p} - \varepsilon_p 10^5 + \hat{\rho}_p (\tilde{H}_g^p - \tilde{q}_{k,p}^p) \frac{\partial \tilde{n}_{\text{eq}}^p}{\partial \tilde{p}^p} \right] \frac{d\tilde{p}_k^p}{dt} \\ & = -\frac{3}{R_p} (H_g N)_{R_p} - \frac{3h_{\text{p,B}}}{R_p} (\tilde{T}_p - \tilde{T}_B) \end{aligned} \quad (4.5)$$

When the sample volume contains no sieve (i.e. is empty) the term $m_r / \hat{\rho}_p = 0$ and these intrapellet ODEs are not required. The final values obtained for the intrapellet coefficients C_K and C_v should be relatively independent of radial discretisation to within experimental error for the sorbent pellets that are modelled within the single control volume. For this reason a range of NDGNAS simulations will be performed where N_r is systematically varied to ascertain the dependence of radial discretisation on final transport coefficient estimates.

Equations (4.2) through (4.5) represent the case where intrapellet temperature T_p is different to interpellet temperature T_B . Their equivalent form for $T_B = T_p$ is not shown here for brevity but the method for combining Eqs. (4.2) through (4.5) has been described previously in §3.2.2. These equations have not introduced any new parameters outside of those quantified in §4.1, leaving C_K and C_v within the intrapellet molar flux only to be found. Coupled to the sample volume equations are the dosing volume ODEs. Given this region contains no sorbent the dosing volume ODEs are equivalent to the sample volume ODEs for $m_p / \hat{\rho}_p = 0$ with "B" replaced by "tank".

$$\frac{V_{\text{tank}}}{R\tilde{T}_{\text{tank}}} \frac{d\tilde{p}^{\text{tank}}}{dt} - \frac{V_{\text{tank}} \tilde{p}^{\text{tank}}}{\tilde{T}_{\text{tank}}^2} \frac{d\tilde{T}_{\text{tank}}}{dt} = -(\rho_g A v)_{\text{tank,bed}} \quad (4.6)$$

$$\begin{aligned} & V_{\text{tank}} \left[\frac{\tilde{p}^{\text{tank}}}{R\tilde{T}_{\text{tank}}} \left(\tilde{c}_g^{\text{tank}} - \frac{\tilde{H}_g^{\text{tank}}}{\tilde{T}_{\text{tank}}} \right) \frac{d\tilde{T}_{\text{tank}}}{dt} + \left(\frac{\tilde{H}_g^{\text{tank}}}{R\tilde{T}_{\text{tank}}} - 10^5 \right) \frac{d\tilde{p}^{\text{tank}}}{dt} \right] \\ & = -(\rho_g A v H_g)_{\text{tank,bed}} - [h_{\text{tank,W}} A_{\text{tank,W}} (\tilde{T}_{\text{tank}} - T_W)] \end{aligned} \quad (4.7)$$

As for the sample volume, the dosing volume heat transfer coefficient $h_{\text{tank,W}}$ needs to be found once V_{tank} is known using helium displacement experiments. $A_{\text{tank,W}}$ is found using approximate estimates on the surface dimensions of the dosing volume, which is $15 \times 10^{-3} \text{ m}^2$.

4.3.2 Experimental Mass-transfer Unit (EMU)

Given the complete set of model equations and physical sorbent properties are now available, the experimental volumetric device will be introduced. This apparatus is called the Experimental Mass-transfer Unit and is affectionately referred to as the EMU given it is skinny and produces a fast response, rather like the native Australian flightless bird of the same name. The EMU was supplied intact and operational from the adsorption research group at Air Products and Chemicals Inc. Please refer to §D.1 of appendix D for a complete description of the EMU including a detailed piping and instrumentation diagram, equipment specification list and photos.

The EMU measures the dynamic change in pressure that occurs when an evacuated sample of sorbent, initially maintained at constant temperature, is suddenly exposed to a dosing volume at higher initial pressure. The dosing and sample volumes are separated by two globe valves that are always fully open, along with a rapid actuating ball valve that is opened at "time equal to zero" according to each EMU simulation. In addition to three valves, approximately 0.30 m of ¼ inch stainless steel tube is present between the two volumes. Given the pressure dynamic is rapid, usually lasting less than one second, a fast response MKS Baratron pressure transducer is used. This pressure transducer, with a response time of 0.02 s and accuracy of ± 0.004 bar over the pressure range 0-1.33 bar.a, is mounted on the dosing volume side of the EMU apparatus.

The pressure transducer is logged at a scan rate of 0.02 s through a PCI-DAS 1200 data acquisition card located within a local PC. Commercially available data acquisition software, Labtech NotebookPro version 10.1, is used to read the pressure signal from the card and log this to file. In addition, temperature within the sample volume is also measured at an approximate scan rate of 0.1 s using a T-type junction exposed thermocouple. Wires leading from the thermocouple tip are housed within a ¼ inch sheath to allow an airtight seal to be made at the entry point of the thermocouple using a compression fitting. The PCI-DAS 1200 card does not have the capability of

measuring thermocouple signals so the LUB data acquisition system described in §4.4.2 was set up in the EMU laboratory to log this temperature.

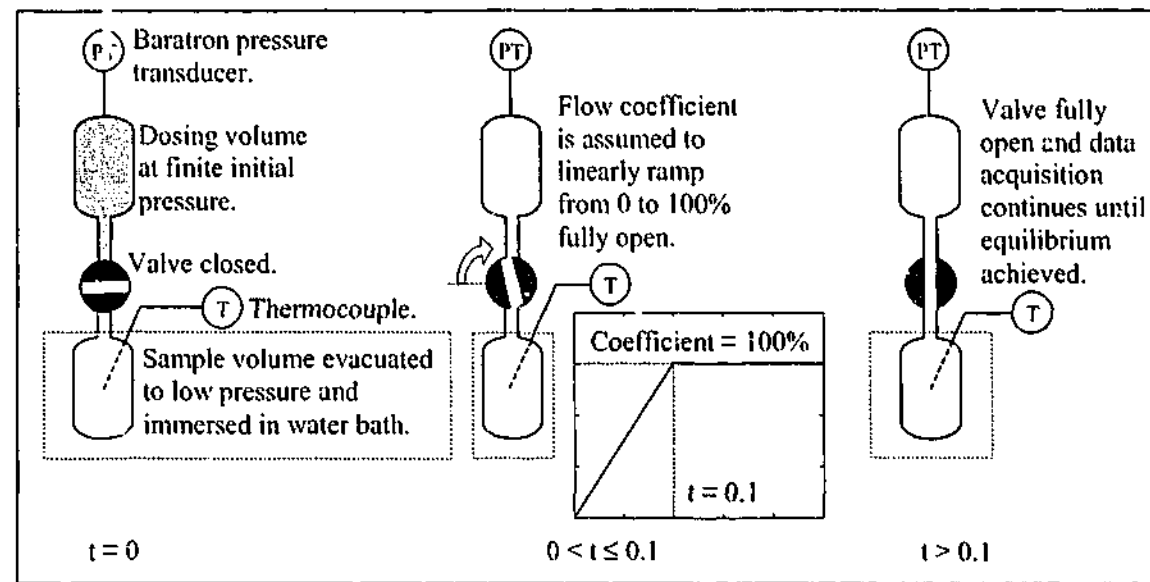


Figure 4.5: Basic schematic arrangement of one EMU run from start, $t = 0$, to end, $t \gg 0.1$.

Before the connecting ball valve is opened the sample volume is evacuated to 1.3×10^{-4} bar.a, which is the minimum resolution of the pressure transducer, for several minutes via an Edwards two-stage high vacuum pump. Once the sample volume is evacuated and isolated, the dosing volume is charged with 99.99 mol% N_2 to a higher initial pressure. The connecting ball valve between the two initially isolated volumes is then pneumatically opened and the pressure response of the dosing volume measured, along with temperature at the center of the cylindrical vessel in the sample volume. A basic schematic arrangement of one EMU run is shown in Fig. 4.5. Figure 4.5 indicates the numerical flow coefficient that connects the two volumes imposes a linear ramp for 0.1 s. This condition was used to numerically capture finite dynamics of the ball valve rate of opening that initially isolates the two volumes from each other. This boundary condition ramp is further discussed in §4.3.3 when experimental data is introduced.

To calibrate the flow coefficient, crushed Zeochem LiLSX with a nominal pellet diameter of $1.0 \pm 0.1 \times 10^{-5}$ m (referred to as “dust”) was used such that $d_{p,eq}$ can be set to zero numerically. This implies ILE in the sample volume. In addition to dust runs, EMU runs with the sample volume empty (referred to as “blank”) were also used. Remaining pellet diameters used within the EMU were obtained by screening many kilograms of sorbent into two size ranges, $1.5 \pm 0.1 \times 10^{-3}$ m and $2.0 \pm 0.1 \times 10^{-3}$ m. All screening and sorbent crushing was performed in a dry air glove box to avoid water contamination from atmospheric air.

4.3.3 Calibrating Numerical Flow and Heat Transfer Coefficients

To numerically simulate each EMU run the rigorous product tank model in NDGNAS was activated for the dosing volume with $V_{\text{tank}} = 59.7 \times 10^{-6}$ m³, while the single node sorbent bed was activated for the sample volume with $V_{\text{bed}} = 16.0 \times 10^{-6}$ m³. With this arrangement there are three parameters that need to be found in order to simulate each EMU run, wall heat transfer coefficients for both volumes and a numerical flow coefficient. To quantify the flow coefficient, three different flow regimes have been investigated.

Regime i: Compressible Flow through a Valve (Valve Equation)

The first flow regime applies the valve equation as specified by the Fluid Controls Institute Inc. for compressible flow [Chou & Huang (1994a)].

$$(\dot{v}A)_{\text{tank,bed}} = 0.07600 K_{\text{valve}} \sqrt{\frac{(p_{\text{up}}^2 - p_{\text{down}}^2)}{SG_{\text{up}} T_{\text{up}}}} \quad \text{for } p_{\text{down}} \geq 0.53 p_{\text{up}} \quad (4.8)$$

$$(\dot{v}A)_{\text{tank,bed}} = 0.06446 K_{\text{valve}} p_{\text{up}} \sqrt{\frac{1}{SG_{\text{up}} T_{\text{up}}}} \quad \text{for } p_{\text{down}} < 0.53 p_{\text{up}} \quad (4.9)$$

p_{up} and p_{down} represent the pressure in bar.a of the upstream (dosing) and downstream (sample) regions respectively. Similarly, SG_{up} and T_{up} represent the specific gravity and temperature respectively of the upstream gas. K_{valve} is a dimensionless fitting coefficient that characterises flow through the seat of the valve. The term $(\dot{v}A)_{\text{tank,bed}}$ represents the volume flow of gas between the two regions and has units of normal m³ s⁻¹. To obtain molar flow between these volumes, normal volumetric flow obtained from either of Eqs. (4.8) or (4.9) is multiplied by gas density at normal conditions, which are 1.013 bar.a and 273.0 K [Chou & Huang (1994a)]. Flow is always directed towards the region with lowest absolute pressure, which in this case is the sample volume. For this option the valve coefficient K_{valve} is used to numerically fit dust and blank runs to experimental data with a valve ramp of 0.1 s active on the magnitude of K_{valve} that begins at zero.

Regime ii: Incompressible Turbulent Flow in a Pipe

The second flow regime considered within NDGNAS is related to incompressible turbulent flow in a pipe ($Re > 2100$) using the Darcy-Weisbach equation [Potter & Wiggert (1991, p 277)].

$$v_{\text{tank,bed}} = K_{\text{turbulent}} \sqrt{\frac{(p_{\text{up}} - p_{\text{down}})}{\hat{\rho}_{\text{g,average}}}} \quad (4.10)$$

$K_{\text{turbulent}}$ represents a pipe K factor that sums individual head loss terms for each pipe section and fitting located between the dosing and sample volumes. Initially, the sample and dosing volumes commence with a very large pressure ratio ($p^{\text{tank}}/p^{\text{B}} \rightarrow \infty$) and the assumption of incompressible flow may seem completely erroneous. However, technical paper 410-C from the Crane Company for flow of fluids through valves, fittings and pipe describe a method of incorporating compressible gas flow within the incompressible form of the Darcy-Weisbach equation [Crane Co. (1976, p 1-9)]. They introduce a compressibility factor Y_{compress} within Eq. (4.10) such that $K_{\text{turbulent}}$ now becomes $Y_{\text{compress}} K'_{\text{turbulent}}$, where Y_{compress} compensates for changes in fluid properties due to expansion. For incompressible flows where $(p_{\text{up}} - p_{\text{down}})$ is less than 40% of p_{up} , $Y_{\text{compress}} \approx 1$ [Crane Co. (1976, p 3-3)]. When $(p_{\text{up}} - p_{\text{down}})$ is greater than 40% of p_{up} , Y_{compress} decreases below 1. The region over which compressibility is important and hence $Y_{\text{compress}} < 1$ according to the Crane Co. (1976) definition is numerically observed for times below 0.2 s.

From this discussion a ramp applied to $K_{\text{turbulent}}$ has the physical analogy of a time-varying compressibility factor Y_{compress} being applied to an incompressible equation for steady flow conditions. However, traditional methods of estimating $K_{\text{turbulent}}$ from literature correlations no longer apply here as the regime of incompressible flow under non-steady conditions is factored into $K_{\text{turbulent}}$. Fitting NDGNAS to experimental blank and dust runs allows $K_{\text{turbulent}}$ to be estimated for the complete pipe manifold. To find molar flow $(\rho_{\text{g}} v A)_{\text{tank,bed}}$ from velocity using Eq. (4.10), $v_{\text{tank,bed}}$ is multiplied by the cross sectional area of the connecting tube and average gas phase density at both ends of the pipe [Crane Co. (1976, p 3-3)].

The heuristic criterion of the Crane Co. (1976) for compressible flow described previously was found to be more appropriate when compared to the traditional criterion based on the Mach number (Ma). $Ma = v_{\text{tank,bed}}/v_{\text{sound}}$ and is defined as the ratio of the average pipe velocity to the speed of sound, where $v_{\text{sound}} = \sqrt{\gamma_{\text{up}} 10^8 RT_{\text{up}}/M_{\text{up}}}$ and $\gamma_{\text{up}} = c_{\text{g}}^{\text{up}}/(c_{\text{g}}^{\text{up}} - 10^5 R)$.

Potter & Wiggert (1991, p 391) indicate that for $Ma < 0.3$ gas flows can be treated as incompressible. The speed of sound for nitrogen at conditions characteristic of an EMU run is approximately 330 m s^{-1} . Calculated pipe velocities from NDGNAS did not exceed 50 m s^{-1} at any stage during any simulation and hence Ma never exceeded 0.2. According to the Ma analysis compressible flow never occurred, a distinctly different conclusion to that reached from the Crane Co. (1976) analysis.

Regime iii: Incompressible Laminar Flow in a Pipe

The third and final flow regime considered is that for incompressible laminar flow in a pipe ($Re < 2100$) with a K factor similar to that adopted for turbulent flow used to replace the analytical coefficients present within the Hagen-Poiseuille equation [McCabe *et. al.* (1993, p 88-89)].

$$v_{\text{tank,bed}} = K_{\text{laminar}} \frac{(p_{\text{up}} - p_{\text{down}})}{10^{-5} \mu_{\text{up}}} \quad (4.11)$$

Note the factor 10^{-5} within the denominator of Eq. (4.11) converts μ_{up} from units of Pa s to bar.a s. Given the temperature of the dosing volume does not change by an appreciable amount the viscosity of the upstream gas, μ_{up} , is approximately constant so that $v_{\text{tank,bed}}$ is approximately proportional to $(p_{\text{up}} - p_{\text{down}})$. As for the turbulent flow equation a ramp is applied to K_{laminar} during the first 0.1 s of the simulation, which can be thought of as compensating for compressible, non-steady conditions that persist at the onset of a valve switch according to the Crane Co. (1976) criterion. To find molar flow $(\rho_{\text{g}} v A)_{\text{tank,bed}}$ from velocity using Eq. (4.11) requires $v_{\text{tank,bed}}$ to be multiplied by tube cross sectional area and average density at both ends of the pipe, similar to that performed with regime ii.

While the assumption of incompressible flow between the connecting pipe work under turbulent conditions appears a rather abstract conclusion from the compressible valve equation discussed in regime i, the application of regime iii for laminar flow appears even more obscure. It will be shown later in this section, however, that the Crane Co. (1976) criterion for compressible flow is not the only parameter to be satisfied for times slightly beyond the allocated ramp time. It has also been found that Re falls below 2100 in a similar time frame, identifying regime iii as the model that best replicates operating conditions beyond the ramp time. This will be discussed with respect to blank and dust runs.

Table 4.4: Summary of experimental operating conditions for all blank and dust EMU runs. Note that blank runs 7 and 8 were not used to optimise each K factor or $h_{\text{tank,w}}$ but instead were used in §4.3.4 to investigate sample volume temperature profiles. Mass of sorbent present in all runs denoted "Dust run ..." was 1.85×10^{-3} kg.

| Run descriptor | p^{tank} for $t \leq 0$ (bar.a) | T_{tank} for $t \leq 0$ (K) | p^{h} for $t \leq 0$ (bar.a) | T_{b} for $t \leq 0$ (K) |
|----------------|--|--------------------------------------|---------------------------------------|-----------------------------------|
| Blank run 1 | 0.267 | 296.7 | 0.0001 | 273.2 (ice bath) |
| Blank run 2 | 0.533 | 297.2 | 0.0001 | 273.2 (ice bath) |
| Blank run 3 | 1.013 | 297.4 | 0.0001 | 273.2 (ice bath) |
| Blank run 4 | 0.267 | 294.5 | 0.0001 | 303.7 |
| Blank run 5 | 0.533 | 294.5 | 0.0001 | 303.7 |
| Blank run 6 | 1.013 | 294.9 | 0.0001 | 303.7 |
| Blank run 7 | 1.248 | 295.4 | 0.0003 | 303.7 |
| Blank run 8 | 0.0003 | 294.5 | 1.277 | 294.5 |
| Dust run 1 | 0.267 | 293.7 | 0.0001 | 273.2 (ice bath) |
| Dust run 2 | 0.534 | 291.7 | 0.0001 | 273.2 (ice bath) |
| Dust run 3 | 1.016 | 293.7 | 0.0001 | 273.2 (ice bath) |
| Dust run 4 | 0.267 | 295.7 | 0.0001 | 303.7 |
| Dust run 5 | 0.534 | 295.7 | 0.0001 | 303.7 |
| Dust run 6 | 1.016 | 295.7 | 0.0001 | 303.7 |

With all of this said, however, conditions that arise between the dosing and sample volumes in reality cover several orders of magnitude in Re as well as compressible-to-incompressible flow within a fraction of a second. To propose a physically realistic picture of this system using anything more complicated than two non-isothermal CSTRs connected through a lumped parameter boundary condition would fall into the category of an exclusive fluid dynamics Ph.D. in itself. For this reason the application of each flow regime to the simulation of blank and dust EMU runs will be scrutinized with respect to experimental data obtained across all conditions where finite pellet diameters are to be used. Table 4.4 summarises experimental initial conditions for the blank and dust runs investigated within this particular subsection.

Definition of a Global Sum Squared Error: Calibrating Flow Coefficients

The foregoing discussion has highlighted three parameters that need to be found using blank and dust runs. In order to find the appropriate fitting coefficients an optimisation routine was incorporated into NDNGAS that aims to minimise a Global Sum Squared Error (GSSE) between the experimental and numerical pressure response obtained in the dosing volume.

$$GSSE = \sum_{m=1}^{\alpha_1} \sum_{n=1}^{\alpha_2} \sum_{p=1}^{\alpha_3} \left[\left(\frac{P_{\text{EMU},m,n,p}^{\text{tank}} - P_{\text{EMU},m,n,\text{min}}^{\text{tank}}}{P_{\text{EMU},m,n,\text{max}}^{\text{tank}} - P_{\text{EMU},m,n,\text{min}}^{\text{tank}}} \right) - \left(\frac{P_{\text{NDGNAS},m,n,p}^{\text{tank}} - P_{\text{EMU},m,n,\text{min}}^{\text{tank}}}{P_{\text{EMU},m,n,\text{max}}^{\text{tank}} - P_{\text{EMU},m,n,\text{min}}^{\text{tank}}} \right) \right]^2 \quad (4.12)$$

where α_1 indicates the number of runs with different initial dosing volume pressures (= 3),

α_2 indicates the number of runs with different water bath temperatures (= 2), and

α_3 indicates the total number of data points obtained from that particular EMU run.

Each individual operating point obtained numerically and experimentally between $0 < t \leq 0.3$ was reduced to dimensionless form using the maximum (initial) and minimum (final steady state) pressures obtained experimentally to provide a relative error value that can be added across all operating conditions. This prevents a bias being placed on runs with high initial pressures in relation to runs with low initial dosing volume pressures when absolute pressure differences are used. GSSE from Eq. (4.12) is minimised by manipulating K_{valves} , $K_{\text{turbulent}}$ or K_{laminar} for each individual flow regime investigated in conjunction with the magnitude of $h_{\text{tank,w}}$.

Table 4.5: Fitted NDGNAS flow coefficients for three different boundary conditions along with the product tank-to-wall heat transfer coefficient using blank and dust results. Also shown to the right of each regime is a percentage difference between the dust and blank fitted K factor, reported in the form $100 \times (K_{\text{regime,blank}} - K_{\text{regime,dust}}) / K_{\text{regime,dust}}$.

| NDGNAS fitted parameter | Blank runs | Dust Runs | |
|--|----------------------|----------------------|----------------------------------|
| K_{valve} regime i (-) | 0.046 | 0.067 | -35 % difference |
| $h_{\text{tank,w}}$ regime i ($W m^2 K^{-1}$) | 4000 | 2760 | |
| GSSE of Eq. (4.12) regime i (-) | 1.8 | 0.80 | |
| $K_{\text{turbulent}}$ regime ii ($kg^{1/2} s^{-1} bar.a^{-1/2} m^{-1}$) | 14 | 22 | -36 % difference |
| $h_{\text{tank,w}}$ regime ii ($W m^2 K^{-1}$) | 4490 | 4830 | |
| GSSE of Eq. (4.12) regime ii (-) | 2.4 | 0.97 | |
| K_{laminar} regime iii (m) | 5.2×10^{-9} | 6.6×10^{-9} | -21% difference, "optimal" |
| $h_{\text{tank,w}}$ regime iii ($W m^2 K^{-1}$) | 1660 | 1730 | |
| GSSE of Eq. (4.12) regime iii (-) | 0.080 | 0.13 | |

Given two parameters are to be independently adjusted the double precision Fortran90 IMSL routine DBCONF was incorporated within NDGNAS that minimises a function of N variables over a bounded space using the quasi-Newton method with finite difference gradients, where N in this case is two. A large solution space was mapped out initially to provide relatively close bounds on both coefficients before starting DBCONF. In addition, this procedure was performed independently for the blank and dust runs to allow final simulation results to be compared for consistency, as summarised in Table 4.5. The final fit to each blank and dust run using all three regimes for flow is compared in Fig. 4.6.

One can see that in all cases the final pressure attained numerically matches the experimental pressure to within 0.02 bar.a across all runs, indicating V_{bed} , V_{tank} and the equilibrium isotherm are well characterised. Figure 4.6 also demonstrates why a boundary condition ramp is required for the first 0.1 s after the valve opens. Experimentally, the first three to four logged pressure points exhibit a slower rate of pressure decrease as opposed to the next 0.2 to 0.3 s. Ultimately, the numerical ramp condition introduces a second fitting coefficient into NDGNAS that assists in the prediction of the corresponding EMU profile. However, a numerical valve ramp is still based on the fact that valve inertia must be overcome when opening from 0 to 100% open.

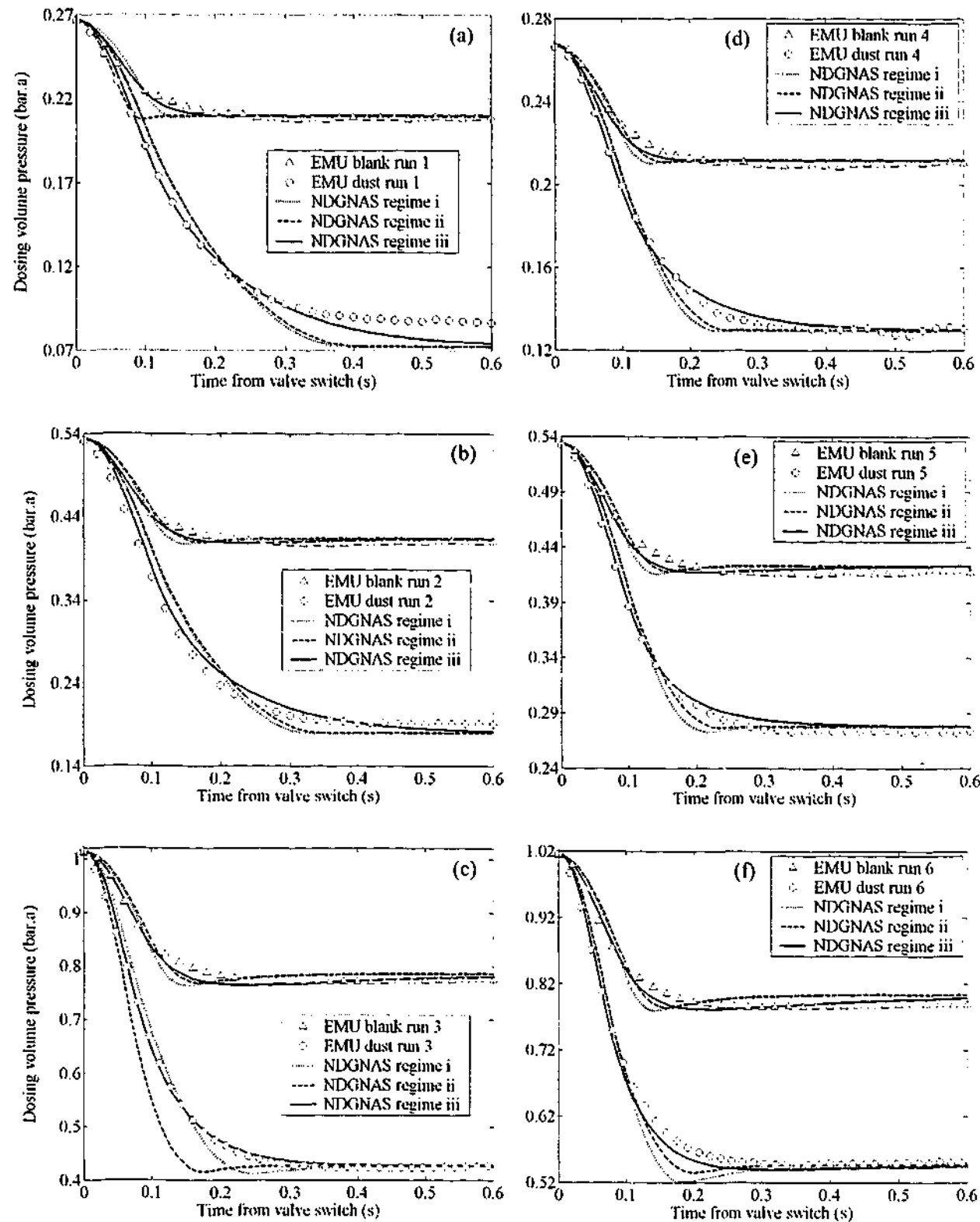


Figure 4.6: Experimental versus numerical pressure response for (a) Blank and dust run 1 (b) Blank and dust run 2 (c) Blank and dust run 3 (d) Blank and dust run 4 (e) Blank and dust run 5 (f) Blank and dust run 6.

Although a range of numerical boundary conditions could be invoked to generate a similar fit to the data, consistently adopting a 0.1 s ramp time across all runs can be considered a close approximation to the real system. Figure 4.6 also demonstrates that regime iii provides the best fit

to experimental data in terms of the lowest GSSE along with the closest predictions on the K factor between blank and dust runs. The resulting values obtained for $h_{\text{tank},W}$ are large to mitigate the temperature depression that occurs numerically when rapid expansion of the gas phase occurs. These values of $h_{\text{tank},W}$ result in an average temperature depression of 5 to 10 K numerically within the dosing volume. However, this could not be verified experimentally as a thermocouple could not be placed inside the dosing volume. Running NDGNAS with $h_{\text{tank},W} \rightarrow \infty$ resulted in a GSSE that was at least one order of magnitude higher than those shown in Table 4.5, so the isothermal product tank option does not adequately reproduce experimental profiles obtained with the non-isothermal option.

Figure 4.6 shows that regimes i and ii predict the initial valve opening dynamic well but tend to overestimate the rate of decay for $t > 0.1$ s in relation to regime iii. The reason for this can be seen in Fig. 4.7 which compares the Crane Co. (1976) compressibility criterion and Re obtained numerically from the blank and dust runs with the largest initial difference in pressures, blank run 3 (Fig. 4.7a) and dust run 3 (Fig. 4.7b). Quantitatively similar trends are observed for blank run 6 and dust run 6 with higher bath temperatures. Other blank and dust runs with smaller initial pressure differences observe shorter convergence times for the Crane Co. (1976) criterion and smaller values of Re over this same time range and hence are not shown for brevity. Therefore, Figs. 4.7a and 4.7b represent the “worst case scenario” conditions for regime iii. Satisfying the Crane Co. (1976) criterion in Fig. 4.7 occurs when lines denoted “ $p^{\text{tank}} - p^B$ ” fall below the corresponding line marked “40% of p^{tank} ”.

Initially, one can see the most extreme blank run is very close to the laminar and incompressible flow regime at $t = 0.1$ s from each of the three boundary conditions investigated (Fig. 4.7a). In fact, apart from Re using regime i, all other trends are within the laminar and incompressible regime. This provides some justification for the improved fit to EMU data obtained using regime iii for a larger portion of the pressure transient in relation to regimes i and ii.

While every blank run safely falls within the laminar and incompressible flow regime for $t \geq 0.1$ s, the same is not rigorously true for dust run 3 (Fig. 4.7b). Although each of the three boundary conditions are close to the laminar and incompressible regime, they have not quite achieved the prescribed conditions that allow regime iii to be used exclusively. While a further 0.1 s at worst is required to fully achieve laminar and incompressible flow, this small window beyond the allocated ramp time may provide some insight as to why K_{laminar} for dust is slightly higher than K_{laminar} for blanks.

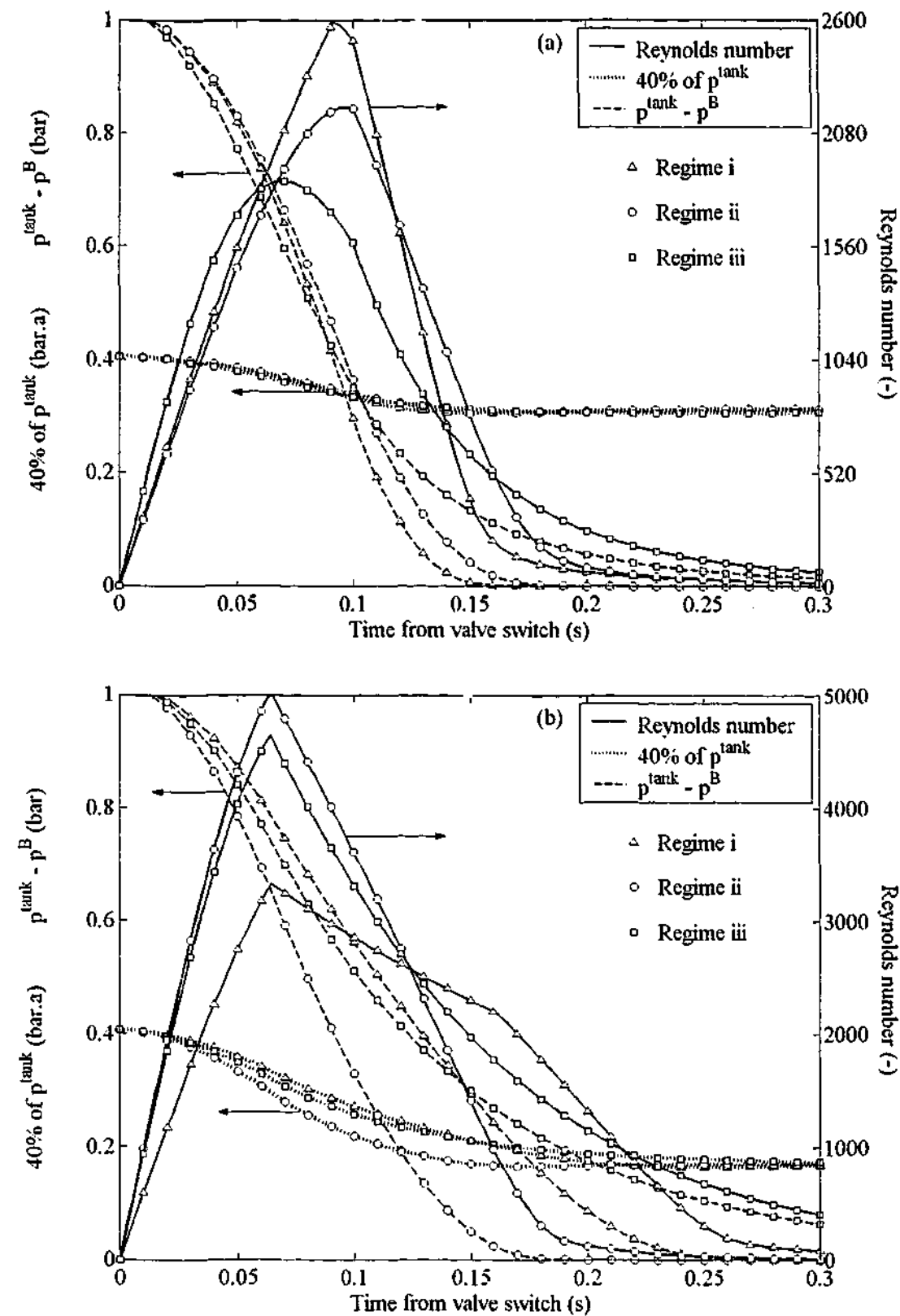


Figure 4.7: Comparative plot of the Crane Co. (1976) compressibility criterion and Re at small values of time obtained from NDGNAS for each regime of flow with (a) Blank run 3 and (b) Dust run 3.

Although dust runs 3 and 6 indicate truly laminar and incompressible conditions have not quite been achieved at $t = 0.1$ s, dust runs 1, 2, 4 and 5 were all at the laminar and incompressible flow regime by $t = 0.1$ s so approximately 33% of the GSSE is being biased by runs that are not within

the fully laminar and incompressible regime. With this said, however, agreement of $K_{laminar}$ to within 20% for blank and dust runs is an encouraging result given the assumptions imposed on NDGNAS.

4.3.4 Temperature Profiles in the Sample Volume

Up to now no reference has been made regarding the magnitude of the sample side heat transfer coefficient $h_{B,W}$. The inability to accurately reproduce the entire experimental pressure response, with small deviations observed around $t = 0.25$ s as profiles begin to plateau can be explained by examining two extremes in the magnitude of $h_{B,W}$ from NDGNAS. At this stage blank run temperature profiles only will be considered. The appropriate value for $h_{B,W}$ to use for dust and pellet finite diameter runs shall be treated separately in §4.3.6.

Once the initial pressure transient is complete and the maxima or minima in temperature due to pressurisation or depressurisation respectively has occurred, the only mechanism that remains is heat transfer to the water bath surrounding the sample volume. NDGNAS assumes the entire volume of the CSTR is at one uniform temperature, which acts through a lumped parameter heat transfer coefficient to exchange energy with the water bath. No allowance for radial or axial conduction of heat through the gas phase to the walls is made. So what impact does radial and axial conduction within the gas phase have inside this volume once the pressure transient is complete? To pursue this issue, temperature profiles within the sample volume at the point where $(p_{up} - p_{down}) \approx 0$ shall be investigated with the aid of an analytical solution for two-dimensional conduction within a medium of assumed constant physical properties.

Consider axial and radial conduction within a cylindrical vessel where gas phase thermal conduction λ_g^B is equivalent in both the r and z directions after the pressure transient is complete (i.e. for $t > 0.3$ s). Each plot in Fig. 4.6 and trends for " $p^{tank} - p^B$ " in Fig. 4.7 indicate pressure is approximately constant beyond this point in time while the experimental temperature variation due to rapid pressurisation or depressurisation is observed to be less than 2 K (see experimental trends in Fig. 4.9). This allows gas phase density $\rho_g^B (= p^B / RT_B)$ to be treated as constant to a good approximation, along with the specific heat capacity at constant pressure c_g^B and thermal conductivity λ_g^B . It is also assumed that film heat transfer resistance from the layer of gas located alongside each face of the cylinder wall limits heat transfer resistance to the environment, which in this case is the water bath. The governing form of the conservation of energy and associated

Boundary and Initial Conditions (BC and IC) can be written as follows [Carslaw & Jaeger (1993, pp 34-35)].

$$\text{IC 1: } \bar{T}_B = 1 \text{ over } 0 \leq r < R \text{ and } -L < z < L \text{ for } t \leq 0,$$

$$\text{BC 1: } \frac{\partial \bar{T}_B}{\partial r} = 0 \text{ at } r = 0 \text{ and } \frac{\partial \bar{T}_B}{\partial z} = 0 \text{ at } z = 0 \text{ for } t > 0, \text{ and}$$

$$\text{BC 2: } \frac{\partial \bar{T}_B}{\partial r} = \left(\frac{h_{B,W}}{\lambda_g^B} \right) \bar{T}_B \text{ at } r = R \text{ and } \frac{\partial \bar{T}_B}{\partial z} = \left(\frac{h_{B,W}}{\lambda_g^B} \right) \bar{T}_B \text{ at } z = \pm L \text{ for } t > 0$$

$$\frac{1}{D_{\text{therm}}} \frac{\partial \bar{T}_B}{\partial t} = \frac{1}{r} \frac{\partial}{\partial r} \left(r \frac{\partial \bar{T}_B}{\partial r} \right) + \frac{\partial^2 \bar{T}_B}{\partial z^2} \quad (4.13)$$

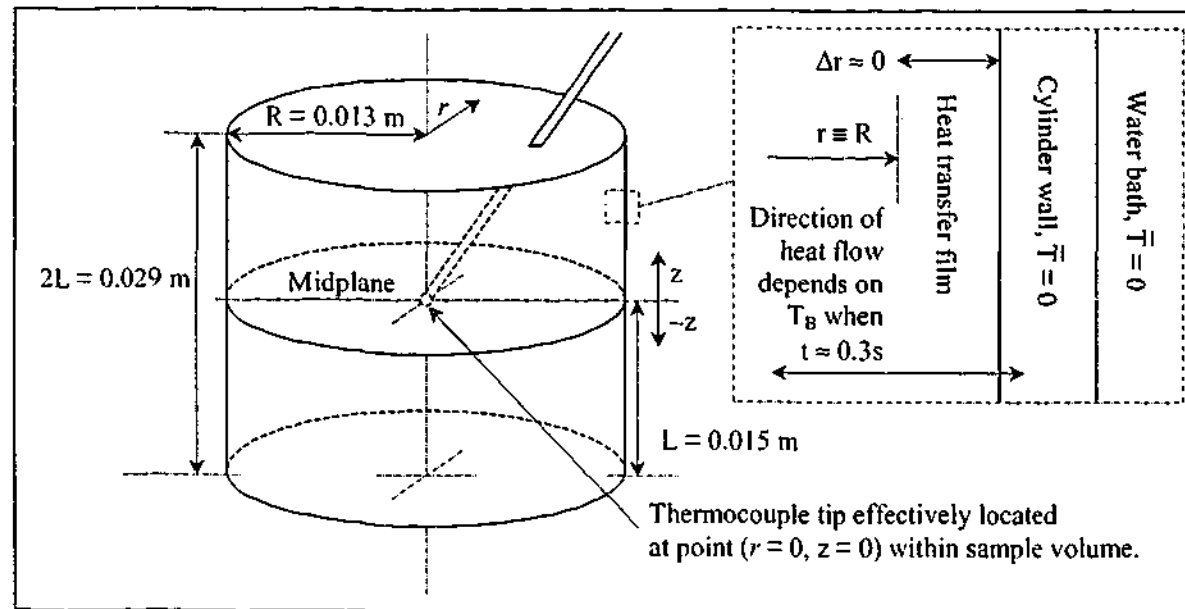


Figure 4.8: A schematic arrangement drawing of the EMU sample volume showing the experimental location of the thermocouple tip and vessel dimensions. Although photos reveal the top and base of this vessel are slightly rounded, the numerical assumption of cylindrical geometry provides a close representation of the real system. Adopted from Incropera & DeWitt (1990, p 264).

Free convection within the vessel is ignored. Temperature is written in dimensionless form using $\bar{T}_B = (T_B - T_W)/(T_{\text{initial}} - T_W)$ while the radial and axial coordinate parameters r and z have units of metres. D_{therm} represents thermal diffusivity of the gas phase and is given by the expression $\lambda_g^B / \rho_g^B c_g^B$. The coordinate system established for this analysis is depicted in Fig. 4.8 along with the experimental location of the thermocouple within the sample volume. For analysis purposes the thermocouple is as close to position $(r = 0, z = 0)$ as could be physically measured. Only a small window for visual inspection was available through the small section of pipe that leads into the sample volume and the thermocouple tip was clearly visible in this field of view.

The analytical solution of Eq. (4.13) subject to the listed boundary and initial conditions involves the multiplication of two separate results, one for a semi-infinite cylinder of finite radius R denoted $\chi(r, t)$ [Carslaw & Jaeger (1993, p 225)] and another for a semi-infinite rectangle of finite half-length L denoted $\Psi(z, t)$ [Carslaw & Jaeger (1993, p 173)]. The resulting expression for \bar{T}_B is given by the following [Carslaw & Jaeger (1993, p 227)].

$$\bar{T}_B(r, z, t) = \chi(r, t) \times \Psi(z, t)$$

$$= \left[\sum_{m=1}^{\infty} \frac{2 \left(\frac{h_{B,W}}{\lambda_g^B} \right) J_0(\alpha_m r) \exp(-D_{\text{therm}} \alpha_m^2 t)}{R \left[\left(\frac{h_{B,W}}{\lambda_g^B} \right)^2 + \alpha_m^2 \right] J_0(\alpha_m R)} \right] \times \left[\sum_{n=1}^{\infty} \frac{2 \left(\frac{h_{B,W}}{\lambda_g^B} \right) \cos(\alpha_n z) \exp(-D_{\text{therm}} \alpha_n^2 t)}{\left[\left(\frac{h_{B,W}}{\lambda_g^B} \right)^2 + \alpha_n^2 \right] L + \left(\frac{h_{B,W}}{\lambda_g^B} \right) \cos(\alpha_n L)} \right]$$

$$\text{where } \alpha_m \text{ are the positive roots of } \alpha_m J_1(\alpha_m R) - \left(\frac{h_{B,W}}{\lambda_g^B} \right) J_0(\alpha_m R) = 0$$

$$\text{and } \alpha_n \text{ are the positive roots of } \alpha_n \tan(\alpha_n L) - \left(\frac{h_{B,W}}{\lambda_g^B} \right) = 0 \quad (4.14)$$

J_0 and J_1 represent the zeroth and first order Bessel functions of the first kind respectively. To compare experimental and NDGNAS temperature profiles against the analytical solution, two additional blank runs were performed. The first involved rapid pressurisation of the sample volume, denoted blank run 7 in Table 4.4, while the second invoked an EMU run in reverse to rapidly depressurise the sample volume, denoted blank run 8 in Table 4.4. Blank runs 7 and 8 were performed with a higher initial pressure to generate a temperature transient large enough to allow comparisons with experimental data to be made. Data from blank runs 1 through 6 lose the small temperature transient due to compression from noise in the measured signal.

A first approach estimate for $h_{B,W}$ to use in both NDGNAS and the analytical solution was made by applying the limiting Nusselt number for heat transfer from a sphere under stagnant conditions, $Nu = h_{B,W} d_{\text{bed}} / \lambda_g^B \approx 2$ [Bird *et al.* (1960, p 409)], which gives $h_{B,W} \approx 2.0 \text{ W m}^{-2} \text{ K}^{-1}$ for nitrogen. In addition, $D_{\text{therm}} = 2.4 \times 10^{-5} \text{ m}^2 \text{ s}^{-1}$ and $8.4 \times 10^{-5} \text{ m}^2 \text{ s}^{-1}$ for blank runs 7 and 8 respectively.

A comparison of the experimental versus numerical temperature and pressure profiles from both runs is provided in Figs. 4.9a through 4.9f. The initial temperature used for the analytical solution is the minimum/maximum temperature measured experimentally, which is assumed to occur at $t =$

0.3 s for both runs. Error in the measured thermocouple signal of ± 0.5 K is reflected in noise present around the average value adopted for the bath temperature. In all cases, boundary conditions obtained from regime iii described in Table 4.5 were used.

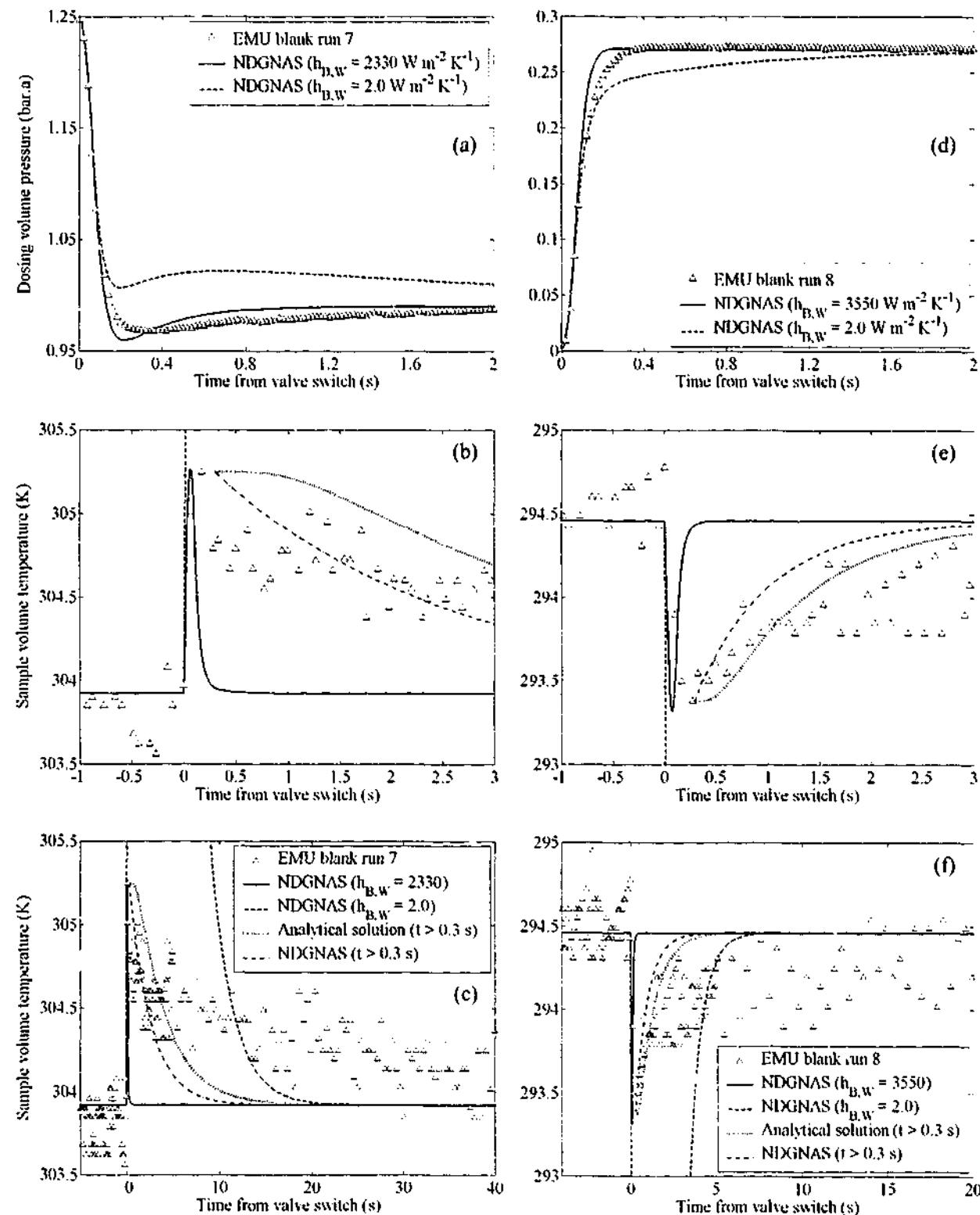


Figure 4.9: Experimental versus numerical profiles obtained from blank runs 7 (left hand side plots) and 8 (right hand side plots) using regime iii. (a) Pressure profiles from blank run 7. (b) Temperature profiles from blank run 7 for short times. (c) Temperature profiles from blank run 7 for long times. (d) Pressure profiles from blank run 8. (e) Temperature profiles from blank run 8 for short times. (f) Temperature profiles from blank run 8 for long times. Note the legends in (c) and (f) also apply identically to (b) and (e) respectively.

Figures 4.9b and 4.9e both show a rapid increase or decrease in temperature across the first three scan times of data acquisition for a rapid pressurisation or depressurisation of the sample volume respectively. However, for $t > 0.3$ s the experimental temperature approaches bath temperature very slowly. These same two plots also highlight two distinctly different responses arise when fitting heat transfer coefficients within NDGNAS. Using the assumed $h_{B,W}$ value of $2.0 \text{ W m}^{-2} \text{ K}^{-1}$ gives rise to a very large temperature transient that deviates from bath temperature by almost 90 K due to gas compression. The analytical solution for compression of an ideal gas into an adiabatic volume that is initially evacuated predicts the temperature will increase to $\gamma_{up} T_{up}$ where "up" denotes upstream gas (i.e. dosing volume) and $\gamma_{up} = c_g^{up} / (c_g^{up} - 10^5 R)$ [Smith *et al.* (1996, p 227-228)]. The maximum temperature from NDGNAS of 385 K is close to the theoretical limit $\gamma_{up} T_{up}$, indicating $h_{B,W} = 2.0 \text{ W m}^{-2} \text{ K}^{-1}$ is close to assuming the sample volume is adiabatic. The corresponding NDGNAS pressure profile with $h_{B,W} = 2.0 \text{ W m}^{-2} \text{ K}^{-1}$ does not accurately follow the EMU pressure profile, with an erroneously slow asymptotic approach to steady state observed (Figs. 4.9a and 4.9d).

To obtain a better match with EMU data requires $h_{B,W}$ to assume a value that correctly predicts the maximum or minimum temperature observed experimentally. Results obtained with these adjusted values of $h_{B,W}$ (2330 and $3550 \text{ W m}^{-2} \text{ K}^{-1}$ respectively for blank runs 7 and 8) indicate NDGNAS now predicts EMU pressure profiles with a greater degree of accuracy. Subsequently, these values of $h_{B,W}$ were used directly in the optimisation routine when ascertaining K factors and $h_{tank,W}$. It is also worth noting that these values are a similar order of magnitude to $h_{tank,W}$, providing an explanation as to why optimal $h_{tank,W}$ values are so large.

These physically unrealistic heat transfer coefficients now damp numerical temperature transients from gas compression but cause temperature to asymptote too quickly towards bath temperature, which is generally complete after 0.5 s. The reason for NDGNAS predicting slightly faster pressure profiles can be attributed to rapid cooling of the sample volume in relation to the rate of temperature decrease observed experimentally (Figs. 4.9c and 4.9f). However, the magnitude of the temperature change between rapid pressurisation/depressurisation and bath temperature is small, less than 2 K, so the resulting deviation between NDGNAS and EMU pressure profiles is also small.

Imposing different magnitudes on $h_{B,W}$ within NDGNAS does not satisfactorily address the reason for poor agreement with EMU temperature profiles. One possible explanation may reside within the CSTR assumption of uniform temperature within the sample volume. To address this issue, the analytical solution at $(r = 0, z = 0)$ is used. Applying the analytical solution to these blank runs

with $h_{b,w} = 2.0 \text{ W m}^{-2} \text{ K}^{-1}$ reveals a gradual decrease (blank run 7) and increase (blank run 8) in temperature towards bath temperature, which provides a better representation of EMU dynamics in both cases once the pressure transient is complete. For $t < 10 \text{ s}$ in Fig. 4.9, the analytical solution matches EMU response very well. Beyond this time, noise in the EMU signal makes it difficult to see the final approach to bath temperature within the sample volume.

To further examine the impact of radial and axial conduction, a third NDGNAS simulation was performed that replicates the input deck from the analytical solution (this run is denoted "NDGNAS ($t > 0.3$)"). Both the analytical solution and "NDGNAS ($t > 0.3$)" trends are shown on each temperature plot of Fig. 4.9. These simulations, which now compare film heat transfer *only* for a CSTR and two-dimensional cylinder, reveal both trends are only a few seconds apart. This suggests gas compression and interpellet gas-to-wall heat transfer terms within the conservation of energy have a significant impact while radial and axial profiles that arise within the vessel are of secondary importance, providing some justification, at least from this preliminary discussion, for adopting a CSTR model within NDGNAS.

This analysis, on the other hand, now brings into doubt the use of gas compression terms within a conservation equation that does not consider the true geometry of a system where rapid pressurisation or depressurisation occurs. Complicated three-dimensional flow patterns with initially large heat transfer coefficients at the wall due to high gas velocities could potentially mitigate gas compression transients estimated from a uniform CSTR model such as NDGNAS. However, to investigate a model of this complexity would encompass an entirely new Ph.D. topic in itself. For this reason it is assumed that matching EMU pressure profiles using a non-isothermal CSTR model and unrealistically large heat transfer coefficients is the most appropriate procedure for simulating EMU blank runs, as well as the dosing volume for all dust and finite pellet diameter runs. The requirement for large bed-to-wall heat transfer coefficients is unnecessary, however, when sorbent is present in the sample volume as the large thermal mass offered by the solid material mitigates temperature transients due to gas compression. This observation is strongly supported by helium decompression experiments performed in §5.3 with a packed bed of sorbent.

4.3.5 Comparing EMU and NDGNAS Results to Find C_K and C_v

With a relatively consistent treatment of blank and dust runs now available from NDGNAS, the remaining task is to simulate EMU runs using finite pellet diameters to elucidate VF+DGM transport coefficients. Each dust run performed in §4.3.3 was also repeated for the 1.5×10^{-3} and $2.0 \times 10^{-3} \text{ m}$ diameter pellets. Experimental operating conditions invoked for each finite pellet diameter run, denoted "Pellet run ...", is presented in Table 4.6.

Table 4.6: Summary of experimental operating conditions across all EMU pellet runs. For pellet runs where $d_p = 1.5 \times 10^{-3} \text{ m}$, $m_p = 2.27 \times 10^{-3} \text{ kg}$. For pellet runs where $d_p = 2.0 \times 10^{-3} \text{ m}$, $m_p = 2.20 \times 10^{-3} \text{ kg}$.

| Run descriptor | d_p (m) | p^{tank} for $t \leq 0$ (bar.a) | T_{tank} for $t \leq 0$ (K) | p^b for $t \leq 0$ (bar.a) | T_b for $t \leq 0$ (K) |
|----------------|----------------------|--|--------------------------------------|------------------------------|--------------------------|
| Pellet run 1 | 1.5×10^{-3} | 0.268 | 293.7 | 0.0001 | 273.2 (ice bath) |
| Pellet run 2 | 2.0×10^{-3} | 0.267 | 293.2 | 0.0001 | 273.2 (ice bath) |
| Pellet run 3 | 1.5×10^{-3} | 0.534 | 294.2 | 0.0001 | 273.2 (ice bath) |
| Pellet run 4 | 2.0×10^{-3} | 0.533 | 294.2 | 0.0001 | 273.2 (ice bath) |
| Pellet run 5 | 1.5×10^{-3} | 1.016 | 294.7 | 0.0001 | 273.2 (ice bath) |
| Pellet run 6 | 2.0×10^{-3} | 1.016 | 294.7 | 0.0001 | 273.2 (ice bath) |
| Pellet run 7 | 1.5×10^{-3} | 0.267 | 293.7 | 0.0001 | 303.8 |
| Pellet run 8 | 2.0×10^{-3} | 0.267 | 295.7 | 0.0001 | 303.7 |
| Pellet run 9 | 1.5×10^{-3} | 0.533 | 294.7 | 0.0001 | 303.8 |
| Pellet run 10 | 2.0×10^{-3} | 0.533 | 295.7 | 0.0001 | 303.7 |
| Pellet run 11 | 1.5×10^{-3} | 1.016 | 294.7 | 0.0001 | 303.8 |
| Pellet run 12 | 2.0×10^{-3} | 1.016 | 295.7 | 0.0001 | 303.7 |

Ruthven (1984b) indicates uptake experiments should be performed at different sorbate step sizes and pellet diameters to ensure the limiting mass transfer resistance, in this case macropore control under spherical geometry, is experimentally observed. Experimental versus NDGNAS results presented in this section reveal the parameter space investigated in Table 4.6 allows the assumption of macropore control in Zeochem LiLSX pellets to be experimentally verified.

The optimisation routine DBCONF was initiated in NDGNAS using a new definition for GSSE.

$$GSSE = \sum_{m=1}^{\alpha_1} \sum_{n=1}^{\alpha_2} \sum_{p=1}^{\alpha_3} \left[\frac{\sum_{q=1}^{\alpha_4} (p_{\text{EMU},m,n,p,q}^{\text{tank}} - p_{\text{NDGNAS},m,n,p,q}^{\text{tank}})^2}{(\text{Relative error scaling parameter})_{m,n,p}} \right] \quad (4.15)$$

where α_1 indicates the number of runs with different initial dosing volume pressures ($= 3$),

α_2 indicates the number of runs with different pellet diameters ($= 2$),

α_3 indicates the number of runs with different water bath temperatures ($= 2$), and

α_4 indicates the total number of data points obtained from that particular EMU run.

(Relative error scaling parameter) $_{m,n,p}$ arising within Eq. (4.15) is present to ensure EMU runs with high initial dosing pressures do not bias the GSSE from runs where the initial dosing pressure is almost an order of magnitude smaller. For completeness (Relative error scaling parameter) $_{m,n,p}$ was set to the numerator of the term in [] brackets of Eq. (4.15) when C_K and C_v attained the largest value considered within the two-parameter space survey, which was 620 and 620 respectively.

Although it may seem more appropriate to define GSSE in a manner similar to that presented in Eq. (4.12), the problem with this earlier definition when comparing pellet runs is that final equilibrium pressure is somewhat lower than pressures dealt with at times close to the valve switch where mass transfer is important, i.e. $0 < t < 1.0$ s. As the pellets slowly cool to bath temperature at times beyond 1.0 s a slow transient period is observed of decreasing pressure. These final equilibrium conditions will be different from run to run and hence incorporating the definition of GSSE from Eq. (4.12) will bias runs where final conditions are not drastically removed from conditions close to $t = 1.0$ s. This means a run with high bath temperature and low initial dosing volume pressure (equilibrium pressure not too far removed from conditions at $t = 1.0$ s) would bias GSSE over a run using a cooler water bath and higher dosing pressure (equilibrium conditions somewhat removed from pressures around $t = 1.0$ s). This new definition of GSSE according to Eq. (4.15) essentially divides the sum squared error for experimental versus NDGNAS results with NDGNAS using a finite pellet diameter against the same error if NDGNAS assumes these same pellets are now acting under ILE conditions.

Final Values Obtained from the Optimisation Routine

Before DBCONF was initiated, a large solution space was mapped out initially to provide relatively close bounds on C_K and C_v . This procedure was repeated using several different levels of radial discretisation within the pellets to examine the impact of N_r on the optimal values for C_K and C_v . Although each individual NDGNAS simulation required anywhere between 0.3 s ($N_r = 3$) and 15 s ($N_r = 50$) on a 650 MHz Compaq XP1000 Dec-Alpha Workstation, in excess of 800,000 individual runs were performed.

Figure 4.10 presents a small window of this two-parameter space initially surveyed by NDGNAS for C_K and C_v . This provides a visual tool that helps to qualitatively describe the impact of transport coefficients on simulated EMU response. Location of the optimal estimates for C_K and C_v from DBCONF are also shown. Figure 4.10 relates to simulation data obtained with $N_r = 30$. Simulation time required to map out a space of this size with $N_r = 50$ was prohibitive so $N_r = 30$ was the highest discretisation level initiated to systematically sweep out the parameter space for transport coefficients. In fact, the bounded parameter space initiated for DBCONF with $N_r = 30$

was also applied directly to DBCONF when $N_r = 50$. Qualitatively similar trends are observed for all other cases with $N_r < 30$. Figure 4.10 indicates the magnitude of C_K has a well-defined minimum for any particular value of C_v . Varying the magnitude of C_v while holding C_K constant, on the other hand, produced a plateau in GSSE once a certain magnitude was exceeded.

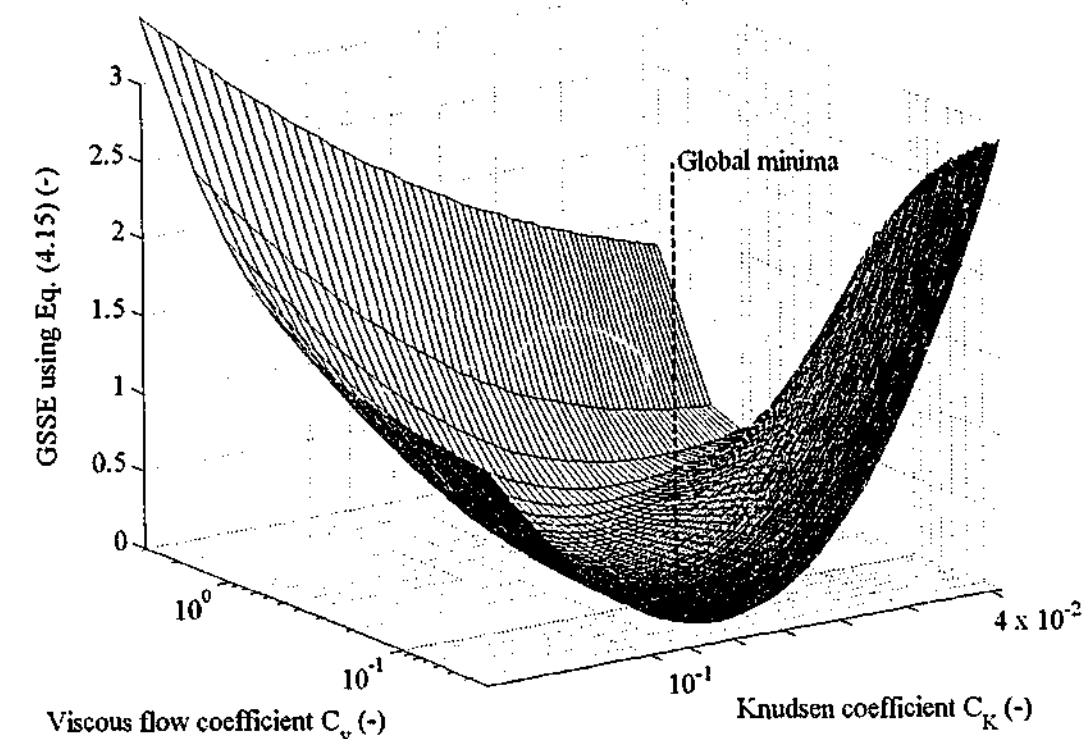


Figure 4.10: GSSE of Eq. (4.15) versus the two independent fitting parameters C_K and C_v obtained from the initial parameter search using $N_r = 30$.

For increasing values of C_v above 0.62 the GSSE increases very rapidly as simulated dosing volume pressure becomes erroneously faster than the equivalent EMU profile, approaching the ILE asymptote for very large values. With decreasing C_v , however, viscous flow has a smaller impact on total intrapellet molar flux and hence the GSSE asymptotes to a Knudsen-only response. Also note the observed minima in C_K did not change significantly for values of C_v much below 0.062, indicating viscous flow has a relatively small impact from this point. Values of C_v much below 0.02 renders viscous flow almost negligible and hence the global search in C_v stopped at this limit given no appreciable change in GSSE was occurring. Final estimates on C_K and C_v obtained by DBCONF for each level of radial discretisation are summarised in Table 4.7.

Table 4.7: Dependence on the level of radial discretisation within the pellet to the optimised transport coefficients obtained across all EMU pellet runs.

| Transport coefficient | Radial discretisation within the pellet, N_r | | | | | | | | | |
|-----------------------|--|--------|--------|--------|--------|--------|--------|--------|--------|--------|
| | 3 | 4 | 5 | 6 | 8 | 10 | 15 | 20 | 30 | 50 |
| C_K | 0.0984 | 0.0901 | 0.0864 | 0.0829 | 0.0856 | 0.0831 | 0.0829 | 0.0827 | 0.0831 | 0.0827 |
| C_v | 0.0321 | 0.0437 | 0.0365 | 0.0392 | 0.0352 | 0.0348 | 0.0508 | 0.0525 | 0.0544 | 0.0608 |

Apart from the run where $N_r = 6$, C_K progressively decreased in magnitude until an approximate asymptote somewhere near 0.083 is approached. On the other hand, C_v showed no monotonically increasing or decreasing trend with increasing N_r , varying randomly between 0.032 and 0.051 until N_r approached 20. For $N_r \geq 20$ a relatively consistent estimate somewhere close to 0.06 was obtained. At this point it is important to ascertain whether experimental uncertainty or radial discretisation presented in Table 4.7 limits the application of final estimates on C_K and C_v for NDGNAS. It is assumed within the following analysis that transport coefficients obtained with $N_r = 50$ are equivalent to results that would be obtained for $N_r \rightarrow \infty$ given relatively consistent estimates are obtained once N_r is greater than 20. Experimental uncertainty in C_K can be found by perturbing all experimentally determined structural coefficients within Knudsen diffusion, namely δ , around its experimental error presented in Table 4.3 and finding the associated deviation in C_K .

$$\text{Error in } C_{K,\text{optimal}} = \text{Maximum} [(C_{K,\text{optimal}} - C_{K,\text{min}}) (C_{K,\text{max}} - C_{K,\text{optimal}})] \quad (4.16)$$

$$\text{where } C_{K,\text{optimal}} \delta = C_{K,\text{min}} (\delta + \Delta\delta), C_{K,\text{optimal}} \delta = C_{K,\text{max}} (\delta - \Delta\delta) \text{ and } C_{K,\text{optimal}} = 0.0827$$

Using this procedure, an experimental error on the Knudsen transport coefficient is 0.083 ± 0.016 . For viscous flow the same structural parameter within B^c to perturb is δ^2 . The equivalent relationship for C_v is as follows.

$$\text{Error in } C_{v,\text{optimal}} = \text{Maximum} [(C_{v,\text{optimal}} - C_{v,\text{min}}) (C_{v,\text{max}} - C_{v,\text{optimal}})] \quad (4.17)$$

$$\text{where } C_{v,\text{optimal}} \delta^2 = C_{v,\text{min}} (\delta + \Delta\delta)^2, C_{v,\text{optimal}} \delta^2 = C_{v,\text{max}} (\delta - \Delta\delta)^2 \text{ and } C_{v,\text{optimal}} = 0.0608$$

Solving Eq. (4.17) gives $C_v = 0.061 \pm 0.025$. For all values of N_r considered in Table 4.7 the maximum deviation in C_K and C_v from their magnitude at $N_r = 50$ was 0.016 and 0.028 respectively. While radial discretisation bounds on C_K lie within the equivalent bounds from experimental uncertainty, C_v does not. Although C_v experiences a larger variation due to radial discretisation than experimental uncertainty, previous discussions within this subsection (and close examination of Fig. 4.10) reveal $C_v < 0.062$ will produce minimal changes in the GSSE. Hence the bounded parameter space provided to DBCONF from the initial searching algorithm becomes relatively insensitive to the initial estimate of C_v once below 0.062.

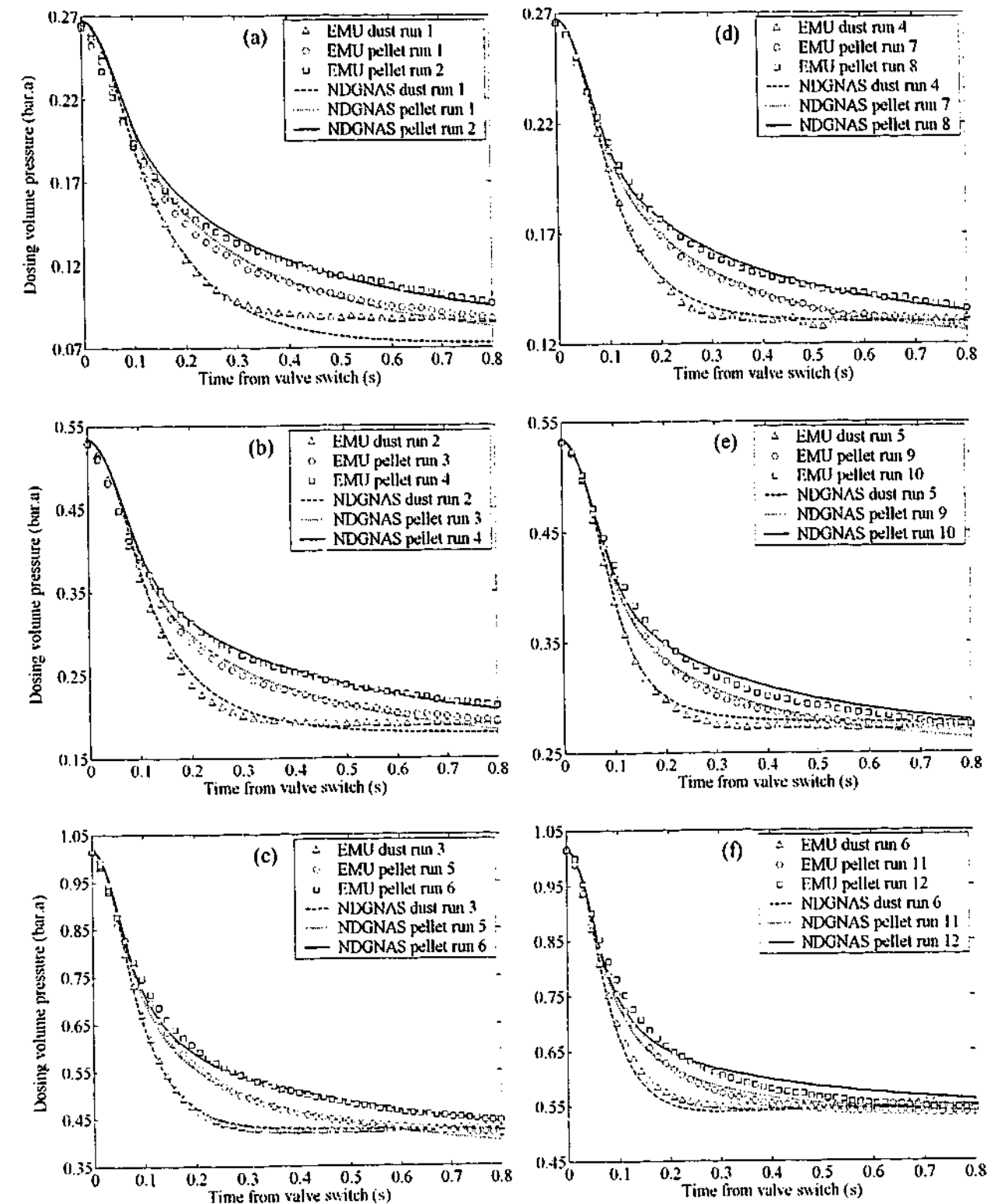


Figure 4.11: NDGNAS and EMU pressure profiles obtained for each dust and pellet run using $N_r = 30$. (a) Dust run 1 and pellet runs 1 and 2. (b) Dust run 2 and pellet runs 3 and 4. (c) Dust run 3 and pellet runs 5 and 6. (d) Dust run 4 and pellet runs 7 and 8. (e) Dust run 5 and pellet runs 9 and 10. (f) Dust run 6 and pellet runs 11 and 12.

The important result to glean from this analysis is that C_K has a strong influence on the GSSE, which was found to lie within experimental uncertainty, while C_v is of lesser importance once its magnitude decreases below 0.062. The fact that C_v does not lie within experimental uncertainty as a function of radial discretisation has more to do with very small errors in the predicted pressure profile of approximately 1.0×10^{-6} bar, accumulating in the calculation of GSSE as opposed to any intrinsic problems with the radial discretisation scheme introduced. Even with relative and absolute ODE tolerances of 10^{-7} , collective results obtained across all EMU simulations required about one month to complete using two 650 MHz Compaq XP1000 Dec-Alpha workstations. Setting error tolerances much tighter and repeating this analysis was deemed time-prohibitive and unnecessary as one could ultimately be trying to fit noise in the signal.

Although presenting every NDGNAS fit for each pellet run as a function of N_r is unnecessary, it was found that each level of radial discretisation did provide a good fit to the corresponding EMU pellet run when using optimised transport coefficients. Only one particular set of profiles have been presented within this dissertation. Figure 4.11 compares each EMU pressure profile against NDGNAS profiles using $N_r = 30$ for all twelve pellet runs, along with the corresponding dust run. Although Fig. 4.11 reveals NDGNAS does not exactly match every EMU run (for example, compare dust run 1, pellet run 10 and pellet run 12), a large majority of these comparative plots show good agreement across a range of pellet diameters, water bath temperatures and initial dosing volume pressures using:

- i. identical boundary conditions to those for dust runs under regime iii, and
- ii. one set of transport coefficients, $C_K = 0.083$ and $C_v = 0.061$, that were assumed for $N_r \rightarrow \infty$.

Figure 4.11 shows the rate of decrease in dosing volume pressure becomes faster as pellet size decreases. The uptake rate of nitrogen into the pellets must therefore be slowing down as pellet diameter increases, a direct result of the increased diffusion path length nitrogen must travel within the pellet to achieve equilibrium between $0 \leq r \leq R_p$. Dust runs are positioned below data obtained from finite pellet diameter runs across each individual graph of Fig. 4.11, while 1.5×10^{-3} m diameter pellet runs are situated in between dust and 2.0×10^{-3} m diameter results on these same graphs. The difference between each result is also in excellent agreement numerically, justifying the assumption that macropore diffusion control is the limiting mechanism for mass transfer in Zeochem LiLSX through an inverse square dependence on uptake rate with pellet diameter.

Having calibrated NDGNAS against EMU data in terms of Knudsen and viscous flow transport coefficients, attention shall now turn towards the impact of non-isothermal behaviour in the

presence of sorbent pellets. A discussion on the magnitude of C_K and C_v will not be initiated until the magnitude of C_m has been determined and hence is reserved until §4.4.3.

4.3.6 Impact of Non-Isothermal Behaviour with Sorbent Pellets

Up to now NDGNAS has imposed the assumption $T_B = T_P$ on all pellet runs by letting $h_{P,B} \rightarrow \infty$. Sircar & Kumar (1984) indicate experimental uptake profiles are initially limited by mass transfer resistance where conditions close to adiabatic arise, which is then followed by a region where external film heat transfer resistance dominates as the pellets cool to bath temperature. If the mass transfer limited regime for Zeochem LiLSX with nitrogen is very fast (i.e. less than 0.3 s) then VF+DGM structural parameters have in fact been calibrated against data that actually falls within the external film heat transfer regime. Given NDGNAS has been calibrated to EMU runs with the assumption $T_B = T_P$ and hence $h_{P,B} \rightarrow \infty$, it should be found that activating $T_B \neq T_P$ and varying $h_{P,B}$ should change the numerical pressure profile whilst holding C_K and C_v constant if external film heat transfer is the limiting resistance. To quantify the impact of each parameter first order sensitivity coefficients of the dosing volume pressure as a function of C_K , C_v and $h_{P,B}$ using NDGNAS have been determined. This method provides a more transparent analysis to describe the impact of each variable on the measured response rather than presenting a large volume of graphs across a wide range of simulation conditions that, in general, look similar from a qualitative point of view.

Before digressing further, it is important to point out that each simulated pellet and dust run applied $h_{B,W} = 2.0 \text{ W m}^{-2} \text{ K}^{-1}$. Now that sorbent material is present within the sample volume large temperature transients no longer arise as the sorbent material provides a large thermal sink to mitigate the effect of rapid gas compression. Given thermal capacitance of the gas phase is negligible in comparison to thermal capacitance of the solid material ($\rho_g^B c_g^B / \rho_P (1 - \epsilon_B) \tilde{c}_s \ll 1$) and heat transfer between these two regions is assumed rapid, the temperature transient due to compression is readily absorbed so T_B essentially follows T_P . Given the sorbent eliminates large temperature transients that result from compression in blank runs the "order of magnitude" estimate for $h_{B,W}$ found in §4.3.4 using the limiting Nu for a sphere is the appropriate value to use. The discussion related to temperature profiles during blank runs in §4.3.4 was used to highlight the importance of large values imposed on $h_{\text{tank},W}$ and the impact of a CSTR model over the rigorous case of axial and radial conduction for a vessel that contains no sorbent.

To establish first order sensitivity coefficients on p^{tank} as a function of C_K , C_v and $h_{P,B}$ a seventh-order Lagrange interpolating polynomial was established [Kreyszig (1993, p 939)]. NDGNAS was

activated eight times with one of the coefficients C_K , C_v or $h_{p,B}$ systematically varying above and below its optimal value while the other two coefficients remained unchanged. With eight slightly different pressure profiles obtained at 0.001 s increments for one particular parameter, denoted $p^{\text{tank}}(t_q, \psi)$ where ψ represents one of either C_K , C_v or $h_{p,B}$, the Lagrange interpolating polynomial was applied. The analytical form of these interpolated pressure profiles can be written in the following manner.

$$p^{\text{tank}}(t_q, \psi) = \sum_{m=0}^{N_L} p_m^{\text{tank}}(t_q) L_m(\psi) \quad \text{where} \quad L_m(\psi) = \frac{\prod_{n=0, n \neq m}^{N_L} (\psi - \psi_n)}{\prod_{n=0, n \neq m}^{N_L} (\psi_m - \psi_n)} \quad (4.18)$$

Within Eq. (4.18) ψ represents one of either C_K , C_v or $h_{p,B}$ and $t_q = (0.001 q)$ for $q = 1$ to 1000. The Π notation in Eq. (4.18) indicates each $(\psi - \psi_n)$ bracket in the numerator and $(\psi_m - \psi_n)$ bracket in the denominator is multiplied, while N_L denotes the order of the Lagrange polynomial and is seven for these runs. To find the first order sensitivity coefficients from Eq. (4.18) the first derivative with respect to ψ is taken.

$$\frac{\partial p^{\text{tank}}(t_q, \psi)}{\partial \psi} = \sum_{m=0}^{N_L} p_m^{\text{tank}}(t_q) \frac{dL_m(\psi)}{d\psi} \quad \text{where} \quad \frac{dL_m(\psi)}{d\psi} = \frac{\left\{ \sum_{n=0, n \neq m}^{N_L} \left[\prod_{p=0, p \neq m, p \neq n}^{N_L} (\psi - \psi_p) \right] \right\}}{\left[\prod_{n=0, n \neq m}^{N_L} (\psi_m - \psi_n) \right]} \quad (4.19)$$

The definition for ψ and t_q introduced in Eq. (4.18) carries over directly into Eq. (4.19). When ψ is C_K incremental step changes of 0.005 were applied for each NDGNAS simulation about 0.083. Then ψ is C_v an incremental step size of 0.005 was also applied to each NDGNAS simulation about 0.061. The third parameter, which is of central interest to the discussion of this subsection, is when ψ is $h_{p,B}$.

For $h_{p,B} \rightarrow \infty$, $(\partial p^{\text{tank}} / \partial h_{p,B}) \rightarrow 0$ as no change in simulated dosing volume pressure can occur once $T_B \equiv T_P$ and no other variable changes. Numerically it was found that $h_{p,B} = 2 \times 10^4 \text{ W m}^{-2} \text{ K}^{-1}$ produced differences between T_P and T_B that, in the worst case, were less than 0.1 K for all $t > 0$ across each EMU pellet run. Hence $h_{p,B} = 2 \times 10^4 \text{ W m}^{-2} \text{ K}^{-1}$ was imposed numerically as the condition equivalent to $h_{p,B} \rightarrow \infty$. To obtain an appropriate value for the sensitivity coefficient $(\partial p^{\text{tank}} / \partial h_{p,B})$ requires values of $h_{p,B} < 2 \times 10^4 \text{ W m}^{-2} \text{ K}^{-1}$ to be used.

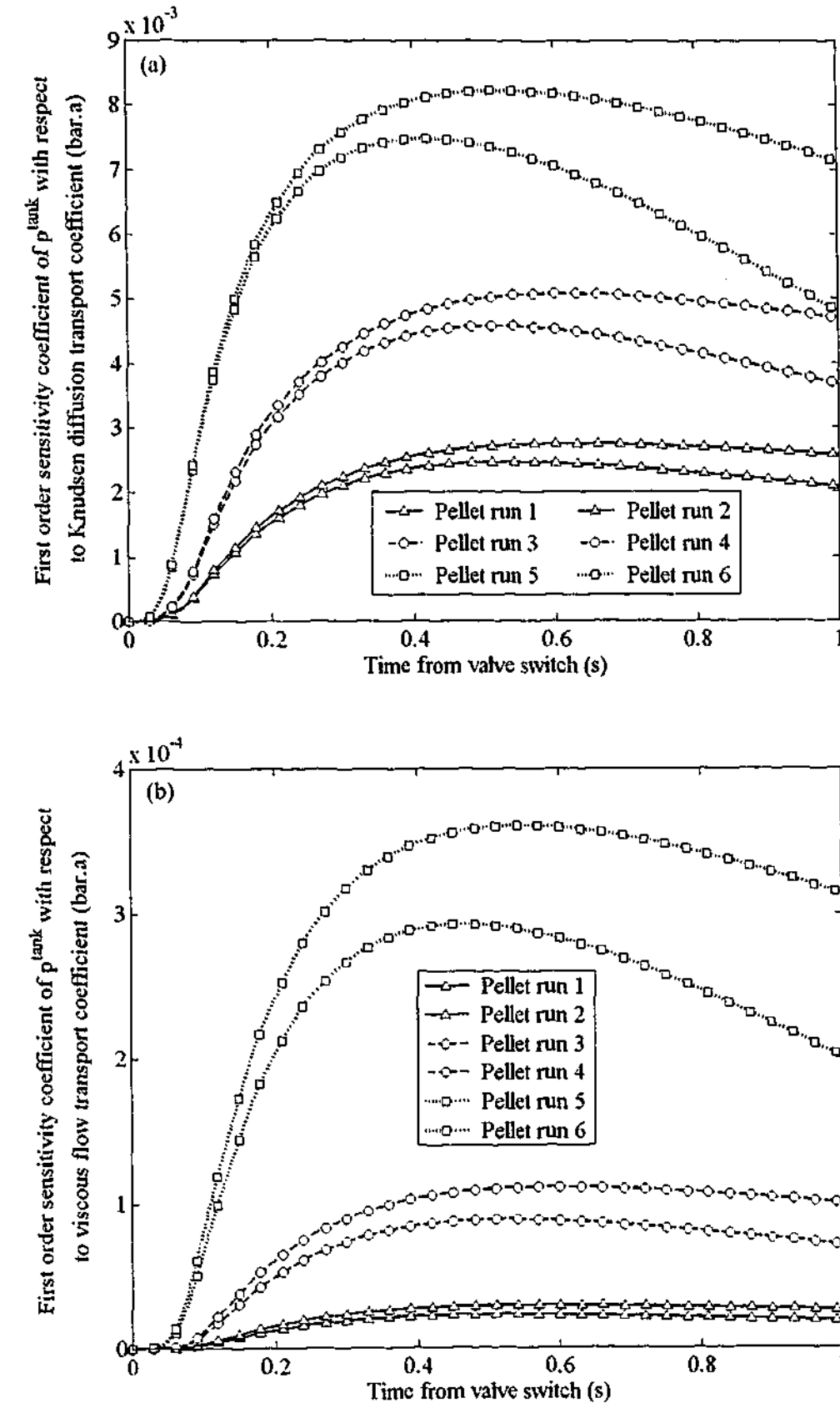


Figure 4.12: First order sensitivity coefficients of p^{tank} obtained from NDGNAS as a function of (a) Knudsen transport coefficient for pellet runs 1 through 6, (b) Viscous flow transport coefficient for pellet runs 1 through 6, and (c) Pellet-to-bed heat transfer coefficient for dust runs 1 through 3 and pellet runs 1 through 6, centred around $h_{p,B} = 40 \text{ W m}^{-2} \text{ K}^{-1}$.

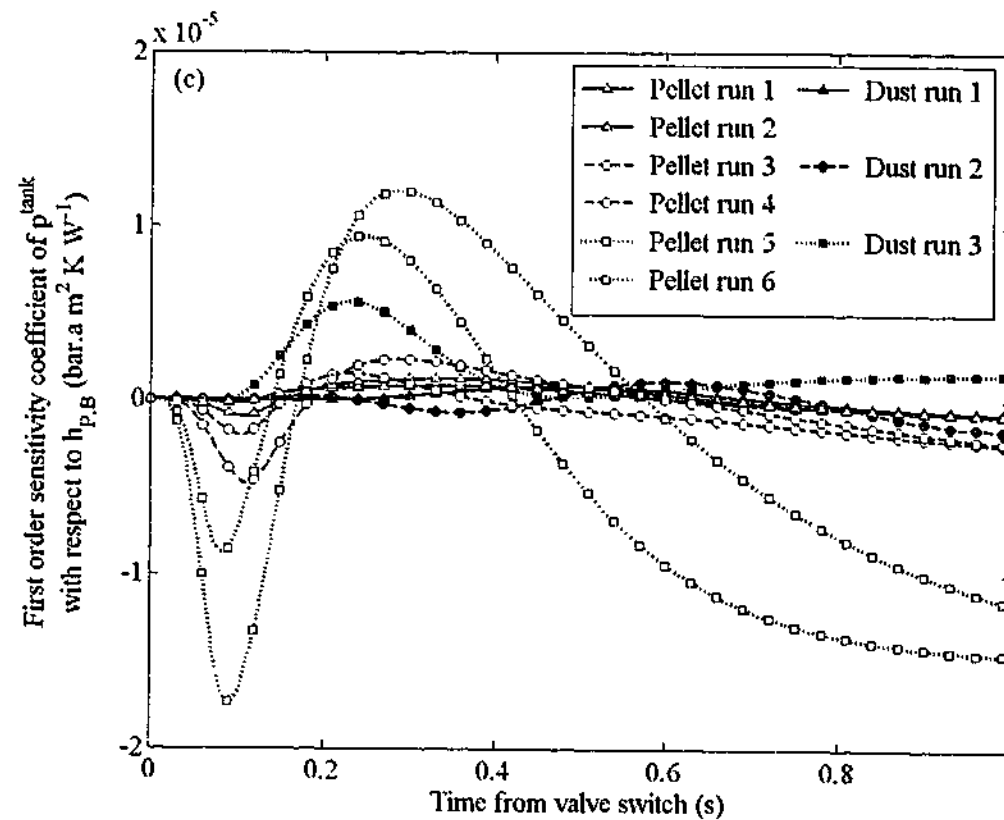


Figure 4.12 continued.

A useful starting point is to consider the lower bound on $h_{p,B}$, which can be inferred from the limiting Nu value of 2 for heat transfer from a single sphere as $Re_p \rightarrow 0$ [Whitaker (1972)]. This provides a lower estimate on $h_{p,B}$ of approximately $40 \text{ W m}^{-2} \text{ K}^{-1}$ under EMU conditions. This value provides the first set of sensitivity coefficients obtained for $h_{p,B}$ to compare against $(\partial p^{\text{tank}}/\partial C_K)$ and $(\partial p^{\text{tank}}/\partial C_v)$. Additional estimates were also obtained for $(\partial p^{\text{tank}}/\partial h_{p,B})$ with $h_{p,B}$ centered around 400 and $4000 \text{ W m}^{-2} \text{ K}^{-1}$.

Comparative plots of each sensitivity coefficient across each time point of the EMU simulation for dust runs 1 through 3 and pellet runs 1 through 6 are presented in Fig. 4.12. Each run presented in Fig. 4.12 relates to the water bath being maintained at a steady temperature of 273 K. Due to the increased adsorption capacity at 273 K over that at 303 K, the non-isothermal transient is greater for ice bath runs and hence the effect of varying $h_{p,B}$ should have the most pronounced effect at the lower temperature. Qualitatively similar results are observed for dust runs 4 through 6 and pellet runs 7 through 12 at 303 K and hence are not shown for brevity. Figure 4.12 indicates the sensitivity coefficient related to Knudsen diffusion, $(\partial p^{\text{tank}}/\partial C_K)$, has the greatest magnitude and hence impact on predicted pressure profiles in relation to the viscous flow transport and pellet-to-bed heat transfer sensitivity coefficients, $(\partial p^{\text{tank}}/\partial C_v)$ and $(\partial p^{\text{tank}}/\partial h_{p,B})$ respectively. The sensitivity coefficients for $(\partial p^{\text{tank}}/\partial h_{p,B})$ centred around values of $h_{p,B}$ greater than $40 \text{ W m}^{-2} \text{ K}^{-1}$ are not

presented in Fig. 4.12 simply because their magnitude are many orders of magnitude smaller than values centred around $h_{p,B} = 40 \text{ W m}^{-2} \text{ K}^{-1}$. Even for a modest estimate of $h_{p,B} = 400 \text{ W m}^{-2} \text{ K}^{-1}$, the peak magnitude obtained for $(\partial p^{\text{tank}}/\partial h_{p,B})$ is below 4×10^{-7} and simply looks like a flat line at $(\partial p^{\text{tank}}/\partial h_{p,B}) = 0$ for $t > 0$ in Fig. 4.12c. When $(\partial p^{\text{tank}}/\partial h_{p,B})$ is centred around $4000 \text{ W m}^{-2} \text{ K}^{-1}$, the peak magnitude of $(\partial p^{\text{tank}}/\partial h_{p,B})$ is less than 7×10^{-9} . This implies a conservative estimate on $h_{p,B}$, which is equivalent to stagnant film heat transfer for the entire duration of an EMU run, has a negligible impact on simulated EMU profiles. To imply that EMU profiles should be numerically modelled with C_K and C_v small (close to ILE) and $h_{p,B}$ the only parameter to vary would produce minimal, if any, differences in the numerical dosing volume pressure suitable enough to match experimental trends presented in Fig. 4.11.

In all cases, the Knudsen sensitivity coefficient is at least one order of magnitude greater than viscous flow and several orders of magnitude greater than pellet-to-bed heat transfer sensitivity coefficients such that Knudsen diffusion can be regarded as the limiting mechanism in terms of measured process response. This result also provides some justification for the numerical observation that C_v has minimal impact on simulated pressure profiles once its magnitude has increased much below 0.062.

While external film heat transfer resistance at the pellet surface can be assumed negligible, a Biot and Fourier heat transfer analysis for the sorbent pellets also reveals intrapellet temperature profiles are negligible (see discussion at the beginning of §2.2). This indicates temperature differences both within the pellet and between the pellets and the surrounding interpellet gas phase are negligible over the course of an EMU run.

Up to this point no mention has been made of the experimental temperature response obtained within the sample volume, mainly because these profiles have been found to confuse rather than clarify this issue. Temperature profiles obtained from dust runs 1 through 3 and pellet runs 1 through 6, along with their numerical counterparts when $h_{p,B} = 2 \times 10^4 \text{ W m}^{-2} \text{ K}^{-1}$ ($T_B = T_p$), are presented in Fig. 4.13. Similar trends are observed for runs with the water bath at 303 K and hence are not shown for brevity. Values of $h_{p,B}$ lower than $2 \times 10^4 \text{ W m}^{-2} \text{ K}^{-1}$ cause T_B to increase above T_p for $t < 1 \text{ s}$ due to the heat of compression but thereafter $T_B \rightarrow T_p$. Presenting these additional profiles for T_B when $h_{p,B} = 40 \text{ W m}^{-2} \text{ K}^{-1}$ in Fig. 4.13 simply clutters the graph for $t < 1 \text{ s}$ that was found to be unimportant towards the discussion that follows when explaining the mismatch between EMU and NDGNAS profiles.

NDGNAS temperature profiles lie much higher than the corresponding EMU profile for time around the valve switch. NDGNAS requires approximately 1-2 s to reach maximum temperature before heat loss to the water bath takes over and the temperature begins to decrease. Contrary to this observation, however, are EMU profiles that require approximately 40 s to reach maximum temperature before heat loss to the water bath becomes evident. The fact that pressure profiles match very well over the initial time period indicates the numerical temperature transient must be somewhere close to the real transient given the amount adsorbed is a strong function of temperature. If a 15 K difference were to arise between the experimental and numerical temperatures as suggested in Figs. 4.13e and 4.13f, it would be very difficult to resolve EMU pressure profiles by adjusting C_K and C_V alone while still matching runs that observe much smaller differences between experimental and numerical temperature, such as dust run 1 and pellet runs 1 and 2 of Figs. 4.13a and 4.13b where a 5 K difference arises.

In fact, a rather unusual observation has been made for temperature profiles obtained within the EMU that will reappear in temperature profiles obtained from the other experimental unit, the LUB apparatus, which operates within a completely different regime to the EMU. A temperature transient that consistently requires 40 seconds to reach a maximum has been observed. Independent experiments that capture rapid temperature transients due to heats of pressurisation and depressurisation in the absence of sorbent indicate the response time of each T-type thermocouple is not the problem. This points the finger towards a mechanism of heat transfer between the sorbent pellets and the thermocouple tip that has not been accounted for. This rather curious observation shall be discussed at length in chapter 5 once a more complete set of experimental data from the LUB apparatus has been introduced.

The fact that EMU and NDGNAS temperature profiles do not match for $t > 40$ s can be resolved by the mechanisms imposed for heat transfer to the water bath within NDGNAS. NDGNAS assumes heat transfer from the gas phase only occurs through the walls of the sample volume to the water bath. In reality, however, large portions of sorbent material are in direct contact with the walls of the sample volume and these walls are essentially at water bath temperature. An additional mechanism of heat transfer via conduction through the contacting sorbent pellets to the internal walls of the cylinder would enhance dissipation of heat as opposed to the NDGNAS assumption of stagnant film heat transfer through the gas phase only. Conduction through the pellets to the wall, while significant over long time scales, does not adequately resolve model mismatch for $t < 1$ s where heat loss via conduction would be minimal in relation to heat generation by adsorption.

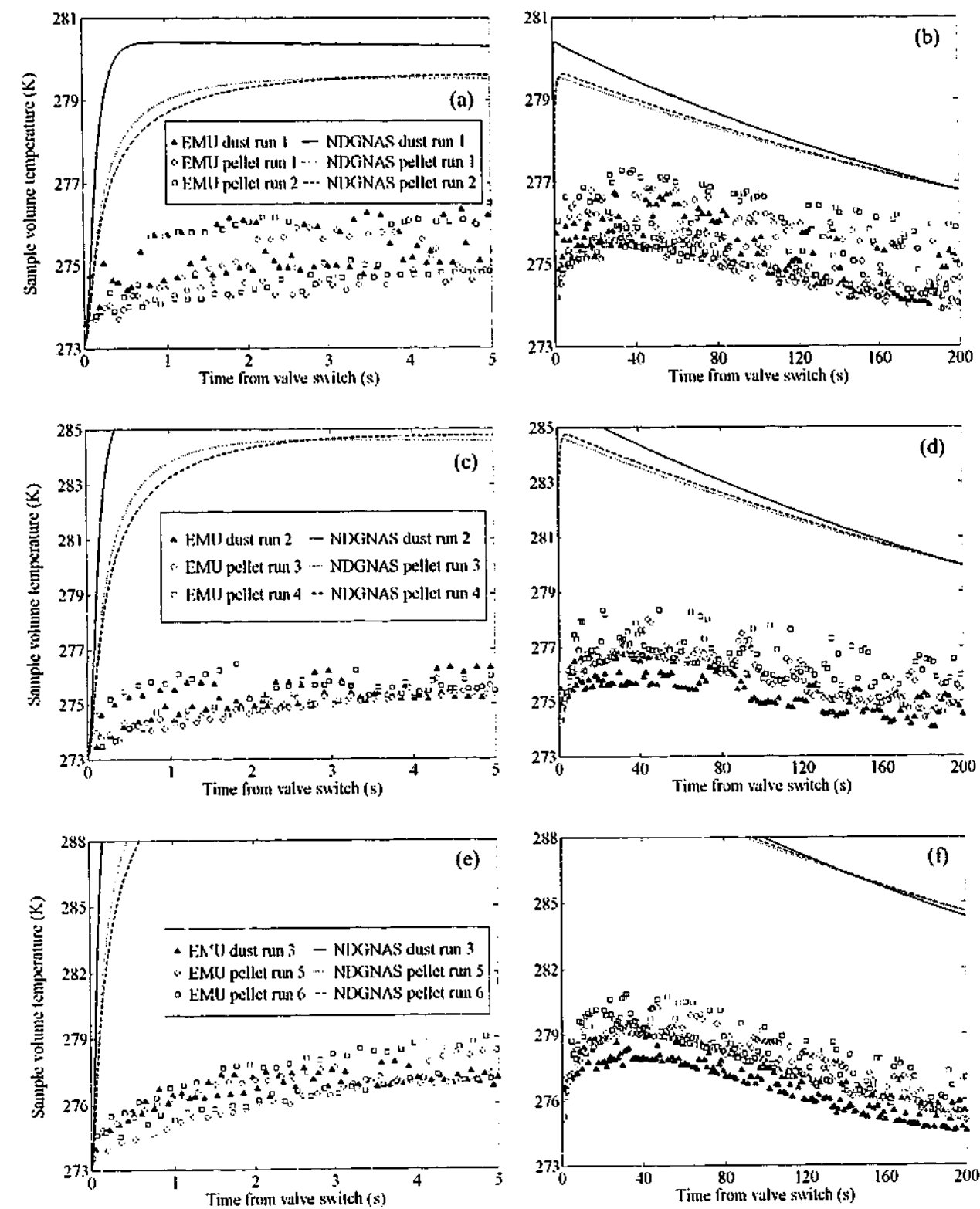


Figure 4.13: EMU and NDGNAS temperature profiles, presented over two different times scales, obtained in the sample volume for each dust and pellet run with the ice water bath. (a) Dust run 1 and pellet runs 1 and 2 for short times. (b) Dust run 1 and pellet runs 1 and 2 for long times. (c) Dust run 2 and pellet runs 3 and 4 for short times. (d) Dust run 2 and pellet runs 3 and 4 for long times. (e) Dust run 3 and pellet runs 5 and 6 for short times. (f) Dust run 3 and pellet runs 5 and 6 for long times. Note the legends from (a), (c) and (e) carry over directly in (b), (d) and (f) respectively.

4.4 Molecular Diffusion Transport Coefficient

With Knudsen and viscous flow transport coefficients now quantified, the final parameter to be ascertained from the VF+DGM intrapellet flux equation is the transport coefficient related to molecular diffusion, C_m . Performing a chromatographic experiment on a binary gas mixture allows this coefficient to be independently determined. To minimise the resistance to mass transfer at the external surface of the pellet, relatively high interpellet gas velocities are required to ensure $Bi_{mass} > 1$ (§1.2.2). Interpellet gas velocities must also ensure $Pe_{U,mass} > 100$ to eliminate axial dispersion of the gas phase (§1.2.1). Experimental conditions maintained within the apparatus introduced in this section will be shown later to satisfy these criteria, provided NDGNAS adequately accounts for the axial pressure gradient that will arise.

4.4.1 Model Options Activated within NDGNAS to Ascertain C_m

Unlike §4.3 that considered an isolated sample of sorbent material, this section now activates the full packed bed model options of NDGNAS. Given a binary component system is of interest ($N_c = 2$), an analytical expression for N_i using the VF+DGM intrapellet flux equation can be derived by solving Eq. (2.20) simultaneously for components 1 and 2.

$$N_i = \left\{ -\frac{1}{RT_p} \frac{\partial p_i^p}{\partial r} - \frac{1}{RT_p} \left[\frac{y_i^p}{D_{m,ij}^c} \left(\frac{1}{D_{k,j}^c} + \frac{y_i^p}{D_{m,ij}^c} \right)^{-1} \right] \frac{\partial p_j^p}{\partial r} - \left(\frac{B^c p^p}{10^{-5} \mu_p RT_p} \right) \right. \\ \left. \times \left[\frac{y_i^p}{D_{k,i}^c} + \frac{y_i^p}{D_{m,ij}^c} \left(\frac{1}{D_{k,j}^c} + \frac{y_i^p}{D_{m,ij}^c} \right)^{-1} \frac{y_j^p}{D_{k,j}^c} \right] \frac{\partial p^p}{\partial r} \right\} / \left[\frac{1}{D_{k,i}^c} + \frac{y_j^p}{D_{m,ij}^c} - \frac{y_i^p y_j^p}{(D_{m,ij}^c)^2} \left(\frac{1}{D_{k,j}^c} + \frac{y_i^p}{D_{m,ij}^c} \right)^{-1} \right] \\ \text{for } i = 1, 2 \text{ and } i \neq j \quad (4.20)$$

Equation (4.20) is a complicated, non-linear function that does not provide an analytical solution when incorporated into the intrapellet conservation equations. However, C_k and C_v have been found previously using EMU data while T_p , p^p and y_i^p are found by discretising the pellet and solving the resulting conservation equations within each spherical control volume. From this, a DPM with the VF+DGM intrapellet flux model for $N_c = 2$ within a chromatographic system reduces Eq. (4.20) to a non-linear parameter fit for C_m through $D_{m,ij}^c$.

Although the intrapellet domain can be reduced to finding just the one parameter, C_m , flowing gas through a packed bed of sorbent pellets at relatively high velocities now introduces two additional

parameters that have yet to be quantified. These parameters are related to the viscous and kinetic components of the steady state momentum equation, $\kappa_{viscous}$ and $\kappa_{kinetic}$ respectively, that characterise pressure drop in the axial direction of the interpellet region.

The study of intrapellet mass transfer and interpellet pressure drop in the presence of adsorption cannot be readily decoupled experimentally for a bulk adsorbing system and hence two distinct mechanisms need to be separately addressed. Interpellet pressure drop is discussed separately in chapter 5 and for this reason chapters 4 and 5 cross-reference each other for experimental coefficients given these two regions cannot be discussed in isolation. Experimental determination of the two steady state pressure drop coefficients is performed in §5.2.2 and the corresponding best-fit parameters obtained were $\kappa_{viscous} = 154$ and $\kappa_{kinetic} = 1.47$. These two parameters will be exclusively used on each NDGNAS simulation for the breakthrough study of oxygen-nitrogen-Zeochem LiLSX described in §4.4.

As was the case in §4.3, the conservation of energy is included to account for temperature changes that occur in the presence of adsorption. In this section it is assumed that the intra- and interpellet regions are both at the same temperature so $T_B = T_p$. The absence of more extensive temperature data from the experimental chromatographic column renders the option $T_B \neq T_p$ redundant. Further to this, NDGNAS profiles obtained from EMU runs with $h_{p,b}$ varying revealed the impact of $T_B \neq T_p$ is negligible in comparison to the more common assumption $T_B = T_p$ (§4.3.6).

The experimental apparatus described in the next section outlines a column that operates at conditions close to adiabatic. The conservation of energy invoked in this section now includes a wall heat transfer term and rigorous wall energy model to investigate the extent of adiabatic behaviour actually attained. The experimental apparatus also contains a finite void space between the inlet valve manifold and sorbent bed interface at the bottom of the column. Hence the lower void volume described in §3.2.6 is activated with $V_{bottom} = 5.70 \times 10^{-4} \text{ m}^3$ (SV2 to sorbent bed interface).

In addition to the steady state momentum equation, the interpellet conservation of energy has also introduced another parameter that needs to be resolved before C_m can be found. This parameter is the bed-to-wall heat transfer coefficient $h_{b,w}$. Ruthven (1984a, p 218) found satisfactory agreement between experimental heat transfer coefficients of Ruthven *et. al.* (1975) and those from Leva's correlation for the adsorption of propylene, *cis*-2-butene and 1-butene from an inert carrier stream in a packed bed of 5A molecular sieve sorbent. For this dissertation it is assumed Leva's correlation is appropriate for the estimation of $h_{b,w}$ [Ruthven (1984a, p 218)].

$$h_{B,W} = \frac{\lambda_B^B}{d_{bed}} \left(\frac{v_B \epsilon_B d_{p,eqv} \hat{p}_B^B}{\mu_B} \right)^{0.19} \exp \left(-6 \frac{d_{p,eqv}}{d_{bed}} \right) \quad (4.21)$$

With all intra- and interpellet parameters characterised except C_m , an experimental apparatus will be introduced that can perform binary component chromatographic experiments in a packed bed of Zeochem LiLSX sorbent pellets.

4.4.2 LUB Apparatus for Binary Chromatographic Experiments

To acquire experimental mass transfer information under adsorbing conditions, a Length of Unused Bed (LUB) apparatus was constructed. This apparatus comprises a single cylindrical column of internal diameter 0.050 m (d_{bed}) and packed bed length of approximately 2 m (L_{bed}) with associated valving and pipe work required to pass gas to and from the column. Please refer to §D.2 of appendix D for a complete description of the LUB apparatus including a detailed piping and instrumentation diagram, column arrangement drawing, equipment specification list and photos. The LUB apparatus also provides experimental data for pressure drop that forms the basis of chapter 5. For now, however breakthrough curves will be the focus of data obtained from the LUB apparatus.

A breakthrough run involves the measurement of the Mass Transfer Zone (MTZ) that traverses the packed bed at the onset of a change in feed gas composition. A basic schematic arrangement of a breakthrough run is depicted in Fig. 4.14. Data acquisition and control was performed from a local PC via a custom written QuickBasic (QB) program. This QB program was specifically developed for rapid data collection with one scan time through the entire code lasting approximately 0.1 s. All analog signals from pressure, temperature, composition and flow metering devices were converted to 12 bit digital integers through two Advantech PCL818HG cards and then logged to file. Valve switching and data logging was activated via user-entered keystrokes through the QB program.

Before solenoid valve SV2 was opened to administer feed gas into the adsorption column, the packed bed was first purged with oxygen for approximately ten minutes to remove pre-adsorbed nitrogen and provide one uniform initial condition for simulation (Fig. 4.14a). Once the bed was purged and temperature uniform to within 0.5 K, feed gas flow was introduced. To ensure a bumpless transfer in pressure and flow occurred during the valve switch, feed gas was initially diverted through a bypass line and adjusted using a pressure modulating valve until the desired conditions were achieved.

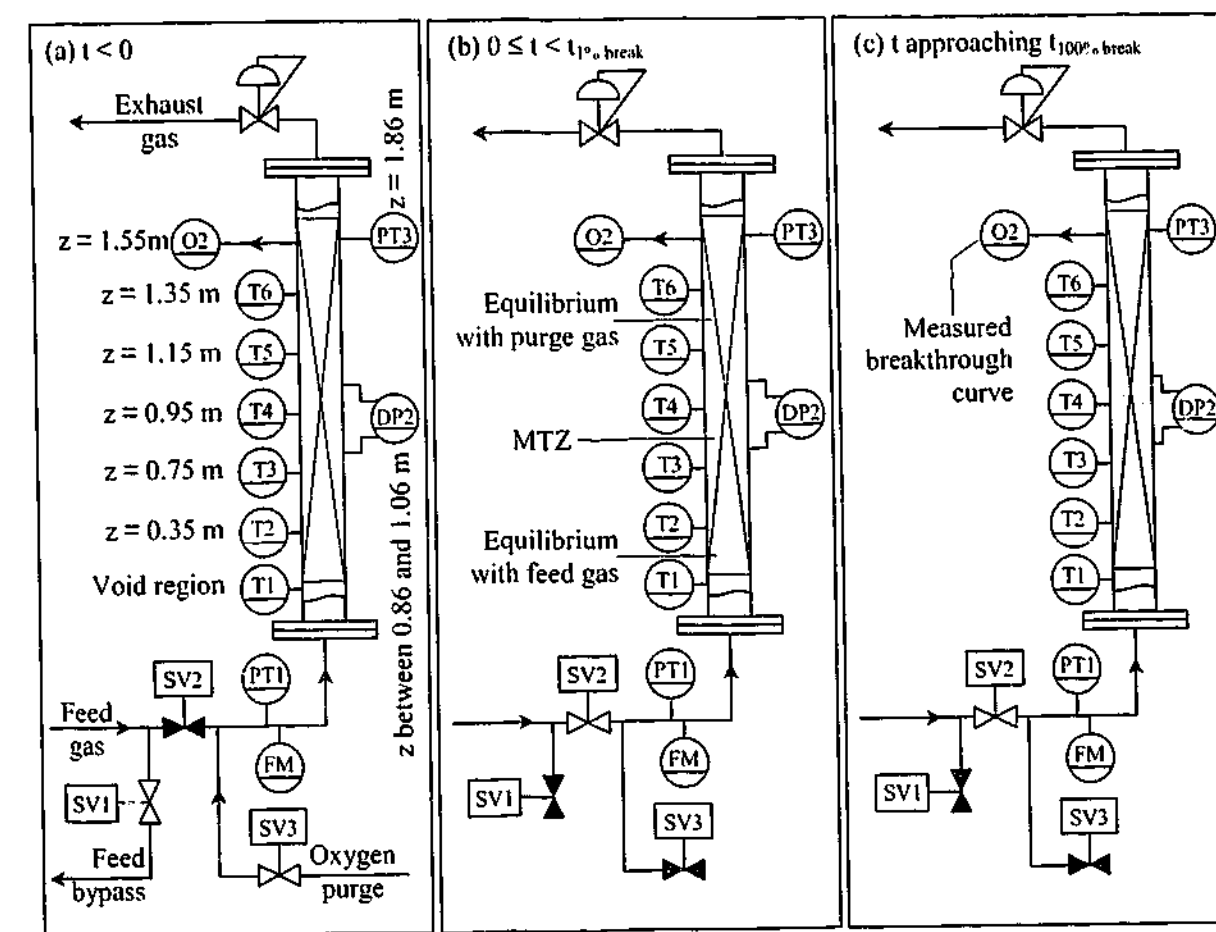


Figure 4.14: Schematic diagram outlining the procedure initiated for one breakthrough experiment performed on the LUB apparatus. (a) The bed is initially purged with oxygen until all measured pressure, composition and temperature profiles are at steady state. (b) At time zero, solenoid valve SV2 is opened while solenoid valves SV1 and SV3 are simultaneously closed to invoke a “bumpless” transfer from purge to feed gas. (c) The MTZ has progressed to the oxygen analyser and the corresponding breakthrough curve is measured.

Once pressure, temperature and composition were at steady state the inlet valve manifold was switched and SV2 opened while SV1 and SV3 simultaneously closed (Fig. 4.14b). As the nitrogen/oxygen feed gas mixture enters the bed, a MTZ forms that progressively moves with speed v_{MTZ} . As the MTZ passes a thermocouple and nitrogen uptake from the inter- to intrapellet region occurs, an increase in temperature is observed that plateaus to a steady value once the MTZ has passed. Given temperature and composition waves move with the same speed for a type I system [Pan & Basmadjian (1967)], temperature profiles indicate the location of the composition wave. The oxygen analyser was placed at a relatively high position within the sorbent bed to ensure any small fluctuations in pressure and flow that occurred around the valve switch had sufficiently decayed by the time the MTZ reached the analyser (Fig. 4.14c). The time for the oxygen analyser reading to fall to feed gas composition is defined as the breakthrough time, $t_{100\% \text{ break}}$. Once breakthrough has occurred and data acquisition ceased, the bed was regenerated with oxygen in readiness for the next breakthrough run, effectively repeating Fig. 4.14.

To validate measured process signals from each equipment item, a series of calibration tests were performed. Temperature was measured using junction exposed T-type thermocouples that were deemed accurate to ± 0.5 K as obtained from several water bath measurements and EMU experiments. Response time for these junction exposed thermocouples was found to be less than one second from various step tests performed between ambient air and controlled water bath conditions in addition to rapid depressurisation experiments (see chapter 5).

Oxygen composition measured at axial position $z = 1.55$ m in the column was obtained from a Servomex ZR733 fast response zirconia oxygen analyser with a rated accuracy of ± 0.5 mol%O₂. The oxygen analyser is connected to the column through a $\frac{1}{8}$ inch stainless steel tube of length 70×10^{-3} m that is located at the centre of the packed section on the inside of the column. Step tests performed on this arrangement revealed a total response time of 0.4 s was required when detecting a transient change from 100 to 22 mol%O₂. Differential Pressure (DP) obtained across a 0.20 m section of packing was accurate to ± 0.001 bar while absolute pressure readings are accurate to ± 0.01 bar.a. The DP cell has a rated response time of 0.5 s due to signal damping while absolute pressure transducers have a rated response time less than 0.1 s (i.e. less than one scan time of the QB data acquisition program).

Each of the above-mentioned equipment items are deemed "primary measured variables" given the experimental signal obtained from each run is used directly for data analysis. Feed flow rate, on the other hand, is classified a "secondary measured variable" as this parameter requires experimental measurements of temperature, absolute pressure and differential pressure drop across the annubar to infer flow rate. The rated accuracy of experimentally measured flow rates is therefore a function of the combined errors for each individual element present within the equation provided from the manufacturer, Fisher-Rosemount, for annubar flow. An approximate estimate for the combined error on feed flow, reported in this dissertation as a velocity, is ± 0.20 m s⁻¹. The DP cell mounted directly on the annubar provides the major limitation towards response time, which is 0.5 s due to signal damping on the output signal.

Although the adsorption column is relatively thin ($d_{bed} = 0.050$ m), the ratio of column-to-pellet diameters is approximately 30 and the assumption of negligible channeling, at least numerically, is satisfied (§1.2.1). The advantage of using a small column diameter that just satisfies the $d_{bed}:d_{p,eqv}$ ratio is that relatively high velocities can be maintained for relatively low feed volume flow rates. The adsorption column itself is a section of PVC storm water pipe with plastic flanges welded at both ends. This arrangement has good mechanical and insulation properties over the duration of a single breakthrough run for pressures up to 2 bar.a. Wrapped around the outside of the column

wall is a 0.020 m thick layer of fiberglass insulation to minimise heat exchange with the environment. This means energy accumulation in the wall, heat conduction along the wall and heat transfer to/from the environment is minimal. Conditions close to adiabatic are maintained within the column to replicate operating conditions typically encountered within an industrial scale unit. This also implies radial temperature gradients will be minimal over the duration of a single breakthrough run [Pentchev *et. al.* (2002)].

To assess the extent of adiabatic behaviour, NDGNAS is run in two different modes. The first involved runs with the rigorous wall model activated and the wall-to-ambient heat transfer coefficient set to zero ($h_{w,a} = 0$) representative of conditions that prevail during a single breakthrough run. The second was a true adiabatic case with the internal heat transfer coefficient from the bed-to-wall set to zero ($h_{b,w} = 0$) and the rigorous wall model deactivated, the ideal case closely approached within an industrial scale unit. NDGNAS results obtained from both cases will be discussed further in the next section. Physical properties of the adsorption column wall are summarised in Table 4.8.

Table 4.8: Physical properties of the adsorption column applied within NDGNAS.

| Parameter | Magnitude | Units |
|----------------|----------------------|------------------------------------|
| Δz_w | 5.0×10^{-3} | m |
| $\hat{\rho}_w$ | 1470 [†] | kg m ⁻³ |
| λ_w | 0.1 [†] | W m ⁻¹ K ⁻¹ |
| \hat{c}_w | 840 [†] | J kg ⁻¹ K ⁻¹ |

[†] Taken from Çengel (1998, p 957) for PVC plastic.

Although pressures of 2 bar.a could be achieved within the column, instabilities in pressure and flow readings at the onset of breakthrough could not be avoided at pressures above 1.3 bar.a, so bed pressure was limited to 1.25 bar.a for the breakthrough study of this chapter. Although a relatively small pressure window is investigated, a wide variation in feed gas composition was considered. Nitrogen-oxygen feed gas mixtures were provided from three different Linde gas cylinders with the following compositions:

- 10.2 mol%N₂ and 89.8 mol%O₂, denoted *mixture A*,
- 20.0 mol%N₂ and 80.0 mol%O₂, denoted *mixture B*, and
- Industrial air, denoted *mixture C*. This is essentially dry air at a dew point of -60°C , so the composition is assumed to be 78.0 mol%N₂ and 22.0 mol%O₂+Ar given argon behaves like oxygen [Chou & Chen (1994)].

While mixture C lumps oxygen and argon together as the one component, mixtures A and B do not require this assumption as both gas bottles were purchased from the vendor with the above

mentioned certified composition. Given absolute pressure arises within $D_{m,ij}$ it is generally assumed that different absolute pressure windows are required to observe any variation in the magnitude of molecular diffusion. Although absolute pressure does appear within $D_{m,ij}$ Eq. (4.20) reveals molecular diffusion arises within the intrapellet molar flux as a ratio with mole fraction. In consultation with Eqs. (2.7) and (2.8) the following is observed.

$$\frac{D_{m,ij}^c}{y_k^p} = C_m \left[1.8829 \times 10^{-7} \frac{\sqrt{T_p^3 (M_i + M_j) / M_i M_j}}{p_k^p \sigma_{ij}^2 \Omega_{ij}^{(1,1)*}} \right] \text{ for } i = 1 \dots N_c, i \neq j \text{ and } k = 1 \dots N_c \quad (4.22)$$

This indicates partial rather than absolute pressure now resides in the intrapellet molar flux through molecular diffusion. Keeping total pressure relatively constant while varying composition and hence partial pressure will have the same effect on Eq. (4.22) as holding composition steady while varying total pressure. In total, two different bed pressures at each feed gas composition was performed experimentally with bed temperature initially at ambient conditions. Experimental boundary conditions measured during each run is summarised in Table 4.9, where bed pressure was measured at axial position $z = 1.86$ m in the bed (PT3 on Fig. 4.14).

Table 4.9: Summary of experimental conditions investigated across each breakthrough run. Note that breakthrough run 3 was used to independently adjust C_m within NDGNAS. The remaining 5 breakthrough runs provide validation data for NDGNAS using C_m obtained from run 3.

| Run descriptor | Feed gas mixture | Feed gas velocity (m s ⁻¹) | Bed pressure at $z = 1.86$ m (bar.a) |
|--------------------|------------------|--|--------------------------------------|
| Breakthrough run 1 | A | 2.95 ± 0.26 | 1.12 ± 0.01 |
| Breakthrough run 2 | A | 4.15 ± 0.21 | 1.25 ± 0.01 |
| Breakthrough run 3 | B | 3.12 ± 0.29 | 1.12 ± 0.01 |
| Breakthrough run 4 | B | 4.44 ± 0.23 | 1.26 ± 0.01 |
| Breakthrough run 5 | C | 2.43 ± 0.35 | 1.11 ± 0.01 |
| Breakthrough run 6 | C | 2.89 ± 0.28 | 1.25 ± 0.01 |

Note that feed gas velocity was measured from the inlet flow meter (denoted FM on Fig. 4.14) as a volume flow. Knowing the internal diameter of the annubar, 15.8×10^{-3} m, volume flow was readily converted to velocity for use as the lower boundary condition at the valve seat of SV2. Error estimates on feed gas velocity was obtained from 95% confidence limits around the average value assuming the data logged to file is normally distributed, which was found to be higher than the rated accuracy of the annubar-DP transducer arrangement. Absolute pressure at $z = 1.86$ m represents the second boundary condition invoked at the top of the sorbent bed. Applying the same 95% confidence limits for pressure at $z = 1.86$ m indicated the rated accuracy of the pressure transducer was higher, hence the error estimate ± 0.01 bar is applied. One last issue regarding

numerical simulation of breakthrough runs will be addressed before NDGNAS results are presented.

Axial Discretisation and Breakthrough Simulation

Webley & He (2000) highlighted the importance axial node distribution can have when modelling breakthrough curves within a packed that that is initially clean with respect to the strongly adsorbed component. They indicate that 10 nodes should be maintained across the MTZ to minimise the effect of numerical dispersion. Given a fundamental transport coefficient is being calibrated against experimental data, NDGNAS simulations must ensure the MTZ is adequately resolved and that numerical dispersion is not limiting the parameter fit. For this reason control volume discretisation was performed in a manner that ensured a minimum of 10 axial nodes were present across the MTZ at $z = 1.55$ m for breakthrough run 3. An appropriate *a priori* estimate of intrapellet radial discretisation, on the other hand, is not generally known and for this reason a range of discretisation levels will be considered to assess the impact of N_r on the optimal molecular transport coefficient. With an appropriate estimate of C_m , the remaining breakthrough runs were simulated using $N_r = 5$ within each axial control volume.

Although $N_r > 5$ was considered when fitting C_m , RPSA simulations performed in chapter 6 use $N_r = 5$. Simulating a full RPSA cycle with the DPM and $N_r > 5$ was not even close to CSS after consuming two weeks of CPU time on the departmental Dec-Alpha workstation. Hence a trade-off between reasonable simulation time and model accuracy had to be made. According to the findings of chapter 2, errors of only a few percent arise when comparing working capacity between $N_r = 5$ and $N_r = 30$ over an individual sorbent pellet operated under non-isothermal RPSA conditions. This provides some justification that $N_r = 5$ will be a suitable discretisation level for a first approach simulation of RPSA data with the DPM. For this reason $N_r = 5$ was adopted once C_m was characterised from breakthrough run 3.

For gas mixtures A and B that involve relatively low feed concentrations of nitrogen, axial control volume spacing of 0.01 m adequately resolved the MTZ. Although the LUB packed section is 2 m in length, NDGNAS simulates the packed bed up to a height of 1.86 m as the boundary condition invoked by PT3 from Fig. 4.14 renders the remaining 0.14 m section of sorbent irrelevant for modelling purposes. An optional input within NDGNAS allows the user to manually set each axial node coordinate within the packed bed. For breakthrough runs 1 through 4 this option was activated and node spacing at 0.01 m increments from the inlet end was specified along with additional points of experimental interest that do not lie exactly on this uniform node spacing. In total, 187 axial nodes were used in the bed ($N_z = 187$) with $L_{bed} = 1.86$ m numerically. Activating

the rigorous wall model, the DPM with $N_r = 5$ and lower void volume resulted in a total of 2,632 simultaneous ODEs being passed to the ODE integrator ($N_{eq} = 2,632$). To reproduce a breakthrough run of 160 s that includes 60 s of oxygen purge before the valve switch required approximately four hours of simulation time on a 650 MHz Compaq XP1000 Dec-Alpha workstation.

Although mixtures A and B result in a relatively broad MTZ, gas mixture C involved bulk adsorption of the strongly adsorbed component and consequently axial node distribution had to be refined to 0.005 m to resolve the MTZ. In this case 373 axial nodes were initiated through the sorbent bed ($N_z = 373$), resulting in a total of 5,236 simultaneous ODEs with the rigorous wall model activated ($N_{eq} = 5,236$). Simulating 140 s of a LUB breakthrough run including 60 s of oxygen purge in this case exceeded three and a half days on the same Dec-Alpha workstation. Even with this level of discretisation and simulation time, the number of axial nodes observed across the MTZ was still found to be slightly under 10 (see Table 4.11). While a more refined level of axial discretisation would have been preferred, breakthrough runs 5 and 6 were close to the runtime memory limit of the Dec-Alpha workstation when 100% CPU time was allocated to NDGNAS. Hence breakthrough runs 5 and 6 are close to the upper limit on computing resources available as a function of adsorption column discretisation using NDGNAS.

Method of Comparing Experimental and Numerical Breakthrough Curves

Webley & Todd (2003) have theoretically and experimentally examined breakthrough profiles obtained with two different UOP sorbents that both exhibit macropore diffusion control using the LUB apparatus of §4.4.2. Their definition of the MTZ carries over in this study and for the sake of brevity shall be discussed only briefly here. To directly compare experimental and numerical results point-by-point, the absolute oxygen reading is normalized with respect to the upper and lower limits from the breakthrough curve.

$$\bar{y}_i^B = \frac{y_i^B - y_{i,99\% \text{ break}}^B}{y_{i,1\% \text{ break}}^B - y_{i,99\% \text{ break}}^B} \quad \text{for } i = 2 \text{ at } z = 1.55 \text{ m} \quad (4.23)$$

Using the difference in time between $y_{i,1\% \text{ break}}^B$ and $y_{i,99\% \text{ break}}^B$ and knowing the speed of the MTZ, the length of the MTZ can be found through the following.

$$L_{\text{MTZ}} = v_{\text{MTZ}} (t_{99\% \text{ break}} - t_{1\% \text{ break}}) \quad (4.24)$$

Webley & Todd (2003) highlight the most reliable experimental estimate of v_{MTZ} is obtained by dividing the mid point time from each temperature transient with the height of this thermocouple in relation to the sorbent bed interface. There are five thermocouples located within the bed so each provides an independent estimate of v_{MTZ} . Experimental error bounds obtained for v_{MTZ} from Table 4.11 reflect 95% confidence limits obtained from this technique. To remove any dependence on the point in time where incipient breakthrough occurs, time is reassigned such that zero now represents the midpoint of the breakthrough curve (i.e. time is given by $t_{\text{valve switch}} - t_{50\% \text{ break}}$ where $t_{50\% \text{ break}}$ occurs when $\bar{y}_i^B = 0.50$ from Eq. (4.23)). Reassigning time in this manner allows the shape of experimental and numerical breakthrough curves to be directly overlaid. The predicted value of $t_{50\% \text{ break}}$ was within 2 to 8% of the same value measured experimentally on the LUB apparatus (see Table 4.11).

4.4.3 Fitting C_m to Breakthrough Run 3

The current discussion indicates C_m is now the only parameter available to independently match NDGNAS with LUB breakthrough data. Breakthrough run 3 from Table 4.9 was arbitrarily designated the fitting run on the basis that runs with higher and lower nitrogen-oxygen partial pressures in Eq. (4.22) could be used as independent verification checks on the resulting magnitude of C_m . To quantify the magnitude of C_m that best matches experimental data a GSSE slightly different again in form to those previously defined in Eqs. (4.12) and (4.15) was used.

$$\text{GSSE} = \sum_{m=1}^{\alpha_i} (\bar{y}_{i,\text{LUB},m}^B - \bar{y}_{i,\text{NDGNAS},m}^B)^2 \quad \text{for } i = 2 \quad (4.25)$$

where α_i indicates the number of experimental data points along the breakthrough curve.

Normalised oxygen composition between $(t_{1\% \text{ break}} - t_{50\% \text{ break}}) \leq (t - t_{50\% \text{ break}}) \leq (t_{99\% \text{ break}} - t_{50\% \text{ break}})$ is compared to the equivalent NDGNAS composition at these time points. Given one parameter only is being adjusted, a custom written optimisation routine that employed a quadratic interpolation scheme [Chapra & Canale (1998, pp 349-351)] was incorporated into NDGNAS that systematically varied C_m until a minimum in the GSSE occurred. The quadratic optimisation routine was initiated with C_m bounded between 0.089 and 0.310. In total, approximately fifteen to twenty individual NDGNAS simulations were required at each level of radial discretisation to converge on an optimal C_m value that was accurate to three significant figures.

To demonstrate the impact of C_m on the obtained fit to the breakthrough curve, Fig. 4.15 plots the GSSE at small increments around the optimal C_m when $N_r = 3$. Figure 4.15 demonstrates a distinct minima in the GSSE exists at one particular C_m value. A monotonically increasing trend in the

GSSE is observed both above and below the optimal value, a result of the numerical MTZ becoming to sharp and broad respectively in relation to the experimental profile. Identical trends in GSSE versus C_m are observed for the higher discretisation levels with the minima in GSSE located at a slightly different C_m value.

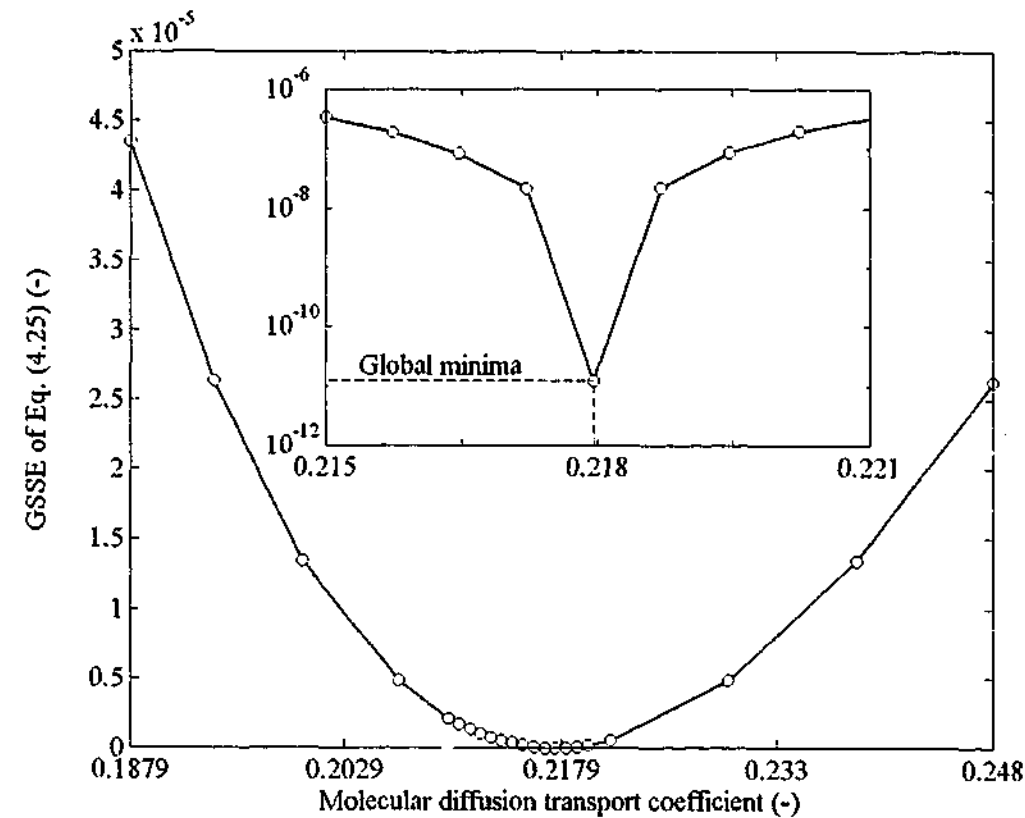


Figure 4.15: GSSE of Eq. (4.25) as a function of the one independent fitting parameter C_m for breakthrough run 3 using NDGNAS with $N_r = 3$ and the rigorous wall model activated.

From Fig. 4.15 the global minima in GSSE for $N_r = 3$ occurs at $C_m = 0.218$. With an increasing number of radial nodes within the sorbent pellet, a decrease in the optimal C_m value was observed (Table 4.10).

Table 4.10: Dependence on the level of radial discretisation within the pellet to the optimised molecular transport coefficient obtained from breakthrough run 3. Also included are experimental bounds on the magnitude of C_m .

| Parameter | Radial discretisation within the pellet, N_r | | | | | | |
|-------------------------------|--|-------|-------|-------|-------|-------|-------|
| | 3 | 4 | 5 | 6 | 8 | 10 | 14 |
| Molecular transport, C_m | 0.218 | 0.183 | 0.166 | 0.156 | 0.146 | 0.141 | 0.136 |
| Number of equations, N_{eq} | 1,884 | 2,258 | 2,632 | 3,006 | 3,754 | 4,502 | 5,998 |

Radial discretisation above 14 was close to the limit in run-time memory allocation for NDGNAS on the Dec-Alpha workstation and hence is as close to $N_r \rightarrow \infty$ as could be achieved with the computing resources available. NDGNAS consumed two and a half weeks of CPU time to

converge on the optimised C_m coefficient with $N_r = 14$, emphasising that $N_r = 14$ was the highest practical discretisation level that could be simulated within a realistic time frame. From this, when $N_r = 5$ we have approached 82% of the value for C_m when $N_r = 14$. As mentioned earlier, with the computing resources available the impact of $N_r = 5$ versus $N_r > 5$ could not be feasibly investigated for anything outside of breakthrough run 3.

The trend of C_m versus N_r from Table 4.10 suggests intrapellet profiles are sharp across the MTZ and approximately 10 nodes are required to maintain a relatively consistent estimate on C_m , at least to the level of radial discretisation that could be achieved in this study. Unlike $D_{K,i}^c$ and B^c that contain an experimentally determined coefficient, namely δ , in addition to the calibrated parameters C_K and C_v , $D_{m,ij}^c$ contains no experimentally determined coefficients outside of C_m and hence C_m should exhibit very small variations in N_r if experimental error on structural parameters is taken into consideration. Nominally, C_m should be $0.136 \pm$ (very small number). Results from Table 4.10 reveal radial discretisation limits the experimental estimate of C_m due to the non-consistent value for C_m obtained as a function of N_r . This result indicates resolution of intrapellet profiles is not entirely adequate at $N_r = 5$ and a possible limit to the experimental estimate of molecular transport within the VF+DGM may reside at the intrapellet as well as interpellet level. To the best knowledge of the author this result has not been discussed anywhere within the literature. From this it was found necessary to apply $C_m = 0.166$ when $N_r = 5$ to all of the remaining breakthrough and RPSA simulations in this dissertation to ensure adequate resolution of the MTZ is maintained with respect to breakthrough run 3.

Contrary to this result for C_m , however, was the fact that C_K was limited by experimental uncertainty according to Eq. (4.16) as revealed in §4.3.5. This allowed the optimal value for C_K as $N_r \rightarrow \infty$ (or $N_r = 50$ numerically) to be applied as a universal value on C_K for any N_r . The viscous flow coefficient, C_v , was also relatively insensitive to N_r from the analysis of §4.3.5 and so C_v assumes the value obtained when $N_r \rightarrow \infty$.

Discussion on the Magnitude of Each Intrapellet Transport Coefficient

The best way to examine the magnitude of C_K , C_v and C_m obtained from the VF+DGM is to transform these into tortuosity coefficients. Section 2.2.1 indicated the transport coefficients C_K , C_v and C_m can be represented in the form $(\epsilon_{p,macro} / \tau_K)$, $(\epsilon_{p,macro} / \tau_v)$ and $(\epsilon_{p,macro} / \tau_m)$ respectively as we are dealing with macropore-based intrapellet diffusion control (§4.2.3). From this,

$$\tau_K = \epsilon_{p,macro} / C_K = 0.343 / 0.083 = 4.15 \quad (4.26)$$

$$\tau_v = \epsilon_{p,macro} / C_v = 0.343 / 0.061 = 5.64 \quad (4.27)$$

$$\tau_m = \epsilon_{p,macro} / C_m = 0.343 / 0.166 = 2.07 \quad (4.28)$$

Tortuosity coefficients have been extensively discussed in the literature and nominal values have been suggested for a range of porous materials. Ruthven (1984a, p 134) indicates experimental tortuosity factors should lie somewhere between 2 and 6 for most porous materials of practical interest, while Satterfield & Sherwood (1963, p 21) indicate tortuosity coefficients vary over a 20-fold range from a review of the published literature on catalytic materials. Feng & Stewart (1973) found the ratio ϵ/τ varied between 0.009 and 0.364 for a range of porous materials using published data.

Mathematical estimates on these tortuosity coefficients include:

- 1.5 ($\tau = 1 - \frac{1}{2} \ln \epsilon_{p,macro}$) for a porous medium that contains randomly packed spheres of either uniform or non-uniform size that do not overlap [Weissberg (1963)],
- 2.9 ($\tau = 1/\epsilon_{p,macro}$) for macro-, micro and series macro-micropore diffusion in a bidisperse medium [Wakao & Smith (1962)],
- 3.0 for a network of randomly interconnected uniform diameter cylindrical pores with no dead ends [Johnson & Stewart (1965)],
- and 5.0 ($\tau = \sqrt{3}/\epsilon_{p,macro}$) for an array of cells that are visualized as cubes or spheres with a fraction $\epsilon_{p,macro}$ of their surface open to the neighbouring cell [Weisz & Schwartz (1962)].

Assessing the coefficients obtained in Eqs. (4.26) through (4.28) with these estimates suggests the results for Knudsen and molecular tortuosity are in excellent agreement with typical magnitudes obtained in the literature while the value obtained for viscous flow is slightly high. It should be pointed out, however, that a majority of these correlations assume one overall tortuosity coefficient for the intrapellet pore network and rarely attribute tortuosity coefficients to each individual

mechanism, as was the case in this chapter. One check that can be made on Knudsen tortuosity is via Monte Carlo simulations performed by Abassi *et al.* (1983) for a monodisperse porous medium. They introduced a structural parameter, defined as k_o , in Eq. (23) of their paper as follows.

$$D_{K,i}^e = \frac{4}{3} \left(\frac{8}{\pi} \frac{10^5 RT}{M_i / 10^3} \right)^{1/2} k_o \text{ where } k_o = (0.1\epsilon - 0.0082) \delta \quad (4.29)$$

Comparing Eq. (4.29) with Eq. (2.9) allows k_o to be rewritten as follows by setting $\epsilon = \epsilon_{p,macro}$.

$$k_o = (0.1\epsilon_p - 0.0082) \delta \equiv \left(\frac{1}{4} C_K \right) \delta \quad (4.30)$$

Performing the left hand side calculation of Eq. (4.30) reveals $k_o = 0.053 \delta$ whereas the right hand side calculation (based on experimental parameters obtained in this chapter) reveals $k_o = 0.021 \delta$. Although these estimates are not exact, the fact that:

- they are approximately within two-fold of each other, a range that generally encompasses tortuosity coefficients for a wide variety of materials that are analysed using simplified pore structure models [Cunningham & Williams (1980, p 225)], and
- viscous flow and adsorption was included in the analysis of this chapter is a favourable result.

Although τ_K and τ_m are in good agreement with accepted literature values, the rather high value for τ_v is attributed to the insensitive nature of fitting C_v when matching numerical data to experimental through the optimization routine DBCONF used within NDGNAS. From this, the EMU is not recommended as an accurate device for estimating viscous flow transport coefficients in macropore-controlled sorbent pellets. Even so, an estimate of 5.6 for a corrected tortuosity coefficient on viscous flow is still reasonable and well within the usual order of magnitude estimates commonly encountered when a review of predicted tortuosity coefficients is made [Satterfield & Sherwood (1963)].

Comparing the Adiabatic versus Rigorous Wall Model Simulation

Using the calibrated molecular transport coefficient at $N_r = 5$, NDGNAS was run under the adiabatic assumption and simulation results compared to the equivalent results obtained with the rigorous wall model activated.

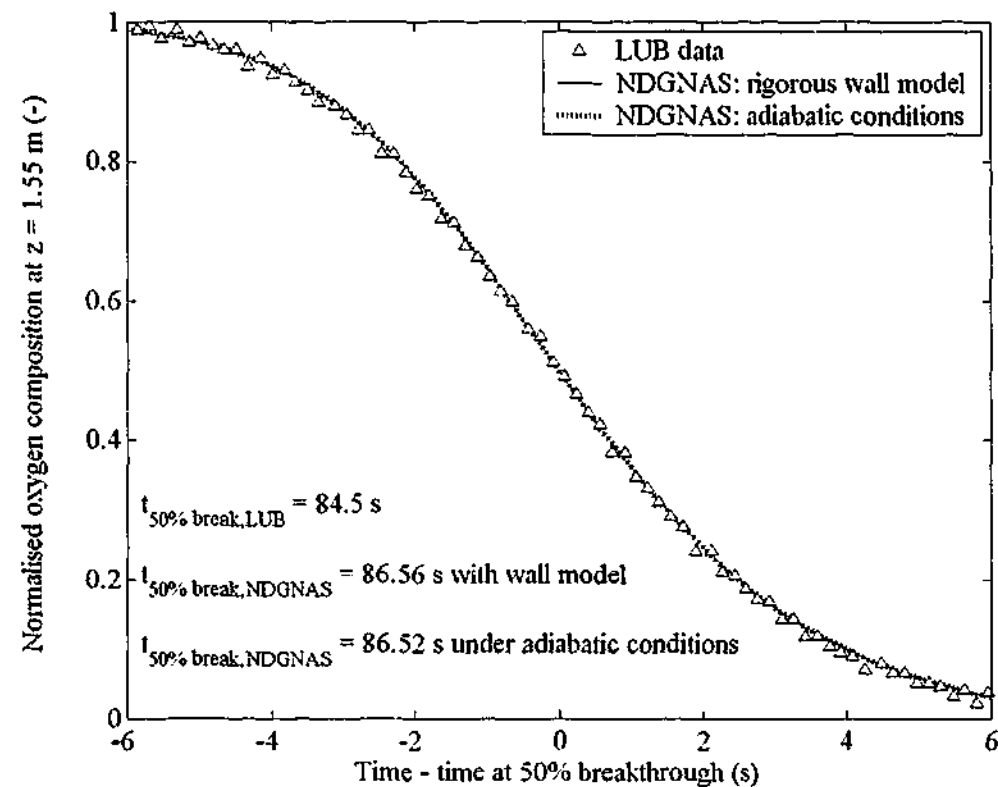


Figure 4.16: NDGNAS breakthrough curves obtained from the rigorous wall model and adiabatic simulations of breakthrough run 3 in comparison to LUB data.

Figure 4.16 compares both NDGNAS breakthrough curves against the corresponding LUB profile. Both NDGNAS profiles show negligible variations along the entire breakthrough curve, providing some justification that the breakthrough curve is being measured at conditions close to adiabatic. In addition, both NDGNAS profiles match LUB data to within experimental error. The time when 50% of the breakthrough curve has passed the oxygen analyser is predicted to within 2 s numerically, a favourable result given:

- i. errors in predicted equilibrium isotherm capacity and selectivity using IAST,
- ii. small fluctuations in velocity and pressure at the onset of a valve switch,
- iii. error in the flow reading obtained at the inlet to the column from the annubar-DP transducer arrangement, and
- iv. real operating conditions that reside somewhere between well mixed and plug flow are modelled as well mixed only within the bottom void volume

all manifest in the prediction of $t_{50\% \text{ break}}$.

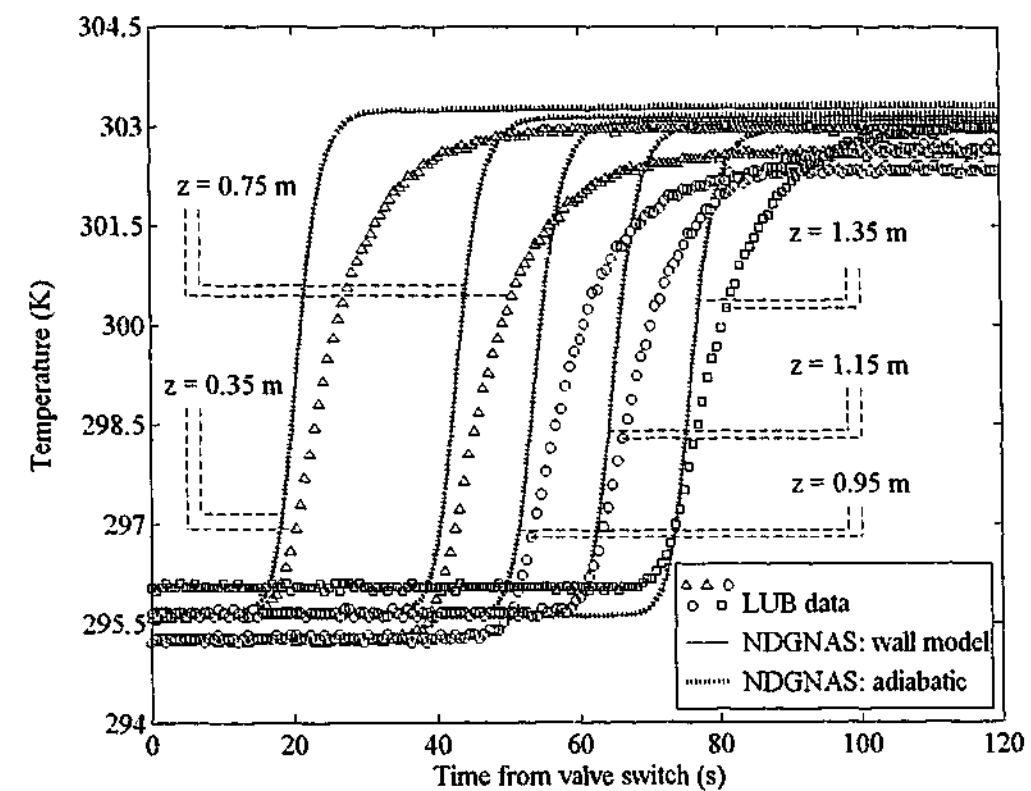


Figure 4.17: NDGNAS temperature profiles obtained from the rigorous wall model and adiabatic simulations of breakthrough run 3 in comparison to experimental temperature profiles.

To further examine the extent of adiabatic behaviour achieved within the column, Fig. 4.17 compares predicted temperature profiles from both NDGNAS runs against LUB data. Figure 4.17 demonstrates the final temperature plateau achieved after the MTZ has traversed the bed is predicted to within experimental error with both NDGNAS simulations. Note error bars of ± 0.5 K are not shown over LUB data in Fig. 4.17 to prevent the graph becoming too cluttered. Temperature does not show any obvious decrease experimentally or numerically with the rigorous wall model activated for the entire duration of the breakthrough experiment, indicating heat loss to the wall and conduction along the wall is negligible and near-adiabatic behaviour is experimentally attained.

The time at which each temperature profile begins to rise from the initial condition is also well predicted along the bed, indicating the speed of the thermal zone and hence MTZ is well captured for the duration of the breakthrough run. NDGNAS imposes a bumpless transfer numerically by maintaining the same boundary condition across the purge and feed steps, so matching experimental temperature profiles in absolute time indicates the transition from oxygen to feed gas was achieved with minimal impact on experimental pressure and velocity profiles.

One mismatch observed between the LUB and corresponding NDGNAS profile for both the adiabatic and rigorous wall model simulations, however, is the rate at which each temperature profile increases as the MTZ traverses the bed. NDGNAS temperature transients rapidly increase as the MTZ passes each point in the bed, mimicking the early shape of the breakthrough curve. However, experimental profiles show a slow asymptotic approach to final bed temperature once local equilibrium is attained behind the MTZ. This discrepancy between experimental and numerical temperature profiles has already been observed from EMU runs discussed in §4.3.6 and will be taken up at length in §5.6.1 once a more comprehensive set of experimental data over a range of operating conditions has been presented.

4.4.4 Sensitivity Analysis of Breakthrough Run 3

Before the remaining five breakthrough runs are discussed, it is useful at this point to investigate the importance of each intrapellet transport mechanism on the predicted breakthrough curve using experimentally calibrated transport coefficients. Comparisons between NDGNAS when run with the adiabatic and rigorous wall model options, Fig. 4.16, indicate the magnitude of $h_{U,W}$ has negligible impact on the predicted breakthrough curve. Hence, this subsection will investigate first order sensitivity coefficients of \bar{y}_i^B for $i = 2$ at $z = 1.55$ m between $(t_{1\% \text{ break}} - t_{50\% \text{ break}}) < (t - t_{50\% \text{ break}}) < (t_{99\% \text{ break}} - t_{50\% \text{ break}})$ with respect to C_K , C_v and C_m only.

The method adopted in §4.3.6 for sensitivity coefficients using EMU runs is also applied here. Lagrange interpolating polynomials will be used to curve fit the response of each breakthrough curve at each increment in time with one parameter systematically varying around its optimal value (either C_K , C_v or C_m) while the other two parameters remain constant. Analytically, these breakthrough curves as a function of time and transport coefficient can be represented in the following form.

$$\bar{y}_i^B(t_q, \psi) \approx \sum_{m=0}^{N_L} \bar{y}_{i,m}^B(t_q) L_m(\psi) \text{ for } i = 2 \text{ where } L_m(\psi) = \frac{\prod_{n=0, n \neq m}^{N_L} (\psi - \psi_n)}{\prod_{n=0, n \neq m}^{N_L} (\psi_m - \psi_n)} \quad (4.31)$$

Within Eq. (4.31) ψ represents one of either C_K , C_v or C_m and $t_q = (0.02 q \pm t_{50\% \text{ break}})$ for $q = 1$ to 350. To find first order sensitivity coefficients from Eq. (4.30), the first derivative with respect to ψ is taken.

$$\frac{\partial \bar{y}_i^B(t_q, \psi)}{\partial \psi} \approx \sum_{m=0}^{N_L} \bar{y}_{i,m}^B(t_q) \frac{dL_m(\psi)}{d\psi} \text{ for } i = 2; \quad \frac{dL_m(\psi)}{d\psi} = \frac{\left\{ \sum_{n=0, n \neq m}^{N_L} \left[\prod_{p=0, p \neq m, p \neq n}^{N_L} (\psi - \psi_p) \right] \right\}}{\left[\prod_{n=0, n \neq m}^{N_L} (\psi_m - \psi_n) \right]} \quad (4.32)$$

The definition for ψ and t_q introduced in Eq. (4.31) carries over directly into Eq. (4.32). For this analysis two values above and below the optimal transport coefficient were considered so N_L is three. A cubic Lagrange interpolating polynomial for breakthrough run 3 was adequate to resolve each sensitivity coefficient given several days were required to generate this data. Each transport coefficient was varied in fractional increments around its optimal value with the Knudsen transport coefficient varying between $0.073 \leq C_K \leq 0.095$, viscous flow between $0.055 \leq C_v \leq 0.067$ and molecular transport coefficient between $0.131 \leq C_m \leq 0.226$. Sensitivity coefficients obtained from this analysis are presented in Fig. 4.18.

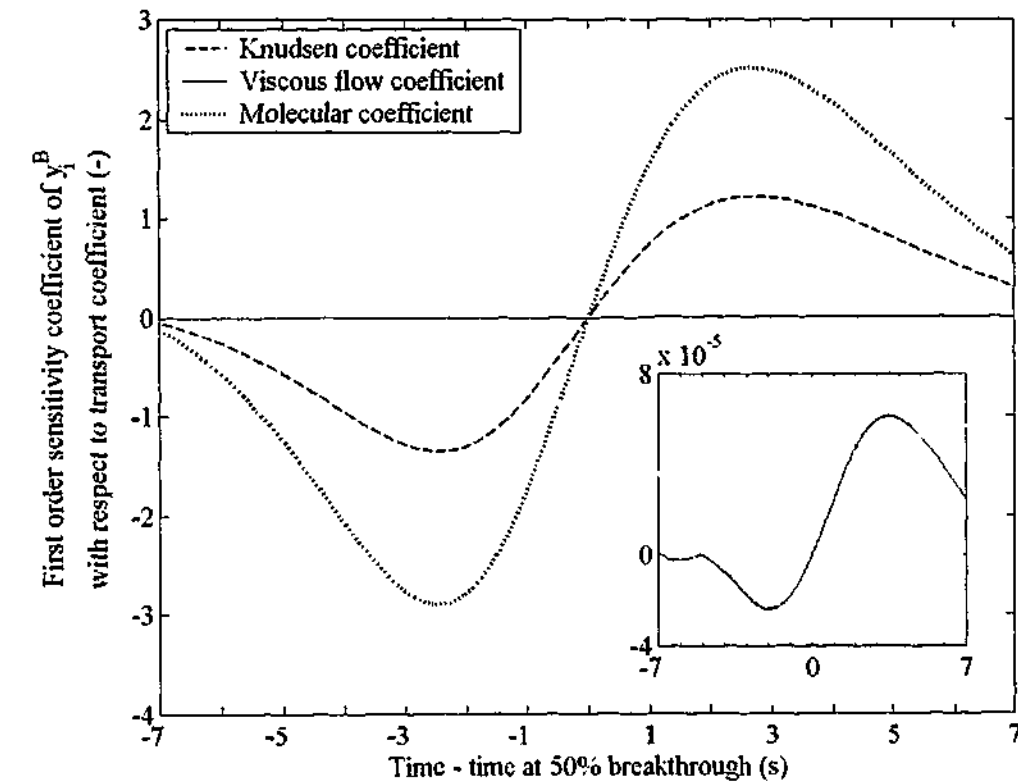


Figure 4.18: First order sensitivity coefficients of \bar{y}_i^B as a function of C_K , C_v and C_m obtained from breakthrough run 3 using NDGNAS. The inlay plot magnifies the y-axis for viscous flow only, so an order of magnitude comparison between the Knudsen and molecular transport coefficients can be made with respect to viscous flow transport coefficient.

Figure 4.18 reveals molecular and Knudsen diffusion are of a similar order of magnitude for the entire passage of the breakthrough curve. While molecular and Knudsen diffusion both contribute significantly to the shape of the breakthrough curve, the inlay plot on Fig. 4.18 indicates viscous flow is more than two orders of magnitude smaller. Sensitivity analysis of EMU runs indicated a

similar difference between Knudsen and viscous flow sensitivity coefficients, which suggests the importance of Knudsen diffusion over viscous flow for a pure component system carries similar weight when a binary gas mixture is introduced into the intrapellet pore network. The time required to achieve 50% breakthrough agreed to within 0.2 seconds numerically for all runs considered during the sensitivity analysis, indicating a variation in the transport coefficient simply stretches or compresses the breakthrough curve around the mid point as expected.

A "kink" in the trend for viscous flow sensitivity coefficient between $-7 < (t - t_{50\% \text{ break}}) < -5$ of Fig. 4.18 is attributed to the numerical derivative of numbers that are very similar being taken from the Lagrange interpolating polynomial, along with very small errors accumulating in the ODE solution vector at the onset of the breakthrough curve emerging at $z = 1.55$ m. All simulations performed in §4.4 set the ODE integrator tolerances $RelTol$ and $AbsTol$ to 5.0×10^{-7} . While these tolerances were more than adequate to compare experimental trends and C_m down to three significant figures, tolerances much tighter than this resulted in excessively long simulation time. Aside from the initial region of the coefficient for viscous flow sensitivity in Fig. 4.18, which will show a similar trend irrespective of the ODE integrator tolerances, no other NDGNAS results presented in §4.4 indicate ODE integrator tolerances might have been too loose.

Revisiting SimPell data from chapter 2 shows the assumed value of 0.20 for C_k and C_m is similar in magnitude to experimental estimates obtained from this analysis. Numerical results of chapter 2 obtained under both isothermal and non-isothermal conditions reveal viscous flow marginally increases the uptake rate of nitrogen from the bulk phase in comparison to a DGM-only response; and this was found with C_v set to 0.20. The current analysis has found an even smaller dependence on viscous flow, providing an order of magnitude realisation that viscous flow arising within Eq. (2.20) is not a significant component of the intrapellet molar flux for Zeochem LiLSX under the macropore assumption.

Although Zeochem LiLSX pellets are assumed macroporous given δ was found experimentally to be 2.5×10^{-7} m, sensitivity analysis of EMU and LUB runs indicate Knudsen diffusion cannot be neglected from the intrapellet molar flux. A discussion on the limiting form of the VF+DGM from §2.2.4 revealed the presence of Knudsen diffusion at the macropore limit implies the transfer of momentum between a gas and stationary dust molecule is still an important aspect of the flux equation to retain.

4.4.5 LUB and NDGNAS Results From Remaining Breakthrough Runs

With a calibrated set of experimental coefficients now available for Zeochem LiLSX, NDGNAS was used to simulate the remaining breakthrough runs using $N_r = 5$ and $C_m = 0.166$. A tabular summary of all six LUB and NDGNAS runs in terms of prescribed points along the breakthrough curve and derived quantities are presented in Table 4.11. This tabular summary complements the graphical presentation of each breakthrough curve obtained numerically and experimentally in Fig. 4.19 while quantifying additional information about each breakthrough run.

Table 4.11: Tabular summary of LUB versus NDGNAS data from each breakthrough run obtained with $N_r = 5$ and $C_m = 0.166$.

| Parameter (mixture A runs) | Breakthrough run 1 | | Breakthrough run 2 | |
|---|--------------------|--------|--------------------|--------|
| | LUB | NDGNAS | LUB | NDGNAS |
| $t_{50\% \text{ break}}$ (s) | 100.5 ± 0.1 | 108.3 | 71.1 ± 0.1 | 73.6 |
| $t_{4\% \text{ break}} - t_{50\% \text{ break}}$ (s) | -9.9 ± 0.5 | -9.9 | -9.9 ± 1.1 | -9.0 |
| $t_{20\% \text{ break}} - t_{50\% \text{ break}}$ (s) | -4.7 ± 0.2 | -4.6 | -4.0 ± 0.1 | -4.3 |
| $t_{40\% \text{ break}} - t_{50\% \text{ break}}$ (s) | -1.4 ± 0.1 | -1.4 | -1.2 ± 0.1 | -1.3 |
| $t_{60\% \text{ break}} - t_{50\% \text{ break}}$ (s) | 1.4 ± 0.1 | 1.4 | 1.2 ± 0.1 | 1.3 |
| $t_{80\% \text{ break}} - t_{50\% \text{ break}}$ (s) | 4.6 ± 0.1 | 4.9 | 3.8 ± 0.1 | 4.6 |
| $t_{96\% \text{ break}} - t_{50\% \text{ break}}$ (s) | 11.5 ± 0.9 | 10.4 | 7.9 ± 0.3 | 9.8 |
| v_{MTZ} ($m s^{-1}$) | 0.0145 ± 0.0009 | 0.0146 | 0.0234 ± 0.0015 | 0.0217 |
| L_{MTZ} (m) | 0.311 ± 0.040 | 0.296 | 0.417 ± 0.060 | 0.407 |
| Axial nodes across MTZ (-) | N/A | ≈ 29 | N/A | ≈ 40 |

| Parameter (mixture B runs) | Breakthrough run 3 (fit C_m) | | Breakthrough run 4 | |
|---|---------------------------------|--------|--------------------|--------|
| | LUB | NDGNAS | LUB | NDGNAS |
| $t_{50\% \text{ break}}$ (s) | 84.5 ± 0.1 | 86.6 | 57.2 ± 0.1 | 58.0 |
| $t_{4\% \text{ break}} - t_{50\% \text{ break}}$ (s) | -4.7 ± 0.1 | -4.6 | -4.9 ± 0.3 | -4.4 |
| $t_{20\% \text{ break}} - t_{50\% \text{ break}}$ (s) | -2.2 ± 0.1 | -2.2 | -2.3 ± 0.1 | -2.1 |
| $t_{40\% \text{ break}} - t_{50\% \text{ break}}$ (s) | -0.6 ± 0.1 | -0.7 | -0.7 ± 0.1 | -0.6 |
| $t_{60\% \text{ break}} - t_{50\% \text{ break}}$ (s) | 0.7 ± 0.1 | 0.7 | 0.6 ± 0.1 | 0.7 |
| $t_{80\% \text{ break}} - t_{50\% \text{ break}}$ (s) | 2.5 ± 0.1 | 2.5 | 2.2 ± 0.1 | 2.4 |
| $t_{96\% \text{ break}} - t_{50\% \text{ break}}$ (s) | 5.5 ± 0.1 | 5.6 | 4.9 ± 0.1 | 5.2 |
| v_{MTZ} ($m s^{-1}$) | 0.0183 ± 0.0002 | 0.0183 | 0.0273 ± 0.0028 | 0.0275 |
| L_{MTZ} (m) | 0.187 ± 0.006 | 0.187 | 0.267 ± 0.039 | 0.263 |
| Axial nodes across MTZ (-) | N/A | ≈ 18 | N/A | ≈ 26 |

| Parameter (mixture C runs) | Breakthrough run 5 | | Breakthrough run 6 | |
|---|--------------------|--------|--------------------|--------|
| | LUB | NDGNAS | LUB | NDGNAS |
| $t_{50\% \text{ break}}$ (s) | 67.0 ± 0.1 | 71.6 | 56.3 ± 0.1 | 58.1 |
| $t_{4\% \text{ break}} - t_{50\% \text{ break}}$ (s) | -0.7 ± 0.1 | -0.4 | -0.6 ± 0.1 | -0.4 |
| $t_{20\% \text{ break}} - t_{50\% \text{ break}}$ (s) | -0.3 ± 0.1 | -0.2 | -0.3 ± 0.1 | -0.2 |
| $t_{40\% \text{ break}} - t_{50\% \text{ break}}$ (s) | -0.1 ± 0.1 | -0.06 | -0.1 ± 0.1 | -0.06 |
| $t_{60\% \text{ break}} - t_{50\% \text{ break}}$ (s) | 0.1 ± 0.1 | 0.07 | 0.1 ± 0.1 | 0.07 |
| $t_{80\% \text{ break}} - t_{50\% \text{ break}}$ (s) | 0.4 ± 0.1 | 0.3 | 0.4 ± 0.1 | 0.3 |
| $t_{96\% \text{ break}} - t_{50\% \text{ break}}$ (s) | 1.1 ± 0.1 | 0.9 | 1.0 ± 0.1 | 1.0 |
| v_{MTZ} ($m s^{-1}$) | 0.0237 ± 0.0050 | 0.0222 | 0.0288 ± 0.0010 | 0.0274 |
| L_{MTZ} (m) | 0.042 ± 0.012 | 0.028 | 0.048 ± 0.007 | 0.039 |
| Axial nodes across MTZ (-) | N/A | ≈ 5 | N/A | ≈ 7 |

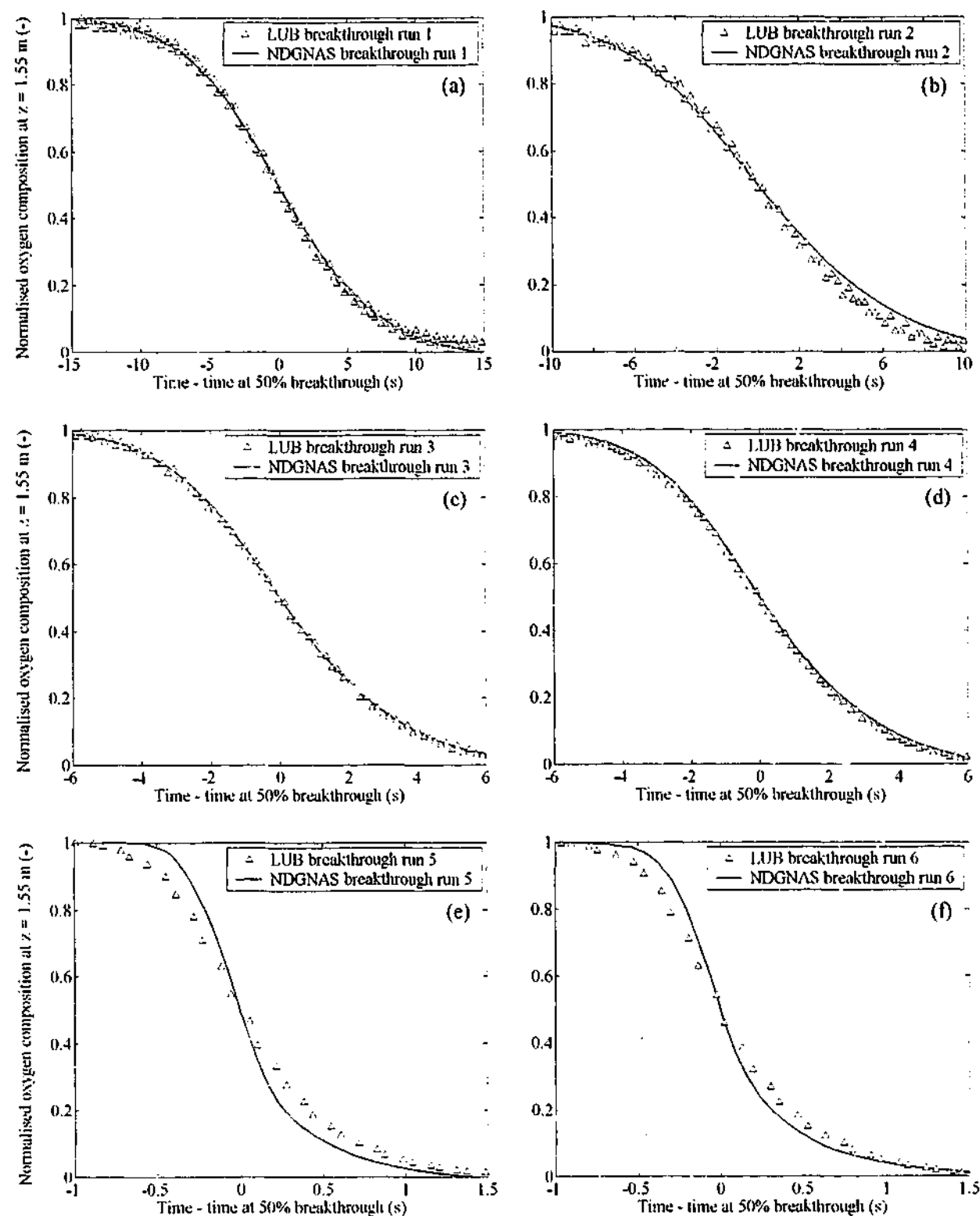


Figure 4.19: Comparison of LUB and NDGNAS breakthrough curves obtained with the rigorous wall model activated for NDGNAS. (a) Breakthrough run 1. (b) Breakthrough run 2. (c) Breakthrough run 3. (d) Breakthrough run 4. (e) Breakthrough run 5. (f) Breakthrough run 6.

All results presented in this subsection, including Table 4.11, relate to rigorous wall model simulations performed using NDGNAS. Adiabatic simulations of the remaining five LUB runs are qualitatively similar to the discussion of §4.4.3 and are deemed unnecessary to repeat in this subsection. Experimental versus numerical results for the speed and width of the MTZ generally

agree to within experimental error. NDGNAS also captures the shape of each breakthrough curve well, from a disperse wave that takes approximately 30 s to pass the analyser to a sharp wave that is complete in less than 2 s (Fig. 4.19). Although it may seem breakthrough runs 1 through 4 provide a better prediction of the breakthrough curve, the time scale for mixture C runs is very short and in general the deviation between NDGNAS and LUB data is less than 0.2 s, which is close to the scan rate of the LUB data acquisition program.

Runs that involve a low nitrogen feed concentration, breakthrough runs 1 through 4, indicate the MTZ is adequately resolved in accordance with the Webley & He (2000) criterion discussed in §4.4.2. Resolving the packed bed into 0.005 m increments for mixture C runs, on the other hand, meant that only 5 and 7 axial nodes for breakthrough runs 5 and 6 respectively were achieved across the MTZ. While Taylor dispersion [Taylor (1953, 1954)] in the $\frac{1}{16}$ inch section of pipe leading from the packed bed to the analyser is negligible, numerical dispersion according to the Webley & He (2000) criterion cannot be neglected. As mentioned in §4.4.2, breakthrough runs 5 and 6 are close to the upper limit of run-time memory available on the Dec-Alpha workstation. Similar issues with available memory prevented these same runs being performed in the Windows environment from a standard desktop PC. Despite this, NDGNAS and LUB data is in good agreement indicating the presence of more nodes across the MTZ would not significantly alter the shape of the numerical breakthrough curve observed in Figs. 4.19e and 4.19f.

This analysis, however, does highlight the efficacy in developing a discretisation scheme that can dynamically adjust node spacing to follow a steep moving front such as those experienced in the passage of a MTZ during a breakthrough run. Node spacing behind and in front of the MTZ can be relatively sparse given these regions are close to equilibrium, while node spacing around the MTZ can be dense in order to resolve the breakthrough curve. This allows the total number of axial nodes to be reduced significantly given the highly refined discretisation scheme is present across the MTZ only. Methods that initiate this very approach have been applied to finite element schemes and are commonly termed Moving Finite Element Methods (MFEM) [Miller (1981), Miller & Miller (1981)]. Kiil & Bhatia (1998) applied a MFEM within a single sorbent pellet that experiences step changes in concentration at $r = R_p$ for a range of dimensionless times, while Sereno *et al.* (1991) applied a MFEM to follow the MTZ within a chromatographic system that operates under ILE. Huang & Chou (1997) incorporated a MFEM into an adsorption simulator for an isothermal, axially dispersed plug flow model that is operating under ILE conditions for a binary system. Further studies by Kaczmarek *et al.* (1997) and Coimbra *et al.* (2001) have investigated MFEMs over a range of conditions where sharp composition profiles arise during an

adsorption process. This is one issue that has not yet been addressed within NDGNAS for the simulation of LUB or RPSA runs.

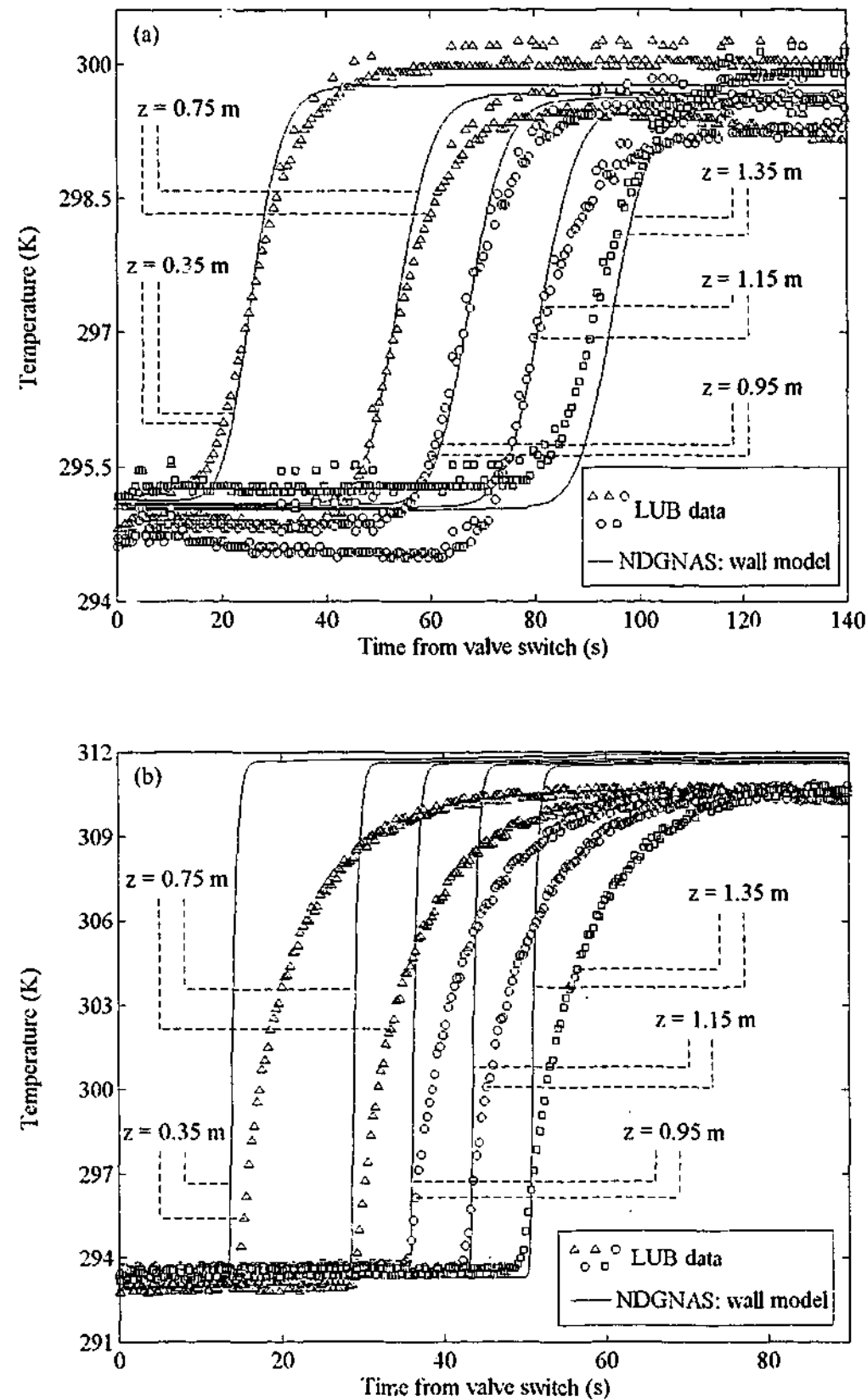


Figure 4.20: A comparison of LUB and NDGNAS temperature profiles obtained with the rigorous wall model activated. (a) Breakthrough run 1. (b) Breakthrough run 6.

Breakthrough curves obtained experimentally and numerically for one particular feed gas mixture (Fig. 4.19) at two different velocities and pressure did not show any significant variation. This suggests large changes in pressure and velocity are required to effect any change on the breakthrough curve for one particular feed gas mixture. Given pressures above 1.30 bar, a could not be initiated, the alternative method of varying feed gas composition was found to significantly alter the shape of the breakthrough curve. This result justifies the use of different feed gas mixtures when examining molecular diffusion through Eq. (4.22). While experimental and numerical breakthrough curves are in good agreement across each breakthrough run, a different trend is observed with the corresponding temperature profile as feed nitrogen composition increases.

Results from mixture B (Fig. 4.17) show the initial portion of the temperature transient is well captured as the MTZ approaches each thermocouple, but the second half of this temperature transient is consistently slower experimentally. This observation is more pronounced with gas mixture C, which employs a high feed nitrogen composition and hence sharper MTZ (Fig. 4.20b), while the numerical and experimental trends follow each other for the majority of the transient using mixture A (Fig. 4.20a). Figures 4.20a and 4.20b relate to breakthrough runs 1 and 6 respectively. Qualitatively identical trends are observed for breakthrough runs 2 and 5 respectively and are not shown for brevity. Section 5.6.1 will discuss breakthrough run temperature profiles in addition to NDGNAS versus LUB pressure drop profiles, so the numerical and experimental comparison of breakthrough runs will stop at this point.

4.4.6 Verifying Intrapellet Mass Transfer as the Limiting Resistance

With each intrapellet transport coefficient now ascertained the remaining discussion of this chapter shall quantify the impact of axial dispersion and external film mass transfer resistance to ensure their omission has been justified.

Second order mass dispersion is characterised through the axial Peclet number $Pe_{B,mass}$ that was first introduced in §1.2.1. To determine $Pe_{B,mass}$ a correlation for D_{ax}^e is required that accounts for intrapellet mass transfer. The model of Gunn (1987) was described in §1.2.1 as a suitable candidate, which takes on the following form using variables defined in this dissertation.

$$D_{ax}^e = \frac{v_B^2 d_{p,eqv}^2 (1 - P_{ax})^2 \left(\frac{\epsilon_B}{1 - \epsilon_B} \right) + \frac{v_B^3 d_{p,eqv}^3 P_{ax} (1 - P_{ax})^3 \left(\frac{\epsilon_B}{1 - \epsilon_B} \right)^2}{535.3 D_{m,ij}^2} \times \left\{ \exp \left[\frac{-23.14 D_{m,ij}}{P_{ax} (1 - P_{ax}) v_B d_{p,eqv} \left(\frac{\epsilon_B}{1 - \epsilon_B} \right)} \right] - 1 \right\} + \frac{D_{m,ij}}{\tau_{ax}} \quad (4.33)$$

Within Eq. (4.33) P_{ax} represents a probability factor for axial dispersion, which is given by the expression $0.17 + 0.33 \exp(-24\mu_B / \nu_B \epsilon_B d_{p,eq} \hat{\rho}_g^B)$ for spherical geometry; and τ_{ax} a transport coefficient that defines the distance a packet of gas travels within the interpellet void space in relation to the "unhindered" distance ($= 1.4$ for spherical geometry). Equation (4.33) is applicable to bulk conditions away from the retaining column walls across all ranges of Re_p investigated in this chapter [Gunn (1987)]. To confirm the plug flow assumption across each breakthrough run, output profiles from NDGNAS were used to calculate D_{ax}^c from Eq. (4.33) and then $Pe_{B,mass}$. Results from this calculation at $z = 1.55$ m, the axial location where the oxygen analyser was located, are shown in Fig. 4.21 for each feed gas mixture considered. The magnitude of $Pe_{B,mass}$ never drops below 700 at any point during each simulation. According to the discussion of §1.2.1, $Pe_{B,mass}$ greater than 100 indicates convective gas motion dominates interpellet mass transfer, justifying the plug flow assumption during the experimental determination of C_m .

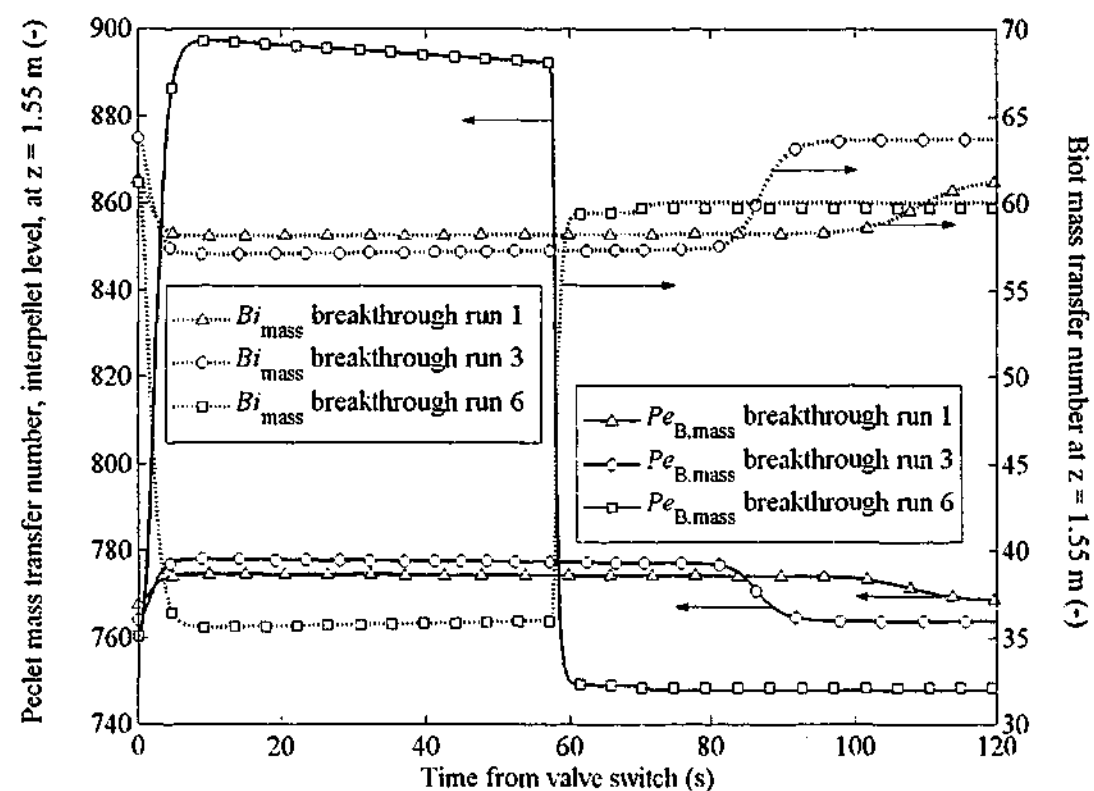


Figure 4.21: Peclet mass transfer number at the bed scale and Biot mass transfer number obtained from NDGNAS data for each gas mixture at $z = 1.55$ m, the location of the oxygen analyser, for breakthrough runs 1, 3 and 6.

In addition to $Pe_{B,mass}$ for breakthrough runs 1, 3 and 6, Fig. 4.21 also shows the corresponding trends for Bi_{mass} . The magnitude of Bi_{mass} was calculated using output profiles obtained from NDGNAS through Eq. (1.10) with the Bosanquet formula used to estimate the effective intrapellet diffusion coefficient D_i^e . For each feed gas mixture Bi_{mass} is of order 30 or greater for the entire duration of each breakthrough run at $z = 1.55$ m, indicating external film mass transfer resistance

was of minimal importance over the period of experimental interest (Bi_{mass} is at least one order of magnitude greater than 1).

While axial dispersion and external film mass transfer resistance can be neglected during the passage of the MTZ, a similar analysis using NDGNAS data also renders axial heat conduction negligible. Equation (3.10) reveals the numerator of the Peclet heat transfer number at the bed scale, $\rho_g^B \epsilon_B \nu_B L_{bed} \left(\sum_{i=1}^2 y_i^B c_{g,i}^B \right)$, is typically 800 to 900 $W m^{-1} K^{-1}$ over a breakthrough run while the denominator, λ_{ax}^c , is around 0.1 $W m^{-1} K^{-1}$. This means $Pe_{B,heat}$ is in excess of 1000 across each breakthrough run, effectively eliminating the transport of heat by conduction along the axial domain of the packed bed.

This analysis, however, has neglected the impact of radial dispersion across the interpellet domain within the column. This parameter is not as simple to quantify for an adsorption system and as such is assumed to have minimal impact on experimental profiles when near adiabatic conditions arise [Pentchev *et al.* (2002)]. In the absence of multiple oxygen analysers placed at the one axial position but different radial coordinates, this mechanism of dispersion is very hard to quantify. Similarly, a radial plus axial discretisation scheme across the interpellet domain, in addition to intrapellet discretisation within NDGNAS would significantly increase computational time beyond those already observed for breakthrough simulations of this chapter. Hence, several months as opposed to several weeks of simulation time may be required when the interpellet domain is discretised axially and radially in addition to the intrapellet domain with a DPM.

4.5 Concluding Remarks

Manipulating a select number of modelling options within NDGNAS allows direct comparisons to be made with experimental data. Quantifying physical and operating parameters for the experimental system of interest allows intrapellet transport coefficients to be directly inferred from one particular experimental response. In this dissertation one sorbent material of commercial interest has been used to compare model predictions against experimental data, a lithium-exchanged LSX-type molecular sieve zeolite denoted Zeochem LiLSX. Characterising the physical properties of Zeochem LiLSX allows the first set of transport coefficients to be found.

A volumetric uptake apparatus using a single component gas, the EMU, allowed Knudsen and viscous flow transport coefficients to be characterized. Experimental estimates on these coefficients are $C_k = 0.083 \pm 0.016$ and $C_v = 0.061 \pm 0.025$. However, it was found that C_v was relatively insensitive to EMU data and it is speculated that the EMU is not an appropriate device

for ascertaining the viscous flow transport coefficient under conditions experimentally investigated in this dissertation. Binary component breakthrough curves generated in a chromatographic apparatus, the LUB unit, allowed the molecular transport coefficient to be obtained. While C_k and C_v were relatively insensitive to N_r , C_m had a strong dependence on radial discretisation that exceeded experimental uncertainty. For this reason only one level of radial discretisation shall be considered for the remainder of this dissertation, $N_r = 5$ using $C_m = 0.166$. These coefficients were also found to be in good agreement with existing literature estimates on the tortuosity coefficient τ .

The molecular diffusion transport coefficient was calibrated using just one breakthrough curve obtained from the LUB apparatus, breakthrough run 3. In conjunction with Knudsen and viscous flow transport coefficients obtained from an independent set of experiments (EMU), excellent agreement was found across all of the remaining five breakthrough runs. The ability to fit all breakthrough curves with just one Ω_i value for each component using the LDF model would be very difficult according to the conclusions of chapter 2 given large differences in pellet surface boundary conditions will arise between mixture runs A, B and C.

Experimental response across all EMU and LUB runs show good agreement with NDGNAS predictions except temperature. While the response time of T-type thermocouples is not the problem, this does present one limitation of the current experimental arrangement being used to measure temperature in the presence of adsorption when rapid temperature transients occur.

CHAPTER 5

EXPERIMENTAL DETERMINATION OF THE INTERPELLET COEFFICIENTS FOR PRESSURE DROP

Having calibrated intrapellet transport coefficients in chapter 4, an additional set of experimental data is generated to calibrate the viscous and kinetic constants of the steady state momentum

equation for pressure drop. The individual objectives for this chapter are as follows:

- i. Provide a background to the methods and models used to quantify pressure drop under non-adsorbing and adsorbing conditions.
 - ii. Obtain experimental estimates of the viscous and kinetic constants within the steady pressure drop equation for one particular sorbent material, Zeochem LiLSX.
 - iii. Validate use of a steady state momentum equation, the Ergun equation, in relation to the full momentum balance under non-adsorbing conditions to predict pressure drop.
 - iv. Validate use of the Ergun equation to predict pressure drop under adsorbing conditions.
-

The movement of gas through a packed bed must overcome the resistance to flow offered by the combined effects of form drag, separation and wake formation around an individual pellet [McCabe *et. al.* (1993, p 151)]. These combined drag forces cause pressure to decrease in the direction of gas flow, characterised in chapter 1 over three different regimes: laminar ($Re_p < 5$), intermediate ($5 < Re_p < 1000$) and turbulent ($Re_p > 1000$). The presence of an axial pressure gradient has a detrimental effect on performance for two reasons.

- i. At one particular temperature adsorbed phase loading is a function of pressure, see Fig. 4.1, so any pressure gradient that arises between the inlet and outlet ends of the packed bed will reduce the adsorption-desorption capacity and hence the ability to remove the strongly adsorbed component(s) from the feed stream. This often requires an increase in the volume of sorbent or a reduction in feed velocity, the end result from both of these solutions ultimately defeat the benefits of miniaturising a PSA process through shorter cycle times.
- ii. A compressor with a larger duty will be required to overcome flow resistance as cycle time decreases, increasing the operating cost (power consumption) for a particular separation.

While these constraints oppose a reduction in cycle time, shorter cycle times reduce the installed capital cost given a smaller sorbent inventory will achieve the same product output (Eq. (1.2)). To quantify these trade-offs an independent assessment of pressure drop needs to be made.

For bulk separations such as oxygen enrichment from air, an additional dynamic related to the uptake of a major component, nitrogen, from the interpellet phase is introduced. To independently quantify pressure drop before adsorption is introduced, the first part of this chapter considers interpellet mass transfer under non-adsorbing conditions (§5.1 through §5.3). Imposing this constraint eliminates mass transfer at the intrapellet level to allow a direct comparison between the Ergun equation, full momentum balance and experimental data to be made. Helium at a purity of 99.996 mol% is used as the feed gas to justify the assumption of negligible adsorption.

The second part of this chapter, §5.4 through §5.6, introduces a sink (adsorption)/source (desorption) term into the experimental analysis to account for the uptake of a bulk component to/from the pellets. As discussed in chapter 1, mass transfer resistance will now be present at the intrapellet level in addition to interpellet pressure drop. To maintain consistent treatments of pressure drop between this chapter and chapters 4 and 6, the VF+EGM flux model will be applied to the DPM with $N_r = 5$. However, the form of this model has little impact on experimental comparisons and the related discussion/conclusions of this chapter can be reached using an LDF approach to intrapellet mass transfer.

Part I. Momentum Equation under Non-Adsorbing Conditions

Various models have been proposed in the literature to correlate the change in pressure across a packed bed as a function of the flowing conditions of the gas stream. Often, complexities associated with packing geometry and arrangement limit such models to a semi-quantitative form applicable to a macroscopically homogeneous medium based on a select number of dimensionless parameters [Dullien (1975)]. These parameters include the friction factor f and pellet Reynolds number Re_p . In general, one or two fitting parameters are used to characterise a particular material within these constitutive models [Bird *et al.* (1960, pp 196-200)]. Restating the Hagen-Poiseuille equation in a form that now reflects flow through a packed bed under laminar conditions in terms of f and Re_p gives the following.

$$f = \kappa_{\text{viscous}} \text{ where } f = \left(-10^5 \frac{\Delta p^B}{\Delta z} \right) \frac{d_{p,\text{eqv}}^2}{\mu_B v_B} \left(\frac{\epsilon_B}{1 - \epsilon_B} \right)^2 \text{ for } Re_p < 5 \quad (5.1)$$

Note the friction factor defined in Eq. (5.1) is consistent with that of Ergun (1952), who described f as the ratio of pressure-to-viscous energy loss. The factor 10^5 that multiplies $\Delta p^B/\Delta z$ converts p^B from units of bar.a to Pascal while the negative sign indicates pressure decreases with gas flowing in the positive z direction. The structural coefficient κ_{viscous} according to the Blake-Kozeny model

for complicated tube-bundle geometries was estimated to be 150, which is equivalent to a tortuosity coefficient of 25/6 for their representation of the interpellet flow path [Bird *et al.* (1960, p 199)]. According to the Carman-Kozeny model, $\kappa_{\text{viscous}} = 180$ from similar arguments [Dullien (1975)]. At the fully turbulent limit a modified form of the equation for turbulent flow in a circular pipe gives rise to the following.

$$f = \kappa_{\text{kinetic}} \frac{Re_p}{(1 - \epsilon_B)} \text{ where } Re_p = \frac{(v_B \epsilon_B) \hat{\rho}_g^B d_{p,\text{eqv}}}{\mu_B} \text{ and } \hat{\rho}_g^B = \frac{\sum_{i=1}^{N_c} M_i p_i^B}{10^3 R T} \text{ for } Re_p > 1000 \quad (5.2)$$

Re_p requires gas phase density in kg m^{-3} , hence the correlation presented for $\hat{\rho}_g^B$ while f is identical to the form presented in Eq. (5.1). The structural coefficient κ_{kinetic} , according to the Burke-Plummer model, was found to be 1.75 assuming all packed beds have a similar "roughness" [Bird *et al.* (1960, p 200)]. Forchheimer, in 1901, was the first to point out the kinetic component of flow should be added to the viscous component [Teng & Zhao (2000)]. Combining Eq. (5.1) for the viscous component with Eq. (5.2) for the kinetic component gives rise the Ergun friction factor, valid across all ranges of Re_p [Ergun & Orning (1949), Ergun (1952)].

$$f = \kappa_{\text{viscous}} + \kappa_{\text{kinetic}} \left[\frac{Re_p}{(1 - \epsilon_B)} \right] \text{ for all } Re_p \quad (5.3)$$

Ergun (1952) estimated the two coefficients κ_{viscous} and κ_{kinetic} to be 150 and 1.75 respectively using a least squares fit of 640 data points from various literature sources. More recently Macdonald *et al.* (1979) proposed $\kappa_{\text{viscous}} = 180$ with κ_{kinetic} now a function of the pellet roughness based on existing experimental data and the smooth/rough pipe analogy of the Moody diagram: $\kappa_{\text{kinetic}} = 1.8$ for "smooth" pellets and $\kappa_{\text{kinetic}} = 4.0$ for "rough" pellets. One can see from this preliminary discussion that both structural coefficients κ_{viscous} and κ_{kinetic} have been differently assigned depending on their source. For this reason the most reliable estimates are obtained from experimental data using the packing material of interest.

5.1 Derivation of the Steady State and Full Momentum Balance

Using an appropriate relationship for f , the inter-conversions of energy within a packed bed can now be investigated through the equation of mechanical energy [Bird *et al.* (1960, p 81)]. The mathematical analysis for a non-adsorbing gas assumes isothermal behaviour based on the following experimental conditions.

- When determining κ_{viscous} and κ_{kinetic} using an adsorbing gas, measurements are performed only when bed saturation has occurred and temperature, pressure and composition profiles are at steady state.
- Helium at a purity of 99.996 mol% is used as the feed gas for all depressurisation experiments, which can be assumed to undergo negligible adsorption.
- The sorbent material has a high heat capacity per unit mass that mitigates any temperature variations resulting from frictional losses associated with viscous transport or heats of compression and/or expansion due to rapid pressure changes across the packed bed.

The equation of mechanical energy needs to allow for flow in both directions given velocity can be oriented in the positive or negative z direction. For a non-adsorbing gas that experiences negligible resistance to mass transfer at the intrapellet level, such as helium, the volume over which the equation of mechanical energy is written relates to the combined inter- and intrapellet void regions. This differential volume is given by $A_B \Delta z [\epsilon_B + \epsilon_P (1 - \epsilon_B)]$. Although viscous and gravitational effects are neglected within the equation of mechanical energy from Bird *et al.* (1960, p 81), an additional term needs to be added for friction loss associated with flow through a packed bed [Serenio & Rodrigues (1993)]. It is worth noting that this loss term, related to the friction factor of Eq. (5.1), maintains interpellet void ϵ_B rather than the combined void $\epsilon_B + \epsilon_P (1 - \epsilon_B)$ as f is directly related to pressure loss associated with flow through the interpellet region only. For a cylindrical column of constant cross-sectional area where no radial gradients arise, the equation of mechanical energy is given by the following.

$$\frac{\partial}{\partial t} \left(\frac{1}{2} \hat{\rho}_g^B v_B |v_B| \right) = - \frac{\partial}{\partial z} \left(\frac{1}{2} \hat{\rho}_g^B v_B^3 \right) - 10^5 v_B \frac{\partial p^B}{\partial z} - \left[\frac{\kappa_{\text{viscous}} \mu_B}{d_{p,\text{eqv}}^2} \left(\frac{1 - \epsilon_B}{\epsilon_B} \right)^2 \right] v_B |v_B| - \left[\frac{\kappa_{\text{kinetic}} \hat{\rho}_g^B}{d_{p,\text{eqv}}} \left(\frac{1 - \epsilon_B}{\epsilon_B} \right) \right] v_B^3 \quad (5.4)$$

Within Eq. (5.4) the Ergun friction factor of Eq. (5.3) has been used. In addition to the equation of mechanical energy, the conservation of mass is also required [Bird *et al.* (1960, p 75)].

$$\frac{\partial \hat{\rho}_g^B}{\partial t} = - \frac{\partial}{\partial z} (\hat{\rho}_g^B v_B) \quad (5.5)$$

Multiplying Eq. (5.5) by $v_B^2/2$ and adding to Eq. (5.4) reduces the equation of mechanical energy to the form commonly referred to as the full momentum balance for an isothermal packed bed of inert material.

$$\frac{\partial}{\partial t} (\hat{\rho}_g^B v_B) = - \frac{\partial}{\partial z} (\hat{\rho}_g^B v_B |v_B|) - 10^5 \frac{\partial p^B}{\partial z} - \left[\frac{\kappa_{\text{viscous}} \mu_B}{d_{p,\text{eqv}}^2} \left(\frac{1 - \epsilon_B}{\epsilon_B} \right)^2 \right] v_B - \left[\frac{\kappa_{\text{kinetic}} \hat{\rho}_g^B}{d_{p,\text{eqv}}} \left(\frac{1 - \epsilon_B}{\epsilon_B} \right) \right] v_B |v_B| \quad (5.6)$$

Under normal operating conditions it is assumed that a solution to the full momentum balance, Eq. (5.6), is often unnecessary given the rate of accumulation of momentum, $\partial(\hat{\rho}_g^B v_B)/\partial t$, and the rate of gain of momentum by convection, $\partial(\hat{\rho}_g^B v_B |v_B|)/\partial z$, are usually smaller than $10^5 \partial p^B/\partial z$ by comparison. Neglecting these two terms from Eq. (5.6) gives rise to the Ergun equation for steady flow through a packed bed as stated previously in dimensionless form (Eq. (5.3)).

$$10^5 \frac{\partial p^B}{\partial z} = - \left[\frac{\kappa_{\text{viscous}} \mu_B}{d_{p,\text{eqv}}^2} \left(\frac{1 - \epsilon_B}{\epsilon_B} \right)^2 \right] v_B - \left[\frac{\kappa_{\text{kinetic}} \hat{\rho}_g^B}{d_{p,\text{eqv}}} \left(\frac{1 - \epsilon_B}{\epsilon_B} \right) \right] v_B |v_B| \quad (5.7)$$

Serenio & Rodrigues (1993) considered the full momentum balance, Eq. (5.6), in comparison to the Ergun equation, Eq. (5.7), for the pressurisation of an inert sorbent bed with air and found the Ergun equation consistently reproduced profiles predicted using the full momentum balance. A pressure ratio of 5:1 between final:initial pressure was used. Chahbani & Tondeur (1998) compared numerical profiles obtained with the full momentum balance, Eq. (5.6), using the Darcy (Eq. (5.1)) and Ergun (Eq. (5.3)) friction factor for hydrogen pressurisation across an inert bed of 0.5×10^{-3} m diameter pellets. A final:initial pressure ratio of 5:1 was also applied. They found the Darcy model predicted pressurisation rates that were erroneously faster than the Ergun model.

Numerical profiles obtained under non-adsorbing, and for that matter, adsorbing conditions will concentrate on the Ergun friction factor only, Eq. (5.3), for both the steady state and full momentum balance. Based on the magnitude of Re_P typically encountered over the analysis sections of this dissertation, $10 < Re_P < 1000$, it is deemed unnecessary to compare numerical results obtained with an exclusively laminar or turbulent friction factor correlation.

5.1.1 Solution of the Equations for a Single Component System

The conservation of mass and steady state/full momentum balance are solved in terms of interpellet pressure p^b rather than density ρ_g^b given isothermal behaviour is assumed. In addition, a single component system is modelled so no dependence on y_i^b arises in the spatial or temporal domain. A solution to the continuity equation using either a steady state or full momentum balance involves a numerical strategy given the non-linear relationship between velocity and pressure. Consequently, the finite volume method previously described in §B.3 of appendix B for cylindrical geometry is applied here. The discretised set of conservation equations were incorporated into NDGNAS through a separate time derivative subroutine and then activated via a user-defined input flag.

Within the first half of this chapter, two different forms of the momentum equation shall be investigated. The first incorporates the full momentum balance of Eq. (5.6) with the conservation of mass, Eq. (5.5), and will be referred to as the *rigorous model*. In finite volume form the rigorous model is given by the two following conservation equations at each node in the bed.

Conservation of momentum for the rigorous model in discretised form

$$\left(\frac{M_{He}}{10^3 RT}\right) \tilde{p}_k^b \frac{d\tilde{v}_{B,k}}{dt} + \left(\frac{M_{He}}{10^3 RT}\right) \tilde{v}_{B,k} \frac{d\tilde{p}_k^b}{dt} = -\frac{1}{\nabla_k z} \nabla_k \left[\left(\frac{M_{He}}{10^3 RT}\right) p^b v_B |v_B| \right] - 10^5 \frac{\nabla_k p^b}{\nabla_k z} - \left[\frac{\kappa_{viscous} \mu_B}{d_{p,eqv}^2} \left(\frac{1-\epsilon_B}{\epsilon_B}\right)^2 \right] \tilde{v}_{B,k} - \left[\frac{\kappa_{kinetic} M_{He}}{10^3 RT d_{p,eqv}} \left(\frac{1-\epsilon_B}{\epsilon_B}\right) \right] \tilde{p}_k^b \tilde{v}_{B,k} |\tilde{v}_{B,k}| \quad \text{for } k = 1 \dots N_z \quad (5.8)$$

Conservation of mass for the rigorous model in discretised form

$$\left(\frac{M_{He}}{10^3 RT}\right) \frac{d\tilde{p}_k^b}{dt} = -\frac{1}{\nabla_k z} \nabla_k \left[\left(\frac{M_{He}}{10^3 RT}\right) p^b v_B \right] \quad \text{for } k = 1 \dots N_z \quad (5.9)$$

As stated in appendix A, the ∇_k operator is introduced for ease of readability only when a difference in two control boundary values surrounding node k is required. The second momentum equation of interest incorporates the steady state Ergun equation, Eq. (5.7), with the conservation of mass and will be referred to as the *approximate model*. The constitutive and conservation equations for the approximate model at each node are given by the following.

Constitutive equation for velocity using the approximate model in discretised form

$$\left[10^5 \frac{(\tilde{p}_{k+1}^b - \tilde{p}_k^b)}{(z_{k+1} - z_k)} \right] = - \left[\frac{\kappa_{viscous} \mu_B}{d_{p,eqv}^2} \left(\frac{1-\epsilon_B}{\epsilon_B}\right)^2 \right] v_{B,k+1/2} - \left[\frac{\kappa_{kinetic} M_{He}}{10^3 RT d_{p,eqv}} \left(\frac{1-\epsilon_B}{\epsilon_B}\right) \right] p_{k+1/2}^b v_{B,k+1/2} |v_{B,k+1/2}| \quad \text{for } k = 1 \dots N_z - 1 \quad (5.10)$$

Conservation of mass for the approximate model in discretised form

$$\left(\frac{M_{He}}{10^3 RT}\right) \frac{d\tilde{p}_k^b}{dt} = -\frac{1}{\nabla_k z} \nabla_k \left[\left(\frac{M_{He}}{10^3 RT}\right) p^b v_B \right] \quad \text{for } k=1 \dots N_z \quad (5.11)$$

Both the rigorous and approximate models require pressure to be found at the boundary to each control volume within the discretised bed. Spatial pressure gradients are assumed relatively smooth so that an average of the two surrounding nodal values, $p_{k+1/2}^b = (\tilde{p}_k^b + \tilde{p}_{k+1}^b)/2$, can be used to resolve pressure boundary values. However, control volume boundary velocity is found using two different methods within the rigorous and approximate models respectively.

The rigorous model requires boundary velocity to be interpolated using nodal velocities obtained from the ODE integrator. While pressure gradients are often smooth enough to invoke an averaging method, velocity gradients can be very severe at the onset of a pressure change [Serenio & Rodrigues (1993), Chahbani & Tondeur (1998)]. To minimise unwanted numerical oscillations around these sharp velocity fronts, control volume boundary velocity is estimated using the quadratic upstream interpolation scheme QUICK [Leonard (1979)] with SMART smoothing [Gaskell & Lau (1988)] outlined in §A.2 of appendix A.

While the rigorous model solves the momentum equation through the ODE integrator to determine velocity at each control volume nodal position, the approximate model calculates control volume boundary velocity directly by inverting the Ergun equation for $v_{B,k+1/2}$ using a finite difference approximation to the pressure gradient from two surrounding nodes. This eliminates the need to integrate N_z temporal velocity ODEs. This procedure renders velocity at each nodal position as irrelevant given the solution strategy requires velocity at the inlet and outlet faces of each control volume only.

5.2 Steady State Pressure Drop Coefficients κ_{viscous} and κ_{kinetic}

Before the rigorous and approximate models of §5.1.1 are compared against experimental data, the steady state coefficients κ_{viscous} and κ_{kinetic} need to be independently determined. The spherical sorbent material introduced in §4.1, Zeochem LiLSX with a nominal diameter of 1.7×10^{-3} m is used exclusively throughout this chapter. Hence physical and structural properties described in chapter 4 also carry over in the following analysis.

5.2.1 Using the LUB Apparatus for Steady State Experiments

A single steady state pressure drop experiment runs the LUB apparatus well beyond 100% breakthrough presented in Fig. 4.14 until temperature, pressure and composition no longer vary to within experimental error. Once steady state has been achieved feed flow rate, bed temperatures and differential pressure drop are recorded via the custom written QB program previously described in §4.4.2. The high and low pressure ports of the differential pressure transducer, denoted DP2 on Fig. 4.14, were directly connected to $\frac{1}{4}$ inch tube fittings located at axial positions $z = 0.86$ and $z = 1.06$ m respectively on the column wall. Feed flow rate was measured using an annubar-differential pressure transducer arrangement (denoted FM on Fig. 4.14) located after the feed line solenoid valve SV2. Under steady conditions the mass flow of gas measured at the inlet line to the column is equivalent to the mass flow through the column and exhaust lines, allowing velocity at any point to be found provided local gas phase density is known. For the entire analysis of this chapter the Servomex fast response oxygen analyser was not used.

5.2.2 Experimental Estimates of κ_{viscous} and κ_{kinetic} for Zeochem LiLSX

The experimental friction factor versus modified pellet Reynolds number obtained with different feed gas mixtures and velocities within the LUB apparatus is shown in Fig. 5.1. Figure 5.1 indicates some scatter in experimental data and 95% confidence limits for the line of best fit is also presented. In addition to the line of best fit is the Ergun (1952) line for Zeochem LiLSX using $\kappa_{\text{viscous}} = 150$ and $\kappa_{\text{kinetic}} = 1.75$, which falls within experimental bounds across the majority of operating conditions investigated. The experimental laminar coefficient ($\kappa_{\text{viscous}} = 154 \pm 14$) agrees well with the value originally proposed by Ergun (1952) while the turbulent coefficient ($\kappa_{\text{kinetic}} = 1.47 \pm 0.13$) is not drastically removed from literature estimates of 1.75 [Ergun (1952)] and 1.8 for smooth pellets [Macdonald *et al.* (1979)]. Although a crude screening method was used to determine the equivalent pellet diameter in §4.1.2, it appears relatively well justified given the experimental coefficients obtained for Zeochem LiLSX fall close to established literature values.

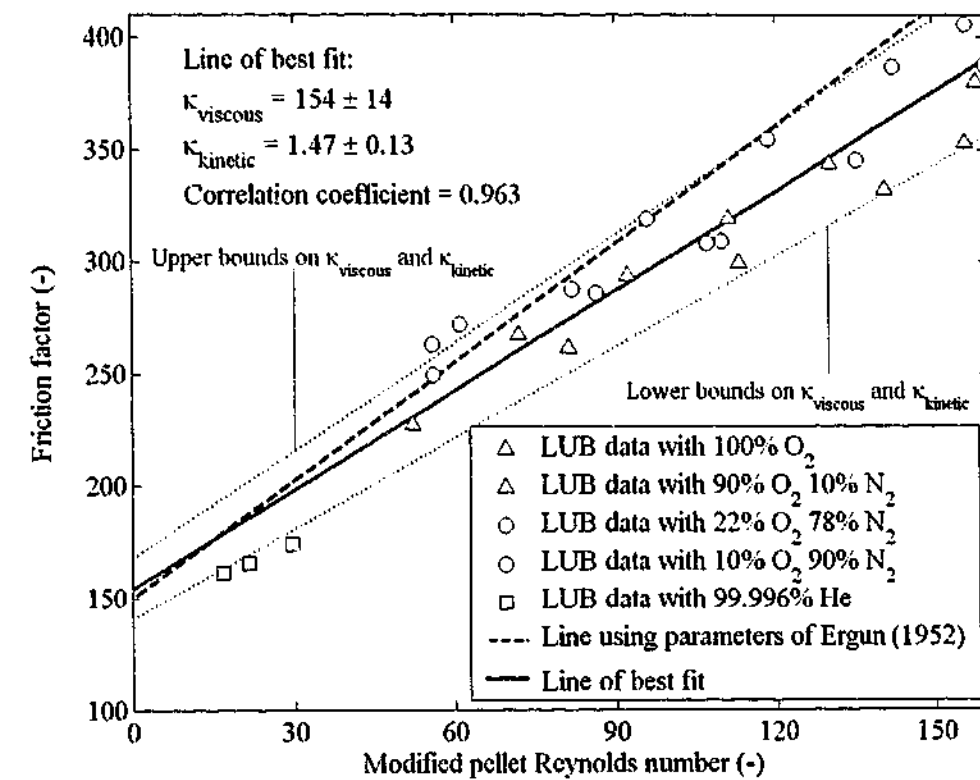


Figure 5.1: Friction factor f versus modified pellet Reynolds number $Re_p / (1 - \epsilon_B)$ for Zeochem LiLSX. Hollow and filled symbols represent experimental data points. Note that each composition presented in the legend is on a molar basis.

The small amount of scatter in experimental data is attributed to fluctuations in measured flow rate obtained from the differential pressure transducer located on the feed line annubar across various runs. Despite these fluctuations, each gas composition is well correlated with an R^2 value of 0.963. This does indicate κ_{viscous} and κ_{kinetic} are relatively independent of the flowing gas composition that would be experienced over a typical RPSA cycle, where oxygen purity can range from almost 10 mol% at the bottom of the sorbent bed during counter-current desorption to almost 100 mol% at the top of the bed during the feed plus make product step. The range of flows implicit to Fig. 5.1 covered the full range of feed line annubar-differential pressure transducer resolution and feed line choked flow conditions. However, all of these were obtained in the intermediate flow regime ($10 < Re_p < 160$) and as such truly laminar or turbulent coefficients were not obtained.

5.3 Pressure Drop During Co-Current Depressurisation

To pursue the applicability of steady state constants κ_{viscous} and κ_{kinetic} for modelling pressure drop under dynamic conditions, co-current depressurisation experiments were performed on the LUB apparatus using 99.996 mol% He as the feed gas.

5.3.1 Using the LUB Apparatus for Depressurisation Experiments

To acquire experimental profiles from the LUB column during a rapid pressure change, the experimental configuration was slightly modified from that described in chapter 4. The response time of the differential pressure transducer DP2 is around 0.5 s, which is too slow to adequately resolve pressure profiles at the onset of a valve switch. For this reason DP2 of Fig. 4.14 was replaced with two absolute pressure transducers located at axial positions $z = 0.06$ m and $z = 1.06$ m respectively. All three pressure transducers now located on the column wall (axial positions $z = 0.06$ m, $z = 1.06$ m and $z = 1.86$ m) have a response time in the order of 0.1 s, which means pressure dynamics at the onset of a valve switch can now be adequately resolved experimentally across each scan time of the QB data acquisition program. However, a sacrifice is made in accuracy when using absolute over differential pressure transducers and experimental pressure profiles are deemed accurate to 0.02 bar.

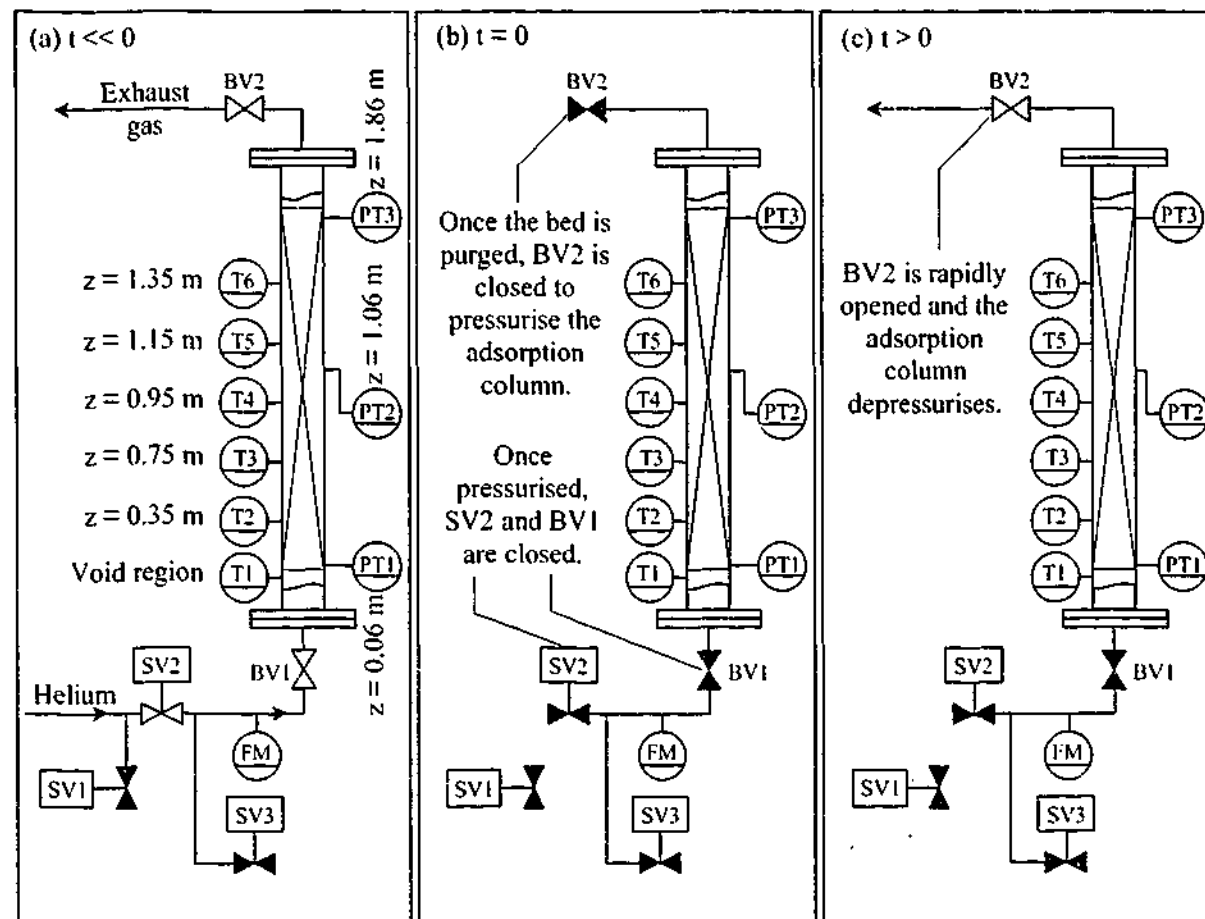


Figure 5.2: Schematic diagram outlining the procedure initiated for one co-current depressurisation experiment on the LUB apparatus. (a) The bed is initially purged with helium. (b) The adsorption column is charged with helium to initial pressure. (c) BV2 has been opened and the column depressurises to atmosphere.

To perform a co-current depressurisation run on the LUB apparatus, the packed bed was initially purged with helium for several minutes and then pressurised to approximately 1.9 bar, which is

approaching the upper limit on safe working pressure and transducer range. Once the column had reached initial pressure, ball valves BV1 and BV2 were closed to isolate the column. Once bed pressure and temperature had stabilised, the ball valve located at the top of the sorbent bed was rapidly opened manually to expose the bed to atmosphere.

Two runs were performed on the LUB apparatus to obtain different depressurisation rates. The first run installed a globe valve a small distance after the manual ball valve to provide a relatively slow depressurisation rate of two seconds from start to finish. The second run exposed the column directly to atmosphere from the outlet side of the ball valve and consequently depressurisation was complete in less than one second. A basic schematic diagram of a co-current depressurisation run, along with the location of each measuring element on the column, is shown in Fig. 5.2.

Fitting NDGNAS to an Experimental Co-Current Depressurisation Run

To compare experimental results against NDGNAS predictions, the boundary condition imposed on BV2 was a valve coefficient or K_{valve} as defined through Eqs. (4.8) and (4.9). Given this ball valve does not instantaneously go from 0 to 100% open, a linear ramp rate was imposed on the coefficient K_{valve} . The reason behind adopting a valve ramp is very similar to the procedure invoked with each EMU simulation described in §4.3.3 and the same duration of time, 0.1 s, was found to consistently reproduce experimental LUB profiles. This duration also encompasses one scan time of the QB data acquisition program. Experimental pressure profiles show a distinct change occurs across the first time scan at the onset of valve opening, providing some justification for the ramp rate of 0.1 s. Although laminar flow in a pipe was the most adequate boundary condition to use when simulating EMU runs in §4.3, all LUB depressurisation runs were best simulated using the compressible valve equation outlined by Eqs. (4.8) and (4.9). The magnitude of the valve coefficient K_{valve} imposed on NDGNAS was systematically adjusted until the numerical profile minimised a Global Sum Square Error (GSSE) with experimental data obtained at one position within the sorbent bed for each scan time beyond the valve switch.

$$\text{GSSE} = \sum_{m=1}^{\alpha_1} (p_{\text{LUB},m}^{\text{B}} - p_{\text{NDGNAS},m}^{\text{B}})^2 \quad (5.12)$$

where α_1 indicates the number of experimental pressure data points obtained at $z = 1.86$ m

The quadratic interpolation optimisation routine adopted in §4.4.3 to fit the molecular transport coefficient was also applied on these runs to optimise K_{valve} . The fastest response to a pressure change was measured at the transducer located closest to the open end, $z = 1.86$ m, so this position was designated for fitting experimental and numerical profiles. The experimental profile at $z =$

1.86 m clearly defines time zero for each depressurisation experiment between two concurrent scan times obtained from the QB data acquisition program. With absolute pressure calibrated numerically at one point in the bed, the remaining two absolute pressure transducers provide experimental validation data for NDGNAS. These experimental profiles are presented as a differential reading by subtracting the measured absolute pressure at two different points in the bed ($z = 1.06$ m and $z = 1.86$ m) from the absolute pressure reading at $z = 0.06$ m. This procedure ensures both differential readings are greater than zero for ease of discussion.

To allow a direct comparison between experimental and numerical data, the bottom and top void volumes were activated and set to the experimental values $V_{\text{bottom}} = 3.99 \times 10^{-4}$ m³ (BV1 to sorbent bed interface) and $V_{\text{top}} = 1.06 \times 10^{-4}$ m³ (sorbent bed interface to BV2). The opposing boundary condition at the closed end to the bed was a no-flow condition such that $v_{\text{valve scat}} = 0$. For each NDGNAS simulation, 100 axial nodes ($N_z = 100$) were used through the bed to adequately resolve all pressure and velocity profiles.

5.3.2 Comparison of Experimental and Numerical Pressure Profiles

Two different co-current depressurisation runs were performed on the LUB apparatus. The first run required two seconds to depressurise the column and is denoted depress run 1. The second involved a faster depressurisation rate that was complete in approximately one second, denoted depress run 2. The initial conditions for both of these runs is summarised in Table 5.1.

Table 5.1: Initial conditions obtained experimentally from the LUB apparatus for both depressurisation runs performed with 99.996 mol%He.

| Run descriptor | p^B for $t \leq 0$ (bar.a) [†] | T_B for $t \leq 0$ (K) |
|----------------|--|-----------------------------|
| Depress run 1 | 1.87 ± 0.01 | 292.7 ± 0.7 |
| Depress run 2 | 1.86 ± 0.01 | 292.6 ± 0.6 |

[†] Initial pressure across the sorbent bed is also applicable to the bottom and top void volumes.

Experimental versus numerical comparison of results from depress run 1 is presented in Fig. 5.3. Figure 5.3a compares NDGNAS predictions against experimental LUB data using the approximate model, while Fig. 5.3b plots the "Relative error in pressure". The relative error in pressure compares the absolute value of pressure obtained from the approximate model with that from the rigorous model and reports this as a percentage error. This parameter is obtained at each spatial increment in the sorbent bed across each time point from the ODE integrator, hence a three-dimensional plot is used to span the duration of depress run 1 at each axial position in the bed.

$$\text{Relative error in pressure} = \left(\frac{p_{\text{approximate}}^B - p_{\text{rigorous}}^B}{p_{\text{rigorous}}^B} \right) \times 100 \text{ at each } t \text{ and } z \text{ point} \quad (5.13)$$

Figure 5.4 compares experimental versus numerical data from depress run 2. In line with Fig. 5.3, Fig. 5.4a compares NDGNAS predictions against experimental LUB data using the approximate model, while Fig. 5.4b compares the relative error in pressure predicted numerically from the approximate and rigorous models.

It is important to point out that time zero allocated to experimental data does not necessarily correspond to a particular data point obtained from the QB data acquisition program. To determine time zero experimentally, the intersection of two straight lines was used. The first straight line is a horizontal asymptote that represents the average initial pressure of the bed before the valve is opened. The second was obtained by placing a straight line through the first two experimental data points that indicate pressure is decreasing at $z = 1.86$ m in the bed. From both plots these two points are clearly visible. The intersection of these two straight lines is designated time zero.

Figures 5.3 and 5.4 indicate the numerical fit obtained with the approximate model to experimental data at $z = 1.86$ m is very good, with a GSSE below 0.005 bar being consistently obtained for the best fit K_{valve} from NDGNAS. For depress run 1 the optimal K_{valve} obtained was 0.256 while $K_{\text{valve}} = 1.35$ for depress run 2. Experimental and numerical results for differential pressure obtained at two different points in the bed also agree to within experimental error, 0.02 bar.

Experimental profiles from depress run 1 run indicate a near-linear decrease in pressure occurs across the bed, which is well captured with the approximate model. While near-linear profiles are observed from depress run 1, depress run 2 shows a curved tail forms as the bed equilibrates to atmospheric pressure, which is also predicted numerically using the approximate model. These results show the coefficients κ_{viscous} and κ_{kinetic} obtained from steady state experiments accurately reproduce dynamic pressure profiles with helium as the feed gas. Figures 5.3b and 5.4b indicate the major difference in numerical pressure between the approximate and rigorous model resides around the open end of the bed ($z = 1.99$ m) at the onset of the top ball valve opening ($t < 0.4$). This error progressively reduces in magnitude as time increases and as one moves further away from the open end. Given the open end at the onset of a valve switch experiences the highest velocities (numerically the maximum velocity is around 1.3 and 4.1 m s⁻¹ for depress runs 1 and 2 respectively), the highest rates of momentum transfer would be expected at these locations. Both plots show this error is negative at the open end after a valve switch, indicating the steady state

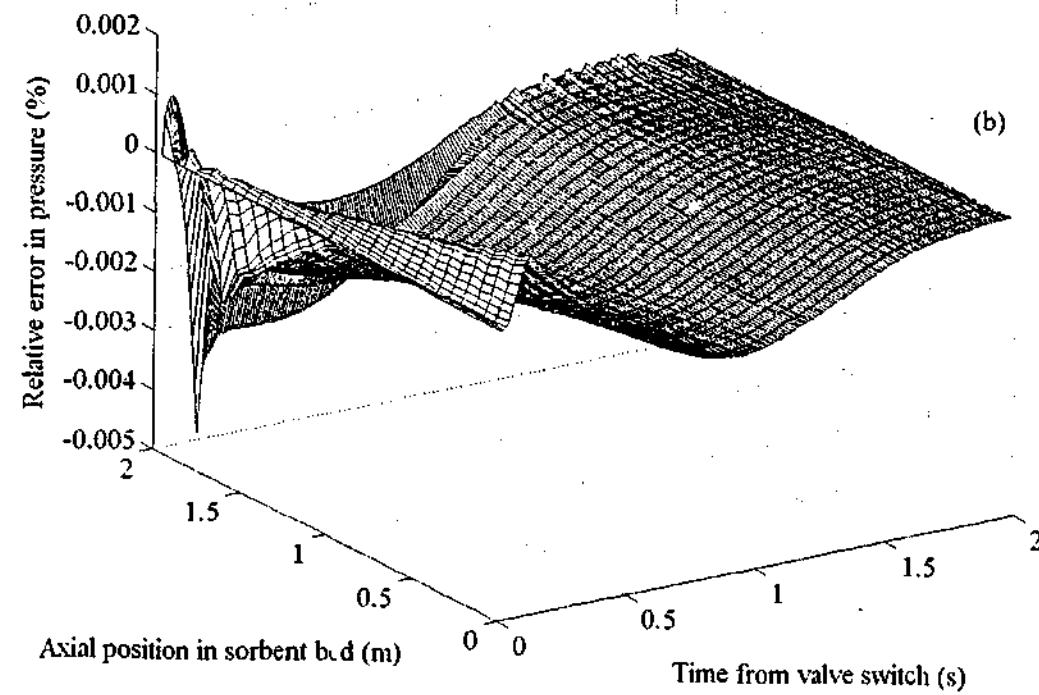
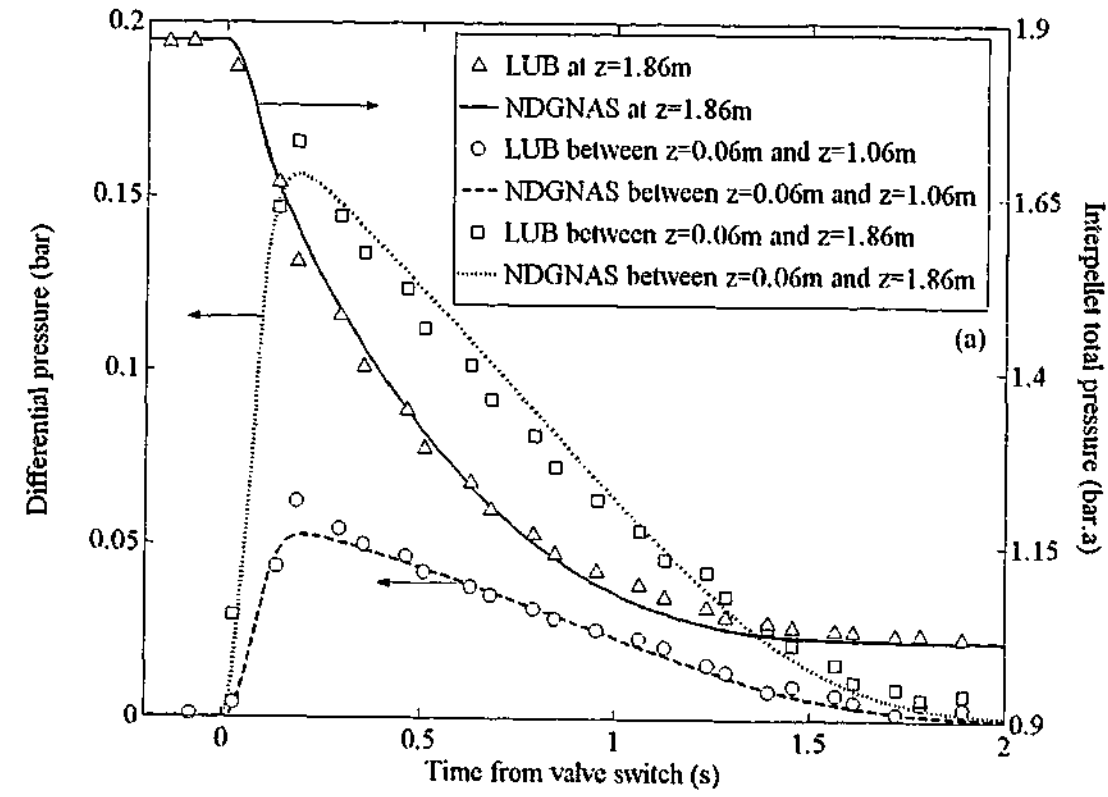


Figure 5.3: (a) Experimental and numerical pressure profiles obtained from depress run 1 using the approximate model. (b) Relative error in pressure obtained from depress run 1.

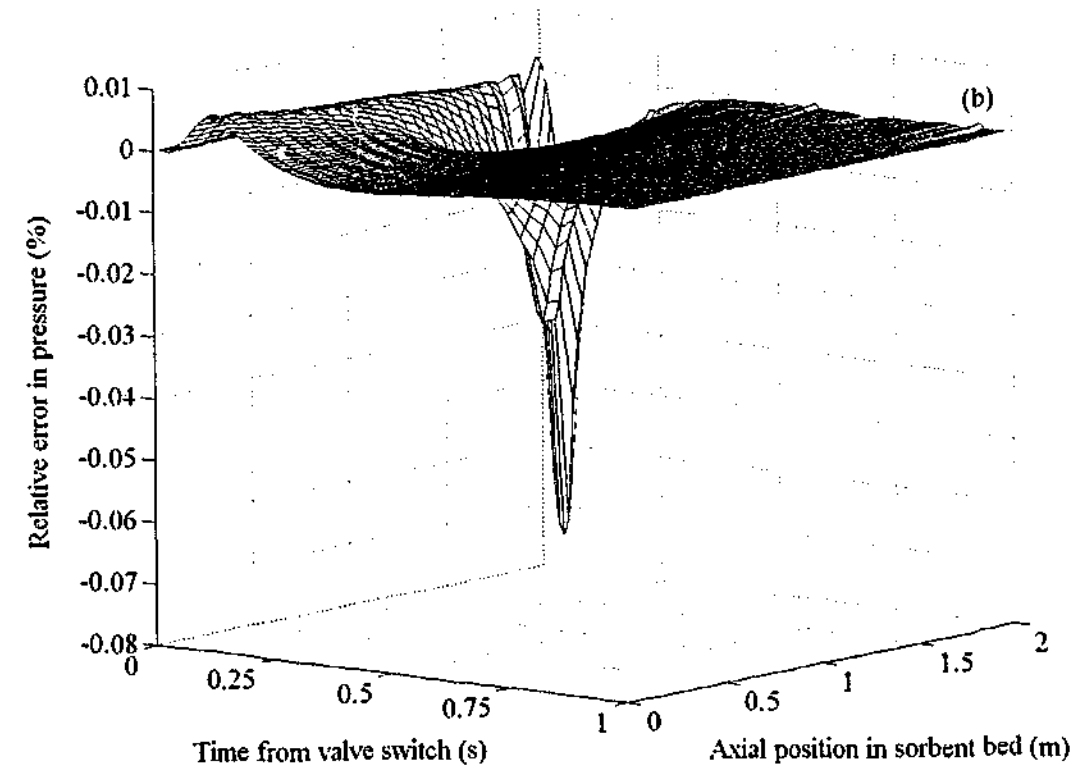
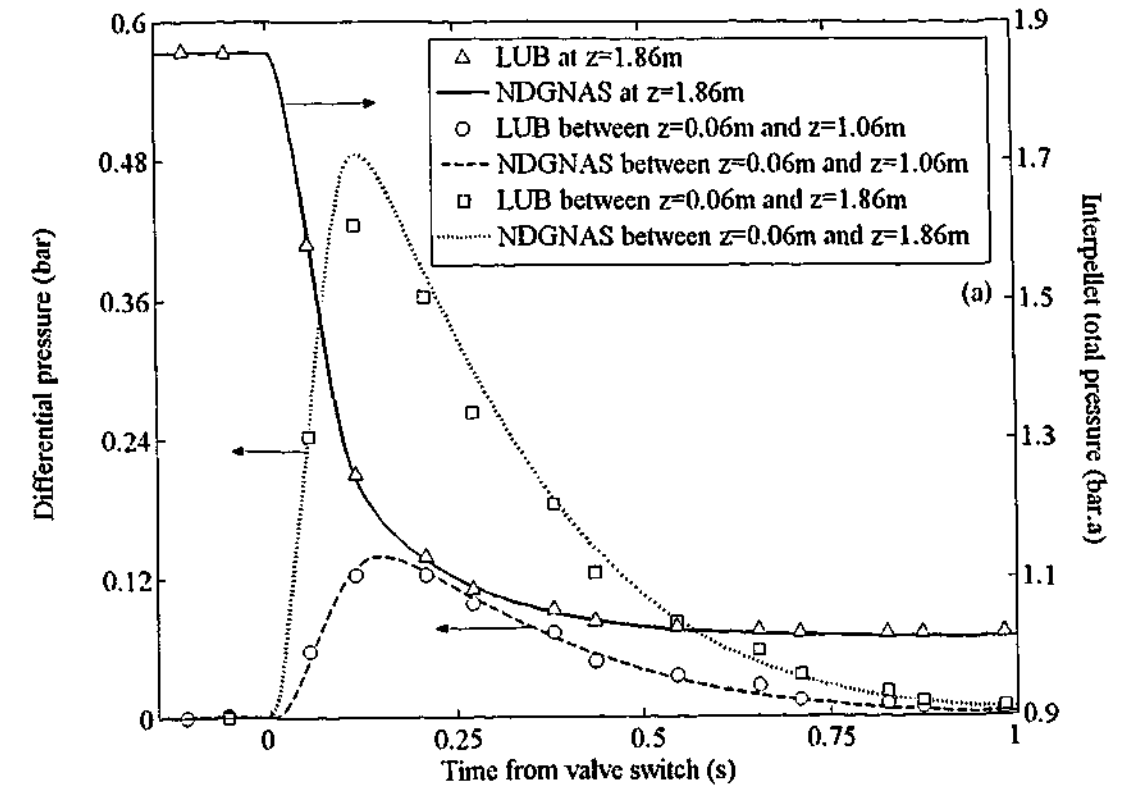


Figure 5.4: (a) Experimental and numerical pressure profiles obtained from depress run 2 using the approximate model. (b) Relative error in pressure obtained from depress run 2.

momentum equation is predicting a slightly faster rate of depressurisation in comparison to a model that includes momentum accumulation and convection. However, these errors are very small and do not exceed an absolute value of 0.1% anywhere within the bed at any point in time. In general, Figs. 5.3b and 5.4b demonstrate the steady state momentum equation accurately reproduces simulation conditions obtained with a full momentum equation for the depressurisation of a sorbent bed using steady state coefficients K_{viscous} and K_{kinetic} .

5.3.3 Validating the Isothermal Assumption

To validate the isothermal assumption for these runs, the experimental temperature profile obtained from depress run 2 is presented in Fig. 5.5. An equivalent trend is observed from depress run 1 and is deemed unnecessary to show. Fig. 5.5 shows each thermocouple recorded no change in temperature apart from the one located inside the bottom void volume. The observed temperature decrease of approximately 6 K within the void is attributed to the rapid expansion of helium in just under a second, which is not observed at any point across the packed section. The large heat capacity of the sorbent and assumed infinite heat transfer rate between the interpellet and intrapellet phases provides the energy required to counteract gas cooling by expansion, mitigating any observable temperature decrease and validating the isothermal assumption.

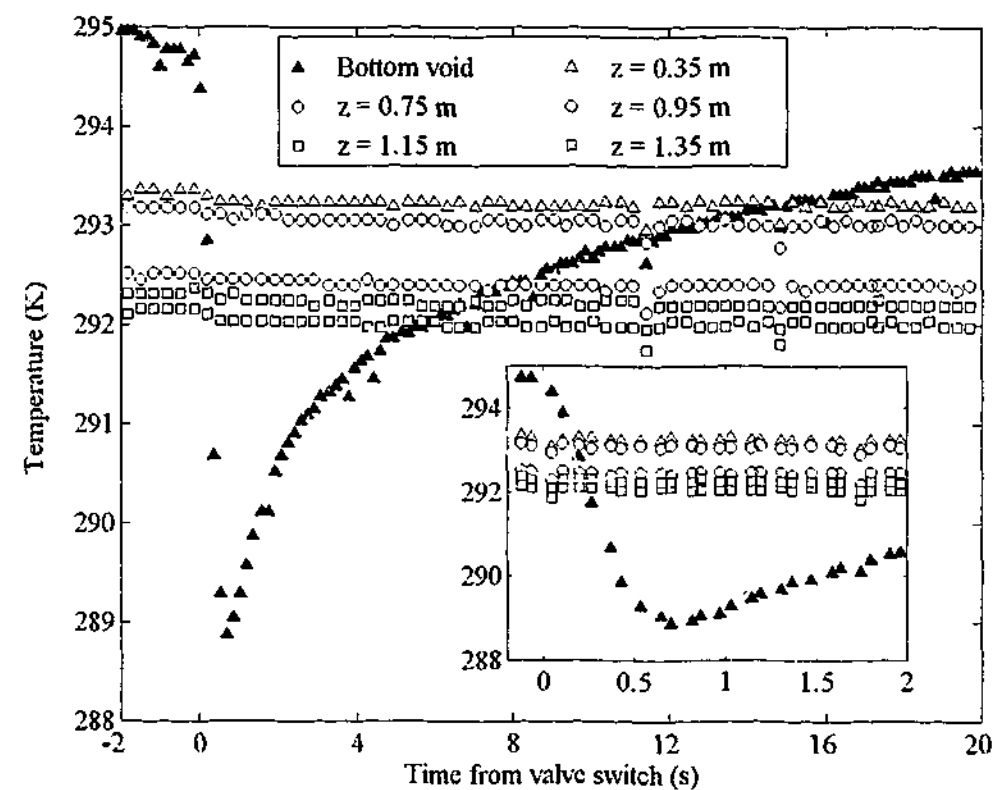


Figure 5.5: Experimental temperature profiles obtained from depress run 2.

Figure 5.5 also provides an excellent example of the rapid response time of junction exposed T-type thermocouples used within the bed. A 6 K swing in temperature is captured in less than one second inside the bottom void, with a distinct change in temperature, almost 1 K, captured across the first three scan times of the QB data acquisition program. This result does suggest that some mechanism of heat transfer within the sorbent bed is creating dispersion in experimental temperature profiles obtained from EMU and LUB runs. This issue will be taken up further in part two of this chapter.

Temperature profiles obtained from the LUB column during a breakthrough run indicate the adiabatic assumption is a very good one. Temperature measured inside the bottom void during depress run 2, however, appears to contradict the adiabatic assumption. Figure 5.4a indicates that 1 s is required to fully depressurise the adsorption column to atmospheric pressure. Experimental temperature within the void space, on the other hand, begins to increase from $t > 0.7$ s despite this region not yet having completely depressurised. The thermocouple located within the void space of the LUB column is approximately 0.06 m below the sorbent bed interface. At atmospheric pressure and 292.6 K, thermal diffusivity of helium is approximately $1.67 \times 10^{-4} \text{ m}^2 \text{ s}^{-1}$. According to Bird *et al.* (1960, p 354) this gives rise to a thermal penetration distance of $0.0517 t^{1/2}$. This implies the temperature should remain constant for approximately 1.3 s once a minimum in temperature is achieved at 0.06 m below the sorbent bed interface if thermal conduction through helium was the only mechanism by which energy was transferred through the void space once depressurisation is complete. The fact that temperature rises before the pressure transient is complete suggests thermal conduction is not the dominant mechanism of heat transfer for $t < 3$ s within the void space.

The observed temperature increase cannot be readily attributed to natural convection either given cold and more dense helium resides in the void space *below* warm (and hence less dense) helium in the sorbent bed. Natural convection arises when cool and more dense gas is situated *above* a packet of warmer and less dense gas [McCabe *et al.* (1993, pp 362-363)]. The only plausible explanation for the observed temperature increase given thermal conduction and natural convection are not suitable answers is that swirling, three dimensional flow patterns must still reside within the void space and interface to the sorbent bed for times slightly beyond 1 s. Although pressure fluctuations at this order of magnitude are too small to measure with absolute pressure transducers, very small pressure fluctuations and hence flow patterns may still be present within the bottom void space and warm gas at the interface to the sorbent bed is mixing with cool gas from the void space. Figure 5.5 indicates a distinct change in the temperature gradient occurs for $t > 3$ s after the valve switch. The fact that temperature begins to increase before the column has completely depressurised further validates this proposition.

To capture these effects mathematically would require a detailed three-dimensional model to be developed that rigorously captures these complicated flow patterns. While this is well beyond the scope of research being pursued in this chapter, it is worth noting that similar observations were made with respect to temperature profiles measured during blank EMU runs from §4.3.4. Although temperature transients within the void space indicate more complex flow dynamics arise within the column, the use of an isothermal, well-mixed CSTR for the void space and steady state momentum equation across the sorbent bed (NDGNAS) suitably captures experimental pressure profiles obtained from the LUB unit.

The mechanisms that dictate a rapid depressurisation experiment, and the subsequent discussion of the last few pages, would also hold during a rapid pressurisation experiment. Although experimental data for pressurisation has not been presented, Baron (1993) obtained experimental pressure profiles across a sorbent bed over a final:initial pressure window of 2:1 bar.a using helium and found excellent agreement using the approximate model and experimentally determined steady state coefficients κ_{viscous} and κ_{kinetic} over a pressurisation time of 3 s. The procedure adopted in this chapter is similar to that of Baron (1993) and so the trends observed here for depressurisation experiments would equivalently hold over a pressurisation experiment. While steady state estimates on κ_{viscous} and κ_{kinetic} obtained in this study agree well with established literature values in addition to predicting dynamic pressure transients, similar analyses performed by Crittenden *et al.* (1994) and Horváth *et al.* (1997) reached different conclusions.

Crittenden *et al.* (1994) found the coefficients obtained from steady state experiments could not adequately simulate dynamic experiments under non-adsorbing conditions when:

- i. step changes in boundary conditions were imposed numerically at $z = 0$, and
- ii. a curve fitted pressure profile obtained at $z = 0.5$ m was imposed numerically.

They go on to say that viscous and kinetic constants ascertained from experiments similar to those performed in §5.2 "is unreliable because it is not fundamentally sound to employ a steady-state pressure drop equation to what is essentially a dynamic situation". Results obtained in part one of this chapter suggest otherwise, indicating the experimental procedure of §5.2 is valid provided the material is well characterised and packing arrangement is not significantly altered during the course of each experiment. Pressure swings as high as 7 bar were performed in the space of 2 s by Crittenden *et al.* (1994), highlighting the potential for bed unsettling during their experiments.

Horváth *et al.* (1997) found $\kappa_{\text{viscous}} = 212\text{-}218$ and $\kappa_{\text{kinetic}} = 2.2$ for a range of gas mixtures over inert and adsorbing materials under steady state conditions, while κ_{viscous} had to be increased beyond 220 to match experimental data under dynamic conditions. Horváth *et al.* (1997) also

found poor agreement numerically when $d_{p,\text{eqv}} > 0.2 \times 10^{-3}$ m. Although their discussion was relatively brief a suitable explanation for poor agreement with $d_{p,\text{eqv}} > 0.2 \times 10^{-3}$ m was not resolved, which appears to be at odds with findings obtained in part one of this chapter. The results of Horváth *et al.* (1997) indicate one of two possibilities; either their packing material was not well characterised or bed unsettling occurred during the course of experiments.

Part II. Momentum Equation for an Adsorbing Bed of Porous Pellets

The subject of pressure drop through a packed bed of adsorbing material has received considerable attention throughout the published literature. The basic equations that describe adsorption and interpellet pressure drop have been introduced previously, so the following discussion shall progress directly into a review of the relevant literature.

5.4 Previous Studies that Consider Pressure Drop and Adsorption

Part one of this chapter revealed the steady state momentum equation provides a very good representation of pressure dynamics under non-steady state conditions, a conclusion that has also been obtained by other researchers. For this reason the steady state momentum equation has been widely used to describe pressure drop across a packed bed of sorbent pellets. Two different forms of the steady state momentum equation are commonly used. The first relates to the laminar regime, often termed Darcy's law, while the second spans both the laminar and turbulent regimes and is termed the Ergun equation.

5.4.1 Adsorption Models that Incorporate Darcy's Law

The simplicity of Darcy's law, which imposes a linear relationship between velocity and pressure drop, has allowed bed profiles during certain steps of a PSA cycle to be solved analytically subject to a certain number of limiting conditions.

Carleton *et al.* (1978) examined the response of a packed bed that is injected with a pulse of an adsorbing component at time zero using moments analysis. Parameters related to the equilibrium isotherm for a linear, isothermal system could be obtained in the presence of a finite pressure gradient from the first moment, implying higher throughputs are possible with no loss of accuracy in parameter estimation or increase in computational difficulty. Experimentally obtained equilibrium parameters for propane, butane, pentane and hexane adsorption on H-type alumina pellets were reported. Sundaram & Wankat (1988) extended the ILE models of Chan *et al.* (1981), Fernandez & Kenney (1983) and Knaebel & Hill (1985) during the pressurisation and

depressurisation steps of a PSA cycle to account for axial pressure gradients using Darcy's law by linearising the overall mass balance. The method of characteristics, in conjunction with the linearised expression for pressure, was used to resolve composition profiles. Scott (1991) considered pressurisation and depressurisation of a sorbent bed from uniform initial conditions with a binary gas mixture under isothermal, plug flow conditions for an assumed infinite bed to obtain a similarity solution for pressure and composition profiles. Andrews & Scott (2000) extended the study of Scott (1991) for the pressurisation step to a multicomponent gas mixture.

To extend the validity of an adsorption model to include additional process effects such as bulk adsorption and non-isothermal behaviour, however, does not readily lend itself to an analytical solution. For this reason numerical adsorption simulators that invoke pressure drop using Darcy's law have also been developed.

Zhong *et al.* (1992) developed a non-isothermal model for single component pressurisation with intrapellet micropore and macropore diffusion resistances to quantify helium (inert) and methanol (adsorbing) profiles over a packed bed of activated carbon. Arumugam *et al.* (1999) compared experimental data for the bulk adsorption of propane on 5A molecular sieve zeolite against ADSIM predictions and found significant pressure transients occurred when a bulk component was adsorbed from the feed stream. Isothermal, plug flow conditions were imposed on ADSIM. Arumugam & Wankat (1998) and Byrne & Wankat (2000) developed a cells-in-series model to characterise flow through a packed bed for adsorption and adsorptive reactors using the SPEEDUP language of Aspen Technology Inc. Compressible laminar flow was assumed in the hypothetical pipe sections connecting each well-mixed cell to simulate pressure drop in the axial direction.

Darcy's law has also been used in several numerical models that describe the performance of RPSA and Rapid Pressure Swing Reactors [Turnock & Kadlec (1971), Kowler & Kadlec (1972), Vaporciyan & Kadlec (1987,1989), Lee & Kadlec (1988), Kenney (1989), Hart & Thomas (1991), Alpay *et al.* (1994), Oh & Pantelides (1996), Serbezov & Sotirchos (1997b), Cheng *et al.* (1998), Nilchan & Pantelides (1998), Ko & Moon (2000, 2002), Choong *et al.* (2002), Huang & Chou (2003)].

5.4.2 Adsorption Models that Incorporate the Ergun Equation

While Darcy's law has been used to describe interpellet pressure drop under PSA and RPSA operating conditions, the assumption of laminar flow is not always valid and the need to incorporate the transitional and turbulent regimes is often required. Several studies have been undertaken that address the limitations of Darcy's law with respect to the Ergun equation.

Lu *et al.* (1993b) investigated the dynamic behaviour of a column subjected to pressurisation and depressurisation with a mixture of one inert and one adsorbing component. Simulation results indicate Darcy's law estimates pressurisation times that are erroneously faster than the Ergun equation when flow conditions outside the laminar regime arise. Yang *et al.* (1998) examined the pressurisation and depressurisation of a packed bed of 5A using an adsorbing mixture of 70 mol% H_2 -30 mol% CO_2 , also concluding that Darcy's law will predict a faster rate of pressurisation in comparison to the Ergun equation.

Unlike Darcy's law, the Ergun equation now provides a non-linear relationship between pressure drop and velocity due to the presence of velocity squared on the kinetic term, making it difficult to provide an analytical solution for bed profiles. Scott (1993) solved the response of a packed bed subject to changes in feed conditions for a trace component adsorbing from an inert carrier, where the inert carrier is subject to pressure and velocity variations according to the Ergun equation. The method of characteristics was applied to an isothermal system with Langmuir and linear isotherms to derive expressions for bed profiles and breakthrough time.

While few studies could be found that analytically solve bed profiles using the Ergun equation, a large number of numerical models have been proposed that incorporate the Ergun equation and adsorption.

Doong & Yang (1988) compared literature data on PSA and RPSA against a non-isothermal process model that incorporates the Ergun equation and found pressure drop is an important aspect of the model to maintain when quantifying process performance. Buzanowski *et al.* (1989) examined the impact of pressure drop on composition profiles for a 2.01 mol% O_2 -97.99 mol%He feed mixture during the adsorption and desorption steps of a cyclic PSA process. Small bead 13X zeolite was used with high feed gas flow rates to maintain near-isothermal behaviour while minimising intrapellet mass transfer resistance, interpellet axial dispersion and external film mass transfer resistance. Experimental and numerical results revealed composition profiles under these conditions broaden during the adsorption step due to increasing flow velocity as a result of pressure drop. On desorption the composition waves sharpened, attributed to the expanded volume of desorbed gas improving desorption along the column. Kikkinides & Yang (1993) used the simplified analytical expression of Buzanowski *et al.* (1989) in addition to a full numerical model to compare breakthrough profiles of oxygen-helium mixtures over 13X zeolite pellets under isothermal and adiabatic conditions.

Lu *et al.* (1992) examined the pressurisation and depressurisation steps of a PSA cycle with a binary feed mixture (one inert, one adsorbing) under isothermal conditions using three different

intrapellet models: the first imposed diffusion plus viscous flow, the second diffusion only and the third imposed ILE. Results show intrapellet resistance to mass transfer increases pressurisation and depressurisation times in relation to ILE, which results in earlier breakthrough on subsequent adsorption steps and increases the amount of purge gas required after depressurisation. Lu *et al.* (1993a) extended this study to assess the importance of these aforementioned intrapellet mass transfer models on an isothermal, one-bed, three-step PSA process. It was found that ILE imposes an upper limit on process performance and the diffusion only model a lower bound, with results obtained from the diffusion plus viscous flow model lying somewhere in between due to an increase in intrapellet mass transfer by viscous flow.

Crittenden *et al.* (1994) examined pressurisation and depressurisation profiles of oxygen and nitrogen over a bed of 5A zeolite, while Crittenden *et al.* (1995) extended this analysis to also consider temperature and composition profiles. Suzuki *et al.* (1996) and Horváth & Suzuki (1998) examined an Ultra Rapid PSA (URPSA) process for oxygen enrichment from air over 5A zeolite. Although bed length was just 0.035 m long, total cycle times in the order of 1 s were imposed and pressure profiles obtained with the Ergun equation matched experimental responses well. Suzuki *et al.* (1997) examined the URPSA process for carbon dioxide recovery from stack gas using a similar model to that of Suzuki *et al.* (1996). The Ergun equation has also been used by Jianyu & Zhenhua (1990), Alpay *et al.* (1993), Baron (1993), Foeth *et al.* (1995), Murray (1996), Betlem *et al.* (1998) and Choong (2000) for the numerical simulation of an RPSA cycle; and Sheikh *et al.* (2001) for a Rapid Pressure Swing Reactor.

Although the previous discussion is not a complete treatise on the subject of pressure drop in the presence of adsorption, the following observations can be made from existing literature information for any numerical model that is applied to experimental data, such as NDGNAS:

- i. Failure to model pressure drop within a system that exhibits finite pressure gradients will delay the point of breakthrough and influence predicted temperature and composition profiles,
- ii. Darcy's law will predict erroneously fast rates of bed pressurisation/depressurisation in relation to the Ergun equation when flow is not within the laminar regime, and
- iii. The Ergun equation has been shown to adequately represent the dynamics of an adsorption column in situations where non-steady flow regimes arise.

5.5 Pressure Drop During Co-Current Depressurisation

Section 5.3 compared experimental and numerical pressure profiles obtained from the LUB apparatus and NDGNAS respectively for co-current depressurisation of a sorbent bed initially filled with helium at a pressure close to 1.9 bar.a. These helium experiments were repeated using oxygen and air as the feed gas to the LUB apparatus. Subsequently, the discussion of §5.3 related to LUB column operation, arrangement, data acquisition and NDGNAS fitting carries over here. These two additional runs are denoted depress runs 3 and 4 respectively and are summarised in Table 5.2. When the column is initially pressurised, the void volumes undergo compression and hence increase in temperature. Also, adsorption occurs and the sorbent bed increases in temperature. This is why void volume temperatures do not generally start at the average conditions of the sorbent bed. Given temperature was not measured in the top void, it was assumed that temperature measured in the bottom void is identical to that in the top void for NDGNAS.

Table 5.2: Initial conditions obtained experimentally from the LUB apparatus for both depressurisation runs performed with an adsorbing gas.

| Run descriptor | Feed gas | p^B for $t \leq 0$ (bar.a) [†] | T_B for $t \leq 0$ (K) | T_{bottom} for $t \leq 0$ (K) |
|----------------|----------|--|-----------------------------|---|
| Depress run 3 | Oxygen | 1.95 ± 0.01 | 294.9 ± 0.5 | 295.5 ± 0.5 |
| Depress run 4 | Air | 1.95 ± 0.01 | 300.8 ± 0.8 | 295.5 ± 0.5 |

[†] Initial pressure across the sorbent bed is also applicable to the bottom and top void volumes.

Now that mass transfer is present from the intrapellet to interpellet phase as pressure decreases, the DPM is activated within NDGNAS using all three intrapellet transport coefficients C_K , C_v and C_m found in chapter 4. NDGNAS still discretises the sorbent bed using 100 control volumes ($N_z = 100$), but now the sorbent pellet at each axial control volume is discretised using 5 radial nodes ($N_r = 5$). No composition gradients form during depress run 3 as pure oxygen is used, while a dispersed composition wave will form during depress run 3 given the favourable shape of the equilibrium isotherm for Zeochem LiLSX. Using this level of discretisation gives $N_{eq} = 814$ and 1,418 for depress runs 3 and 4 respectively, which is assumed adequate to resolve all profiles considered in part two of this chapter. NDGNAS exclusively considers the steady state momentum equation in the presence of adsorption and no comparison is made here with results obtained using a full momentum balance.

For all NDGNAS simulations performed in this section, the non-isothermal option with $T_B = T_P$ was activated. Given an ideal gas is expanded within the bottom and top void spaces inside a column that operates at conditions close to adiabatic, artificially large heat transfer coefficients between the gas and column wall had to be used in order to match the void space experimental

temperature profile. This procedure was required to avoid temperature depressions approaching the analytical result $T_{\text{initial}} \left(p_{\text{final}}^n / p_{\text{initial}}^n \right)^{(1-\gamma)/\gamma}$ being achieved numerically, where $\gamma = c_p / (c_p - 10^5 R)$ [Bird *et al.* (1960, p 337)]. This procedure, discussed at length for blank EMU runs in §4.3.4 had minimal impact on bed profiles for all values of $h_{\text{bottom,W}}$ and $h_{\text{top,W}}$ considered in this section. Given experimental temperature was not measured in the top void space, the value obtained for $h_{\text{bottom,W}}$ was applied directly to $h_{\text{top,W}}$.

The first set of pressure profiles, Fig. 5.6, compares experimental data against NDGNAS predictions from depress run 3. The analysis technique applied in §5.3 was also used on depress run 3 with an optimal value of $K_{\text{valve}} = 1.25$ obtained. In fact, outside of K_{valve} that is automatically adjusted to minimise the GSSE of Eq. (5.12) at $z = 1.86$ m, there are no adjustable parameters left within NDGNAS and both depress runs 3 and 4 allow an independent assessment of the Ergun equation to be made under dynamic, adsorbing conditions using experimentally calibrated values for κ_{viscous} and κ_{kinetic} . NDGNAS predictions agree very well with experimental LUB profiles obtained from the two differential readings obtained across the bed. For this experiment ball valve BV2 was directly exposed to atmosphere and as such is equivalent to the experimental arrangement of depress run 2.

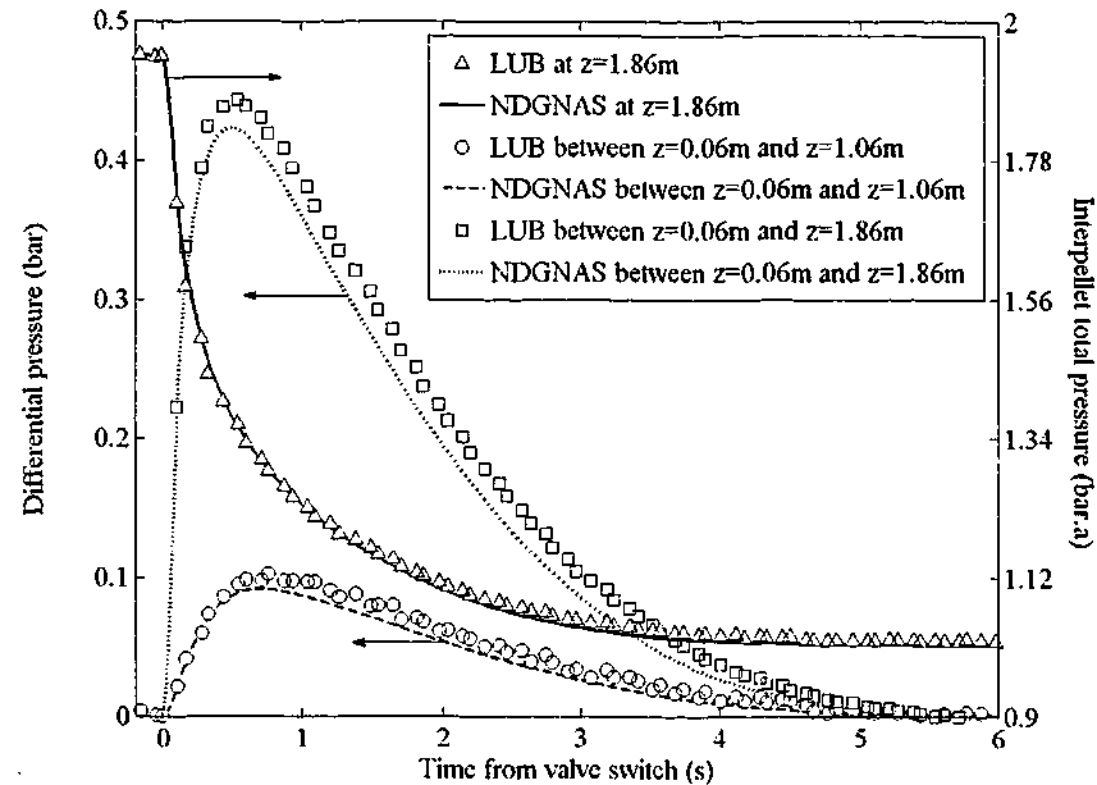


Figure 5.6: Experimental and numerical pressure profiles obtained from depress run 3.

What is immediately obvious from Fig. 5.6 in comparison to depress run 2 (Fig. 5.4a) is the time required to depressurise the column, almost 6 s, in the presence of a component that is initially adsorbed. An inventory of the adsorption column at time zero from NDGNAS reveals 68% of the oxygen is initially contained in the adsorbed phase. As pressure decreases and gas is swept from the interpellet phase to atmosphere, gas desorbs and replaces interpellet gas being swept from the column. Given the interpellet phase is being replenished with oxygen from the pellets, bed pressure consequently takes longer to reach atmospheric conditions. It is also worth noting the final valve coefficient fitted to experimental data for depress run 3 ($K_{\text{valve}} = 1.25$) is similar to the equivalent value fitted to depress run 2 of $K_{\text{valve}} = 1.35$, indicating valve dynamics are similar across both runs. From this NDGNAS is capturing bed dynamics well for a single component depressurisation experiment in the presence or absence of adsorption.

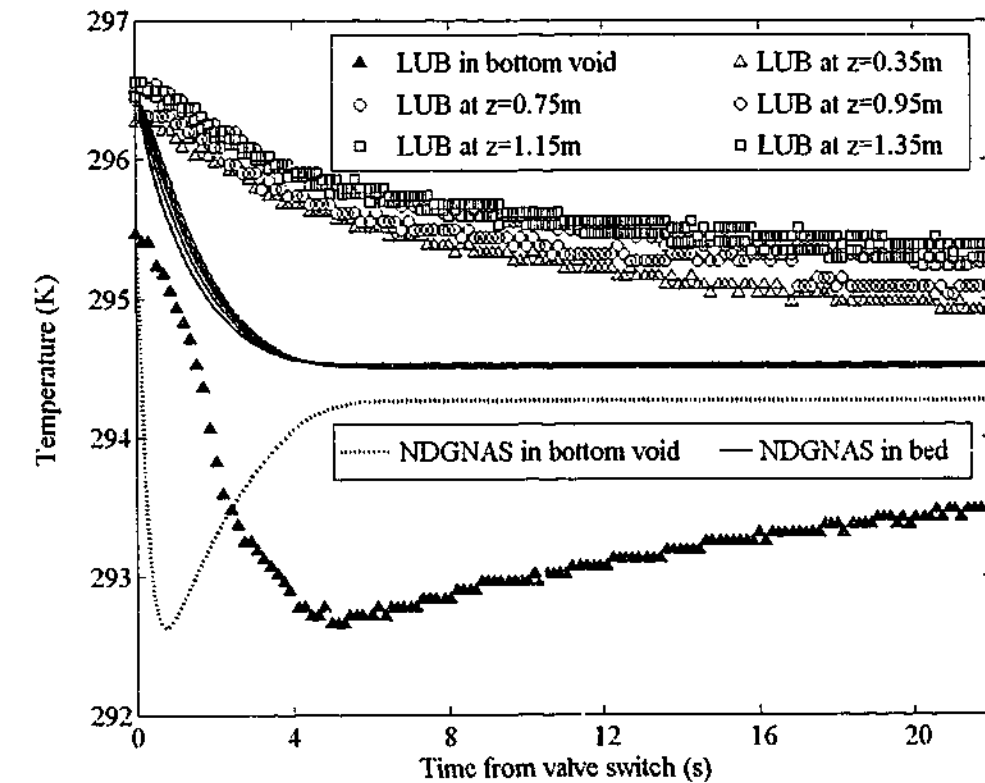


Figure 5.7: Experimental and numerical temperature profiles obtained from depress run 3.

With good agreement observed between experimental and numerical pressure profiles, a similar comparison is made between experimental and numerical temperature profiles (Fig. 5.7). Unlike pressure profiles, however, the transient temperature response predicted numerically is significantly faster than the experimental response. Numerical temperature profiles follow the pressure transient through the assumption of an equivalent inter-intrapellet temperature, so NDGNAS reaches thermal equilibrium after 6 s as the pressure approaches atmospheric conditions.

The expansion of oxygen in the bottom void results in an experimental temperature depression that also follows the pressure transient, again highlighting the fact that thermocouple response time is not in question. Note the numerical temperature in the bottom void reaches a minimum much earlier than the experimental response due to the artificial nature of heat transfer between the column wall and bottom void gas to mitigate large temperature depressions. To match the absolute value of temperature obtained from the LUB apparatus, $h_{\text{bottom,w}}$ had to be set to $283 \text{ W m}^{-2} \text{ K}^{-1}$. Although data acquisition was prematurely stopped before 40 s had elapsed experimentally, one can see that after 22 s the experimental temperature profile (Fig. 5.7) has approached 0.5 K of the numerical result and the asymptotic nature of the transient response suggests temperature will not decrease by much more than 1 K at steady conditions. This indicates the overall change in temperature and hence adsorbed phase loading is well predicted but the transient response is in error. The next set of profiles relate to depress run 3. Experimental pressure profiles are compared against NDGNAS predictions in Fig. 5.8 while experimental and numerical temperature profiles are compared in Fig. 5.9.

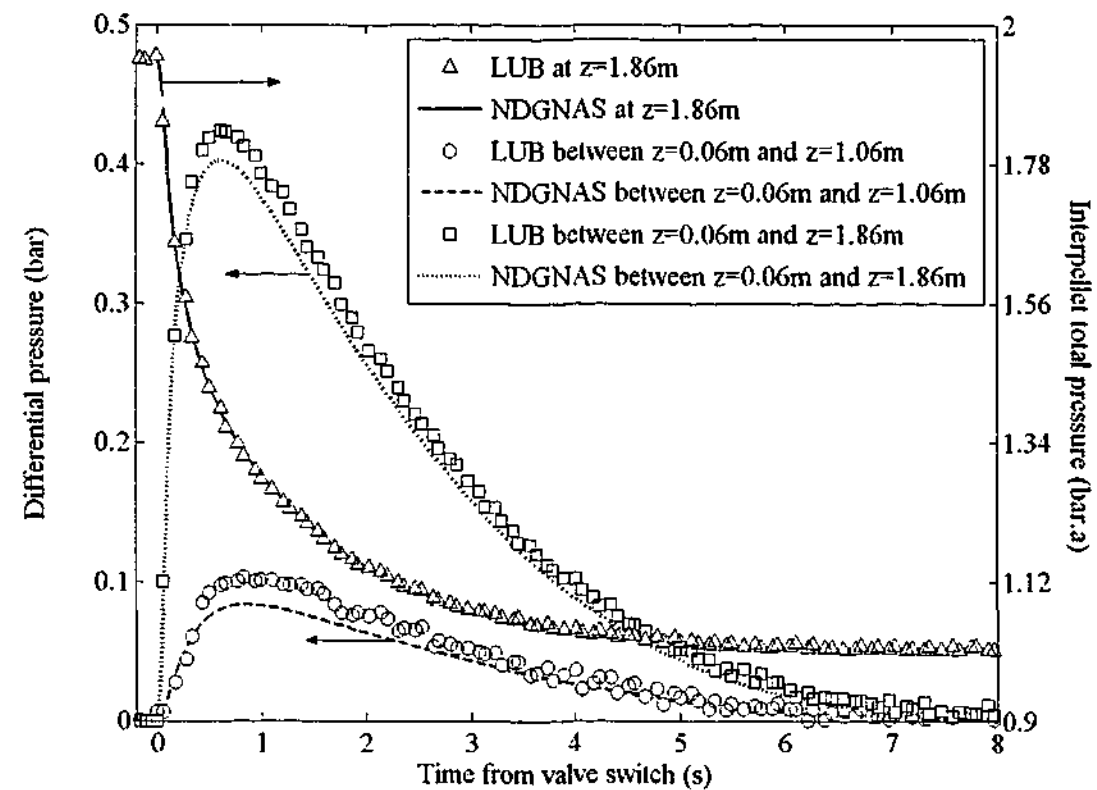


Figure 5.8: Experimental and numerical pressure profiles obtained from depress run 4.

Figure 5.8 indicates pressure profiles are generally in good agreement across the bed with small mismatch observed between NDGNAS and LUB data at times around 1 s after valve opening. It is worth pointing out that depress run 4 was performed several months after depress runs 1 through 3, with the LUB column packed using a fresh batch of regenerated Zeochem LiLSX. It is an encouraging result to find numerical data, which assumes the physical properties of the packed bed

are identical across all depress runs, matches experimental data very well from a separate packing of the same material. The only obvious difference between the results of this run and those from the other three depress runs is the optimised K_{valve} coefficient obtained numerically. Although this run is similar in nature to depress runs 2 and 3, the K_{valve} coefficient obtained here was 0.745, attributed to small differences in flow geometries and packing arrangement that may have manifested in this and the previous set of LUB experiments. While pressure profiles are in general agreement across depress run 4, the temperature profiles again are not (Fig. 5.9).

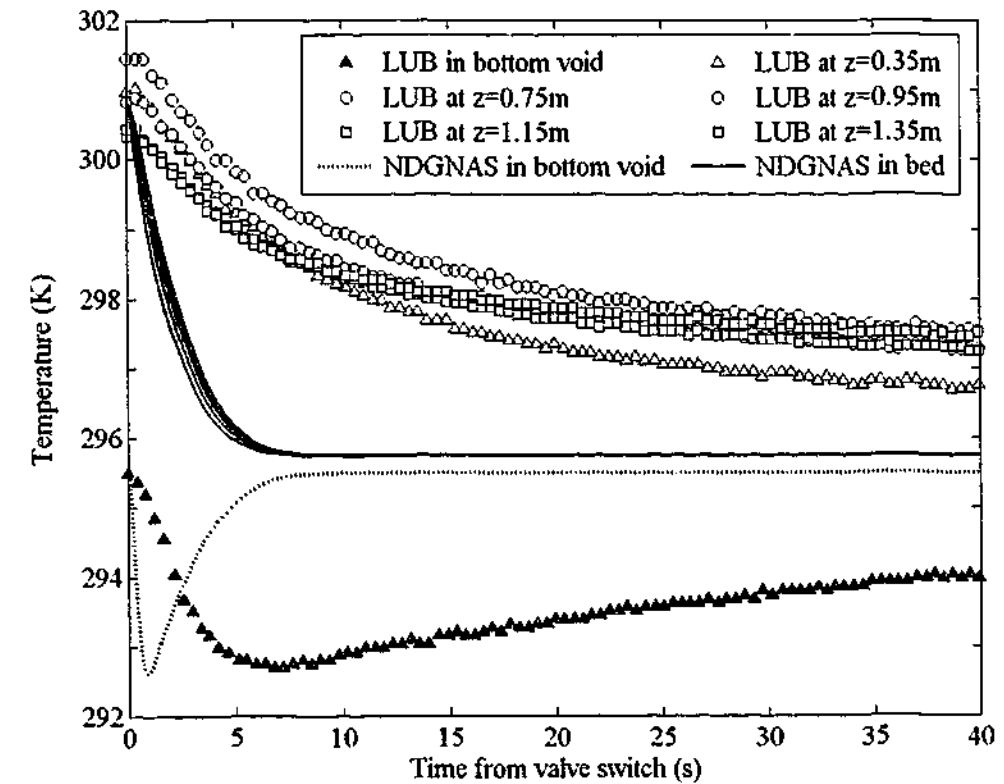


Figure 5.9: Experimental and numerical temperature profiles obtained from depress run 4.

Differences between the final and initial temperatures of the sorbent bed generally agree to within 1 K once the column reaches steady state, a favourable result given the regeneration procedure for Zeochem LiLSX on this batch may not have been as complete as that achieved on the first packing of the column. However, as found for all operating conditions considered thus far where the numerical temperature transient is rapid, the experimental response is in error. Approximately 50 s is required for experimental temperature profiles to steady out. Temperature measured inside the bottom void follows the pressure transient with the cooling due to expansion complete in 8 to 9 s, showing response time of T-type junction exposed thermocouples in the absence of sorbent will consistently follow the pressure transient. To match the experimental minima in temperature measured experimentally, an artificial gas to wall heat transfer coefficient of $133 \text{ W m}^{-2} \text{ K}^{-1}$ was applied to $h_{\text{bottom,w}}$. This issue of thermocouple response, first revealed in chapter 4, shall be taken up in the next section given all LUB runs have now been presented.

5.6 Pressure Drop During Breakthrough Runs

NDGNAS predictions for pressure drop across a sorbent bed over a single depressurisation experiment are in good agreement with experimental data. Now, the issue of pressure drop in the presence of a MTZ travelling through the bed is addressed during a breakthrough run. Each graph shown in this section was obtained during three of the six breakthrough runs described in §4.4. Unlike their depressurisation counterparts, pressure drop during a breakthrough run was measured using a true differential pressure transducer (DP2 depicted in Fig. 4.14) located between axial positions $z = 0.86$ m and $z = 1.06$ m. One experimental response from each of the three compositions is presented and these graphs, Figs. 5.10 through 5.12, relate to breakthrough runs 1, 3 and 6 from Table 4.9 respectively. Qualitatively similar plots are observed from breakthrough runs 2, 4 and 5 in relation to breakthrough runs 1, 3 and 6 respectively and are not shown for brevity.

Results with low nitrogen feed composition, gas mixture A of Fig. 5.10, indicate pressure drop is well captured numerically in relation to the experimental trend across the MTZ. Although some noise is present in the experimental response of DP2, a slight increase in bed pressure drop of approximately 0.001 bar is observed as the MTZ moves through this region, which is in good agreement numerically. Experimental results from Table 4.11 indicate the MTZ for breakthrough run 1 was moving through the bed with a velocity of 0.0145 m s^{-1} . From this the MTZ would take approximately 14 s to pass the high and low pressure ports of DP2. Experimental and numerical data from Fig. 5.10 generally agree with this estimate, which does not take into account the actual width of the MTZ that could potentially increase the time for this transient.

With an increase in feed composition to 20 mol% N_2 , gas mixture B of Fig. 5.11, a significant increase in pressure drop is observed before and after the MTZ has arrived, which again is well captured through NDGNAS. For this run the MTZ was moving with a velocity of 0.0183 m s^{-1} so the MTZ would pass DP2 in approximately 11 s. Again, this result agrees well with experimental and numerical results obtained in Fig. 5.11. With a further increase in feed composition to around 78 mol% N_2 , gas mixture C of Fig. 5.12, the pressure drop across 0.2 m of packing increases by more than double that measured/predicted before and after the MTZ has passed this region of the bed. For breakthrough run 6 the MTZ was experimentally determined to be traveling at a speed of 0.0288 m s^{-1} , which means it will pass DP2 in approximately 7 s. Again, the time to complete the transient in pressure drop is similar to that observed experimentally and numerically, suggesting constant pattern behaviour has been achieved before axial position $z = 0.86$ m across all three feed compositions investigated in the LUB apparatus.

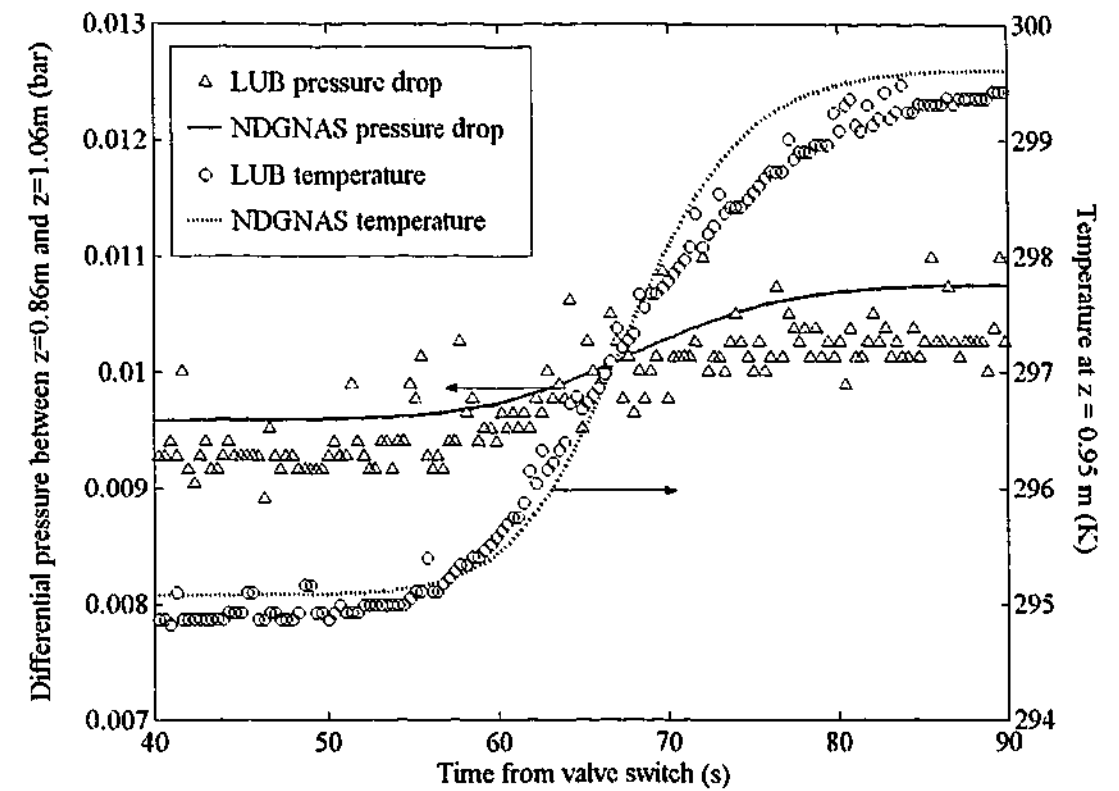


Figure 5.10: Experimental and numerical pressure drop and temperature profiles from breakthrough run 1 using gas mixture A.

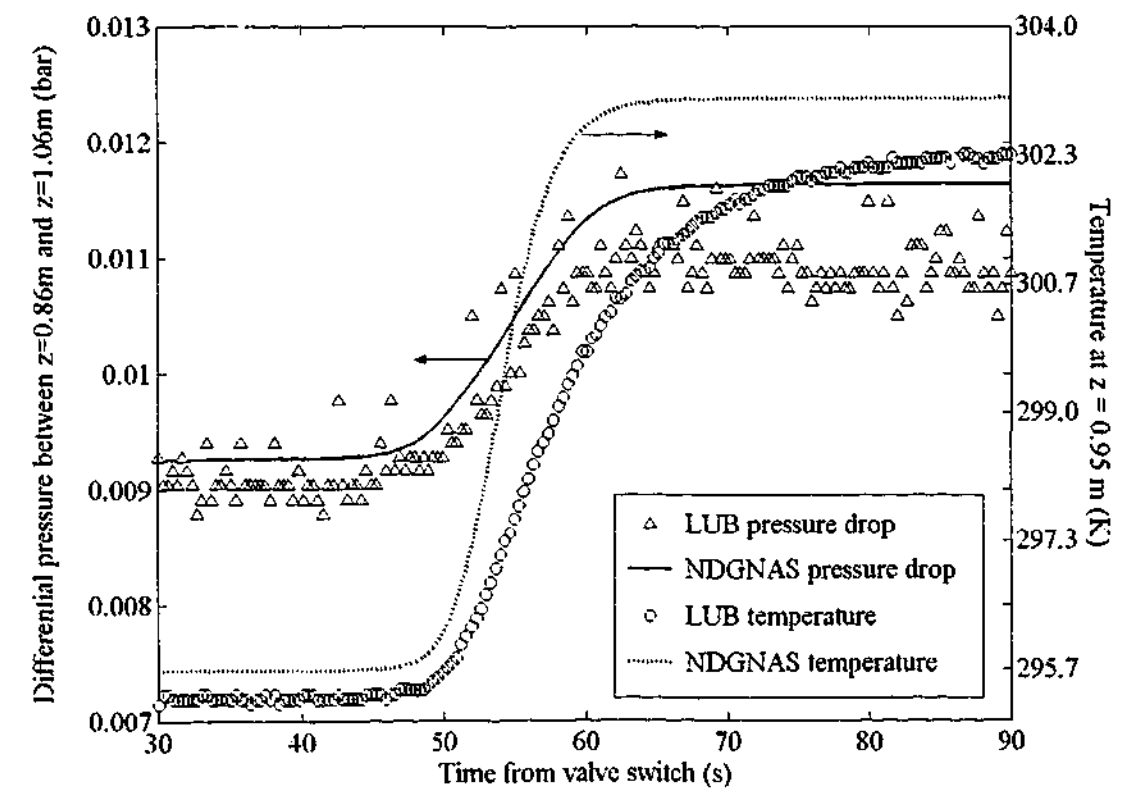


Figure 5.11: Experimental and numerical pressure drop and temperature profiles from breakthrough run 3 with gas mixture B.

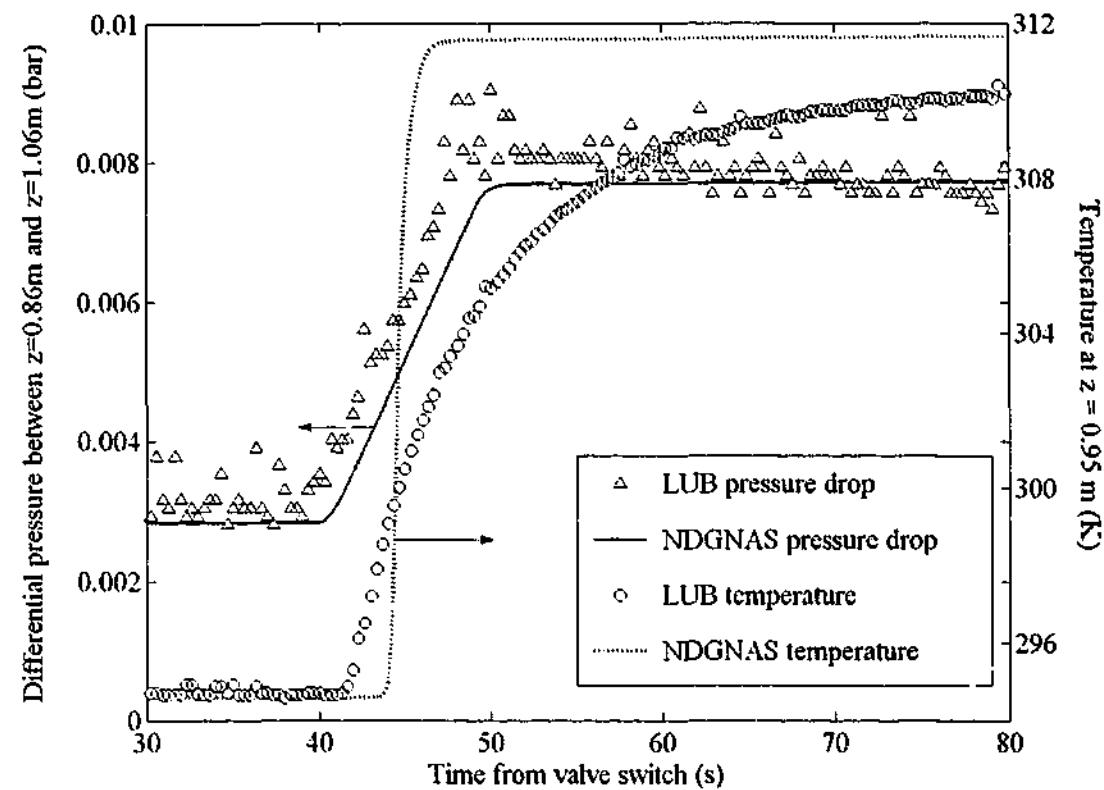


Figure 5.12: Experimental and numerical pressure drop and temperature profiles from breakthrough run 6 with gas mixture C.

Generally speaking, a process that involves adsorption of 10 wt% or more of the feed mixture is regarded a bulk separation [Yang (1987, p 3)]. In mass fraction terms, gas mixture A contains 8.9 wt% N_2 . The bed is initially saturated with oxygen so one can assume that nitrogen is the only component being taken up from the interpellet gas to intrapellet adsorbed phase over the duration of a breakthrough experiment. The delineating composition of 10 wt% adsorbing component for a bulk separation appears to be in good agreement with the observed change in pressure drop across a 0.20 m section of the bed obtained with gas mixture A (8.9 wt% N_2 in the feed) and gas mixtures B and C (18 and 76 wt% N_2 respectively), reinforcing the statement that purification processes can generally be distinguished by adsorption of 10 wt% or less of the feed stream.

5.6.1 The Issue of Temperature Measurement in the LUB Apparatus

In addition to experimental and numerical pressure drop obtained between $z = 0.86$ m and $z = 1.06$ m from breakthrough runs 1, 3 and 6 (Figs. 5.10 through 5.12 respectively), the experimental and numerical temperature profile obtained between these two locations, $z = 0.95$ m, is also shown. From the plots for feed mixtures A and B (Figs. 5.10 and 5.11), the experimental and numerical temperature profile at $z = 0.95$ m begins to increase around the same time the bed begins to experience a change in pressure drop between $z = 0.86$ m and $z = 1.06$ m. This suggests the MTZ

is wide enough such that nitrogen is breaking through at $z = 0.95$ m around the same time a significant change in pressure drop is about to occur a distance of 0.09 m before this point. This observation is confirmed when comparing L_{MTZ} from Table 4.11. The length of the MTZ, L_{MTZ} , obtained from feed mixtures A and B was between 0.19 and 0.41 m wide and hence half of L_{MTZ} indicates the first traces of nitrogen will pass $z = 0.95$ m around the same time the majority of the MTZ is passing $z = 0.86$ m.

With feed mixture C, however, a delay of approximately 4 s between half the MTZ passing $z = 0.86$ m and the first traces of nitrogen passing $z = 0.95$ m is predicted numerically. Although some noise is present in the reading from the DP cell around $t = 40$ s from the valve switch, a short delay of a couple seconds between the DP cell and thermocouple transients is observed (Fig. 5.12). This indicates numerical and experimental predictions across the MTZ for the initial period of breakthrough is in very good agreement. Each of these three graphs, Figs. 5.10 through 5.12, show the temperature profile from NDGNAS increasingly becomes sharper as nitrogen feed composition increases, but experimentally the temperature profile experiences an almost identical transient of 40 s from start to end. Similar temperature transients of 40 s were observed from dust runs 1 through 3 and pellet runs 1 through 6 from the EMU (Fig. 4.13) and depress runs 3 and 4 (Figs. 5.7 and 5.9 respectively) from the LUB apparatus.

If the experimental temperature transient that has been consistently measured from the EMU and LUB units really was the temperature present within that local region of the sorbent bed, then adsorbed phase loading would be significantly affected as differences of almost 10 K have been observed. This would mean uptake rates obtained from the EMU and breakthrough curves obtained from the LUB apparatus would not match NDGNAS uptake rates and breakthrough curves respectively once conditions outside of those used to fit each intrapellet transport coefficient were investigated. Good agreement was found across all EMU runs with just one set of transport coefficients that consistently reproduced experimental trends as a function of pellet diameter. Also, the molecular transport coefficient obtained for gas mixture B (breakthrough run 3) provided an excellent representation of breakthrough curves for feed mixtures A and C. If C_m really did correct the breakthrough curve for feed gas mixture B, then C_m would provide a poor representation of the breakthrough curve for feed mixtures A and C.

Results obtained from the EMU for various blank runs and the LUB apparatus within the bottom void volume during depressurisation experiments indicate the response time of junction exposed T-type thermocouples is not the mechanism giving rise to model mismatch. Sensitivity coefficients obtained from §4.3.6 indicate the mechanism of pellet-to-bed heat transfer, as quantified through $h_{p,b}$, is negligible for most conditions of practical interest within the EMU. Serbezov & Sotirchos

(1998) reached a similar conclusion through detailed numerical modelling of an individual sorbent pellet within a packed bed, suggesting external film heat transfer is not the mechanism at work here. If external film heat transfer at the pellet surface was the limiting mechanism and knowing the Nusselt number is a function of pellet Reynolds number for flow over spherical geometries [Incropera & DeWitt (1990, pp 417-418)], the experimentally measured temperature transient should be quite different between the EMU and LUB apparatus given two distinctly different flow regimes arise.

Instead, these combined results of a 40 s transient in measuring a temperature increase point to a particular mechanism of heat transfer that questions the method adopted within these units for measuring temperature. It is also worth pointing out that Figure 8 from Webley & Todd (2003) demonstrates a 40 s transient arises for their temperature profiles obtained using two different sorbent materials that exhibit macropore diffusion control, NaX (UOP PSO2HP) and CaX (UOP VSA2). Despite this, good agreement between theoretical and experimental LDF rate constants was obtained for pure and pseudo mixtures of these two sorbents. Thermocouple response within a packed bed may also explain poor agreement between experimental and numerical temperature profiles obtained in the oxygen RPSA study of Teague & Edgar (1999). They attributed poor agreement to some unmodelled temperature gradient within their UOP OxySiv-5 13X zeolite pellets. It is the opinion of the author, however, that they have directly observed the same phenomena disclosed here. A detailed evaluation of their results shall be taken up in §6.7.6 once RPSA pilot plant data has been introduced. These two independent studies provide further evidence that the 40 s response time is a function of the method used to measure the temperature transient within a packed bed as opposed to any intrinsic heat transfer limitation specific to Zeochem LiLSX itself.

Each thermocouple was pre-mounted inside the EMU and LUB units before sorbent was added. Once mounted and the respective vessels pressure tested, sorbent was poured in through the top and settled before the vessel was subjected to the relevant set of experimental conditions. This means sorbent pellets were allowed to randomly settle around each thermocouple tip. When fully regenerated, sorbent pellets contain a high level of static charge and it is not uncommon to see these pellets move unassisted 5 or even 10 centimeters to a surface such as the plastic wall of a bucket. This may suggest pellets will preferentially agglomerate around the junction-exposed tip of each thermocouple, creating a small pocket or dead zone where no flow occurs. In this small region the experimental temperature transient may be a strong function of thermal conduction through the local sorbent pellets and gas surrounding the thermocouple tip. To quantify such an arrangement, however, is rather difficult without more conclusive photographic or visual evidence.

From this preliminary discussion a very small cage should possibly be placed over the junction-exposed tip of a thermocouple located within an adsorption column that is being used to measure rapid temperature transients. This approach, however, would require a more advanced method of placing thermocouples in the bed to ensure the cage space does not introduce large void spaces while maintaining an airtight seal between the thermocouple and column wall. In addition, the thermal mass of this cage device should be small relative to the bed capacitance to ensure the cage itself is not mitigating rapid temperature transients. Limitations in time prevented this approach being pursued and is recommended as a future research topic to close the argument between experimental EMU/LUB data and NDGNAS predictions.

5.7 Concluding Remarks

The use of experimentally determined steady state coefficients have been shown to match dynamic pressure changing experiments well for an assumed non-adsorbing gas, helium, across a packed bed of Zeochem LiLSX pellets. The magnitude of these coefficients, $\kappa_{\text{viscous}} = 154 \pm 14$ and $\kappa_{\text{kinetic}} = 1.47 \pm 0.13$, were obtained from a series of runs using various compositions of oxygen and nitrogen as the feed gas, along with pure helium.

Numerical simulation shows the steady state form of the momentum balance, the Ergun equation, produces errors less than 0.1% in magnitude when compared to the equivalent set of data obtained with the full momentum equation over a pressure window of 2:1 bar.a between initial:final pressure. These observations were made with experimental depressurisation rates approaching 1 s, justifying the steady state momentum equation for interpellet pressure drop.

Helium depressurisation experiments were repeated with oxygen and air as the feed gas, both of which undergo adsorption and good agreement was found when using the Ergun equation to match experimental LUB data. The only discrepancy observed across all validation runs performed with NDGNAS from chapters 4 and 5 relate to experimental versus numerical temperature profiles. A closer examination of these profiles revealed the experimental temperature transient consistently lasted for 40 s across a range of operating conditions, suggesting a possible heat transfer limitation is arising between a local packet of sorbent pellets directly surrounding a thermocouple and the thermocouple tip itself. Apart from model mismatch between experimental and numerical temperature profiles, NDGNAS has provided an accurate description of process operating conditions from two different experimental units developed specifically to quantify mass transfer through C_k , C_v and C_m and interpellet pressure drop through κ_{viscous} and κ_{kinetic} for a real system.

CHAPTER 6

COMPARING MATHEMATICAL PREDICTIONS AGAINST PILOT PLANT DATA

The preceding five chapters have introduced a numerical model for an adsorption process and calibrated various transport coefficients at the intra- and interpellet level. With no fitting coefficients remaining, NDGNAS predictions are compared against experimental data obtained from a suitably instrumented pilot plant. The individual objectives for this chapter are as follows:

- i. Summarise RPSA pilot plant data obtained previously from various literature sources.
 - ii. Compare experimental data obtained from a pilot scale RPSA plant against NDGNAS predictions under various modelling assumptions.
 - iii. Investigate any differences in separation performance as a function of cycle time between the DPM and LDFP model.
 - iv. Investigate the impact of interpellet pressure drop on process performance at the limit of short cycle times.
-

Mathematical models of varying complexity have been extensively studied throughout the literature for the prediction of PSA process performance. Common examples include the work of Yang & Doong (1985), Cen & Yang (1986), Doong & Yang (1987), Kumar *et al.* (1994), Yang *et al.* (1995, 1997), Ahn *et al.* (1999) and Park *et al.* (2000) for hydrogen PSA; Hassan *et al.* (1986), Shin & Knaebel (1988), Ruthven & Farooq (1990), Farooq & Ruthven (1990b, 1991), Kim *et al.* (1995) and LaCava & Lemcoff (1996) for nitrogen PSA; and Fernandez & Kenney (1983), Kayser & Knaebel (1986), Farooq *et al.* (1989), Chou & Huang (1994b), Hofmann *et al.* (1999), Shin *et al.* (2000) and Mendes *et al.* (2001b) for oxygen PSA.

6.1 Previous Studies that have Investigated RPSA

The volume of literature related to the mathematical prediction of RPSA process performance, on the other hand, is not as extensive. Turnock & Kadlec (1971) provide the first known study that compares mathematical predictions against experimental data obtained from an RPSA pilot plant. A chronological summary of these studies that began with Turnock & Kadlec (1971) is provided in Table 6.1.

Table 6.1: Published studies that have investigated RPSA process performance. Some of these studies do not compare experimental data with simulation results. These have been included to provide a relatively concise summary of the existing literature that complements Table 1.1.

| Author(s) | Separation/Cycle | Experimental Regime | Mathematical Comparison |
|-------------------------|--|--|---|
| Turnock & Kadlec (1971) | <ul style="list-style-type: none"> Nitrogen enrichment from a nitrogen-methane feed stream over Linde 5A zeolite. One-bed, two-step cycle: feed plus make product followed by counter-current depressurisation. | <ul style="list-style-type: none"> $L_{bed} = 1.52$ m. $d_{bed} = 0.019$ m. $d_p = 42-60$ mesh ($0.40-0.25 \times 10^{-3}$ m). Four cycle times considered: 2.5 s, 5s, 10s and 20 s. Product purity varied between 35 and ≈ 99 mol%N₂ with cycle time. Total product flow rate between 0.24 and 0.94 normal litres min⁻¹. Nitrogen recovery low and further processing of exhaust stream suggested for this process. Negligible difference in performance when system operates at 273 and 297 K. Operation at 196 K poor, attributed to intrapellet mass transfer resistance. | <p>Binary component, plug flow model imposed. Isothermal behaviour assumed along with ILE locally in the bed. Darcy's law used to represent bed pressure drop. Pure component Freundlich isotherm used with co-adsorption neglected. Good qualitative agreement with experimental data found.</p> |
| Kowler & Kadlec (1972) | <ul style="list-style-type: none"> Nitrogen enrichment from a nitrogen-methane feed stream over Davison 5A zeolite. One-bed, three-step cycle: feed plus make product, co-current depressurisation and counter-current depressurisation. | <ul style="list-style-type: none"> $L_{bed} = 1.52$ m. $d_{bed} = 0.019$ m. $d_p = 20-50$ mesh ($0.84-0.30 \times 10^{-3}$ m). Range of cycle times investigated: 3 s cycle time, however, was optimal and this data set presented. Product purity varied between 43 and 66 mol%N₂. Total product flow rate between 0.55 and 1.1 normal litres min⁻¹. Co-current depressurisation time small (< 6%) at optimal t_{cycle} to reduce exhaust rate and improve performance. | <p>Binary component, plug flow model imposed. Isothermal behaviour assumed along with ILE locally in the bed. Darcy's law used to represent bed pressure drop. Pure component Freundlich isotherm used with co-adsorption neglected. Used to determine feed step duration that optimises product purity and exhaust rate.</p> |
| Jones & Keller (1981) | <ul style="list-style-type: none"> O₂ enrichment from air over 5A zeolite; N₂ enrichment from a N₂-C₂H₄ stream over activated carbon; and H₂ enrichment from a H₂-CH₄ stream One-bed, three-step cycle: feed plus make product, co-current depressurisation; and counter-current depressurisation. | <ul style="list-style-type: none"> $L_{bed} = 0.51$ and 1.5 m (O₂ from air) and 1.2 m (N₂ from N₂/C₂H₄). Little information provided on arrangement of hydrogen enrichment system. $d_{bed} = 0.076$ m. $d_p = 40-80$ mesh ($0.42-0.18 \times 10^{-3}$ m) for 5A and 28-60 mesh ($0.6-0.2 \times 10^{-3}$ m) for activated carbon. Total cycle times between 8 and 18.5 s (O₂ from air) and 6.5 s (N₂ from N₂/C₂H₄) considered. Product purity of 90 mol%O₂; 55 to 98 mol%N₂; and 98 mol%H₂ considered Various tables and plots presented for recovery and product flow as a function of step times and feed/exhaust pressure. | <p>No comparison to simulation data made.</p> |

Table 6.1 continued

| Author(s) | Separation/Cycle | Experimental Regime | Mathematical Comparison |
|----------------------------|---|---|---|
| Pritchard & Simpson (1986) | <ul style="list-style-type: none"> Oxygen enrichment from air over 5A zeolite. One-bed, three-step cycle: feed plus make product; co-current depressurisation; and counter-current depressurisation. | <ul style="list-style-type: none"> $L_{bed} = 0.23$ m (low purity) and 0.61 m (high purity) $d_{bed} = 0.038$ m $d_p = 40-60$ mesh ($0.42-0.25 \times 10^{-3}$ m); 60-80 mesh ($0.25-0.18 \times 10^{-3}$ m); 30-40 mesh ($0.5-0.42 \times 10^{-3}$ m); and 22-30 mesh ($0.8-0.5 \times 10^{-3}$ m). A range of cycle times between 3.0 to 11.5 s considered Product purity between 28 and 98 mol%O₂ considered. Oxygen enrichment (moles O₂ separated per mole O₂ fed) between 5 and 15%. Total product flow rate between 0.25 and 2 litres min⁻¹. | <p>No comparison to simulation data made.</p> |
| Jianyu & Zhenhua (1990) | <ul style="list-style-type: none"> Oxygen enrichment from air over 13X zeolite. One-bed, three-step cycle: feed plus make product; feed delay; and counter-current depressurisation. | <ul style="list-style-type: none"> $L_{bed} = 1.21$ m. $d_{bed} = 0.016$ m. $d_{p,eqv} = 4.6 \times 10^{-4}$ m. Three cycle times of 13.5, 15.7 and 20.7 s considered. Product purity between 30 and 98 mol%O₂ considered. Oxygen recovery between 11% (at 98 mol%O₂) and 62% (at 35 mol%O₂) reported. Total product flow rate between 0.1 and 0.6 litres min⁻¹. | <p>RPSA process simulation represented in the form of an equivalent electrical analog circuit. Binary, isothermal, plug flow conditions assumed. Ergun equation used for pressure drop. ILE assumed locally in the sorbent bed. Non-isobaric product tank model included. Pure component Langmuir isotherms used with co-adsorption neglected. Errors of 15% for product purity and 25% for exhaust flow found with this model.</p> |
| Hart & Thomas (1991) | <ul style="list-style-type: none"> Methane enrichment from methane/carbon dioxide over activated carbon and 5A zeolite. One-bed three-step cycle: feed pressurisation; feed plus make product (invoked by pressure relief valve opening); and counter-current depressurisation. | <ul style="list-style-type: none"> $L_{bed} = 1.0$ m. $d_{bed} = 0.010$ m. $d_p = 0.25-0.50 \times 10^{-3}$ m (some additional results presented for $0.50-0.70 \times 10^{-3}$ m). Total cycle times between 0.4 and 10.0 s investigated. CH₄ purities of 72 mol% (activated carbon) and 92 mol% (5A zeolite) obtained. CH₄ recoveries between 7-19% (activated carbon) and 14-15% (5A zeolite) reported. Separation factor (ratio of CH₄ concentration in product to feed) of 1.02 to 1.6 reported. | <p>Binary component, plug flow model imposed. Isothermal behaviour assumed, along with ILE locally in the bed. Darcy's law represents bed pressure drop. Pure component Langmuir isotherms used with co-adsorption neglected. While separation factor overestimated, product recovery and exhaust flow rate estimated fairly well.</p> |

Table 6.1 continued

| Author(s) | Separation/Cycle | Experimental Regime | Mathematical Comparison |
|---|--|--|---|
| Alpay et al. (1994) | <ul style="list-style-type: none"> Oxygen enrichment from air over Bayer 5A zeolite. One-bed, two-step cycle: feed plus make product; and counter-current depressurisation. | <ul style="list-style-type: none"> $L_{bed} = 1.00$ m $d_{bed} = 0.050$ m Five different pellet diameters considered, $0.15-0.25 \times 10^{-3}$ m; $0.25-0.36 \times 10^{-3}$ m; $0.36-0.43 \times 10^{-3}$ m; $0.43-0.50 \times 10^{-3}$ m; and $0.50-0.71 \times 10^{-3}$ m Total cycle time ranged between 1.0 and 5.0 s. Product purity varied between 39 and 92 mol%O₂. Oxygen recovery varied between 2.4 and 58%. Total product flow rate was maintained between 0.60 and 1.2 normal litres min⁻¹. | Binary component, isothermal, axially dispersed plug flow model applied. Darcy's law assumed for bed pressure drop. Linear isotherms with no co-adsorption imposed. LDF model with mass transfer coefficient of Alpay & Scott (1992) used. Also, ILE model compared. Good agreement observed between ILE and LDF for d_p below 0.40×10^{-3} m, but LDF better for higher d_p . |
| Chou & Wu (1994) | <ul style="list-style-type: none"> Oxygen enrichment from air over UOP 5A zeolite. One-bed, three-step cycle: feed plus make product; co-current depressurisation; and counter-current depressurisation. | <ul style="list-style-type: none"> $L_{bed} = 0.51$ m. $d_{bed} = 0.055$ m. $d_p = 60-80$ mesh ($0.25-0.18 \times 10^{-3}$ m). Total cycle times ranged between 2.5 and 30.5 s. Product purity varied between 40 and 95 mol%O₂. Oxygen recovery between 10 and 18%. Total product flow rates of 0.25, 0.50 and 1.0 litres min⁻¹ obtained. | No comparison to simulation data made. |
| Sircar & Hanley (1995) | <ul style="list-style-type: none"> Oxygen enrichment from air over a NaX zeolite. Two-bed, two-step cycle: feed plus make product and provide purge; followed by co-current depressurisation and receive purge. Termed spilt bed RPSA. | <ul style="list-style-type: none"> $L_{bed} = 0.18$ m. $d_{bed} = 0.15$ m. $d_p = 30-50$ mesh ($0.50-0.30 \times 10^{-3}$ m). Total cycle time varied between 6 and 20 s Product purity between 40 and 85 mol%O₂. Oxygen recovery varied between 10% (at 85 mol%O₂) and 45% (at 40 mol%O₂). Total product flow approximately between 3.5 and 21 normal litres min⁻¹ at 85 and 40 mol%O₂ respectively. | No comparison to simulation data made, only a brief discussion on the limitations of intrapellet mass transfer under RPSA conditions made. |
| A small portion of experimental and numerical results from this paper was first presented in Alpay et al. (1993). | | | |
| This same process was also discussed by Sircar (1996). | | | |

Table 6.1 continued

| Author(s) | Separation/Cycle | Experimental Regime | Mathematical Comparison |
|--|---|---|--|
| Chou & Kuang (1996) | <ul style="list-style-type: none"> Oxygen enrichment from air over UOP 5A zeolite. One-bed, three-step cycle: feed plus make product; co-current depressurisation followed by counter-current depressurisation. Some runs, however, set the duration of the co-current depressurisation step to zero. | <ul style="list-style-type: none"> Three different bed lengths were considered, 0.23, 0.508 and 0.71 m. $d_{bed} = 0.055$ m. Three different size ranges for d_p investigated: $0.15-0.18 \times 10^{-3}$ m, $0.18-0.25 \times 10^{-3}$ m and $0.25-0.45 \times 10^{-3}$ m. Optimal cycle time for each sorbent bed configuration varied between 3.5 and 15.5 s. Product purity varied between 20 and 65 mol%O₂. Purity was used as the sole parameter to determine optimum performance. Oxygen recovery varied between 5% and 22% from a select number of runs presented in paper. Total product flow approximately between 0.25 and 1.0 litre min⁻¹ over a range of purities. | No comparison to simulation data made. |
| Murray (1996) | <ul style="list-style-type: none"> Oxygen enrichment from air over 5A zeolite. One-bed, two-step cycle: feed plus make product; followed by counter-current depressurisation. Equal times assigned for both operating steps. | <ul style="list-style-type: none"> $L_{bed} = 0.20$ m. $d_{bed} = 0.050$ m. Four different pellet diameters in the size range $0.09-0.13 \times 10^{-3}$ m; $0.12-0.15 \times 10^{-3}$ m; $0.25-0.35 \times 10^{-3}$ m; and $0.35-0.45 \times 10^{-3}$ m investigated. Total cycle time varied between 0.2 and 6.0 s. Product purity varied between 30 and 80 mol%O₂. The maximum oxygen recovery attained was 15%. Total product flow rate was in the range 0.2 to 1.0 normal litres min⁻¹. | Binary, isothermal, axially dispersed plug flow model. Pressure drop modelled using Ergun equation and linear isotherms with no co-adsorption imposed. LDF model of Glueckauf (1955) used. Good qualitative agreement found with feed pressure BC modelled using a harmonic function. A similar model developed by Choong (2000) found better qualitative agreement using a feed pressure ramp BC. |
| This same data set was also used in the Ph.D. dissertation of Choong (2000). | | | |
| Suzuki et al. (1996) | <ul style="list-style-type: none"> Oxygen enrichment from air over 5A zeolite. One-bed, four-step cycle based on four-stroke piston motion: introduce feed gas; compress feed gas and make product; counter-current depressurisation; and remove desorbed gas. Termed Ultra Rapid PSA (URPSA). | <ul style="list-style-type: none"> $L_{bed} = 0.035$ m. $d_{bed} = 0.060$ m. Various ranges of pellet diameters used including 48-80 mesh ($0.30-0.18 \times 10^{-3}$ m); 80-150 mesh ($0.18-0.10 \times 10^{-3}$ m); and 200-350 mesh ($0.07-0.04 \times 10^{-3}$ m). Total cycle time varied between 0.5 and 1.7 s Product purity varied between 21 and 60 mol%O₂. Maximum oxygen recovery of 5% attained. Total product flow between 5×10^{-4} and 0.33 normal litres min⁻¹. High oxygen production capacity obtained at the expense of oxygen recovery. | Binary component, isothermal, plug flow model applied. Bed pressure drop represented by the Ergun equation. Linear isotherms with no co-adsorption imposed. LDF model using time corrected mass transfer coefficient of Nakao & Suzuki (1983). Non-isobaric void volume below bed included. General trends with experimental data captured through numerical model. |
| This same data set was also presented by Horváth & Suzuki (1998). | | | |

Table 6.1 continued

| Author(s) | Separation/Cycle | Experimental Regime | Mathematical Comparison |
|----------------------|--|---|--|
| Zhu et al. (1996) | <ul style="list-style-type: none"> Oxygen enrichment from air over 13X with binder, 13X without binder and 5A zeolite with binder. One-bed, three-step cycle; feed plus make product; co-current depressurisation followed by counter-current depressurisation. | <ul style="list-style-type: none"> $L_{bed} = 1.0$ m and 1.6 m. $d_{bed} = 0.0125$ m. $d_p = 35$-60 mesh (0.25-0.43×10^{-3} m). Total cycle time varied between 1.7 and 26 s Product purity varied between 21 and 95 mol%O₂ over the range of pressure windows and cycle times investigated. Oxygen recovery varied between 5% and 60% across product purities investigated. No experimental values for product flow reported. | Binary component, isothermal, plug flow model used with mass transfer described using the LDF model. Bed pressure drop represented by the Ergun equation. Langmuir isotherms used. Void volumes around sorbent bed included. Numerical results with 5A agree well (micropore diffusion control), but 13X simulations do not agree as well (macropore diffusion control). |
| Suzuki et al. (1997) | <ul style="list-style-type: none"> Carbon dioxide recovery from stack gas (assumed to be 15 mol%CO₂, 2 mol%O₂ and 83 mol%N₂) over 5A zeolite and hydrophobic Y zeolite. One-bed, four-step cycle identical to URPSA cycle of Suzuki et al. (1996) applied. | <ul style="list-style-type: none"> $L_{bed} = 0.010$ m (5A) and 0.010 and 0.035 m (Y zeolite). $d_{bed} = 0.060$ m. $d_p = 80$-150 mesh for both 5A and Y zeolites (0.18-0.10×10^{-3} m). Total cycle time = 0.5 s. Product purity did not exceed 20 mol%CO₂. Recoveries of carbon dioxide from the feed stream exceeded 50%. Maximum total product flow rates of 6.6 and 7.5 normal litres min⁻¹ obtained with 5A and Y zeolite respectively. | The numerical model developed by Suzuki et al. (1996) is applied directly to this process. Equilibrium isotherms for 5A represented by linear and Langmuir isotherms assuming no co-adsorption, while Langmuir isotherms with no co-adsorption applied to Y zeolite. The model predicted qualitative trends obtained from experimental data. |
| Zhang et al. (1998) | <ul style="list-style-type: none"> Carbon dioxide enrichment from a nitrogen-carbon dioxide feed stream using a macroporous silica gel. One- and two-bed process of three-steps: feed plus make product; backfill with gas obtained from counter-current depressurisation; and counter-current depressurisation. | <ul style="list-style-type: none"> $L_{bed} = 1.60$ m $d_{bed} = 0.020$ m $d_{p,eqv} = 0.44 \times 10^{-3}$ m Cycle time = 10.5 s CO₂ purity = 89.5 mol% from one-bed arrangement and 93.5 mol% from two-bed arrangement. CO₂ recovery = 70% (one-bed) and 72.3% (two-bed). CO₂ product flow around 2.5×10^{-3} gmole 100% CO₂/cycle (one-bed) and 2.7×10^{-3} gmole 100% CO₂/cycle (two-bed). | No comparison to simulation data made. |

Table 6.1 continued

| Author(s) | Separation/Cycle | Experimental Regime | Mathematical Comparison |
|-----------------------|--|---|--|
| Teague & Edgar (1999) | <ul style="list-style-type: none"> Oxygen enrichment from air over UOP OxySiv-5 zeolite (13X). Two-bed, two-step cycle. Step 1 performs feed pressurisation, make product and provide purge together; while step 2 performs counter-current depressurisation and receive purge together. | <ul style="list-style-type: none"> $L_{bed} = 0.62$ m. $d_{bed} = 0.051$ m. $d_{p,eqv} = 1.0 \times 10^{-3}$ m. Total cycle time between 9.6 and 40.7 s. Product purity varied between 50 and 96 mol%O₂. Oxygen recoveries between 7 and 29% obtained. Total product flow varied between 0.001 and 0.003 gmole s⁻¹. | Binary component, non-isothermal, axially dispersed plug flow model with intrapellet mass transfer described using the LDF model. The LDF coefficient is evaluated using the Glueckauf (1955) model. Isobaric conditions assumed. Multicomponent adsorption described using the SSTM isotherm equation of Ruthven (1976). Good agreement was found for cycle averaged feed rate, product composition and pressure from experimental runs |
| Arvind et al. (2002) | <ul style="list-style-type: none"> Oxygen and nitrogen enrichment from air over 13X zeolite. One-bed, two-step cycle: feed plus make product; followed by counter-current depressurisation. This cycle is achieved using pistons above and below the sorbent bed. | <ul style="list-style-type: none"> $L_{bed} = 0.40$ m (blank calibration runs) and 0.30 m (sorbent runs). $d_{bed} = 0.02$ m (blank) and 0.03 m (sorbent). Two pellet diameters considered, 8-12 mesh (2.4-1.7×10^{-3} m) and 12-24 mesh (1.7-0.7×10^{-3} m). Total cycle time between 3 and 6 s (pistons operating at 21 and 10 RPM respectively). For runs where product gas was taken, purities of 20 to 30 mol%O₂ and 80 to 95 mol%N₂ obtained. For these runs, oxygen recovery was between 35 and 95%, while nitrogen recovery was between 20 and 80%. | Binary component, isobaric, isothermal, axially dispersed plug flow model using the LDF assumption imposed. The LDF coefficient of Glueckauf (1955) used. Langmuir isotherms for the co-adsorption of nitrogen and oxygen applied. CSTR models used for void volumes around sorbent bed. Good agreement between numerical and experimental trends observed. |

From this preliminary discussion it is readily seen that a large gap remains in the literature with regards to the predictive ability of the partial pressure form of the LDF model and DPM for macropore diffusion control over an RPSA cycle and for that matter, a traditional PSA cycle. Although several studies have applied the DPM using a VF+DGM approach to intrapellet mass transfer as discussed in §3.1.3, such process simulators have not been fully characterised with respect to pilot plant data. In addition, the intrusion of pressure drop as a function of cycle time for a non-isothermal, bulk adsorbing separation has received minimal attention across the published literature. It is the aim of this chapter and ultimately, this dissertation to address these issues using experimentally calibrated intrapellet transport and interpellet pressure drop coefficients through NDGNAS.

6.2 Description of the RPSA Pilot Plant

To provide operating data representative of an industrial installation, a pilot scale RPSA plant was constructed. This plant was designed in-house using existing schematic arrangements of typical PSA installations and was constructed on a single skid frame by a local company in Victoria, IWI Cryoquip. All aspects of process design, project management, equipment sourcing, plant commissioning, operation and maintenance was performed by myself with guidance from Dr. P. A. Webley and funding provided by Air Products and Chemicals Inc. Process equipment was sourced from both local and overseas vendors. A complete piping and instrumentation diagram for the RPSA pilot plant is shown in §D.3 of appendix D, along with equipment lists, arrangement drawings of the adsorption column and various photos.

6.2.1 One-Bed as Opposed to Two-Bed Operation

The RPSA pilot plant allows for two-bed operation to perform bed-to-bed pressure equalisation and purge commonly invoked on a commercial installation [Batta (1973), Warmuzinski (2002)]. While successful process operation has been previously reported for the RPSA pilot plant when operating in two-bed mode [Todd & Webley (2001)], the two-bed arrangement shall not be discussed in this dissertation given the additional level of model mismatch that can potentially arise with asymmetrical profiles [Doong & Propsner (1988)]. Although NDGNAS does contain the "store-and-retrieve" technique commonly invoked for single-bed simulators that attempt to predict multi-bed data such as SIMPAC [Kumar *et al.* (1994)], SAXS [Da Silva *et al.* (1999)] and MINSA [Todd *et al.* (2001)], validation using this approach adds another level of complexity that may obscure mass transfer/pressure drop arguments under consideration here. Therefore, one-bed runs with purge initiated from the product tank shall be the only cycle of experimental interest.

6.2.2 Solenoid and Modulating Valves

One important aspect of process operation was rapid actuation of the solenoid valves that invoke each process step for any arbitrary RPSA cycle. For this purpose eight 1½ inch pneumatically actuated Nippon-Valqua cylinder valves were imported from Japan. These valves were selected on the basis of durability and lifetime for on-off actuation, rated to over one million switches, along with actuation time of approximately 0.1 s. These solenoid valves require air-to-open and air-to-close (pneumatic line pressure = 7.5 bar.a) so actuation times are rapid when the valve is both opened and closed. Each solenoid valve can be independently actuated to expose the sorbent bed to four different process lines: the exhaust, feed, product and purge line. Along with eight solenoid valves for on-off control, four manual modulating valves are located on each of the four process

lines to invoke end of step pressure and purity control. Pressure control on the exhaust and feed lines was initiated using 1½ inch ball valves while pressure control on the purge line was performed using a 1½ inch pneumatic piston valve. Product purity was controlled through a ½ inch manual globe valve on the product line. Stem position on each modulating valve was adjusted cycle-by-cycle until the desired operating conditions were achieved. One issue that became evident during RPSA pilot plant operation was loop interaction between each modulating valve when achieving desired end of step conditions.

Although advanced control schemes for PSA and VSA operation have been extensively studied through the Ph.D. dissertation of Beh (2003), it was found in this instance that manual control for a large portion of the transient period was adequate to achieve required set points. In some cases, however, only small perturbations from a previous CSS condition was desired but large deviations in pressure and purity arose, making control at times rather difficult to say the least. From this perspective the implementation of advanced control schemes [Beh (2003)] should be considered for future operation to reduce downtime often associated with my poor selection of modulating valve stem position.

6.2.3 Adsorption Column Design

Although column diameters required to achieve true adiabatic behaviour are not generally feasible at the pilot scale with diameters exceeding one metre required [Chihara & Suzuki (1983)], current data in the literature often falls below this mark (see Table 6.1), tending more towards the near-isothermal limit. For this reason the columns were designed with an internal diameter d_{bed} of 0.156 m, large enough to obtain significant temperature deviations representative of a near-adiabatic process without the need for excessively large feed gas flow rates or sieve quantity. Also, the column-to-particle diameter ratio is very large ($d_{bed}:d_{p,eqv} \approx 92:1$ with Zeochem LiLSX), avoiding gas maldistribution and channeling effects common with small diameter columns from a modelling perspective. A large number of ⅛ and ⅙ inch compression fittings are located axially down the column wall to allow temperature and pressure measuring devices to be inserted directly into the sorbent bed. This allows interpellet conditions to be determined at a pre-selected number of axial positions at any point during the cycle.

The adsorption column itself is manufactured from a sheet of 0.0034 m thick stainless steel 304 that has been formed into a cylindrical vessel. Stainless steel flanges were welded to the top and bottom of this cylinder to allow pipe sections to be connected at both ends. Oxygen compatible gaskets are used to seal flanged ends. Static pressure tests with the column mounted in the skid frame and packed with sorbent revealed an airtight seal was maintained for at least three weeks,

the longest period for which the RPSA pilot plant was in shut down mode with sorbent packed in the column.

Each column contains a sorbent support mechanism welded in position at the base of the packed bed. At the top of the bed, the sorbent support mechanism is mounted upon a high-tension 0.10 m diameter spring to take up settling and prevent fluidisation under rapid cycling. With this variable position support mechanism located at the top of the column packed bed length was typically 1.00 ± 0.03 m.

6.2.4 In-Line Process Equipment to Measure Operating Conditions

The feed line emanates from a 0.64 m^3 air receiver which contains dry air at a relatively steady pressure of 7.5 bar.a and dew point of -60°C . The exhaust line is piped directly into a soundproof vessel that contains a large number of venting ports to remain at atmospheric conditions. This vessel was installed to reduce noise created by rapid venting of desorbed gas obtained from the bottom of the sorbent bed. The product line is designated as the section of piping located between SV7 at the top of the column and the product line modulating valve (see Figure 6.1). The product line also includes a 0.07 m^3 buffer tank used to smooth out intermittent changes in pressure and composition obtained from the top of the column over a cycle. Hence the purge line is designated to be the relatively short section of piping that connects SV5, SV6 and SV8 to the top of the sorbent bed.

Located on each of the exhaust, feed and product lines are pressure transducers, junction exposed T-type thermocouples and flow metering devices. Each pressure transducer was rated to an accuracy of 0.03 bar over the pressure range 1.01-6.00 bar.a. Response time of these transducers, like those located on the LUB apparatus of chapter 4, is approximately 0.1 s. Thermocouples mounted inside each process line, in addition to those mounted inside the sorbent bed through compression fittings on the column wall were all calibrated at three different temperatures and are accurate to 0.5 K. Response time of junction exposed T-type thermocouples, as revealed in the previous two chapters, is around 0.1 s. However, this response time should be considered separate to that found when measuring temperature transients in a packed bed and this point will be addressed further in §6.7.4 and §6.7.6.

A Dry Test Meter (DTM) was used on the product line to measure accumulated flow obtained from the RPSA pilot plant. In addition to the DTM, a soap bubble flow meter was used to verify product flow rate. These two readings generally agreed to within 5% over the full range of product

flowrates investigated. A steady flow of product is obtained across the entire duration of an RPSA cycle and hence response time for these two flow meters is not an issue.

Flow metering on the exhaust line was performed using an annubar-Differential Pressure (DP) cell arrangement similar to that used on the LUB apparatus. Response time of the exhaust line flow meter is limited by damping on the output signal of the DP cell, which is 0.5 s. Several calibration tests were performed on this arrangement and it was found that flow transients accurate to around 5% could be attained for depressurisation rates approaching 8 s in duration from the adsorption column over a pressure window of 4.0 to 1.0 bar.a. In general, flow calibration experiments revealed the more severe the flow spike from the column, the larger the error will be in measured flow rate. This will become important when RPSA cycles of 14 and 8 s in duration are discussed. The rated accuracy of this device, as with the LUB arrangement, is a function of the pressure, temperature and DP cell used to calculate flow using the annubar equation provided by the vendor (i.e. a secondary measured variable). In general, flow rates obtained from the annubar-DP cell arrangement on the RPSA pilot plant were found to be accurate to approximately two significant figures.

Although a similar annubar-DP cell arrangement was mounted on the feed line, significant errors were found when performing the same flow calibration tests initiated on the exhaust line. This means accumulated feed flow rates could not be directly measured experimentally. Given pressure tests performed over each section of the plant revealed gas leaks were negligible, feed flow had to be inferred as the sum of the exhaust plus product line flows. At CSS, accumulation of mass in the bed over a cycle is negligibly small and the total quantity of gas passed into the column must equal the quantity of gas obtained in the exhaust and product lines. Both of these flows are measured experimentally. This approach has been successfully used by Air Products and Chemicals Inc. to obtain an estimate of feed flow in several of their pilot scale PSA plants [APCI (2002)].

Product line composition is measured using a Servomex 1440C paramagnetic oxygen analyser. Calibration of this analyser was performed using pure nitrogen, pure oxygen and a 90 mol% O_2 /10 mol% N_2 gas mixture. The rated accuracy of this analyser is ± 0.5 mol% O_2 over the full range of oxygen compositions expected from the RPSA pilot plant. Response time is typically less than 10 s, which is more than adequate given this analyser was located after the product buffer tank. DP cells mounted directly on the adsorption column wall are deemed accurate to 0.001 bar. Common to all DP cells discussed in this dissertation, however, is the minimum signal damping time constant of 0.5 s.

To protect equipment items located around the sorbent bed, filter elements of mesh size 50 micron were installed to remove any coarse sorbent particles becoming entrained in the exhaust and product lines. These elements are sized and mounted in such a way that minimal void volume and pressure drop are present. Filter elements along with ancillary pipe work and void space between the sorbent support mechanism and solenoid valves comprise all dead volumes located around the sorbent bed. Relatively large swings in pressure are performed very rapidly on the RPSA pilot plant in the presence of high purity oxygen. This gives rise to a potentially dangerous situation of an oxygen fire should a small amount of grease somewhere in the top piping manifold be ignited due to adiabatic compression. For this reason all piping and equipment items located on the purge and product lines were cleaned for oxygen service using a CFC solution by IWI Cryoquip.

6.2.5 PLC Control and Remote Data Acquisition

Plant operation is controlled through a GE Fanuc 90-30 PLC that operates each valve while continually monitoring all analog input devices. The PLC was programmed in ladder logic using Logicmaster90 software provided from the PLC vendors. A preset scan rate of 0.025 s was activated for one sweep through the program, which was entirely written by myself. Given the RPSA pilot plant ran twenty-four hours a day for several months, trip and alarm conditions had to be incorporated into program logic that shut down the plant to safe mode the very instant a dangerously high pressure, temperature or incorrect valve sequence arose.

A commercially available SCADA software package, Citect version 5.21, was used to log all process operating variables on line via a remote PC using an ethernet connection available through the PLC. A minimum scan rate of 0.5 s was allowed through Citect so all experimental plots presented in this chapter have a resolution of 0.5 s. The computer used to log all Citect variables, however, had difficulties maintaining this scan rate during data acquisition and a resolution of 0.5 s was not always maintained.

6.3 One-Bed, Four-Step Cycle of Experimental Interest

In this chapter the impact of changing cycle time on the separation performance of Zeochem LiLSX for oxygen enrichment over one particular cycle configuration will be investigated. This one cycle arrangement will consider two different product purities and pressure windows with cycle time covering the PSA and RPSA operating regime. For this particular study the form of the cycle initiated on the RPSA pilot plant is of little consequence given separation performance as a function of cycle time is the primary parameter of interest here. For this purpose a relatively standard four-step cycle is used that contains most of the essential elements of a PSA cycle except,

obviously, bed-to-bed purge and equalisation steps. The arrangement of this four-step cycle on the RPSA pilot plant is shown schematically in Fig. 6.1.

Step 1 involves co-current pressurisation with feed gas. This terminates and step 2 begins when the pressure in the void space at the top of the sorbent bed is equal to or greater than product tank pressure. Logic incorporated into the PLC ensured SV7 did not open until this condition was met. This eliminates partial bed pressurisation with product gas, which not only complicates numerical comparisons but can also reduce oxygen recovery. Although times for steps 1 and 2 were not pre-set before starting a run, the total time for these two combined steps was and this time was allocated as half of the total cycle. This condition was based purely on the definition of θ , provided at the start of chapter 2. This effectively means the time for which "adsorption" and "desorption" are being performed now constitutes half of the total cycle time.

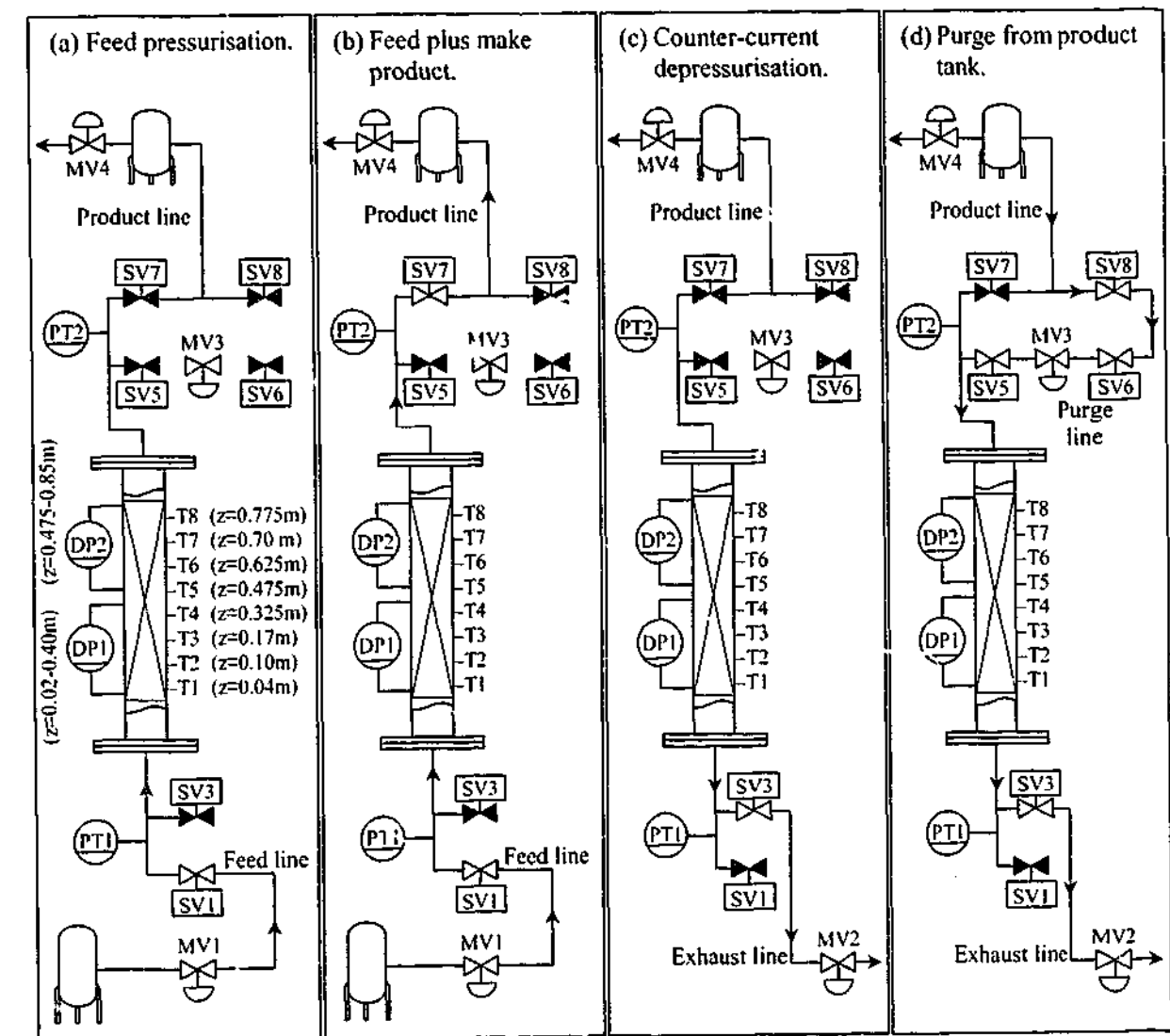


Figure 6.1: One-bed, four-step cycle initiated on the RPSA pilot plant.

- (a) In step 1, gas from the feed tank is used to pressurise the sorbent bed.
 (b) When $p^{\text{top}} > p^{\text{tank}}$, step 2 starts and product gas is withdrawn from the column.
 (c) In step 3, the sorbent bed is depressurised to atmosphere.
 (d) In step 4, a small amount of gas from the product tank flows back through the bed as purge.

At the completion of step 2, all solenoid valves on the top manifold are closed and the bed is depressurised in the counter-current direction through SV3 to atmosphere. Once the bed has reached a designated minimum in pressure, counter-current purge is performed by allowing a small amount of product gas to flow back into the bed from the product tank while desorbed gas is still being withdrawn from the bottom of the column.

6.3.1 Target Values for End of Step Pressures and Product Purity

When the RPSA pilot plant was running, three target pressures and one target purity was maintained at CSS using each of the four modulating valves located around the plant. A summary of these target values and the corresponding valve used to achieve that particular control target is provided in Table 6.2.

Table 6.2: Parameters that were controlled around the RPSA pilot plant.
Given two different pressure windows and product purities are considered, the first two entries in this table are set to one of two possible combinations.

| Parameter of interest | Target value(s) | Valve used to achieve target value |
|---|--|------------------------------------|
| Average product gas purity over cycle | 80.0 ± 1.0 mol%O ₂ 90.0 ± 1.0 mol%O ₂ | Modulating valve on product line |
| Pressure at bottom of bed, end step 2 † | 4.00 ± 0.03 bar.a 5.00 ± 0.03 bar.a | Modulating valve on feed line |
| Pressure at bottom of bed, end step 3 † | 1.20 ± 0.03 bar.a | Modulating valve on exhaust line |
| Pressure at bottom of bed, end step 4 † | 1.40 ± 0.03 bar.a | Modulating valve on purge line |

† Note that the "bottom of bed" is represented by the void volume located between the sorbent bed interface and SV1 and SV3.

Note the range for each target value on pressure is assigned as the uncertainty in each pressure reading. In this chapter two different pressure windows are considered. Bed pressure increases slightly during the purge step so the pressure at the end of steps 2 and 3 define the pressure window over which the cycle operates and hence two parameters to control. The first pressure window involved a high:low ratio of 4.00:1.20 bar.a while the second ratio was maintained at 5.00:1.20 bar.a. The lower pressure limit of 1.20 bar.a was always maintained on step 3 to ensure the sorbent bed was higher than atmospheric pressure throughout the cycle, this avoids atmospheric air flowing back into the sorbent bed should the column completely depressurise before purge commences.

End of step purge pressure, 1.40 bar.a, was an arbitrary value that was selected according to the following heuristics. An increase in pressure from the end of counter-current depressurisation to purge was desired so that gas was always flowing in the negative z direction (i.e. from the product

tank to exhaust line) to ensure the nitrogen MTZ was pushed further back in the bed. The ensuing feed plus make product step will therefore commence with the upper region of the bed relatively clean when SV7 opens to the product line. While the pressure should increase, end of step purge pressure should not be too high with respect to the pressure window otherwise the bed will be over-purged. This means the volume of product gas passing back into the bed as purge is greater than the minimum required to maintain purity with specific productivity and recovery decreasing as a result. From these two heuristics end of step purge pressure is now a parameter that needs to be optimised for each cycle under consideration if process performance is to be optimised. This chapter is not concerned with end of step purge pressure that corresponds to the optimal operating condition but instead shall address the impact of intrapellet mass transfer and interpellet pressure drop on cycle time over a fixed PSA cycle. Further to this, a reduction in cycle time may potentially alter optimum end of step purge pressure due to the changing influence of intrapellet mass transfer and interpellet pressure drop. For this reason 1.40 bar.a was deemed suitable without the need to perform additional runs at each cycle time and pressure window under investigation. Maintaining purge pressure constant, however, does not imply the moles of gas required for purge will be constant.

Each end of step pressure presented in Table 6.2 relates to conditions in the bottom void volume, which constitutes the section of tubing between the sorbent bed interface and solenoid valves SV1 and SV3. As cycle time decreases and gas velocity increases to maintain the same end of step pressure, bed pressure drop increases and hence differential pressure between the bottom and top void volume changes. While end of step pressure in the bottom void was effectively constant according to Table 6.2, end of step pressure in the top void was a function of bed pressure drop and this changed with decreasing cycle time.

Product purity was controlled in addition to end of step pressure to maintain the same extent of breakthrough across each run as a function of cycle time. Reducing t_{cycle} increases interpellet velocity for the same pressure window that in turn will alter the shape of the breakthrough curve (Table 4.11 readily shows L_{MTZ} increases with increasing velocity for minor changes in bed pressure). Maintaining the same extent of breakthrough (i.e. purity) with L_{MTZ} changing as a function of cycle time can provide some insights into the impact of intrapellet mass transfer on recovery. The high purity target of 90 mol%O₂ is a typical purity required from most industrial PSA plants [Michael (1997)]. This same target value also indicates a large majority of the MTZ should remain within the bed to maintain purity. Although the second purity target of 80 mol%O₂ is not so common industrially, this does allow partial breakthrough to occur and hence the MTZ is not necessarily confined to the sorbent bed.

6.3.2 Cycle Times Investigated

The longest cycle time used on the RPSA pilot plant that allowed CSS to be maintained was 50 s. This time represents the slowest cycle performed in this study. As mentioned earlier, the combined times for steps 1 and 2 was half of the total cycle time. The remaining two steps of the cycle used fixed step times. In assigning these times, it was arbitrarily stipulated that 12 to 14% of the cycle be devoted to purge to the nearest second. From this the balance in cycle time was designated for step 3, counter-current depressurisation. As discussed earlier, the implemented cycle is arbitrary and does not necessarily represent the optimum regime to operate Zeochem LiLSX over. Table 6.3 provides a summary of the five cycle times investigated. Table 6.3 also provides an approximate estimate on the magnitude of the dimensionless time parameter θ_i commonly encountered in the RPSA literature.

Table 6.3: Individual step and cycle times considered on the RPSA pilot plant.

Also included are the calculated values of θ_i for nitrogen and oxygen in each of these cycles. Note that steps 1 and 2 initially are not assigned individual times due to the constraint that step 2 starts when top void pressure is greater than or equal to product tank pressure, which is not known *a priori*.

| Total cycle time (s) | Steps 1 and 2 combined (s) | Step 3 (s) | Step 4 (s) | θ_i for nitrogen (-) | θ_i for oxygen (-) |
|----------------------|----------------------------|------------|------------|-----------------------------|---------------------------|
| 50 | 25 | 19 | 6 | ≈ 4.2 | ≈ 11 |
| 36 | 18 | 13 | 5 | ≈ 3.0 | ≈ 8.5 |
| 22 | 11 | 8 | 3 | ≈ 1.9 | ≈ 5.2 |
| 14 | 7 | 5 | 2 | ≈ 1.2 | ≈ 3.3 |
| 8 | 4 | 3 | 1 | ≈ 0.7 | ≈ 1.9 |

To calculate θ_i for nitrogen and oxygen, the Bosanquet assumption for combined intrapellet molecular and Knudsen diffusion was used [Pollard & Present (1948)]. Given this effective coefficient is often stated in surface diffusion form, a correction for the equilibrium isotherm derivative discussed at the beginning of chapter 2 is required. The governing form of θ_i can be described analytically as follows.

$$\theta_i = \frac{t}{R_p^2} \left[\frac{\left(\frac{p^p \sigma_{ij}^2 \Omega_{ij}^{(1,1)*}}{1.8829 \times 10^{-7} C_m \sqrt{T_p^3 (M_i + M_j) / M_i M_j}} + \frac{1}{48.5 C_K \delta \sqrt{T_p}} \right)^{-1}}{\epsilon_p + \hat{p}_p R T_p \left(\frac{\partial n_{i,eq}^p}{\partial p_i^p} \right)} \right] \text{ for } i = 1, 2 \text{ and } j \neq i \quad (6.1)$$

Values of θ_i were obtained by assuming intrapellet gas is at "average" conditions: 3.0 bar.a, 290 K and feed composition (78 mol%N₂/22 mol%O₂). This number provides a first approach estimate to the academic definition of an RPSA cycle (see §1.1). From these estimates the shortest cycle time is close but still above this limit. However, numerical comparisons obtained from SimPell indicate the assumption of equimolar counterdiffusion was becoming invalid for $\theta_i < 1.0$, which is experimentally achieved in the RPSA pilot plant. With respect to industrial literature the 22, 14 and 8 s cycle times are classified as true RPSA cycles.

6.3.3 Defining Parameters of Experimental Interest

A select number of variables are used to delineate one experimental RPSA pilot plant run from another. The most important of these, which are required when simulating each run, include:

- Product purity, reported in mol%O₂. Note this value was measured directly as one steady reading from the paramagnetic oxygen analyser at CSS. As binary component simulations are performed, product purity is also reported as mol%O₂+Ar. Air contains approximately 1 mol% argon. Given argon and oxygen behave in a similar manner under adsorption conditions [Chou & Chen (1994)] argon can be lumped with oxygen to form the one effective component referred to as oxygen. Hence product purity measured experimentally must reflect the additional contribution from argon.
- End of step pressures, reported in bar.a. These values were measured directly from transducers located around the RPSA pilot plant at CSS.
- Ambient conditions, namely pressure and temperature, at the time CSS results are obtained.

Once an operating regime has been established and CSS achieved, a large volume of data can be obtained from an adsorption process. In this study, a select number of these parameters will be of primary interest when comparing NDGNAS results against experimental data. In addition to pressure and temperature profiles obtained within the adsorption column, these include:

- Total mole flow obtained in the exhaust lines during counter-current depressurisation and purge, reported in units of gmole cycle⁻¹.

$$\text{Exhaust flow, step } m = \frac{P_A}{RT_A} \times (\text{Gas volume out of exhaust line, step } m) \quad (6.2)$$

- Total flow in the product line, reported in units of gmole cycle⁻¹.

$$\text{Total product flow} = \frac{P_A}{RT_A} \times (\text{Gas volume out of product line over cycle}) \quad (6.3)$$

- Recovery of oxygen (plus argon) in the product line, reported as a percentage. Note the total flow of oxygen fed into the process is found by adding the total flow of gas obtained in the product and exhaust lines.

$$\text{Recovery} = \frac{100 \times (\text{Total product flow}) \times (\text{O}_2 + \text{Ar composition as a \%})}{22 \times \frac{P_A}{RT_A} \times (\text{Gas volume out of exhaust and product lines over cycle})} \quad (6.4)$$

- iv. The amount of oxygen (plus argon) obtained from the process per unit mass of sorbent per day, denoted specific productivity with units of $(\text{kg O}_2 + \text{Ar}) \text{ kg}^{-1} \text{ day}^{-1}$.

$$\text{Specific productivity} = \frac{27.65 \times (\text{Total product flow}) \times (\text{O}_2 + \text{Ar composition as a \%})}{m_{\text{bed}} \times t_{\text{cycle}}} \quad (6.5)$$

(Gas volume out of product line over cycle) was measured using the DTM and soap bubble flow meters on the product line while (Gas volume out of exhaust line over cycle) was measured with the annubar-DP cell arrangement discussed in §6.2.4. All three of these flow meters are located after their respective modulating valves and hence measure volume flow at atmospheric conditions. To perform the calculations of Eqs. (6.2) through (6.5), ambient pressure p_A was obtained from the digital display of the MKS Baratron pressure transducer (EMU) while a pre-calibrated junction exposed T-type thermocouple was used to measure ambient temperature, T_A . The mass of Zeochem LiLSX added to the adsorption column, m_{bed} , was 11.29 ± 0.05 kg. This batch of sorbent was regenerated within our furnace according to the procedure described in §4.1.1 before being packed into the adsorption column.

6.4 Simulating the RPSA Pilot Plant with NDGNAS

The preceding two sections form a complete treatise on the design and operation of the RPSA pilot plant relevant to this chapter. From this discussion a concise summary is presented, Table 6.4, that collects the important parameters required by NDGNAS to simulate the RPSA pilot plant. Physical properties of the sorbent, Zeochem LiLSX, are identical to those discussed in chapters 4 and 5 and so are not repeated in Table 6.4 for brevity.

For all simulations performed in this chapter, bottom and top void volume models were activated and set to the corresponding experimental value shown in Table 6.4. In addition to the top void region, which is related to the volume between SV7 and sorbent bed interface, the additional section of tubing that is opened to the column during purge is also accounted for. NDGNAS allows the void volume on each step to be separately defined. The top void on step 4, which was set to $V_{\text{top}} + V_{\text{top,extra}}$, was the only region over the cycle that differed from V_{bottom} and V_{top} shown in Table 6.4. V_{bottom} between adsorption and desorption steps was essentially the same and hence two separate values are not required.

Table 6.4: A summary of experimental parameters that characterise the RPSA pilot plant.

| Parameter | Magnitude | Units |
|------------------------|-------------------------------|----------------------------------|
| L_{bed} | 1.00 | m |
| d_{bed} | 0.156 | m |
| V_{bottom} | 2.68×10^{-3} | m^3 |
| V_{top} | 2.28×10^{-3} | m^3 |
| $V_{\text{top,extra}}$ | $1.60 \times 10^{-3} \dagger$ | m^3 |
| m_{bed} | 11.29 | kg |
| Δz_w | 0.0034 | m |
| $\hat{\rho}_w$ | 7900 ‡ | kg m^{-3} |
| λ_w | 14.9 ‡ | $\text{W m}^{-1} \text{K}^{-1}$ |
| \hat{c}_w | 477 ‡ | $\text{J kg}^{-1} \text{K}^{-1}$ |

† This value denotes the volume of pipework associated with the purge line on step 4 only.

‡ Taken from Çengel (1998, p 949) for stainless steel 304.

An approximate estimate of the heat transfer coefficient between the void region and column wall was calculated using the correlation of Sieder & Tate (1936). Leva's correlation was used to calculate a local heat transfer coefficient between the sorbent bed and wall at each axial coordinate within the adsorption column (Eq. (4.21)). External film heat transfer coefficients from the wall to ambient, $h_{w,A}$, were set to zero given the column was wrapped with insulation.

6.4.1 Experimentally Fitting Product Tank Response

The EMU study of §4.3 revealed the non-isothermal CSTR model used within NDGNAS required unrealistic heat transfer coefficients to match experimental data. Deviations from the adiabatic, well-mixed assumption are also prominent within the product tank located on the RPSA pilot plant. Section 4.3 stated the dynamics that dictate the response of a tank that deviates from the CSTR assumption is not being pursued in this dissertation. This statement also applies to simulations performed in this chapter. To independently characterise the response of the product tank on the RPSA pilot plant using one adjustable heat transfer coefficient was not possible across all runs. Instead, the product tank profile obtained experimentally from each individual RPSA pilot plant run was passed directly into NDGNAS as the modulating pressure to use on the other side of the compressible valve equation at the top of the adsorption column. An uninsulated stainless steel pipe of length 2 m and internal diameter 0.038 m connects the product tank to SV5 and SV7, so NDGNAS stipulates gas passing back into the bed as purge is at ambient temperature.

Each simulation performed in this chapter was executed with a new product tank model that allows end of step pressures for the tank to be entered and straight lines then used to connect these pressures across each step. In general, experimental product tank profiles presented later in this chapter were found to match linearly fitted profiles very well. This method eliminates any influence artificial $h_{\text{tank},A}$ values can have on simulated profiles as real tank profiles are now being

used. In fact, one can think of this as being equivalent to adjusting $h_{\text{tank},w}$ artificially throughout the cycle to match experimental profiles. End of step product tank pressures obtained experimentally for every run simulated in this chapter have also been provided in Table 6.6 for completeness. Numerically, product flow per cycle is calculated from the accumulated moles obtained downstream of SV7 on step 2 minus the moles of gas passing back into the bed as purge on step 4. Hence product gas purity is calculated as the ratio of oxygen to total flow obtained during step 2 of the cycle. After step 2 of each simulated cycle, NDGNAS updates product gas composition based on this ratio and passes this composition back into the top void on step 4.

With numerical valve coefficients controlled to achieve end of step pressure and purity targets (see §6.4.4), no fitting parameters remain within NDGNAS to match experimental data. All equilibrium isotherm, intrapellet transport and pressure drop parameters quantified in chapters 4 and 5 were used directly in this chapter to characterise the sorbent bed. Although experimental profiles have been used to fit product tank response, this procedure is valid as we are mainly concerned here with dynamics that reside within the adsorption column. The product tank is an external device that provides the boundary condition on steps 2 and 4. Fitting this experimentally means that errors in the product tank model do not manifest in any deviations observed numerically for the sorbent bed, allowing valid conclusions to be made regarding bed response that is independent of the tank model.

6.4.2 Defining CSS from Experimental and Numerical Data

NDGNAS employs a successive substitution approach to CSS from an arbitrary set of initial conditions over a predefined cycle arrangement. For all RPSA pilot plant simulations of this chapter, the CSS check described in §B.4 of appendix B was activated. The LDFP model and DPM are both used so the Mass-transfer Model Switch (MMS) introduced in §3.3.1 is also activated. However, *a priori* estimates on the actual magnitude of these CSS tolerance parameters is rather arbitrary and no definitive guidelines are readily available. In this respect assignment of suitable tolerance parameters was simply based on the fact that additional tightening resulted in negligible differences to CSS conditions when compared to RPSA pilot plant data.

One argument in favour of the values adopted in Table 6.5, however, is the fact that corresponding parameters measured experimentally, such as pressure and temperature, have a resolution that is at least one order of magnitude greater. While the mathematical definition of CSS for a numerical simulator is relatively straight forward and easily implemented, the same cannot be said for the experimental determination of CSS on the RPSA pilot plant. Ambient pressure and temperature fluctuate continuously and uncontrollably within the laboratory where the RPSA pilot plant is

located and hence influences the performance of the process at that particular point in time. Further to this, small fluctuations in feed air supply pressure from the screw compressor meant the pressure difference across the feed line modulating valve was not exactly constant, occasionally giving rise to small drifts in bed pressure of around 0.05 bar.

Table 6.5: Magnitude of the tolerances applied to each CSS parameter used by NDGNAS when simulating RPSA pilot plant data. A complete definition of these parameters can be found in Table B.1 of appendix B.

| Parameter | Magnitude | Units |
|---|----------------------|---|
| $E_{j,\max}^B$ for p_i^B | 5.0×10^{-4} | bar.a for $i = 1 \dots N_c$ ($j = 1 \dots N_c$) |
| $E_{j,\max}^B$ for n_i^P | 2.0×10^{-4} | gmole kg^{-1} for $i = 1 \dots N_c$ ($j = N_c + 1 \dots 2N_c$) |
| $E_{j,\max}^B$ for T | 1.0×10^{-2} | K ($j = 2N_c + 1$) |
| $E_{j,\text{rms}}^B$ for p_i^B | 1.0×10^{-4} | bar.a for $i = 1 \dots N_c$ ($j = 1 \dots N_c$) |
| $E_{j,\text{rms}}^B$ for n_i^P | 1.0×10^{-4} | gmole kg^{-1} for $i = 1 \dots N_c$ ($j = N_c + 1 \dots 2N_c$) |
| $E_{j,\text{rms}}^B$ for T | 5.0×10^{-3} | K ($j = 2N_c + 1$) |
| $E_{i,\text{mole}}^B$ | 1.0×10^{-2} | % for $i = 1 \dots N_c$ |
| E_{energy}^B and E_{grad}^B | 1.0×10^{-1} | % |

Each of these mechanisms indicate CSS for the RPSA pilot plant is not truly defined by one single set of operating conditions but rather a range of values that will be a function of local conditions at the time CSS readings are taken. One example of this is shown in Fig. 6.2. For the particular run depicted in Fig. 6.2 (RPSA run 15 from Table 6.6) ambient pressure did not vary by a significant amount, nor did feed air supply pressure so the transients depicted in Fig. 6.2 are primarily due to changes in ambient room temperature. This graph starts from a point where CSS has just been achieved so Fig. 6.2 represents thirty-six hours of operating data obtained at CSS.

Over this period, bed temperature and product gas purity are seen to track ambient temperature even though bed pressures, which are not shown here, were relatively steady throughout. As ambient temperature decreases so does bed temperature and vice versa. It is interesting to note the thermocouple located at $z = 0.040$ m experiences a change in temperature that closely follows ambient while the highest thermocouple in the bed, located at $z = 0.775$ m, sees this same change a few hours later. Further to this, product gas purity closely follows the temperature transient at $z = 0.775$ m indicating a change in ambient temperature takes approximately three hours to make its way through to the product line for RPSA run 15. Although product purity loosely remains within tolerances defined in Table 6.2, Fig. 6.2 does highlight the fact that a formal definition of CSS applied to NDGNAS will, in general, not be achieved experimentally given small perturbations are always present on the RPSA pilot plant.

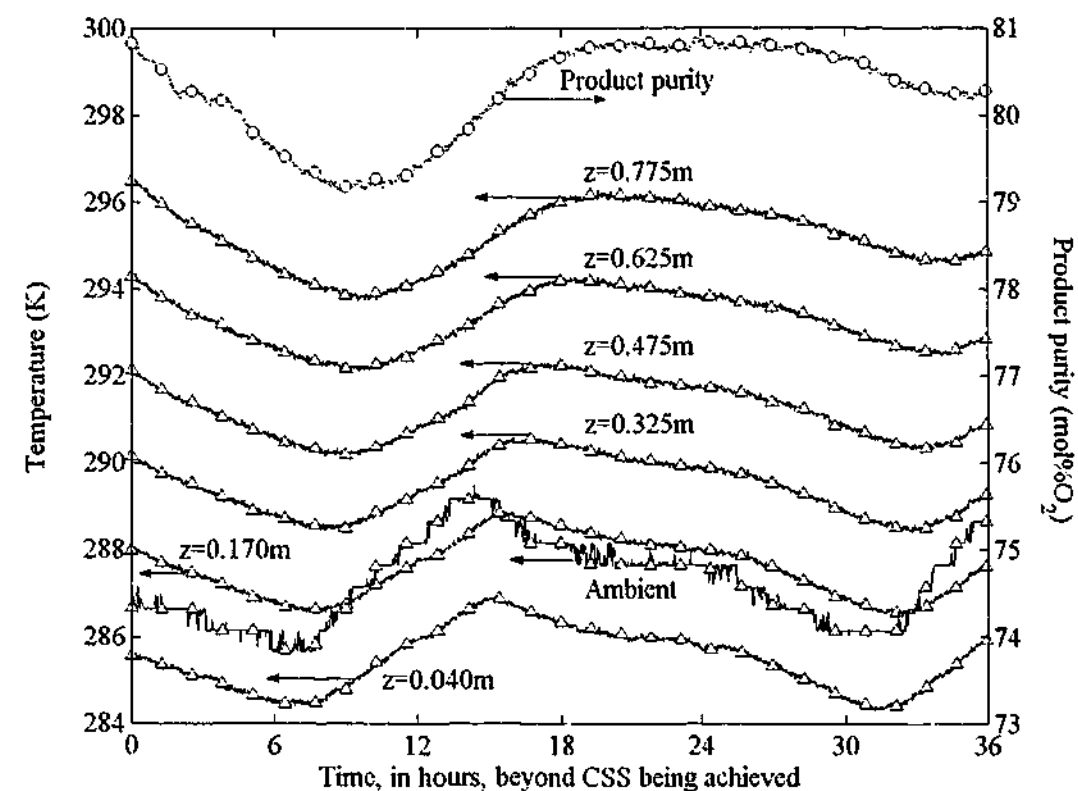


Figure 6.2: Experimental temperature and product purity that track changes in ambient temperature once a steady CSS condition has been achieved. This particular data set relates to RPSA run 15.

As such a strict definition of CSS was not incorporated into PLC logic and CSS is determined at the discretion of the operator. Typically, twelve to eighteen hours of steady purity, pressure and product flow was maintained before any parameters defined as being at CSS were taken. This in general means that each set of CSS data was obtained at a frequency that varied between two and five days, depending on how difficult it was to bring all four control target values to their designated tolerance in Table 6.2.

6.4.3 An Appropriate Level of Axial and Radial Discretisation?

One limitation inherent with numerical models and adsorption simulation is the appropriate level of axial discretisation, N_z , required to suitably resolve all spatial profiles across the sorbent bed. In addition to this, chapter 4 revealed some dependence on the level of radial discretisation within the pellet, N_r , for single step breakthrough experiments performed on the LUB apparatus. *A priori* estimates on these parameters for the simulation of an RPSA cycle when producing oxygen enriched air is not generally available. From this point an appropriate level of discretisation across both domains had to be selected that:

- i. allows a solution to be attained within a reasonable period of time (i.e. does not require several months to attain a single CSS operating point), and

- ii. adequately resolves spatial profiles to an accuracy that readily allows a number of comparisons to be made with experimental data at the interpellet level.

At this point a certain level of intuition has to be granted given a digression into the performance of NDGNAS as a function of N_z and N_r was not possible within the timeframe of this Ph.D.

An axial discretisation level of 41 nodes was assumed adequate to resolve spatial profiles across the interpellet domain of the sorbent bed ($N_z = 41$), while the radial domain of the pellet was discretised into five equal volumes ($N_r = 5$). The manual assignment of axial node locations similar to that used on the LUB apparatus in chapter 4 was also applied to allow data at select locations in the sorbent bed to be compared experimentally. Chapter 4 provides some discussion regarding the use of $N_r = 5$, the main emphasis being that C_m should be set to 0.166 while C_K and C_v , 0.083 and 0.061 respectively, are relatively insensitive to this value. Resolving the axial domain into 41 volumes produces a node spacing of approximately 0.025 m. Webley & He (2000) indicate spatial resolution does not need to be as fine for a cyclic process in relation to a single step given initial profiles are smeared as a result of the preceding counter-current depressurisation and purge steps.

For a binary component simulation with the rigorous wall model and bottom/top void volumes activated, the number of ODEs required to solve the LDFP model is 265 ($N_{eq} = 256$) while this same number is 593 ($N_{eq} = 593$) when the DPM is activated. Although these values of N_{eq} are not enormous, the length of time for which these ODEs are numerically integrated over is large, being in the order of several days. The ODE tolerances $RelTol$ and $AbsTol$ were both set to 5.0×10^{-7} on every simulation. To reduce the burden of numerical simulation from the same initial condition every time, NDGNAS has an added option of restarting a simulation from a complete set of CSS profiles obtained from a previous run by outputting a formatted file that can be read back in at program initialisation. When using the MMS these initial conditions relate to the LDFP portion of the simulation only and marginal differences in CPU time were observed. Section 3.5 found the LDFP model only occupies a small portion of the total CPU time required to converge the DPM, which was also the case in this chapter.

6.4.4 Implementing Numerical Control Loops

Section 6.3.1 introduced four target values that are maintained during each run on the RPSA pilot plant. These same constraints were also imposed on NDGNAS in the form of numerical proportional-only control loops [Marlin (1995, pp 266-270)]. Proportional-only control loops were used without integral or derivative action given full PID control often caused the simulation to become unstable. The implementation of PID control loops within NDGNAS, which is identical to the scheme adopted through MINSA, is discussed in Todd *et al.* (2001). At the end of each cycle NDGNAS extracts the required parameters for control and then systematically adjusts the relevant boundary condition assigned to that variable, which in this case are numerical valve coefficients K_{valve} , until the desired tolerance is achieved. While tolerances of 0.03 bar and 1.0 mol%O₂ were enforced experimentally (Table 6.2), NDGNAS enforced tolerances of 0.01 bar and 0.1 mol%O₂. Satisfying these control tolerances required anywhere from 300 to 5000 cycles to be simulated.

To ensure CSS data that is written to file also satisfies these target values, the CSS check invoked by NDGNAS stipulates each control loop must be within tolerance in addition to profile and mass/energy balance closure checks performed using parameters from Table 6.5. In general, an additional 500 to 1000 cycles were simulated once control loops had converged to achieve final CSS conditions. This means anywhere from 2,000 to 12,000 cycles per simulation in total was being performed with the MMS activated.

Now that a rigorous product tank model is no longer simulated, product gas purity was controlled by manipulating K_{valve} that connects the sorbent bed to the product tank at the top of the bed on step 2. To control end of feed plus make product step pressure, K_{valve} at the bottom of the bed across steps 1 and 2 were manipulated. In order to control vent pressure on step 3, K_{valve} at the bottom of the bed was manipulated and the corresponding magnitude carried across directly onto step 4 for K_{valve} at the bottom of the bed. End of step purge pressure was manipulated using K_{valve} that connects the product tank to the sorbent bed on step 4. All numerical valve coefficients assigned to NDGNAS were effectively manipulated as per the RPSA pilot plant to achieve four target values assigned by Table 6.2. The logic adopted within the PLC code at the top of the bed between steps 1 and 2 also has a numerical analog, which means the valve at the top of the sorbent bed between steps 1 and 2 within NDGNAS does not open until pressure in the top void volume is greater than or equal to product tank pressure. The time required to achieve this condition was consistently within 0.2 s of the experimentally observed value.

6.5 Introducing the Simplified RPSA Analysis

Before NDGNAS predictions are compared against experimental results, an alternative to the rigorous numerical approach shall be introduced that allows certain trends in process performance to be found analytically. A full description of the simplified RPSA analysis is provided in appendix C with the essential elements of that discussion presented in this chapter. It is important to point out, however, that results obtained from this simplified RPSA analysis will not be extensively analysed. Instead, this model is used as a tool that can provide certain trends in process performance under the assumption that intrapellet mass transfer, interpellet pressure drop and heat transfer through the sorbent bed have the same influence on process performance across all cycle times under consideration.

The simplified RPSA analysis transforms a mass balance performed over the entire one-bed, four-step cycle of Fig. 6.1 into analytical expressions for oxygen productivity and recovery as a function of working selectivity, $WS_{N_2:O_2}$. Working selectivity is a parameter that defines the separation efficiency of a sorbent material over the primary steps of adsorption and desorption [Notaro *et al.* (1999)]. A full process simulator such as NDGNAS is generally required to quantify each physical mechanism that can influence working selectivity, so the simplified RPSA analysis assumes working selectivity is constant with respect to cycle time at one particular purity and pressure window. The corresponding expressions for specific productivity and recovery obtained from this analysis are as follows.

$$\text{Specific productivity} = \frac{2765N_{O_2, BD} \left[WS_{N_2:O_2} - \left(\frac{1-y_{FD}}{y_{FD}} \right) \right]}{m_{\text{bed}} t_{\text{cycle}} \left[\left(\frac{1-y_{FD}}{y_{FD}} \right) - \left(\frac{1-y_{PD}}{y_{PD}} \right) \right]} \approx \frac{\text{constant}}{t_{\text{cycle}}} \quad (6.6)$$

$$\text{Recovery} = (1-X) \frac{\left[WS_{N_2:O_2} - \left(\frac{1-y_{FD}}{y_{FD}} \right) \right]}{\left[WS_{N_2:O_2} - \left(\frac{1-y_{PD}}{y_{PD}} \right) \right]} \approx \text{constant} \quad (6.7)$$

The symbol N represents the total moles of gas obtained over one cycle and y the mole fraction of oxygen in the relevant stream. The parameter X defines the amount of feed gas lost in the purge exhaust stream, $N_{\text{PG out}} = X N_{\text{FD}}$, that has to be made in order to derive analytical expressions in the form shown above. A justification for the introduction of X can be found in Table C.1 of appendix

C. The assumption of working selectivity (and moles of oxygen recovered during blowdown) being constant implies specific productivity has an inverse dependence on cycle time and recovery should be constant, as indicated by Eqs. (6.6) and (6.7). For working selectivity to remain constant the moles of nitrogen to oxygen removed over a cycle should be independent of any transport mechanisms within the bed; namely intrapellet mass transfer, interpellet pressure drop and heat transport. Calibrating the constants of Eqs. (6.6) and (6.7) at one particular cycle time from NDGNAS and the RPSA pilot plant allows ideal trend lines to be generated. The approximations of Eqs. (6.6) and (6.7) are equivalent to the scaling rules generated by Rota & Wankat (1990), see §1.1.2, so any deviations from ideal trend lines is a reflection of the changing impact of intrapellet mass transfer, interpellet heat transfer and heat transport as a function of cycle time.

In addition to the ideal trend lines of Eqs. (6.6) and (6.7), the simplified RPSA analysis provides a convenient parameter that allows different sorbent materials to be evaluated over one particular operating regime, namely working selectivity. Notaro *et al.* (1999) indicate the adiabatic working selectivity is most appropriate for oxygen PSA and so temperature variations need to be accounted for within the calculation of WS_{N_2/O_2} . To introduce adiabatic behaviour, a simple energy balance very similar to that proposed by Wilson (2001) is performed. This method effectively lumps the capacitance of the sorbent bed into one average term that allows the temperature of gas exiting the bed during adsorption and desorption steps to be found. This also assumes the sorbent bed is swinging by an amount ΔT_{bed} between adsorption and desorption such that a linear temperature gradient arises through the bed (refer to appendix C for more details). Final expressions for temperature around the sorbent bed are as follows.

$$T_{BD} = T_{FD} - \frac{1}{2} \Delta T_{bed} \quad (6.8)$$

$$T_{PD} = T_{FD} + \frac{1}{2} \left(\frac{N_{FD}}{F_{PD} + N_{PG in}} \right) \left(\frac{N_{BD}}{N_{FD}} + X \right) \Delta T_{bed} \quad (6.9)$$

$$\Delta T_{bed} = \frac{m_{bed} [\Delta H_1 (n_{1,eq}^{FD} - n_{1,eq}^{PG}) + \Delta H_2 (n_{2,eq}^{FD} - n_{2,eq}^{PG})]}{[m_{bed} \hat{c}_s + m_{bed} c_g^{ave} n_{BD,ave}^{eq} + \varepsilon_T V_{bed} c_g^{ave} \rho_{g,ave}^{BD} + \frac{1}{2} (N_{BD} + X N_{FD}) c_g^{BD}]} \quad (6.10)$$

Having introduced the simplified RPSA analysis, attention will now turn towards a comparison of individual RPSA pilot plant runs with respect to NDGNAS. The simplified RPSA analysis shall be used in §6.7 to examine the use of IAST regressed equilibrium isotherm parameters in addition to comparing ideal trend lines against RPSA pilot plant and NDGNAS data.

6.6 Results - RPSA Pilot Plant versus NDGNAS Data

With the experimental arrangement of the RPSA pilot plant fully represented within NDGNAS, a comparison of experimental and numerical separation performance can be made. In total, eighteen different CSS operating points have been obtained from the RPSA pilot plant and are denoted RPSA run 1 through 18. A tabular summary of the relevant parameters that identify each RPSA run is presented in Table 6.6. Data presented in Table 6.6 was also used by NDGNAS to simulate each run hence RPSA pilot plant values only are shown.

Table 6.6: Tabular summary of experimentally obtained step times, product purity and end of step pressures that identify the operating conditions for each RPSA run.

| Parameter | RPSA run 1 | RPSA run 2 |
|--|---------------------|---------------------|
| Step 1 time (s) | 11.3 ± 0.1 | 11.1 ± 0.1 |
| Total cycle time (s) † | 50.0 ± 0.1 | 50.0 ± 0.1 |
| Product purity (mol%O ₂) # | 90.0 ± 0.5 (94.0) ‡ | 79.1 ± 0.5 (82.6) ‡ |
| Feed temperature (K) * | 287.9 ± 0.6 | 286.5 ± 0.9 |
| T _A (K) | 288.7 ± 0.5 | 287.7 ± 0.5 |
| p _A (bar.a) | 1.015 ± 0.001 | 1.018 ± 0.001 |
| p ^{tank} end step 1 (bar.a) | 3.41 ± 0.04 | 3.33 ± 0.05 |
| p ^{tank} end step 2 (bar.a) | 3.98 ± 0.03 | 3.97 ± 0.03 |
| p ^{tank} end step 3 (bar.a) | 3.87 ± 0.03 | 3.85 ± 0.03 |
| p ^{tank} end step 4 (bar.a) | 3.44 ± 0.05 | 3.36 ± 0.06 |

| Parameter | RPSA run 3 | RPSA run 4 |
|--|---------------------|---------------------|
| Step 1 time (s) | 7.3 ± 0.1 | 8.0 ± 0.1 |
| Total cycle time (s) † | 36.0 ± 0.1 | 36.0 ± 0.1 |
| Product purity (mol%O ₂) # | 89.2 ± 0.5 (93.2) ‡ | 80.1 ± 0.5 (83.7) ‡ |
| Feed temperature (K) * | 286.4 ± 0.6 | 284.7 ± 0.6 |
| T _A (K) | 287.7 ± 0.5 | 285.7 ± 0.5 |
| p _A (bar.a) | 0.999 ± 0.001 | 1.008 ± 0.001 |
| p ^{tank} end step 1 (bar.a) | 3.22 ± 0.03 | 3.25 ± 0.03 |
| p ^{tank} end step 2 (bar.a) | 3.91 ± 0.03 | 3.95 ± 0.03 |
| p ^{tank} end step 3 (bar.a) | 3.81 ± 0.03 | 3.84 ± 0.03 |
| p ^{tank} end step 4 (bar.a) | 3.27 ± 0.03 | 3.28 ± 0.03 |

† Step time 2 = Cycle time - step time 1 - step time 3 - step time 4 (see Table 6.3 for step times 3 and 4).

‡ The number in brackets represents the adjusted purity mol%O₂+Ar used for each NDGNAS simulation.

Denotes a parameter that is controlled according to Table 6.2.

* Feed temperature represents the average temperature of gas passed into the bed over the cycle at CSS. The plus-minus value represents 95% confidence limits on feed temperature.

Table 6.6 continued

| Parameter | RPSA run 5 | RPSA run 6 |
|---|--------------------------------|--------------------------------|
| Step 1 time (s) | 4.2 ± 0.1 | 4.0 ± 0.1 |
| Total cycle time (s) [†] | 22.0 ± 0.1 | 22.0 ± 0.1 |
| Product purity (mol%O ₂) [#] | 89.3 ± 0.5 (93.3) [‡] | 80.7 ± 0.5 (84.3) [‡] |
| Feed temperature (K) [*] | 289.2 ± 1.3 | 287.8 ± 0.6 |
| T _A (K) | 290.2 ± 0.5 | 288.3 ± 0.5 |
| p _A (bar.a) | 1.012 ± 0.001 | 1.011 ± 0.001 |
| p ^{tank} end step 1 (bar.a) | 3.28 ± 0.03 | 3.20 ± 0.03 |
| p ^{tank} end step 2 (bar.a) | 3.93 ± 0.03 | 3.93 ± 0.03 |
| p ^{tank} end step 3 (bar.a) | 3.83 ± 0.03 | 3.83 ± 0.03 |
| p ^{tank} end step 4 (bar.a) | 3.34 ± 0.03 | 3.28 ± 0.03 |

| Parameter | RPSA run 7 | RPSA run 8 |
|---|--------------------------------|--------------------------------|
| Step 1 time (s) | 2.7 ± 0.1 | 2.6 ± 0.1 |
| Total cycle time (s) [†] | 14.0 ± 0.1 | 14.0 ± 0.1 |
| Product purity (mol%O ₂) [#] | 89.8 ± 0.5 (93.8) [‡] | 80.4 ± 0.5 (84.0) [‡] |
| Feed temperature (K) [*] | 288.3 ± 0.8 | 288.4 ± 0.6 |
| T _A (K) | 288.2 ± 0.5 | 289.6 ± 0.5 |
| p _A (bar.a) | 1.016 ± 0.001 | 1.003 ± 0.001 |
| p ^{tank} end step 1 (bar.a) | 3.18 ± 0.03 | 3.09 ± 0.03 |
| p ^{tank} end step 2 (bar.a) | 3.91 ± 0.03 | 3.89 ± 0.03 |
| p ^{tank} end step 3 (bar.a) | 3.86 ± 0.03 | 3.82 ± 0.03 |
| p ^{tank} end step 4 (bar.a) | 3.27 ± 0.03 | 3.20 ± 0.03 |

| Parameter | RPSA run 9 | RPSA run 10 |
|---|--------------------------------|--------------------------------|
| Step 1 time (s) | 1.5 ± 0.1 | 9.7 ± 0.2 |
| Total cycle time (s) [†] | 8.0 ± 0.1 | 50.0 ± 0.1 |
| Product purity (mol%O ₂) [#] | 80.0 ± 0.5 (83.6) [‡] | 89.4 ± 0.5 (93.4) [‡] |
| Feed temperature (K) [*] | 290.8 ± 0.5 | 288.7 ± 2.4 |
| T _A (K) | 290.8 ± 0.5 | 288.3 ± 0.5 |
| p _A (bar.a) | 1.008 ± 0.001 | 1.011 ± 0.001 |
| p ^{tank} end step 1 (bar.a) | 2.97 ± 0.03 | 4.32 ± 0.05 |
| p ^{tank} end step 2 (bar.a) | 3.76 ± 0.03 | 4.99 ± 0.03 |
| p ^{tank} end step 3 (bar.a) | 3.76 ± 0.03 | 4.87 ± 0.03 |
| p ^{tank} end step 4 (bar.a) | 3.14 ± 0.03 | 4.35 ± 0.05 |

| Parameter | RPSA run 11 | RPSA run 12 |
|---|--------------------------------|--------------------------------|
| Step 1 time (s) | 9.4 ± 0.2 | 5.5 ± 0.1 |
| Total cycle time (s) [†] | 50.0 ± 0.1 | 36.0 ± 0.1 |
| Product purity (mol%O ₂) [#] | 79.6 ± 0.5 (83.1) [‡] | 90.4 ± 0.5 (94.4) [‡] |
| Feed temperature (K) [*] | 290.3 ± 2.3 | 290.2 ± 1.5 |
| T _A (K) | 290.5 ± 0.5 | 290.8 ± 0.5 |
| p _A (bar.a) | 0.989 ± 0.001 | 1.004 ± 0.001 |
| p ^{tank} end step 1 (bar.a) | 4.23 ± 0.05 | 4.22 ± 0.03 |
| p ^{tank} end step 2 (bar.a) | 4.97 ± 0.03 | 4.98 ± 0.03 |
| p ^{tank} end step 3 (bar.a) | 4.82 ± 0.03 | 4.86 ± 0.03 |
| p ^{tank} end step 4 (bar.a) | 4.26 ± 0.06 | 4.27 ± 0.03 |

[†] Step time 2 = Cycle time - step time 1 - step time 3 - step time 4 (see Table 6.3 for step times 3 and 4).

[‡] The number in brackets represents the adjusted purity mol%O₂+Ar used for each NDGNAS simulation.

[#] Denotes a parameter that is controlled according to Table 6.2.

^{*} Feed temperature represents the average temperature of gas passed into the bed over the cycle at CSS. The plus-minus value represents 95% confidence limits on feed temperature.

Table 6.6 continued

| Parameter | RPSA run 13 | RPSA run 14 |
|---|--------------------------------|--------------------------------|
| Step 1 time (s) | 5.7 ± 0.2 | 3.2 ± 0.1 |
| Total cycle time (s) [†] | 36.0 ± 0.1 | 22.0 ± 0.1 |
| Product purity (mol%O ₂) [#] | 79.1 ± 0.5 (82.6) [‡] | 90.7 ± 0.5 (94.7) [‡] |
| Feed temperature (K) [*] | 287.9 ± 1.4 | 287.9 ± 1.4 |
| T _A (K) | 289.7 ± 0.5 | 288.3 ± 0.5 |
| p _A (bar.a) | 0.996 ± 0.001 | 1.008 ± 0.001 |
| p ^{tank} end step 1 (bar.a) | 4.12 ± 0.05 | 4.18 ± 0.03 |
| p ^{tank} end step 2 (bar.a) | 4.99 ± 0.03 | 4.92 ± 0.03 |
| p ^{tank} end step 3 (bar.a) | 4.84 ± 0.03 | 4.83 ± 0.03 |
| p ^{tank} end step 4 (bar.a) | 4.15 ± 0.05 | 4.28 ± 0.03 |

| Parameter | RPSA run 15 | RPSA run 16 |
|---|--------------------------------|--------------------------------|
| Step 1 time (s) | 3.0 ± 0.1 | 2.6 ± 0.1 |
| Total cycle time (s) [†] | 22.0 ± 0.1 | 14.0 ± 0.1 |
| Product purity (mol%O ₂) [#] | 79.5 ± 0.5 (83.0) [‡] | 89.6 ± 0.5 (93.6) [‡] |
| Feed temperature (K) [*] | 287.6 ± 1.2 | 289.8 ± 0.7 |
| T _A (K) | 289.1 ± 0.5 | 289.7 ± 0.5 |
| p _A (bar.a) | 1.009 ± 0.001 | 1.008 ± 0.001 |
| p ^{tank} end step 1 (bar.a) | 4.07 ± 0.03 | 4.51 ± 0.03 |
| p ^{tank} end step 2 (bar.a) | 4.90 ± 0.03 | 4.96 ± 0.03 |
| p ^{tank} end step 3 (bar.a) | 4.79 ± 0.03 | 4.89 ± 0.03 |
| p ^{tank} end step 4 (bar.a) | 4.19 ± 0.03 | 4.26 ± 0.03 |

| Parameter | RPSA run 17 | RPSA run 18 |
|---|--------------------------------|--------------------------------|
| Step 1 time (s) | 2.5 ± 0.1 | 1.3 ± 0.1 |
| Total cycle time (s) [†] | 14.0 ± 0.1 | 8.0 ± 0.1 |
| Product purity (mol%O ₂) [#] | 80.0 ± 0.5 (83.6) [‡] | 80.5 ± 0.5 (84.1) [‡] |
| Feed temperature (K) [*] | 288.9 ± 1.2 | 288.6 ± 0.5 |
| T _A (K) | 289.5 ± 0.5 | 288.3 ± 0.5 |
| p _A (bar.a) | 1.007 ± 0.001 | 1.011 ± 0.001 |
| p ^{tank} end step 1 (bar.a) | 4.01 ± 0.03 | 3.98 ± 0.03 |
| p ^{tank} end step 2 (bar.a) | 4.94 ± 0.03 | 4.90 ± 0.03 |
| p ^{tank} end step 3 (bar.a) | 4.84 ± 0.03 | 4.86 ± 0.03 |
| p ^{tank} end step 4 (bar.a) | 4.13 ± 0.03 | 4.22 ± 0.03 |

[†] Step time 2 = Cycle time - step time 1 - step time 3 - step time 4 (see Table 6.3 for step times 3 and 4).

[‡] The number in brackets represents the adjusted purity mol%O₂+Ar used for each NDGNAS simulation.

[#] Denotes a parameter that is controlled according to Table 6.2.

^{*} Feed temperature represents the average temperature of gas passed into the bed over the cycle at CSS. The plus-minus value represents 95% confidence limits on feed temperature.

Experimental data presented in Table 6.6 (as well as Table 6.7) represent average values obtained over ten cycles of data acquisition at CSS. The corresponding plus-minus value represents 95% confidence limits on the reported average. In situations where the plus-minus value is smaller than experimental error discussed in §6.2.4, experimental error is reported as the 95% confidence limit. Table 6.6 presents two values for purity, the first represents average purity that was experimentally obtained from the paramagnetic oxygen analyser over ten cycles and the second (in brackets) represents product purity when oxygen and argon are lumped together as the one component.

For ease in the numerical calculation of Ω_i , the LDFP model is evaluated using the Alpay & Scott (1992) analytical result for Ω_i when $\theta_i < 0.1$. For $\theta_i \geq 0.1$ the constant value $\Omega_i = \pi^2$ is adopted as shown on Fig. 2.2. The Alpay & Scott (1992) expression fits the Nakao & Suzuki (1983) result well for $\theta_i < 0.1$ and eliminates the need to independently determine Ω_i through a separate numerical routine or graphical look-up procedure. Table 6.3, however, reveals θ_i is greater than 0.1 across each cycle time so $\Omega_i = \pi^2$ for all runs that use the LDFP model.

Having presented parameters that define the operating conditions from each of the eighteen RPSA runs, the next set of results presented in Table 6.7 compare experimental results for the parameters of interest, discussed in §6.3.3, to their corresponding NDGNAS predictions.

Table 6.7: Comparing experimental and numerical parameters of interest as outlined in §6.3.3.

| RPSA run 1 ($t_{\text{cycle}} = 50$ s at 90.0 mol%O ₂) | RPSA pilot plant | NDGNAS | |
|---|------------------|--------|-------|
| | | LDFP | DPM |
| Parameter | | | |
| p^{bottom} end step 1 (bar.a) | 3.43 ± 0.04 | 3.42 | 3.43 |
| p^{top} end step 1 (bar.a) | 3.42 ± 0.04 | 3.41 | 3.42 |
| p^{bottom} end step 2 (bar.a) [#] | 4.00 ± 0.03 | 4.00 | 4.01 |
| p^{top} end step 2 (bar.a) | 3.99 ± 0.03 | 3.99 | 4.00 |
| p^{bottom} end step 3 (bar.a) [#] | 1.21 ± 0.03 | 1.22 | 1.21 |
| p^{top} end step 3 (bar.a) | 1.22 ± 0.03 | 1.22 | 1.22 |
| p^{bottom} end step 4 (bar.a) [#] | 1.40 ± 0.04 | 1.40 | 1.39 |
| p^{top} end step 4 (bar.a) | 1.42 ± 0.04 | 1.42 | 1.42 |
| Exhaust flow step 3 (gmole cycle ⁻¹) | 7.09 ± 0.06 | 7.35 | 7.39 |
| Exhaust flow step 4 (gmole cycle ⁻¹) | 1.16 ± 0.06 | 1.19 | 1.14 |
| Total product flow (gmole cycle ⁻¹) | 0.410 ± 0.020 | 0.492 | 0.507 |
| Recovery (%O ₂ +Ar) | 20.0 ± 0.8 | 23.2 | 24.2 |
| Specific productivity ((kg O ₂ +Ar) kg ⁻¹ day ⁻¹) | 1.89 ± 0.06 | 2.26 | 2.33 |

| RPSA run 2 ($t_{\text{cycle}} = 50$ s at 79.1 mol%O ₂) | RPSA pilot plant | NDGNAS | |
|---|------------------|--------|-------|
| | | LDFP | DPM |
| Parameter | | | |
| p^{bottom} end step 1 (bar.a) | 3.35 ± 0.05 | 3.35 | 3.33 |
| p^{top} end step 1 (bar.a) | 3.33 ± 0.05 | 3.34 | 3.32 |
| p^{bottom} end step 2 (bar.a) [#] | 4.00 ± 0.03 | 4.00 | 4.00 |
| p^{top} end step 2 (bar.a) | 3.99 ± 0.03 | 3.99 | 3.99 |
| p^{bottom} end step 3 (bar.a) [#] | 1.21 ± 0.03 | 1.21 | 1.21 |
| p^{top} end step 3 (bar.a) | 1.22 ± 0.03 | 1.22 | 1.22 |
| p^{bottom} end step 4 (bar.a) [#] | 1.40 ± 0.05 | 1.40 | 1.40 |
| p^{top} end step 4 (bar.a) | 1.43 ± 0.05 | 1.43 | 1.43 |
| Exhaust flow step 3 (gmole cycle ⁻¹) | 7.10 ± 0.06 | 7.23 | 7.27 |
| Exhaust flow step 4 (gmole cycle ⁻¹) | 1.16 ± 0.06 | 1.17 | 1.15 |
| Total product flow (gmole cycle ⁻¹) | 0.490 ± 0.020 | 0.611 | 0.627 |
| Recovery (%O ₂ +Ar) | 20.8 ± 0.8 | 25.5 | 26.0 |
| Specific productivity ((kg O ₂ +Ar) kg ⁻¹ day ⁻¹) | 1.98 ± 0.06 | 2.47 | 2.54 |

[#] Denotes a parameter that is controlled according to Table 6.2.

Table 6.7 continued

| RPSA run 3 ($t_{\text{cycle}} = 36$ s at 89.2 mol%O ₂) | RPSA pilot plant | NDGNAS | |
|---|------------------|--------|-------|
| | | LDFP | DPM |
| Parameter | | | |
| p^{bottom} end step 1 (bar.a) | 3.25 ± 0.03 | 3.23 | 3.25 |
| p^{top} end step 1 (bar.a) | 3.22 ± 0.03 | 3.21 | 3.23 |
| p^{bottom} end step 2 (bar.a) [#] | 4.00 ± 0.03 | 4.01 | 4.00 |
| p^{top} end step 2 (bar.a) | 3.98 ± 0.03 | 4.00 | 3.99 |
| p^{bottom} end step 3 (bar.a) [#] | 1.18 ± 0.03 | 1.19 | 1.17 |
| p^{top} end step 3 (bar.a) | 1.19 ± 0.03 | 1.21 | 1.19 |
| p^{bottom} end step 4 (bar.a) [#] | 1.41 ± 0.03 | 1.40 | 1.40 |
| p^{top} end step 4 (bar.a) | 1.45 ± 0.03 | 1.45 | 1.45 |
| Exhaust flow step 3 (gmole cycle ⁻¹) | 7.23 ± 0.06 | 7.44 | 7.52 |
| Exhaust flow step 4 (gmole cycle ⁻¹) | 1.39 ± 0.06 | 1.53 | 1.50 |
| Total product flow (gmole cycle ⁻¹) | 0.474 ± 0.020 | 0.547 | 0.636 |
| Recovery (%O ₂ +Ar) | 21.8 ± 0.9 | 24.3 | 27.8 |
| Specific productivity ((kg O ₂ +Ar) kg ⁻¹ day ⁻¹) | 3.00 ± 0.07 | 3.46 | 4.03 |

| RPSA run 4 ($t_{\text{cycle}} = 36$ s at 80.1 mol%O ₂) | RPSA pilot plant | NDGNAS | |
|---|------------------|--------|-------|
| | | LDFP | DPM |
| Parameter | | | |
| p^{bottom} end step 1 (bar.a) | 3.28 ± 0.03 | 3.27 | 3.26 |
| p^{top} end step 1 (bar.a) | 3.26 ± 0.03 | 3.25 | 3.24 |
| p^{bottom} end step 2 (bar.a) [#] | 4.00 ± 0.03 | 4.01 | 4.01 |
| p^{top} end step 2 (bar.a) | 3.98 ± 0.03 | 4.00 | 4.00 |
| p^{bottom} end step 3 (bar.a) [#] | 1.22 ± 0.03 | 1.22 | 1.21 |
| p^{top} end step 3 (bar.a) | 1.23 ± 0.03 | 1.24 | 1.23 |
| p^{bottom} end step 4 (bar.a) [#] | 1.40 ± 0.03 | 1.41 | 1.40 |
| p^{top} end step 4 (bar.a) | 1.44 ± 0.03 | 1.45 | 1.44 |
| Exhaust flow step 3 (gmole cycle ⁻¹) | 7.01 ± 0.06 | 7.19 | 7.27 |
| Exhaust flow step 4 (gmole cycle ⁻¹) | 1.38 ± 0.06 | 1.46 | 1.42 |
| Total product flow (gmole cycle ⁻¹) | 0.516 ± 0.020 | 0.596 | 0.639 |
| Recovery (%O ₂ +Ar) | 21.8 ± 0.8 | 24.6 | 26.0 |
| Specific productivity ((kg O ₂ +Ar) kg ⁻¹ day ⁻¹) | 2.94 ± 0.06 | 3.41 | 3.64 |

| RPSA run 5 ($t_{\text{cycle}} = 22$ s at 89.3 mol%O ₂) | RPSA pilot plant | NDGNAS | |
|---|------------------|--------|-------|
| | | LDFP | DPM |
| Parameter | | | |
| p^{bottom} end step 1 (bar.a) | 3.32 ± 0.03 | 3.32 | 3.31 |
| p^{top} end step 1 (bar.a) | 3.28 ± 0.03 | 3.28 | 3.27 |
| p^{bottom} end step 2 (bar.a) [#] | 4.00 ± 0.03 | 4.01 | 4.00 |
| p^{top} end step 2 (bar.a) | 3.98 ± 0.03 | 3.99 | 3.98 |
| p^{bottom} end step 3 (bar.a) [#] | 1.21 ± 0.03 | 1.21 | 1.22 |
| p^{top} end step 3 (bar.a) | 1.24 ± 0.03 | 1.24 | 1.24 |
| p^{bottom} end step 4 (bar.a) [#] | 1.41 ± 0.03 | 1.41 | 1.41 |
| p^{top} end step 4 (bar.a) | 1.50 ± 0.03 | 1.49 | 1.49 |
| Exhaust flow step 3 (gmole cycle ⁻¹) | 6.97 ± 0.06 | 7.15 | 7.30 |
| Exhaust flow step 4 (gmole cycle ⁻¹) | 1.30 ± 0.06 | 1.43 | 1.40 |
| Total product flow (gmole cycle ⁻¹) | 0.415 ± 0.020 | 0.387 | 0.515 |
| Recovery (%O ₂ +Ar) | 20.0 ± 0.9 | 18.3 | 23.6 |
| Specific productivity ((kg O ₂ +Ar) kg ⁻¹ day ⁻¹) | 4.32 ± 0.11 | 4.02 | 5.35 |

[#] Denotes a parameter that is controlled according to Table 6.2.

Table 6.7 continued.

| RPSA run 6 ($t_{\text{cycle}} = 22$ s at 80.7 mol%O ₂) | RPSA pilot plant | NDGNAS | |
|---|------------------|--------|-------|
| | | LDFP | DPM |
| Parameter | | | |
| p^{bottom} end step 1 (bar.a) | 3.26 ± 0.03 | 3.24 | 3.25 |
| p^{top} end step 1 (bar.a) | 3.21 ± 0.03 | 3.20 | 3.20 |
| p^{bottom} end step 2 (bar.a) [#] | 4.01 ± 0.03 | 4.02 | 4.02 |
| p^{top} end step 2 (bar.a) | 3.99 ± 0.03 | 4.00 | 4.00 |
| p^{bottom} end step 3 (bar.a) [#] | 1.21 ± 0.03 | 1.21 | 1.21 |
| p^{top} end step 3 (bar.a) | 1.23 ± 0.03 | 1.23 | 1.23 |
| p^{bottom} end step 4 (bar.a) [#] | 1.41 ± 0.03 | 1.41 | 1.41 |
| p^{top} end step 4 (bar.a) | 1.50 ± 0.03 | 1.49 | 1.49 |
| Exhaust flow step 3 (gmole cycle ⁻¹) | 6.95 ± 0.06 | 7.18 | 7.29 |
| Exhaust flow step 4 (gmole cycle ⁻¹) | 1.28 ± 0.06 | 1.44 | 1.39 |
| Total product flow (gmole cycle ⁻¹) | 0.500 ± 0.020 | 0.535 | 0.627 |
| Recovery (%O ₂ +Ar) | 21.7 ± 0.8 | 22.4 | 25.8 |
| Specific productivity ((kg O ₂ +Ar) kg ⁻¹ day ⁻¹) | 4.70 ± 0.12 | 5.02 | 5.89 |

| RPSA run 7 ($t_{\text{cycle}} = 14$ s at 89.8 mol%O ₂) | RPSA pilot plant | NDGNAS | |
|---|------------------|--------|-------|
| | | LDFP | DPM |
| Parameter | | | |
| p^{bottom} end step 1 (bar.a) | 3.27 ± 0.03 | 3.23 | 3.24 |
| p^{top} end step 1 (bar.a) | 3.18 ± 0.03 | 3.17 | 3.17 |
| p^{bottom} end step 2 (bar.a) [#] | 4.02 ± 0.03 | 4.02 | 4.02 |
| p^{top} end step 2 (bar.a) | 3.97 ± 0.03 | 3.98 | 3.98 |
| p^{bottom} end step 3 (bar.a) [#] | 1.21 ± 0.03 | 1.21 | 1.22 |
| p^{top} end step 3 (bar.a) | 1.27 ± 0.03 | 1.25 | 1.27 |
| p^{bottom} end step 4 (bar.a) [#] | 1.42 ± 0.03 | 1.42 | 1.42 |
| p^{top} end step 4 (bar.a) | 1.64 ± 0.03 | 1.58 | 1.58 |
| Exhaust flow step 3 (gmole cycle ⁻¹) | 6.41 ± 0.18 | 6.60 | 7.06 |
| Exhaust flow step 4 (gmole cycle ⁻¹) | 1.38 ± 0.06 | 1.45 | 1.46 |
| Total product flow (gmole cycle ⁻¹) | 0.327 ± 0.020 | 0.199 | 0.397 |
| Recovery (%O ₂ +Ar) | 15.6 to 17.0 | 10.3 | 18.9 |
| Specific productivity ((kg O ₂ +Ar) kg ⁻¹ day ⁻¹) | 5.37 ± 0.17 | 3.26 | 6.51 |

| RPSA run 8 ($t_{\text{cycle}} = 14$ s at 80.4 mol%O ₂) | RPSA pilot plant | NDGNAS | |
|---|------------------|--------|-------|
| | | LDFP | DPM |
| Parameter | | | |
| p^{bottom} end step 1 (bar.a) | 3.19 ± 0.03 | 3.17 | 3.17 |
| p^{top} end step 1 (bar.a) | 3.10 ± 0.03 | 3.10 | 3.08 |
| p^{bottom} end step 2 (bar.a) [#] | 4.01 ± 0.03 | 4.01 | 4.01 |
| p^{top} end step 2 (bar.a) | 3.95 ± 0.03 | 3.97 | 3.96 |
| p^{bottom} end step 3 (bar.a) [#] | 1.20 ± 0.03 | 1.20 | 1.21 |
| p^{top} end step 3 (bar.a) | 1.26 ± 0.03 | 1.25 | 1.26 |
| p^{bottom} end step 4 (bar.a) [#] | 1.40 ± 0.03 | 1.40 | 1.41 |
| p^{top} end step 4 (bar.a) | 1.62 ± 0.03 | 1.57 | 1.58 |
| Exhaust flow step 3 (gmole cycle ⁻¹) | 6.38 ± 0.10 | 6.87 | 7.14 |
| Exhaust flow step 4 (gmole cycle ⁻¹) | 1.36 ± 0.06 | 1.51 | 1.48 |
| Total product flow (gmole cycle ⁻¹) | 0.462 ± 0.020 | 0.379 | 0.565 |
| Recovery (%O ₂ +Ar) | 19.2 to 21.3 | 16.5 | 23.4 |
| Specific productivity ((kg O ₂ +Ar) kg ⁻¹ day ⁻¹) | 6.79 ± 0.16 | 5.57 | 8.29 |

[#] Denotes a parameter that is controlled according to Table 6.2.

Table 6.7 continued.

| RPSA run 9 ($t_{\text{cycle}} = 8$ s at 80.0 mol%O ₂) | RPSA pilot plant | NDGNAS | |
|---|------------------|--------|-------|
| | | LDFP | DPM |
| Parameter | | | |
| p^{bottom} end step 1 (bar.a) | 3.18 ± 0.03 | 3.09 | 3.13 |
| p^{top} end step 1 (bar.a) | 2.98 ± 0.03 | 2.97 | 2.97 |
| p^{bottom} end step 2 (bar.a) [#] | 3.98 ± 0.03 | 3.98 | 3.97 |
| p^{top} end step 2 (bar.a) | 3.80 ± 0.03 | 3.89 | 3.87 |
| p^{bottom} end step 3 (bar.a) [#] | 1.20 ± 0.03 | 1.21 | 1.21 |
| p^{top} end step 3 (bar.a) | 1.35 ± 0.03 | 1.30 | 1.31 |
| p^{bottom} end step 4 (bar.a) [#] | 1.39 ± 0.03 | 1.39 | 1.39 |
| p^{top} end step 4 (bar.a) | 2.00 ± 0.03 | 1.76 | 1.76 |
| Exhaust flow step 3 (gmole cycle ⁻¹) | 4.97 ± 0.20 | 5.85 | 6.47 |
| Exhaust flow step 4 (gmole cycle ⁻¹) | 1.27 ± 0.06 | 1.09 | 1.09 |
| Total product flow (gmole cycle ⁻¹) | 0.263 ± 0.020 | 0.114 | 0.338 |
| Recovery (%O ₂ +Ar) | 12.6 to 15.2 | 6.09 | 16.2 |
| Specific productivity ((kg O ₂ +Ar) kg ⁻¹ day ⁻¹) | 6.77 ± 0.25 | 2.91 | 8.67 |

| RPSA run 10 ($t_{\text{cycle}} = 50$ s at 89.4 mol%O ₂) | RPSA pilot plant | NDGNAS | |
|---|------------------|--------|-------|
| | | LDFP | DPM |
| Parameter | | | |
| p^{bottom} end step 1 (bar.a) | 4.34 ± 0.05 | 4.33 | 4.35 |
| p^{top} end step 1 (bar.a) | 4.32 ± 0.05 | 4.32 | 4.33 |
| p^{bottom} end step 2 (bar.a) [#] | 5.01 ± 0.03 | 5.01 | 5.01 |
| p^{top} end step 2 (bar.a) | 5.00 ± 0.03 | 5.01 | 5.00 |
| p^{bottom} end step 3 (bar.a) [#] | 1.19 ± 0.03 | 1.18 | 1.19 |
| p^{top} end step 3 (bar.a) | 1.19 ± 0.03 | 1.19 | 1.20 |
| p^{bottom} end step 4 (bar.a) [#] | 1.40 ± 0.04 | 1.40 | 1.41 |
| p^{top} end step 4 (bar.a) | 1.44 ± 0.05 | 1.44 | 1.44 |
| Exhaust flow step 3 (gmole cycle ⁻¹) | 9.15 ± 0.06 | 9.30 | 9.46 |
| Exhaust flow step 4 (gmole cycle ⁻¹) | 1.31 ± 0.06 | 1.37 | 1.35 |
| Total product flow (gmole cycle ⁻¹) | 0.543 ± 0.020 | 0.673 | 0.682 |
| Recovery (%O ₂ +Ar) | 20.7 ± 0.7 | 25.2 | 25.8 |
| Specific productivity ((kg O ₂ +Ar) kg ⁻¹ day ⁻¹) | 2.48 ± 0.06 | 3.08 | 3.15 |

| RPSA run 11 ($t_{\text{cycle}} = 50$ s at 79.6 mol%O ₂) | RPSA pilot plant | NDGNAS | |
|---|------------------|--------|-------|
| | | LDFP | DPM |
| Parameter | | | |
| p^{bottom} end step 1 (bar.a) | 4.25 ± 0.04 | 4.25 | 4.25 |
| p^{top} end step 1 (bar.a) | 4.24 ± 0.05 | 4.23 | 4.23 |
| p^{bottom} end step 2 (bar.a) [#] | 4.99 ± 0.03 | 4.99 | 4.99 |
| p^{top} end step 2 (bar.a) | 4.98 ± 0.03 | 4.98 | 4.98 |
| p^{bottom} end step 3 (bar.a) [#] | 1.19 ± 0.03 | 1.19 | 1.19 |
| p^{top} end step 3 (bar.a) | 1.20 ± 0.03 | 1.20 | 1.20 |
| p^{bottom} end step 4 (bar.a) [#] | 1.40 ± 0.05 | 1.40 | 1.40 |
| p^{top} end step 4 (bar.a) | 1.43 ± 0.05 | 1.43 | 1.43 |
| Exhaust flow step 3 (gmole cycle ⁻¹) | 8.98 ± 0.06 | 9.09 | 9.13 |
| Exhaust flow step 4 (gmole cycle ⁻¹) | 1.33 ± 0.06 | 1.35 | 1.32 |
| Total product flow (gmole cycle ⁻¹) | 0.618 ± 0.020 | 0.787 | 0.801 |
| Recovery (%O ₂ +Ar) | 21.2 ± 0.7 | 26.4 | 26.9 |
| Specific productivity ((kg O ₂ +Ar) kg ⁻¹ day ⁻¹) | 2.52 ± 0.06 | 3.20 | 3.26 |

[#] Denotes a parameter that is controlled according to Table 6.2.

Table 6.7 continued

| RPSA run 12 ($t_{\text{cycle}} = 36$ s at 90.4 mol%O ₂) Parameter | RPSA pilot plant | NDGNAS | |
|---|------------------|--------|-------|
| | | LDFP | DPM |
| p^{bottom} end step 1 (bar.a) | 4.25 ± 0.03 | 4.26 | 4.25 |
| p^{top} end step 1 (bar.a) | 4.22 ± 0.03 | 4.23 | 4.22 |
| p^{bottom} end step 2 (bar.a) [#] | 5.01 ± 0.03 | 5.01 | 5.01 |
| p^{top} end step 2 (bar.a) | 5.00 ± 0.03 | 5.00 | 5.00 |
| p^{bottom} end step 3 (bar.a) [#] | 1.19 ± 0.03 | 1.20 | 1.19 |
| p^{top} end step 3 (bar.a) | 1.21 ± 0.03 | 1.21 | 1.20 |
| p^{bottom} end step 4 (bar.a) [#] | 1.42 ± 0.03 | 1.41 | 1.42 |
| p^{top} end step 4 (bar.a) | 1.47 ± 0.03 | 1.46 | 1.47 |
| Exhaust flow step 3 (gmole cycle ⁻¹) | 8.89 ± 0.06 | 9.21 | 9.28 |
| Exhaust flow step 4 (gmole cycle ⁻¹) | 1.54 ± 0.06 | 1.70 | 1.67 |
| Total product flow (gmole cycle ⁻¹) | 0.576 ± 0.020 | 0.645 | 0.761 |
| Recovery (%O ₂ +Ar) | 22.2 ± 0.7 | 23.9 | 27.8 |
| Specific productivity ((kg O ₂ +Ar) kg ⁻¹ day ⁻¹) | 3.70 ± 0.07 | 4.14 | 4.89 |

| RPSA run 13 ($t_{\text{cycle}} = 36$ s at 79.1 mol%O ₂) Parameter | RPSA pilot plant | NDGNAS | |
|---|------------------|--------|-------|
| | | LDFP | DPM |
| p^{bottom} end step 1 (bar.a) | 4.15 ± 0.05 | 4.14 | 4.14 |
| p^{top} end step 1 (bar.a) | 4.12 ± 0.05 | 4.11 | 4.11 |
| p^{bottom} end step 2 (bar.a) [#] | 5.00 ± 0.03 | 5.01 | 5.01 |
| p^{top} end step 2 (bar.a) | 5.00 ± 0.03 | 5.00 | 5.01 |
| p^{bottom} end step 3 (bar.a) [#] | 1.18 ± 0.03 | 1.19 | 1.17 |
| p^{top} end step 3 (bar.a) | 1.19 ± 0.03 | 1.20 | 1.19 |
| p^{bottom} end step 4 (bar.a) [#] | 1.41 ± 0.05 | 1.40 | 1.40 |
| p^{top} end step 4 (bar.a) | 1.46 ± 0.06 | 1.45 | 1.45 |
| Exhaust flow step 3 (gmole cycle ⁻¹) | 8.93 ± 0.06 | 9.17 | 9.26 |
| Exhaust flow step 4 (gmole cycle ⁻¹) | 1.54 ± 0.06 | 1.68 | 1.64 |
| Total product flow (gmole cycle ⁻¹) | 0.701 ± 0.020 | 0.818 | 0.898 |
| Recovery (%O ₂ +Ar) | 23.3 ± 0.8 | 26.3 | 28.6 |
| Specific productivity ((kg O ₂ +Ar) kg ⁻¹ day ⁻¹) | 3.94 ± 0.07 | 4.60 | 5.05 |

| RPSA run 14 ($t_{\text{cycle}} = 22$ s at 90.7 mol%O ₂) Parameter | RPSA pilot plant | NDGNAS | |
|---|------------------|--------|-------|
| | | LDFP | DPM |
| p^{bottom} end step 1 (bar.a) | 4.27 ± 0.03 | 4.25 | 4.26 |
| p^{top} end step 1 (bar.a) | 4.19 ± 0.03 | 4.17 | 4.17 |
| p^{bottom} end step 2 (bar.a) [#] | 5.00 ± 0.03 | 5.00 | 5.00 |
| p^{top} end step 2 (bar.a) | 4.99 ± 0.03 | 4.98 | 4.98 |
| p^{bottom} end step 3 (bar.a) [#] | 1.18 ± 0.03 | 1.19 | 1.19 |
| p^{top} end step 3 (bar.a) | 1.22 ± 0.03 | 1.22 | 1.22 |
| p^{bottom} end step 4 (bar.a) [#] | 1.41 ± 0.03 | 1.40 | 1.40 |
| p^{top} end step 4 (bar.a) | 1.52 ± 0.03 | 1.50 | 1.50 |
| Exhaust flow step 3 (gmole cycle ⁻¹) | 8.67 ± 0.06 | 9.02 | 9.25 |
| Exhaust flow step 4 (gmole cycle ⁻¹) | 1.44 ± 0.06 | 1.62 | 1.59 |
| Total product flow (gmole cycle ⁻¹) | 0.486 ± 0.020 | 0.434 | 0.637 |
| Recovery (%O ₂ +Ar) | 19.6 ± 0.7 | 16.9 | 23.9 |
| Specific productivity ((kg O ₂ +Ar) kg ⁻¹ day ⁻¹) | 5.15 ± 0.12 | 4.58 | 6.72 |

[#] Denotes a parameter that is controlled according to Table 6.2.

Table 6.7 continued

| RPSA run 15 ($t_{\text{cycle}} = 22$ s at 79.5 mol%O ₂) Parameter | RPSA pilot plant | NDGNAS | |
|---|------------------|--------|-------|
| | | LDFP | DPM |
| p^{bottom} end step 1 (bar.a) | 4.17 ± 0.03 | 4.15 | 4.15 |
| p^{top} end step 1 (bar.a) | 4.08 ± 0.03 | 4.06 | 4.06 |
| p^{bottom} end step 2 (bar.a) [#] | 4.99 ± 0.03 | 4.99 | 5.01 |
| p^{top} end step 2 (bar.a) | 4.98 ± 0.03 | 4.98 | 4.99 |
| p^{bottom} end step 3 (bar.a) [#] | 1.20 ± 0.03 | 1.20 | 1.20 |
| p^{top} end step 3 (bar.a) | 1.24 ± 0.03 | 1.24 | 1.23 |
| p^{bottom} end step 4 (bar.a) [#] | 1.41 ± 0.03 | 1.41 | 1.41 |
| p^{top} end step 4 (bar.a) | 1.52 ± 0.03 | 1.51 | 1.51 |
| Exhaust flow step 3 (gmole cycle ⁻¹) | 8.55 ± 0.06 | 8.92 | 9.06 |
| Exhaust flow step 4 (gmole cycle ⁻¹) | 1.44 ± 0.06 | 1.61 | 1.55 |
| Total product flow (gmole cycle ⁻¹) | 0.650 ± 0.020 | 0.676 | 0.817 |
| Recovery (%O ₂ +Ar) | 22.8 ± 0.8 | 22.7 | 26.9 |
| Specific productivity ((kg O ₂ +Ar) kg ⁻¹ day ⁻¹) | 6.01 ± 0.11 | 6.25 | 7.55 |

| RPSA run 16 ($t_{\text{cycle}} = 14$ s at 89.6 mol%O ₂) Parameter | RPSA pilot plant | NDGNAS | |
|---|------------------|--------|-------|
| | | LDFP | DPM |
| p^{bottom} end step 1 (bar.a) | 4.28 ± 0.03 | 4.24 | 4.26 |
| p^{top} end step 1 (bar.a) | 4.17 ± 0.03 | 4.15 | 4.15 |
| p^{bottom} end step 2 (bar.a) [#] | 5.01 ± 0.03 | 5.01 | 5.00 |
| p^{top} end step 2 (bar.a) | 4.98 ± 0.03 | 4.98 | 4.97 |
| p^{bottom} end step 3 (bar.a) [#] | 1.20 ± 0.03 | 1.20 | 1.21 |
| p^{top} end step 3 (bar.a) | 1.28 ± 0.03 | 1.25 | 1.27 |
| p^{bottom} end step 4 (bar.a) [#] | 1.40 ± 0.03 | 1.40 | 1.40 |
| p^{top} end step 4 (bar.a) | 1.66 ± 0.03 | 1.58 | 1.58 |
| Exhaust flow step 3 (gmole cycle ⁻¹) | 7.98 ± 0.07 | 8.24 | 8.76 |
| Exhaust flow step 4 (gmole cycle ⁻¹) | 1.54 ± 0.06 | 1.59 | 1.59 |
| Total product flow (gmole cycle ⁻¹) | 0.401 ± 0.020 | 0.236 | 0.489 |
| Recovery (%O ₂ +Ar) | 15.7 to 17.0 | 10.0 | 19.2 |
| Specific productivity ((kg O ₂ +Ar) kg ⁻¹ day ⁻¹) | 6.59 ± 0.17 | 3.86 | 8.02 |

| RPSA run 17 ($t_{\text{cycle}} = 14$ s at 80.0 mol%O ₂) Parameter | RPSA pilot plant | NDGNAS | |
|---|------------------|--------|-------|
| | | LDFP | DPM |
| p^{bottom} end step 1 (bar.a) | 4.15 ± 0.03 | 4.12 | 4.12 |
| p^{top} end step 1 (bar.a) | 4.02 ± 0.03 | 4.02 | 4.00 |
| p^{bottom} end step 2 (bar.a) [#] | 5.00 ± 0.03 | 5.00 | 5.00 |
| p^{top} end step 2 (bar.a) | 4.98 ± 0.03 | 4.97 | 4.96 |
| p^{bottom} end step 3 (bar.a) [#] | 1.19 ± 0.03 | 1.19 | 1.19 |
| p^{top} end step 3 (bar.a) | 1.27 ± 0.03 | 1.25 | 1.25 |
| p^{bottom} end step 4 (bar.a) [#] | 1.40 ± 0.03 | 1.41 | 1.41 |
| p^{top} end step 4 (bar.a) | 1.67 ± 0.03 | 1.62 | 1.62 |
| Exhaust flow step 3 (gmole cycle ⁻¹) | 7.95 ± 0.12 | 8.61 | 8.91 |
| Exhaust flow step 4 (gmole cycle ⁻¹) | 1.54 ± 0.06 | 1.72 | 1.65 |
| Total product flow (gmole cycle ⁻¹) | 0.597 ± 0.020 | 0.469 | 0.716 |
| Recovery (%O ₂ +Ar) | 20.1 to 22.3 | 16.5 | 24.1 |
| Specific productivity ((kg O ₂ +Ar) kg ⁻¹ day ⁻¹) | 8.75 ± 0.17 | 6.87 | 10.5 |

[#] Denotes a parameter that is controlled according to Table 6.2.

Table 6.7 continued

| RPSA run 18 ($t_{\text{cycle}} = 8$ s at 80.5 mol%O ₂) Parameter | RPSA pilot plant | NDGNAS | |
|---|------------------|--------|-------|
| | | LDFP | DPM |
| p^{bottom} end step 1 (bar.a) | 4.41 ± 0.03 | 4.21 | 4.31 |
| p^{top} end step 1 (bar.a) | 4.01 ± 0.04 | 3.99 | 3.99 |
| p^{bottom} end step 2 (bar.a) [#] | 5.02 ± 0.03 | 5.02 | 5.02 |
| p^{top} end step 2 (bar.a) | 4.95 ± 0.03 | 4.95 | 4.95 |
| p^{bottom} end step 3 (bar.a) [#] | 1.21 ± 0.03 | 1.21 | 1.22 |
| p^{top} end step 3 (bar.a) | 1.39 ± 0.03 | 1.32 | 1.34 |
| p^{bottom} end step 4 (bar.a) [#] | 1.41 ± 0.03 | 1.41 | 1.40 |
| p^{top} end step 4 (bar.a) | 2.13 ± 0.03 | 1.86 | 1.87 |
| Exhaust flow step 3 (gmole cycle ⁻¹) | 6.35 ± 0.27 | 7.37 | 8.25 |
| Exhaust flow step 4 (gmole cycle ⁻¹) | 1.48 ± 0.06 | 1.24 | 1.24 |
| Total product flow (gmole cycle ⁻¹) | 0.341 ± 0.020 | 0.105 | 0.435 |
| Recovery (%O ₂ +Ar) | 13.1 to 15.8 | 4.61 | 16.7 |
| Specific productivity ((kg O ₂ +Ar) kg ⁻¹ day ⁻¹) | 8.84 ± 0.27 | 2.71 | 11.2 |

[#] Denotes a parameter that is controlled according to Table 6.2.

Tables 6.6 and 6.7 reveal that eighteen of a possible twenty combinations for product purity, pressure window and cycle time have been covered (see Tables 6.2 and 6.3 for all possible combinations). The high purity run, 90 mol%O₂, at the shortest cycle time, $t_{\text{cycle}} = 8$ s, could not be achieved on the RPSA pilot plant without fully closing the product line modulating valve and letting the plant undergo complete internal purge. Even at this extreme limit of operation, twenty-four hours of continuous operation with a tiny amount of product gas being withdrawn for purity measurement could barely achieve 87 mol%O₂ under the 4.00:1.20 and 5.00:1.20 bar.a pressure windows respectively. Therefore, total cycle time somewhere between 8 and 14 s represents the limiting value of t_{cycle} on the RPSA pilot plant that could maintain process operation with a finite quantity of product gas being withdrawn per cycle at high purity. This operating constraint means two RPSA runs have not been considered in this analysis in relation to a product purity of 90 mol%O₂ and cycle time of 8 s.

Entries for recovery in RPSA runs 7, 8, 9, 16, 17 and 18 represent two extremes in exhaust flow. The assignment of these two values is discussed further in §6.7 with reference to error bars on the graphical presentation of this data. It is also worth mentioning at this point that eighteen RPSA runs presented in Table 6.7 took approximately three months to simulate using three separate 650 MHz Compaq XP1000 Dec-Alpha workstations. While the LDFP portion of each simulation generally consumed two to five days of CPU time, anything from two weeks to a month was required for the DPM once the MMS occurred.

6.6.1 Experimental Results Obtained from a Repeat of RPSA Run 2

Before discussing these results, one important question that must be addressed is whether fast cycle times significantly altered sorbent bed configuration before all runs were complete. To answer this, a repeat of RPSA run 2 was performed after RPSA runs 1 through 18 inclusive were complete as a final check on sorbent condition, denoted here as RPSA run 2 (repeat) in Table 6.8. Any significant deviations that arise between RPSA run 2 and 2 (repeat) would indicate shorter cycle times might have altered sorbent bed configuration.

Table 6.8: Experimental results obtained from RPSA runs 2 (repeat) and 2. Note the definition of each superscript symbol is identical to those in Table 6.6.

| Parameter | RPSA run 2 (repeat) | RPSA run 2 |
|--|--------------------------------|--------------------------------|
| Step 1 time (s) | 9.4 ± 0.1 | 11.1 ± 0.1 |
| Total cycle time (s) [†] | 50.0 ± 0.1 | 50.0 ± 0.1 |
| Product purity (mol%O ₂ +Ar) [#] | 80.5 ± 0.5 (84.1) [‡] | 79.1 ± 0.5 (82.6) [‡] |
| Feed temperature (K) [*] | 287.8 ± 1.6 | 286.5 ± 0.9 |
| T_A (K) | 288.7 ± 0.5 | 287.7 ± 0.5 |
| p_A (bar.a) | 1.002 ± 0.001 | 1.018 ± 0.001 |
| p^{tank} end step 1 (bar.a) | 3.32 ± 0.03 | 3.33 ± 0.05 |
| p^{tank} end step 2 (bar.a) | 3.97 ± 0.03 | 3.97 ± 0.03 |
| p^{tank} end step 3 (bar.a) | 3.85 ± 0.03 | 3.85 ± 0.03 |
| p^{tank} end step 4 (bar.a) | 3.34 ± 0.03 | 3.36 ± 0.06 |
| p^{bottom} end step 1 (bar.a) | 3.34 ± 0.03 | 3.35 ± 0.05 |
| p^{top} end step 1 (bar.a) | 3.33 ± 0.03 | 3.33 ± 0.05 |
| p^{bottom} end step 2 (bar.a) [#] | 4.00 ± 0.03 | 4.00 ± 0.03 |
| p^{top} end step 2 (bar.a) | 3.99 ± 0.03 | 3.99 ± 0.03 |
| p^{bottom} end step 3 (bar.a) [#] | 1.19 ± 0.03 | 1.21 ± 0.03 |
| p^{top} end step 3 (bar.a) | 1.20 ± 0.03 | 1.22 ± 0.03 |
| p^{bottom} end step 4 (bar.a) [#] | 1.40 ± 0.03 | 1.40 ± 0.05 |
| p^{top} end step 4 (bar.a) | 1.42 ± 0.03 | 1.43 ± 0.05 |
| Exhaust flow step 3 (gmole cycle ⁻¹) | 7.28 ± 0.06 | 7.10 ± 0.06 |
| Exhaust flow step 4 (gmole cycle ⁻¹) | 1.24 ± 0.06 | 1.16 ± 0.06 |
| Total product flow (gmole cycle ⁻¹) | 0.483 ± 0.020 | 0.490 ± 0.020 |
| Recovery (%O ₂) | 20.3 ± 0.7 | 20.8 ± 0.8 |
| Specific productivity ((kg O ₂) kg ⁻¹ day ⁻¹) | 1.99 ± 0.05 | 1.98 ± 0.05 |

Although each RPSA run was not performed in the numerical order described by Tables 6.6 and 6.7, RPSA runs 1 and 2 were the first and second cycles performed respectively. The fact that RPSA run 2 and 2 (repeat) are in relatively close agreement is an encouraging result given that:

- End of step pressures are similar and the creation of a significant amount of fine material, which would increase pressure drop, is not evident and
- Specific productivity per unit kilogram of sorbent was equal to within experimental error indicating large amounts of crushed sorbent, if created, was not lost from the sorbent bed.

Differences between individual operating conditions can be attributed to small deviations in the final settings on each modulating valve stem position ascribed to RPSA runs 2 and 2 (repeat).

6.6.2 Maintaining CSS at the Shortest Cycle Time - RPSA Run 18

While the sorbent bed remained intact during all RPSA runs presented in Tables 6.6 and 6.7, one important point to address is how stable was the RPSA pilot plant once CSS was achieved at the shortest cycle time. Observations made in this subsection are important towards the implementation of RPSA cycle times at the industrial level. The RPSA pilot plant was assembled from equipment items that are commercially used on standard PSA facilities. In addition, it is large enough in scale to capture a majority of the process effects present at an industrial level. Therefore, stable operation of the RPSA pilot plant at $t_{\text{cycle}} = 8$ s once CSS has been achieved would provide some confidence in the ability to perform RPSA at the commercial level.

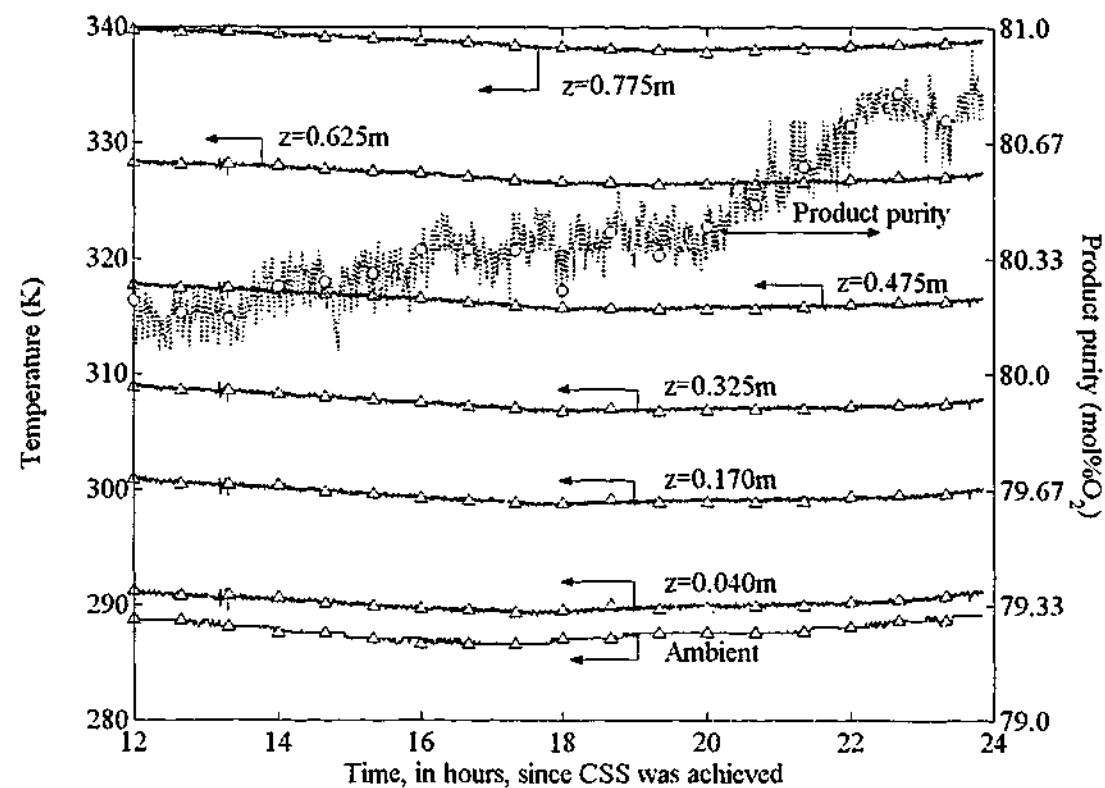


Figure 6.3: Experimental temperature and product purity at CSS from RPSA run 18 over a twelve hour period. This data was obtained approximately twelve hours after CSS had been achieved.

The DTM located on the product line was not logged electronically into the PLC but instead was manually read at predefined time intervals during process operation. Therefore, specific productivity was not recorded often enough over this time period to accurately follow this parameter. Instead a direct measure can be inferred by examining temperature, pressure and product purity measured through the SCADA system. If these three parameters drift significantly in time beyond that imposed through changes in ambient conditions then specific productivity will also drift. Temperature and purity profiles over a 12 hour period are shown in Fig. 6.3 while three different pressure profiles obtained over this same 12 hour period are shown in Fig 6.4.

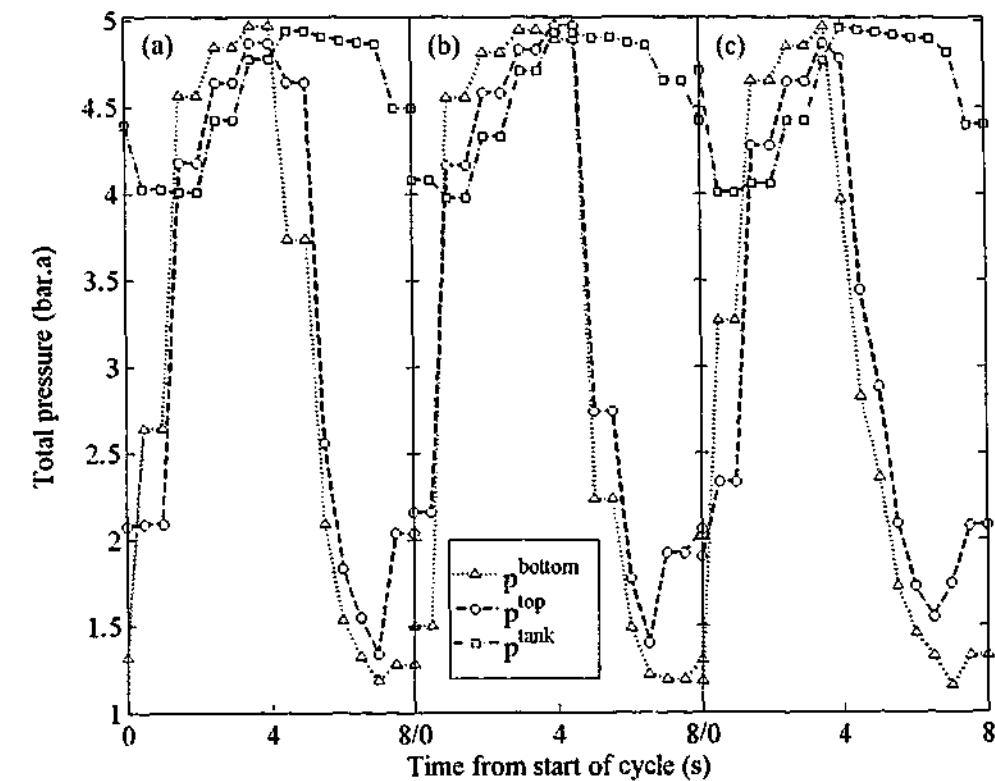


Figure 6.4: Experimental pressure profiles obtained at CSS from RPSA run 18.
(a) Pressure profile approximately twelve hours after CSS achieved.
(b) Pressure profile approximately eighteen hours after CSS achieved.
(c) Pressure profile approximately twenty-four hours after CSS achieved.

The temperature profile spans almost 50 K across the bed (Fig. 6.3) and reasons behind the formation of such a temperature gradient are discussed in §6.7.4. Trends in Fig. 6.3 closely follow those shown in Fig. 6.2 indicating ambient temperature was the only parameter that was uncontrollably fluctuating at CSS. Three different pressure profiles obtained over this same 12 hour period, Fig. 6.4, indicate the pressure window was relatively steady to within variations on ambient pressure. Figure 6.4 also reveals the computer used to log data from the SCADA system struggled to maintain 0.5 s resolution. It was found that the same operating parameter, such as pressure and temperature, was carried over for one second instead of sampling at 0.5 s intervals. In addition the computer did not always maintain sampling frequency at 0.5 s, sometimes overstepping this pre-set scan rate. This problem was observed across all RPSA runs making it difficult to accurately compare experimental versus mathematical trends for $t_{\text{cycle}} < 22$ s.

Irrespective of sampling problems at short cycle times, these results show temperature, pressure and product purity obtained from the RPSA pilot plant were steady to within ambient fluctuations for at least one day of continuous operation once CSS had been achieved. In addition RPSA run 2 (repeat) indicates the sorbent bed was not significantly altered for the entire duration of RPSA pilot plant runs. While operation of RPSA run 18 for several months was not feasible within the

time constraints of a Ph.D., this preliminary investigation reveals RPSA can be performed at a capacity that is comparable on some level to an industrial facility. The main issue that needs to be addressed when increasing process capacity is an appropriate hold down mechanism for the sorbent bed. Once internal column diameter increases much beyond those considered here, spring-loaded hold down plates become difficult to mount and a new method that can prevent fluidisation without crushing the packed bed becomes crucial.

6.7 Discussion - Mathematical Predictions versus Experimental Data

An extensive tabular summary of RPSA pilot plant data versus NDGNAS predictions with the DPM and LDFP model was provided in §6.6. The purpose of this section is to discuss these findings in addition to introducing performance results obtained with the simplified RPSA analysis. Numerically generated pressure and temperature profiles are also compared against experimental data to explain discrepancies between the DPM and LDFP model at the RPSA limit.

6.7.1 Quantifying Mismatch between Simulated and Experimental Results

To assist in the following discussion eight graphs have been produced that compare specific productivity and recovery as a function of cycle time from the RPSA pilot plant, NDGNAS and simplified RPSA analysis across each pressure window (Figs. 6.6, 6.7, 6.11 and 6.12). The most striking trend from these graphs, which was evident in the tabular summary, is that NDGNAS consistently overestimates specific productivity and recovery at the longest cycle times; RPSA runs 1, 2, 10 and 11; where the form of the intrapellet mass transfer model has little impact on predicted separation performance (i.e. compare DPM and LDFP model results from these RPSA runs). To investigate a potential cause for this mismatch, the definition of working selectivity introduced through the simplified RPSA analysis is used.

The equilibrium isotherm for Zeochem LiLSX was regressed using pure component experimental data in addition to multicomponent data generated from IAST as discussed in §4.1.1. Although IAST has been shown to reproduce multicomponent data for non-polar molecules such as nitrogen and oxygen when steric effects are unimportant [Sorial *et al.* (1983)], Myers (1983) and Valenzuela *et al.* (1988) indicate IAST is a poor model in situations where an energy distribution for adsorption sites exists across the surface of the sorbent. X-type crystal structures have several different sites available for adsorption [Ruthven (1984a, pp 14-16)] and as such the energy distribution would not be expected to be homogeneous through a crystal, potentially limiting the application of IAST. To investigate these potential deviations, equilibrium isotherms obtained from Air Products and Chemicals Inc. (APCI) for two different lithium exchanged X-type zeolite

sorbent materials are presented. Both of these materials are proprietary and as such equilibrium isotherm parameters are not presented. The first material is an 85% lithium exchanged LSX zeolite that is denoted APCI LiLSX in the following discussion. The second material is a faujasite NaX crystal that has been exchanged with 85% lithium and 15% zinc. This LiZnX is called Class 2 MCI and hence shall be denoted APCI Class 2 MCI in the following discussion.

APCI have regressed two sets of equilibrium isotherm parameters for both of these materials:

- i. One set of parameters for the equilibrium isotherm was regressed using true binary component equilibrium data for nitrogen and oxygen obtained from a multicomponent equilibrium measuring device.
- ii. The second set of parameters was regressed using IAST with pure component equilibrium data obtained for nitrogen and oxygen, very similar to the procedure adopted for Zeochem LiLSX described in §4.1.1.

With two independent sets of regressed equilibrium isotherm parameters for nitrogen and oxygen over materials that are similar in structure to Zeochem LiLSX, particularly APCI LiLSX, a comparison of the adiabatic working selectivity from the simplified RPSA analysis can be made. This is performed by comparing the ratio of true binary to IAST working selectivity, which should provide a good indication of the potential error in the use of IAST for Zeochem LiLSX. A plot of the true binary and IAST working selectivity under adiabatic conditions for APCI LiLSX and APCI Class 2 MCI is provided in Fig. 6.5. This same graph also shows the adiabatic working selectivity for Zeochem LiLSX using IAST over the same conditions. The pressure window used in this analysis is 4.00:1.20 bar.a, which constitutes the low pressure window applied on the RPSA pilot plant. The product purity y_{PD} selected for this same analysis is 90 mol%O₂. Similar trends in working selectivity are also observed when this same value was set to 80 mol%O₂.

The inlay graph on Fig. 6.5 compares the ratio of working selectivity obtained with true binary component equilibrium data in relation to the same working selectivity obtained with IAST regressed parameters. One can see the difference is in the range of 10 to 15% at feed temperatures typically encountered on the RPSA pilot plant. The working selectivity for true binary and IAST equilibrium isotherms relate to conditions where intrapellet mass transfer is not assumed to be important. Results from the inlay graph of Fig. 6.5 show that IAST regressed equilibrium isotherm parameters will overestimate true binary data by approximately 10 to 15% for the nitrogen-oxygen-zeolite system, which is very similar to the errors observed at the long cycle time between NDGNAS and the RPSA pilot plant. Therefore, it is speculated that a large majority of the error between experimental and simulated data for the RPSA pilot plant can be attributed to the error introduced when IAST is used to regress multicomponent equilibrium isotherm parameters.

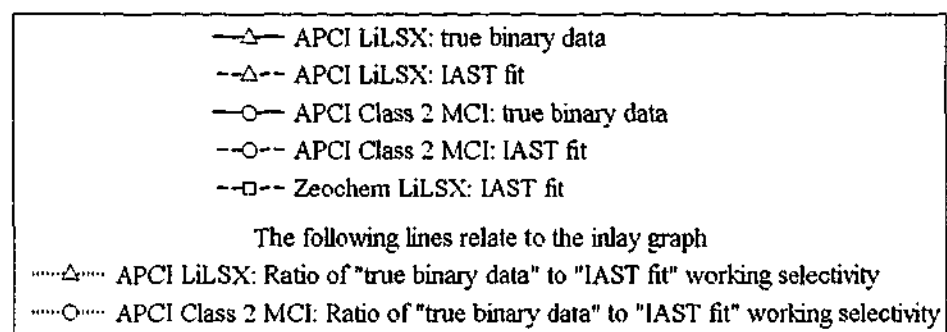
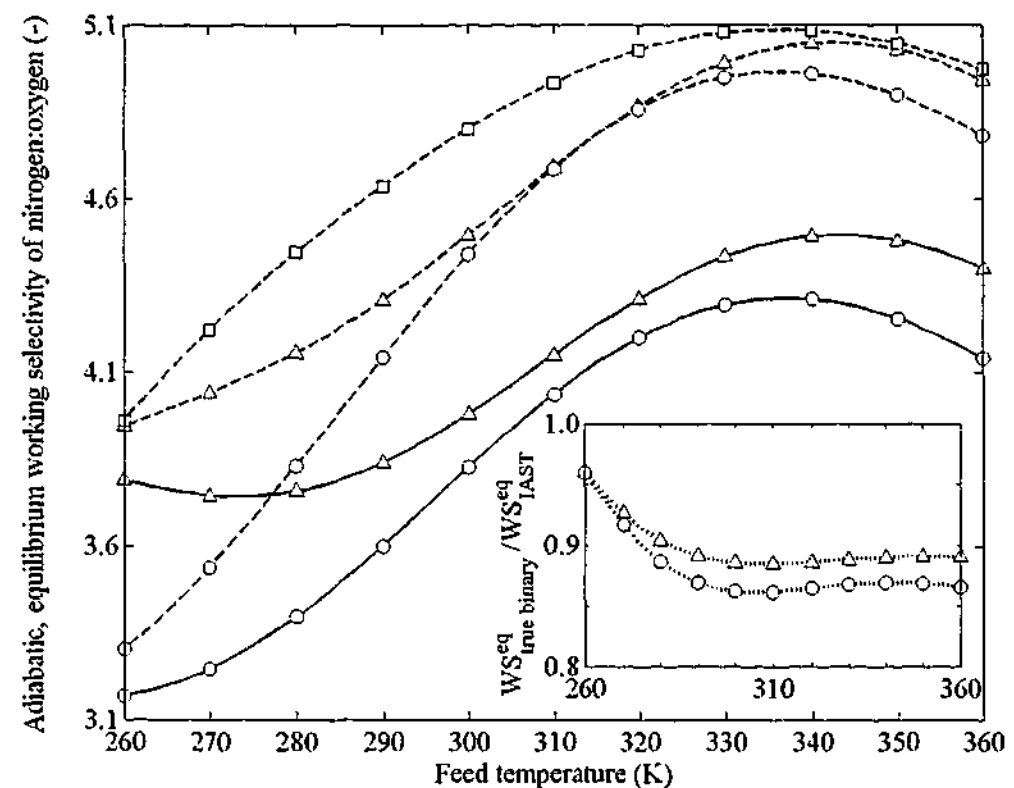


Figure 6.5: True binary versus IAST fitted adiabatic working selectivity of APCI LiLSX and APCI Class 2 MCI. The working selectivity of Zeochem LiLSX using IAST is also shown for comparison.

Although IAST regressed equilibrium isotherm parameters were not sufficient to reproduce absolute values for performance obtained from the RPSA pilot plant, the same parameters were adequate to compare numerical versus experimental data from the EMU and LUB apparatus of chapters 4 and 5. Predicted uptake curves for a single component system using nitrogen was in good agreement with experimental data from the EMU. Therefore, any errors in multicomponent equilibrium loadings introduced through IAST will not be seen in EMU data. Although binary feed mixtures were used within the LUB apparatus, each breakthrough experiment was performed at relatively low pressures in comparison to the RPSA pilot plant. Extensive equilibrium data was available up to a pressure of 1.33 bar.a (1000 torr) from two Baratron pressure transducers that are used on the equilibrium isotherm measuring device described in §4.1.1. Above 1.33 bar.a a third transducer is used that is ranged to 33.3 bar.a (25,000 torr), making isotherm measurement difficult

at pressures approaching 5 bar.a due to transducer resolution (Fig. 4.1 shows a distinct change in frequency of data collection above 1.33 bar.a). Hence the RPSA pilot plant operates over a pressure window where pure component equilibrium data was not as extensive as that obtained for breakthrough experiments.

While errors in predicted adsorbed phase loading and equilibrium selectivity for a multicomponent mixture would be the major source of mismatch when absolute values of specific productivity and recovery are compared, this has little bearing on qualitative trends that have been observed between the DPM and LDFP model in relation to the RPSA pilot plant as a function of t_{cycle} . This preliminary discussion has raised one important feature that should be remembered when comparing NDGNAS results against RPSA pilot plant data: predicted separation performance using either the DPM or LDFP model should consistently overestimate the equivalent results from the RPSA pilot plant. The fact that this statement does not hold for the LDFP model when compared to the DPM at the RPSA limit provides one central discussion point of this chapter. Before progressing any further, a brief mention will be made here regarding error bars on each RPSA pilot plant data point across Figs. 6.6, 6.7, 6.11 and 6.12.

6.7.2 Comparing Overall Process Performance at CSS

Error margins for specific productivity found in Table 6.7 are based on the ability to measure product flow using the DTM and soap bubble flow meters under steady conditions and hence are relatively small. On the other hand, recovery had to be inferred from the accumulated moles of gas obtained in the product and exhaust lines. At short cycle times the annubar-DP cell arrangement struggled to capture the flow spike that occurs when the column depressurises to atmosphere and consequently underestimates gas volume passing through the exhaust line. The upper part of the error band therefore represents exhaust volume measured experimentally while the lower part of the error bar represents exhaust volume obtained using NDGNAS with the DPM activated. Product volume obtained experimentally is used in both of these calculations according to Eq. (6.4). The actual data point ascribed to the short cycle time represents experimentally measured recovery and hence sits at the top of the error bar. This also explains why two values are presented for recovery instead of a plus-minus error on RPSA runs 7, 8, 9, 16, 17 and 18 in Table 6.7.

Results from the 4.00:1.20 bar.a Pressure Window

Accumulated moles of gas obtained in the exhaust line with the DPM and LDFP model generally agree to within 5% of the same value measured experimentally at the long and intermediate cycle times (i.e. $t_{\text{cycle}} > 14$ s). For RPSA runs where t_{cycle} was 14 s or less, deviations of 5-11% arose

between predicted and experimentally observed exhaust gas flows during step 3. As mentioned in §6.2.4 these flow transients are very difficult to capture and the experimental value in Table 6.7 would be expected to underestimate the actual moles of gas obtained from the column during step 3. It is interesting to note, however, that exhaust flow during purge, step 4, generally agree to within 11% of numerical predictions using the DPM and LDFP across all cycle times. During purge the flow of gas leaving the bed is relatively steady such that flow transients that arose just a few seconds earlier have subsided enough to allow a reliable estimate of accumulated moles to be obtained.

Accumulated moles of gas obtained during purge and counter-current depressurisation for long cycle times agree relatively well against experimental values. However, the moles of gas obtained in the product line show consistently different trends between the DPM and LDFP model. For the DPM total product flow is consistently overestimated by 20% to 30% across all cycle times. On the other hand, the LDFP model initially overestimates total product flow by 20% as expected but once t_{cycle} is 14 s or less, underestimates total product flow by as much as 60%. This result shows the two intrapellet mass transfer models predict significantly different gas flows out of the top of the bed at the RPSA limit with the DPM consistently overestimating total product flow in comparison to the LDFP model.

In general the predicted amount of nitrogen and oxygen adsorbed onto the bed at the end of step 2 is in relatively close agreement with experimental loading given the volume of gas passing out of the bed during step 3, in addition to the end of step pressure, are similar in magnitude. However, selectivity for the adsorption of nitrogen over oxygen predicted using IAST appears to overestimate actual selectivity of the sorbent bed packed into the RPSA pilot plant, which means an increased volume of gas can be obtained numerically in the product line.

Figures 6.6 and 6.7 are presented to discuss trends in specific productivity and recovery obtained numerically and experimentally from RPSA runs 1 through 9. The first set of results at 90 mol%O₂ from Fig. 6.6 show specific productivity and recovery actually increase above the ideal line when cycle time decreased from 50 to 36 s. A significant change in the role of intrapellet mass transfer and interpellet pressure drop from 50 to 36 s would not be expected as θ_i was greater than 1 for nitrogen and oxygen from Table 6.3 and end of step pressures are similar across RPSA runs 1 and 3. While the assumption of working selectivity being independent of any changes to mass transfer and pressure drop appears suitable at these cycle times, the impact of maintaining 1.40 bar.a for end of step purge pressure may have had a very different impact. This suggests the bed may have been over-purged at 50 s with end of step purge pressure set to 1.40 bar.a whereas 1.40 bar.a was closer to the optimum end of step purge pressure at $t_{\text{cycle}} = 36$ s.

Below 36 s (Fig. 6.6) the RPSA pilot approaches the equivalent ideal line, crossing over somewhere near 22-25 s before decreasing below the ideal line as cycle time decreased further. While the DPM is in good agreement with the RPSA pilot plant for the point where the ideal line is crossed, the LDFP crosses at a cycle time of 30-32 s. At the shortest cycle time the LDFP model is less than one half of the ideal specific productivity whereas the DPM and RPSA pilot plant have both decreased by approximately 20% from the ideal line. Given the DPM is in good qualitative agreement with respect to deviations observed from the ideal line using the RPSA pilot plant highlights the fact that the LDFP model has overemphasised the impact of intrapellet mass transfer resistance at cycle times approaching the RPSA limit.

Trends observed at the lower product purity of 80 mol%O₂ (Fig. 6.7) show a different trend to those found at 90 mol%O₂. Firstly, a large improvement in specific productivity and recovery above the ideal line is not observed when t_{cycle} decreased from 50 to 22 s with the DPM and RPSA pilot plant. This suggests the relative importance of intrapellet mass transfer, interpellet pressure drop and end of step purge pressure is not drastically altering working selectivity across these cycle times. End of step pressure profiles across RPSA runs 2, 4 and 6 are similar in magnitude, with major differences becoming evident across RPSA runs 8 and 9 only, supporting the notion of interpellet pressure drop being minimal in impact up to $t_{\text{cycle}} = 22$ s. The fact that the LDFP model predicts a significant reduction in specific productivity and recovery from the ideal line at $t_{\text{cycle}} = 22$ s with respect to the RPSA pilot plant and DPM again indicates the LDFP model is overemphasising the impact of intrapellet mass transfer resistance. Once the shortest cycle time is reached at 80 mol%O₂, the LDFP model is not even in qualitative agreement with the RPSA pilot plant or DPM. The LDFP model at $t_{\text{cycle}} = 8$ s suggests specific productivity is decreasing rapidly, whereas the RPSA pilot plant and DPM indicate specific productivity has reached something close to a local maximum as a function of cycle time.

From this initial discussion it is evident intrapellet mass transfer resistance is overemphasised within the LDFP model in relation to the DPM and RPSA pilot plant for $t_{\text{cycle}} < 30$ s. At cycle times approximately greater than 22 s it also appears that interpellet pressure drop is of minor importance given the general agreement between end of step pressure profiles. At shorter cycle times, however, end of step pressure changes and the role of interpellet pressure drop may become important.

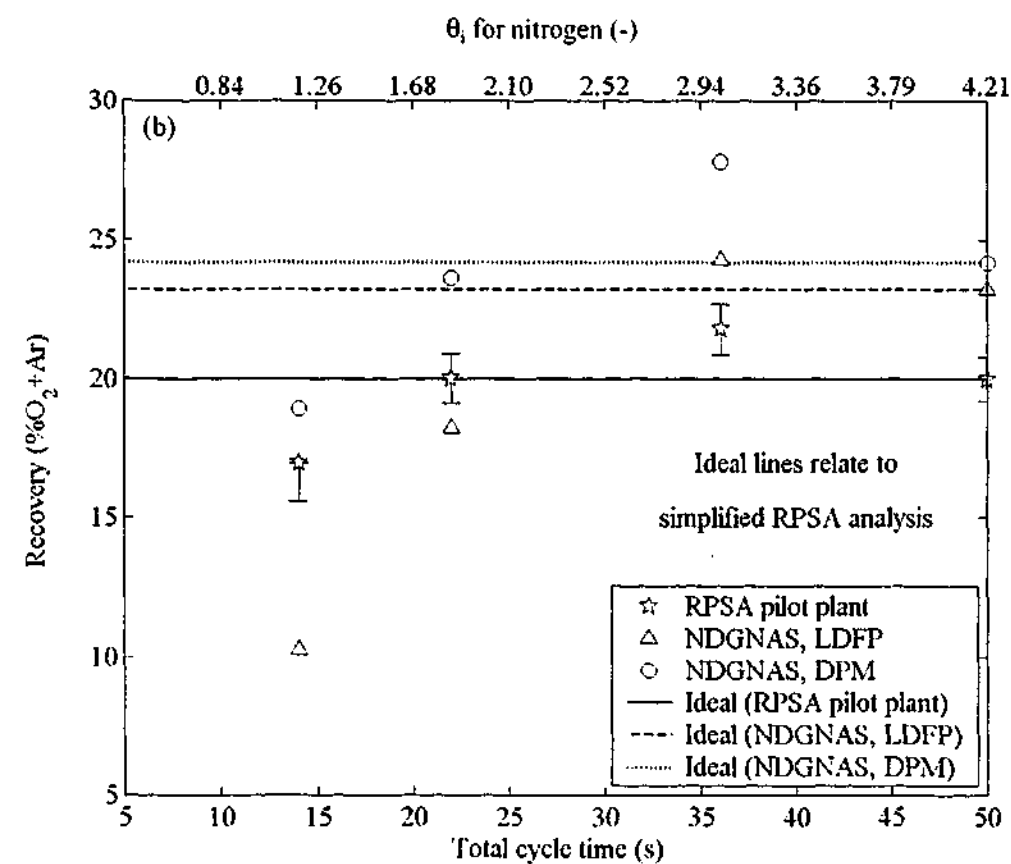
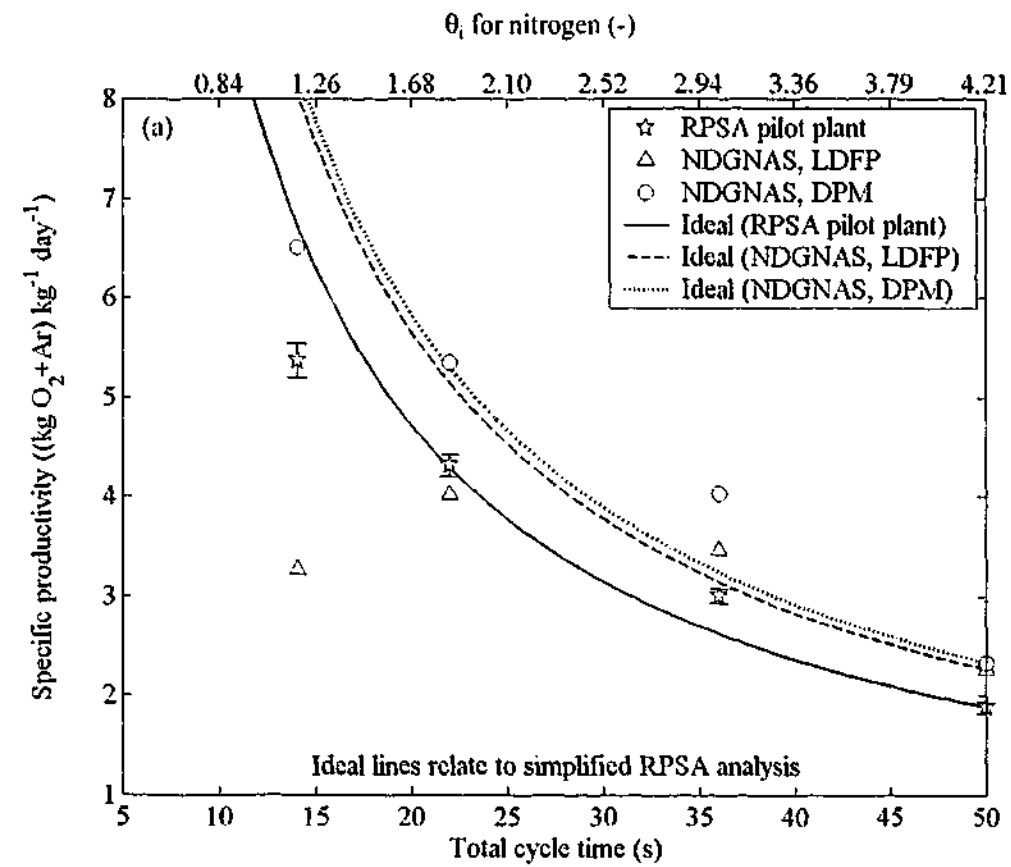


Figure 6.6: Comparing process performance results between RPSA pilot plant data, NDGNAS and simplified RPSA analysis over a 4.00:1.20 pressure window at a target purity of 90 mol% O_2 for (a) specific productivity and (b) recovery.

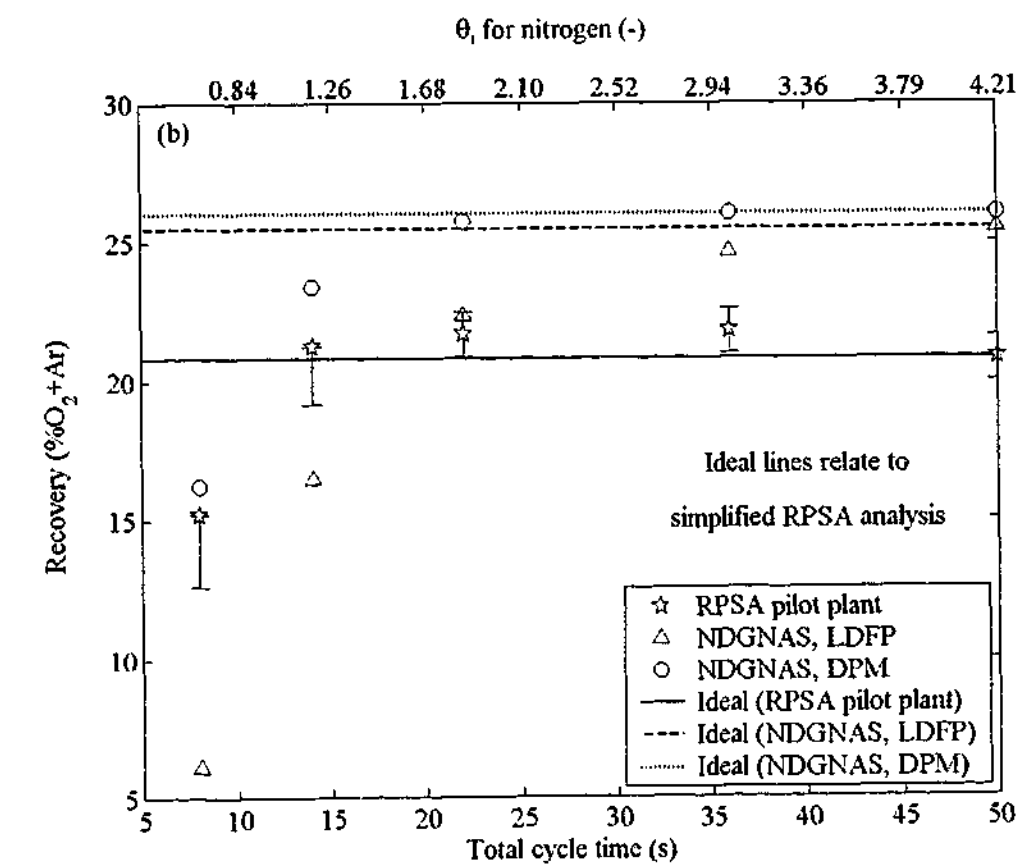
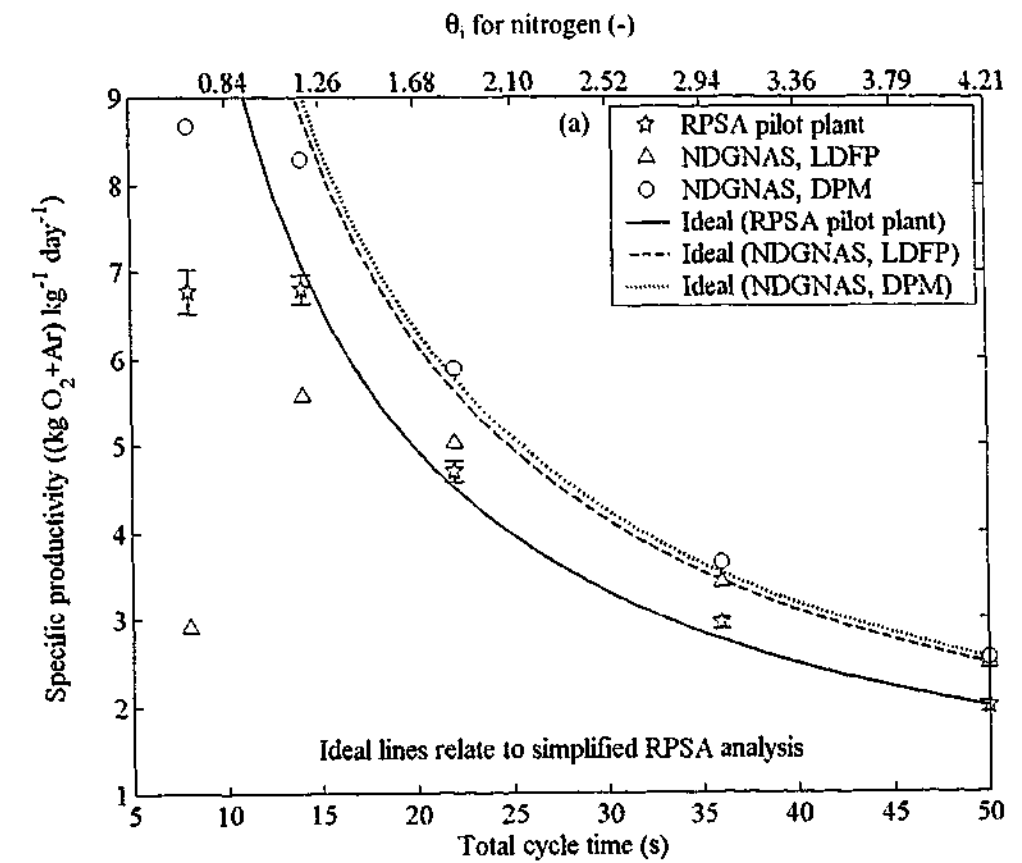


Figure 6.7: Comparing process performance results between RPSA pilot plant data, NDGNAS and simplified RPSA analysis over a 4.00:1.20 pressure window at a target purity of 80 mol% O_2 for (a) specific productivity and (b) recovery.

To address this issue of intrapellet mass transfer versus interpellet pressure drop resistance at the RPSA limit, four additional simulations have been performed using NDGNAS at the shortest cycle times experimentally achieved for both the 80 and 90 mol%O₂ purities and 4.00:1.20 bar.a pressure window.

- The first of these additional simulations activated something very close to the ILE assumption by assigning Ω_i the constant value 1.0×10^{10} within the LDFP model. This same run did not change any other parameter that constitutes the NDGNAS input deck so this compares separation performance at the RPSA limit in the presence of interpellet pressure drop and non-isothermal behaviour only.
- The second and third runs were performed under conditions where the constants of the pressure drop equation κ_{viscous} and κ_{kinetic} are two orders of magnitude smaller than their corresponding values obtained experimentally in chapter 5. With all other parameters that constitute the NDGNAS input deck unchanged this second run effectively compares separation performance in the presence of intrapellet mass transfer (DPM and LDFP model) and non-isothermal behaviour only.
- The final run combines ILE by setting Ω_i to 1.0×10^{10} for both nitrogen and oxygen within the LDFP model in addition to reducing the numerical constants of the steady state pressure drop equation. With all other parameters that constitute the NDGNAS input deck unchanged apart from κ_{viscous} , κ_{kinetic} and Ω_i , this run effectively compares separation performance in the presence of non-isothermal behaviour only.

It should be pointed out that numerical difficulties arose with inversion of the Ergun equation for cases ii. and iii. above given the a term within the quadratic equation $(-b \pm \sqrt{b^2 - 4ac})/2a$ is now very small. Hence the kinetic term had to be deactivated on these simulations. This effectively means a simulation where interpellet pressure drop is very small (denoted $\Delta p^B \approx 0$) was in fact performed with Darcy's law and a very low permeability coefficient. The use of Darcy's law here, however, is inconsequential as the goal of decreasing interpellet pressure drop to the point where $\partial p^B / \partial z$ is something close to zero is the desired outcome. This means just three lines of many thousands were executed differently within the source code: here v_B is found using a relationship of the form $(-\partial p^B / \partial z) / (\text{very small permeability})$ instead of the quadratic equation mentioned a few lines earlier.

For the present discussion an additional set of simulations that assume isothermal behaviour have not been performed given significant deviations in process performance will obviously arise due to the temperature dependence of adsorbed phase loading. Further to this, chapter 2 revealed the impact of isothermal versus non-isothermal behaviour at the pellet level had little impact on the

transport of gas when bulk flow (DGM and VF+DGM), equimolar counterdiffusion (FFL) and time corrected Ω_i parameters (LDFP model) was applied. Assigning the initial conditions as those obtained from CSS for the corresponding LDFP model run described in Table 6.7 required a minimum of 2000 cycles to achieve CSS in all cases simulated. Numerical simulation results from both NDGNAS simulations for RPSA runs 7 and 9 are summarised in Table 6.9.

Table 6.9: NDGNAS predictions at CSS for RPSA run 7 (shortest t_{cycle} at 90 mol%O₂+Ar) and RPSA run 9 (shortest t_{cycle} at 80 mol%O₂+Ar) under various assumptions for intrapellet mass transfer and interpellet pressure drop. ILE denotes a simulation where $\Omega_i = 1.0 \times 10^{10}$ for nitrogen and oxygen using the LDFP model. Δp^B finite denotes a simulation where $\kappa_{\text{viscous}} = 154$ and $\kappa_{\text{kinetic}} = 1.47$ using the Ergun equation. $\Delta p^B \approx 0$ denotes a simulation where $\kappa_{\text{viscous}} = 1.54$ using Darcy's law.

| RPSA run 7 ($t_{\text{cycle}} = 14$ s at 89.8 mol%O ₂) | Δp^B finite using ... | | | $\Delta p^B \approx 0$ using ... | | |
|---|-------------------------------|-------|------------------|----------------------------------|-------|-------|
| | Parameter | ILE | DPM [†] | LDFP [‡] | ILE | DPM |
| p^{bottom} end step 1 (bar.a) | 3.26 | 3.24 | 3.23 | 3.17 | 3.17 | 3.17 |
| p^{top} end step 1 (bar.a) | 3.18 | 3.17 | 3.17 | 3.17 | 3.17 | 3.17 |
| p^{bottom} end step 2 (bar.a) | 4.03 | 4.02 | 4.02 | 4.03 | 4.03 | 4.03 |
| p^{top} end step 2 (bar.a) | 3.99 | 3.98 | 3.98 | 4.03 | 4.03 | 4.03 |
| p^{bottom} end step 3 (bar.a) | 1.21 | 1.22 | 1.21 | 1.22 | 1.22 | 1.22 |
| p^{top} end step 3 (bar.a) | 1.26 | 1.27 | 1.25 | 1.22 | 1.22 | 1.22 |
| p^{bottom} end step 4 (bar.a) | 1.43 | 1.42 | 1.42 | 1.43 | 1.42 | 1.42 |
| p^{top} end step 4 (bar.a) | 1.62 | 1.58 | 1.58 | 1.43 | 1.42 | 1.42 |
| Exhaust flow step 3 (gmole cycle ⁻¹) | 7.22 | 7.06 | 6.60 | 7.39 | 7.42 | 6.92 |
| Exhaust flow step 4 (gmole cycle ⁻¹) | 1.47 | 1.46 | 1.45 | 1.53 | 1.55 | 1.53 |
| Total product flow (gmole cycle ⁻¹) | 0.631 | 0.397 | 0.199 | 0.599 | 0.398 | 0.185 |
| Recovery (%O ₂ +Ar) | 28.8 | 18.9 | 10.3 | 26.8 | 18.1 | 9.10 |
| Specific productivity ((kg O ₂ +Ar) kg ⁻¹ day ⁻¹) | 10.4 | 6.51 | 3.26 | 9.82 | 6.53 | 3.03 |

| RPSA run 9 ($t_{\text{cycle}} = 8$ s at 80.0 mol%O ₂) | Δp^B finite using ... | | | $\Delta p^B \approx 0$ using ... | | |
|---|-------------------------------|-------|------------------|----------------------------------|-------|-------|
| | Parameter | ILE | DPM [†] | LDFP [‡] | ILE | DPM |
| p^{bottom} end step 1 (bar.a) | 3.16 | 3.13 | 3.09 | 2.96 | 2.98 | 2.96 |
| p^{top} end step 1 (bar.a) | 2.98 | 2.97 | 2.97 | 2.96 | 2.98 | 2.96 |
| p^{bottom} end step 2 (bar.a) | 3.97 | 3.97 | 3.98 | 3.98 | 3.98 | 3.98 |
| p^{top} end step 2 (bar.a) | 3.85 | 3.87 | 3.89 | 3.98 | 3.98 | 3.98 |
| p^{bottom} end step 3 (bar.a) | 1.21 | 1.21 | 1.21 | 1.21 | 1.21 | 1.21 |
| p^{top} end step 3 (bar.a) | 1.33 | 1.31 | 1.30 | 1.21 | 1.21 | 1.21 |
| p^{bottom} end step 4 (bar.a) | 1.39 | 1.39 | 1.39 | 1.40 | 1.39 | 1.39 |
| p^{top} end step 4 (bar.a) | 1.83 | 1.76 | 1.76 | 1.40 | 1.39 | 1.39 |
| Exhaust flow step 3 (gmole cycle ⁻¹) | 6.70 | 6.47 | 5.85 | 7.27 | 7.20 | 6.45 |
| Exhaust flow step 4 (gmole cycle ⁻¹) | 1.08 | 1.09 | 1.09 | 1.22 | 1.23 | 1.21 |
| Total product flow (gmole cycle ⁻¹) | 0.629 | 0.338 | 0.114 | 0.609 | 0.334 | 0.069 |
| Recovery (%O ₂ +Ar) | 28.3 | 16.2 | 6.09 | 25.4 | 14.5 | 3.38 |
| Specific productivity ((kg O ₂ +Ar) kg ⁻¹ day ⁻¹) | 16.1 | 8.67 | 2.91 | 15.6 | 8.56 | 1.76 |

[†] These results have been taken directly from the "NDGNAS, DPM" entries of Table 6.7.

[‡] These results have been taken directly from the "NDGNAS, LDFP" entries of Table 6.7.

ILE results with Δp^B finite at both purities show separation performance is significantly higher than the equivalent DPM and LDFP model results. Therefore, intrapellet mass transfer resistance is present at the intrapellet level and the relative importance of this resistance is overemphasised within the LDFP model. Lu *et al.* (1993a) found separation performance predicted from a DPM

that incorporates intrapellet viscous flow will fall somewhere between a DPM that incorporates diffusion only and the ILE assumption. There appears to be a similar analogy from Table 6.9 as cycle time approaches the RPSA limit: predicted separation performance obtained from the VF+DGM using a DPM will lie somewhere between the LDFP model and ILE assumption.

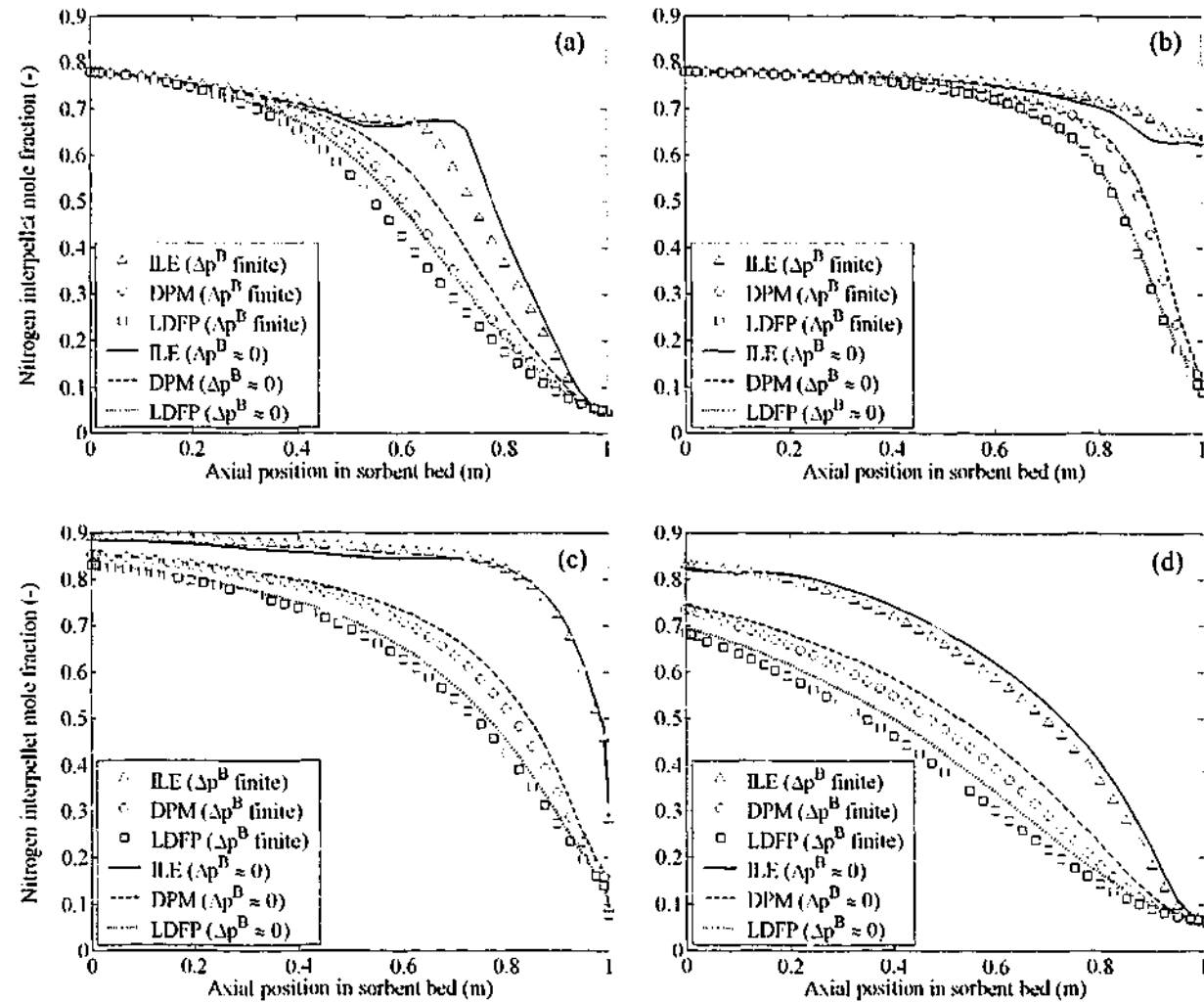


Figure 6.8: Composition profiles obtained from RPSA run 7 (89.8 mol%O₂) using six different modelling options within NDGNAS at the end of step (a) 1, (b) 2, (c) 3 and (d) 4.

Although intrapellet mass transfer is important at the RPSA limit when Δp^B is finite, a rather curious observation from Table 6.9 is made when $\Delta p^B \approx 0$. Both RPSA runs 7 and 9 show separation performance actually decreased when the ILE assumption, DPM and LDFP model was activated using $\Delta p^B \approx 0$ (note, however, that a very small increase in specific productivity was observed with the DPM on RPSA run 7). To assist in the following discussion, end of step composition profiles obtained from all five modelling options using NDGNAS for RPSA runs 7 and 9 are presented in Figs. 6.8 and 6.9 respectively.

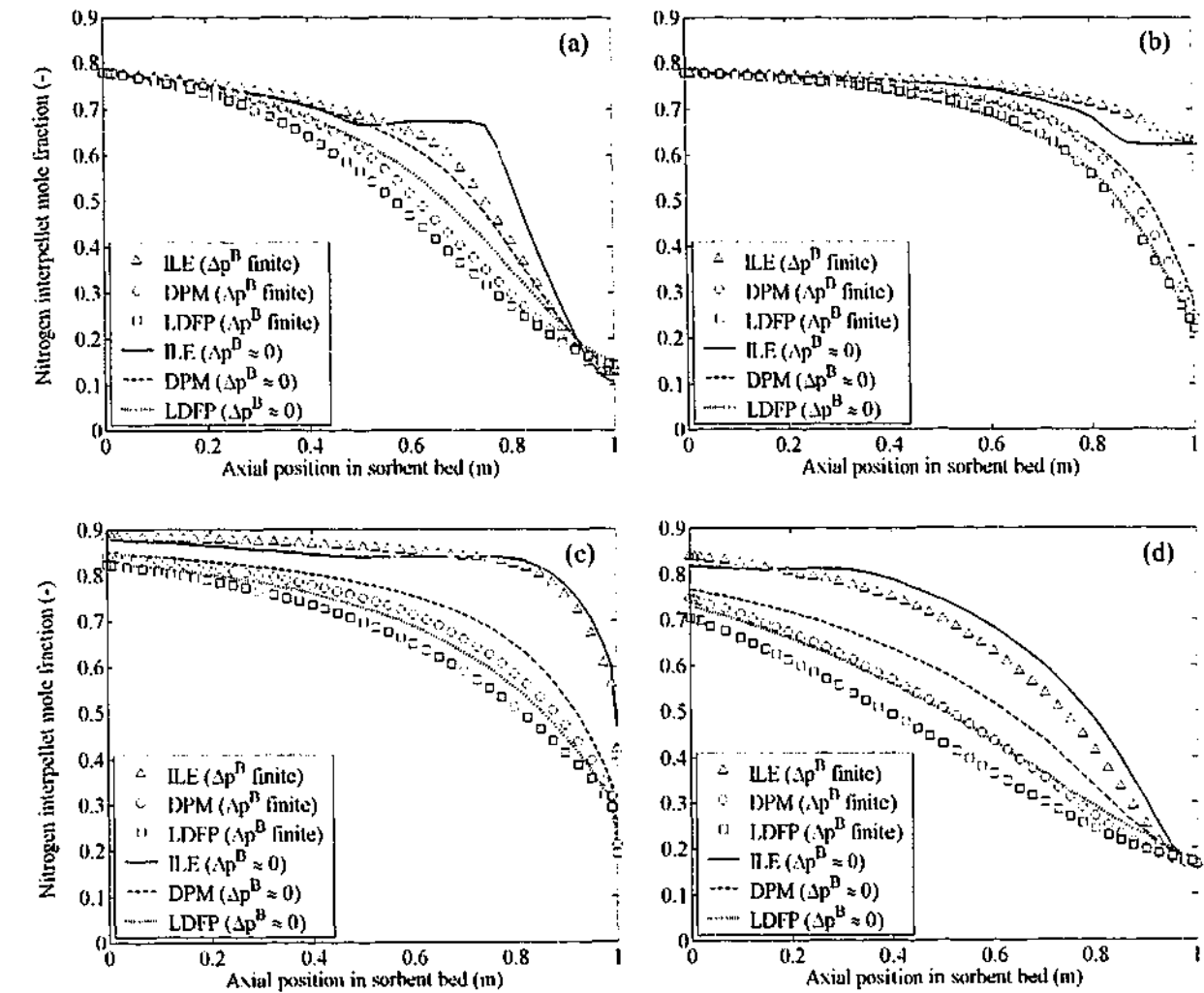


Figure 6.9: Composition profiles obtained from RPSA run 9 (80.0 mol%O₂) using six different modelling options within NDGNAS at the end of step (a) 1, (b) 2, (c) 3 and (d) 4.

During feed pressurisation, Figs. 6.8a and 6.9a both show the penetration distance of nitrogen increases when $\Delta p^B \approx 0$ with respect to the same simulation using Δp^B finite. Feed pressurisation (step 1) terminates and the product line opens (step 2) when the pressure in the top void matches product tank pressure. For the simulation where $\Delta p^B \approx 0$ the entire bed is effectively at tank pressure whereas bed pressure is higher, on average, with Δp^B finite as bottom void pressure is greater than top void pressure (see p^{bottom} and p^{top} entries in Table 6.9 for step 1). The capacity for nitrogen adsorption across the bed is slightly higher with Δp^B finite and hence a larger portion of feed gas is adsorbed, allowing the nitrogen front to be held further back in the bed. By the end of step 2 the axial pressure gradient is relatively flat and the final shape of the composition profile is similar between Δp^B finite and $\Delta p^B \approx 0$ to maintain product purity. The reason for specific productivity and recovery being slightly lower with $\Delta p^B \approx 0$ can be largely attributed to this difference in working capacity for nitrogen adsorption between steps 1 and 2 than any intrinsic influence from the presence of intrapellet mass transfer alone.

Nitrogen composition is similar at the end of step 2 whether Δp^B is finite or $\Delta p^B \approx 0$ (Figs. 6.8b and 6.9b) given the role of intrapellet mass transfer does not change between these runs. A similar observation is also made for nitrogen composition by the end of counter-current depressurisation, step 3. The only noticeable difference between a simulation where Δp^B is finite and $\Delta p^B \approx 0$ for step 3 is the moles of gas exhausted from the bed (Table 6.9). A simulation where Δp^B is finite produces a pressure gradient from top to bottom that is approximately 0.06 bar.a (RPSA run 7) and 0.10 bar.a (RPSA run 9) in magnitude, which is not significant enough to influence interpellet nitrogen mole fraction in comparison to $\Delta p^B \approx 0$ according to Figs. 6.8c and 6.9c. However, a simulation where Δp^B is finite means the bed, on average, is slightly higher in pressure so the equivalent simulation where $\Delta p^B \approx 0$ must exhaust a larger volume of gas to achieve end of step pressure.

A similar argument reveals purge, step 4, is performed at a higher pressure on average when Δp^B is finite. With purge now performed at a slightly higher pressure when Δp^B is finite with respect to $\Delta p^B \approx 0$ the gas phase is not enriched with desorbed nitrogen to the same extent. The axial pressure gradient is significant on RPSA run 9, approximately 0.35-0.40 bar.a, in comparison to RPSA run 7, which is approximately 0.15-0.20 bar.a. Consequently the difference between nitrogen composition when Δp^B is finite and $\Delta p^B \approx 0$ is most pronounced on RPSA run 9 (Fig. 6.9d) with respect to RPSA run 7 (Fig. 6.8d).

Overall, the difference in specific productivity and recovery for the ILE assumption/DPM/LDFP model between Δp^B finite and $\Delta p^B \approx 0$ is not as large as the difference observed between the ILE assumption, DPM and LDFP model when Δp^B is finite. Small differences between the ILE assumption, DPM and LDFP model for Δp^B finite versus $\Delta p^B \approx 0$ could also be rationalised on the basis that nitrogen working capacity between steps 1 and 2 was slightly different and mass transfer had a minor impact on changes in process performance (i.e. compare the relative differences in performance between the ILE assumption for Δp^B finite and $\Delta p^B \approx 0$, where no transfer arises, and then for the LDFP model where mass transfer is overemphasised: there is not a great deal of difference in the relative change in performance).

On this basis interpellet pressure drop mainly alters the available working capacity for nitrogen adsorption. If the choice to start step 2 had been made on the bottom void pressure being a certain value rather than top void pressure equalling product tank pressure (and consequently the bed would be lower in pressure, on average, with Δp^B finite at the end of step 1) performance with $\Delta p^B \approx 0$ would most probably be slightly *greater* than runs where Δp^B is finite.

One last comparison shall be made using data obtained from NDGNAS simulations presented in Table 6.9 with respect to RPSA pilot plant data. Applying different assumptions on intrapellet mass transfer using Δp^B finite, in each case, gave rise to an axial pressure gradient across the sorbent bed that was generally in good agreement with RPSA pilot plant data. Both DP cells located across the bed struggled to capture these rapid pressure transients so the difference between p^{bottom} and p^{top} is presented (Fig. 6.10).

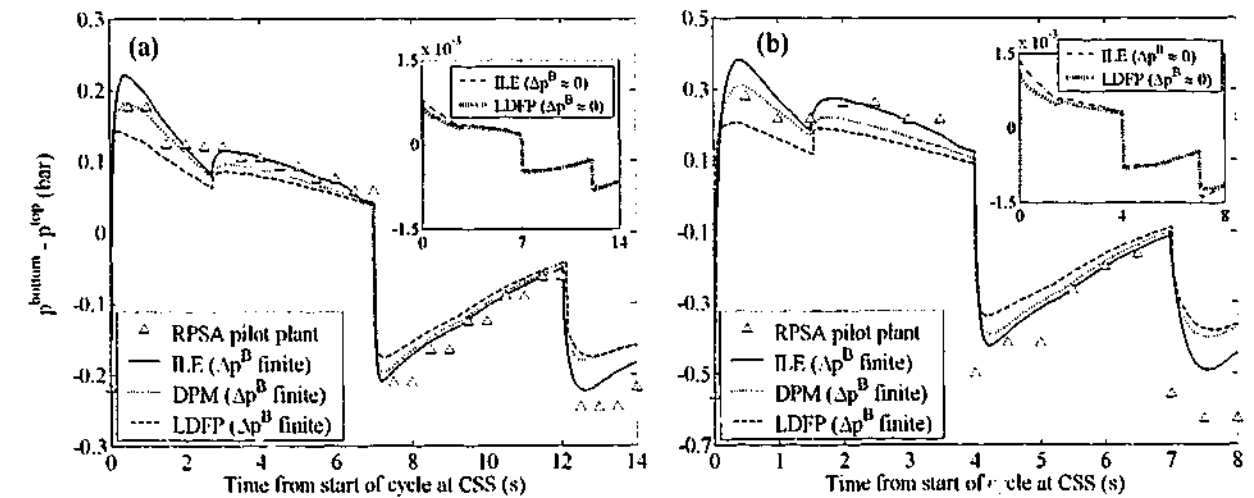


Figure 6.10: Magnitude of the pressure gradient across the sorbent bed obtained experimentally and numerically under various modelling assumptions for (a) RPSA run 7 and (b) RPSA run 9. Inlay graphs of (a) and (b) are provided as a visual guide only to the magnitude of the numerical pressure gradient that arose for simulations where $\Delta p^B \approx 0$. DPM lines for $\Delta p^B \approx 0$ are not shown for brevity but lie between the ILE and LDFP lines on both inlay graphs.

The pressure gradient is highest when the bed behaves under ILE conditions, with the pressure gradient subsiding in magnitude as NDGNAS progressively introduces intrapellet mass transfer into the system. Under ILE conditions the rate of nitrogen adsorption/desorption is the highest as the gas can be taken up/released from the pellets instantaneously, therefore gas flows must be high to achieve the required end of step pressure. With the LDFP model, intrapellet mass transfer is limiting and the bed is partially inert with respect to a DPM or ILE run, hence gas flows do not need to be as high to reach end of step pressure and consequently bed pressure drop is lower.

Despite small differences in simulated pressure drop, the general trend from RPSA run 7 (Fig. 6.10a) and RPSA run 9 (Fig. 6.10b) is that NDGNAS pressure profiles compare well against experimental data with the exception of the purge step, where NDGNAS generally underestimates the pressure gradient from top to bottom. This issue is taken up further in §6.7.3 when pressure profiles over various RPSA runs are presented.

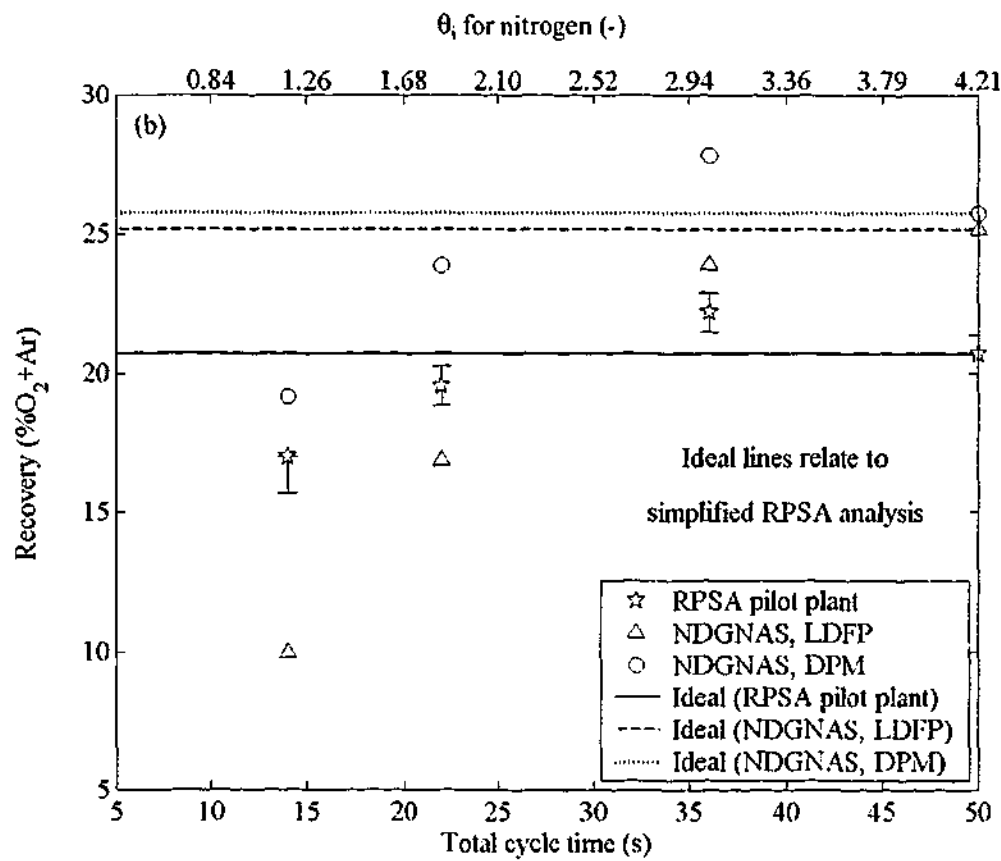
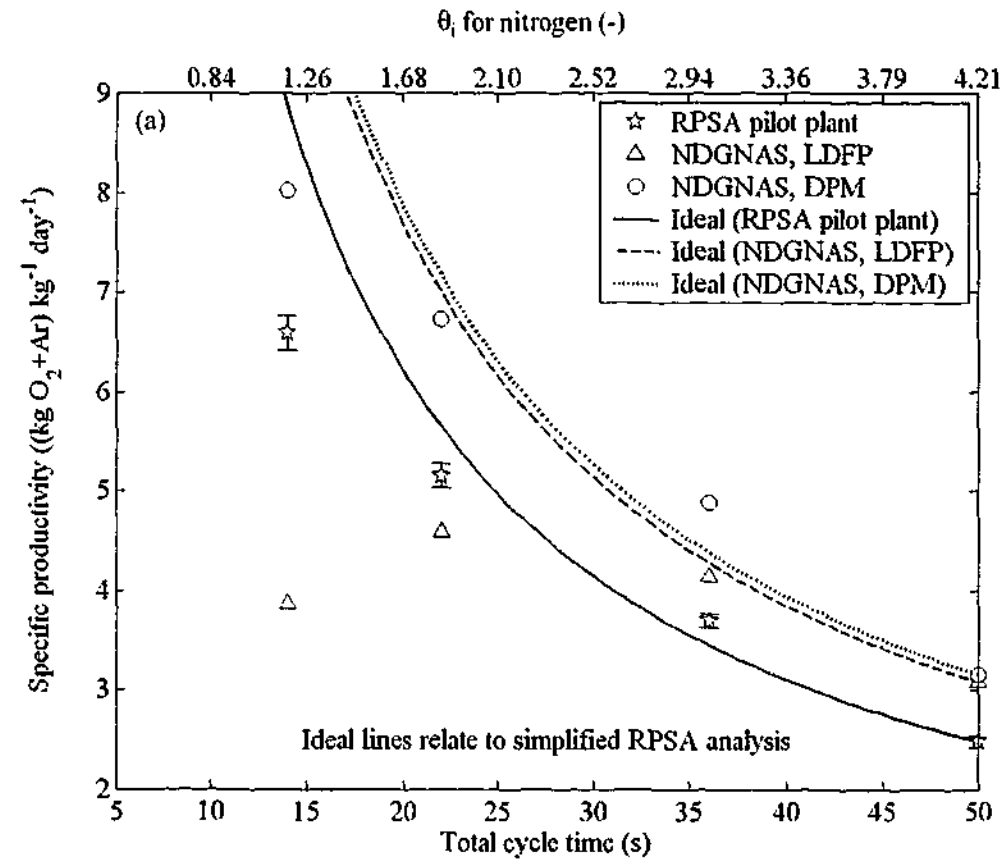


Figure 6.11: Comparing process performance results between RPSA pilot plant data, NDGNAS and simplified RPSA analysis over a 5.00:1.20 pressure window at a target purity of 90 mol%O₂ for (a) specific productivity and (b) recovery.

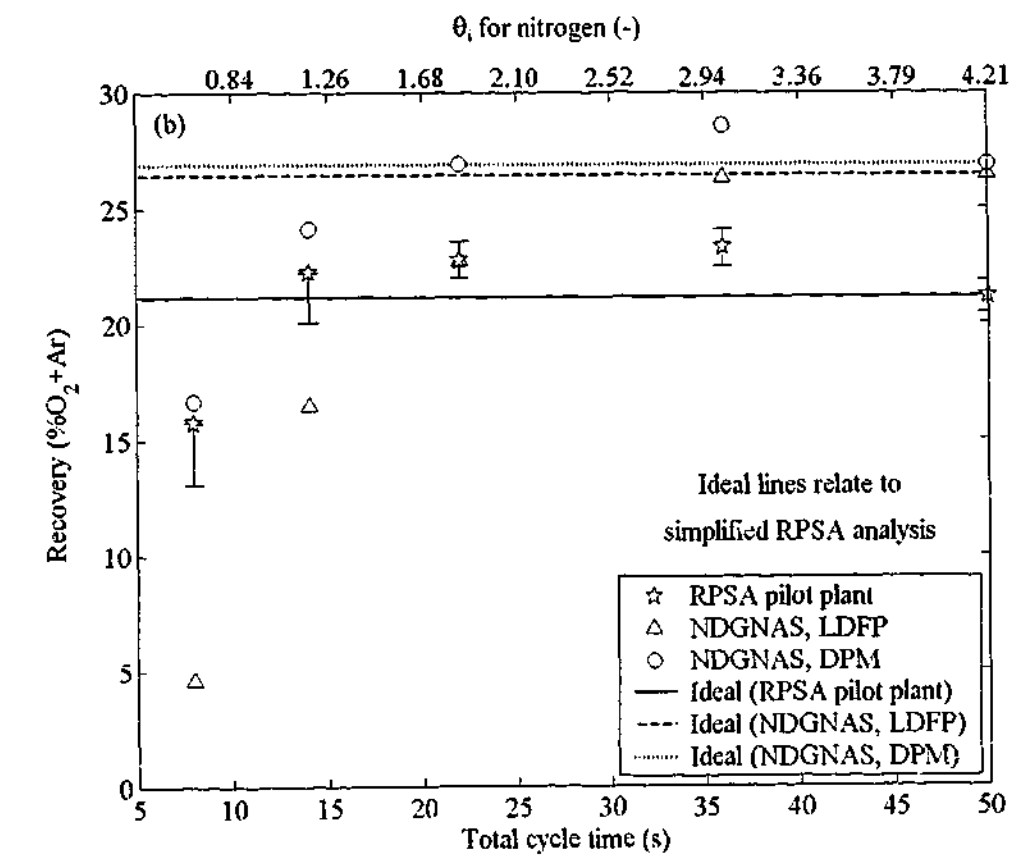
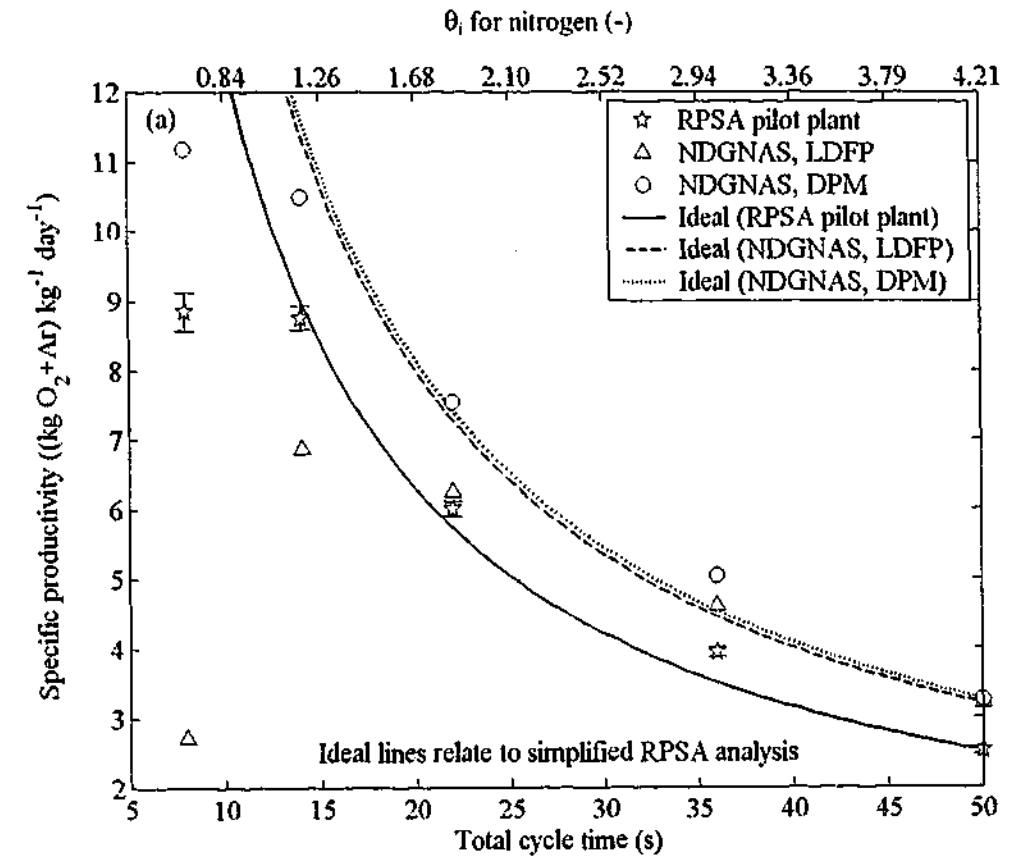


Figure 6.12: Comparing process performance results between RPSA pilot plant data, NDGNAS and simplified RPSA analysis over a 5.00:1.20 pressure window at a target purity of 80 mol%O₂ for (a) specific productivity and (b) recovery.

Results from the 5.00:1.20 bar.a Pressure Window

Trends and percentage errors in the exhaust and total product flows described for the 4.00:1.20 bar.a pressure window also carry over when comparing experimental versus numerical data for the 5.00:1.20 bar.a pressure window. A premature drop in total product flow at the same cycle time observed from the 4.00:1.20 bar.a window, $t_{\text{cycle}} = 22$ s for purity = 90 mol%O₂ and $t_{\text{cycle}} = 14$ s for purity = 80 mol%O₂, also occurs here. Subsequent graphs for specific productivity and recovery as a function of t_{cycle} for the 5.00:1.20 bar.a pressure window are presented in Figs. 6.11 and 6.12.

The same trends in simulated versus experimental data discussed for the 4.00:1.20 bar.a pressure window also applies to the Figs. 6.11 and 6.12. The only obvious difference in trends between the 5.00:1.20 and 4.00:1.20 bar.a pressure window is that a slight increase in specific productivity and recovery occurred for the 80 mol%O₂ runs when t_{cycle} decreased from 50 to 36 s. This suggests end of step purge pressure may have a strong influence on the optimal conditions at the high pressure window with respect to the low pressure window. While the DPM and RPSA pilot plant are again in good agreement, the LDFP model fails to capture the improvement in performance at 80 and 90 mol%O₂ around $t_{\text{cycle}} = 36$ s. In fact the LDFP model at 90 mol%O₂ predicts specific productivity is limited by intrapellet mass transfer resistance to the extent where specific productivity will not improve greatly with a further reduction in cycle time (Fig. 6.11a).

For each simulation performed in this chapter the same values of C_k and C_m used with the VF+DGM, 0.083 and 0.061 respectively, were used in $D_{m,ij}^e$ and $D_{k,i}^e$ for the LDFP model. Although some may argue independent values of C_k and C_m should be found for the LDFP model, this statement is not correct given Fick's first law of diffusion, Eq. (2.16), assumes the intrapellet pore network is identical to that imposed on the VF+DGM. In fact the only difference between the VF+DGM and FFL constitutive equations is the assumption of equimolar counterdiffusion imposed on FFL. Volume averaging the pellet using one radial node over the sorbent pellet was required to generate the LDFP model, which introduced the parameter Ω_i . It is important to remember that both FFL and volume averaging with $N_r = 1$ does not alter the general nature of the intrapellet pore network and transport coefficients obtained in chapter 4 should be general to each transport mechanism within Zeochem LLSX. Viscous flow has a minimal impact on intrapellet mass transfer so the mechanisms of Knudsen and molecular diffusion are dominant; the LDFP model suitably accounts for both of these diffusion mechanisms within a pore network that is assumed equivalent to that imposed on the VF+DGM as FFL underlies the LDF assumption. The discussion of §4.4.3 found transport coefficients obtained in this dissertation agree well against existing literature estimates so the magnitude of C_k and C_m should not be all that different from the

values found using the VF+DGM anyhow. Instead, the finger should be pointed towards the time adjusted coefficient Ω_i ; given this value is the only coefficient that cannot be suitably assigned from EMU or LUB experiments. Conclusions from chapter 2 revealed the assignment of Ω_i for a general PSA cycle was a limiting assumption at the pellet level, data obtained in this chapter further reinforces this statement.

The use of a conventional LDF model to simulate an RPSA cycle, from the preceding discussion, indicates a new limiting value for θ ; that is greater than 0.1 should be adopted: a value closer to 1.0 is recommended from this analysis. While the LDFP model failed to predict general trends at cycle times approaching the RPSA limit, transport coefficients obtained from an independent set of EMU and LUB experiments (chapter 4) with the VF+DGM approach have captured general trends in RPSA pilot plant data (Figs. 6.6, 6.7, 6.11 and 6.12) at cycle times approaching the RPSA limit.

6.7.3 Comparing Pressure Profiles at CSS

Having addressed process performance as a function of cycle time, a comparison of experimental and numerical pressure profiles using both the VF+DGM and LDF intrapellet mass transfer models shall be made. From here the simplified RPSA analysis is not considered since it does not predict pressure profiles. Six of the eighteen RPSA runs have been graphically presented in this dissertation, Figs. 6.13 and 6.14, as a representative sample of the entire data set. The longest and shortest cycle times, along with an intermediate cycle time between these two extremes are presented from both the 4.00:1.20 and 5.00:1.20 bar.a pressure windows. These trends all relate to 80 mol%O₂ runs. Qualitatively identical profiles are observed for the 90 mol%O₂ RPSA runs and are not shown for brevity.

At cycle times reminiscent of a PSA cycle, $t_{\text{cycle}} = 50$ s, excellent agreement is seen between experimental and numerical pressure profiles. At these cycle times interpellet pressure drop has minimal impact on pressure profiles according to difference in p^{bottom} and p^{top} from Table 6.7 and the discussion of §6.7.2, justifying the well-mixed assumption with no flow channeling discussed in §1.2.1 for $d_{\text{bed}}:d_{p,\text{eqv}} > 30:1$. These results also justify the use of void volumes and the compressible valve equation to independently reproduce pressure profiles expected from a typical PSA cycle. Good agreement between linear fitted and experimental product tank pressure profiles from end of step data shown in Figs. 6.13 and 6.14 also validates this assumption across each cycle time investigated.

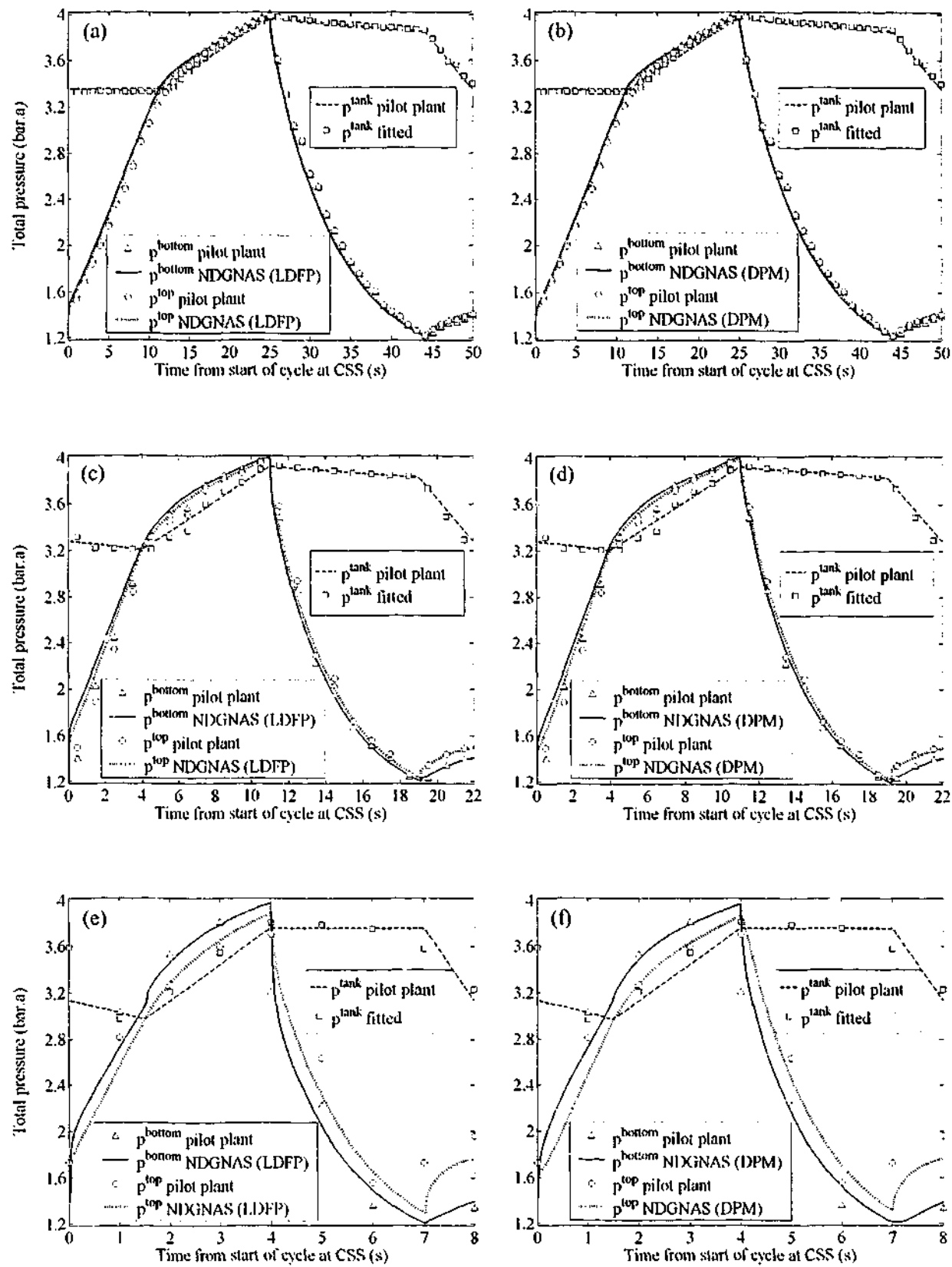


Figure 6.13: Comparing experimental versus simulated pressure profiles with time at CSS over a 4.00:1.20 bar.a pressure window using both intrapellet mass transfer models of NDGNAS. (a) RPSA run 2 with LDFP. (b) RPSA run 2 with DPM. (c) RPSA run 6 with LDFP. (d) RPSA run 6 with DPM. (e) RPSA run 9 with LDFP. (f) RPSA run 9 with DPM.

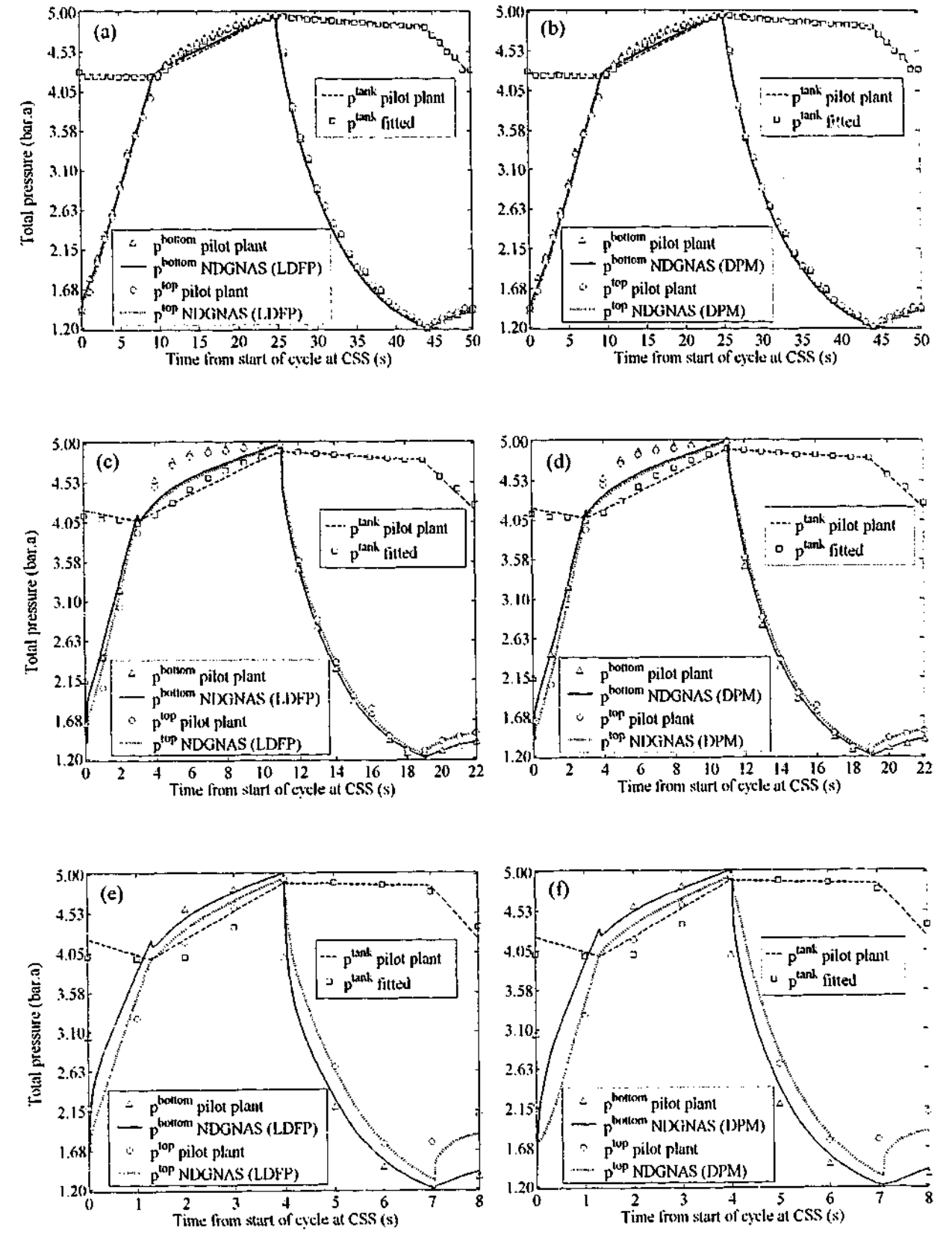


Figure 6.14: Comparing experimental versus simulated pressure profiles with time at CSS over a 5.00:1.20 bar.a pressure window using both intrapellet mass transfer models of NDGNAS. (a) RPSA run 11 with LDFP. (b) RPSA run 11 with DPM. (c) RPSA run 15 with LDFP. (d) RPSA run 15 with DPM. (e) RPSA run 18 with LDFP. (f) RPSA run 18 with DPM.

Numerical versus experimental predictions from the 4.00:1.20 bar.a pressure window, Fig. 6.13, show the DPM and LDFP model both reproduce experimental pressure profiles well from the long to short cycle times. On this basis comparing pressure profiles alone does not reveal any significant deviations between the DPM and LDFP model, which goes against the trend observed from Figs. 6.6, 6.7, 6.11 and 6.12 in relation to process performance numbers. However, two regions where the DPM and LDFP models do show some discrepancy occurs at the start of feed pressurisation and counter-current depressurisation, steps 1 and 3 respectively. As cycle time reduces, the LDFP model predicts the bed initially pressurises and depressurises faster than the DPM. This is starting to become evident at $t_{\text{cycle}} = 22$ s (Figs. 6.13c and 6.13d) and is quite pronounced at $t_{\text{cycle}} = 8$ s (Figs. 6.13e and 6.13f). These observations can be attributed to the rate at which pellets take up/release sorbate molecules from/to the interpellet region using a VF+DGM versus LDF approach. The discussion that follows is closely related to the discussion of Fig. 2.7 and the reasons behind trends in that graph carry over in this discussion.

At short contact times bulk gas motion and viscous flow (VF+DGM) are crucial components of intrapellet mass transfer with respect to gas entering and leaving a sorbent pellet. The LDFP model, on the other hand, imposes equimolar counterdiffusion on gas transport. During feed pressurisation gas can enter the pellets and be adsorbed much faster using the VF+DGM approach, hence the interpellet region takes longer to pressurise. During counter-current depressurisation, the opposing argument holds and desorbed gas leaves the pellets much faster (VF+DGM) to replenish the interpellet region. The importance of desorbed gas replenishing the interpellet region was evident between the adsorbing and non-adsorbing conditions for rapid depressurisation experiments performed in §5.5. The LDFP model "depletes" and "replenishes" interpellet gas slower than the VF+DGM. Hence the sorbent bed is almost semi-inert during the early stages of steps 1 and 3 giving rise to a sharp increase and decrease in pressure respectively. Difficulties in data acquisition at short cycle times prevent this statement from being experimentally validated.

While each numerical profile over the 4.00:1.20 pressure window of Fig. 6.13 matches experimental data well, the agreement is not so good for the 5.00:1.20 bar.a pressure window presented in Fig. 6.13. In general, NDGNAS profiles during feed plus make product, step 2, is lower than the equivalent experimental trend. This has a big impact on the volume of gas obtained as product that in turn affects predicted separation performance. This was evident when comparing experimental versus numerical results from the 4.00:1.20 and 5.00:1.20 bar.a pressure window. Errors in the regressed equilibrium isotherm parameters discussed in §6.7.1 are believed to be the cause of this offset. The equilibrium isotherm used by NDGNAS does not require pressure to be as high in the sorbent bed to invoke the same separation when compared to the RPSA pilot plant. A

lack of more extensive equilibrium data for a binary component mixture of oxygen and nitrogen makes it difficult to quantify this observation.

Figures 6.13 and 6.14 reveal the largest discrepancy between experimental and numerical pressure resides in the top void region during purge, step 4, at short cycle times. NDGNAS predictions for p^{top} at the end of step 4 with $t_{\text{cycle}} = 14$ s is approximately 0.05 bar.a lower than those from the RPSA pilot plant. At $t_{\text{cycle}} = 8$ s this discrepancy has increased to 0.20 bar.a. Given purge is performed in 1 s when $t_{\text{cycle}} = 8$ s, errors in flow geometry simulated between the product tank and sorbent bed interface at $z = L_{\text{bed}}$ will be most pronounced. Numerically the top void is a CSTR that can accumulate a small volume of gas between $z = L_{\text{bed}}$ and the product tank. This same region, however, does not provide any pressure drop. On the RPSA pilot plant the top void comprises several pipe sections with 90° bends in addition to a filter element that removes entrained sorbent dust. To purge the bed with pressure increasing from 1.20 to 1.40 bar.a in 1 s suggests momentum transfer in the top pipe manifold was important in comparison to longer cycle times. Despite this, good qualitative agreement is observed and the inclusion of a pipe K factor into the upper void CSTR of NDGNAS may assist in closing this mismatch.

6.7.4 Comparing Temperature Profiles at CSS

Before a single graph is presented in this subsection it should be evident from the discussion of chapters 4 and 5 that NDGNAS will overestimate temperatures obtained experimentally within the RPSA pilot plant. Eight pre-calibrated junction exposed T-type thermocouples were placed in the centre of the sorbent bed at different axial locations to measure temperature, identical to that used in the previous two chapters. The 40 s response time discussed in §5.6.1 indicates the full swing in temperature expected during each step of the cycle will not be seen experimentally. The corresponding temperature versus time graphs of Figs. 6.13 and 6.14 are shown in Figs. 6.15 and 6.16 and, as expected, the numerical profile lies above the corresponding experimental profile.

Figures 6.15 and 6.16 show NDGNAS predicts a more rapid temperature change than those experimentally observed. During feed pressurisation NDGNAS temperatures rapidly increase as pressure increases and nitrogen adsorbs. Once the product line opens and gas is withdrawn from the bed, the rate of change of pressure decreases and so does the rate of change of temperature. For the longest cycle time, $t_{\text{cycle}} = 50$ s, this trend over the first two steps of the cycle is loosely observed on the RPSA pilot plant. As cycle time reduces, the experimental transients do not show this distinct change in gradient commonly observed numerically between steps 1 and 2, obviously being a strong function of thermocouple response just mentioned.

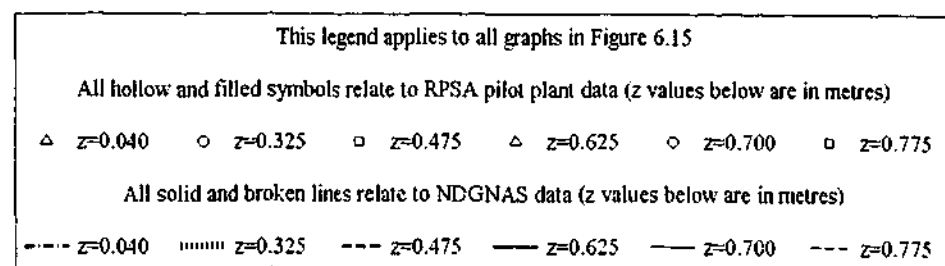
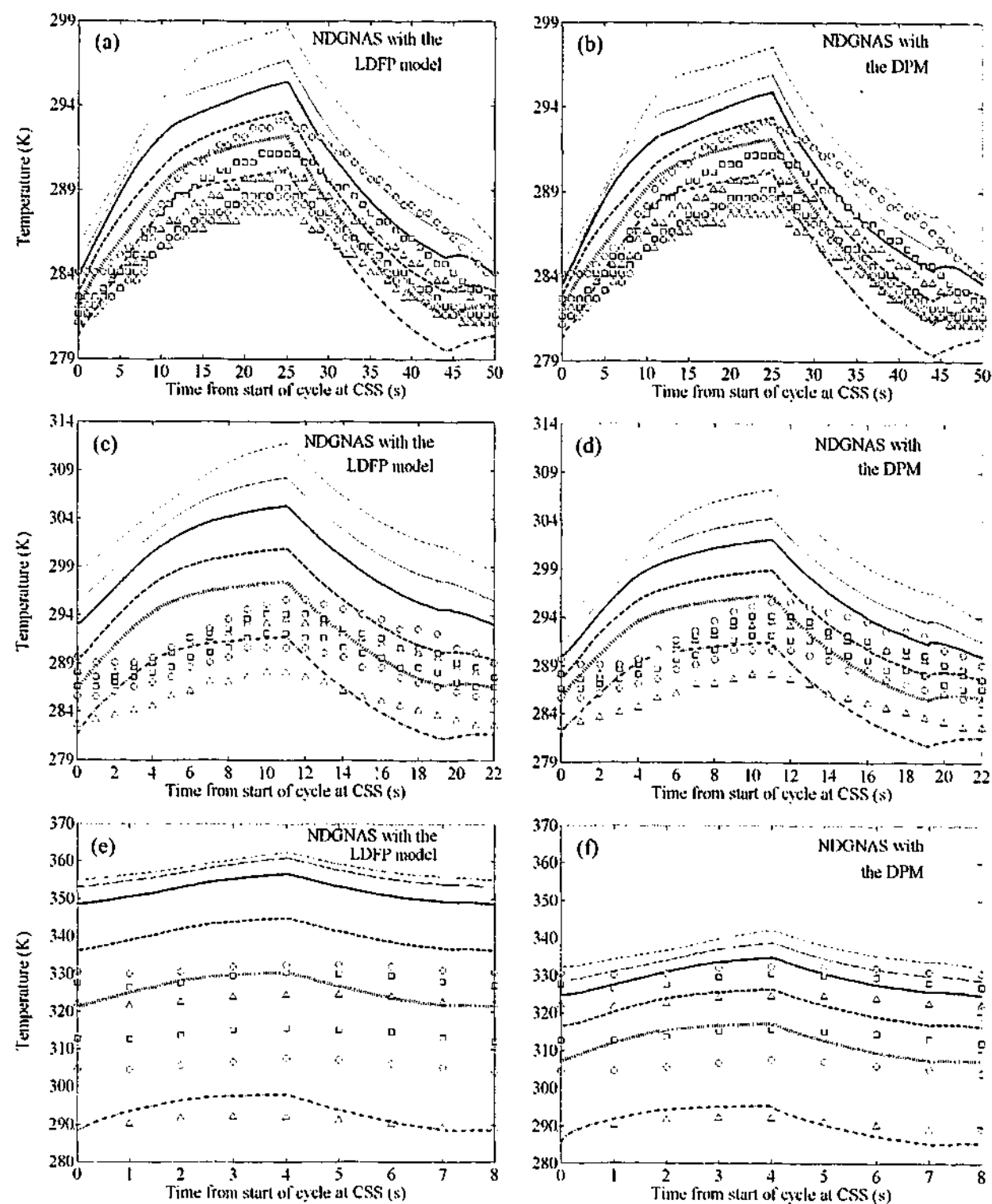


Figure 6.15: Comparing experimental versus simulated temperature profiles with time at CSS over a 4.00:1.20 bar.a pressure window using both intrapellet mass transfer models of NDGNAS. (a) RPSA run 2 with LDFP. (b) RPSA run 2 with DPM. (c) RPSA run 6 with LDFP. (d) RPSA run 6 with DPM. (e) RPSA run 9 with LDFP. (f) RPSA run 9 with DPM.

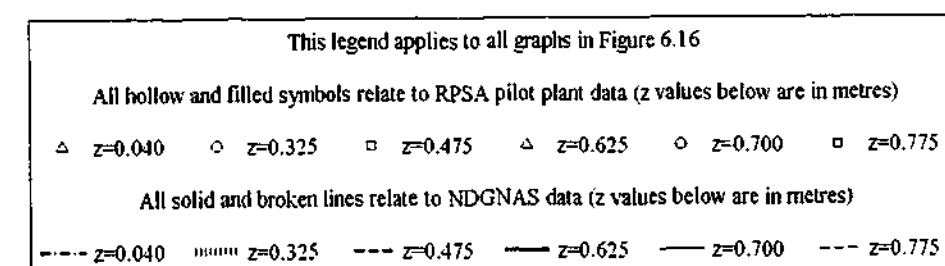
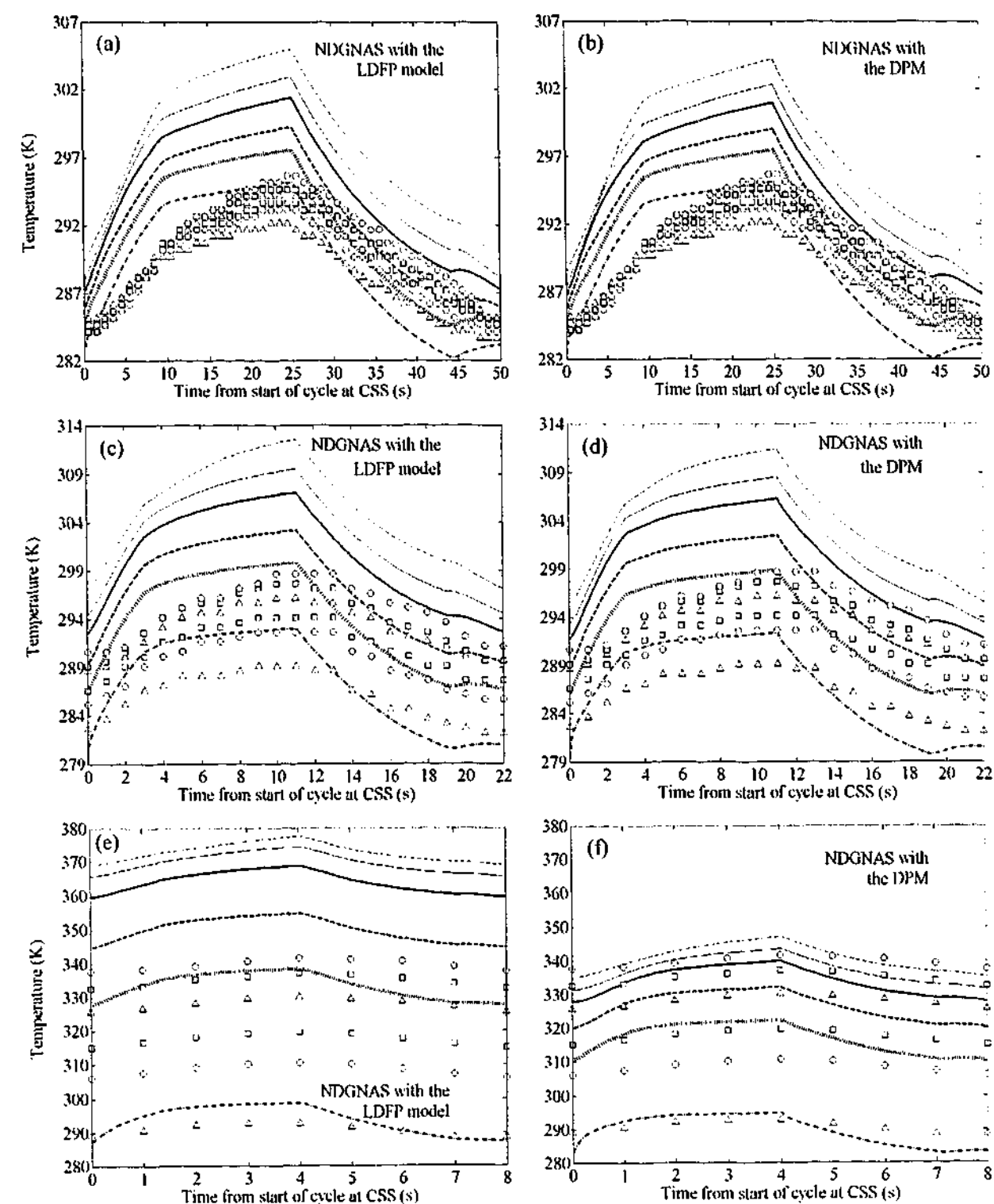


Figure 6.16: Comparing experimental versus simulated temperature profiles with time at CSS over a 5.00:1.20 bar.a pressure window using both intrapellet mass transfer models of NDGNAS. (a) RPSA run 11 with LDFP. (b) RPSA run 11 with DPM. (c) RPSA run 15 with LDFP. (d) RPSA run 15 with DPM. (e) RPSA run 18 with LDFP. (f) RPSA run 18 with DPM.

For the shortest cycle time, temperature swing predicted numerically at any one point in the bed was smaller than that observed for the longest cycle time. The predicted swing in temperature from both the DPM and LDFP model during RPSA run 2 is approximately 11-12 K (Figs. 6.15a and 6.15b), while they are approximately 8-9 K during RPSA run 9 (Figs. 6.15e and 6.15f). Although thermocouple response time is a major issue during RPSA run 9, temperature swing observed experimentally for RPSA run 2 is approximately 8-9 K, which compares well with the numerical estimate of 11-12 K. Although not drastic (i.e. θ , ranges between 4.2 to 0.7 for nitrogen across RPSA runs 1 through 18), the trend of decreasing temperature swing with cycle time at any one point in the bed is directly in line with single pellet non-isothermal simulations discussed around Figs. 2.16 and 2.18. The effective working volume of the pellet is decreasing with cycle time so adsorption-desorption capacity is progressively moving to the outer layers of the sorbent pellet. The assumption of intrapellet thermal equilibrium means a constant thermal capacitance is available to absorb a smaller quantity of heat being released during adsorption and taken up during desorption. Although the scale on Figs. 6.15e and 6.15f make it difficult to compare temperature swing directly against Figs. 6.15a and 6.15b, the observation of a decreasing temperature swing with cycle time observed here is consistent with single pellet studies performed in chapter 2.

What has drastically changed between the long and short cycle time, however, is the axial temperature gradient across the sorbent bed. To further examine this result, Figs. 6.18 and 6.19 compare end of step temperature profiles obtained from the RPSA pilot plant and NDGNAS. Each graph in Figs. 6.18 and 6.19 is the end of step counterpart to pressure profiles in Figs. 6.13 and 6.14 and temperature profiles in Figs. 6.15 and 6.16. Simulation data at long cycle times show temperature increases rather sharply across the upper regions of the bed. To help explain these results, numerical composition profiles obtained from the DPM and LDFP model from RPSA runs 2 and 9 are useful to consider (see Fig. 6.17). The mole fraction of nitrogen at the end of step 1 from RPSA run 2 (Fig. 6.17a) indicates the bed is similar in composition to air for $z < 0.7$ m. During step 2 the MTZ moves from $z \approx 0.7$ to $z \approx 1.0$ m and 100% breakthrough is imminent. A significant amount of nitrogen adsorbs between $0.7 < z < 1.0$ that liberates a large amount of heat in comparison to the rest of the sorbent bed below $z \approx 0.7$ m. This increased amount of nitrogen adsorption explains the sharp increase in numerical bed temperature for axial regions above $z \approx 0.7$ m. Although axial temperature gradient increases sharply above $z \approx 0.7$ m, the actual swing in temperature itself is similar as the entire bed moves from high to low pressure with time (i.e. pressure drop is relatively low so working capacity is similar from $z = 0$ to $z = L_{\text{bed}}$).

In general, predicted temperature profiles obtained with both the DPM and LDFP model for the long cycle time (Fig. 6.18a and 6.18b) are in good qualitative agreement with experimental trends.

Figures 6.18a and 6.18b show RPSA pilot plant temperature is beginning to increase at an axial coordinate similar to that predicted from both the DPM and LDFP model. The form of the composition profile depicted in Fig. 6.17a is in accordance with experimentally observed temperature profiles. Long time scale temperature profiles obtained from the 5.00:1.20 bar.a pressure window using NDGNAS also show good qualitative agreement with experimental data (Figs. 6.19a and 6.19b).

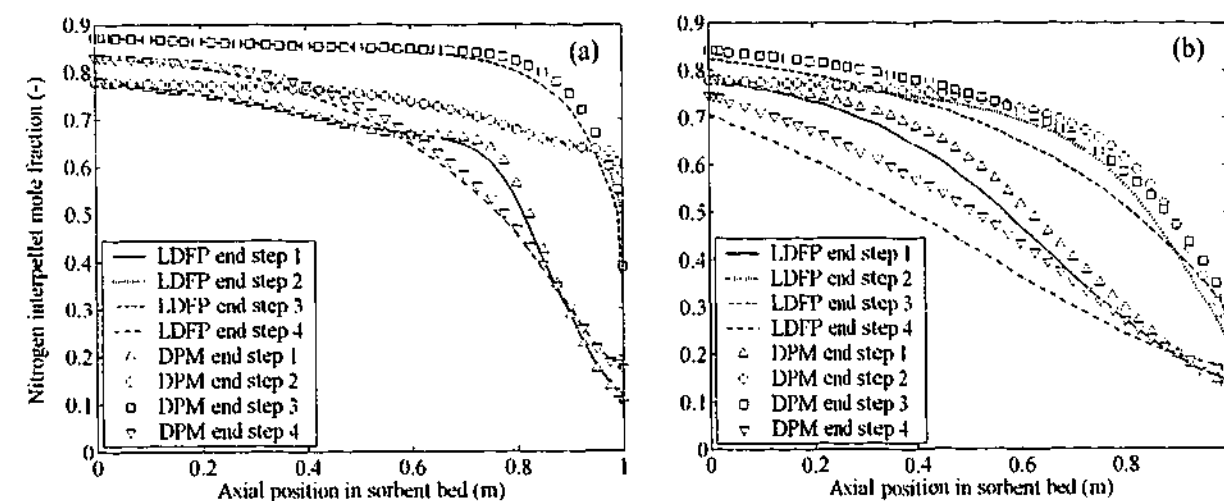


Figure 6.17: NDGNAS end of step composition profiles for nitrogen obtained with the DPM and LDFP model from (a) RPSA run 2 and (b) RPSA run 9.

The other trend evident from Figs. 6.18 and 6.19 is the gradual increase in sorbent bed temperature with axial position as cycle time decreases. At these shorter cycle times interpellet velocities increase to maintain the same pressure window and consequently the MTZ broadens. This requires the MTZ to be held further back in the bed to maintain product purity over step 2. To contain the MTZ within the bed, the amount of gas withdrawn from the top of the bed has to decrease and product recovery drops accordingly. For a system where heat loss to the environment is a small component of the total energy passing through the bed (§6.7.5 indicates near-adiabatic conditions are maintained), enthalpy entering the bed at $z = 0$ simply accumulates as less enthalpy is taken out as product. This explains the gradual sharpening of axial temperature profiles across Figs. 6.18 and 6.19 as cycle time decreases. The fact that the LDFP model draws less gas out of the bed in relation to the DPM to maintain purity for RPSA runs 9 and 18 means the temperature increases by almost 100 K from feed gas temperature. The DPM allows more gas to exit the bed using a VF+DGM approach and hence the temperature is significantly lower, increasing by approximately 60 K from feed conditions. The DPM is also in good agreement with experimental temperature profiles at the short cycle time.

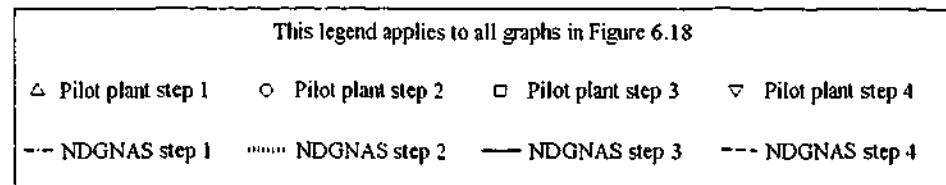
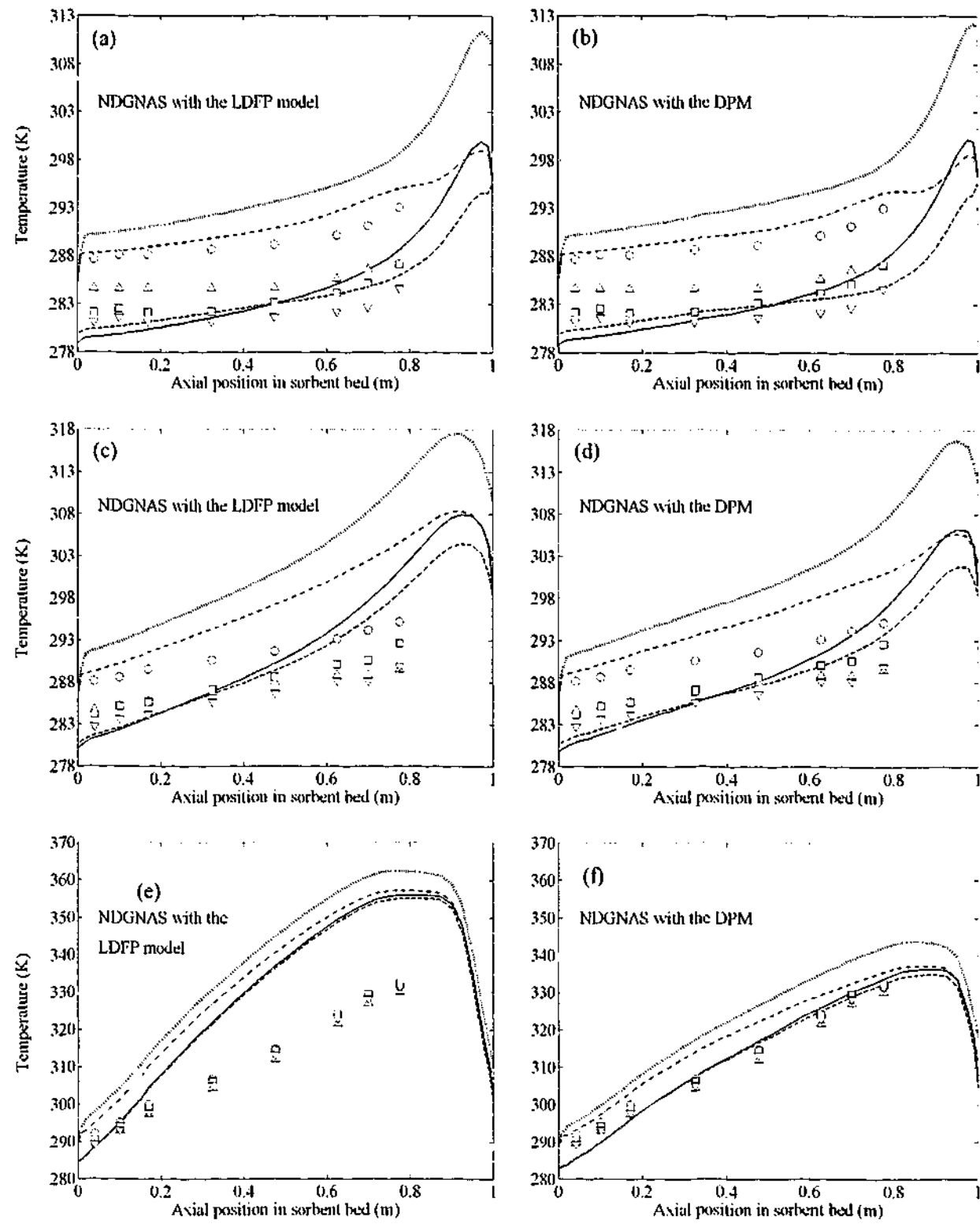


Figure 6.18: Comparing experimental versus simulated end of step temperature profiles at CSS with a 4.00:1.20 bar.a pressure window using both intrapellet mass transfer models of NDGNAS. (a) RPSA run 2 with LDFP. (b) RPSA run 2 with DPM. (c) RPSA run 6 with LDFP. (d) RPSA run 6 with DPM. (e) RPSA run 9 with LDFP. (f) RPSA run 9 with DPM.

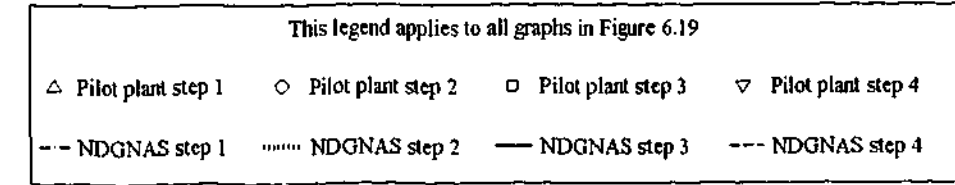
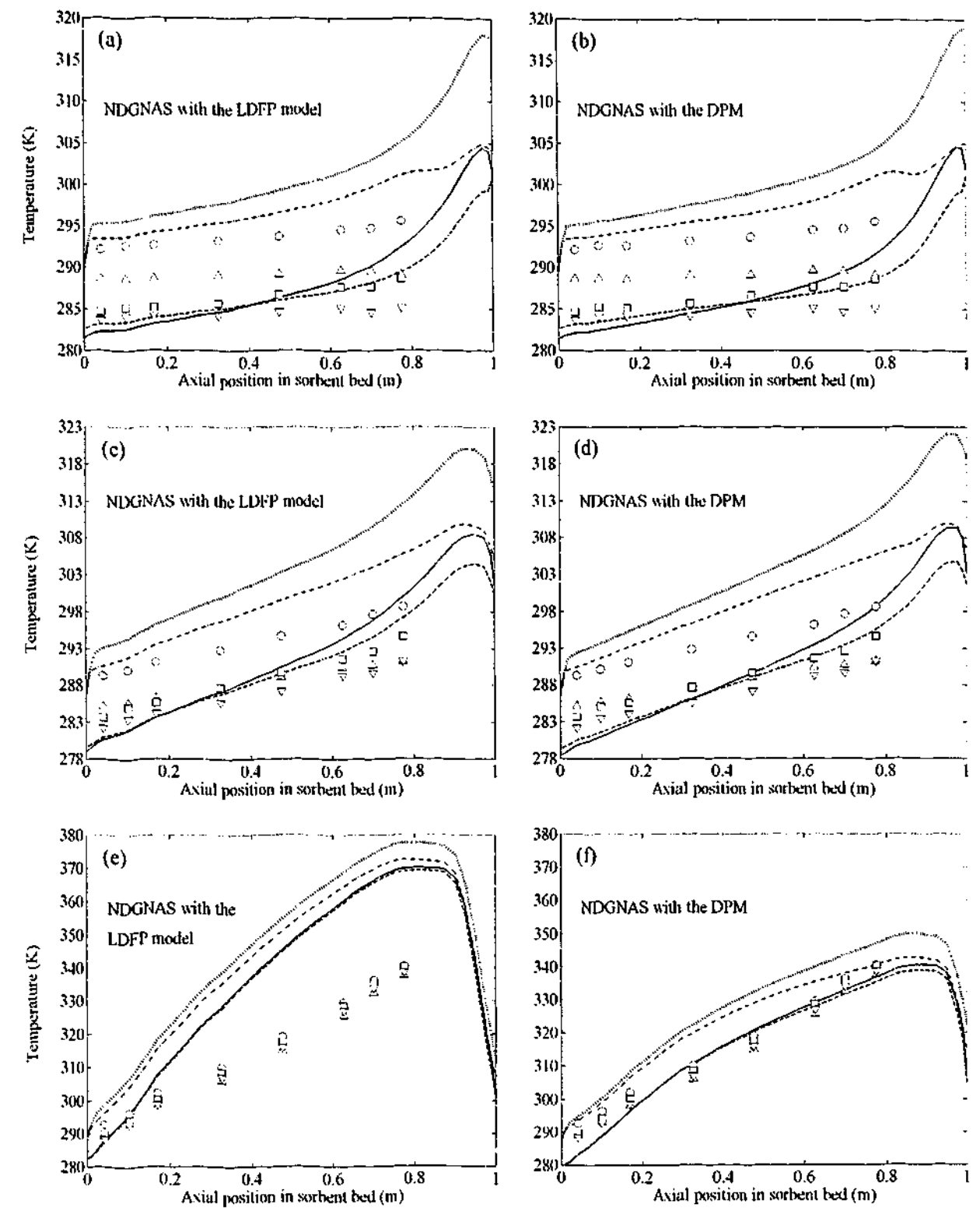


Figure 6.19: Comparing experimental versus simulated end of step temperature profiles at CSS with a 5.00:1.20 bar.a pressure window using both intrapellet mass transfer models of NDGNAS. (a) RPSA run 11 with LDFP. (b) RPSA run 11 with DPM. (c) RPSA run 15 with LDFP. (d) RPSA run 15 with DPM. (e) RPSA run 18 with LDFP. (f) RPSA run 18 with DPM.

6.7.5 Adiabatic versus Non-Isothermal Assumption

Up to this point, numerical versus experimental comparisons have been made with the rigorous wall model activated on both the DPM and LDF portions of each simulation. Although deviations between the DPM and LDFP model were observed, the purpose of this section is to investigate the impact of the adiabatic versus non-isothermal assumption with just one of the intrapellet mass transfer models. In the present discussion "non-isothermal" refers to simulations where the rigorous wall model was activated and hence the bed is not completely adiabatic. Although the sorbent bed itself was not adiabatic, the combined regions of the column wall plus sorbent bed is adiabatic given insulation was wrapped around the outside of the adsorption column. These additional simulations effectively compare the impact of energy accumulation and conduction along the walls of the adsorption column.

The following discussion considers the LDFP model only due to time constraints inherent with the DPM. Even with good estimates for valve coefficients and CSS bed profiles from the initial file of the corresponding non-isothermal run, each simulation still required in excess of 1,000 cycles to converge. With this said, however, concentration is focused on RPSA runs where the LDFP model was still in relatively good agreement with the DPM and RPSA pilot plant. For this reason one additional simulation was performed on RPSA runs 2 and 8 respectively to investigate the impact of the adiabatic versus non-isothermal assumption on CSS results. For both of these RPSA runs simulation conditions identical to those summarised previously were used, the only difference here being the appropriate flag from the input deck has now deactivated the rigorous wall model. A comparison of simulation results obtained with the LDFP model under adiabatic and non-isothermal conditions from RPSA runs 2 and 8 respectively are presented in Table 6.10, along with the corresponding error between simulations results.

The most obvious result from Table 6.10 is that errors were less than 1% for each parameter compared. The accumulation and transport of energy along the walls of the adsorption column is seen to have a negligible impact on process performance with respect to the adiabatic case. This result also shows conditions close to adiabatic have been attained within the RPSA pilot plant using a metal walled column with an internal diameter of 0.156 m that is insulated on the outside. This has of course neglected heat transfer to the environment that can occur experimentally from both metal flanges located at the top and bottom of the column. While non-isothermal versus adiabatic simulation results are similar at cycle times representative of a PSA and RPSA process, numerical temperature profiles obtained from the non-isothermal run lie below their equivalent adiabatic profile (Fig. 6.20).

Table 6.10: Numerical performance results obtained from RPSA runs 2 and 8 under non-isothermal and adiabatic conditions with the LDFP model activated on NDGNAS.

| RPSA run 2 ($t_{\text{cycle}} = 50$ s at 79.1 mol% O ₂) | NDGNAS, LDFP | | Error (%) [‡] |
|---|--------------|-----------------------------|------------------------|
| | Parameter | Non-isothermal [†] | |
| p^{bottom} end step 1 (bar.a) | 3.348 | 3.333 | -0.43 |
| p^{top} end step 1 (bar.a) | 3.338 | 3.323 | -0.44 |
| p^{bottom} end step 2 (bar.a) | 4.001 | 4.000 | -0.02 |
| p^{top} end step 2 (bar.a) | 3.994 | 3.994 | -0.01 |
| p^{bottom} end step 3 (bar.a) | 1.212 | 1.214 | 0.16 |
| p^{top} end step 3 (bar.a) | 1.221 | 1.223 | 0.17 |
| p^{bottom} end step 4 (bar.a) | 1.401 | 1.396 | -0.35 |
| p^{top} end step 4 (bar.a) | 1.427 | 1.422 | -0.35 |
| Exhaust flow step 3 (gmole cycle ⁻¹) | 7.232 | 7.239 | 0.09 |
| Exhaust flow step 4 (gmole cycle ⁻¹) | 1.170 | 1.162 | -0.69 |
| Total product flow (gmole cycle ⁻¹) | 0.6112 | 0.6132 | 0.33 |
| Recovery (%O ₂ +Ar) | 25.48 | 25.53 | 0.20 |
| Specific productivity ((kg O ₂ +Ar) kg ⁻¹ day ⁻¹) | 2.474 | 2.480 | 0.20 |

| RPSA run 8 ($t_{\text{cycle}} = 14$ s at 80.4 mol% O ₂) | NDGNAS, LDFP | | Error (%) [‡] |
|---|--------------|-----------------------------|------------------------|
| | Parameter | Non-isothermal [†] | |
| p^{bottom} end step 1 (bar.a) | 3.171 | 3.153 | -0.57 |
| p^{top} end step 1 (bar.a) | 3.098 | 3.081 | -0.55 |
| p^{bottom} end step 2 (bar.a) | 4.007 | 4.006 | -0.03 |
| p^{top} end step 2 (bar.a) | 3.966 | 3.964 | -0.05 |
| p^{bottom} end step 3 (bar.a) | 1.199 | 1.205 | 0.53 |
| p^{top} end step 3 (bar.a) | 1.249 | 1.256 | 0.52 |
| p^{bottom} end step 4 (bar.a) | 1.399 | 1.407 | 0.56 |
| p^{top} end step 4 (bar.a) | 1.573 | 1.580 | 0.41 |
| Exhaust flow step 3 (gmole cycle ⁻¹) | 6.869 | 6.812 | -0.80 |
| Exhaust flow step 4 (gmole cycle ⁻¹) | 1.514 | 1.506 | -0.54 |
| Total product flow (gmole cycle ⁻¹) | 0.3790 | 0.3790 | 0.01 |
| Recovery (%O ₂ +Ar) | 16.47 | 16.58 | 0.67 |
| Specific productivity ((kg O ₂ +Ar) kg ⁻¹ day ⁻¹) | 5.568 | 5.563 | -0.08 |

[†] These results have been taken directly from the "NDGNAS, LDFP" entries of Table 6.7.

[‡] "Error" is defined as $[(\psi_{\text{adiabatic}} - \psi_{\text{non-isothermal}}) / \psi_{\text{non-isothermal}}] \times 100$, where ψ represents the corresponding "Parameter" listed on the left hand side of the table.

Although the bed is slightly cooler in the presence of a wall that can accumulate and conduct energy, general trends in temperature as a function of axial position are identical. This suggests the transport of energy from a warm to cool region of the bed via conduction is only a very small percentage of the energy that accumulates within the column wall. The bed swings by a similar magnitude between adsorption and desorption and the small offset in absolute temperature can therefore be attributed to a slight increase in thermal capacitance offered by the adsorption column walls. The common method of increasing \hat{c}_p to account for the presence of a metal wall without rigorously modelling the column wall itself appears to be a valid assumption provided conditions close to adiabatic arise between the external surface of the wall and the surrounding environment.

From this preliminary study, operating an RPSA cycle at the industrial scale would lead to severe temperature profiles on a magnitude similar to those observed here. At the limit of short cycle

times the LDFF model will significantly overestimate the axial temperature gradient through the bed while the DPM provides a much better representation of the temperature profile.

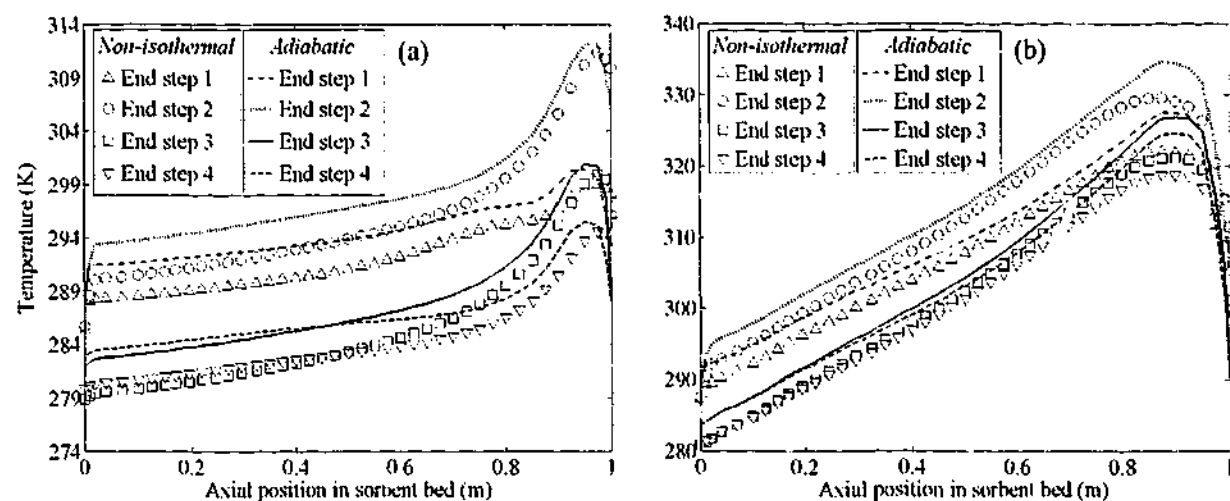


Figure 6.20: Comparing adiabatic versus non-isothermal temperature profiles obtained with the LDFF model activated on NDGNAS from (a) RPSA run 2 and (b) RPSA run 8.

It should be pointed out here that pure component isotherms were measured up to a temperature of 321.9 K. As temperatures were exceeding 340 K numerically in the sorbent bed at the RPSA limit, the applicability of the equilibrium isotherm under these conditions becomes a contentious issue. These observations suggest equilibrium isotherm measurements should be performed over a wider range of temperatures to ensure regressed parameters cover the full range of temperatures expected within the sorbent bed under near-adiabatic RPSA conditions.

6.7.6 Comparing Temperature Profiles from Teague & Edgar (1999)

The discussion of this chapter shall conclude with a review of data obtained from a previous study that, according to the author, may validate the hypothesis that thermocouple response within a packed bed of sorbent may be causing mismatch between experimental and numerical temperature profiles. Teague & Edgar (1999) found numerical temperature profiles overestimated their experimental counterparts within a two-bed PSA system performing oxygen enrichment from air over a packed bed of UOP Oxysiv-5 13X zeolite at cycle times comparable to those performed here. Although a two-bed arrangement was used, their cycle comprised feed pressurisation, feed plus make product, counter-current depressurisation and purge; very similar to the cycle performed in this study. As a comparison, Figs. 19 and 20 from their paper have been reproduced and are shown above similar trends obtained in this dissertation (Fig. 6.21). Although a different sorbent was used, experimental versus numerical trends are similar between these two independent studies.

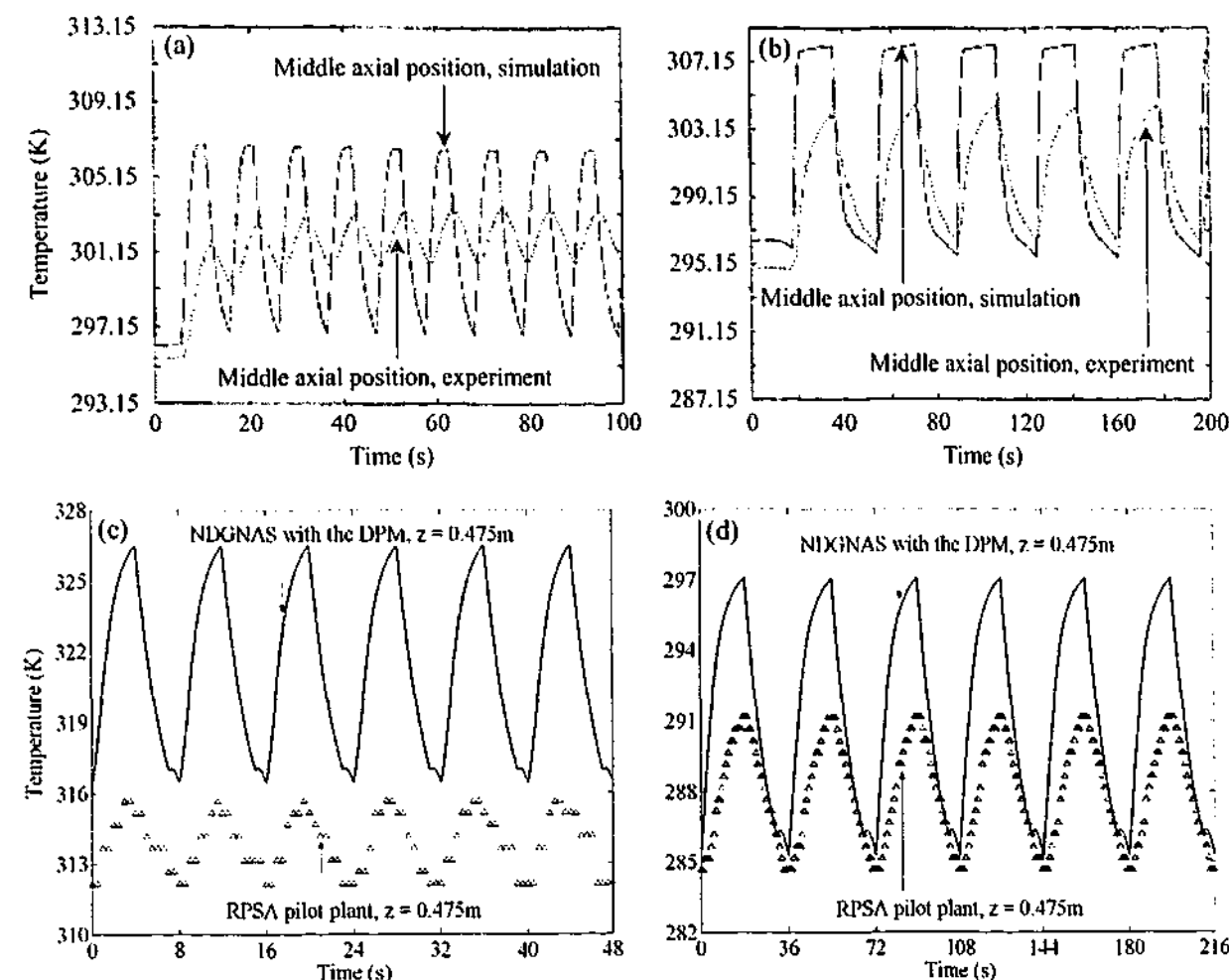


Figure 6.21: Comparing experimental versus numerical temperature profiles obtained by Teague & Edgar (1999) against those obtained in this dissertation.

- (a) Teague & Edgar (1999): $t_{\text{cycle}} = 10.4$ s, pressure window = 4.5:1.1 bar.a and purity = 70.6 mol%O₂.
 (b) Teague & Edgar (1999): $t_{\text{cycle}} = 35.6$ s, pressure window = 4.5:1.1 bar.a and purity = 88.3 mol%O₂.
 (c) RPSA run 9: $t_{\text{cycle}} = 8.0$ s, pressure window = 4.00:1.20 bar.a and purity = 80.9 mol%O₂.
 (d) RPSA run 3: $t_{\text{cycle}} = 36.0$ s, pressure window = 4.00:1.20 bar.a and purity = 89.2 mol%O₂.
 Note that (a) and (b) were reproduced from Figures 19 and 20 of Teague & Edgar (1999) respectively.

Teague & Edgar (1999) mounted K-type thermocouples at axial positions close to the inlet, outlet and middle regions of the packed bed. Figures 6.21a and 6.21b relate to data obtained at the middle axial position of the bed which is why $z = 0.475$ m was selected from data obtained in this dissertation. What is immediately obvious from Figs. 6.21a and 6.21b is the experimental transient decreases much more rapidly than the numerical transient in a similar manner to that observed in Figs. 6.21c and 6.21d. Using the data of Teague & Edgar (1999), experimental temperature swing is approximately 3 K at $t_{\text{cycle}} = 10.4$ s while at $t_{\text{cycle}} = 35.6$ s is approximately 8 K. Their numerical model predicts these same swings to be 10 and 15 K respectively. Performing these same calculations on data presented in Figs. 6.21c and 6.21d reveals experimental temperature swing is approximately 4 K and 7 K at $t_{\text{cycle}} = 8.0$ s and 36.0 s respectively, while numerically these same values are 10 K and 12 K. Across both studies temperature swing decreases by $\approx 50\%$ experimentally while the same reduction is $\approx 20\%$ numerically.

Teague & Edgar (1999) argue heat loss from the bed cannot account for these discrepancies. They go on to say "a more probable explanation (for differences between numerical and experimental temperature swing) is that there is a significant unmodeled temperature gradient within the zeolite pellets at the end of the (combined feed) pressurisation/production step". While temperature swing numerically is decreasing with cycle time as found earlier, the drastic reduction in temperature swing observed experimentally, in my opinion, can be attributed to this issue of thermocouple response within a packed bed. The fact that their model agreed well against experimental data except for temperature, as found here, again questions the method of inserting a junction exposed thermocouple directly into the sorbent bed to measure temperature when something close to a 40 s response time arises.

6.8 Concluding Remarks

A large body of work is currently available on the experimental validation of numerical adsorption simulators under PSA and VSA conditions. However, the amount of work devoted to experimental validation under RPSA conditions is not as extensive. Although some RPSA studies have considered non-isothermal and non-isobaric behaviour, none could be found that use a VF+DGM approach to intrapellet mass transfer. Using experimentally calibrated intrapellet transport and interpellet pressure drop coefficients from chapters 4 and 5, simulation data obtained with the DPM and LDFP model under non-isothermal and non-isobaric conditions have been compared to RPSA pilot plant data for oxygen enrichment at cycle times approaching the RPSA limit.

Simulation results from both the DPM and LDFP model were very similar at long cycle times, indicating the form of the intrapellet mass transfer model under typical PSA conditions is not a crucial aspect of process simulation to maintain. However, NDGNAS results at long cycle times overestimated experimental data and this was attributed to errors in the regressed equilibrium isotherm parameters using IAST. As cycle time decreased the LDFP model failed to match experimental trends in separation performance, predicting recovery and specific productivity will drop due to intrapellet mass transfer resistance at a cycle time higher than the DPM and RPSA pilot plant predicted. This observation was attributed to the assumption of equimolar counterdiffusion at the pellet level in addition to the assignment of an appropriate Ω_i value at cycle times approaching the RPSA limit.

Performing additional NDGNAS simulations at the shortest cycle times experimentally achieved using various assumptions on process operation found the ILE assumption predicted significantly higher production rates and oxygen recovery in comparison to the DPM and LDFP model, hence

intrapellet mass transfer is present at the RPSA limit. This result also indicates the LDFP model provides a conservative estimate of performance, overemphasising intrapellet mass transfer when approaching the RPSA limit. A second set of simulations reduced interpellet pressure drop to an almost insignificant level for the ILE assumption and LDFP model. Results from these simulations revealed process operation changed only slightly from the case where pressure drop was finite and this small change was attributed to the different working capacity of the sorbent bed: intrapellet mass transfer had a minimal impact on process operation between pressure drop finite and the same run where pressure drop is negligible at the RPSA limit.

Using the LDFP model with existing correlations for Ω_i [i.e. Nakao & Suzuki (1983), Alpay & Scott (1992)] do not appear suitable based on the unpredictable nature of boundary conditions that arise at the pellet surface when approaching the RPSA limit. In order for the LDFP model to correctly match experimental trends at these cycle times, Ω_i would have to increase before θ_i is 0.1. Independent pellet simulations of chapter 2 and RPSA process simulation from this chapter indicate Ω_i would need to begin increasing at a θ_i value closer to 2. To develop a new plot for Ω_i as a function of θ_i based on data of Figs. 6.6, 6.7, 6.11 and 6.12 may not be suitable, however, when a new cycle arrangement is used.

While interpellet pressure profiles obtained from the DPM and LDFP model matched experimental trends across all cycle times, small differences in pressure between the DPM and LDFP model around rapid changes in pressure was attributed to differences in the rate of mass transfer from the intra- to interpellet region and vice versa when bulk gas motion (VF+DGM) is included. Numerical temperature profiles, on the other hand, were found to overestimate experimental profiles due to the 40 s response time for junction-exposed thermocouples within a packed bed observed across chapters 4 and 5. Despite this, end of step temperature at long cycle times was in good qualitative agreement using both the DPM and LDFP model. End of step temperature at short cycle times was generally well predicted with the DPM and an axial temperature gradient close to 60 K arose. The LDFP model incorrectly predicted this same axial temperature gradient to be almost 100 K.

Results obtained from this chapter suggest intrapellet transport and interpellet pressure drop parameters that are independently characterised from EMU and LUB experiments can be used to reproduce experimental trends across the PSA and RPSA cycle times when a VF+DGM approach to intrapellet mass transfer is used. The one limitation with this approach, however, is CPU time required to achieve CSS. While the MMS alleviated some of the burden computationally, CPU

time was approximately one order of magnitude higher with the DPM when compared to the LDFP model.

6.8.1 Effective Diffusion Coefficients from the RPSA Pilot Plant

A final assessment of data obtained from the RPSA pilot plant is to estimate effective diffusion coefficients over the range of operating conditions investigated in this chapter. These are presented in Table 6.11 as a reference data set for nitrogen and oxygen in Zeochem LiLSX.

Table 6.11: Effective diffusion coefficients for nitrogen and oxygen in Zeochem LiLSX over a range of operating conditions investigated in the RPSA pilot plant.

| Temperature (K) | Pressure (bar.a) | D_m^e for N ₂ -O ₂ (m ² s ⁻¹) | D_K^e for N ₂ (m ² s ⁻¹) | D_K^e for O ₂ (m ² s ⁻¹) | $B^e p^0/10^{-5} \mu_P$ (m ² s ⁻¹) |
|-----------------|------------------|--|--|--|---|
| 290 | 1.0 | 3.27×10^{-6} | 3.22×10^{-6} | 3.02×10^{-6} | 6.43×10^{-7} |
| 290 | 5.0 | 6.55×10^{-7} | 3.22×10^{-6} | 3.02×10^{-6} | 3.22×10^{-6} |
| 320 | 1.0 | 3.90×10^{-6} | 3.39×10^{-6} | 3.17×10^{-6} | 6.43×10^{-7} |
| 320 | 5.0 | 7.79×10^{-7} | 3.39×10^{-6} | 3.17×10^{-6} | 3.22×10^{-6} |

CHAPTER 7

CONCLUSIONS AND RECOMMENDATIONS FOR FUTURE WORK

This dissertation has addressed several issues of both academic and industrial importance regarding the mathematical prediction of PSA performance for oxygen enrichment at cycle times approaching the RPSA limit. It is the intention of this chapter to briefly summarise these findings and suggest future research topics that have arisen from this study.

7.1 Conclusions

- The LDF model has been extensively used throughout the adsorption literature as a tool for quantifying mass transfer resistance under PSA conditions. However, studies over a single pellet and a full RPSA pilot plant under macropore diffusion control reveal the LDF model has several inherent limitations when predicting uptake profiles as dimensionless time θ_i falls below ≈ 1 and fails to predict RPSA performance when $\theta_i < 2$.
- LDF uptake rates significantly underestimate those predicted using the DGM when the time scale for transport into and out of a pellet is comparable to individual step times due to the assumption of equimolar counterdiffusion (i.e. $\theta_i < \approx 1$). The contribution from viscous flow to intrapellet mass transfer was found to be minimal. Another limitation with LDF models around the RPSA limit resides in the use of a time adjusted Ω coefficient due to the unpredictable nature of boundary conditions that arise at the surface of a sorbent pellet. These observations were relatively insensitive to the assumption of isothermal or non-isothermal behaviour at the pellet level.
- The simulation of a general RPSA cycle is a time consuming exercise when non-isothermal behaviour arises and a DPM is adopted, this makes CPU optimisation schemes highly desirable. Two novel schemes have been investigated using a custom developed adsorption simulator, NDCNAS, and both were found to reduce simulation time when a successive substitution approach to CSS is adopted. The first proposed CPU optimisation technique exploits computational improvements offered through the ODE integrator BzzOde while the

second utilises CSS profiles obtained from the LDF model as an improved initial guess on CSS profiles for the DPM.

- Volumetric and chromatographic uptake experiments allowed all three intrapellet transport coefficients of one particular sorbent material, Zeochem LiLSX, to be found using the VF+DGM approach to mass transfer. The volumetric device, however, was not the most suitable experimental apparatus for determination of the viscous flow transport coefficient. The magnitude of these parameters was found to be in good agreement with established literature estimates.
- The steady state Ergun equation can accurately reproduce dynamic pressure profiles obtained under non-adsorbing conditions in comparison with experimental data and the full momentum balance provided the viscous and kinetic numerical constants κ_{viscous} and κ_{kinetic} are experimentally determined.
- The Ergun equation can accurately reproduce dynamic pressure profiles obtained under adsorbing conditions using the numerical constants κ_{viscous} and κ_{kinetic} obtained from non-adsorbing experiments.
- At long cycle times, predicted separation performance between the DPM and LDFP models are in good agreement. Small differences in separation performance between NDGNAS and the RPSA pilot plant at long cycle times could be attributed to errors in the use of IAST regressed equilibrium isotherm parameters. At the RPSA limit, however, qualitative trends from the LDFP model were in disagreement with the DPM and RPSA pilot plant. The LDFP model significantly underestimated process performance due to the assumption of equimolar counterdiffusion and assignment of an appropriate Ω_i value. In contrast, the DPM correctly predicted experimental trends across all cycle times.
- Comparing NDGNAS results between the ILE assumption, DPM and LDFP model at short cycle times reveals intrapellet mass transfer is important at the RPSA limit, with the LDFP model overemphasising the importance of intrapellet mass transfer. When these same RPSA cycles were simulated under the assumption of negligible pressure drop, marginal changes in performance arose from the equivalent finite pressure drop case. Therefore interpellet pressure drop primarily changes working capacity of the sorbent bed and has minimal impact on intrapellet mass transfer in its absence. Therefore, experimental and mathematical data obtained from the nitrogen-oxygen-zeolite system imply the LDF model is inadequate

when predicting separation performance at conditions approaching but not quite exceeding the RPSA limit of $\theta_i \leq 0.1$ (i.e. θ_i closer to 1 is a more appropriate definition of RPSA for the nitrogen-oxygen-zeolite system under macropore diffusion control).

- Predicted pressure profiles obtained with the DPM and LDFP model are in good agreement across all cycle times, indicating experimental pressure profiles are not a sensitive test when comparing different intrapellet mass transfer models. The only difference that did arise, which was relatively small in comparison to the overall pressure profile, was attributed to the rate of intrapellet mass transfer when bulk gas motion is included (VF+DGM) and excluded (LDFP model) around the initial period of a pressure changing step under short cycle times.
- While numerical temperature profiles at long cycle times compare well against experimental data, at short cycle times the LDFP model significantly overestimated temperature in relation to the DPM. This was attributed to the additional accumulation of energy within the bed given a smaller volume of gas passes through the top as product. Comparing adiabatic versus non-isothermal simulation results revealed the RPSA pilot plant was operating at conditions close to adiabatic.

7.2 Recommendations for Future Work

This body of work represents the first Ph.D. project initiated within the adsorption research group at Monash University to investigate RPSA process performance in any form. Understandably, a large number of issues have arisen during this Ph.D. that warrant further consideration.

This dissertation has concentrated on macropore diffusion control in X-type zeolites for the enrichment of oxygen from air under non-isothermal conditions. Given this system is ultimately equilibrium driven, fast cycle times are required before intrapellet mass transfer at the macropore level becomes important. Consideration should therefore be given to systems where micropore diffusion control is important. The intrapellet mass transfer model of NDGNAS should be extended to include this mechanism. The EMU could still be used as the experimental apparatus by which these additional models could be investigated provided viscous flow and Knudsen diffusion are correctly accounted for.

The DPM approach to intrapellet mass transfer is very demanding computationally, even for moderate levels of discretisation pursued in this dissertation. Following Moore's Law, the advent of faster computers will make adsorption simulation using NDGNAS much more practical in the

years to come. As stated in chapter 6, however, anything short of a state-of-the-art super computer using today's computing technology significantly hampers the ability to explore the true impact of interpellet axial and intrapellet radial discretisation, N_z and N_r respectively, on the predictive ability of NDGNAS. This also limited the ability to perform a sensitivity analysis and optimisation studies using NDGNAS with the DPM. In the absence of advanced computing resources, serious consideration should be given towards improved solution techniques such as direct determination and moving finite element techniques for adsorption simulation. To the best knowledge of the author these techniques have not yet to been pursued for a non-isothermal process using the VF+DGM constitutive equation, making this a Ph.D. worthy research topic in itself.

One major limitation with adsorption simulation is accurate equilibrium isotherm data for a multicomponent system. In this dissertation pure component equilibrium data was extended to multicomponent data using IAST. Chapter 6 revealed this was a poor assumption when comparing equilibrium working selectivity for a range of lithium based X-type zeolite systems. Experimental techniques should be investigated that can provide multicomponent data for an adsorbing system to further narrow potential sources of experimental discrepancy that hamper direct comparisons between the DPM and LDFP model.

The importance of non-isothermal behaviour on RPSA simulation, according to the author, has not been adequately emphasised across the published literature. Experimental temperature profiles obtained in chapter 6 reveal isothermal behaviour is a poor assumption to make on any process model at cycle times approaching the RPSA regime. This important finding should focus research towards experimental and theoretical treatments of heat transfer coefficients, specific heat capacities, adsorbed phase thermodynamics and heats of adsorption that influence temperature profiles obtained during an adsorption based separation.

The issue of experimental temperature measurement within a packed bed of sorbent material should be readdressed. The common technique of inserting a junction-exposed thermocouple directly into the packed bed, as used throughout this study, does not appear to match numerical data across a wide range of operating conditions despite good agreement found with a majority of the other parameters experimentally measured. This was also evident when comparing experimental temperature profiles from Teague & Edgar (1999). The use of a small cage like device should be considered around the thermocouple tip to provide a small clearance between surrounding sorbent pellets. This would ensure interpellet gas temperature is actually being measured in addition to providing useful experimental data concerning the equivalence in temperature between the intra- and interpellet regions.

APPENDIX A

DERIVATION OF SIMPELL

Isothermal and non-isothermal behaviour is allowed for at the pellet level and hence both forms of the conservation equations are presented for completeness. Throughout the following analysis ideal gas behaviour is assumed such that gas phase density, $\rho_{g,i}^p$, is given by p_i^p/RT_p .

A.1 Differential form of the Conservation Equations

The conservation equations are derived using a radial coordinate system that is fixed with respect to the pellet center, $r = 0$. Hence the molar flux N_i is defined with respect to a stationary coordinate system.

A.1.1 Isothermal Conditions

The conservation of mass begins with a shell balance [Bird *et. al.* (1960)] over a differential volume within an assumed spherical pellet. The region of interest is $4\pi r^2 \Delta r$ with no assumed angular dependence on gas properties, only radial dependence from the pellet center to surface.

$$4\pi r^2 \Delta r \frac{\epsilon_p}{RT_p} \frac{\partial p_i^p}{\partial t} + 4\pi r^2 \Delta r \rho_p \frac{\partial n_i^p}{\partial t} = -[4\pi(r + \Delta r)^2 N_i - 4\pi r^2 N_i] \text{ for } i = 1 \dots N_c \quad (\text{A.1})$$

Local equilibrium is assumed within each radial volume of the pellet, allowing the adsorbed phase loading derivative to be rewritten in the following form.

$$\frac{\partial n_i^p}{\partial t} = \sum_{j=1}^{N_c} \frac{\partial n_{i,eq}^p}{\partial p_j^p} \frac{\partial p_j^p}{\partial t} \text{ for } i = 1 \dots N_c \quad (\text{A.2})$$

Dividing Eq. (A.1) through by $4\pi r^2 \Delta r$, taking the limit as $\Delta r \rightarrow 0$ and rewriting the adsorption uptake term using Eq. (A.2) gives the following.

$$\left(\frac{\varepsilon_p}{RT_p} + \hat{\rho}_p \frac{\partial n_{i,eq}^p}{\partial p_i^p} \right) \frac{\partial p_i^p}{\partial t} + \sum_{j=1, j \neq i}^{N_c} \left(\hat{\rho}_p \frac{\partial n_{i,eq}^p}{\partial p_j^p} \right) \frac{\partial p_j^p}{\partial t} = -\frac{1}{r^2} \frac{\partial}{\partial r} (r^2 N_i) \quad \text{for } i = 1 \dots N_c \quad (\text{A.3})$$

A.1.2 Non-Isothermal Conditions

Under non-isothermal conditions the temperature and partial pressure terms resulting from the expansion of the temporal derivative on gas phase density must be maintained. The partial time derivative of the equilibrium isotherm, Eq. (A.2), also needs to incorporate $\partial T_p / \partial t$.

$$\frac{\partial n_i^p}{\partial t} = \sum_{j=1}^{N_c} \frac{\partial n_{i,eq}^p}{\partial p_j^p} \frac{\partial p_j^p}{\partial t} + \frac{\partial n_{i,eq}^p}{\partial T_p} \frac{\partial T_p}{\partial t} \quad \text{for } i = 1 \dots N_c \quad (\text{A.4})$$

Applying the shell balance technique under these conditions gives the following.

$$\left(\frac{\varepsilon_p}{RT_p} + \hat{\rho}_p \frac{\partial n_{i,eq}^p}{\partial p_i^p} \right) \frac{\partial p_i^p}{\partial t} + \sum_{j=1, j \neq i}^{N_c} \left(\hat{\rho}_p \frac{\partial n_{i,eq}^p}{\partial p_j^p} \right) \frac{\partial p_j^p}{\partial t} + \left(\hat{\rho}_p \frac{\partial n_{i,eq}^p}{\partial T_p} - \frac{\varepsilon_p p_i^p}{RT_p^2} \right) \frac{\partial T_p}{\partial t} = -\frac{1}{r^2} \frac{\partial}{\partial r} (r^2 N_i) \quad \text{for } i = 1 \dots N_c \quad (\text{A.5})$$

Within the pellet there are three regions where energy can accumulate, the gas void, adsorbed and solid phases. Using the definition of internal energy and taking the limit as $\Delta r \rightarrow 0$, the conservation of energy can be written in the following general form.

$$\varepsilon_p \frac{\partial (\rho_g^p U_g^p)}{\partial t} + \hat{\rho}_p \frac{\partial \hat{U}_a^p}{\partial t} + \hat{\rho}_p \frac{\partial \hat{U}_s^p}{\partial t} = -\frac{1}{r^2} \frac{\partial}{\partial r} \left(r^2 \sum_{i=1}^{N_c} N_i H_{g,i}^p \right) - \frac{1}{r^2} \frac{\partial}{\partial r} \left(r^2 \lambda_p^c \frac{\partial T_p}{\partial r} \right) \quad (\text{A.6})$$

Coupled to the conservation of energy are the following thermodynamic correlations for each phase.

$$\rho_g^p U_g^p = \sum_{i=1}^{N_c} \rho_{g,i}^p U_{g,i}^p = \sum_{i=1}^{N_c} \rho_{g,i}^p (H_{g,i}^p - 10^5 RT_p) \quad \text{where } H_{g,i}^p = H_{g,i}^{p,ref} + \int_{T_{ref}}^T c_{g,i}^p dT \quad (\text{A.7})$$

$$\hat{U}_a^p = \sum_{i=1}^{N_c} \hat{U}_{a,i}^p = \sum_{i=1}^{N_c} \hat{H}_{a,i}^p \quad \text{where } \hat{H}_{a,i}^p = \text{function}(n_{1,eq}^p, \dots, n_{N_c,eq}^p, T_p) \quad (\text{A.8})$$

$$\hat{U}_s^p = \hat{H}_s^p \quad \text{where } \hat{H}_s^p = \hat{H}_{s,ref}^p + \int_{T_{ref}}^T \hat{c}_s dT \quad (\text{A.9})$$

The reference gas phase enthalpy, $H_{g,ref}^p$, defined through Eq. (A.7) is arbitrarily set to zero at T_{ref} . The factor 10^5 that multiplies RT_p in Eq. (A.7) is present to convert bar.a to Pascal. A third order polynomial for the temperature dependence of the gas phase specific heat capacity is used [Reid *et al.* (1987, appendix A)].

$$c_{g,i}^p = a_{0,i} + a_{1,i} T_p + a_{2,i} T_p^2 + a_{3,i} T_p^3 \quad (\text{A.10})$$

$$H_{g,i}^p = a_{0,i} (T_p - T_{ref}) + \frac{a_{1,i}}{2} (T_p^2 - T_{ref}^2) + \frac{a_{2,i}}{3} (T_p^3 - T_{ref}^3) + \frac{a_{3,i}}{4} (T_p^4 - T_{ref}^4) \quad (\text{A.11})$$

Gibb's surface excess model is used to represent adsorbed phase thermodynamics in Eq. (A.8) [Sircar (1985, 1999)]. The adsorbed phase enthalpy, $\hat{H}_{a,i}^p$, becomes a function of the N_c component equilibrium adsorbed phase loadings $n_{i,eq}^p$ and pellet temperature T_p according to this analysis. The rigorous Clausius-Clapeyron equation is used to estimate the heat of adsorption for each component.

$$q_i^p = 10^5 RT_p^2 \left(\frac{\partial \ln p_i^p}{\partial T_p} \right)_{n_{i,eq}^p, n_{j,eq}^p} = \frac{10^5 RT_p^2}{p_i^p} \left(\frac{\partial p_i^p}{\partial T_p} \right)_{n_{i,eq}^p, n_{j,eq}^p} \quad \text{for } i = 1 \dots N_c \quad (\text{A.12})$$

The solid phase heat capacity \hat{c}_s is assumed to be independent of pressure, temperature and gas/adsorbed phase composition. The reference enthalpy for the solid phase, $\hat{H}_{s,ref}^p$, is also set to zero at the reference temperature. Taking the respective time derivatives of the energy balance using Eqs. (A.7) through (A.9) gives the following.

$$\frac{\partial (\rho_g^p U_g^p)}{\partial t} = \left[\sum_{i=1}^{N_c} \frac{p_i^p}{RT_p} \left(c_{g,i}^p - \frac{H_{g,i}^p}{T_p} \right) \right] \frac{\partial T_p}{\partial t} + \left[\sum_{i=1}^{N_c} \frac{\partial p_i^p}{\partial t} \left(\frac{H_{g,i}^p}{RT_p} - 10^5 \right) \right] \quad (\text{A.13})$$

$$\frac{\partial \hat{U}_a^p}{\partial t} = \left\{ \xi + \sum_{i=1}^{N_c} \left[n_{i,eq}^p c_{g,i}^p + (H_{g,i}^p - q_i^p) \frac{\partial n_{i,eq}^p}{\partial T_p} \right] \right\} \frac{\partial T_p}{\partial t} + \sum_{i=1}^{N_c} \left[(H_{g,i}^p - q_i^p) \sum_{j=1}^{N_c} \frac{\partial n_{i,eq}^p}{\partial p_j^p} \frac{\partial p_j^p}{\partial t} \right] \quad (\text{A.14})$$

$$\frac{\partial \hat{U}_s^p}{\partial t} = \hat{c}_s \frac{\partial T_p}{\partial t} \quad (\text{A.15})$$

ξ within Eq. (A.14) involves equilibrium isotherm and surface chemical potential ($\hat{\xi}$) derivatives.

$$\xi = -T_p \left(\frac{\partial^2 \hat{\xi}}{\partial T_p^2} \right) + \sum_{i=1}^{N_c} \left[-\frac{2RT_p n_{i,eq}^p}{p_i^p} \left(\frac{\partial p_i^p}{\partial T_p} \right)_{n_{j,eq}^p} - \frac{RT_p^2 n_{i,eq}^p}{p_i^p} \left(\frac{\partial^2 p_i^p}{\partial T_p^2} \right)_{n_{j,eq}^p} \right] \quad (\text{A.16})$$

For equilibrium isotherms that possess a linear gradient the resulting analytical form of ξ reduces to zero. Each sorbent used within the analysis of this dissertation possesses linear or near-linear equilibrium isotherm gradients. This indicates ξ is small in comparison to the other terms that comprise the adsorbed phase internal energy temporal derivative, allowing ξ to be neglected. Doing so does not affect mole or energy balance closure over a single step or cycle [Wilson (2001)]. The inclusion of Eqs. (A.13) through (A.15) into Eq. (A.6) gives the complete form of the conservation of energy for the pellet in terms of partial pressure and temperature derivatives.

$$\left[\sum_{i=1}^{N_c} \frac{\varepsilon_p p_i^p}{RT_p} \left(c_{g,i}^p - \frac{H_{g,i}^p}{T_p} \right) + \sum_{i=1}^{N_c} \hat{\rho}_p n_{i,eq}^p c_{g,i}^p + \sum_{i=1}^{N_c} \hat{\rho}_p (H_{g,i}^p - q_i^p) \frac{\partial n_{i,eq}^p}{\partial T_p} + \hat{\rho}_p \hat{c}_s \right] \frac{\partial T_p}{\partial t} + \left\{ \sum_{i=1}^{N_c} \frac{\partial p_i^p}{\partial t} \left[\frac{\varepsilon_p H_{g,i}^p}{RT_p} - \varepsilon_p 10^5 + \sum_{j=1}^{N_c} \hat{\rho}_p (H_{g,j}^p - q_j^p) \frac{\partial n_{j,eq}^p}{\partial p_i^p} \right] \right\} = -\frac{1}{r^2} \frac{\partial}{\partial r} \left(r^2 \sum_{i=1}^{N_c} N_i H_{g,i}^p \right) - \frac{1}{r^2} \frac{\partial}{\partial r} \left(r^2 \lambda_p^c \frac{\partial T_p}{\partial r} \right) \quad (\text{A.17})$$

A.2 Numerical Solution of the Discretised Pellet Model

Each of the intrapellet flux equations considered in chapter 2 all require the differential form of the conservation equations from §A.1 to be solved using an appropriate discretisation scheme. The scheme adopted within this dissertation is the finite volume method. Discretisation is performed on an iso-volumetric basis [Sun & LeVan (1995)] to reduce the pellet to a series of equal volume regions, ΔV_k^p , shown schematically in Fig. A.1.

$$\Delta V_k^p = \frac{4\pi}{3} (r_{k+1/2}^3 - r_{k-1/2}^3) = \frac{4\pi}{3} \nabla_k r^3 \quad \text{for } k = 1 \dots N_r \quad (\text{A.18})$$

Introduction of the ∇_k operator has been used to simplify the written form of a discretised PDE that requires a difference in a variable surrounding node k . This terminology greatly improves the readability of the discretised form of the conservation equations presented over the following pages and in other sections of this dissertation.

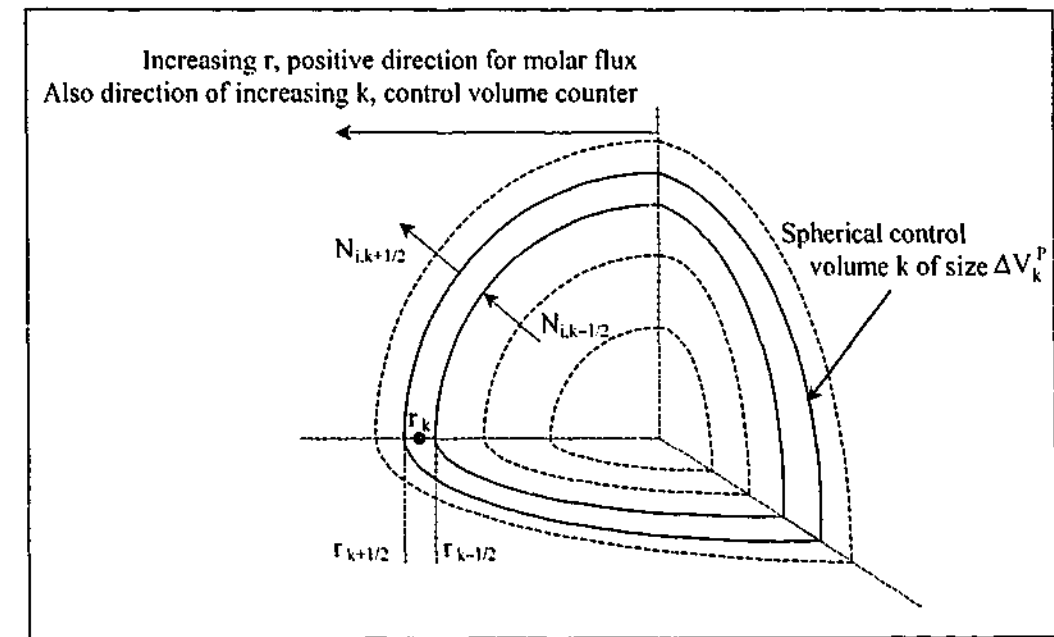


Figure A.1: Cutaway diagram of a spherical sorbent pellet showing the arrangement of control volumes. The grey shaded area represents one spherical control volume. Each node resides at the center of its corresponding control volume.

The finite volume method integrates the governing conservation equations over each spherical control volume to reduce spatial and temporal derivatives to a series of temporal ODEs coupled through the contacting boundaries at $r_{k+1/2}$ and $r_{k-1/2}$. In the following ψ represents any state variable that is differentiated with respect to time and a tilde ($\tilde{\psi}$) indicates ψ has been volume-averaged over control volume k .

$$\int_{r_{k-1/2}}^{r_{k+1/2}} \left(\frac{\partial \psi}{\partial t} \right) 4\pi r^2 dr = 4\pi \frac{d\tilde{\psi}_k}{dt} \frac{1}{3} (r_{k+1/2}^3 - r_{k-1/2}^3) \equiv \frac{d\tilde{\psi}_k}{dt} \frac{4\pi}{3} \nabla_k r^3 \quad \text{for } k = 1 \dots N_r \quad (\text{A.19})$$

The volume-averaged quantity is defined at the center of each control volume, location r_k of Fig. A.1. Integrating a molar flux term (partial radial derivative) over control volume k gives the following, where ψ represents any state variable that is differentiated with respect to radial position.

$$\int_{r_{k-1/2}}^{r_{k+1/2}} \frac{1}{r^2} \left(\frac{\partial \psi}{\partial r} \right) 4\pi r^2 dr = 4\pi (\psi_{k+1/2} - \psi_{k-1/2}) \equiv 4\pi \nabla_k \psi \quad \text{for } k = 1 \dots N_r \quad (\text{A.20})$$

A.2.1 Isothermal Conditions

Rewriting the differential form of the isothermal conservation of mass, Eq. (A.3), in terms of the finite volume method at volume k gives the following.

Intrapellet conservation of mass with the isothermal DPM

$$\left(\frac{\epsilon_p}{RT_p} + \hat{\rho}_p \frac{\partial \tilde{n}_{i,eq}^p}{\partial \tilde{p}_i^p} \right) \frac{d\tilde{p}_{i,k}^p}{dt} + \sum_{j=1, j \neq i}^{N_c} \left(\hat{\rho}_p \frac{\partial \tilde{n}_{i,eq}^p}{\partial \tilde{p}_j^p} \right) \frac{d\tilde{p}_{j,k}^p}{dt} = -\frac{3}{\nabla_k r^3} [\nabla_k (r^2 N_i)]$$

for $i = 1 \dots N_c$ and $k = 1 \dots N_r$ (A.21)

A volume-averaged temperature \tilde{T}_p for the pellet is not required here as the initial temperature is used for the entire duration of the simulation.

A.2.2 Non-Isothermal Conditions

The beginning of §2.2 justified the uniform temperature assumption across the pellet so one volume-averaged temperature, \tilde{T}_p , is used. This provides a convenient volume, the entire pellet domain, to write the discretised conservation of energy. At the pellet center, symmetry in all profiles is assumed and enthalpy and conduction fluxes reduce to zero.

Using the finite volume method requires the accumulation of energy for each phase to be summed over all N_r radial control volumes contained within the pellet. The resulting form of the conservation of energy across the pellet domain can be written in the following manner.

$$\sum_{k=1}^{N_r} \nabla_k r^3 \left[\epsilon_p \frac{d(\tilde{p}_g^p \tilde{U}_g^p)}{dt} \right]_k + \hat{\rho}_p \frac{d\tilde{U}_s^p}{dt} + \hat{\rho}_p \frac{d\tilde{U}_s^p}{dt} \Big|_k = -3R_p^2 \left(\sum_{i=1}^{N_c} N_i H_{g,i}^p \right)_{R_p} - 3R_p^2 h_{p,b} (T_p - T_b)$$

(A.22)

Inserting the equivalent finite volume form of Eqs. (A.13) through (A.15) into Eq. (A.22) allows $d\tilde{T}_p/dt$ to be factored out given one unique value exists over the pellet. The discretised conservation of mass and energy respectively are given by the following.

Intrapellet conservation of mass with the non-isothermal DPM

$$\left(\frac{\epsilon_p}{R\tilde{T}_p} + \hat{\rho}_p \frac{\partial \tilde{n}_{i,eq}^p}{\partial \tilde{p}_i^p} \right) \frac{d\tilde{p}_{i,k}^p}{dt} + \sum_{j=1, j \neq i}^{N_c} \left(\hat{\rho}_p \frac{\partial \tilde{n}_{i,eq}^p}{\partial \tilde{p}_j^p} \right) \frac{d\tilde{p}_{j,k}^p}{dt} + \left(\hat{\rho}_p \frac{\partial \tilde{n}_{i,eq}^p}{\partial \tilde{T}_p} - \frac{\epsilon_p \tilde{p}_{i,k}^p}{R\tilde{T}_p^2} \right) \frac{d\tilde{T}_p}{dt}$$

$$= -\frac{3}{\nabla_k r^3} \nabla_k (r^2 N_i) \text{ for } i = 1 \dots N_c \text{ and } k = 1 \dots N_r \quad (A.23)$$

Intrapellet conservation of energy with the DPM

$$\sum_{k=1}^{N_r} \frac{\nabla_k r^3}{R_p^3} \left\{ \sum_{i=1}^{N_c} \left[\frac{\epsilon_p \tilde{p}_{i,k}^p}{R\tilde{T}_p} \left(\tilde{c}_{g,i}^p - \frac{\tilde{H}_{g,i}^p}{\tilde{T}_p} \right) + \hat{\rho}_p \tilde{n}_{i,eq,k}^p \tilde{c}_{g,i}^p + \hat{\rho}_p (\tilde{H}_{g,i}^p - \tilde{q}_{i,k}^p) \frac{\partial \tilde{n}_{i,eq}^p}{\partial \tilde{T}_p} \right] \right\} \frac{d\tilde{T}_p}{dt}$$

$$+ \hat{\rho}_p \tilde{c}_s \frac{d\tilde{T}_p}{dt} + \sum_{k=1}^{N_r} \frac{\nabla_k r^3}{R_p^3} \left\{ \sum_{i=1}^{N_c} \left[\frac{\epsilon_p \tilde{H}_{g,i}^p}{R\tilde{T}_p} - \epsilon_p 10^5 + \sum_{j=1}^{N_c} \hat{\rho}_p (\tilde{H}_{g,j}^p - \tilde{q}_{j,k}^p) \frac{\partial \tilde{n}_{j,eq}^p}{\partial \tilde{p}_i^p} \right] \right\} \frac{d\tilde{p}_{i,k}^p}{dt}$$

$$= -\frac{3}{R_p} \left(\sum_{i=1}^{N_c} N_i H_{g,i} \right)_{R_p} - \frac{3h_{p,b}}{R_p} (\tilde{T}_p - T_b) \quad (A.24)$$

A.2.3 Finding Intrapellet Molar Flux at each Finite Volume Boundary

In order to calculate the intrapellet molar flux N_i at each control volume boundary, a set of operating conditions at these locations is required in addition to their first derivatives. At the center of the pellet, symmetry in all profiles is assumed which gives rise to the following boundary conditions.

$$\frac{\partial y_i^p}{\partial r} = \frac{\partial p_i^p}{\partial r} = 0 \text{ for } i = 1 \dots N_c \text{ and } \frac{\partial p^p}{\partial r} = 0 \text{ at } r = 0 \quad (A.25)$$

The result of Eq. (A.25) at $r = 0$ ultimately reduces N_i to zero. Numerically this implies the conditions that persist at the center of the pellet are equivalent to the conditions at the first node.

$$y_{i,1/2}^p = \tilde{y}_{i,1}^p \text{ and } p_{i,1/2}^p = \tilde{p}_{i,1}^p \text{ for } i = 1 \dots N_c \text{ and } p_{1/2}^p = \tilde{p}_1^p \quad (A.26)$$

First derivatives between $k = 2$ and $k = N_r - 1$ are evaluated using a central difference approximation between two successive nodes [Leonard (1979)].

$$\frac{\partial \psi}{\partial r} \Big|_{k+1/2} = \frac{\tilde{\psi}_{k+1} - \tilde{\psi}_k}{r_{k+1} - r_k} \text{ for } k = 2 \dots N_r - 1 \quad (A.27)$$

Here $\tilde{\psi}$ is used to represent volume-averaged variables \tilde{p}_i^p or \tilde{p}^p . To determine the conditions at each boundary to a control volume, namely $p_{k+1/2}^p$ and $y_{i,k+1/2}^p$ for $i = 1 \dots N_c$ with $k = 1 \dots N_r - 1$, an interpolation scheme that uses values from the respective node positions is required. Intrapellet pressure gradients are assumed relatively smooth during most operating cycles such that individual control volume boundary pressures can be resolved through an average of the two surrounding nodal values, $p_{k+1/2}^p = (\tilde{p}_k^p + \tilde{p}_{k+1}^p)/2$. While pressure gradients are often smooth enough to invoke an average of this form, composition gradients on the other hand may be quite sharp around a step change in pressure at the surface of the pellet. To minimise unwanted numerical oscillations around these sharp wave fronts using a minimal number of radial nodes, control volume boundary mole fraction is estimated using the quadratic upstream interpolation scheme QUICK (acronym for Quadratic Upstream Interpolation using Convective Kinematics) [Leonard (1979)] with a SMART (acronym for Sharp and Monotonic Algorithm for Realistic Transport by convection) smoothing algorithm [Gaskell & Lau (1988)].

The QUICK scheme uses one downstream and two upstream nodal values obtained from the previous time increment of the numerical integration routine to interpolate the corresponding control volume boundary quantity for the next time increment, which leads to a third order asymptotic truncation error. This requires a minimum of three radial nodes ($N_r \geq 3$) to be present within the pellet. Webley & He (2000) provide a detailed account of the QUICK scheme with SMART smoothing adopted in this simulator.

Given external film mass transfer is neglected, parameters at $r = R_p$ represent external forcing boundary conditions on the pellet. At this location the QUICK scheme with SMART smoothing is not invoked and instead a user-defined flag selects the desired boundary condition to apply.

- Mole fraction, pressure and temperature are constant over a defined period of time.
- Mole fraction, pressure and temperature vary according to a functional relationship that is exponential or trigonometric in form.
- Mole fraction, pressure and temperature vary according to pre-entered data points at specified time intervals, fitted using linear or cubic splines.

First derivatives at the surface of the pellet are evaluated using a backward difference formula between $r = R_p$ and the N_r -th node located at $r = (R_p - \Delta r/2)$.

With a set of state variables and their associated numerical derivatives at each control volume boundary, a set of N_c equations for the molar flux can be established. For 1 or 2 components the VF+DGM and DGM can be solved analytically for the molar flux. For 3 or more components the VF+DGM and DGM are solved using a matrix inversion routine given the implicit nature of the

resulting flux equations. The FFL equation can be solved explicitly for N_i^p with any number of components.

A.3 Derivation of the Linear Driving Force Model

Unlike the $N_r N_c$ set of conservation equations for the DPM, the LDF model only requires N_c ODEs to be solved across the pellet domain under isothermal conditions. When non-isothermal behaviour is assumed the number of ODEs for all pellet models increase by 1 to allow for the volume-averaged temperature derivative. Dynamic response obtained through the LDF model is now based on the magnitude of the molar flux entering and leaving the pellet at $r = R_p$. The following provides one particular derivation of the LDF model and several alternatives have been proposed within the literature (see introduction to chapter 2).

A.3.1 Isothermal Conditions

Both LDF models considered within this dissertation start by integrating the conservation of mass, Eq. (A.3), over the entire pellet domain.

$$\left[\frac{\varepsilon_p}{RT_p} + \hat{\rho}_p \frac{\partial \tilde{n}_{i,eq}^p}{\partial \tilde{p}_i^p} \right] \frac{d\tilde{p}_i^p}{dt} + \sum_{j=1, j \neq i}^{N_c} \left[\hat{\rho}_p \frac{\partial \tilde{n}_{i,eq}^p}{\partial \tilde{p}_j^p} \right] \frac{d\tilde{p}_j^p}{dt} = -\frac{3}{R_p} N_{i,R_p} \quad \text{for } i = 1 \dots N_c \quad (\text{A.28})$$

This reduces a matrix of intrapellet partial pressures for each component at each node to a vector of partial pressures at the "volume-averaged" conditions of the pellet. From this an estimate of the surface molar flux N_{i,R_p} is required. Applying the FFL flux model gives the following.

$$-\frac{3}{R_p} N_{i,R_p} = \frac{3}{R_p} \frac{D_i^*}{RT_p} \left. \frac{\partial p_i^p}{\partial r} \right|_{R_p} \quad \text{for } i = 1 \dots N_c \quad (\text{A.29})$$

Adopting the n -th order analysis of Do & Mayfield (1987) allows the intrapellet partial pressure profile to be represented by $p_i^p(r, t) = a_0(t) + a_n(t)r^n$. At the pellet surface one boundary condition is available, $p_i^p(r = R_p, t) = p_i^b$. The second boundary condition is obtained from the integral of the summation of the adsorbed phase loading and intrapellet gas using the n -th order profile between $0 \leq r \leq R_p$.

$$\text{Moles}_i = \left(\hat{\rho}_p \tilde{n}_{i,eq}^p + \frac{\varepsilon_p \tilde{p}_i^p}{RT_p} \right) \frac{4}{3} \pi R_p^3 = \int_0^{R_p} \left(\hat{\rho}_p n_{i,eq} + \frac{\varepsilon_p p_i^p}{RT_p} \right) 4\pi r^2 dr \quad \text{for } i = 1 \dots N_c \quad (\text{A.30})$$

To allow a tractable analytical solution to be obtained from the integral of Eq. (A.30), a linear uncoupled isotherm is assumed as a first approximation to the equilibrium equation. After several algebraic manipulations the following is obtained.

$$-\frac{3}{R_p} N_{i,RP} = \frac{3(n+3)D_i^c}{RT_p R_p^2} (p_i^B - \tilde{p}_i^P) \text{ for } i = 1 \dots N_c \quad (\text{A.31})$$

Given the order of the intrapellet partial pressure profile n is not known *a priori* and continually changes during a step [Do & Mayfield (1987)], $3(n+3)$ can be assumed equivalent to Ω , the numerical constant of the LDF model. The resulting form of the conservation equation is termed the partial pressure form of the Linear Driving Force (LDFP) model.

Intrapellet conservation of mass with the isothermal LDFP model

$$\left(\frac{\epsilon_p}{RT_p} + \hat{\rho}_p \frac{\partial \tilde{n}_{i,eq}^P}{\partial \tilde{p}_i^P} \right) \frac{d\tilde{p}_i^P}{dt} + \sum_{j=1, j \neq i}^{N_c} \left(\hat{\rho}_p \frac{\partial \tilde{n}_{i,eq}^P}{\partial \tilde{p}_j^P} \right) \frac{d\tilde{p}_j^P}{dt} = \frac{\Omega_i D_i^c}{RT_p R_p^2} (p_i^B - \tilde{p}_i^P) \text{ for } i = 1 \dots N_c \quad (\text{A.32})$$

If we impose a linear uncoupled equilibrium isotherm for $n_{i,eq}^P$ and multiply Eq. (A.32) through by H_i , the surface diffusion form of the Linear Driving Force (LDFS) model is obtained.

Intrapellet conservation of mass with the isothermal LDFS model

$$\frac{d\tilde{n}_i^P}{dt} = \left[\frac{\Omega_i D_i^c}{R_p^2} \frac{1}{(\epsilon_p + \hat{\rho}_p RT_p H_i)} \right] (n_{i,eq}^B - \tilde{n}_i^P) \text{ for } i = 1 \dots N_c \quad (\text{A.33})$$

Equation (A.33) is the most common form of the LDF model in use today although it strictly applies to a linear, uncoupled equilibrium isotherm operated under isothermal conditions. Equation (A.33) is equivalent to the LDF model of Nakao & Suzuki (1983) and hence their method of finding Ω_i for a given θ_i (Fig. 2.2) is used as an option within SimPell.

A.3.2 Non-Isothermal Conditions

Arguments presented in chapter 2 indicate the LDFP model provides the only consistent treatment under non-isothermal conditions when compared to the DPM, as given by the following.

Intrapellet conservation of mass with the non-isothermal LDFP model

$$\left(\frac{\epsilon_p}{R\tilde{T}_p} + \hat{\rho}_p \frac{\partial \tilde{n}_{i,eq}^P}{\partial \tilde{p}_i^P} \right) \frac{d\tilde{p}_i^P}{dt} + \sum_{j=1, j \neq i}^{N_c} \left(\hat{\rho}_p \frac{\partial \tilde{n}_{i,eq}^P}{\partial \tilde{p}_j^P} \right) \frac{d\tilde{p}_j^P}{dt} + \left(\hat{\rho}_p \frac{\partial \tilde{n}_{i,eq}^P}{\partial \tilde{T}_p} - \frac{\epsilon_p \tilde{p}_i^P}{R\tilde{T}_p^2} \right) \frac{d\tilde{T}_p}{dt} = \frac{\Omega_i D_i^c}{R\tilde{T}_p R_p^2} (p_i^B - \tilde{p}_i^P) \text{ for } i = 1 \dots N_c \quad (\text{A.34})$$

Intrapellet conservation of energy with the LDFP model

$$\left\{ \hat{\rho}_p \tilde{c}_s + \sum_{i=1}^{N_c} \left[\frac{\epsilon_p \tilde{p}_i^P}{R\tilde{T}_p} \left(\tilde{c}_{g,i}^P - \frac{\tilde{H}_{g,i}^P}{\tilde{T}_p} \right) + \hat{\rho}_p \tilde{n}_{i,eq}^P \tilde{c}_{g,i}^P + \hat{\rho}_p (\tilde{H}_{g,i}^P - \tilde{q}_i^P) \frac{\partial \tilde{n}_{i,eq}^P}{\partial \tilde{T}_p} \right] \right\} \frac{d\tilde{T}_p}{dt} + \left\{ \sum_{i=1}^{N_c} \left[\frac{\epsilon_p \tilde{H}_{g,i}^P}{R\tilde{T}_p} - \epsilon_p 10^5 + \sum_{j=1}^{N_c} \hat{\rho}_p (\tilde{H}_{g,j}^P - \tilde{q}_j^P) \frac{\partial \tilde{n}_{j,eq}^P}{\partial \tilde{p}_i^P} \right] \frac{d\tilde{p}_i^P}{dt} \right\} = \sum_{i=1}^{N_c} \left[\frac{\Omega_i D_i^c}{R\tilde{T}_p R_p^2} (p_i^B - \tilde{p}_i^P) H_{g,i,RP}^P \right] - \frac{3h_{p,B}}{R_p} (\tilde{T}_p - T_B) \quad (\text{A.35})$$

The reason for neglecting the LDFS model under non-isothermal conditions resides in the manner by which the LDF equations are solved. The LDFP model, in its most general form correctly handles each of the three intrapellet phases under non-isothermal conditions that allows a direct comparison with the DPM to be made. The same cannot be said, however, for the LDFS model that introduces the additional assumption of a linear equilibrium isotherm. This means the traditional form of the LDFS model $\partial n_i^P / \partial t = k_i (n_{i,eq}^B - n_i^P)$ no longer holds given the temperature derivative is now locked up in the conservation of mass and vice versa for the volume-averaged adsorbed phase loading. Virtually all LDF models proposed in the literature under non-isothermal conditions use this form, indicating those pellet models are not consistent with the underlying assumptions imposed on the governing conservation equations. Given mass and energy balance closure is essential to define CSS within NDGNAS when the LDFP model is activated, a conservative set of intrapellet PDEs is essential.

A.4 Definition of Cyclic Steady State Applied within SimPell

At the end of each cycle SimPell performs a check to see whether CSS has been reached. The definition of CSS adopted for the pellet is presented in Table A.1, equivalent to the CSS check performed on the adsorption simulator MINSA [Todd *et al.* (2001)].

Table A.1: Parameters that define CSS within SimPell.

| Physical Meaning | Notation | Calculation |
|--|----------------|--|
| Maximum difference in state vector X between cycle k and k - 1. Variables within X include intrapellet partial pressure for component 1 ... N_c and temperature. | $E_{j,max}^P$ | $\max \left[\text{abs} \left(X_{j,k} - X_{j,k-1} \right) \right]$ obtained over the radial domain of pellet. $j = 1 \dots (N_c + 1)$. |
| The root mean square error between cycles k and k - 1 for each variable contained within the state vector X described above. | $E_{j,rms}^P$ | $\sqrt{\frac{\sum_{i=1}^{N_c} \left(X_{i,j,k} - X_{i,j,k-1} \right)^2}{N_r}}$ |
| Relative accumulation of moles for component i over the pellet ($r = R_p$) over one cycle. | $E_{i,mole}^P$ | (Total moles i into and out of the pellet) / (Total moles i entering the pellet) |
| Relative accumulation of energy over the adsorbent pellet ($r = R_p$) over one cycle. | E_{energy}^P | (Total enthalpy into and out of the pellet) / (Total enthalpy entering the pellet) |
| Average gradient of the accumulation of energy between cycles k and k - 5. | E_{grad}^P | $\frac{E_{energy,k}^P - E_{energy,k-5}^P}{5}$ |

The parameters $E_{j,max}^P$ and $E_{j,rms}^P$ check for reproducibility in the end of step pellet temperature and partial pressure profiles between two successive cycles. When both of these " $N_c + 1$ " terms are all below a predefined tolerance this part of the CSS check is complete. Given the pellet is assumed to be at local equilibrium within each control volume, CSS profiles satisfying partial pressure and temperature convergence will automatically satisfy adsorbed phase loading. Hence the loading for each component is not included as one of the profiles to satisfy CSS.

To ensure a correct CSS condition is met, tight tolerances are often required on the end of step profiles. For this reason the terms $E_{i,mole}^P$ and E_{energy}^P are included to ensure the accumulation of mass and energy over the pellet has closed to predefined tolerances. For the pellet models initiated in chapter 2 the FFL was the only one used to determine CSS. When the FFL has reached CSS according to the criteria of Table A.1, SimPell assumes all flux models activated during the simulation are at CSS. The assumption required to derive the FFL from the DGM is equimolar

counterdiffusion and the assumption required to derive the DGM from the VF+DGM is negligible permeability of the porous matrix. Both of these assumptions reduce the magnitude of the molar flux at the pellet surface. The smaller the flux entering and leaving the pellet, the longer it takes to wash out initial conditions and hence approach CSS. This means the DGM and VF+DGM will converge to CSS faster than FFL and hence CSS based on closure of the VF+DGM or DGM may prematurely stop the FFL before it has reached CSS. Testing this observation for select cases of chapter 2 with each of the three discretised pellet models found the FFL was the pellet model that consistently required the most cycles to reach CSS.

Although a CSS check on every pellet model could be initiated, a significant amount of computer memory must be allocated to store all profiles from each step in order to compare current and previous cycle profiles, particularly in cases where $N_r = 30$. From arguments presented in the previous paragraph this is unnecessary and hence a reduction in computational overheads can be afforded by concentrating on the limiting pellet model for CSS closure. Given both LDF models volume average conditions over the pellet, these are not considered useful in determining CSS in relation to the discretised pellet models. Hence the LDFS/LDFP models assume CSS once the FFL model has converged to CSS. While this result is not as obvious as the DGM and VF+DGM to justify, negligible changes to the adsorbed phase loading over a cycle at CSS were observed with the LDFS/LDFP models once the FFL reached CSS for various cases examined in chapter 2.

APPENDIX B

DERIVATION OF NDGNAS

The adsorption process simulator NDGNAS discussed in this dissertation considers three different forms on the conservation of energy. The first allows intra- and interpellet temperatures to differ so that $T_B \neq T_P$. The second assumes intra- and interpellet temperatures are equivalent, $T_B = T_P$, while the third option deactivates the conservation of energy altogether (i.e. isothermal behaviour). For the isothermal and " $T_B = T_P$ " options, no distinction will be made between interpellet (T_B) and intrapellet (T_P) temperatures so a generic temperature (T) will be used.

In addition, two different mass transfer models can be activated for the uptake of species i from the inter- to intrapellet region with any one of these three options activated for the conservation of energy. The first uses a DPM while the second instigates a linear driving force approximation based on the LDFP assumption. For this reason the conservation equations are discussed using both formulations. Note, however, that the LDFP model is not used in this dissertation with $T_B \neq T_P$ so this particular option will not be discussed. Within appendix A the molar flux was defined as positive when gas flows from the center ($r = 0$) to the surface ($r = R_p$) of the pellet (i.e. positive when gas flows out of the pellet, Fig. A.1). This terminology carries over in the following discussion.

For the derivation of each conservation equation in this discussion, the shell balance technique of Bird *et al.* (1960) has been applied to a cylindrical volume of cross sectional area $A_{bed} (= \pi d_{bed}^2 / 4)$ between z and $z + \Delta z$. In accordance with appendix A, ideal gas behaviour is assumed such that $\rho_{g,i}^B = p_i^B / RT_B$. It is further assumed no interpellet radial profiles form across the constant cross sectional area of the column. Further to this, interpellet conservation equations only shall be presented here. The corresponding intrapellet conservation equations introduced in appendix A are identical in form to those required here and so are not repeated for brevity.

B.1 Isothermal Conditions

B.1.1 Conservation Equation with the DPM

Derivation of the conservation equations based on the isothermal assumption simplifies the analysis significantly given all temporal and spatial temperature gradients are zero. The conservation of mass across a small cylindrical element of the sorbent bed is given by the following.

$$\frac{A_{bed} \Delta z}{RT} \frac{\partial p_i^B}{\partial t} = - \left[\left(\frac{A_{bed} p_i^B v_B}{RT} \right)_{z+\Delta z} - \left(\frac{A_{bed} p_i^B v_B}{RT} \right)_z \right] + \frac{3A_{bed} \Delta z}{R_p} \left(\frac{1-\epsilon_B}{\epsilon_B} \right) N_{i,R,P}$$

for $i = 1 \dots N_c$ (B.1)

The mechanism of axial dispersion within the interpellet region is neglected based on the magnitude of the axial Peclet number (§1.2.1). The flux term at the pellet surface $N_{i,R,P}$ is not given by a simple analytical expression and hence is left unchanged within the interpellet conservation equation. This term is found through numerical solution of the governing intrapellet flux model discussed in appendix A. Dividing Eq. (B.1) through by $A_{bed} \Delta z$ and taking the limit as $\Delta z \rightarrow 0$ gives the differential form of the conservation of mass for the DPM.

$$\frac{1}{RT} \frac{\partial p_i^B}{\partial t} = - \frac{\partial}{\partial z} \left(\frac{p_i^B v_B}{RT} \right) + \left(\frac{1-\epsilon_B}{\epsilon_B} \right) \frac{3}{R_p} N_{i,R,P} \quad \text{for } i = 1 \dots N_c \quad (B.2)$$

B.1.2 Conservation Equation with the LDFP Model

The form of the conservation of mass with the LDFP model is identical to that of the DPM except here the surface flux $N_{i,R,P}$ is given by an analytical expression derived in appendix A. Inserting Eq. (A.31) into Eq. (B.2) gives the LDFP form of the interpellet conservation of mass.

$$\frac{1}{RT} \frac{\partial p_i^B}{\partial t} = - \frac{\partial}{\partial z} \left(\frac{p_i^B v_B}{RT} \right) - \left(\frac{1-\epsilon_B}{\epsilon_B} \right) \frac{\Omega_i D_i^c}{RTR_p^2} (p_i^B - \tilde{p}_i^P) \quad \text{for } i = 1 \dots N_c \quad (B.3)$$

B.2 Non-Isothermal Conditions

B.2.1 Intra- and Interpellet Temperatures Differ: $T_B \neq T_P$

Under these conditions Eq. (B.2) is now supplemented by $\partial T_B / \partial t$ that arises when expanding the temporal derivative on gas phase density.

$$\frac{1}{RT_B} \frac{\partial p_i^B}{\partial t} - \frac{p_i^B}{RT_B^2} \frac{\partial T_B}{\partial t} = - \frac{\partial}{\partial z} \left(\frac{p_i^B v_B}{RT_B} \right) + \left(\frac{1-\epsilon_B}{\epsilon_B} \right) \frac{3}{R_p} N_{i,R,P} \quad \text{for } i = 1 \dots N_c \quad (B.4)$$

The corresponding equation for the conservation of energy includes convection through the interpellet region, energy transfer to/from the column wall and heat transfer to/from sorbent pellets. There are two components of energy transferred between the intra- and interpellet regions to consider when using the DPM, the first is attributed to the enthalpy of gas that is convected through the surface layer of the pellet and the second is attributed to external film heat transfer.

$$\frac{\partial (\rho_g^B U_g^B)}{\partial t} = - \frac{\partial}{\partial z} \left[\sum_{i=1}^{N_c} \left(\frac{p_i^B v_B}{RT_B} H_{g,i}^B \right) \right] - \frac{4h_{B,W}}{d_B \epsilon_B} (T_B - T_W) + \frac{(1-\epsilon_B)}{\epsilon_B} \frac{3}{R_p} \left[\sum_{i=1}^{N_c} (N_{i,R,P} H_{g,i}^P) + h_{P,B} (T_P - T_B) \right] \quad (B.5)$$

Making use of Eq. (A.13), Eq. (B.5) can be rewritten in terms of partial pressure and temperature derivatives as follows.

$$\left[\sum_{i=1}^{N_c} \frac{p_i^B}{RT_B} \left(c_{g,i}^B - \frac{H_{g,i}^B}{T_B} \right) \right] \frac{\partial T_B}{\partial t} + \left[\sum_{i=1}^{N_c} \frac{\partial p_i^B}{\partial t} \left(\frac{H_{g,i}^B}{RT_B} - 10^5 \right) \right] = - \frac{\partial}{\partial z} \left[\sum_{i=1}^{N_c} \left(\frac{p_i^B v_B}{RT_B} H_{g,i}^B \right) \right] - \frac{4h_{B,W}}{d_B \epsilon_B} (T_B - T_W) + \frac{(1-\epsilon_B)}{\epsilon_B} \frac{3}{R_p} \left[\sum_{i=1}^{N_c} (N_{i,R,P} H_{g,i}^P) + h_{P,B} (T_P - T_B) \right] \quad (B.6)$$

Note the term $\sum_{i=1}^{N_c} 10^5 (\partial p_i^B / \partial t)$ present within Eq. (B.6) is associated with heat generation due to compression and cooling due to expansion that occurs when the gas phase increases or decreases in pressure respectively [LaCava & Krishnan (1998)].

B.2.2 Intra- and Interpellet Temperatures are Equivalent: $T_b = T_p = T$

The control volume for the conservation of energy now includes the intrapellet region in addition to the interpellet region. Hence intrapellet gas, adsorbed and solid phases along with interpellet gas all need to be combined into the one conservation equation for energy.

Conservation Equations with the DPM

The conservation of mass is identical to that of Eq. (B.4) except here a T replaces T_b .

$$\frac{1}{RT} \frac{\partial p_i^b}{\partial t} - \frac{p_i^b}{RT^2} \frac{\partial T}{\partial t} = -\frac{\partial}{\partial z} \left(\frac{p_i^b v_B}{RT} \right) + \left(\frac{1-\epsilon_B}{\epsilon_B} \right) \frac{3}{R_p} N_{i,R_p} \quad \text{for } i = 1 \dots N_c \quad (\text{B.7})$$

To derive one combined PDE for the conservation of energy requires Eq. (A.6) at the intrapellet level to be integrated between $0 \leq r \leq R_p$, multiplied by $-3(1-\epsilon_B)/\epsilon_B R_p^2$ and then substituted into the right hand side of Eq. (B.5) in place of the terms that represent intra- to interpellet energy transfer. Performing these operations give rise to the following form of the conservation of energy in its most fundamental form.

$$\begin{aligned} & \frac{\partial(\rho_g^b U_g^b)}{\partial t} + \frac{3(1-\epsilon_B)}{\epsilon_B} \left\{ \int_0^{R_p} \left[\epsilon_p \frac{\partial(\rho_g^p U_g^p)}{\partial t} + \hat{\rho}_p \frac{\partial \hat{U}_{a,i}^p}{\partial t} + \hat{\rho}_p \frac{\partial \hat{U}_s^p}{\partial t} \right] r^2 dr \right\} \\ & = -\frac{\partial}{\partial z} \left[\sum_{i=1}^{N_c} \left(\frac{p_i^b v_B}{RT} H_{g,i}^b \right) \right] - \frac{4h_{b,w}}{d_B \epsilon_B} (T - T_w) \end{aligned} \quad (\text{B.8})$$

Analytical expressions for the integrated differential on each intrapellet internal energy term is not possible so Eq. (B.8) represents the most general form of the combined intra- and interpellet conservation of energy. The discretisation scheme applied within the pellet (see §A.2 of appendix A) allows Eq. (B.8) to be simplified to a form suitable for numerical implementation.

Conservation Equations with the LDFP Model

Incorporating $\partial T/\partial t$ into Eq. (B.3) gives rise to the conservation of mass under non-isothermal conditions for the LDFP model.

$$\frac{1}{RT} \frac{\partial p_i^b}{\partial t} - \frac{p_i^b}{RT^2} \frac{\partial T}{\partial t} = -\frac{\partial}{\partial z} \left(\frac{p_i^b v_B}{RT} \right) - \left(\frac{1-\epsilon_B}{\epsilon_B} \right) \frac{\Omega_i D_i^c}{RTR_p^2} (p_i^b - \tilde{p}_i^p) \quad \text{for } i = 1 \dots N_c \quad (\text{B.9})$$

The conservation of energy for the LDFP model in its most general form is identical to that given by Eq. (B.8) and so is not repeated for brevity. The numerical implementation of Eq. (B.8), however, will be slightly different between the DPM and LDFP model given the two different treatments of intrapellet radial discretisation.

B.3 Numerical Solution of the Conservation Equations

Solution of the conservation equations is performed numerically using the finite volume method. In appendix A the finite volume method was applied to a spherical control volume within a sorbent pellet to solve the resulting conservation equations. Here a similar procedure is adopted but now cylindrical geometry for each control volume is imposed. The resulting discretisation scheme and associated mechanisms of heat and mass transfer at the boundary of this control volume for cylindrical geometry is shown in Fig. B.1.

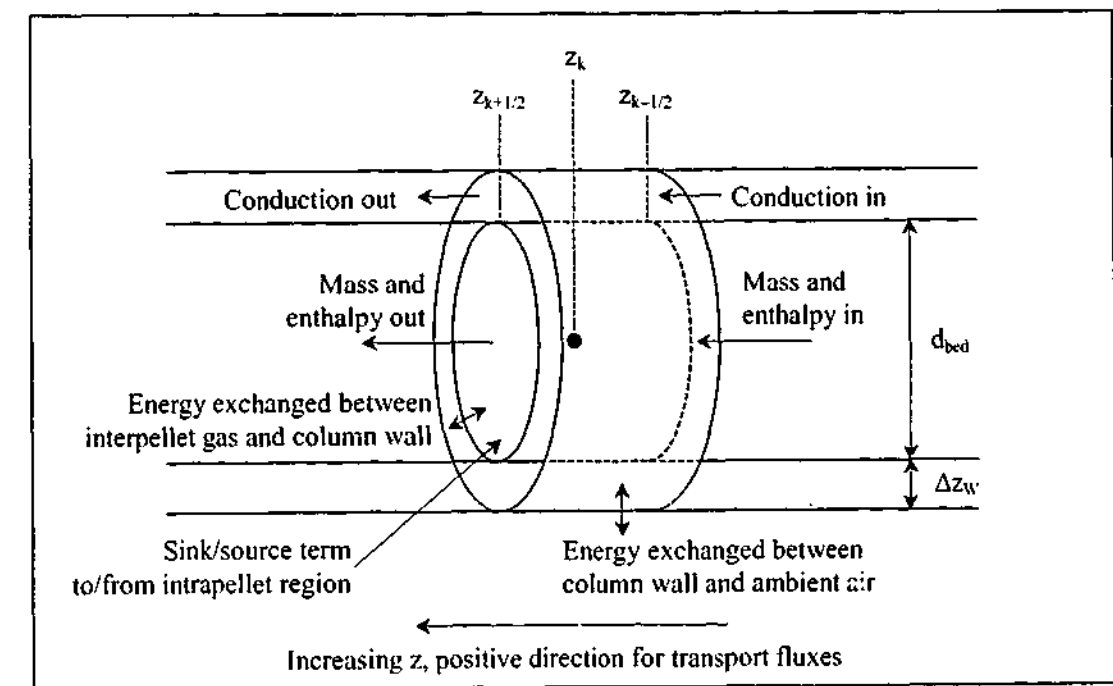


Figure B.1: Diagram of a single control volume within the sorbent bed detailing the mechanisms that dictate heat and mass transfer. This diagram includes mechanisms associated with the wall model.

The interpellet control volume ΔV_k^{bed} has the following size.

$$\Delta V_k^{\text{bed}} = A_{\text{bed}}(z_{k+1/2} - z_{k-1/2}) \equiv A_{\text{bed}} \nabla_k z \text{ for } k = 1 \dots N_z \quad (\text{B.10})$$

As for the DPM, the discretised interpellet conservation equations also apply to nodal points located at the center of each control volume. The ∇_k operator is used to simplify the written form of a discretised equation when a difference in two control volume boundaries surrounding the corresponding node is required (introduced in appendix A). Volume discretisation is not necessarily performed on an iso-volumetric basis across the bed domain. Around the inlet and outlet regions a reduced control volume size can be used as optional user input within NDGNAS. This ensures adequate control volume spacing to capture spatial profiles that determine mole and enthalpy flows into and out of the bed [Webley & He (2000)].

Integrating a partial time derivative within a cylindrical control volume produces the equivalent volume-averaged ODE. In the following equation ψ represents any variable differentiated with respect to time and a tilde (\sim) indicates ψ has been volume averaged over control volume k .

$$\int_{z_{k-1/2}}^{z_{k+1/2}} \left(\frac{\partial \psi}{\partial t} \right) dz = \frac{d\tilde{\psi}_k}{dt} (z_{k+1/2} - z_{k-1/2}) \equiv \frac{d\tilde{\psi}_k}{dt} \nabla_k z \text{ for } k = 1 \dots N_z \quad (\text{B.11})$$

Integrating a flux term (partial z derivative) over the same control volume produces the following.

Here ψ represents any variable differentiated with respect to axial position.

$$\int_{z_{k-1/2}}^{z_{k+1/2}} \left(\frac{\partial \psi}{\partial z} \right) dz = \psi_{k+1/2} - \psi_{k-1/2} \equiv \nabla_k \psi \text{ for } k = 1 \dots N_z \quad (\text{B.12})$$

With the finite volume method, quantities located at each nodal position are found using interpolated values at the neighbouring control volume boundaries. In order to determine these control volume boundary values for mole fraction and temperature, the QUICK scheme with SMART smoothing introduced in appendix A is applied, while node averaging is applied to total pressure as discussed in appendix A also.

B.3.1 Isothermal Conditions

Applying the finite volume method (i.e. Eqs. (B.11) and (B.12)) to Eq. (B.2) for the DPM gives the following.

$$\text{Interpellet conservation of mass with the isothermal DPM}$$

$$\frac{1}{RT} \frac{d\tilde{p}_{i,k}^B}{dt} = -\frac{1}{\nabla_k z} \left[\nabla_k \left(\frac{p_i^B v_B}{RT} \right) \right] + \left(\frac{1-\epsilon_B}{\epsilon_B} \right) \frac{3}{R_p} N_{i,R,p,k} \text{ for } i = 1 \dots N_c \text{ and } k = 1 \dots N_z \quad (\text{B.13})$$

The equivalent form of the conservation equation when applied to the LDFP model, Eq. (B.3), is as follows.

$$\text{Interpellet conservation of mass with the isothermal LDFP model}$$

$$\frac{1}{RT} \frac{d\tilde{p}_{i,k}^B}{dt} = -\frac{1}{\nabla_k z} \left[\nabla_k \left(\frac{p_i^B v_B}{RT} \right) \right] - \left(\frac{1-\epsilon_B}{\epsilon_B} \right) \frac{\Omega_i D_{i,k}^s}{RTR_p^2} (\tilde{p}_{i,k}^B - \tilde{p}_{i,k}^P)$$

for $i = 1 \dots N_c$ and $k = 1 \dots N_z$ (B.14)

B.3.2 Non-Isothermal Conditions and $T_B \neq T_P$

Applying Eqs. (B.11) and (B.12) to Eqs. (B.4) and (B.6) gives the following.

$$\text{Interpellet conservation of mass with the non-isothermal DPM}$$

$$\frac{1}{RT_{B,k}} \frac{d\tilde{p}_{i,k}^B}{dt} - \frac{\tilde{p}_{i,k}^B}{RT_{B,k}^2} \frac{dT_{B,k}}{dt} = -\frac{1}{\nabla_k z} \left[\nabla_k \left(\frac{p_i^B v_B}{RT_B} \right) \right] + \frac{3}{R_p} \left(\frac{1-\epsilon_B}{\epsilon_B} \right) N_{i,R,p,k}$$

for $i = 1 \dots N_c$ and $k = 1 \dots N_z$ (B.15)

$$\text{Interpellet conservation of energy with the DPM}$$

$$\left[\sum_{i=1}^{N_c} \frac{\tilde{p}_{i,k}^B}{RT_{B,k}} \left(\tilde{c}_{g,i,k}^B - \frac{\tilde{H}_{g,i,k}^B}{T_{B,k}} \right) \right] \frac{dT_{B,k}}{dt} + \left[\sum_{i=1}^{N_c} \frac{d\tilde{p}_{i,k}^B}{dt} \left(\frac{\tilde{H}_{g,i,k}^B}{RT_{B,k}} - 10^5 \right) \right] = -\frac{1}{\nabla_k z} \left[\sum_{i=1}^{N_c} \nabla_k \left(\frac{p_i^B v_B}{RT_B} H_{g,i}^B \right) \right]$$

$$- \frac{4h_{B,w,k}}{d_B \epsilon_B} (\tilde{T}_{B,k} - \tilde{T}_{w,k}) + \frac{(1-\epsilon_B)}{\epsilon_B} \frac{3}{R_p} \left[\sum_{i=1}^{N_c} (N_{i,R,p,k} \tilde{H}_{g,i,k}^P) + h_{P,B,k} (\tilde{T}_{P,k} - \tilde{T}_{B,k}) \right]$$

$k = 1 \dots N_z$ (B.16)

B.3.3 Non-Isothermal Conditions and $T_B = T_P = T$

Applying Eqs. (B.11) and (B.12) to Eqs. (B.7) and (B.8) using the DPM formulation gives the following.

Interpellet conservation of mass with the non-isothermal DPM

$$\frac{1}{R\tilde{T}_k} \frac{d\tilde{p}_{i,k}^B}{dt} - \frac{\tilde{p}_{i,k}^B}{R\tilde{T}_k^2} \frac{d\tilde{T}_k}{dt} = -\frac{1}{V_{k,z}} \left[\nabla_k \left(\frac{p_i^B v_B}{RT} \right) \right] + \frac{3}{R_p} \left(\frac{1-\epsilon_B}{\epsilon_B} \right) N_{i,R,p,k}$$

for $i = 1 \dots N_c$ and $k = 1 \dots N_z$ (B.17)

Conservation of energy with the DPM

$$\left\{ \sum_{m=1}^{N_c} \frac{\nabla_m r^3}{R_p^3} \left(\frac{1-\epsilon_B}{\epsilon_B} \right) \left[\sum_{i=1}^{N_c} \left(\frac{\epsilon_p \tilde{p}_{i,m}^P}{R\tilde{T}_k} \left(\tilde{c}_{g,i,k}^P - \frac{\tilde{H}_{g,i,k}^P}{\tilde{T}_k} \right) + \hat{\rho}_P \tilde{n}_{i,eq,m}^P \tilde{c}_{g,i,k}^P \right. \right. \right. \\ \left. \left. \left. + \hat{\rho}_P \left(\tilde{H}_{g,i,k}^P - \tilde{q}_{i,m}^P \right) \frac{\partial \tilde{n}_{i,eq}^P}{\partial \tilde{T}_k} \right] \right] \right\} + \hat{\rho}_P \left(\frac{1-\epsilon_B}{\epsilon_B} \right) \tilde{c}_s + \sum_{i=1}^{N_c} \frac{\tilde{p}_{i,k}^B}{R\tilde{T}_k} \left(\tilde{c}_{g,i,k}^B - \frac{\tilde{H}_{g,i,k}^B}{\tilde{T}_k} \right) \left\} \frac{d\tilde{T}_k}{dt} \right. \\ \left. + \sum_{m=1}^{N_c} \frac{\nabla_m r^3}{R_p^3} \left(\frac{1-\epsilon_B}{\epsilon_B} \right) \left\{ \sum_{i=1}^{N_c} \left[\frac{\epsilon_p \tilde{H}_{g,i,k}^P}{R\tilde{T}_k} - \epsilon_p 10^5 + \sum_{j=1}^{N_c} \hat{\rho}_P \left(\tilde{H}_{g,i,k}^P - \tilde{q}_{j,m}^P \right) \frac{\partial \tilde{n}_{j,eq}^P}{\partial \tilde{p}_i^P} \right] \frac{d\tilde{p}_{i,m}^P}{dt} \right\} \right. \\ \left. + \sum_{i=1}^{N_c} \left(\frac{\tilde{H}_{g,i,k}^B}{R\tilde{T}_k} - 10^5 \right) \frac{d\tilde{p}_{i,k}^B}{dt} = -\frac{1}{\nabla_{k,z}} \left[\sum_{i=1}^{N_c} \nabla_k \left(\frac{p_i^B v_B}{RT} H_{g,i}^B \right) \right] - \frac{4h_{B,W,k}}{d_{col} \epsilon_B} (\tilde{T}_k - \tilde{T}_{w,k})$$

$k = 1 \dots N_z$ (B.18)

Adopting the same procedure on the corresponding LDFP model conservation equations gives a slightly different form to the conservation of energy. With the LDFP model, no radial discretisation at the intrapellet level arises for terms that represent intrapellet accumulation of energy.

Interpellet conservation of mass with the non-isothermal LDFP model

$$\frac{1}{R\tilde{T}_k} \frac{d\tilde{p}_{i,k}^B}{dt} - \frac{\tilde{p}_{i,k}^B}{R\tilde{T}_k^2} \frac{d\tilde{T}_k}{dt} = -\frac{1}{\nabla_{k,z}} \left[\nabla_k \left(\frac{p_i^B v_B}{RT} \right) \right] - \left(\frac{1-\epsilon_B}{\epsilon_B} \right) \frac{\Omega_i D_{i,k}^c}{R\tilde{T}_k R_p^2} (\tilde{p}_{i,k}^B - \tilde{p}_{i,k}^P)$$

for $i = 1 \dots N_c$ and $k = 1 \dots N_z$ (B.19)

Conservation of energy with the LDFP model

$$\left\{ \hat{\rho}_P \left(\frac{1-\epsilon_B}{\epsilon_B} \right) \tilde{c}_s + \sum_{i=1}^{N_c} \left[\frac{\tilde{p}_{i,k}^B}{R\tilde{T}_k} \left(\tilde{c}_{g,i,k}^P - \frac{\tilde{H}_{g,i,k}^P}{\tilde{T}_k} \right) + \frac{\epsilon_p \tilde{p}_{i,k}^P}{R\tilde{T}_k} \left(\frac{1-\epsilon_B}{\epsilon_B} \right) \left(\tilde{c}_{g,i,k}^P - \frac{\tilde{H}_{g,i,k}^P}{\tilde{T}_k} \right) \right. \right. \\ \left. \left. + \hat{\rho}_P \left(\frac{1-\epsilon_B}{\epsilon_B} \right) \tilde{n}_{i,eq,k}^P \tilde{c}_{g,i,k}^P + \hat{\rho}_P \left(\frac{1-\epsilon_B}{\epsilon_B} \right) \left(\tilde{H}_{g,i,k}^P - \tilde{q}_{i,k}^P \right) \frac{\partial \tilde{n}_{i,eq}^P}{\partial \tilde{T}_k} \right] \right\} \frac{d\tilde{T}_k}{dt} + \sum_{i=1}^{N_c} \left[\frac{d\tilde{p}_{i,k}^B}{dt} \left(\frac{\tilde{H}_{g,i,k}^B}{R\tilde{T}_k} - 10^5 \right) \right] \\ + \sum_{i=1}^{N_c} \left[\frac{d\tilde{p}_{i,k}^P}{dt} \left(\frac{1-\epsilon_B}{\epsilon_B} \right) \left(\frac{\epsilon_p \tilde{H}_{g,i,k}^P}{R\tilde{T}_k} - \epsilon_p 10^5 + \sum_{j=1}^{N_c} \hat{\rho}_P \left(\tilde{H}_{g,i,k}^P - \tilde{q}_{j,k}^P \right) \frac{\partial \tilde{n}_{j,eq}^P}{\partial \tilde{p}_i^P} \right) \right] \\ = -\frac{1}{\nabla_{k,z}} \left[\sum_{i=1}^{N_c} \nabla_k \left(\frac{p_i^B v_B}{RT} H_{g,i}^B \right) \right] - \frac{4h_{B,W,k}}{d_{col} \epsilon_B} (\tilde{T}_k - \tilde{T}_{w,k}) \text{ for } k = 1 \dots N_z \quad (B.20)$$

Solution of the full bed and pellet model at each control volume requires an $[N_c(1 + N_c) + 1]$ matrix of intra- and interpellet ODEs to be inverted. A Gaussian elimination method is applied within NDGNAS. Despite the complete form of the conservation of energy for the DPM and LDFP being complicated in form, three very important points are worth noting about their application:

- i. Equations (B.16), (B.18) and (B.20) are in conservative form which means the energy entering and leaving the bed balances the accumulation of energy across the four phases over each step and cycle to within tolerances on the ODE integrator, irrespective of the parameters initiated with any particular simulation.
- ii. Equations (B.16), (B.18) and (B.20) both result in zero accumulation of energy over the bed at CSS to within tolerances on the ODE integrator. To imply the temperature profiles between two concurrent steps of an arbitrary PSA cycle are identical means the energy entering and leaving the bed over an entire cycle should match (to within integrator tolerances) the energy accumulated in each phase. This allows the relative accumulation of energy to serve as one check for CSS convergence.
- iii. Equations (B.16), (B.18) and (B.20) are insensitive to the magnitude of T_{ref} to within tolerances on the ODE integrator. To validate this statement, isolate terms that contain only T_{ref} within the conservation of energy. Doing so gives rise to the conservation of mass for each component multiplied by $c_{g,i} T_{ref}$. The conservation of mass is a conservative equation, so any scalar number multiplying a conservative equation is in itself insensitive to the scalar number.

The rather complex form of the conservation of energy presented for both the DPM and LDFP model resides in the constraint that the final equation satisfies these three points.

B.3.4 Additional Model Options Established within NDGNAS

The finite volume method is also applied to the conservation of energy for the column wall, Eq. (3.15), to provide a discretised wall temperature $\tilde{T}_{w,k}$ at each bed void control volume k . The corresponding finite volume form of Eq. (3.15) is given by the following.

$$\begin{aligned} &\text{Conservation of energy for the adsorption column wall} \\ &\hat{\rho}_w \hat{c}_w \frac{d\tilde{T}_{w,k}}{dt} = \frac{1}{\nabla_k z} \left[\nabla_k \left(\lambda_w \frac{\partial T_w}{\partial z} \right) \right] + \left[\frac{4d_B h_{B,W,k}}{(d_{col}^2 - d_{bed}^2)} (\tilde{T}_k^B - \tilde{T}_{w,k}) \right] \\ &\quad - \left[\frac{4d_{col} h_{W,A,k}}{(d_{col}^2 - d_{bed}^2)} (\tilde{T}_{w,k} - T_A) \right] \text{ for } k = 1 \dots N_z \end{aligned} \quad (B.21)$$

Both the product tank and upper/lower void volume models discussed in chapter 3 are based on well-mixed CSTR models that can be numerically implemented within NDGNAS as written. Hence the discussion of §3.2.6 is relatively well contained for these three options and no additional discussion is required in this appendix.

B.4 Definition of Cyclic Steady State Applied within NDGNAS

At the end of each cycle NDGNAS performs a check to see whether CSS has been reached. The definition of CSS adopted within NDGNAS is equivalent to the check performed on the bed model MINSA developed in-house at Monash University [Todd *et al.* (2001)].

The state vector X of operating parameters compared between two cycles includes the N_c component partial pressures, adsorbed phase loading and temperature profiles. At the end of a cycle where CSS has been achieved, X returns identically to its value at the start of the cycle. This condition is mathematically sufficient for determining CSS but from a practical standpoint requires very tight tolerances with correspondingly small ODE tolerances ($RelTol$ and $AbsTol < 10^{-9}$) resulting in excessive CPU time. The same result can be achieved more quickly if closure in the accumulation of mass and energy are also included as appropriate criteria (in addition to closure in X) with an ODE tolerance around 10^{-6} .

In summary Table B.1 shows the set of CSS criterion that is implemented within NDGNAS to establish automatically whether CSS has been achieved. The usual error quantities $E_{j,max}^B$ and

$E_{j,rms}^B$ are used along with closure terms for the accumulation of mass and energy over the bed, $E_{i,mole}^B$ and E_{energy}^B respectively. The last criterion, E_{grad}^B , is required to avoid picking up false zeroes with the evolution of the oscillating energy accumulation term E_{energy}^B . Thus E_{grad}^B enforces detection of CSS only when the energy balance oscillation has decayed out. It is important that NDGNAS automatically detects the presence of CSS because evaluation of additional cycles is expensive computationally.

Table B.1: Parameters that define CSS within NDGNAS.

| Physical Meaning | Notation | Calculation |
|--|----------------|---|
| Maximum difference in state vector X between cycle k and $k-1$. Variables within X include interpellet partial pressure for component 1 ... N_c , intrapellet adsorbed phase loading for component 1 ... N_c and temperature. | $E_{j,max}^B$ | $\max \left[\text{abs}(X_{j,k} - X_{j,k-1}) \right]$ obtained over the axial domain of the bed. $j = 1 \dots (2N_c + 1)$. |
| The root mean square error between cycles k and $k-1$ for each variable contained within the state vector X described above. | $E_{j,rms}^B$ | $\sqrt{\frac{\sum_{j=1}^{N_z} (X_{i,j,k} - X_{i,j,k-1})^2}{N_z}}$ |
| Relative accumulation of moles for component i over the sorbent bed over one cycle. | $E_{i,mole}^B$ | (Total moles i into and out of the bed) / (Total moles i entering the bed) |
| Relative accumulation of energy over the sorbent bed over one cycle. | E_{energy}^B | (Total enthalpy into and out of the bed) / (Total enthalpy entering the bed) |
| Average gradient of the accumulation of energy between cycles k and $k-5$. | E_{grad}^B | $\frac{E_{energy,k}^B - E_{energy,k-5}^B}{5}$ |

APPENDIX C

SIMPLIFIED RPSA ANALYSIS

To complement trends obtained from the numerical simulator NDGNAS, an alternative mathematical approach is used that performs simple mass and energy balances over a one-bed, four-step RPSA cycle. This model is not intended to provide quantitative agreement with experimental or simulation data but rather allow general trends in process performance to be found when intrapellet mass transfer and interpellet pressure drop have the same impact as a function of cycle time.

C.1 Mass Balance Over One Cycle

The particular cycle of interest for this analysis has been depicted previously in Fig. 6.1. Here, a hypothetical boundary is drawn around that entire cycle to define the system as follows.

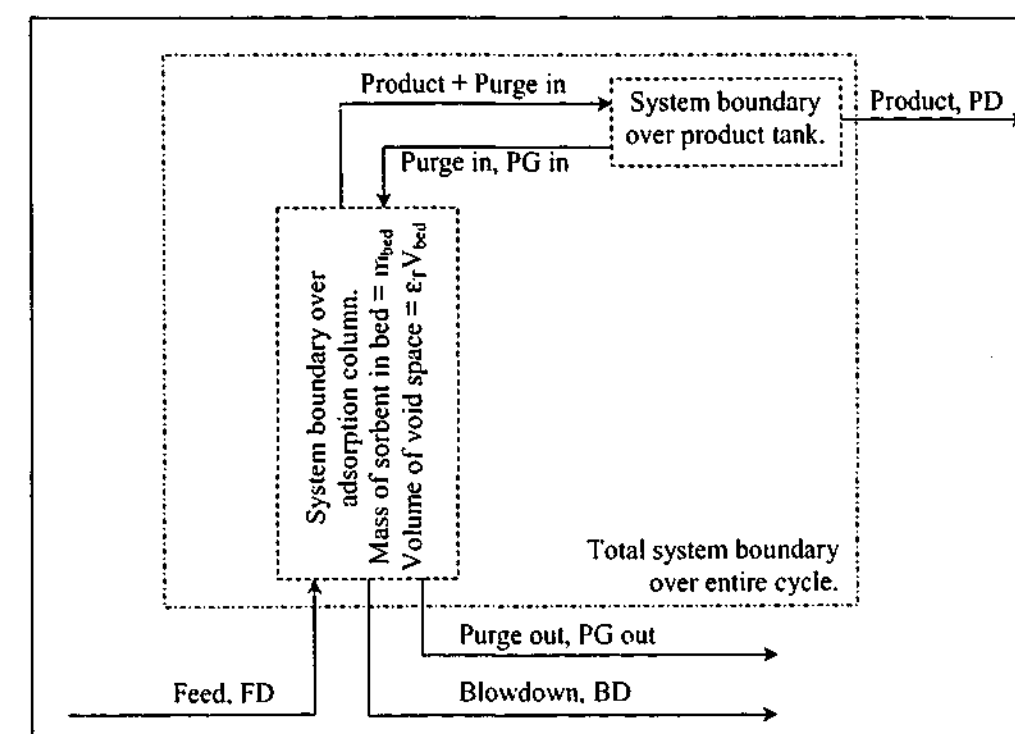


Figure C.1: System boundary and streams of interest for the simplified RPSA analysis.

A binary mixture of nitrogen and oxygen, with nitrogen the preferentially adsorbed component, is considered. $N_{PG, in}$ is composed of gas lost in the purge out stream plus the moles of gas required to partially pressurise the bed after the blowdown step. This means there is a quantity of gas equal to

the moles required to partially pressurise the sorbent bed during purge that passes between the bed and product tank without leaving the system. An analytical expression for $N_{PG\ in}$ is given by Eq. (C.13). Within the following N represents the total flow in gmols obtained over one cycle for the stream of interest. To solve this system it is stipulated that purge out is some fraction X of the feed stream passed into the bed. This allows the moles of gas recovered in the purge out stream to be written as follows.

$$N_{PG\ out} = X N_{FD} \quad (C.1)$$

To justify Eq. (C.1), the calculated ratio of $N_{PG\ out}$ to N_{FD} obtained from all eighteen experimental and simulated RPSA runs is shown in Table C.1 (see Table 6.7 for a tabular summary of $N_{PG\ out}$ and N_{FD}). One can see that a relatively consistent value is obtained from all three systems so Eq. (C.1) is a relatively good assumption for the particular cycle under consideration.

Table C.1: Experimental and numerical values of the fraction of feed lost as purge out, X .

| RPSA run | RPSA pilot plant | NDGNAS | | RPSA run | RPSA pilot plant | NDGNAS | |
|----------|------------------|--------|-------|----------|------------------|--------|-------|
| | | LDFP | DPM | | | LDFP | DPM |
| 1 | 0.134 ± 0.009 | 0.132 | 0.126 | 10 | 0.119 ± 0.007 | 0.120 | 0.118 |
| 2 | 0.132 ± 0.009 | 0.130 | 0.127 | 11 | 0.122 ± 0.007 | 0.120 | 0.117 |
| 3 | 0.153 ± 0.009 | 0.161 | 0.156 | 12 | 0.140 ± 0.007 | 0.147 | 0.143 |
| 4 | 0.155 ± 0.009 | 0.158 | 0.153 | 13 | 0.138 ± 0.007 | 0.144 | 0.139 |
| 5 | 0.150 ± 0.010 | 0.159 | 0.152 | 14 | 0.136 ± 0.008 | 0.147 | 0.139 |
| 6 | 0.147 ± 0.009 | 0.157 | 0.150 | 15 | 0.135 ± 0.008 | 0.144 | 0.136 |
| 7 | 0.169 ± 0.013 | 0.176 | 0.164 | 16 | 0.155 ± 0.009 | 0.158 | 0.147 |
| 8 | 0.166 ± 0.011 | 0.173 | 0.161 | 17 | 0.152 ± 0.009 | 0.159 | 0.147 |
| 9 | 0.195 ± 0.018 | 0.155 | 0.138 | 18 | 0.181 ± 0.016 | 0.142 | 0.125 |

Average of RPSA pilot plant X values = 0.149 ± 0.040

Average of NDGNAS LDFP X values = 0.149 ± 0.032

Average of NDGNAS DPM X values = 0.141 ± 0.028

Performing a nitrogen balance around the total system boundary of Fig. C.1 gives the following.

$$N_{N_2,FD} = N_{N_2,PD} + N_{N_2,BD} + X N_{N_2,FD} \quad (C.2)$$

The identical relation for oxygen simply replaces the subscript N_2 with O_2 in Eq. (C.2). Knowing $N_{N_2,FD} = N_{O_2,FD} (1 - y_{FD}) / y_{FD}$ and $N_{N_2,PD} = N_{O_2,PD} (1 - y_{PD}) / y_{PD}$, where y represents the mole fraction of oxygen, the following expression is obtained.

$$N_{O_2,PD} = \frac{N_{O_2,BD} \left[WS_{N_2:O_2} - \frac{(1 - y_{FD})}{y_{FD}} \right]}{\left[\frac{(1 - y_{FD})}{y_{FD}} \right] - \left[\frac{(1 - y_{PD})}{y_{PD}} \right]} \quad \text{where } WS_{N_2:O_2} = \frac{N_{N_2,BD}}{N_{O_2,BD}} \quad (C.3)$$

Equation (C.3) reveals that for any separation to occur, $WS_{N_2:O_2} > (1 - y_{FD}) / y_{FD} \approx 3.5$ for oxygen enrichment from air. Using the definition for specific productivity and recovery discussed in chapter 6, Eq. (C.3) can be used to derive the following.

$$\text{Specific productivity} = \frac{2765 N_{O_2,BD} \left[WS_{N_2:O_2} - \frac{(1 - y_{FD})}{y_{FD}} \right]}{m_{bed} t_{cycle} \left[\frac{(1 - y_{FD})}{y_{FD}} \right] - \left[\frac{(1 - y_{PD})}{y_{PD}} \right]} \quad (C.4)$$

$$\text{Recovery} = (1 - X) \frac{\left[WS_{N_2:O_2} - \frac{(1 - y_{FD})}{y_{FD}} \right]}{\left[WS_{N_2:O_2} - \frac{(1 - y_{PD})}{y_{PD}} \right]} \quad (C.5)$$

$WS_{N_2:O_2}$ is commonly termed the working selectivity and is calculated from the ratio of the moles of nitrogen to oxygen recovered during blowdown. The calculation of $N_{N_2,BD}$ and $N_{O_2,BD}$ should therefore account for the difference in adsorbed phase loading and void space gas between the end of feed and blowdown steps. These calculations can be related to the equilibrium working capacity of nitrogen ($WC_{N_2}^{eq}$) and oxygen ($WC_{O_2}^{eq}$) assuming ILE applies.

$$WC_{N_2}^{eq} = m_{bed} (n_{N_2,eq}^{FD} - n_{N_2,eq}^{BD}) + \epsilon_T V_{bed} \left[\frac{(1 - y_{FD}) p_{FD}}{RT_{FD}^{ave}} - \frac{(1 - y_{BD}) p_{BD}}{RT_{BD}^{ave}} \right] \quad (C.6)$$

$$WC_{O_2}^{eq} = m_{bed} (n_{O_2,eq}^{FD} - n_{O_2,eq}^{BD}) + \epsilon_T V_{bed} \left[\frac{y_{FD} p_{FD}}{RT_{FD}^{ave}} - \frac{y_{BD} p_{BD}}{RT_{BD}^{ave}} \right] \quad (C.7)$$

The ILE assumption implies the bed is at one average composition (y_{FD} and y_{BD}), pressure (p_{FD} and p_{BD}) and temperature (T_{FD}^{ave} and T_{BD}^{ave}) which effectively implies 100% bed utilisation. ILE theory proposed by Knaebel & Hill (1985) can be used to determine bed composition at the end of

blowdown, y_{BD} , provided the equilibrium isotherm is linearised around these compositions. While this is a limiting assumption, it does provide a starting estimate on working capacity for these two components. The composition of y_{BD} typically obtained from such a calculation (i.e. Eq. (12) of Knaebel & Hill (1985)) yields values around 0.08 to 0.02. The ratio of $WC_{N_2}^{eq}$ to $WC_{O_2}^{eq}$ yields the equilibrium working selectivity.

$$WS_{N_2:O_2}^{eq} = \frac{WC_{N_2}^{eq}}{WC_{O_2}^{eq}} \quad (C.8)$$

Comparing Eqs. (C.3) and (C.8) shows the working capacity is equivalent to the calculated moles of each component obtained during blowdown for long cycle times where intrapellet mass transfer and interpellet pressure drop are minimal. Although equilibrium working selectivity defined through Eq. (C.8) will not match true working selectivity $WS_{N_2:O_2}$ at the RPSA limit, it does provide a useful quantity that helps to compare different equilibrium isotherms for a range of sorbent materials over a particular pressure window, $p_{FD}:p_{BD}$. This makes equilibrium working selectivity a convenient tool that explains observed differences between experimental and simulated separation performance uncovered in chapter 6.

If the impact of intrapellet mass transfer and interpellet pressure drop remains unchanged within Eqs. (C.4) and (C.5) as cycle time decreases, then trends in specific productivity and recovery should follow the relations set out below.

$$\text{Specific productivity} \propto \frac{1}{t_{\text{cycle}}} = \frac{(\text{constant, evaluated at longest cycle time})}{t_{\text{cycle}}} \quad (C.9)$$

$$\text{Recovery} = (\text{constant, evaluated at longest cycle time}) \quad (C.10)$$

Equations (C.9) and (C.10) are "ideal" trend lines that quantify the relationship between cycle time and process performance when the impact of intrapellet mass transfer, interpellet pressure drop and heat transport through the bed do not change with cycle time. The constants are evaluated from conditions obtained at the longest cycle time considered. Any deviations in simulated and experimental data below these ideal lines as t_{cycle} reduces indicate the mechanisms of heat and mass transfer are changing predicted separation performance in relation to the conditions present at longer cycle times.

C.2 Introducing Non-Isothermal Behaviour - Simple Energy Balance

To provide a realistic estimate of equilibrium working selectivity, non-isothermal behaviour is introduced using a simplified picture for the axial temperature profile within the sorbent bed. The energy balance that follows is closely related to the work of Wilson (2001), which was largely based on experimental observations for the axial temperature profile commonly observed within a single layered sorbent bed operated over a cycle very similar to that considered in this dissertation. This simple energy balance assumes the sorbent bed is well insulated (i.e. adiabatic) that rises in temperature during adsorption and decreases during blowdown by an amount ΔT_{bed} . The purge step is assumed to be at the same temperature as the blowdown step for simplicity. Given the change in pressure and hence delta in adsorbed phase loading is relatively small during purge, this is a good first approximation. These assumptions give rise to the following trends for temperature within the system (Fig. C.2). One can see these are in relatively good qualitative agreement with experimental temperature profiles presented in chapter 6 for the RPSA pilot plant.

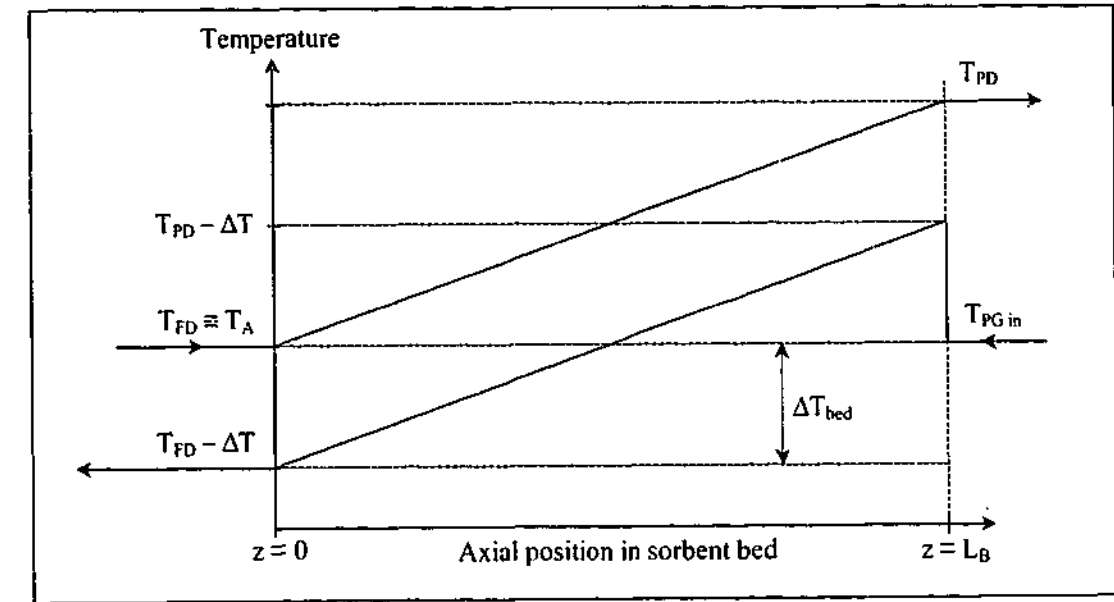


Figure C.2: Qualitative representation of temperature profiles assumed to arise at the end of the feed and blowdown steps. Note the purge profile is assumed identical to the blowdown profile.

For the current analysis reference temperature is assigned at feed gas conditions, which is assumed constant, so all enthalpy flows are in relation to feed gas. A total energy balance based on convective flows around the sorbent bed can be written as follows.

$$N_{PG\text{ in}} c_g^{PG\text{ in}} (T_A - T_{FD}) = (N_{PD} + N_{PG\text{ in}}) c_g^{PD} (T_{PD} - T_{FD}) + (N_{BD} + \lambda N_{FD}) c_g^{BD} (T_{BD} - T_{FD}) \quad (C.11)$$

Using Fig. C.2 the temperature of gas exhausted from the bed during blowdown is the average of T_{FD} and $(T_{FD} - \Delta T_{bed})$ so $T_{BD} = (T_{FD} - \frac{1}{2} \Delta T_{bed})$ whereas $T_{BD}^{ave} = [\frac{1}{2} (T_{FD} + T_{PD}) - \Delta T_{bed}]$. A similar argument leads to $T_{FD}^{ave} = \frac{1}{2} (T_{FD} + T_{PD})$. Assuming $T_A = T_{FD}$, which was the case to approximately 3 K across all RPSA pilot plant runs allows Eq. (C.11) to be solved for T_{PD} using the expression for T_{BD} just described.

$$T_{PD} = T_{FD} + \frac{1}{2} \left(\frac{N_{FD}}{N_{PD} + N_{PGin}} \right) \left(\frac{N_{BD}}{N_{FD}} + X \right) \Delta T_{bed} \quad (C.12)$$

N_{PGin} is calculated as follows.

$$N_{PGin} = m_{bed} (n_{N_2,eq}^{PG} - n_{N_2,eq}^{BD}) + \frac{\epsilon_T V_{bed} (1 - y_{BD})}{RT_{BD}^{ave}} (p_{PG} - p_{BD}) + m_{bed} (n_{O_2,eq}^{PG} - n_{O_2,eq}^{BD}) + \frac{\epsilon_T V_{bed} y_{BD}}{RT_{BD}^{ave}} (p_{PG} - p_{BD}) + \lambda N_{FD} \quad (C.13)$$

The last remaining parameter to find now is the magnitude of the temperature swing ΔT_{bed} . To do this, apply a simple energy balance over the blowdown step. Given the sorbent bed cools down during desorption, the "Average accumulation" and "Heat generated" terms are negative.

$$- \{ \text{Average accumulation} \} = \{ \text{Enthalpy in} \} - \{ \text{Enthalpy out} \} - \{ \text{Heat generated} \} \quad (C.14)$$

$$- \Delta T_{bed} (m_{bed} \hat{c}_s + m_{bed} c_g^{ave} n_{BD,ave}^{eq} + \epsilon_T V_{bed} c_g^{ave} \rho_{g,ave}^{BD}) = - (N_{BD} + \lambda N_{FD}) c_g^{BD} (T_{BD} - T_{FD}) - \Delta H_{total} \quad (C.15)$$

ΔH_{total} represents the total heat of adsorption released during the feed step and is equal to $m_{bed} [\Delta H_{N_2} (n_{N_2,eq}^{FD} - n_{N_2,eq}^{PG}) + \Delta H_{O_2} (n_{O_2,eq}^{FD} - n_{O_2,eq}^{PG})]$, so $-\Delta H_{total}$ represents the heat of desorption required by sorbate molecules to reenter the gas phase from the adsorbed phase. Solving Eq. (C.15) for ΔT_{bed} gives the following.

$$\Delta T_{bed} = \frac{m_{bed} [\Delta H_{N_2} (n_{N_2,eq}^{FD} - n_{N_2,eq}^{PG}) + \Delta H_{O_2} (n_{O_2,eq}^{FD} - n_{O_2,eq}^{PG})]}{[m_{bed} \hat{c}_s + m_{bed} c_g^{ave} n_{BD,ave}^{eq} + \epsilon_T V_{bed} c_g^{ave} \rho_{g,ave}^{BD} + \frac{1}{2} (N_{BD} + \lambda N_{FD}) c_g^{BD}]} \quad (C.16)$$

Although the simplified RPSA analysis is not recommended as a predictive tool for RPSA, it does allow:

- i. Separation performance as a function of temperature to be compared for a range of different sorbent materials under non-isothermal conditions through equilibrium working selectivity.
- ii. General trends in process performance to be compared against the ideal trend line that assumes intrapellet mass transfer and interpellet pressure drop have the same impact across all cycle times.

C.2.1 Proposed Solution Strategy

Although calculation of adiabatic working selectivity is analytical in so much as algebraic expressions have been derived, it is an iterative approach as initial estimates for temperature are required to calculate adsorbed phase loading that in turn are used to calculate mole flows that are finally used to update temperature according to Eqs. (C.12) and (C.16). A bootstrap technique was used, where updated temperatures are passed back in as initial estimates, until starting and final estimates were within 10^{-8} K of each other (Fig. C.3).

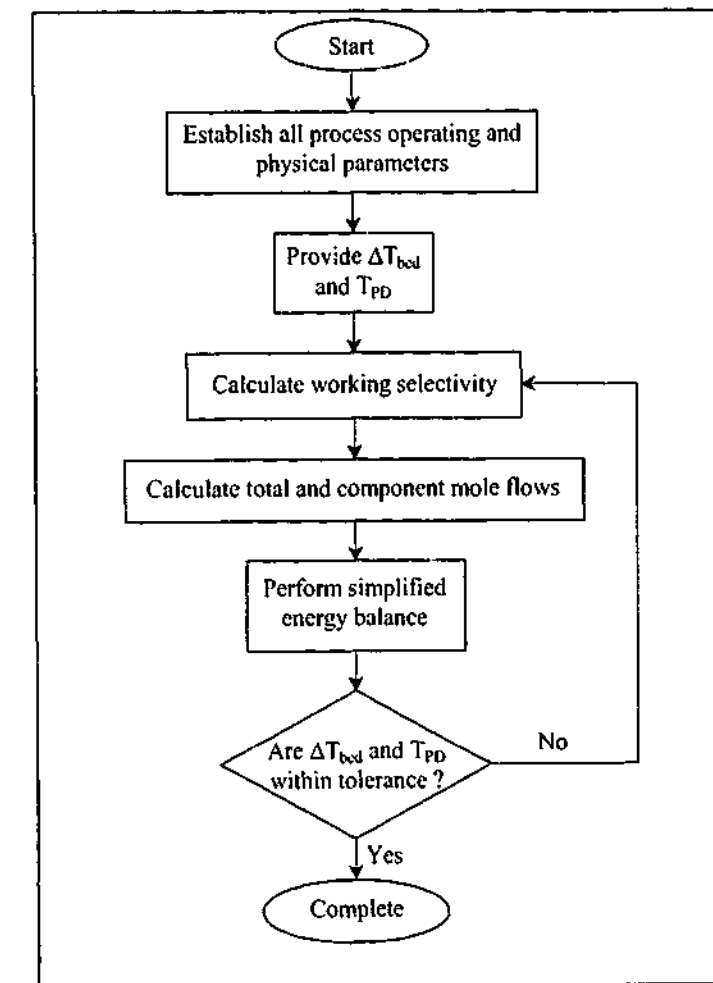


Figure C.3: Flowchart outlining calculation procedure for the simplified RPSA analysis.

APPENDIX D

DETAILS ON EACH EXPERIMENTAL APPARATUS

This appendix provides dimensional drawings, equipment specifications and photographs on each experimental apparatus used in this dissertation. I would again like to acknowledge Air Products and Chemicals Inc. for providing the EMU in its complete form and the financial provisions to allow the LUB apparatus and RPSA pilot plant to be constructed.

D.1 Experimental Mass-transfer Unit (EMU)

For each equipment specification table (Tables D.1 through D.3) the items deemed relevant to experimental profiles/parameters reported in this dissertation only are presented. A complete description of each individual fitting and equipment item is unnecessary for this dissertation.

Table D.1: Equipment specifications on the EMU.

| Tag | Description | Range | Accuracy | Response time |
|----------|--|-------------------------------------|--------------|--|
| PT1 | MKS Baratron type 627B absolute pressure transducer ¹ | 0 to 1000 torr (0 to 1.33 bar.a) | 0.0013 bar.a | Approximately 0.020 s |
| BV3 | Swagelok pneumatically actuated solenoid valve ² | Not relevant | Not relevant | Around 0.1 s (assumed for purposes of EMU simulation) |
| P1 to P5 | Analog pressure gauges ³ | 1.013 to 1.50 bar.a | 0.05 bar.a | Less than 1 s |

Notes:

¹ The signal obtained from the transducer is processed through an MKS Baratron type 660B digital readout unit. With analog-to-digital signal conversion in the local PC, an additional error was introduced. Although the transducer and digital display itself are accurate to 0.0013 bar.a, observations on the recorded signal at steady state gave an error of 0.0040 bar.a that is considered to be the accuracy of recorded pressure profiles obtained in chapter 4.

² Actuated via nitrogen from the feed line through a manual release mechanism.

³ Provided for visual checks on inlet line pressures only.

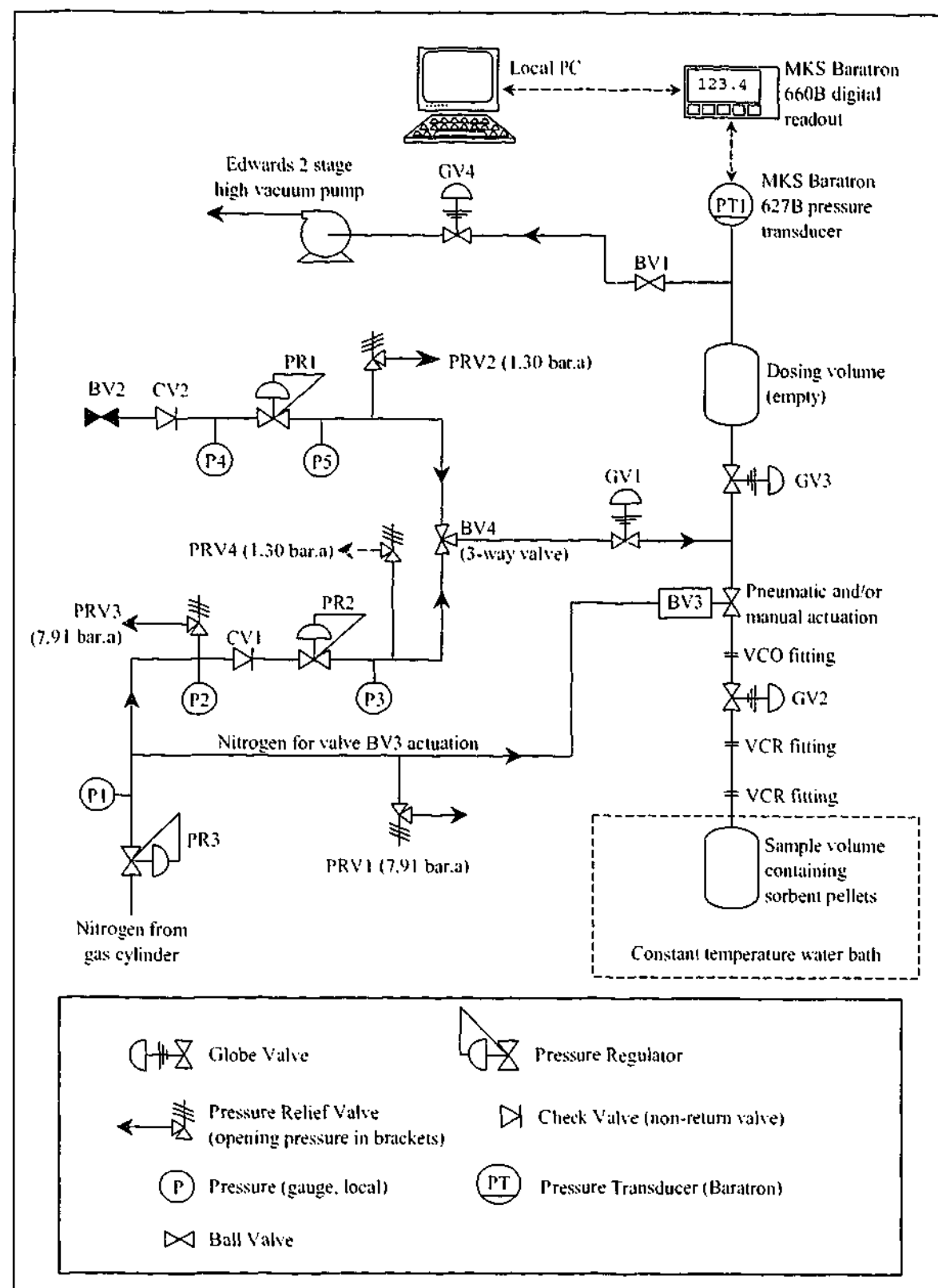


Figure D.1: Detailed piping and instrumentation diagram of the EMU.

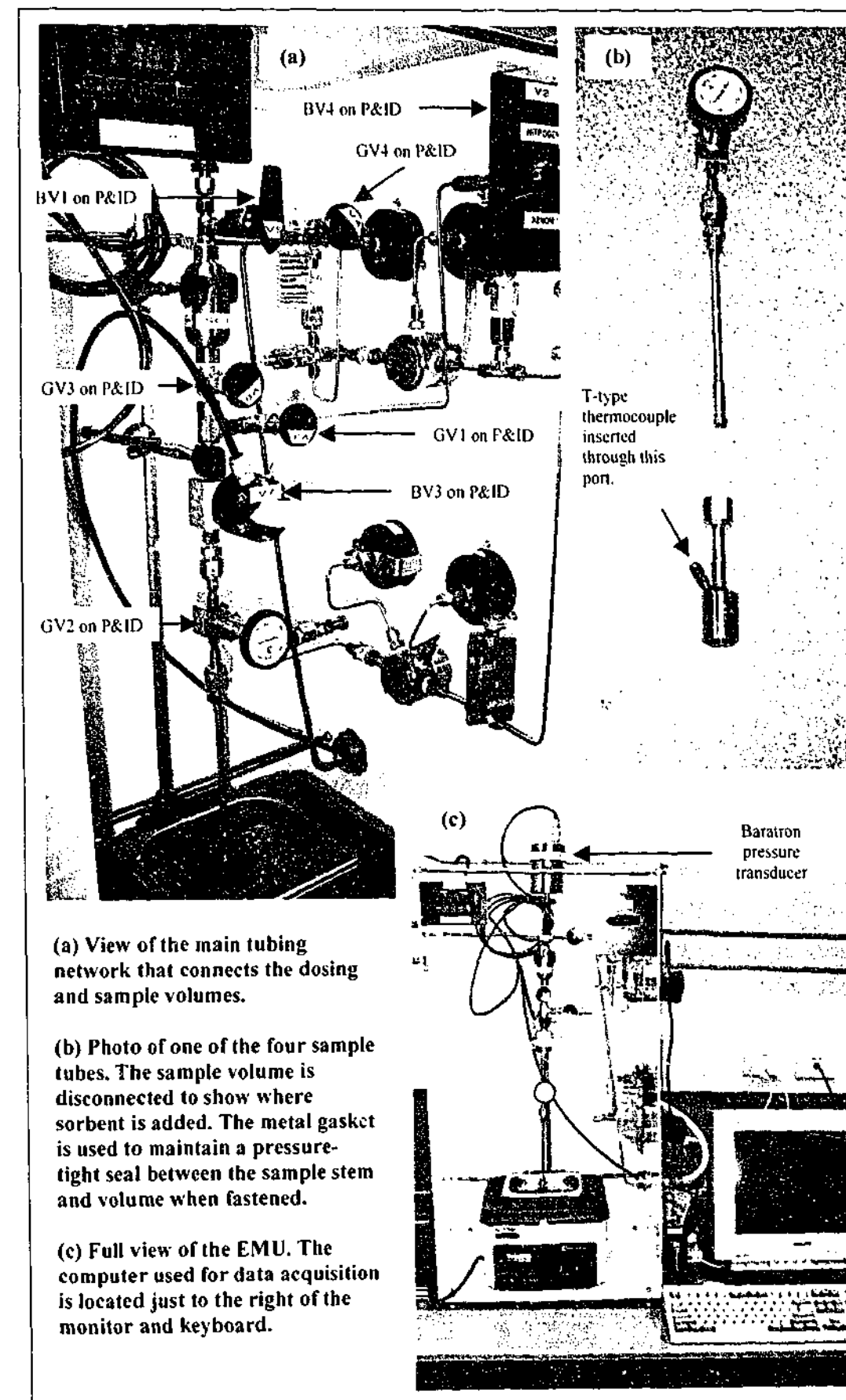


Figure D.2: Various photos of the EMU.

D.2 Length of Unused Bed (LUB) Apparatus

Table D.2: Equipment specifications on the LUB apparatus.

| P&ID Tag | Description | Range | Accuracy | Response time |
|------------|---|--|------------------------|---|
| PT1 to PT3 | Druck PTX1400 pressure transducers ¹ | 0 to 100 kPa.g (1.013 to 2.013 bar.a) | 0.01 bar.a | Around 0.1 s |
| DP1 | Yokogawa EJA110 model differential pressure transducer ² | 0 to 40 mbar (0 to 0.040 bar) | 0.0008 bar | Around 1.0 s |
| DP2 | Foxboro IDP10-A model differential pressure transducer ³ | -100 to 100 kPa (-1.0 to 1.0 bar) | 0.001 bar | Around 0.5 s |
| T1 to T6 | Pyrosales Type T junction exposed thermocouples ⁴ | 0 to 45 °C (273 to 318 K) | 0.5 K | Less than 1.0 s |
| O2 | Servomex Zr733 fast response zirconia oxygen sensor ⁵ | 1 to 100 mol%O ₂ | 0.5 mol%O ₂ | Step tests indicate response time approximately 0.4 s for 100% of response. |

Notes:

- ¹ The response time for these transducers was observed to fall within one scan time of the data acquisition program. All three transducers were consistent to within 0.01 bar.a when the column was at one steady and uniform pressure.
- ² Located on feed line annubar to measure flow rate to adsorption column.
- ³ Mounted directly onto the adsorption column to measure pressure drop when finding steady state Ergun friction factor coefficients. This transducer was also used during breakthrough runs to measure pressure drop across the MTZ, but was disconnected for pressurisation and depressurisation runs.
- ⁴ Although measured range within the data acquisition program was 70 K to 373 K, each thermocouple was calibrated between an ice bath (0.0 °C) and various water bath temperatures up to 45.0 °C using a mercury-in-glass thermometer as the "true" temperature. The calibrated readings also include analog-to-digital conversion offset/error. T7 is a type K thermocouple and only used to monitor and control oxygen analyser temperature to be 750 ± 5 °C.
- ⁵ $\frac{1}{16}$ inch tubing between column and analyser minimal (around 0.07 m) to reduce dead time and dispersion.

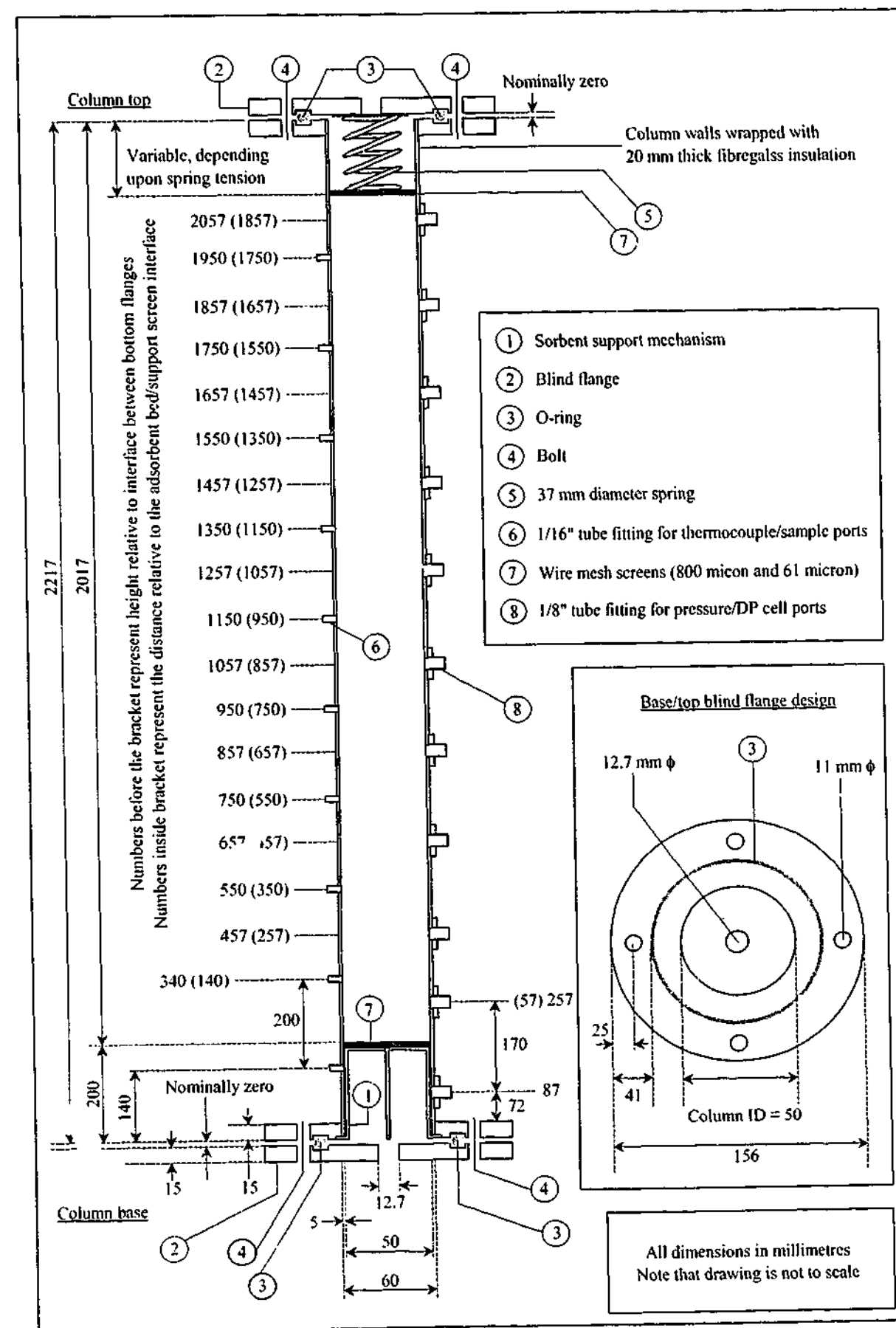


Figure D.3: Detailed arrangement drawing of the LUB adsorption column.

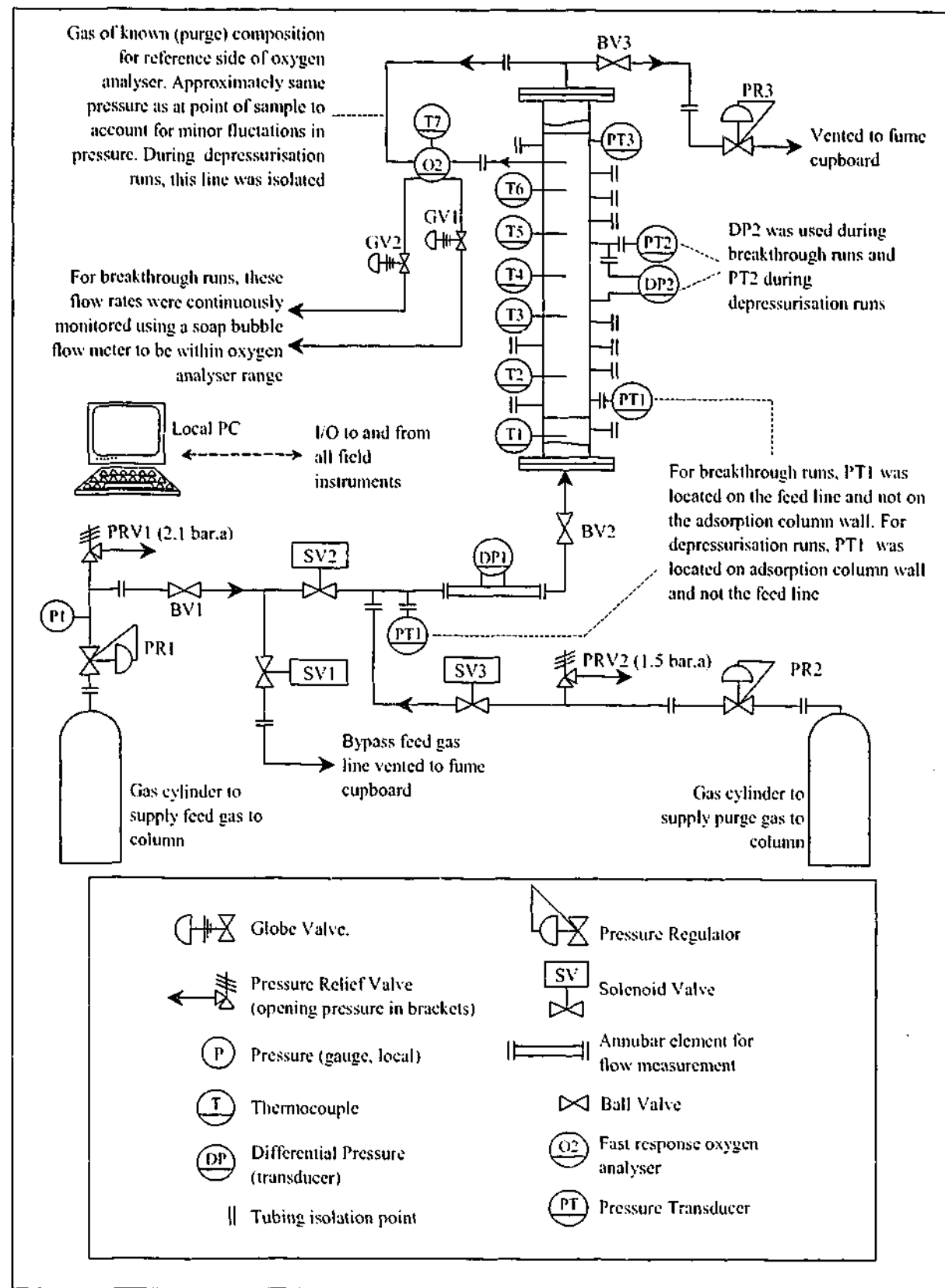


Figure D.4: Detailed piping and instrumentation diagram of LUB apparatus.

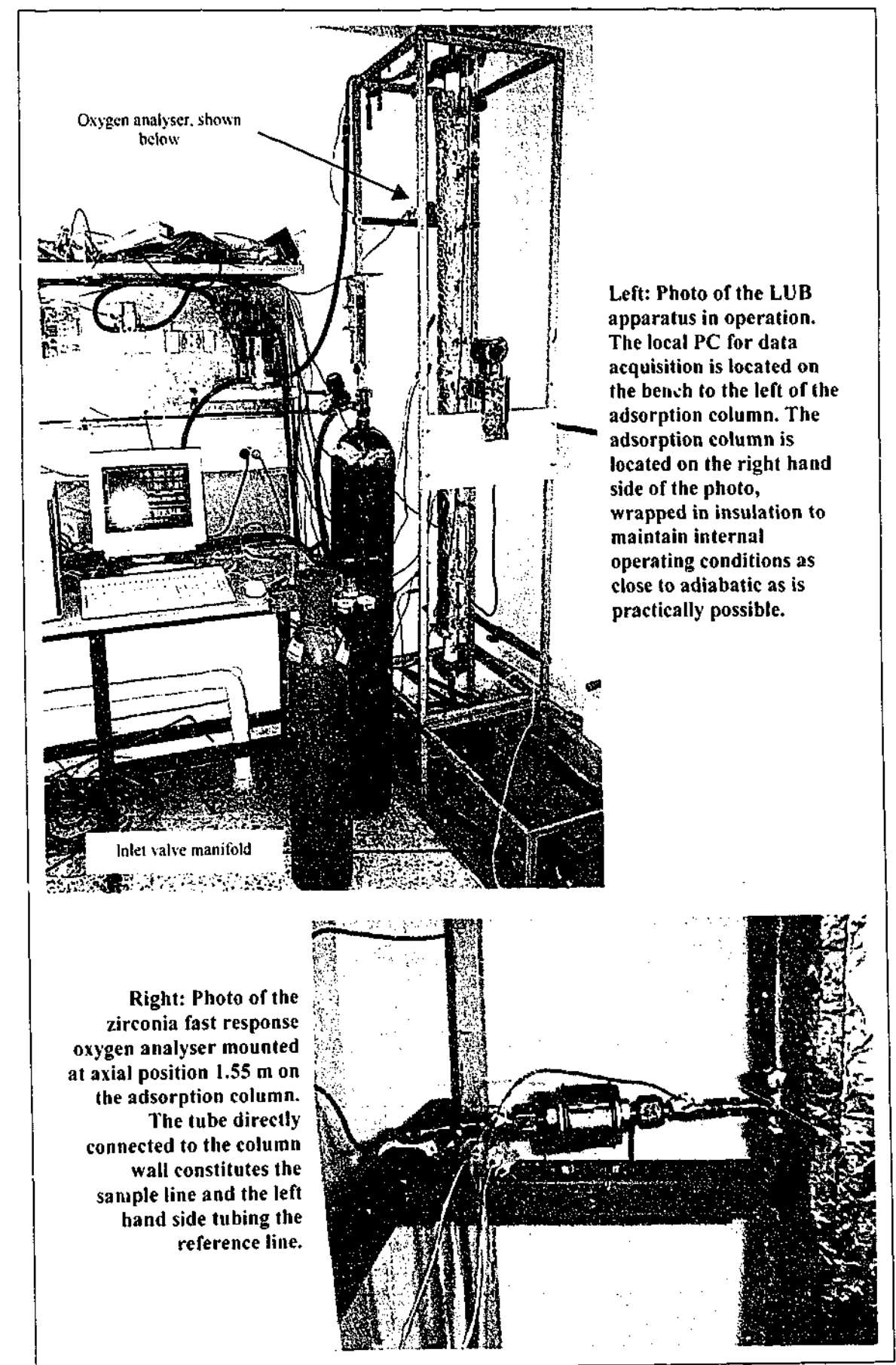


Figure D.5: Various photos of the LUB apparatus.

D.3 RPSA Pilot Plant

Table D.3: Equipment specifications on the RPSA pilot plant.

| P&ID Tag | Description | Range | Accuracy ¹ | Response time |
|------------------------------|---|---|---------------------------|-----------------|
| PT1, PT2 and PT5 | Ellison sensors GS4200-4 pressure transducers | 0 to 10 bar.g (1.013 to 11.013 bar.a) | 0.05 bar.a | Less than 0.1 s |
| PT3, PT4, PT6 and PT7 | Ellison sensors GS4200-4 pressure transducers | 0 to 6 bar.g (1.013 to 7.013 bar.a) | 0.03 bar.a | Less than 0.1 s |
| DP1 and DP2 | Foxboro IDP10-A differential pressure transducer | -70 to 200 kPa (-0.7 to 2.0 bar) | 0.007 bar | Around 0.5 s |
| DP3 | Foxboro IDP10-A differential pressure transducer | 0 to 250 mmH ₂ O (0 to 0.025 bar) | 6.1×10^{-5} bar | Around 0.5 s |
| DP4 | Foxboro IDP10-A differential pressure transducer | 0 to 250 mmH ₂ O (0 to 0.025 bar) | 6.1×10^{-5} bar | Around 0.5 s |
| DTM | Dry test meter | 0 to 6.22 kPa (0 to 0.0622 bar) | 1.24×10^{-4} bar | Around 1.0 s |
| SV1 to SV8 | 1.5" Nippon Valqua rapid actuation cylinder valves ² | Either 0 or 100 % open | Not relevant | Around 0.2 s |
| T1 to T12 | Pyrosales Type T junction exposed thermocouples ³ | 0 to 40 °C (273 to 313 K) | 0.5 K | Less than 1.0 s |
| Para-magnetic O ₂ | Servomex 1440 paramagnetic oxygen sensor ⁴ | 0 to 100 mol%O ₂ | 0.5 mol%O ₂ | Less than 10 s. |

Notes (most of the observations from the notes of Table D.2 also carry over here):

¹ Reported accuracy includes all offset and non-linearities from individual sensor specifications, along with analog-to-digital conversion performed by the PLC.

² These valves require air too open and close (actuated with 7.5 bar.a air from PSA dryer).

³ The calibration procedure performed on each LUB thermocouple was also performed on each RPSA pilot plant thermocouple. Thermocouple A/D cards located within the PLC report temperature in increments of 0.5 K.

⁴ This analyser measures product gas composition after the product tank.

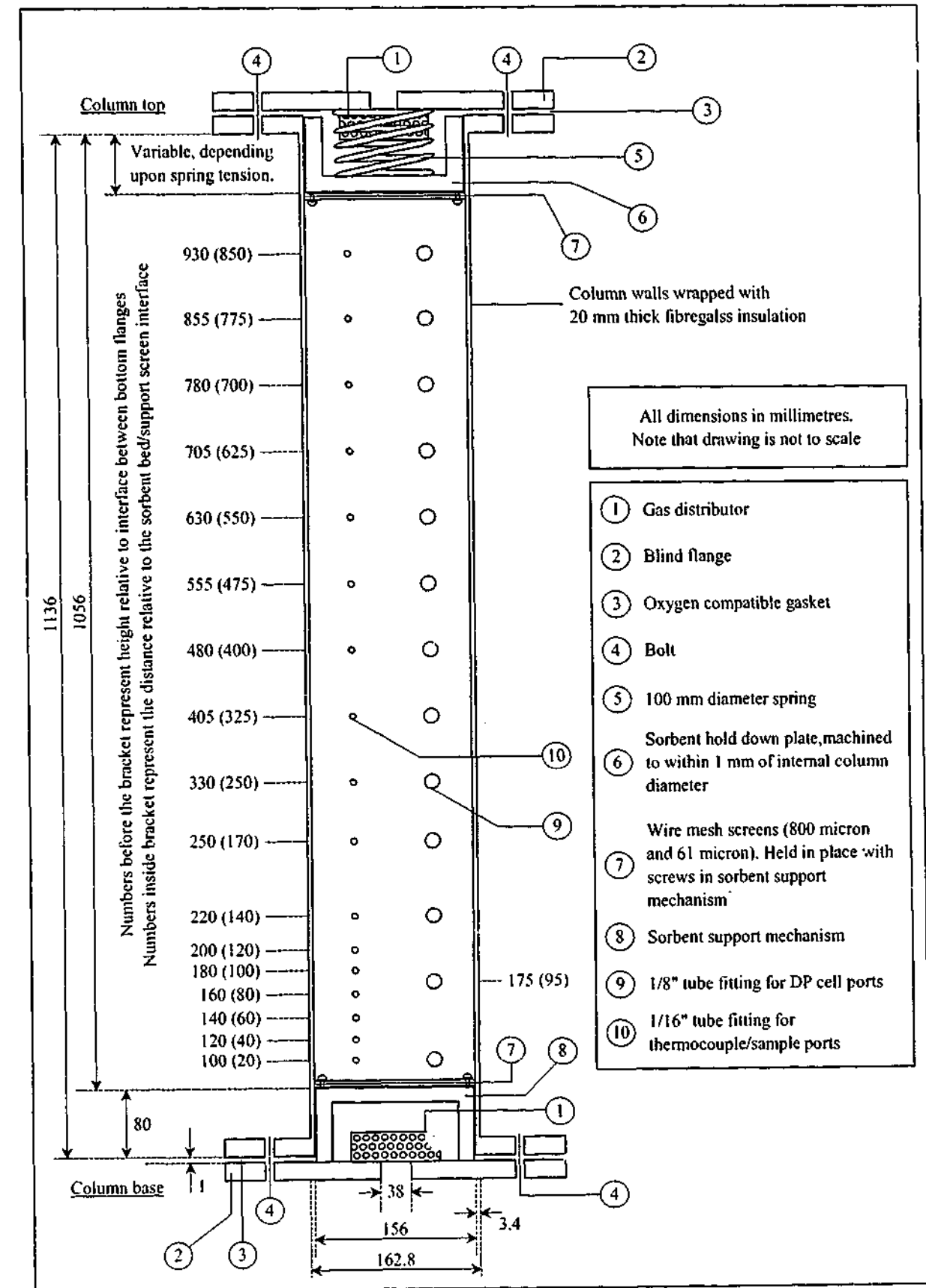


Figure D.6: Detailed arrangement drawing of the RPSA pilot plant adsorption column.

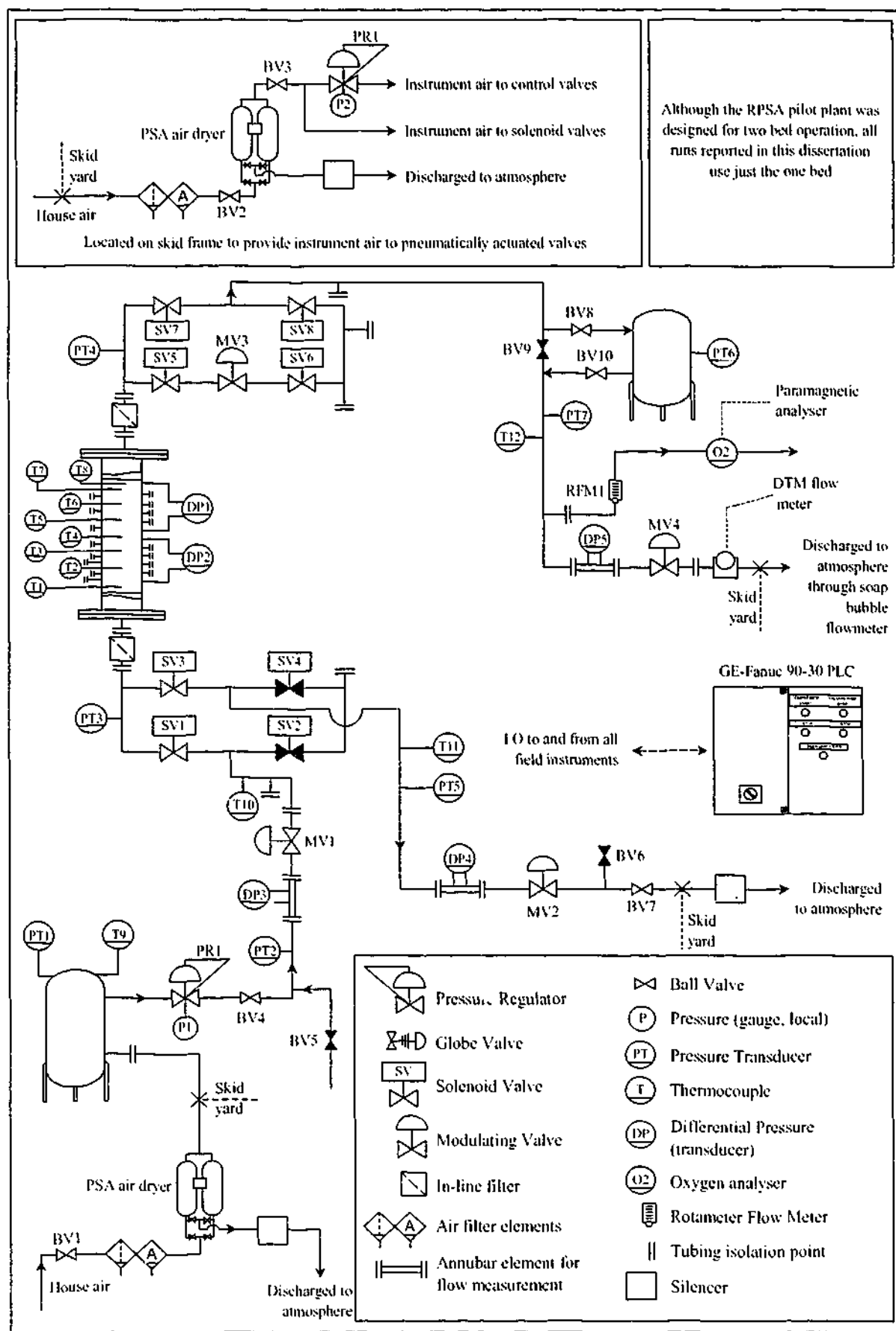


Figure D.7: Detailed piping and instrumentation diagram of the RPSA pilot plant.

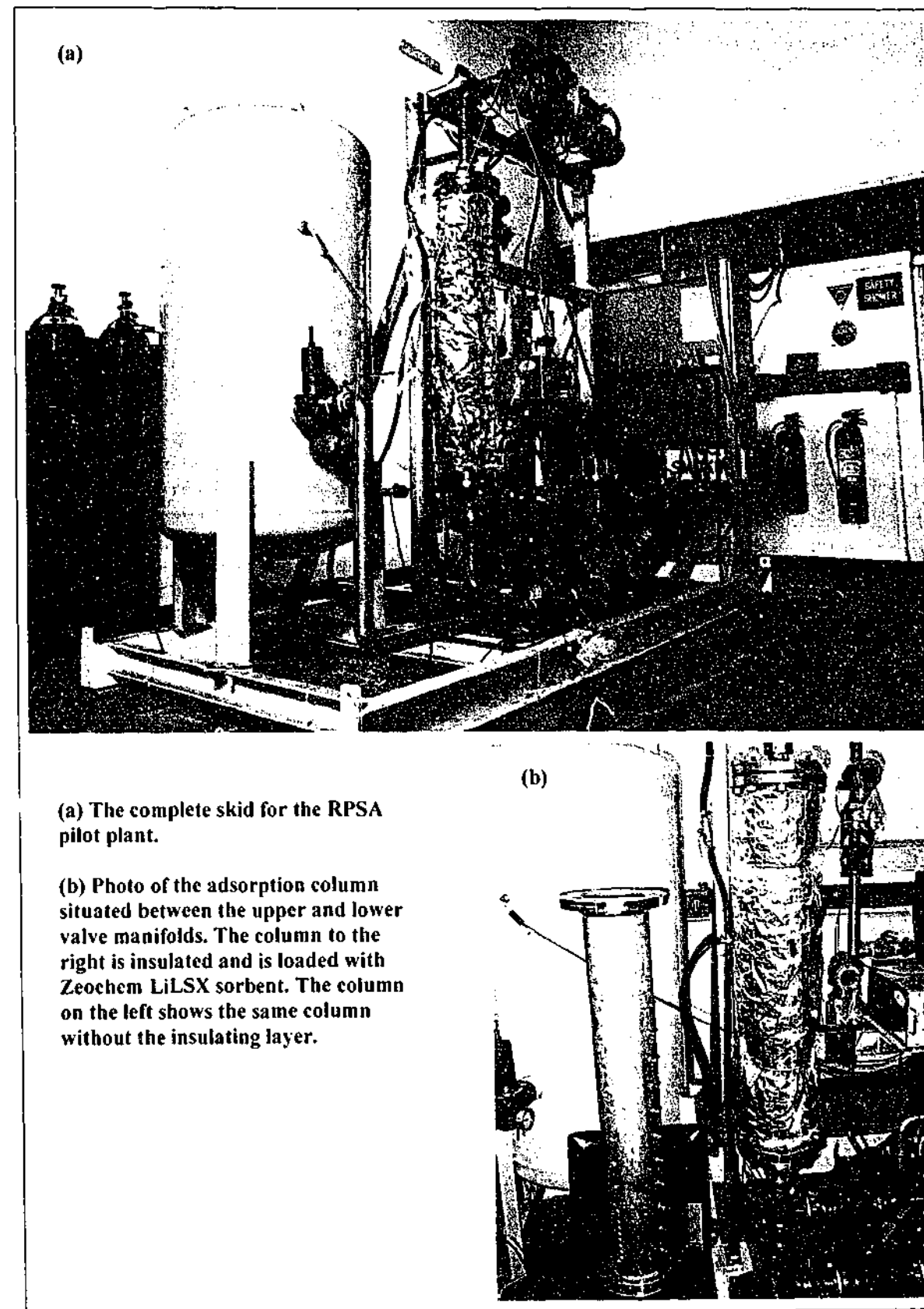


Figure D.8: Various photos of the RPSA pilot plant and adsorption column.

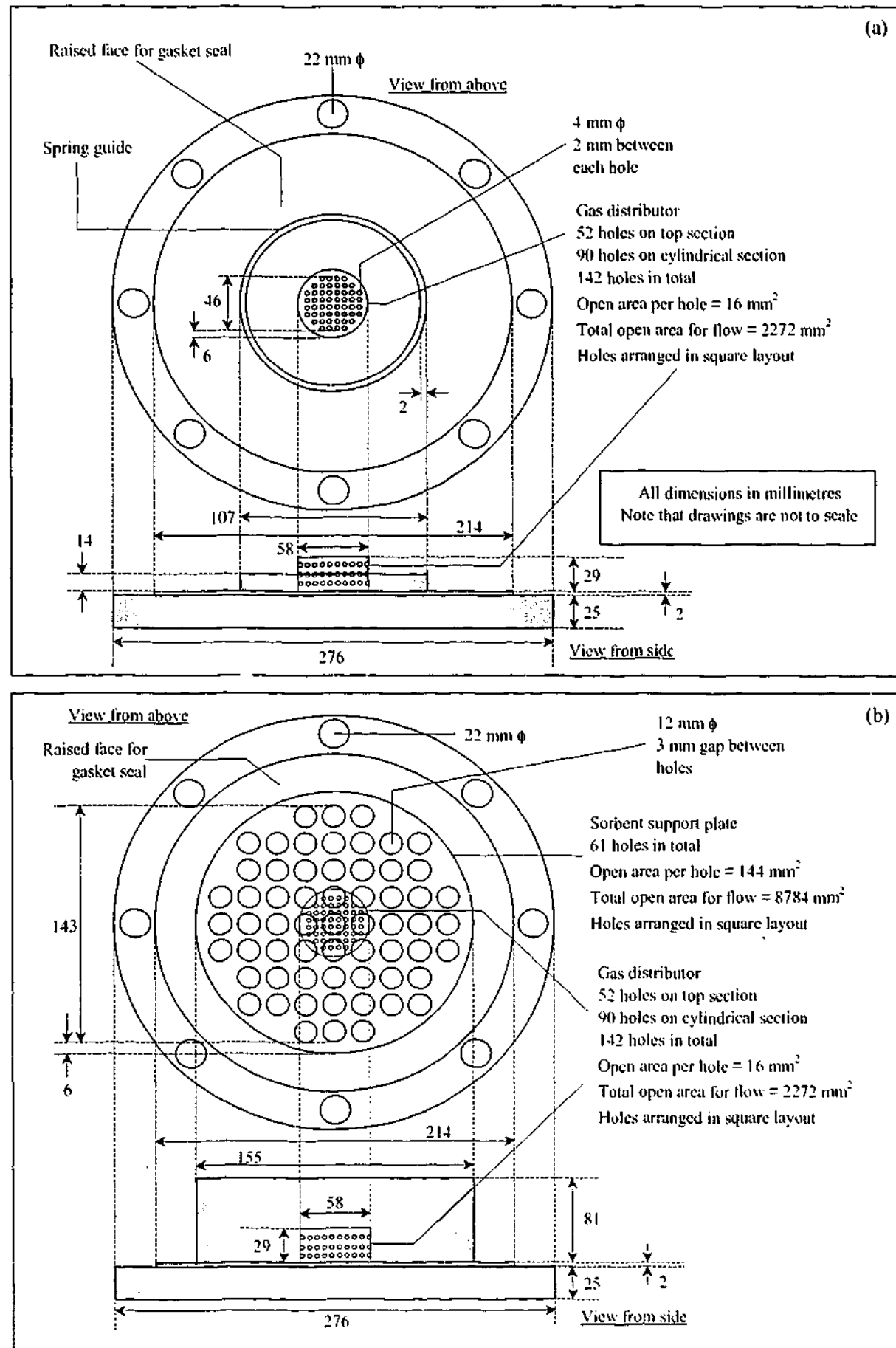


Figure D.9: Detailed arrangement drawing of the (a) top flange and (b) bottom flange.

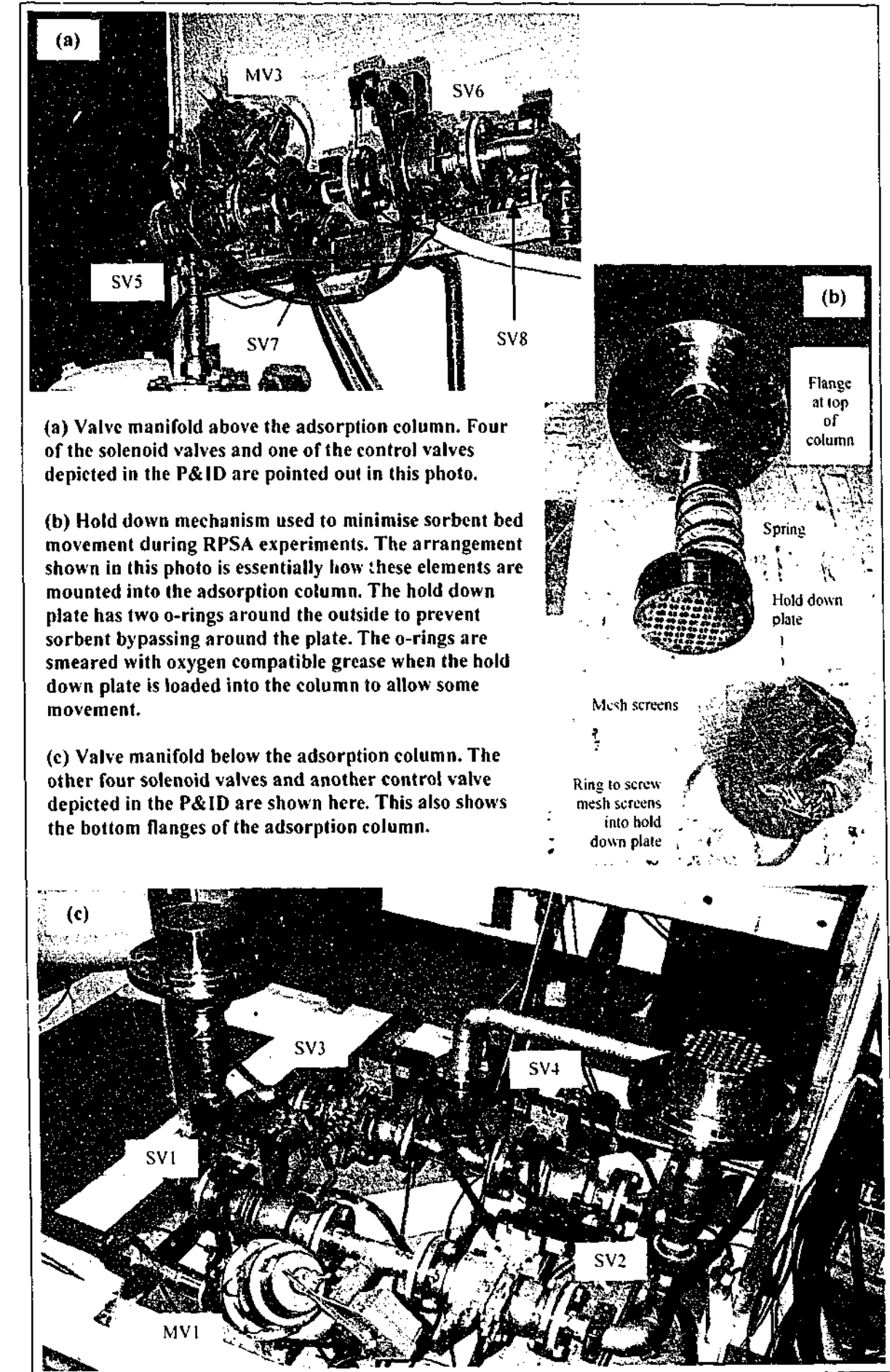


Figure D.10: Photos of the RPSA pilot plant valve manifolds and column internals.

LIST OF REFERENCES

- Abbasi M. H., Evans J. W. & Abramson I. S. (1983) Diffusion of Gases in Porous Solids: Monte Carlo Simulations in the Knudsen and Ordinary Diffusion Regimes, *AIChE J.*, **29**, 617 – 624
- Ackley M. W., Smolarek J. & Leavitt F. W. (2003) *Pressure Swing Adsorption Gas Separation Method, Using Adsorbents with High Intrinsic Diffusivity and Low Pressure Ratios*, US Patent 6 506 234, January 14
- Ackley M. W. & Zhong G. (2003) *Medical Oxygen Concentrator*, US Patent 6 551 384, April 22
- Ahn H., Lee C.-H., Seo B., Yang J. & Baek K. (1999) Backfill Cycle of a Layered Bed H₂ PSA Process, *Adsorption*, **5**, 419 – 433
- Alpay E. & Scott D. M. (1992) The Linear Driving Force Model for Fast-Cycle Adsorption and Desorption in a Spherical Particle, *Chem. Eng. Sci.*, **47**, 499 – 502
- Alpay E., Kenney C. N. & Scott D. M. (1993) Simulation of Rapid Pressure Swing Adsorption and Reaction Processes, *Chem. Eng. Sci.*, **48**, 3173 – 3186
- Alpay E., Kenney C. N. & Scott D. M. (1994) Adsorbent Particle Size Effects in the Separation of Air by Rapid Pressure Swing Adsorption, *Chem. Eng. Sci.*, **49**, 3059 – 3075
- Anderson B. G., de Gauw F. J. M. M., Noordhoek N. J., van Ijzendoorn L. J., van Santen R. A. & de Voigt M. J. A. (1998) Mass Transfer of Alkanes in Zeolite Packed-Bed Reactors Studied with Positron Emission Profiling (PEP). 1. Experiments, *Ind. & Eng. Chem. Res.*, **37**, 815 – 824
- Andrews J. R. G. & Scott D. M. (2000) Similarity Solutions for Multicomponent Nonlinear Diffusion, *Chem. Eng. Sci.*, **55**, 1033 – 1037
- Andrieu J. & Smith J. M. (1980) Rate Parameters for Adsorption of CO₂ in Beds of Carbon Particles, *AIChE J.*, **26**, 944 – 948
- APCI (2001) *Air Products and Chemicals Inc. Annual Report 2001*
- APCI (2002) *Series of Private Communications*
- Arnošt D. & Schneider P. (1995) Dynamic Transport of Multicomponent Mixtures of Gases in Porous Solids, *Chem. Eng. J.*, **57**, 91 – 99
- Arumugam B. K. & Wankat P. C. (1998) Pressure Transients in Gas Phase Adsorptive Reactors, *Adsorption*, **4**, 345 – 354
- Arumugam B. K., Banks J. F. & Wankat P. C. (1999) Pressure Effects in Adsorption Systems, *Adsorption*, **5**, 261 – 278
- Arvind R., Farooq S. & Ruthven D. M. (2002) Analysis of a Piston PSA Process for Air Separation, *Chem. Eng. Sci.*, **57**, 419 – 433
- AspenTech (1997) *ADSIM Library Manual (Release 6.1)*, Aspen Technology Inc., United States

- Baiker A., New M. & Richarz W. (1982) Determination of Intraparticle Diffusion Coefficients in Catalyst Pellets – A Comparative Study of Measuring Methods, *Chem. Eng. Sci.*, **37**, 643 – 656
- Bär N.-K., McDaniel P. L., Coe C. G., Seiffert G. & Kärger J. (1997) Measurement of Intracrystalline Diffusion of Nitrogen in Zeolites NaX and NaCaA using Pulsed Field Gradient N.M.R., *Zeolites*, **18**, 71 – 74
- Baerlocher C., Meier W. M. & Olson D. H. (2001) *Atlas of Zeolite Framework Types (Fifth Edition)*, Elsevier, Amsterdam
- Baron G. (1993) Modelling PSA Processes, *Gas. Sep. Purif.*, **7**, 111 – 117
- Basagaoglu H., Ginn T. R., McCoy B. J. & Mariño M. A. (2000) Linear Driving Force Approximation to a Radial Diffusive Model, *AIChE J.*, **46**, 2097 – 2105
- Batta L. B. (1973) *Selective Adsorption Process for Air Separation*, US Patent 3 717 974, February 27
- Beeckman J. W. & Froment G. F. (1982) Deactivation of Catalysts by Coke Formation in the Presence of Internal Diffusional Limitation, *Ind. Eng. Chem. Fundam.*, **27**, 243 – 250
- Beh C. C. K. (2003) *The Vacuum Swing Adsorption Process for Oxygen Enrichment. A Study into the Dynamics, Modelling and Control*, Ph.D. Dissertation, Monash University, Australia
- Betlem B. H. L., Gotink R. W. M. & Bosch H. (1998) Optimal Operation of Rapid Pressure Swing Adsorption with Slop Recycling, *Comput. Chem. Eng.*, **22 Suppl.**, S633 – S636
- Bhaskar G. V. & Do D. D. (1989) A Simple Solution for Nonisothermal Adsorption in a Single Particle, *Chem. Eng. Sci.*, **44**, 1215 – 1219
- Bhatia S. K. (1985) Directional Autocorrelation and the Diffusional Tortuosity of Capillary Porous Media, *J. Catalysis*, **93**, 192 – 196
- Bhatia S. K. (1986) Stochastic Theory of Transport in Inhomogeneous Media, *Chem. Eng. Sci.*, **41**, 1311 – 1324
- Bhatia S. K. (1988) Combined Surface and Pore Volume Diffusion in Porous Media, *AIChE J.*, **34**, 1094 – 1105
- Bird R., Stewart W. & Lightfoot E. (1960) *Transport Phenomena*, John Wiley and Sons, New York
- Boniface II. A. & Ruthven D. M. (1985) The Use of Higher Moments to Extract Transport Data from Chromatographic Adsorption Experiments, *Chem. Eng. Sci.*, **40**, 1401 – 1409
- Boss B. D., Stejskal E. O. & Ferry J. D. (1967) Self-Diffusion in High Molecular Weight Polyisobutylene-Benzene Mixtures Determined by the Pulsed-Gradient, Spin-Echo Method, *J. Phys. Chem.*, **71**, 1501 – 1506
- Botte G. G., Ritter J. A. & White R. E. (2000) Comparison of Finite Difference and Control Volume Methods for Solving Differential Equations, *Comput. Chem. Eng.*, **24**, 2633 – 2654
- Bourdin V., Grenier Ph., Meunier F. & Sun L. M. (1996) Thermal Frequency Response Method for the Study of Mass-Transfer Kinetics in Adsorbents, *AIChE J.*, **42**, 700 – 712

- Brandani S. (1998) Effects of Nonlinear Equilibrium on Zero Length Column Experiments, *Chem. Eng. Sci.*, **53**, 2791 – 2798
- Brandani S. (2002) Heat Effects in the Zero Length Column Technique, *AIChE Annual Meeting*, Dallas, Texas, USA, October 31-November 5
- Brandani S., Cavalcante C., Guimarães A. & Ruthven D. M. (1998) Heat Effects in ZLC Experiments, *Adsorption*, **4**, 275 – 285
- Brandani S., Hufton J. & Ruthven D. M. (1995a) Self-Diffusion of Propane and Propylene in 5A and 13X Zeolite Crystals Studied by the Tracer ZLC Method, *Zeolites*, **15**, 624 – 631
- Brandani S., Jama M. A. & Ruthven D. M. (2000a) ZLC Measurements under Non-Linear Conditions, *Chem. Eng. Sci.*, **55**, 1205 – 1212
- Brandani S., Jama M. A. & Ruthven D. M. (2000b) Diffusion, Self-Diffusion and Counter-Diffusion of Benzene and *p*-Xylene in Silicalite, *Microporous & Mesoporous Materials*, **35-36**, 283 – 300
- Brandani S., Ruthven D. M. & Kärger J. (1995b) Concentration Dependence of Self-Diffusivity of Methanol in NaX Zeolite Crystals, *Zeolites*, **15**, 494 – 495
- Brandani S., Ruthven D. M. & Kärger J. (1997) Diffusion in a Unidimensional Zeolite Pore System: Propane in AlPO₄-5, *Microporous Materials*, **8**, 193 – 200
- Brandani S., Xu Z. & Ruthven D. M. (1996) Transport Diffusion and Self-Diffusion of Benzene in NaX and CaX Zeolite Crystals studied by ZLC and Tracer ZLC Methods, *Microporous Materials*, **7**, 323 – 331
- Brown P. N., Byrne G. D. & Hindmarsh A. C. (1989) VODE: A Variable-Coefficient ODE Solver, *SIAM J. Sci. Stat. Comput.*, **10**, 1038 – 1051
- Brunovská A., Hlaváček V., Ilavský J. & Valtýni J. (1978) An Analysis of a Nonisothermal One-Component Sorption in a Single Adsorbent Particle, *Chem. Eng. Sci.*, **33**, 1385 – 1391
- Bülow M. (2002) Complex Sorption Kinetics of Carbon Dioxide in NaX-Zeolite Crystals, *Adsorption*, **8**, 9 – 14
- Burganos V. N. (1998) Gas Diffusion in Random Binary Media, *J. Chem. Phys.*, **109**, 6772 – 6779
- Burganos V. N. & Sotirchos S. V. (1987) Diffusion in Pore Networks: Effective Medium Theory and Smooth Field Approximation, *AIChE J.*, **33**, 1678 – 1689
- Burganos V. N. & Sotirchos S. V. (1988) Simulation of Knudsen Diffusion in Random Networks of Parallel Pores, *Chem. Eng. Sci.*, **43**, 1685 – 1694
- Burganos V. N. & Sotirchos S. V. (1989) Knudsen Diffusion in Parallel, Multidimensional or Randomly Oriented Capillary Structures, *Chem. Eng. Sci.*, **44**, 2451 – 2462
- Burghardt A., Rogut J. & Gotkowska J. (1988) Diffusion Coefficients in Bidisperse Porous Structures, *Chem. Eng. Sci.*, **43**, 2463 – 2476
- Burghardt A. & Smith J. M. (1979) Dynamic Response of a Single Catalyst Pellet, *Chem. Eng. Sci.*, **34**, 267 – 273

- Buzanowski M. A. & Yang R. T. (1989) Extended Linear Driving-Force Approximation for Intraparticle Diffusion Rate Including Short Times, *Chem. Eng. Sci.*, **44**, 2683 – 2689
- Buzanowski M. A. & Yang R. T. (1991a) Approximations for Intraparticle Diffusion Rates in Cyclic Adsorption and Desorption. *Chem. Eng. Sci.*, **46**, 2589 – 2598
- Buzanowski M. A. & Yang R. T. (1991b) A Nondriving-Force Approximation for Intraparticle Diffusion in Cyclic Adsorption and Desorption with Short Cycle Times, *Chem. Eng. Commun.*, **104**, 257 – 266
- Buzanowski M. A., Yang R. T. & Haas O. W. (1989) Direct Observation of the Effects of Bed Pressure Drop on Adsorption and Desorption Dynamics, *Chem. Eng. Sci.*, **44**, 2392 – 2394
- Buzzi Ferraris G. & Manca D. (1998) BzzOde: A New C++ Class for the Solution of Stiff and Non-stiff Ordinary Differential Equation Systems, *Comput. Chem. Eng.*, **22**, 1595 – 1621
- Byrne M. E. & Wankat P. C. (2000) Pressure Effects in Adsorbers and Adsorptive Reactors, *Sepr. Sci. Tech.*, **35**, 323 – 351
- Čapek P., Hejtmánek V., Šolcová O., Klusáček K. & Schneider P. (1997) Gas Transport in Porous Media under Dynamic Conditions, *Catalysis Today*, **38**, 31 – 38
- Čapek P., Hejtmánek V. & Šolcová O. (2001) Permeation of Gases in Industrial Porous Catalysts, *Chem. Eng. J.*, **81**, 281 – 285
- Čapek P. & Seidel-Morgenstern A. (2001) Multicomponent Mass Transport in Porous Solids and Estimation of Transport Parameters, *Applied Catalysis A: General*, **211**, 227 – 237
- Carberry J. J. (1975) On the Relative Importance of External-Internal Temperature Gradients in Heterogeneous Catalysis, *Ind. Eng. Chem. Fundam.*, **14**, 129 – 131
- Carleton F. B., Kershenbaum L. S. & Wakeham W. A. (1978) Adsorption in Non-Isobaric Fixed Beds, *Chem. Eng. Sci.*, **33**, 1239 – 1246
- Carlson, N. W. & Dranoff, J. S. (1985) On the Adsorption of Ethane by 4A Zeolite Pellets, *Ind. Eng. Chem. Process Des. Dev.*, **24**, 1300 – 1302
- Carslaw H. S. & Jaeger J. C. (1993) *Conduction of Heat in Solids (Reprint of the 1959 Second Edition)*, Oxford University Press, Oxford
- Carta G. (1988) Exact Analytical Solution of a Mathematical Model for Chromatographic Operations, *Chem. Eng. Sci.*, **43**, 2877 – 2883
- Carta G. (1993) The Linear Driving Force Approximation for Cyclic Mass Transfer in Spherical Pellets, *Chem. Eng. Sci.*, **48**, 622 – 625
- Cassidy R. T. & Holmes E. S. (1984). Twenty-five years of Progress in "Adiabatic" Adsorption Processes, *AIChE Symp. Series*, No. 233, **80**, 68 – 75
- Cavalcante C. L., Azevêdo D. C. S., Souza I. G., Silva C. M., Alsina O. L. S., Lima V. E. & Araujo A. S. (2000) Sorption and Diffusion of *p*-Xylene and *o*-Xylene in Aluminophosphate Molecular Sieve AIPO₄-11, *Adsorption*, **6**, 53 – 59
- Cavalcante C. L., Brandani S. & Ruthven D. M. (1997) Evaluation of the Main Diffusion Path in Zeolites from ZLC Desorption Curves, *Zeolites*, **18**, 282 – 285

- Cen P. L. & Yang R. T. (1986) Analytic Solution for Adsorber Breakthrough Curves with Bidisperse Sorbents (Zeolites), *AIChE J.*, **32**, 1635 – 1641
- Çengel Y. A. (1998) *Heat Transfer: A Practical Approach*, McGraw-Hill, Boston
- Çengel Y. A. & Boles M. A. (1994) *Thermodynamics: An Engineering Approach (Second Edition)*, McGraw-Hill, New York
- Chahbani M. H. & Tondeur D. (1998) Modeling Compression and Decompression in Pressure-Swing-Adsorption, 811 – 816, *Proc. 6th. Int. Conf. Fundamentals of Adsorption*, presqu'île de Giens, France, 24-28 May
- Chahbani M. H. & Tondeur D. (2000) Mass Transfer Kinetics in Pressure Swing Adsorption, *Sepr. & Purif. Tech.*, **20**, 185 – 196
- Chan Y. N. I., Hill F. B. & Wong Y. W. (1981) Equilibrium Theory of a Pressure Swing Adsorption Process, *Chem. Eng. Sci.*, **36**, 243 – 251
- Chapra S. C. & Canale R. P. (1998) *Numerical Methods for Engineers (Third Edition)*, McGraw-Hill, New York
- Cheng Y. S., Alpay E. & Kershenbaum L. S. (1998) Simulation and Optimisation of a Rapid Pressure Swing Reactor, *Comput. Chem. Eng.*, **22 Suppl.**, S45 – S52
- Chiang A. S. T. (1996) An Analytical Solution to Equilibrium PSA Cycles, *Chem. Eng. Sci.*, **51**, 207 – 216
- Chihara K. & Suzuki M. (1983) Simulation of Nonisothermal Pressure Swing Adsorption, *J. Chem. Eng. Japan*, **16**, 53 – 61
- Choong T. S.-Y. (2000) *Algorithm Synthesis for Modelling Cyclic Processes: Rapid Pressure Swing Adsorption*, Ph.D. Dissertation, University of Cambridge, England
- Choong T. S.-Y., Paterson W. R. & Scott D. M. (1998) Axial Dispersion in Rich, Binary Gas Mixtures: Model Form and Boundary Conditions, *Chem. Eng. Sci.*, **53**, 4147 – 4149
- Choong T. S.-Y., Paterson W. R. & Scott D. M. (2002) Development of Novel Algorithm Features in the Modelling of Cyclic Processes, *Comput. Chem. Eng.*, **26**, 95 – 112
- Choong T. S.-Y. & Scott D. M. (1998) The Linear Driving Force Model for Cyclic Adsorption and Desorption: the Effect of External Fluid-Film Mass Transfer, *Chem. Eng. Sci.*, **53**, 847 – 851
- Chou C.-T. & Chen L.-H. (1994) Ternary Component Simulation of a Pressure Swing Adsorption Process for Air Separation, *J. Chin. Inst. Chem. Eng.*, **25**, 361 – 365
- Chou C.-T. & Huang W.-C. (1994a) Incorporation of a Valve Equation into the Simulation of a Pressure Swing Adsorption Process, *Chem. Eng. Sci.*, **49**, 75 – 84
- Chou C.-T. & Huang W.-C. (1994b) Simulation of a Four-Bed Pressure Swing Adsorption Process for Oxygen Enrichment, *Ind. & Eng. Chem. Res.*, **33**, 1250 – 1258
- Chou C.-T. & Kuang S.-C. (1996) Experiments on a Rapid Pressure Swing Adsorption Process for Air Separation, 195 – 202, *Fundamentals of Adsorption*, Kluwer Academic Publishers, Boston, Massachusetts

- Chou C.-T. & Wu C.-L. (1994) Oxygen Enrichment over Zeolite 5A by a Rapid Pressure Swing Adsorption Process, *Studies Surf. Sci. & Technol.*, **84**, 1255 – 1260
- Chun C. & Lee C.-H. (2000) Comparison of Adsorption Dynamics of a Ternary Hydrogen Mixture in Equilibrium and Kinetic Separation Beds, 371 – 375, *Proc. 2nd. Pacific Basin Conf. Adsorption Sci. and Tech.*, Brisbane, Queensland, Australia, 14-18 May
- Cohen Y. & Metzner A. B. (1981) Wall Effects in Laminar Flow of Fluid through Packed Beds, *AIChE J.*, **27**, 705 – 715
- Coimbra M. C., Sereno C. & Rodrigues A. (2001) Applications of a Moving Finite Element Method, *Chem. Eng. J.*, **84**, 23 – 29
- Crane Co., Engineering Division (1976) *Technical Paper 410-C: Flow of Fluids through Valves, Fittings and Pipe (Sixteenth Edition)*, Crane Company, Canada
- Crank J. (1975) *The Mathematics of Diffusion (Second Edition)*, Clarendon Press, Oxford
- Crittenden B. D., Guan J., Ng W. N. & Thomas W. J. (1994) Dynamics of Pressurization and Depressurization during Pressure Swing Adsorption, *Chem. Eng. Sci.*, **49**, 2657 – 2669
- Crittenden B. D., Guan J., Ng W. N. & Thomas W. J. (1995) Pressure, Concentration and Temperature Profiles in a 5A Zeolite Adsorbent Bed during Pressurisation and Depressurisation with Air, *Chem. Eng. Sci.*, **50**, 1417 – 1428
- Croft D. T. & LeVan M. D. (1994) Periodic States of Adsorption Cycles - I. Direct Determination and Stability, *Chem. Eng. Sci.*, **49**, 1821 – 1829
- Cui C. L., Authelin J. R., Schweich D. & Villiermaux J. (1990) Consequence of Distributed Properties on Effective Diffusivities in Porous Solids, *Chem. Eng. Sci.*, **45**, 2611 – 2617
- Cunningham R. E. & Williams R. J. J. (1980) *Diffusion in Gases and Porous Media*, Plenum Press, New York
- Czepirski L. & Laciak B. (2000) Interpretation of High-Pressure Adsorption Equilibrium and Kinetic Data for Active Carbons, 164 – 168, *Proc. 2nd. Pacific Basin Conf. Adsorption Sci. and Tech.*, Brisbane, Queensland, Australia, 14-18 May
- Da Silva F. A., Silva J. A. & Rodrigues A. E. (1999) A General Package for the Simulation of Cyclic Adsorption Processes, *Adsorption*, **5**, 229 – 244
- Dangieri T. J. & Cassidy R. T. (1983) *RPSA Process*, US Patent 4 406 675, September 27
- Deepak P. D. & Bhatia S. K. (1994) Transport in Capillary Network Models of Porous Media: Theory and Simulation, *Chem. Eng. Sci.*, **49**, 245 – 247
- Demontis P., Fois E. S., Suffritti G. B. & Quartieri S. (1990) Molecular Dynamics Studies on Zeolites. 4. Diffusion of Methane in Silicalite, *J. Phys. Chem.*, **94**, 4329 – 4334
- Delmas M. P. F. & Ruthven D. M. (1995) Measurement of Intracrystalline Diffusion in NaX Zeolite by Capillary Column Gas Chromatography, *Microporous Materials*, **3**, 581 – 592
- Ding Y. & LeVan M. D. (2001) Periodic States of Adsorption Cycles III. Convergence Acceleration for Direct Determination. *Chem. Eng. Sci.*, **56**, 5217 – 5230

- Do D. D. (1990) Hierarchy of Rate Models for Adsorption and Desorption in Bidispersed Structured Adsorbents, *Chem. Eng. Sci.*, **45**, 1373 – 1381
- Do D. D. (1995) Dynamics of a Semi-Batch Adsorber with Constant Molar Supply Rate: A Method for Studying Adsorption Rate of Pure Gases, *Chem. Eng. Sci.*, **50**, 549 – 553
- Do D. D. (1998) *Adsorption Analysis: Equilibria and Kinetics*, ICP, London
- Do D. D. & Do H. D. (1998a) A Maxwell-Stefan Analysis of Convective Flow, Pore and Surface Diffusion, Heat Transfer and Adsorption of Hydrocarbon Mixtures in Activated Carbon, 689 – 694, *Proc. 6th. Int. Conf. Fundamentals of Adsorption*, presqu'île de Giens, France, 24-28 May
- Do D. D. & Do H. D. (2001) Surface Diffusion of Hydrocarbons in Activated Carbon: Comparison between Constant Molar Flow, Differential Permeation and Differential Adsorption Bed Methods, *Adsorption*, **7**, 189 – 209
- Do D. D., Do H. D. & Prasetyo I. (2000) Constant Molar Flow Semi-Batch Adsorber as a Tool to Study Adsorption Kinetics of Pure Gases and Vapours, *Chem. Eng. Sci.*, **55**, 1717 – 1727
- Do D. D. & Mayfield P. L. J. (1987) A New Simplified Model for Adsorption in a Single Particle, *AIChE J.*, **33**, 1397 – 1400
- Do D. D. & Rice R. G. (1986) Validity of the Parabolic Profile Assumption in Adsorption Systems, *AIChE J.*, **32**, 149 – 154
- Do D. D. & Rice R. G. (1995) Revisiting Approximate Solutions for Batch Adsorbents: Explicit Half Time, *AIChE J.*, **41**, 426 – 429
- Do D. D. & Wang K. (1998) Dual Diffusion and Finite Mass Exchange Model for Adsorption Kinetics in Activated Carbon, *AIChE J.*, **44**, 68 – 82
- Do H. D. & Do D. D. (1998b) Maxwell-Stefan Analysis of Multicomponent Transient Diffusion in a Capillary and Adsorption of Hydrocarbons in Activated Carbon Particle, *Chem. Eng. Sci.*, **53**, 1239 – 1252
- Doğu G. & Ercan C. (1983) Dynamic Analysis of Adsorption on Bidisperse Porous Catalysts, *Canadian J. Chem. Eng.*, **61**, 660 – 664
- Doğu G., Keskin A. & Doğu T. (1987) Macropore and Micropore Effective Diffusion Coefficients from Dynamic Single-Pellet Experiments, *AIChE J.*, **33**, 322 – 324
- Doğu G. & Smith J. M. (1975) A Dynamic Method for Catalyst Diffusivities, *AIChE J.*, **21**, 58 – 61
- Doğu G. & Smith J. M. (1976) Rate Parameters from Dynamic Experiments with Single-Catalyst Pellets, *Chem. Eng. Sci.*, **31**, 123 – 135
- Dominguez J. A., Psaras D. & LaCava A. I. (1988) Langmuir Kinetics as an Accurate Simulation of the Rate of Adsorption of Oxygen and Nitrogen Mixtures on Non-Fickian Carbon Molecular Sieves, *AIChE Symp. Series*, No. 264, **84**, 73 – 82
- Doong S.-J. & Propsner P. (1998) Effect of Operation Symmetry on Pressure Swing Adsorption Process, *Adsorption*, **4**, 149 – 158

- Doong S.-J. & Yang R. T. (1986) Parametric Study of the Pressure Swing Adsorption Process for Gas Separation: A Criterion for Pore Diffusion Limitation, *Chem. Eng. Commun.*, **41**, 163 – 180
- Doong S.-J. & Yang R. T. (1987) Bidisperse Pore Diffusion Model for Zeolite Pressure Swing Adsorption, *AIChE J.*, **33**, 1045 – 1049
- Doong S.-J. & Yang R. T. (1988) The Role of Pressure Drop in Pressure Swing Adsorption, *AIChE Symp. Series*, No. 264, **84**, 145 – 154
- Dullien F. A. L. (1975) Invited Review: Single Phase Flow through Porous Media and Pore Structure, *Chem. Eng. J.*, **10**, 1 – 34
- Duncan W. L. & Möller K. P. (2002) The Effect of a Crystal Size Distribution on ZLC Experiments, *Chem. Eng. Sci.*, **57**, 2641 – 2652
- Earls D. E. & Long G. N. (1980) *Multiple Bed Rapid Pressure Swing Adsorption for Oxygen*, US Patent 4 194 891, March 25
- Eiç M. & Ruthven D. M. (1988) A New Experimental Technique for Measurement of Intracrystalline Diffusivity, *Zeolites*, **8**, 40 – 45
- Eiç M., Micke A., Kočirik M., Jama M. & Kikánová A. (2002) Diffusion and Immobilization Mechanisms in Zeolites Studied by ZLC Chromatography, *Adsorption*, **8**, 15 – 22
- Eriksson R. (1979) *Fractionating Apparatus*, US Patent 4 169 715, October 2
- Ergun S. (1952) Fluid Flow through Packed Columns, *Chem. Eng. Prog.*, **48**, 89 – 94
- Ergun S. & Orning A. A. (1949) Fluid Flow through Randomly Packed Columns and Fluidized Beds, *Ind. Eng. Chem.*, **41**, 1179 – 1184
- Evans J. W., Abbasi M. H. & Sarin A. (1980) A Monte Carlo Simulation of the Diffusion of Gases in Porous Solids, *J. Chem. Phys.*, **72**, 2967 – 2973
- Evans III R. B., Watson G. M. & Mason E. A. (1961) Gaseous Diffusion in Porous Media at Uniform Pressure, *J. Chem. Phys.*, **35**, 2076 – 2083
- Farooq S. (1995) Sorption and Diffusion of Oxygen and Nitrogen in Molecular Sieve RS-10, *Gas Sep. Purif.*, **9**, 205 – 212
- Farooq S. & Ruthven D. M. (1990a) Heat Effects in Adsorption Column Dynamics. 1. Comparison of One- and Two-Dimensional Models, *Ind. & Eng. Chem. Res.*, **29**, 1076 – 1084
- Farooq S. & Ruthven D. M. (1990b) A Comparison of Linear Driving Force and Pore Diffusion Models for a Pressure Swing Adsorption Bulk Separation Process, *Chem. Eng. Sci.*, **45**, 107 – 115
- Farooq S. & Ruthven D. M. (1991) Numerical Simulation of a Kinetically Controlled Pressure Swing Adsorption Bulk Separation Process based on a Diffusion Model, *Chem. Eng. Sci.*, **46**, 2213 – 2224
- Farooq S., Ruthven D. M. & Boniface H. A. (1989) Numerical Simulation of a Pressure Swing Adsorption Oxygen Unit, *Chem. Eng. Sci.*, **44**, 2809 – 2816
- Farooq S., Tharon C. & Ruthven D. M. (1998) Numerical Simulation of a Parallel-Passage Piston-Driven PSA Unit, *Sepr. & Purif. Tech.*, **13**, 181 – 193

- Feng C., Kostrov V. V. & Stewart W. E. (1974) Multicomponent Diffusion of Gases in Porous Solids. Models and Experiments, *Ind. Eng. Chem. Fundam.*, **13**, 5 – 9
- Feng C. & Stewart W. E. (1973) Practical Models for Isothermal Diffusion and Flow of Gases in Porous Solids, *Ind. Eng. Chem. Fundam.*, **12**, 143 – 147
- Fernandez G. F. & Kenney C. N. (1983) Modelling of the Pressure Swing Air Separation Process, *Chem. Eng. Sci.*, **38**, 827 – 834
- Foeth F., Bootsma E. S., Bosch H. & Reith T. (1995), Implementation of the Dynamics of a Rapid Pressure Swing Adsorption Model using the Numerical Method of Lines, 1 – 4, *Proc. Lezing Faculteit Polytechnique de Mons*, Mons, België, June 28
- Frost A. C. (1981) Measurement of Effective Diffusivity from Effluent Concentration of a Flow Through Diffusion Cell, *AIChE J.*, **27**, 813 – 818
- Gaskell P. H. & Lau A. K. C. (1988) Curvature-Compensated Convective Transport: SMART, A new Boundedness-Preserving Transport Algorithm, *Int. J. Num. Meth. Fluids*, **8**, 617 – 641
- Gelbin D. & Fiedler K. (1980) On the Concentration Dependence of Diffusion Coefficients in Zeolites, *AIChE J.*, **26**, 510 – 513
- Gladden L. F. (1991) Influence of Pellet Structure on Selectivity during Pressure Swing Adsorption Separations, *Chem. Eng. Sci.*, **46**, 2455 – 2464
- Gladden L. F. (1994) Review Article Number 46. Nuclear Magnetic Resonance in Chemical Engineering: Principles and Applications, *Chem. Eng. Sci.*, **49**, 3339 – 3408
- Gladden L. F. (2003) Magnetic Resonance: Ongoing and Future Role in Chemical Engineering Research, *AIChE J.*, **49**, 2 – 9
- Glueckauf E. (1955) Theory of Chromatography. Part 10.-Formulae for Diffusion into Spheres and their Application to Chromatography, *Trans. Faraday Soc.*, **51**, 1540 – 1551
- Glueckauf E. & Coates J. I. (1947) Theory of Chromatography. Part IV. The Influence of Incomplete Equilibrium on the Front Boundary of Chromatograms and on the Effectiveness of Separation, *J. Chem. Soc.*, 1315 – 1321
- Golden T. C., Golden C. M. A., Zwillig D. P. (2003) *Self-Supported Structured Adsorbent for Gas Separation*, US Patent 6 565 627, May 20
- Grenier Ph., Malka-Edery A. & Bourdin V. (1999) A Temperature Frequency Response Method for Adsorption Kinetics Measurements, *Adsorption*, **5**, 135 – 143
- Guan J. & Ye Z. (1990) Analog Circuit for Simulation of Pressure Swing Adsorption, *Chem. Eng. Sci.*, **45**, 3063 – 3069
- Guan J. & Ye Z. (1993) Analog Circuit for Simulation of Pressure Swing Adsorption: Kinetic Model, *Chem. Eng. Sci.*, **48**, 2821 – 2823
- Gunn D. J. (1987) Axial and Radial Dispersion in Fixed Beds, *Chem. Eng. Sci.*, **42**, 363 – 373
- Guo J., Shah D. B. & Talu O. (1998) Transport through a Single Commercial Adsorbent Pellet/Bead by Steady-state Wicke-Kallenbach Technique, 1195 – 1200, *Proc. 6th. Int. Conf. Fundamentals of Adsorption*, presqu'île de Giens, France, 24-28 May

- Harriot G. M. (1993) Memory-Integral Mass-Transfer Models for Adsorption Process Simulation, *AIChE J.*, **39**, 422 – 433
- Harriot G. M. (1996) Direct Finite Element Computation of Periodic Adsorption Processes, *Comp. Fluid Dyn.*, **7**, 201 – 211
- Hart J. & Thomas W. J. (1991) Gas Separation by Pulsed Pressure Swing Adsorption, *Gas Sep. Purif.*, **5**, 125 – 133
- Hartmann R. & Mersmann A. (1994) Simulation of Single Pellet Adsorption Kinetics with Experimentally Determined Dusty-Gas Coefficients, *Studies Surf. Sci. Catal.*, **84**, 1151 – 1158
- Hartzog D. G. & Sircar S. (1995) Sensitivity of PSA Process Performance to Input Variables, *Adsorption*, **1**, 133 – 151
- Hashimoto N. & Smith J. M. (1974) Diffusion in Bidisperse Porous Catalyst Pellets, *Ind. Eng. Chem. Fundam.*, **13**, 115 – 120
- Hassan M. M., Ruthven D. M. & Raghavan N. S. (1986) Air Separation by Pressure Swing Adsorption on a Carbon Molecular Sieve, *Chem. Eng. Sci.*, **41**, 1333 – 1343
- Haugaard J. & Livbjerg H. (1998) Models of Pore Diffusion in Porous Catalysts, *Chem. Eng. Sci.*, **53**, 2941 – 2948
- Hejtmánek V., Capek P. & Šolcová O., Schneider P. (1998) Dynamics of Pressure Build-up Accompanying Multicomponent Gas Transport in Porous Solids: Inert Gases, *Chem. Eng. J.*, **74**, 189 – 195
- Hejtmánek V., Capek P., Šolcová O. & Schneider P. (1999) Dynamics of Pressure Build-up Accompanying Multicomponent Gas Transport in Porous Solids: Adsorbable Gases, *Chem. Eng. J.*, **74**, 171 – 179
- Henry J. P., Chennakesavan B. & Smith J. M. (1961) Diffusion Rates in Porous Catalysts, *AIChE J.*, **7**, 10 – 12
- Henry J. P., Cunningham R. S. & Geankoplis C. J. (1967) Diffusion of Gases in Porous Solids over a Thousand-Fold Pressure Range, *Chem. Eng. Sci.*, **22**, 11 – 20
- Hirooka E., Wheatland J. P. & Doong S.-J. (1992) *Process for Producing Oxygen Enriched Product Stream*, US Patent 5 122 164, June 16
- Hirose T. & Minoda T. (1986) Periodic Steady-State Solution to Pressure Swing Adsorption with Short Cycle Time, *J. Chem. Eng. Japan*, **19**, 300 – 306
- Hirschfelder J. O., Curtiss C. F. & Bird R. B. (1954) *Molecular Theory of Gases and Liquids*, John Wiley and Sons, New York
- Hite R. H. & Jackson R. (1977) The Dynamical Behaviour of Catalyst Pellets in the Limiting Cases of Finely Porous and Coarsely Porous Structures, *Chem. Eng. Sci.*, **32**, 917 – 924
- Hofmann U., Loehr M. & Straub M. (1999) Sensitivity Analysis of PSA Processes Supported by Numerical Simulation, *AIChE Annual Meeting*, Dallas, Texas, USA, 31 October-5 November
- Hoogschagen J. (1953) Equal Pressure Diffusion in Porous Substances, *J. Chem. Phys.*, **21**, 2096 – 2097

- Hoogschagen J. (1955) Diffusion in Porous Catalysts and Adsorbents, *Ind. Eng. Chem.*, **47**, 906 – 913
- Hopfinger E. J. & Altman M. (1969) Experimental Verification of the Dusty-Gas Theory for Thermal Transpiration through Porous Media, *J. Chem. Phys.*, **50**, 2417 – 2428
- Horváth G., Kutics K. & Suzuki M. (1997) Adsorption Engineering. Hydrodynamics of PSA Columns, *NATO ASI Ser., Ser. C (Physical Adsorption: Experiment, Theory and Applications)*, **491**, 511 – 524
- Horváth G. & Suzuki M. (1998) Advanced Technical Tools for the Solution of High Capacity Adsorption Separation, *Stud. Surf. Sci. Catal. (Adsorption and its Applications in Industry and Environmental Protection)*, **120**, 275 – 300
- Hsiang T. C.-S. & Haynes H. W. (1977) Axial Dispersion in Small Diameter Beds of Large, Spherical Particles, *Chem. Eng. Sci.*, **32**, 678 – 681
- Hsuen H.-K. (2000) An Improved Linear Driving Force Approximation for Intraparticle Adsorption, *Chem. Eng. Sci.*, **55**, 3475 – 3480
- Huang W.-C. & Chou C.-T. (1997) A Moving Finite Element Simulation of a Pressure Swing Adsorption Process, *Comput. Chem. Eng.*, **21**, 301 – 315
- Huang W.-C. & Chou C.-T. (2003) Comparison of Radial- and Axial-Flow Rapid Pressure Swing Adsorption Processes, *Ind. Eng. Chem. Res.*, **42**, 1998 – 2006
- Incropera F. P. & DeWitt D. P. (1990) *Fundamentals of Heat and Mass Transfer (Third Edition)*, John Wiley and Sons, New York
- Ilavský J., Brunovská A. & Hlaváček V. (1980) Experimental Observation of Temperature Gradients occurring in a Single Zeolite Pellet, *Chem. Eng. Sci.*, **35**, 2475 – 2479
- Jackson R. (1977) *Transport in Porous Catalysts*, Elsevier, Amsterdam
- Jaffe S. M. & Contescu C. (2002a) Nanocomposite Parallel Passage Contactor for High Purity Separations, *AIChE Annual Meeting*, Indianapolis, Indiana, USA, 3-8 November
- Jaffe S. M., Contescu C. & Ritter J. A. (2002b) Zeolite Parallel Passage Contactor, *AIChE Annual Meeting*, Indianapolis, Indiana, USA, 3-8 November
- Jiangu G. & Zhenhua Y. (1990) Analog Circuit for Simulation of Pressure Swing Adsorption, *Chem. Eng. Sci.*, **45**, 3063 – 3069
- Jobic H. (2000) Diffusion of Linear and Branched Alkanes in ZSM-5. A Quasi-Elastic Neutron Scattering Study, *J. Molecular Catalysis A: Chemical*, **158**, 135 – 142
- Jobic H., Paoli H., Méthivier A., Ehlers G., Kärger J. & Krause C. (2003) Diffusion of *n*-hexane in 5A Zeolite Studied by the Neutron Spin-Echo and Pulsed-Field Gradient NMR techniques, *Microporous & Mesoporous Materials*, **59**, 113 – 121
- Johnson M. F. L. & Stewart W. E. (1965) Pore Structure and Gaseous Diffusion in Solid Catalysts, *J. Catalysis*, **4**, 248 – 252
- Jones R. L., Keller II G. E. & Wells R. C. (1980) *Rapid Pressure Swing Adsorption Process with High Enrichment Factor*, US Patent 4 194 892, March 25

- Jones R. L. & Keller II G. E. (1981) Pressure Swing Parametric Pumping - A New Adsorption Process, *J. Separ. Proc. Technol.*, **2**, 17 - 23
- Jordi R. G. & Do D. D. (1994) Analysis of the Frequency Response Method Applied to Non-Isothermal Sorption Studies, *Chem. Eng. Sci.*, **49**, 957 - 979
- June R. L., Bell A. T. & Theodorou D. N. (1990) Prediction of Low Occupancy Sorption of Alkanes in Silicalite, *J. Phys. Chem.*, **94**, 1508 - 1516
- June R. L., Bell A. T. & Theodorou D. N. (1992) Molecular Dynamics Studies of Butane and Hexane in Silicalite, *J. Phys. Chem.*, **96**, 1051 - 1060
- Jury S. H. (1967) An Improved Version of the Rate Equation for Molecular Diffusion in a Dispersed Phase, *AIChE J.*, **13**, 1124 - 1126
- Kaczmarzki K., Mazzotti M., Storti G. & Morbidelli M. (1997) Modeling Fixed-Bed Adsorption Columns through Orthogonal Collocations on Moving Finite Elements, *Comput. Chem. Eng.*, **21**, 641 - 660
- Kaiser L. G., Meersmann T., Logan J. W. & Pines A. (2000) Visualization of Gas Flow and Diffusion in Porous Media, *Proc. Natl. Acad. Sci. U.S.A.*, **97**, 2414 - 2418
- Kapoor A. & Yang R. T. (1989) Kinetic Separation of Methane-Carbon Dioxide Mixture by Adsorption on Molecular Sieve Carbon, *Chem. Eng. Sci.*, **44**, 1723 - 1733
- Kapteijn F., Bakker W. J. W., Zheng G., Poppe J. & Moulijn J. A. (1995) Permeation and Separation of Light Hydrocarbons through a Silicate-1 Membrane. Application of the Generalized Maxwell-Stefan Equations, *Chem. Eng. J.*, **57**, 145 - 153
- Kärger J. (2003) Measurement of Diffusion in Zeolites - A Never Ending Challenge?, *Adsorption*, **9**, 29 - 35
- Kärger J., Kočirik M. & Zikánová A. (1981) Molecular Transport through Assemblages of Microporous Particles, *J. Colloid & Interface Sci.*, **84**, 240 - 249
- Kärger J., Pfeifer H., Stallmach F. & Spindler H. (1990) ^{129}Xe NMR Self-Diffusion Measurements - A Novel Method to Probe Diffusional Barriers on the External Surface of Zeolite Crystallites, *Zeolites*, **10**, 288 - 292
- Kärger J., Pfeifer H., Stallmach F., Feoktistova N. & Zhdanov S. P. (1993) ^{129}Xe and ^{13}C PFG NMR Study of the Intracrystalline Self-Diffusion of Xe, CO_2 and CO, *Zeolites*, **13**, 50 - 55
- Kärger J., Stallmach F. & Vasenkov S. (2003) Structure-Mobility Relations of Molecular Diffusion in Nanoporous Materials, *Magnetic Resonance Imaging*, **21**, 185 - 191
- Kawazoe K. & Takeuchi Y. (1974) Mass Transfer in Adsorption on Bidisperse Porous Materials - Macro- and Micro-pore Series Diffusion Model, *J. Chem. Eng. Japan*, **7**, 431 - 437
- Kayser J. C. & Knaebel K. S. (1986) Pressure Swing Adsorption: Experimental Study of an Equilibrium Theory, *Chem. Eng. Sci.*, **41**, 2931 - 2938
- Keefer B. G. & McLean C. R. (2000) *High Frequency Rotary Pressure Swing Adsorption Apparatus*, US Patent 6 056 804, May 2

- Keefer B. G. & McLean C. R. (2003) *Life Support Oxygen Concentrator*, US Patent 6 514 319, February 4
- Kehoe J. P. G. & Butt J. B. (1972) Interactions of Inter- and Intraparticle Gradients in a Diffusion Limited Catalytic Reaction, *AIChE J.*, **18**, 347 - 355
- Keller II G. E. & Kuo C. A. (1982) *Enhanced Gas Separation by Selective Adsorption*, US Patent 4 354 859, October 19
- Kenney C. N. (1989) The Bed Dynamics of Pressure Swing Adsorption, 273 - 286, *Separation of Gases: Proc. 5th. BOC Priestley Conf.*, Birmingham, England, 19-21 September
- Kiil S. & Bhatia S. K. (1998) Solution of Adsorption Problems involving Steep Moving Profiles, *Comput. Chem. Eng.*, **22**, 893 - 896
- Kikkinides E. S. & Yang R. T. (1993) Effects of Bed Pressure Drop on Isothermal and Adiabatic Adsorber Dynamics, *Chem. Eng. Sci.*, **48**, 1545 - 1555
- Kim D. H. (1990) Single Effective Diffusivities for Dynamic Adsorption in Bidisperse Adsorbents, *AIChE J.*, **36**, 302 - 306
- Kim J.-N., Chue K.-T., Cho S.-H. & Kim J.-D. (1995) Production of High-Purity Nitrogen from Air by Pressure Swing Adsorption on Zeolite X, *Sepr. Sci. Tech.*, **30**, 347 - 368
- Knaebel K. S. & Hill F. B. (1985) Pressure Swing Adsorption: Development of an Equilibrium Theory for Gas Separations, *Chem. Eng. Sci.*, **40**, 2351 - 2360
- Ko D. & Moon I. (2000) Optimization of Start-up Operating Condition in RPSA, *Sepr. & Purif. Tech.*, **21**, 17 - 26
- Ko D. & Moon I. (2002) Multiobjective Optimization of Cyclic Adsorption Processes, *Ind. Eng. Chem. Res.*, **41**, 93 - 104
- Ko D., Siriwardane R. & Biegler L. T. (2002) Optimization of PSA using Zeolite 13X for CO_2 Sequestration, *AIChE Annual Meeting*, Indianapolis, Indiana, USA, 3-8 November
- Ko D., Siriwardane R. & Biegler L. T. (2003) Optimization of a Pressure-Swing Adsorption Process using Zeolite 13X for CO_2 Sequestration, *Ind. Eng. Chem. Res.*, **42**, 339 - 348
- Kolaczowski S. T. & Ullah U. (1989) Measurement of Effective Diffusivities using a Spinning Basket Reactor, *Chem. Eng. Sci.*, **44**, 2843 - 2852
- Kowler D. E. & Kadlec R. H. (1972) The Optimal Control of a Periodic Adsorber, *AIChE J.*, **18**, 1207 - 1219
- Kreyszig E. (1993) *Advanced Engineering Mathematics (Seventh Edition)*, John Wiley and Sons, Singapore
- Krishna R. (1990) Multicomponent Surface Diffusion of Adsorbed Species: A Description based on the Generalized Maxwell-Stefan Equations, *Chem. Eng. Sci.*, **45**, 1779 - 1791
- Krishna R. (1993a) Problems and Pitfalls in the use of the Fick Formulation for Intraparticle Diffusion, *Chem. Eng. Sci.*, **48**, 845 - 861

- Krishna R. (1993b) A Unified Approach to the Modelling of Intraparticle Diffusion in Adsorption Processes, *Gas Sep. Purif.*, **7**, 91 – 104
- Krishna R. (1995) Experimental Verification of the Maxwell-Stefan Theory for Micropore Diffusion, *Chem. Eng. Sci.*, **50**, 2507 – 2522
- Krishna R. & Van den Broeke L. J. P. (1995) The Maxwell-Stefan Description of Mass Transport across Zeolite Membranes, *Chem. Eng. J.*, **57**, 155 – 162
- Krishna R., Vlugt T. J. H. & Smit B. (1999) Influence of Isotherm Inflection on Diffusion in Silicalite, *Chem. Eng. Sci.*, **54**, 1751 – 1757
- Krishna R. & Wesselingh J. A. (1997) Review Article Number 50. The Stefan-Maxwell Approach to Mass Transfer, *Chem. Eng. Sci.*, **52**, 861 – 911
- Kulish S. & Swank R. P. (1998) *Rapid Cycle Pressure Swing Adsorption Oxygen Concentration Method and Apparatus*, US Patent 5 827 358, October 27
- Kulish S. & Swank R. P. (2000) *Rapid Cycle Pressure Swing Adsorption Oxygen Concentration Method and Apparatus*, US Patent 6 068 680, May 30
- Kumar R. (1996) Vacuum Swing Adsorption Process for Oxygen Production - A Historical Perspective, *Sepr. Sci. Tech.*, **31**, 877 – 893
- Kumar R., Fox V. G., Hartzog D. G., Larson R. E., Chen Y. C., Houghton P. A. & Naheiri T. (1994) A Versatile Process Simulator for Adsorptive Separations, *Chem. Eng. Sci.*, **49**, 3115 – 3125
- Kvamsdal H. M. & Hertzberg T. (1997) Optimization of PSA Systems - Studies on Cyclic Steady State Convergence, *Comput. Chem. Eng.*, **8**, 819 – 832
- Labouriau A., Pietrass T, Weber W. A, Gates B. C. & Earl W. L. (1999) Temperature Dependence of Nuclear Magnetic Resonance Chemical Shifts of ^{129}Xe in the α -Cages of NaY Zeolite, *J. Phys. Chem. B*, **103**, 4323 – 4329
- LaCava A. I. & Lemcoff N. O. (1996) Single Bed Pressure Swing Adsorption Process to Generate High Purity Nitrogen, *Gas Sep. Purif.*, **10**, 113 – 115
- LaCava A. I. & Krishnan S. V. (1998) Thermal Effects of Compression and Expansion of Gas in a Pressure Swing Adsorption Process, 787 – 792, *Proc. 6th. Int. Conf. Fundamentals of Adsorption*, presqu'île de Giens, France, 24-28 May
- Lai C.-C. & Tan C.-S. (1991) Approximate Models for Nonlinear Adsorption in a Packed-Bed Adsorber, *AIChE J.*, **37**, 461 – 465
- Langer G., Roethe A., Roethe K.-P. & Gelbin D. (1978) Heat and Mass Transfer in Packed Beds - III. Axial Mass Dispersion, *Int. J. Heat & Mass Transfer*, **21**, 751 – 759
- Lee I.-L. & Kadlec R. H. (1988) Effects of Adsorbent and Catalyst Distributions in Pressure Swing Reactors, *AIChE Symp. Series*, No. 264, **84**, 167 – 176
- Leis J. R. & Kramer M. A. (1988) The Simultaneous Solution and Sensitivity Analysis of Systems described by Ordinary Differential Equations, *ACM Transactions Mathematical Software*, **14**, 45 – 60

- Leonard B. P. (1979) A Stable and Accurate Convective Modelling Procedure based on Quadratic Upstream Interpolation, *Comp. Meth. Appl. Mech. & Eng.*, **19**, 59 – 98
- LeVan M. D. (1998) Adsorption Process and Modeling: Present and Future, 19 – 29, *Proc. 6th. Int. Conf. Fundamentals of Adsorption*, presqu'île de Giens, France, 24-28 May
- LeVan M. D. & Vermeulen T. (1984) Channeling and Bed-diameter Effects in Fixed-bed Adsorber Performance, *AIChE Symp. Series*, No. 233, **80**, 34 – 43
- Li Z. & Yang R. T. (1999) Concentration Profile for Linear Driving Force Model for Diffusion in a Particle, *AIChE J.*, **45**, 196 – 200
- Liao H.-S. & Shiau C.-Y. (2000) Analytical Solution to an Axial Dispersion Model for the Fixed-Bed Adsorber, *AIChE J.*, **46**, 1168 – 1176
- Liaw C. H., Wang J. S. P., Greenkorn R. A. & Chao K. C. (1979) Kinetics of Fixed-Bed Adsorption: A New Solution, *AIChE J.*, **25**, 376 – 381
- Loos J.-B. W. P., Verheijen P. J. T. & Moulijn J. A. (2000) Improved Estimation of Zeolite Diffusion Coefficients from Zero-Length Column Experiments, *Chem. Eng. Sci.*, **55**, 51 – 65
- Lu Y., Acharya D. R., Shirley A. I. & Lemcoff N. O. (2003) *Adsorption Processes*, US Patent 6 503 297, January 7
- Lu Z. P., Loureiro J. M., LeVan M. D. & Rodrigues A. E. (1992) Intraparticle Convection Effect on Pressurization and Blowdown of Adsorbers, *AIChE J.*, **38**, 857 – 867
- Lu Z. P., Loureiro J. M., LeVan M. D. & Rodrigues A. E. (1993a) Pressure Swing Adsorption Processes: Intraparticle Diffusion/Convection Models, *Ind. & Eng. Chem. Res.*, **32**, 2740 – 2751
- Lu Z. P., Loureiro J. M., Rodrigues A. E. & LeVan M. D. (1993b) Pressurization and Blowdown of Adsorption Beds-II. Effect of the Momentum and Equilibrium Relations on Isothermal Operation, *Chem. Eng. Sci.*, **48**, 1699 – 1707
- Lust K., Roose D., Spence A. & Champneys A. R. (1998) An Adaptive Newton-Picard Algorithm with Subspace Iteration for Computing Periodic Solutions, *SIAM J. Sci. Comput.*, **19**, 1188 – 1209
- Ma Y. H. & Lee T. Y. (1976) Transient Diffusion in Solids with a Bipore Distribution, *AIChE J.*, **22**, 147 – 152
- Macdonald I. F., El-Sayed M. S. & Dullien F. A. L. (1979) Flow through Porous Media - the Ergun Equation Revisited, *Ind. Eng. Chem. Fundam.*, **18**, 199 – 208
- Macdougall H., Ruthven D. M. & Brandani S. (1999) Sorption and Diffusion of SF_6 in Silicalite Crystals, *Adsorption*, **5**, 369 – 372
- Maginn E. J., Bell A. T. & Theodorou D. N. (1996) Dynamics of Long n -Alkanes in Silicalite: A Hierarchical Simulation Approach, *J. Phys. Chem.*, **100**, 7155 – 7173
- Maheshwary A., Wang B. B., Ambriano J. R. & Thomson T. P. (2001) *Oxygen Production*, US Patent 6 524 370, June 15
- Marlin T. E. (1995) *Process Control: Designing Processes and Control Systems for Dynamic Performance*, McGraw-Hill, Singapore

- Mason E. A. & Evans III R. B. (1969) Graham's Laws: Simple Demonstrations of Gases in Motion. Part 1, Theory, *J. Chem. Ed.*, **46**, 358 – 364
- Mason E. A. & Kronstadt B. (1967) Graham's Laws of Diffusion and Effusion, *J. Chem. Ed.*, **44**, 740 – 744
- Mason E. A. & Malinauskas A. P. (1983) *Gas Transport in Porous Media: The Dusty-Gas Model*, Elsevier, Amsterdam
- Matz M. J. & Knaebel K. S. (1988) Pressure Swing Adsorption: Effects of Incomplete Purge, *AIChE J.*, **34**, 1486 – 1492
- Mayfield P. L. J. & Do D. D. (1991) Measurement of Single-Component Adsorption Kinetics of Ethane, Butane, and Pentane onto Activated Carbon using a Differential Adsorption Bed, *Ind. Eng. Chem. Res.*, **30**, 1262 – 1270
- McCabe W. L., Smith J. C. & Harriott P. (1993) *Unit Operations of Chemical Engineering (Fifth Edition)*, McGraw-Hill, New York
- McDaniel P. L., Coe C. G., Kärger J. & Moyer J. D. (1996) Direct Observation of N₂ Self-Diffusion in Zeolitic Adsorbents Using ¹⁵N PFG NMR, *J. Phys. Chem.*, **100**, 16263 – 16267
- Mendes A. M. M. (1993) *Pressure Swing Adsorption: Application to the Separation of Oxygen from Air*, Ph.D. Dissertation, University of Porto, Portugal
- Mendes A. M. M., Costa C. A. V. & Rodrigues A. E. (1994) Linear Driving Force Approximation for Diffusion in Spherical Adsorbents with Binary Non-linear Adsorption, *Gas Sep. Purif.*, **8**, 229 – 236
- Mendes A. M. M., Costa C. A. V. & Rodrigues A. E. (1995) Linear Driving Force Approximation for Non-Isobaric Diffusion/Convection with Binary Langmuir Adsorption, *Gas Sep. Purif.*, **9**, 259 – 270
- Mendes A. M. M., Costa C. A. V. & Rodrigues A. E. (1996) Extension of the Linear Driving Force - Dusty Gas Model Approximation to include Surface or Micropore Diffusion, *Gas Sep. Purif.*, **10**, 141 – 148
- Mendes A. M. M., Costa C. A. V. & Rodrigues A. E. (2001a) PSA Simulation using Particle Complex Models, *Sepr. & Purif. Tech.*, **24**, 1 – 11
- Mendes A. M. M., Costa C. A. V. & Rodrigues A. E. (2001b) Oxygen Separation from Air by PSA: Modelling and Experimental Results Part I: Isothermal Operation, *Sepr. & Purif. Tech.*, **24**, 173 – 188
- Michael K. (1997) Industrial Gas: Surveying Onsite Supply Options, *Chemical Engineering*, January, 72 – 79
- Miller G. W. (1987) Adsorption of Nitrogen, Oxygen, Argon, and Ternary Mixtures of these Gases in 13X Molecular Sieve, *AIChE Symp. Series*, No. 259, **83**, 28 – 39
- Miller G. W. & Theis C. F. (1989) *Secondary Oxygen Purifier for Molecular Sieve Oxygen Concentrator*, US Patent 4 813 979, March 21
- Miller K. (1981) Moving Finite Elements. II, *SIAM J. Numer. Anal.*, **18**, 1033 – 1057

- Miller K. & Miller R. N. (1981) Moving Finite Elements. I, *SIAM J. Numer. Anal.*, **18**, 1019 – 1032
- Mohamadinejad H., Knox J. C. & Smith J. E. (2000) Experimental and Numerical Investigation of Adsorption/Desorption in Packed Sorption Beds under Ideal and Nonideal Flows, *Sepr. Sci. Tech.*, **35**, 1 – 22
- Morton K. W. (1996) *Numerical Solution of Convection-Diffusion Problems*, Chapman & Hall, London
- Mugge J., Bosch H. & Reith T. (2000) Gas Adsorption in Activated Carbon, 451 – 455, *Proc. 2nd. Pacific Basin Conf. Adsorption Sci. and Tech.*, Brisbane, Queensland, Australia, 14-18 May
- Mugge J., Bosch H. & Reith T. (2001) Measuring and Modelling Gas Adsorption Kinetics in Single Porous Particles, *Chem. Eng. Sci.*, **56**, 5351 – 5360
- Murray J. W. (1996) *Air Separation by Rapid Pressure Swing Adsorption*, Ph.D. Dissertation, University of Cambridge, England
- Myers A. L. (1983) Activity Coefficients of Mixtures Adsorbed on Heterogeneous Surfaces, *AIChE J.*, **29**, 691 – 693
- Myers A. L. & Prausnitz J. M. (1965) Thermodynamics of Mixed-Gas Adsorption, *AIChE J.*, **11**, 121 – 127
- Nakano Y. & Evans J. W. (1983) Monte Carlo Simulation of Diffusion of Gases in a Porous Solid: Calculations for a New Class of Solids, *J. Chem. Phys.*, **78**, 2568 – 2572
- Nakao S.-I. & Suzuki M. (1983) Mass Transfer Coefficient in Cyclic Adsorption and Desorption, *J. Chem. Eng. Japan*, **16**, 114 – 119
- Naphtali L. M. & Polinski L. M. (1963) A Novel Technique For Characterization Of Adsorption Rates On Heterogeneous Surfaces, *J. Phys. Chem.*, **67**, 369 – 375
- Neale G. H. & Nader W. K. (1973) Prediction of Transport Processes within Porous Media: Diffusive Flow Processes within an Homogeneous Swarm of Spherical Particles, *AIChE J.*, **19**, 112 – 119
- Nguyen C. & Do D. D. (2000) Dual Langmuir Kinetic Model for Adsorption in Carbon Molecular Sieve Materials, *Langmuir*, **16**, 1868 – 1873
- Nijhuis T. A., Van den Broeke L. J. P., Van de Graaf J. M., Kapteijn F., Makkee M. & Moulijn J. A. (1997) Bridging the Gap between Macroscopic and NMR Diffusivities, *Chem. Eng. Sci.*, **52**, 3401 – 3404
- Nilchan S. & Pantelides C. C. (1998) On the Optimisation of Periodic Adsorption Processes, *Adsorption*, **4**, 113 – 147
- Niven R. K. (2002) Physical Insight into the Ergun and Wen & Yu Equations for Fluid Flow in Packed and Fluidised Beds, *Chem. Eng. Sci.*, **57**, 527 – 534
- Noordhoek N. J., van Ijzendoorn L. J., Anderson B. G., de Gauw F. J. M. M., van Santen R. A. & de Voigt M. J. A. (1998) Mass Transfer of Alkanes in Zeolite Packed-Bed Reactors Studied with Positron Emission Profiling. 2. Modeling, *Ind. & Eng. Chem. Res.*, **37**, 825 – 833

- Notaro F., Ackley M. W. & Smolarek J. (1999) Recover Industrial Gases via Adsorption, *Chemical Engineering*, April, 104 – 108
- Novák M., Ehrhardt K., Klusáček K. & Schneider P. (1988) Dynamics of Non-Isobaric Diffusion in Porous Catalysts, *Chem. Eng. Sci.*, **43**, 185 – 193
- Nowak A. K., den Ouden C. C. J., Pickett S. D., Smit B., Cheetham A. K., Post M. F. M. & Thomas J. M. (1991) Mobility of Adsorbed Species in Zeolites: Methane, Ethane, and Propane Diffusivities, *J. Phys. Chem.*, **95**, 848 – 854
- O'Shea J. D. & Liapis A. I. (1990) Evaluation of Simple and Complex Models for Mass Transfer in the Nonisothermal Gas Adsorption of Multiple Adsorbates in a Single Adsorbent Particle, *Trans. IChemE, Chem. Eng. Res. Des.*, **68A**, 242 – 250
- Oh M. & Pantelides C. C. (1996) A Modelling and Simulation Language for Combined Lumped and Distributed Parameter Systems, *Comput. Chem. Eng.*, **20**, 611 – 633
- Onyestyák G., Valyon J. & Rees L. V. C. (2000) Frequency-Response Study of Ammonia Sorption in Zeolites A, X and Y. 477 – 481, *Proc. 2nd. Pacific Basin Conf. Adsorption Sci. and Tech.*, Brisbane, Queensland, Australia, 14-18 May
- Palekar M. G. & Rajadhyaksha R. A. (1985) Sorption in Zeolites - I Sorption of Single Component and Binary Sorbate Systems, *Chem. Eng. Sci.*, **40**, 1085 – 1091
- Pan C. Y. & Basmadjian D. (1967) Constant Pattern Adiabatic Fixed-Bed Adsorption, *Chem. Eng. Sci.*, **22**, 285 – 297
- Park J.-H., Kim J.-D., Kim J.-N. & Cho S.-H. (1999) Analysis of Equilibrium PSA Performance with an Analytical Solution, *Adsorption*, **5**, 245 – 259
- Park J.-H., Kim J.-N. & Cho S.-H. (2000) Performance Analysis of Four-Bed H₂ PSA Process using Layered Beds, *AIChE J.*, **46**, 790 – 802
- Parkinson G., D'Aquino R. & Ondrey G. (1999) O₂ Breathes New Life into Processes, *Chemical Engineering*, September, 28 – 31
- Pel L., Valckenborg R. M. E., Kopinga K., Aarden F. B. & Kerkhof P. J. A. M. (2003) Nitrobenzene Adsorption in Activated Carbon as Observed by NMR, *AIChE J.*, **49**, 232 – 236
- Pentchev I., Paev K. & Seikova I. (2002) Dynamics of Non-Isothermal Adsorption in Packed Beds of Biporous Zeolites, *Chem. Eng. J.*, **85**, 245 – 257
- Petzold L. (1983) Automatic Selection of Methods for Solving Stiff and Nonstiff Systems of Ordinary Differential Equations, *SIAM J. Sci. Stat. Comput.*, **4**, 136 – 148
- Pollard W.G. & Present R. D. (1948) On Gaseous Self-Diffusion in Long Capillary Tubes, *Phys. Rev.*, **73**, 762 – 774
- Potter M. C. & Wiggert D. C. (1991) *Mechanics of Fluids*, Prentice-Hall, New Jersey
- Prasetyo I. & Do D. D. (1998) Adsorption Rate of Methane and Carbon Dioxide on Activated Carbon by the Semi-Batch Constant Molar Flow Rate Method, *Chem. Eng. Sci.*, **19**, 3459 – 3467
- Present R. D. (1958) *Kinetic Theory of Gases*, McGraw-Hill, New York

- Pritchard C. L. & Simpson G. K. (1986) Design of an Oxygen Concentrator using the Rapid Pressure-Swing Adsorption Principle, *Chem. Eng. Res. Des.*, **64**, 467 – 472
- Qinglin H., Sundaram S. M. & Farooq S. (2003) Revisiting Transport of Gases in the Micropores of Carbon Molecular Sieves, *Langmuir*, **19**, 393 – 405
- Raghavan N. S., Hassan M. M. & Ruthven D. M. (1986) Numerical Simulation of a PSA System using a Pore Diffusion Model, *Chem. Eng. Sci.*, **41**, 2787 – 2793
- Rasmuson A. (1981) Exact Solution of a Model for Diffusion and Transient Adsorption in Particles and Longitudinal Dispersion in Packed Beds, *AIChE J.*, **27**, 1032 – 1035
- Rasmuson A. (1982) Time Domain Solutions of a Model for Transport Processes in Bidisperse Structured Catalysts, *Chem. Eng. Sci.*, **37**, 787 – 788
- Rasmuson A. & Neretnieks I. (1980) Exact Solution of a Model for Diffusion in Particles and Longitudinal Dispersion in Packed Beds, *AIChE J.*, **26**, 686 – 690
- Reed D. A. & Ehrlich G. (1981) Surface Diffusion, Atomic Jump Rates and Thermodynamics, *Surface Science*, **102**, 588 – 609
- Reid R. C. & Prausnitz J. M., Poling B. E. (1987) *The Properties of Gases and Liquids*, (Fourth Edition), McGraw-Hill, New York
- Reyes S. & Jensen K. F. (1985) Estimation of Effective Transport Coefficients in Porous Solids based on Percolation Concepts, *Chem. Eng. Sci.*, **40**, 1723 – 1734
- Reyes S. C. & Iglesia E. (1991) Effective Diffusivities in Catalyst Pellets: New Model Porous Structures and Transport Simulation Techniques, *J. Catalysis*, **129**, 457 – 472
- Riekert L. (1971) Rates of Sorption and Diffusion of Hydrocarbons in Zeolites, *AIChE J.*, **17**, 446 – 454
- Rittig F., Coe C. G. & Zielinski J. M. (2002) Predicting Gas Transport in Formed Zeolite Adsorbents from NMR Studies, *J. American Chem. Soc.*, **124**, 5264 – 5265
- Rittig F., Coe C. G. & Zielinski J. M. (2003) Pure and Multicomponent Gas Diffusion within Zeolitic Adsorbents: Pulsed Field Gradient NMR Analysis and Model Development, *J. Phys. Chem. B*, **107**, 4560 – 4566
- Robinson H. & Lillerud K. P. (2001) *Verified Synthesis of Zeolitic Materials (Second Edition)*, Elsevier, Amsterdam
- Rosen J. B. (1952) Kinetics of a Fixed Bed System for Solid Diffusion into Spherical Particles, *J. Chem. Phys.*, **20**, 387 – 394
- Rota R. & Wankat P. C. (1990) Intensification of Pressure Swing Adsorption Processes, *AIChE J.*, **36**, 1299 – 1312
- Runnebaum R. C. & Magim. E. J. (1997) Molecular Dynamics Simulations of Alkanes in the Zeolite Silicalite: Evidence for Resonant Diffusion Effects, *J. Phys. Chem. B*, **101**, 6394 – 6408
- Ruckenstein E., Vaidyanathan A. S. & Youngquist G. R. (1971) Sorption by Solids with Bidisperse Pore Structures, *Chem. Eng. Sci.*, **26**, 1305 – 1318

- Rutherford S. W. & Coons J. E. (2002) Adsorption Dynamics of Carbon Dioxide and Methane in Molecular Sieving Carbon. *AIChE Annual Meeting*, Indianapolis, Indiana, USA, 3-8 November
- Rutherford S. W. & Do D. D. (1999) Knudsen, Slip, and Viscous Permeation in a Carbonaceous Pellet, *Ind. Eng. Chem. Res.*, **38**, 565 – 570
- Rutherford S. W. & Do D. D. (2000) Characterization of Carbon Molecular Sieve 3A, *Langmuir*, **16**, 7245 – 7254
- Ruthven D. M. (1976) Sorption of Oxygen, Nitrogen, Carbon Monoxide, Methane, and Binary Mixtures of these Gases in 5A Molecular Sieve, *AIChE J.*, **22**, 753 – 759
- Ruthven D. M. (1984a) *Principles of Adsorption and Adsorption Processes*, John Wiley and Sons, New York
- Ruthven D. M. (1984b) Intracrystalline Diffusion in Zeolites and Carbon Molecular Sieves, *AIChE Symp. Series*, No. 253, **80**, 21 – 33
- Ruthven D. M. (2000) Commentaries. Past Progress and Future Challenges in Adsorption Research, *Ind. & Eng. Chem. Res.*, **39**, 2127 – 2131
- Ruthven D. M. & Doetsch I. H. (1976) Diffusion of Hydrocarbons in 13X Zeolite, *AIChE J.*, **22**, 882 – 886
- Ruthven D. M. & Farooq S. (1990) Air Separation by Pressure Swing Adsorption, *Gas Sep. Purif.*, **4**, 141 – 148
- Ruthven D. M., Farooq S. & Knaebel K. S. (1994) *Pressure Swing Adsorption*, VCH Publishers, New York
- Ruthven D. M., Garg D. R. & Crawford R. M. (1975) The Performance of Molecular Sieve Adsorption Columns: Non-isothermal Systems, *Chem. Eng. Sci.*, **30**, 803 – 810
- Ruthven D. M., Lee L. K. & Yucel H. (1980) Kinetics of Non Isothermal Sorption in Molecular Sieve Crystals, *AIChE J.*, **26**, 16 – 23
- Ruthven D. M. & Loughlin K. F. (1971) The Effect of Crystalline Shape and Size Distribution on Diffusion Measurements in Molecular Sieve, *Chem. Eng. Sci.*, **26**, 577 – 584
- Ruthven D. M. & Loughlin K. F. (1972) The Diffusional Resistance of Molecular Sieve Pellets, *Canadian J. Chem. Eng.*, **50**, 550 – 552
- Ruthven D. M. & Xu Z. (1993) Diffusion of Oxygen and Nitrogen in 5A Zeolite Crystals and Commercial 5A Pellets, *Chem. Eng. Sci.*, **48**, 3307 – 3312
- Satterfield C. N. & Sherwood T. K. (1963) *The Role of Diffusion in Catalysis*, Addison-Wesley Publishing, Massachusetts
- Schalles D. G. & Danner R. P. (1988) Adsorption of Oxygen and Nitrogen on Carbon Molecular Sieve Type 3A, *AIChE Symp. Series*, No. 264, **84**, 83 – 88
- Schneider P. (1978) Multicomponent Isothermal Diffusion and Forced Flow in Capillaries, *Chem. Eng. Sci.*, **33**, 1311 – 1319

- Schneider P. & Gelbin D. (1985) Direct Transport Parameters Measurement versus their Estimation from Mercury Penetration in Porous Solids, *Chem. Eng. Sci.*, **40**, 1093 – 1099
- Scholl S. E. & Mersmann A. B. (1991a) Influence of Intraparticle Total Pressure Change on Pore Mass Transport, *Chem. Eng. Technol.*, **14**, 213 – 218
- Scholl S. E. & Mersmann A. B. (1991b) On Intraparticle Total Pressure Change during Gas Phase Adsorption, *Gas Sep. Purif.*, **5**, 77 – 82
- Scott D. M. (1991) Similarity Solutions for Pressurisation and Depressurisation with a Two-Component Gas in an Adsorbing Bed, *Chem. Eng. Sci.*, **46**, 2977 – 2982
- Scott D. M. (1993) Effects of Bed Pressure Drop on Adsorption and Desorption with Langmuir Isotherms, *Chem. Eng. Sci.*, **48**, 3001 – 3006
- Scott D. M. (1994) The Linear Driving Force Model for Cyclic Adsorption and Desorption: The Effect of Shape, *Chem. Eng. Sci.*, **49**, 914 – 916
- Scott D. S. & Dullien F. A. L. (1962) Diffusion of Ideal Gases in Capillaries and Porous Solids, *AIChE J.*, **8**, 113 – 117
- Scott D. S., Lee W. & Papa J. (1974) The Measurement of Transport Coefficients in Gas-Solid Heterogeneous Reactions, *Chem. Eng. Sci.*, **29**, 2155 – 2167
- Serbezov A. (1997) *Adsorptive Separation of Multicomponent Gaseous Mixtures*, Ph.D. Dissertation, University of Rochester, USA
- Serbezov A. & Sotirchos S. V. (1997a) Multicomponent Transport Effects in Sorbent Particles under Pressure Swing Conditions, *Ind. & Eng. Chem. Res.*, **36**, 3002 – 3012
- Serbezov A. & Sotirchos S. V. (1997b) Mathematical Modelling of the Adsorptive Separation of Multicomponent Gaseous Mixtures, *Chem. Eng. Sci.*, **52**, 79 – 91
- Serbezov A. & Sotirchos S. V. (1998) Mathematical Modeling of Multicomponent Nonisothermal Adsorption in Sorbent Particles under Pressure Swing Conditions, *Adsorption*, **4**, 93 – 111
- Serbezov A. & Sotirchos S. V. (1999) Particle-Bed Model for Multicomponent Adsorption-based Separations: Application to Pressure Swing Adsorption, *Chem. Eng. Sci.*, **54**, 5647 – 5666
- Sereno C., Rodrigues A. & Villadsen J. (1991) The Moving Finite Element Method with Polynomial Approximation of Any Degree, *Comput. & Chem. Eng.*, **15**, 25 – 33
- Sereno C. & Rodrigues A. (1993) Can Steady-State Momentum Equations be used in Modelling Pressurization of Adsorption Beds?, *Gas Sep. Purif.*, **7**, 167 – 174
- Sharma R. K., Creswell D. L. & Newson E. J. (1991) Effective Diffusion Coefficients and Tortuosity Factors for Commercial Catalysts, *Ind. & Eng. Chem. Res.*, **30**, 1428 – 1433
- Sheikh J., Kershenbaum L. S. & Alpay E. (2001) 1-Butene Dehydrogenation in Rapid Pressure Swing Reaction Processes, *Chem. Eng. Sci.*, **56**, 1511 – 1516
- Shelley S. (1991), Out of Thin Air: Noncryogenic Air Separation is not new, but it is Changing the way Atmospheric Gases are used, *Chemical Engineering*, June, 30 – 39

- Shendalam L. H. & Mitchell J. E. (1972) A Study of Heatless Adsorption in the Model System CO₂ in He, I, *Chem. Eng. Sci.*, **27**, 1449 – 1458
- Shin H.-S., Kim D.-H., Koo K.-K. & Lee T.-S. (2000) Performance of a Two-Bed Pressure Swing Adsorption Process with Incomplete Pressure Equalization, *Adsorption*, **6**, 233 – 240
- Shin H.-S. & Knaebel K. S. (1988) Pressure Swing Adsorption: An Experimental Study of Diffusion-Induced Separation, *AIChE J.*, **34**, 1409 – 1416
- Sieder E. N. & Tate G. E. (1936) Heat Transfer and Pressure Drop of Liquids in Tubes, *Ind. Eng. Chem.*, **28**, 1429 – 1435
- Singh K. & Jones J. (1997) Numerical Simulation of Air Separation by Piston-Driven Pressure Swing Adsorption, *Chem. Eng. Sci.*, **52**, 3133 – 3145
- Sircar S. (1983) Linear-Driving-Force Model for Non-Isothermal Gas Adsorption Kinetics, *J. Chem. Soc., Faraday Trans. 1.*, **79**, 785 – 796
- Sircar S. (1985) Excess Properties and Thermodynamics of Multicomponent Gas Adsorption, *J. Chem. Soc., Faraday Trans. 1.*, **81**, 1527 – 1540
- Sircar S. (1991) *Gas Separation by Rapid Pressure Swing Adsorption*, US Patent 5 071 449, December 10
- Sircar S. (1994) Non-Isothermal Differential Adsorption Kinetics for Binary Gas Mixture, *Ind. & Eng. Chem. Res.*, **33**, 1585 – 1592
- Sircar S. (1996) Production of Oxy-Rich Air by RPSA for Combustion Use, *Adsorption*, **2**, 323 – 326
- Sircar S. (1999) Gibbsian Surface Excess for Gas Adsorption - Revisited, *Ind. & Eng. Chem. Res.*, **38**, 3670 – 3682
- Sircar S. (2001) Applications of Gas Separation by Adsorption for the Future, *Adsorption Science & Technology*, **19**, 347 – 366
- Sircar S. (2002) Commentaries. Pressure Swing Adsorption, *Ind. Eng. Chem. Res.*, **41**, 1389 – 1392
- Sircar S. & Hanley B. F. (1995) Production of Oxygen Enriched Air by Rapid Pressure Swing Adsorption, *Adsorption*, **1**, 313 – 320
- Sircar S. & Hufton J. R. (2000) Intraparticle Adsorbate Concentration Profile for Linear Driving Force Model, *AIChE J.*, **46**, 659 – 660
- Sircar S. & Kumar R. (1984) Non-isothermal Surface Barrier Model for Gas Sorption Kinetics on Porous Adsorbents, *J. Chem. Soc., Faraday Trans. 1.*, **80**, 2489 – 2507
- Smit B. & den Ouden C. C. J. (1988) Monte Carlo Simulations on the Relation between the Structure and Properties of Zeolites: The Adsorption of Small Hydrocarbons, *J. Phys. Chem.*, **92**, 7169 – 7171
- Smith J. M., Van Ness H. C. & Abbott M. M. (1996) *Introduction to Chemical Engineering Thermodynamics (Fifth Edition)*, McGraw-Hill, New York

- Smith IV O. J. & Westerberg A. W. (1992) Acceleration of Cyclic Steady State Convergence for Pressure Swing Adsorption Models, *Ind. & Eng. Chem. Res.*, **31**, 1569 – 1573
- Snurr R. Q. & Karger J. (1997) Molecular Simulations and NMR Measurements of Binary Diffusion in Zeolites, *J. Phys. Chem. B*, **101**, 6469 – 6473
- Šolcová O. & Schneider P. (1994) Axial Dispersion in Single-Pellet-String Columns Packed with Cylindrical Particles, *Chem. Eng. Sci.*, **49**, 401 – 408
- Šolcová O., Šnajdaufová H. & Schneider P. (2001) Multicomponent Counter-Current Gas Diffusion in Porous Solids: The Graham's-Law Diffusion Cell, *Chem. Eng. Sci.*, **56**, 5231 – 5237
- Song L. & Rees L. V. C. (1996) Frequency Response Diffusion of Propane in Silicalite-1, *Microporous Materials*, **6**, 363 – 374
- Sorial G.A., Granville W. H. & Daly W. O. (1983) Adsorption Equilibria for Oxygen and Nitrogen Gas Mixtures on 5A Molecular Sieves, *Chem. Eng. Sci.*, **38**, 1517 – 1523
- Sotirchos S. V. (1989) Multicomponent Diffusion and Convection in Capillary Structures, *AIChE J.*, **35**, 1953 – 1961
- Sotirchos S. V. (1992) Steady-State versus Transient Measurement of Effective Diffusivities in Porous Media using the Diffusion-Cell Method, *Chem. Eng. Sci.*, **47**, 1187 – 1198
- Sotirchos S. V. & Burganos V. N. (1988) Analysis of Multicomponent Diffusion in Pore Networks, *AIChE J.*, **34**, 1106 – 1118
- Srinivasan R., Auvil S. R. & Schork J. M. (1995) Mass Transfer in Carbon Molecular Sieves - An Interpretation of Langmuir Kinetics, *Chem. Eng. J.*, **57**, 137 – 144
- Stallmach F. & Kärger J. (1999) The Potentials of Pulsed Field Gradient NMR for Investigation of Porous Media, *Adsorption*, **5**, 117 – 133
- Stallmach F., Kärger J. & Pfeifer H. (1993) ¹³C Pulsed-Field-Gradient Diffusion Studies of Guest Molecules in Zeolites, *J. Magnetic Resonance, Series A*, **102**, 270 – 273
- Stejskal E. O. & Tanner J. E. (1965) Use of Spin Echoes in a Pulsed Magnetic-Field Gradient to Study Anisotropic, Restricted Diffusion and Flow, *J. Chem. Phys.*, **43**, 3597 – 3603
- Stiel L. I. & Thodos G. (1961) The Viscosity of Nonpolar Gases at Normal Pressures, *AIChE J.*, **7**, 611 – 615
- Sun L. M. & LeVan M. D. (1995) Numerical Solution of Diffusion Equations by the Finite Difference Method: Efficiency Improvement by Iso-Volumetric Spatial Discretization, *Chem. Eng. Sci.*, **50**, 163 – 166
- Sun L. M., Meunier F., Grenier Ph. & Ruthven D. M. (1994) Frequency Response for Nonisothermal Adsorption in Biporous Pellets, *Chem. Eng. Sci.*, **49**, 373 – 381
- Sundaram N. & Wankat P. C. (1988) Pressure Drop Effects in the Pressurization and Blowdown Steps of Pressure Swing Adsorption, *Chem. Eng. Sci.*, **43**, 123 – 129
- Suzuki M. (1988) State of the Art in Pressure Swing Adsorption in Japan, *AIChE Symp. Series*, No. 264, **84**, 119 – 128

- Suzuki M. (1990) *Adsorption Engineering*, Kodansha Ltd., Japan
- Suzuki M., Suzuki T., Sakoda A. & Izumi J. (1996) Piston-Driven Ultra Rapid Pressure Swing Adsorption, *Adsorption*, **2**, 111 – 119
- Suzuki T., Sakoda A., Suzuki M. & Izumi J. (1997) Recovery of Carbon Dioxide from Stack Gas by Piston-Driven Ultra Rapid PSA, *J. Chem. Eng. Japan*, **30**, 1026 – 1033
- Sward B. K. & LeVan M. D. (1999) Simple Apparatus for Measurement of Adsorption Equilibrium and Dynamics by Frequency Response, *AIChE Annual Meeting*, Dallas, Texas, USA, October 31-November 5
- Szostak R. (1992) *Handbook of Molecular Sieves*, Van Nostrand Reinhold, New York
- Tanner J. E. & Stejskal E. O. (1968) Restricted Self-Diffusion of Protons in Colloidal Systems by the Pulsed-Gradient, Spin-Echo Method, *J. Chem. Phys.*, **49**, 1768 – 1777
- Taylor G. I. (1953) Dispersion of Solute Matter in Solvent Flowing Slowly through a Tube, *Proc. Roy. Soc. (London) Series A*, **219**, 186 – 203
- Taylor G. I. (1954) The Dispersion of Matter in Turbulent Flow through a Pipe, *Proc. Roy. Soc. (London) Series A*, **223**, 446 – 468
- Taylor R. & Krishna R. (1993) *Multicomponent Mass Transfer*, John Wiley and Sons, New York
- Teague K. G. & Edgar T. F. (1999) Predictive Dynamic Model of a Small Pressure Swing Adsorption Air Separation Unit, *Ind. & Eng. Chem. Res.*, **38**, 3761 – 3775
- Teng H. & Zhao T. S. (2000) An Extension of Darcy's Law to Non-Stokes Flow in Porous Media, *Chem. Eng. Sci.*, **55**, 2727 – 2735
- Thomas W. J. & Crittenden B. D. (1998) *Adsorption Technology and Design*, Butterworth-Heinemann, Oxford
- Tien C. (1994) *Adsorption Calculations and Modelling*, Butterworth-Heinemann, Massachusetts
- Tobis J. & Vortmeyer D. (1988). The Near-Wall Channelling Effect on Isothermal Constant-Pattern Adsorption, *Chem. Eng. Sci.*, **43**, 1363 – 1369
- Todd R. S., He J., Webley P. A., Beh C., Wilson S. & Lloyd M. A. (2001) Fast Finite-Volume Method for PSA/VSA Cycle Simulation - Experimental Validation, *Ind. & Eng. Chem. Res.*, **40**, 3217 – 3224
- Todd R. S. & Webley P. A. (2001) Low Purity Oxygen Production by Rapid Pressure Swing Adsorption, *Proc. 6th. World Congress Chemical Engineering*, Melbourne, Victoria, Australia, 23-27 September
- Todd R. S. & Webley P. A. (2002a) Limitations of the LDF/Equimolar Counterdiffusion Assumption for Mass Transport within Porous Adsorbent Pellets, *Chem. Eng. Sci.*, **57**, 4227 – 4242
- Todd R. S. & Webley P.A. (2002b) Limitations of the LDF and Equimolar Counterdiffusion Assumption for an Adsorbent Pellet under Non-Isothermal Conditions, *AIChE Annual Meeting*, Indianapolis, Indiana, USA, 3-8 November

- Todd R. S., Buzzi Ferraris G., Manca D. & Webley P. A. (2003) Improved ODE Integrator and Mass Transfer Approach for Simulating a Cyclic Adsorption Process, *Comput. & Chem. Eng.*, **27**, 883 – 899
- Tomadakis M. M. & Sotirchos S. V. (1993) Ordinary, Transition and Knudsen Regime Diffusion in Random Capillary Structures, *Chem. Eng. Sci.*, **48**, 3323 – 3333
- Tomida T. & McCoy B. J. (1987) Polynomial Profile Approximation for Intraparticle Diffusion, *AIChE J.*, **33**, 1908 – 1911
- Turnock P. H. & Kadlec R. H. (1971) Separation of Nitrogen and Methane via Periodic Adsorption, *AIChE J.*, **17**, 335 – 342
- Valenzuela D. P., Myers A. L., Talu O. & Zwiebel I. (1988) Adsorption of Gas Mixtures: Effect of Energetic Heterogeneity, *AIChE J.*, **34**, 397 – 402
- Valuš J. & Schneider P. (1981) A Novel Cell for Gas-Counterdiffusion Measurements in Porous Pellets, *Applied Catalysis*, **1**, 355 – 366
- Valuš J. & Schneider P. (1985a) Transport Characteristics of Bidisperse Porous α -aluminas, *Applied Catalysis*, **16**, 329 – 341
- Valuš J. & Schneider P. (1985b) Transport Parameters of Porous Catalysts via Chromatography with a Single-Pellet-String Column, *Chem. Eng. Sci.*, **40**, 1457 – 1462
- Valyon J., Onyestyák G. & Rees L. V. C. (2000) The Diffusion and Sorption of *n*- and *i*-Butanes in MFI Zeolites, 482 – 486, *Proc. 2nd. Pacific Basin Conf. Adsorption Sci. and Tech.*, Brisbane, Queensland, Australia, 14-18 May
- Valyon J., Lónyi F., Onyestyák G. & Papp J. (2003) DRIFT and FR spectroscopic Investigation of N_2 and O_2 Adsorption on Zeolites, *Microporous & Mesoporous Materials*, **61**, 147 – 158
- van Noorden T. L., Verduyn Lunel S. M. & Bliet A. (2002) Acceleration of the Determination of Periodic States of Cyclically Operated Reactors and Separators, *Chem. Eng. Sci.*, **57**, 1041 – 1055
- van Noorden T. L., Verduyn Lunel S. M. & Bliet A. (2003) Optimization of Cyclically Operated Reactors and Separators, *Chem. Eng. Sci.*, **58**, 4115 – 4127
- Vaporciyan G. G. & Kadlec R. H. (1987) Equilibrium-Limited Periodic Separating Reactors, *AIChE J.*, **33**, 1334 – 1343
- Vaporciyan G. G. & Kadlec R. H. (1989) Periodic Separating Reactors: Experiments and Theory, *AIChE J.*, **35**, 831 – 844
- Vasenkov S., Böhlmann W., Galvosas P., Geier O., Liu H. & Kärger J. (2001) PFG NMR Study of Diffusion in MFI-Type Zeolites: Evidence of the Existence of Intracrystalline Transport Barriers, *J. Phys. Chem. B*, **105**, 5922 – 5927
- Vermeulen T. (1953) Theory for Irreversible and Constant-Pattern Solid Diffusion, *Ind. Eng. Chem.*, **45**, 1664 – 1670
- Vortmeyer D. & Michael K. (1985) The Effect of Non-Uniform Flow Distribution on Concentration Profiles and Breakthrough Curves of Fixed Bed Adsorbers, *Chem. Eng. Sci.*, **40**, 2135 – 2138

- Wakao N. & Smith J. M. (1962) Diffusion in Catalyst Pellets, *Chem. Eng. Sci.*, **17**, 825 – 834
- Wang C. T. & Smith J. M. (1983) Tortuosity Factors for Diffusion in Catalyst Pellets, *AIChE J.*, **29**, 132 – 136
- Wang K., Qiao S., Hu Y. & Do D. D. (2001) Discrimination of Adsorption Kinetic Models for the Description of Hydrocarbon Adsorption in Activated Carbon, *Adsorption*, **7**, 51 – 63
- Warmuzinski K. (2002) Effect of Pressure Equalization of Power Requirements in PSA Systems, *Chem. Eng. Sci.*, **57**, 1475 – 1478
- Webb P. A. & Orr C. (1997) *Analytical Methods in Fine Particle Technology*, Micromeritics Instrument Corp., Georgia
- Webley P. A., Beh C., He J., Wilson S. & Todd R. S. (2000) Numerical Simulation and Experimental Validation of Multiple-Layer, Non-Isothermal, Bulk Gas Pressure Swing Adsorption, 658 – 662, *Proc. 2nd. Pacific Basin Conf. Adsorption Sci. and Tech.*, Brisbane, Queensland, Australia, 14-18 May
- Webley P. A. & He J. (2000) Fast Solution-Adaptive Finite Volume Method for PSA/VSA Cycle Simulation; 1 Single Step Simulation, *Comput. Chem. Eng.*, **23**, 1701 – 1712
- Webley P.A. & Todd R. S. (2003) Kinetics of Mixed Adsorbent Systems in Gas-Solid Adsorption, *Adsorption Science & Technology*, **21**, 9 – 34
- Weissberg H. L. (1963) Effective Diffusion Coefficient in Porous Media, *J. Appl. Phys.*, **34**, 2636 – 2639
- Weisz P. B. & Schwartz A. B. (1962) Diffusivity of Porous-Oxide-Gel-Derived Catalyst Particles, *J. Catalysis*, **1**, 399 – 406
- Wells A. A. (1991) *Pressure Swing Gas Separation*, US Patent 5 069 688, December 3
- Whitaker S. (1972) Forced Convection Heat Transfer Correlations for Flow in Pipes, Past Flat Plates, Single Cylinders, Single Spheres, and for Flow in Packed Beds and Tube Bundles, *AIChE J.*, **18**, 361 – 371
- Wicke E. & Kallenbach R. (1941) Surface Diffusion of Carbon Dioxide in Activated Charcoals, *Kolloid Zeitschrift*, **97**, 135 – 151
- Wilke C. R. (1950a) Diffusional Properties of Multicomponent Gases, *Chem. Eng. Prog.*, **46**, 95 – 104
- Wilke C. R. (1950b) A Viscosity Equation for Gas Mixtures, *J. Chem. Phys.*, **18**, 517 – 519
- Wilson S. J. (2001) *Thermal Profiles in Oxygen VSA - Modelling, Observations and Optimisation*, Ph.D. Dissertation, Monash University, Australia
- Wilson S. J., Beh C. C. K., Webley P. A. & Todd R. S. (2001) The Effects of a Readily Adsorbed Trace Component (Water) in a Bulk Separation PSA Process: The Case of Oxygen VSA, *Ind. & Eng. Chem. Res.*, **40**, 2702 – 2713
- Wilson S. J. & Webley P. A. (2002) Perturbation Techniques for Accelerated Convergence of Cyclic Steady State (CSS) in Oxygen VSA Simulations, *Chem. Eng. Sci.*, **57**, 4145 – 4159

- Wloch J. (2003) Effect of Surface Etching of ZSM-5 Zeolite Crystals on the Rate of *n*-hexane Sorption, *Microporous & Mesoporous Materials*, **62**, 81 – 86
- Yang J., Han S., Cho C., Lee C.-H. & Lee H. (1995) Bulk Separation of Hydrogen Mixtures by a One-column PSA Process, *Sepns. Tech.*, **5**, 239 – 249
- Yang J., Lee C.-H. & Chang J.-W. (1997) Separation of Hydrogen Mixtures by a Two-Bed Pressure Swing Adsorption Process using Zeolite 5A, *Ind. & Eng. Chem. Res.*, **36**, 2789 – 2798
- Yang J., Park M.-W., Chang J.-W., Ko S.-M. & Lee C.-H. (1998) Effects of Pressure Drop in a PSA Process, *Korean J. Chem. Eng.*, **15**, 211 – 216
- Yang R. T. (1997) *Gas Separation by Adsorption Processes (Reprint)*, Imperial College Press, London
- Yang R. T. & Doong S.-J. (1985) Gas Separation by Pressure Swing Adsorption: A Pore-Diffusion Model for Bulk Separation, *AIChE J.*, **31**, 1829 – 1842
- Yasuda Y. (1982) Determination of Vapour Diffusion Coefficients in Zeolite by the Frequency Response Method, *J. Phys. Chem.*, **95**, 2486 – 2492
- Yasuda Y., Suzuki Y. & Fukada H. (1991) Kinetic Details of a Gas/Porous Adsorbent System by the Frequency Response Method, *J. Phys. Chem.*, **95**, 2486 – 2492
- Zhang H. & Cheng D. (2000) Mathematical Model for a Fixed Bed Adsorptive Reactor, *Carbon*, **38**, 877 – 880
- Zhang Z., Guan J. & Ye Z. (1998) R & D Note: Separation of a Nitrogen-Carbon Dioxide Mixture by Rapid Pressure Swing Adsorption, *Adsorption*, **4**, 173 – 177
- Zhadanov V. P. (1988) Diffusion of Coadsorbed Particles, *Surface Science*, **194**, 1 – 12
- Zhong G. M., Meunier F., Huberson S. & Chalfen J. B. (1992) Pressurization of a Single-Component Gas in an Adsorption Column, *Chem. Eng. Sci.*, **47**, 543 – 550
- Zhu L.-Q., Baron G. V. & Verelst H. (1996) RPSA Air Separation: Influence of Selectivities and Transport Properties of the Adsorbents on the Performance, 1067 – 1074, *Fundamentals of Adsorption*, Kluwer Academic Publishers, Massachusetts
- Zhu W., Kapteijn F. & Moulijn J. A. (2001) Diffusion of Linear and Branched C₆ Alkanes in Silicalite-1 Studied by the Tapered Element Oscillating Microbalance, *Microporous & Mesoporous Materials*, **47**, 157 – 171